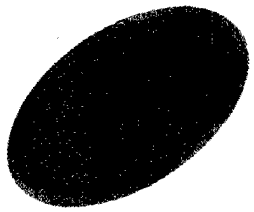
IEEE

MHS'99

Proceedings of the 1999 International Symposium on Micromechatronics and Human Science

Nagoya Congress Center &
Nagoya Municipal Industrial Research Institute
November 23-26,1999

- Towards the New Century -



IEEE Catalog Number:99TH8478
ISBN: 0-7803-5790-6
Library of Congress Number:99-65524

Cosponsored by
IEEE Industrial Electronics Society
IEEE Robotics and Automation Society
Nagoya University

19991207 045

REPORT DOCUMENTATION PAGE

Form Approved

OMB No. 0704-0188

The public reporting burden for this collection of information is estimated to average 1 hour per response, including the time for reviewing instructions, searching existing data sources, gathering and maintaining the data needed, and completing and reviewing the collection of information. Send comments regarding this burden estimate or any other aspect of this collection of information, including suggestions for reducing the burden, to Department of Defense, Washington Headquarters Services, Directorate for Information Operations and Reports (0704-0188), 1215 Jefferson Davis Highway, Suite 1204, Arlington, VA 22202-4302. Respondents should be aware that notwithstanding any other provision of law, no person shall be subject to any penalty for failing to comply with a collection of information if it does not display a currently valid OMB control number.

PLEASE DO NOT RETURN YOUR FORM TO THE ABOVE ADDRESS.

1. REPORT DATE *(DD-MM-YYYY)*	2. REPORT TYPE	3. DATES COVERED *(From - To)*
29-11-1999	Conference Proceedings	

4. TITLE AND SUBTITLE

1999 International Symposium on Micromechatronics and Human Science

5a. CONTRACT NUMBER

F6256299M9216

5b. GRANT NUMBER

5c. PROGRAM ELEMENT NUMBER

6. AUTHOR(S)

Conference Committee

5d. PROJECT NUMBER

5e. TASK NUMBER

5f. WORK UNIT NUMBER

7. PERFORMING ORGANIZATION NAME(S) AND ADDRESS(ES)

Dept. of Micro System Engineering, Nagoya University
1, Furo-cho, Chikusa-ku
Nagoya 464-8603
Japan

8. PERFORMING ORGANIZATION REPORT NUMBER

N/A

9. SPONSORING/MONITORING AGENCY NAME(S) AND ADDRESS(ES)

AOARD
UNIT 45002
APO AP 96337-5002

10. SPONSOR/MONITOR'S ACRONYM(S)

AOARD

11. SPONSOR/MONITOR'S REPORT NUMBER(S)

CSP-991009

12. DISTRIBUTUION/AVAILABILITY STATEMENT

Approved for public release; distribution is unlimited.

13 SUPPLEMENTARY NOTES

14. ABSTRACT

The conference proceeding includes topics in the following areas:
"Micro/namo-manipulation and Control"
"Microfabrication, Material, and Property I"
"Microrobot"
"Microfabrication, Material, and Property II"
"Microcomponents and Microdevices I"
"Microcomponents and Microdevices II"
"Measurement and System"

15. SUBJECT TERMS

MEMs, Microelectronics, Micromechatronics

16. SECURITY CLASSIFICATION OF:			17. LIMITATION OF ABSTRACT	18. NUMBE OF PAGES	19a. NAME OF RESPONSIBLE PERSON
a. REPORT	b. ABSTRACT	c. THIS PAGE			Michele Gaudreault, Maj., USAF
U	U	U	UU	287	19b. TELEPHONE NUMBER *(Include area code)* +81-3-5410-4409

MHS'99

PROCEEDINGS OF 1999 INTERNATIONAL SYMPOSIUM ON MICROMECHATRONICS AND HUMAN SCIENCE

Nagoya Congress Center
&
Nagoya Municipal Industrial Research Institute
November 23-26, 1999

IEEE Catalog Number: 99TH8478
ISBN: 0-7803-5790-6
Library of Congress Number: 99-65524

Cosponsored by
IEEE Industrial Electronics Society
IEEE Robotics and Automation Society
Nagoya University

Technically Sponsored by
Japan Society of Mechanical Engineers
Robotics Society of Japan
Society of Instrument and Control Engineers
Research Committee on Micromechatronics
Technical Committee on Micro-mechanisms of
Japan Society of Precision Engineering

Copyright © 1999 by the Institute of Electrical and Electronics Engineers, Inc.
All rights reserved.

Copyright and Reprint Permission: Abstracting is permitted with credit to the source. Libraries are permitted to photocopy beyond the limit of U.S. copyright law for private use of patrons those articles in this volume that carry a code at the bottom of the first page, provided the per-copy fee indicated in the code is paid through Copyright Clearance Center, 222 Rosewood Drive, Danvers, MA 01923.

For other copying, reprint, or republication permission, write to IEEE Copyrights Manager, IEEE Operations Center, 445 Hoes Lane, P. O. Box 1331, Piscataway, NJ 08855-1331.

IEEE Catalog Number: 99TH8478
ISBN:0-7803-5790-6
Library of Congress Number: 99-65524

Additional Copies may be obtained from:

IEEE Operations Center
445 Hoes Lane, P.O. Box 1331
Piscataway
NJ 08855-1331, USA

The papers in this book comprise the proceedings of the meeting mentioned on the cover and title page. They reflect the authors' opinions and, in the interests of timely dissemination, are published as presented and without change. Their inclusion in this publication does not necessarily constitute endorsement by the editors, The IEEE Industrial Electronics Society, The IEEE Robotics and Automation Society and Nagoya University.

Welcome Remarks

Issues affecting the global environment are our current focus of attention. Considered to be effective in the conservation of resources and energy, micromachine technology is increasing in importance as the need to achieve harmonious coexistence between man and nature becomes a priority.

The applied research of micromechatronics technology, a seminal technology for the 21st century, extends from basic areas such as semiconductors, sensors, and machine tools to much wider technological areas such as medical equipment, construction machinery, and space aeronautics. More recent developments have delved into new areas such as welfare engineering, where R & D is now underway.

The Chubu region, which is a hub of mechatronics technology, has been hosting this symposium on micromechatronics and human science, organized with the full support of industry, public bodies, and academic institutions. The Symposium this year is the 10th in the series. In 1997, its name was changed from "Micromachine" to "Micromechatronics," expanding the scope of discussion into wider research areas, which in turn is aimed at encouraging active exchange of opinions and information that will be useful for future R & D. I am pleased to report that the Department of Microsystem Engineering of Nagoya University's Graduate School of Engineering is now in its sixth year since its establishment. Research into micromachines and micromechatronics is rapidly progressing.

"Towards the New Century" is the theme of this year's symposium. I hope that we will be able to provide new technology to the industrial sector, which remains the mainstay of the Japanese economy, and to explore the possibilities of creating exciting new industries for the new century. I await lively discussions from our participants so that we may learn of the work to be undertaken and to explore the vision of the future through micromechatronics technology.

On behalf of the sponsors and on behalf of the Nagoya University's Graduate School of Engineering, I would like to express my heartfelt gratitude to all those who have spared no effort in planning and organizing this Symposium. Finally, I wish to sincerely thank all the participants for your interest and dedication.



Y Inagaki

Yasuyoshi Inagaki
Dean of the Graduate School of Engineering
Nagoya University

Symposium Organization

General Chair:	Toshio Fukuda	(Nagoya University)
Program Chair:	Fumihito Arai	(Nagoya University)
Advisory Committee:	Fernando Aldana	(University of Politec. de Madrid, Spain)
	Iwao Fujimasa	(National Graduate Institute for Policy Studies)
	Fumio Harashima	(The Tokyo Metropolitan Institute of Technology)
	Teruo Kurokouchi	(The Chubu Industrial Advancement Center)
	Hirofumi Miura	(Kagawa University)
	Naomasa Nakajima	(The University of Tokyo)
	Hiroyuki Okabe	(Chubu Science & Technology Center)
	Yukio Terakura	(City of Nagoya)
	Yoshio Tsukio	(The University of Tokyo)
	Akihiko Uchiyama	(Waseda University)
Steering Committee:	Mark G. Allen	(Georgia Institute of Technology)
	Wolfgang Benecke	(University of Bremen)
	Edwards Colgate	(North Western University)
	Paolo Dario	(Scuola Superiore, Pisa)
	Takeyoshi Dohi	(The University of Tokyo)
	Masayoshi Esashi	(Tohoku University)
	Ronald S. Fearing	(University of California, Berkeley)
	A. Bruno Frazier	(Georgia Institute of Technology)
	Hiroyuki Fujita	(The University of Tokyo)
	Mizuho Fukushima	(Nagoya Urban Industries Promotion Corporation)
	Henry Guckel	(University of Wisconsin-Madison)
	Hideki Hashimoto	(The University of Tokyo)
	Tadashi Hattori	(DENSO Co., Ltd.)
	Iwao Hayashi	(Tokyo Institute of Technology)
	Toshiro Higuchi	(The University of Tokyo)
	Takanobu Hori	(AISIN COSMOS R&D CO., Ltd.)
	Roger T. Howe	(University of California, Berkeley)
	Koji Ikuta	(Nagoya University)
	J. D. Irwin	(Auburn University)
	Hidenori Ishihara	(Kagawa University)
	Hideaki Ota	(Chubu Science & Technology Center)
	Shogo Kito	(The Chubu Industrial Advanced Center)
	Satoshi Konishi	(Ritsumeikan University)
	Kazuhiro Kosuge	(Tohoku University)
	Katsutoshi Kuribayashi	(Yamaguchi University)
	Yoshitaka Kuwahara	(National Industrial Research Institute of Nagoya)
	Ren C. Luo	(National Chung Cheng University)
	Noel C. MacDonald	(Cornell University)
	Takahisa Masuzawa	(The University of Tokyo)
	Mehran Mehregany	(Case Western Reserve University)
	Wolfgang Menz	(Universität Feiburg)
	Yasunaga Mitsuya	(Nagoya University)
	Khalil Najafi	(University of Michigan)
	Jean-Daniel Nicoud	(Swiss Federal Institute of Technology)
	Kouhei Ohnishi	(Keio University)
	Nobutada Ohno	(Nagoya University)
	Shigeru Okuma	(Nagoya University)
	Albert P. Pisano	(University of California, Berkeley)
	Micheal L. Reed	(Carnegie Mellon University)
	Nico F. de Rooij	(University of Neuchatel)
	Katsumi Sakaguchi	(Nagoya Urban Industries Promotion Corporation)
	Kazuo Sato	(Nagoya University)
	Isao Shimoyama	(The University of Tokyo)
	Goran Stemme	(Royal Institute of Technology)
	Susumu Sugiyama	(Ritsumeikan University)
	Osamu Tabata	(Ritsumeikan University)
	William Trimmer	(Bell Mead Research Center)
	H. S. Tzou	(University of Kentucky)
	Bernd Wagner	(Fraunhofer Institute for Silicon Technology)
Education & Standard Committee Chair:	Yasushi Yamashita	(Takayama Technical High School)
Education & Standard Committee:	Tomohiro Kakumu	(Takayama Techinical High School)
	Kazuhiro Takeuchi	(Gifu Technical High School)
	Yasuhisa Hasegawa	(Nagoya University)
	Futoshi Kobayashi	(Nagoya University)

Program at a Glance

November 23 (Tue.) International Micro Robot Maze Contest

13:00 - 15:00	Preliminaries Category 0: Teleoperated Micro Racer Category 1: Teleoperated Mountain Climbing Micro Robots
15:00 - 15:30	Break
15:30 - 16:30	Finals Category 0: Teleoperated Micro Racer Category 1: Teleoperated Mountain Climbing Micro Robots Category 2: Wireless Autonomous Mobile Robots
16:30 - 16:50	Break
16:50 - 17:20	Closing

November 24 (Wed.) Opening Ceremony, Keynote and Plenary Lectures

10:00-10:30	**Opening Ceremony**
10:30-11:30	**Keynote Lecture** Collaboration between Industry and University for the Creation of New Buisinesses *Dr. Toshiaki Ikoma, Texas Instruments Japan Ltd., Japan*
11:30-12:30	**Plenary Lectures** Recent Trend of Piezoelectric Actuator Developments *Prof. Kenji Uchino, The Pennsylvania State University, USA*
12:30-14:00	Lunch
14:00-15:00	Chemical Processing and Properties of Functional Ceramics *Prof. Shin-ichi Hirano, Nagoya University, Japan*
15:00-16:00	Integrated Sample Preparation Systems for Miniaturized Biochemical Analysis *Prof. A. Bruno Frazier, Georgia Institute of Technology, USA*
16:00-16:30	Coffee Break
16:30-17:30	Mechatronic Micro Devices Dr. Frank Michel, Institute of Microtechnology Mainz GmbH (IMM), Germany
17:40-19:00	Beer Party

November 25 (Thu.) Invited Lectures and Technical Sessions

9:10 - 10:00	**Invited Lecture** Challenge to Micro/Nanomanipulation Using Atomic Force Microscope *Prof. Hideki Hashimoto, University of Tokyo, Japan*	
10:00 - 10:20	Coffee Break	
10:20 - 12:00	Conference Room 1	Conference Room 2
	Session A-1: Micro/nano-manipulation and Control	Session A-2: Microfabrication, Material, and Property I
12:00-13:10	Lunch	
13:10-15:10	Conference Room 1	Conference Room 2
	Session B-1: Microrobot	Session B-2: Microfabrication, Material, and Property II
15:10-15:30	Coffee Break	
15:30-16:50	Conference Room 1	Conference Room 2
	Session C-1: Round Table Discussion on Micro Robot Maze Contest	SessionC-2: Microcomponents and Microdevices I
17:00-17:30	Explanation of Exhibit	
17:40-19:00	Reception Party	

November 26 (Fri.) Technical Sessions and Laboratory Tour

9:10-10:00	**Invited Lecture** Preparation and Properties of Carbon Nanotubes *Prof. Yahachi Saito, Mie University, Japan*	
10:00-10:20	Coffee Break	
10:20-12:00	Conference Room 1	Conference Room 2
	Session D-1: Microcomponents and Microdevices II	Session D-2: Measurement and System Control
12:00 - 14:00	Lunch	
14:00 -	Laboratory Tour Nagoya University	

Table of Contents

Welcome Remark i
Symposium Organization ii
Program at a Glance iii
Keynote and Plenary Lectures
Collaboration between Industry and University for the Creation of New Buisinesses 1
Dr. Toshiaki Ikoma, Texas Instruments Japan Ltd., Japan
Recent Trend of Piezoelectric Actuator Developments 3
Prof. Kenji Uchino, The Pennsylvania State University, USA
Chemical Processing and Properties of Functional Ceramics 11
Prof. Shin-ichi Hirano, Nagoya University, Japan
Integrated Sample Preparation Systems for Miniaturized Biochemical Analysis 19
Prof. A. Bruno Frazier, Georgia Institute of Technology, USA
Mechatronic Micro Devices 27
Dr. Frank Michel, Institute of Microtechnology Mainz GmbH (IMM), Germany

Invited Lectures
Challenge to Micro/Nanomanipulation Using Atomic Force Microscope 35
Prof. Hideki Hashimoto, University of Tokyo, Japan
Preparation and Properties of Carbon Nanotubes 43
Prof. Yahachi Saito, Mie University, Japan

Session A-1: Micro/nano-manipulation and Control
Stochastic Dynamics of Molecular Machine; It's Nanomachine Which is Based on Nyquist Theory 51
H. Matsuura, National Graduate Institute for Policy Studies, Japan, M. Nakano
Application of Atomic Force Microscopy to an Encoder 59
M. Shimodaira, A. Torii and A. Ueda, Aichi Institute of Technology, Japan
Contact Motion Control of a Micro Operation Hand 65
T. Nakamura, Y. Kogure and K. Shimamura, Tokyo Metropolitan University, Japan
3D Bio-Micromanipulation (Bilateral Control System Using Micro Tri-axial Force Sensor) 71
F. Arai, Nagoya University, Japan, T. Sugiyama, Poom L., A. Kawaji, T. Fukuda, K. Itoigawa and A. Maeda
A Model for Operating Spherical Micro Objects 79
Q. Zhou, Tampere University of Technology, Finland, P. Kallio, F. Arai, T. Fukuda and H. N. Koivo

Session A-2: Microfabrication, Material, and Property I
Study on Fabrication of Sub-micron Structures for MEMS Using Deep X-ray Lithography 87
H. Ueno, N. Nishi and S. Sugiyama, Ritsumeikan University, Japan
3-dimensional Micromachining of PTFE Using Synchrotron Radiation Direct Photo-etching 93
N. Nishi, Ritsumeikan University, Japan, T. Katoh, H. Ueno, S. Konishi and S. Sugiyama

Mechanical and Electrical Characteristics of Poly-silicon Film Deposited by a New LPCVD Using Lamp Heating 99
T. Ueda, Central Engineering Co., Ltd., Japan, K. Kuribayashi and S. Hasegawa
Evaluation of Strength Property of HAp - Tyranno Fiber Composite by Flexural Test and Process of Sintering Condition 107
K. Yagi, Tokyo Metropolitan University of Health Sciences, Japan, M. Tokuda, K. Suzuki and H. Yoshidome
Design of Functional Hydrogel and Evaluation of its Material Properties 113
K. Yagi, Tokyo Metropolitan University of Health Sciences, Japan, M. Tokuda, T. Yoshikawa and Y. Ichiminami

Session B-1: Microrobot

Frequency Modulation Velocity Control of Multiple Cybernetic Actuators for Two-lead-wire Drive 123
M. Nokata and K. Ikuta, Nagoya University, Japan
LAMAlice : A Nanorover for Planetary Exploration 129
M. Freese, M. Kaelin, J-M. Lehky, G. Caprari, T. Estier and R. Siegwart, Swiss Federal Institute of Technology Lausanne (EPFL), Switzerland
Development of an Artificial Fish Microrobot 135
S. Guo, Kagawa University, Japan, T. Fukuda and K. Oguro
In-Pipe Wireless Micro Locomotive System 141
H. Nishikawa, T. Sasaya, T. Shibata, T. Kaneko, N. Mitumoto, S. Kawakita and N. Kawahara, Denso Corporation, Japan
Screw Principle Microrobot Passing Steps in a Small Pipe 149
T. Yamaguchi, NEC Corporation, Japan, Y. Kagawa, I. Hayashi, N. Iwatsuki, K. Morikawa and K. Nakamura
Improvement of Characteristics of In-Pipe Micro Robot 153
L. Sun, P. Sun, L. Lian, X. Qin and Z. Gong, Shanghai University, P.R.China

Session B-2: Microfabrication, Material, and Property II

The Design and Synthesis of Magnetic Ultra-fine Poly-Saccharide Particles 157
K. Yagi, Tokyo Metropolitan University of Health Sciences, Japan, M. Tokuda, T. Kobayashi and T. Kishita
Study of XeF_2 Pulse Etching Using Wagon Wheel Pattern 163
K. Sugano and O. Tabata, Ritsumeikan University, Japan
Excimer Laser Processing in Nano-Technology 169
Y P Kathuria, Laser X Co. Ltd., Japan
Movable Microstructures Made by Two-photon Three-dimensional Microfabrication 173
S. Maruo and K. Ikuta, Nagoya University, Japan
3D Microstructuring of Glass Using Electrochemical Discharge Machining (ECDM) 179
V. Fascio, R. Wüethrich, D. Viquerat and H. Langen Swiss Federal Institute of Technology Lausanne (EPFL), Switzerland
In Situ Measurement and Micromachining of Glass 185
R. Wüethrich, V. Fascio, D. Viquerat and H. Langen Swiss Federal Institute of Technology Lausanne (EPFL), Switzerland

Session C-2: Microcomponents and Microdevices I

A Design and Production Framework for Modular Microsystems 193
V. Grosser, Fraunhofer Institute for Reliability and Microintegration (IZM), Germany, M. Schuenemann, B. Michel and H. Reichl

Thermal Analysis of Fingerprint Sensor Having a Microheater Array 199
J. Han, T. Kadowaki, K. Sato and M. Shikida, Nagoya University, Japan

A New ID Acquiring Method for Personal Identification System with Fingerprint 207
T. Fukuda, Nagoya University, Japan, F. Arai, J. Tsuruno and K. Itoigawa

A New Piezoresistive High Pressure Sensor Utilizing Combination of Three-axis Normal Stress Components 215
T. Toriyama, K. Sawa, Y. Tanimoto and S. Sugiyama, Ritsumeikan University, Japan

Session D-1: Microcomponents and Microdevices II

Fabrication of Micromotors Using LIGA Process 221
S. Takimoto, Ritsumeikan University, Japan, R. Kondo, K. Suzuki and S. Sugiyama

Development of a Planar Type Micro Electro Magnetic Distance Sensor Using High Aspect Ratio Photoresist and Its Application 227
X. Ding, K. Kuribayashi and T. Hashida, Yamaguchi University, Japan

Structure of Microrobots Using Electromagnetic Actuators 235
A. Torii, T. Koyanagi and A. Ueda, Aichi Institute of Technology, Japan

Optical Micro Energy and Information Transmission System 243
H. Ishihara, Kagawa University, Japan, and T. Fukuda

Improvement of Sensing and Actuating Property of Parallel Beam Gyroscope 249
H. Sato, Nagoya University, Japan, T. Fukuda, F. Arai, K. Itoigawa and Y. Tsukahara

Session D-2: Measurement and System

Fire Flame Detection Algorithm Using a Color Camera 255
H. Yamagishi and J. Yamaguchi, Sogo Keibi Hosho Co., Ltd., Japan

Analysis of Left Ventricular Wall Locus Tracing and Motion by Optical-Flow Using MRI ... 261
K. Yagi, Tokyo Metropolitan University of Health Sciences, Japan, M. Tokuda, Y. Sawaki, T. Inaba, A. Yamamoto and K. Sekioka

Distributed Behavior Arbitration Network: An Autonomous Control Architecture for Humanoid Robots 267
M. Shimizu, T. Furuta and K. Tomiyama, Aoyama Gakuin University, Japan

Fuzzy-Neural Based Multi-Agent Strategy for Biped Motion Control 275
A. Khoukhi and L. Khoukhi, Institut d'Informatique USTHB, Algeria

International Micro Robot Maze Contest

Authors Index

Keynote & Plenary Lectures

Collaboration between Industry and University for the Creation of New Businesses

Toshiaki Ikoma

Texas Instruments Japan Ltd., Japan

Nishi-Shinjuku Mitsui Bldg.

6-24-1 Nishi-Shinjuku, Shinjuku-ku, Tokyo 160-8366

Japan

In recent years, Japan has been struggling under economic slowdown, while the U.S. and European economies have been enjoying prosperity. Asia appears to have found its way out of the currency crisis to get on the recovery track. A substantial portion of U.S. industry, the locomotive of the world economy, is made up of new telecommunications businesses using new technologies, including the Internet. In creating such new businesses, universities have played a pivotal role and still do today, through collaboration with industry. In Europe, Britain led the other countries in introducing the American-type economic mechanism, and succeeded in rebuilding its economy. And with creation of the European Union as momentum, even France, which is under the tightest state control in Europe, as well as Germany, a country with a conservative economic mechanism, started working to build American-type economies and industrial structures. France, in particular, leads the world in telecommunications technology, and is enthusiastic about making investments in this field. Japan, in comparison, has seen much less progress in deregulation in the telecommunications industry and, even though Internet and cell phones users have been increasing rapidly, growth in this new sector has not been substantial enough to lead the entire Japanese economy. And this is not all the bad news about Japan. In the semiconductor industry, of which Japan was believed to be the world leader, the U.S., Europe, South Korea and Taiwan are gaining the upper hand over our country. Under these circumstances, there is increasing expectation that universities are the key to Japan's breaking through the current difficulties and making a comeback as the No. 1 country in both technology and industry.

Meanwhile, the environment surrounding the universities is rapidly changing. One of the changes comprises the fact that, with the enactment of the Fundamental Law on Science and Technology, a much greater amount of money than before is being spent on research and study, ¥17 trillion will be spent over the 5-year period of the basic plan. In the past, it was only the Ministry of Education, Science and Culture that funded university research activities. But today, grants are available from the Ministry of International Trade and Industry, the Ministry of Posts and Telecommunications, and the Science and Technology Agency as well, so the universities can tackle a wider spectrum of themes instead of conventional basic studies. Another change is that, with the lifting of the rule banning civil servants from part-time side work, university professors are now able to do research work at companies. In addition, the Law on Technology Transfer Involving Universities and Colleges came into effect, making it easier for universities to acquire patents and start their businesses using TLO. The law also allows professors to earn patent royalties. Until the enactment of this law, it was

1999 INTERNATIONAL SYMPOSIUM ON
MICROMECHATRONICS AND HUMAN SCIENCE
0-7803-5790-6/99/ $10.00 ©1999 IEEE.

considered undesirable, both legally and morally, for someone to earn profit from technological transfer carried out by universities, but this reluctance is expected to ease, to a certain extent. The third change is that, with national universities made independent administrative juridical bodies, it has become legally mandatory to evaluate each university, which naturally leads to more active and frequent evaluation of the performance of individual professors. If the criteria for performance evaluation include not only the number of papers written, but also the impact of an individual's performance on technology transfer and on the industrial community, this will make a lot of difference in the way universities work and interact with society. All these changes indicate the ongoing transformation of the foundation on which industry and university collaborate.

Although the environment is changing, it must be noted that there are some sectors wherein technology transfer from university will easily result in the emergence of new businesses, while other sectors remain relatively unaffected. In the mature industries, on one hand, technology is extremely advanced, so it is hard to put into practical application in original form the kind of technologies resulting from scientific researches. In the materials and pharmaceuticals industries, on the other hand, it is highly possible that new and useful materials are created as a result of basic scientific research. In micromechatronics, research activities are conducted not so much for the sake of basic scientific study as for the sake of application and practical use. So if the universities work in the right direction, this field can demonstrate model collaboration between industry and university. In my presentation, I would like to share my views on how collaboration between industry and university should be carried out, the more effectively to cope with the changing industrial and university environment.

Recent Trend of Piezoelectric Actuator Developments

Kenji Uchino
International Center for Actuators and Transducers
Materials Research Laboratory, The Pennsylvania State University
University Park, PA 16802, USA

Abstract:

In these several years, piezoelectric materials have bocome key components in smart actuator/sensor systems such as precision positioners, miniature ultrasonic motors and adaptive mechanical dampers. This paper reviews recent developments of piezoelectric and related ceramic actuators with particular focus on the improvement of actuator materials, device designs and applications.

1. INTRODUCTION

Piezoelectric actuators are forming a new field between electronic and structural ceramics [1-4]. Application fields are classified into three categories: positioners, motors and vibration suppressors. The manufacturing precision of optical instruments such as lasers and cameras, and the positioning accuracy for fabricating semiconductor chips, which must be adjusted using solid-state actuators, is of the order of 0.1 μm. Regarding conventional electromagnetic motors, tiny motors smaller than 1 cm are often required in office or factory automation equipment and are rather difficult to produce with sufficient energy efficiency. Ultrasonic motors whose efficiency is insensitive to size are superior in the mini-motor area. Vibration suppression in space structures and military vehicles using piezoelectric actuators is also a promising technology.

This article reviews recent developments of piezoelectric and related ceramics to smart actuator/sensor systems, including the improvement of actuator materials, design of the devices, and applications.

2 CERAMIC ACTUATOR MATERIALS

Recent four topics are reviewed here.

2.1 Relaxor Single Crystal Transducers

In 1981, we firstly reported an enormously large electromechanical coupling factor k_{33} = 92 - 95% and piezoelectric constant d_{33} = 1500 pC/N in solid solution single crystals between relaxor and normal ferroelectrics, $Pb(Zn_{1/3}Nb_{2/3})O_3$-$PbTiO_3$ [5,6]. This discovery has not been marked for more than 10 years until high k materials have been paid attention in medical acoustics recently. These date have been reconfirmed, and much more improved data were obtained recently, aiming at medical acoustic applications [7,8]. The strains as large as 1.7% can be induced practically for a morphotropic phase boundary composition of the PZN-PT solid solution single crystals. It is notable that the highest values are observed for a rhombohedral composition only when the single crystal is poled along the perovskite [001] axis, not along the [111] spontaneous polarization axis.

2.2 Epitaxial PZT Films

A series of theoretical calculations made on perovskite type ferroelectric crystals suggests that large d and k values in similar magnitudes to PZN-PT can also be expected in PZT. Crystal orientation dependence of piezoelectric properties was phenomenologically calculated for compositions around the morphotropic phase boundary of PZT [9]. The maximum longitudinal piezoelectric constant d_{33} (4 - 5 times enhancement) and electromechanical coupling factor k_{33} (more than 90 %) in the rhombohedral composition were found to be at 57° and 51° angles, respectively, canted from the spontaneous polarization direction [111], which correspond roughly to the perovskite [100] axis.

Figure 1 shows the principle of the enhancement in electromechanical couplings. Because the shear coupling d_{15} is the highest in perovskite piezoelectric crystals, the applied filed should be canted from the spontaneous polarization direction to obtain the maximum strain.

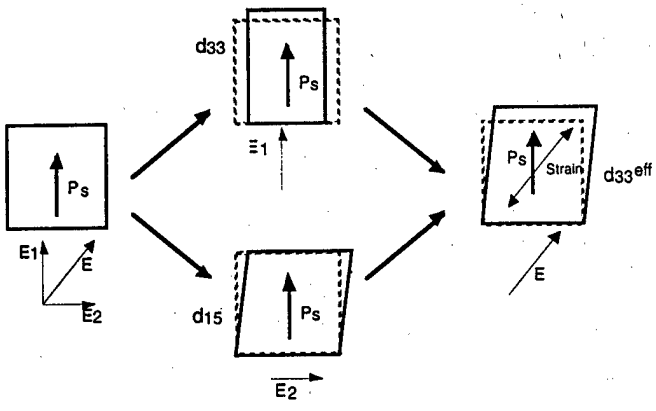


Fig.1 Principle of the enhancement in electromechanical couplings.

1999 INTERNATIONAL SYMPOSIUM ON
MICROMECHATRONICS AND HUMAN SCIENCE
0-7803-5790-6/99/ $10.00 ©1999 IEEE.

We are demonstrating [001] oriented epitaxially grown thin/thick films using a rhomboherial PZT compostion, which are expected to enhance the effective piezoelectric constant by 4-5 times.

2.3 Phase-Change Materials

Concerning the phase-change-related strains, polarization induction by switching from an antiferroelectric to a ferroelectric state, has been proposed [10]. Figure 2 shows the field-induced strain curves taken for the lead zirconate stannate based $Pb_{0.99}Nb_{0.02}((Zr_xSn_{1-x})_{1-y}Ti_y)_{0.98}O_3$ system. The longitudinally induced strain reaches up to 0.4%, which is larger than that expected in normal piezostrictors or electrostrictors. A rectangular-shape hysteresis in Fig.2 top, referred to as a "digital displacement transducer" because of the two on/off strain states, is interesting. Moreover, this field-induced transition exhibits a shape memory effect in appropriate compositions (Fig.2 bottom). Once the ferroelectric phase has been induced, the material will "memorize" its ferroelectric state even under zero-field conditions, although it can be erased with the application of a small reverse bias field [11]. This shape memory ceramic is used in energy saving actuators. A latching relay is composed of a shape memory ceramic unimorph and a mechanical snap action switch, which is driven by a pulse voltage of 4ms. Compared with the conventional electromagnetic relays, the new relay is much simple and compact in structure with almost the same response time.

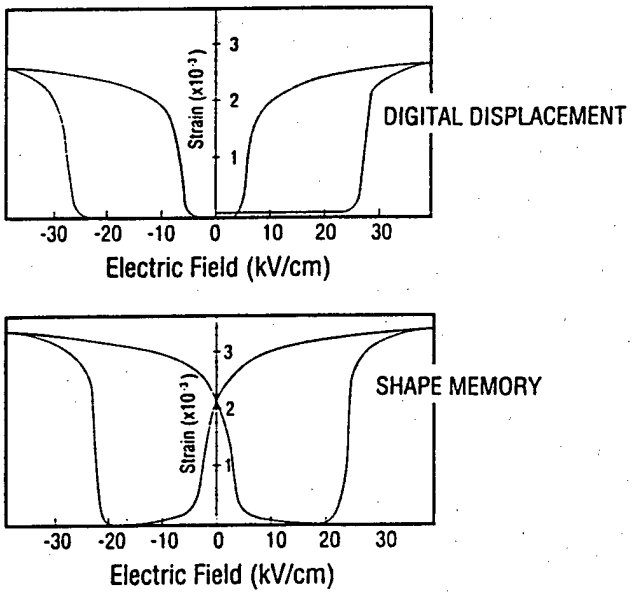


Fig.2 Field-induced strain curves for the lead zirconate stannate system $Pb_{0.99}Nb_{0.02}((Zr_xSn_{1-x})_{1-y}Ti_y)_{0.98}O_3$. Top: x = 0.060, and bottom: x = 0.065.

2.4 Photostrictive Actuators

A photostrictive actuator is a fine example of an intelligent material, incorporating "illumination sensing" and self production of "drive/control voltage" together with final "actuation." In certain ferroelectrics, a constant electromotive force is generated with exposure of light, and a photostrictive strain results from the coupling of this bulk photovoltaic effect to inverse piezoelectricity. A bimorph unit has been made from PLZT 3/52/48 ceramic doped with slight addition of tungsten [12]. The remnant polarization of one PLZT layer is parallel to the plate and in the direction opposite to that of the other plate. When a violet light is irradiated to one side of the PLZT bimorph, a photovoltage of 1 kV/mm is generated, causing a bending motion. The tip displacement of a 20mm bimorph 0.4mm in thickness was 150μm, with a response time of 1 sec.

A photo-driven micro walking device, designed to begin moving by light illumination, has been developed [13]. It is simple in structure, having neither lead wires nor electric circuitry, with two bimorph legs fixed to a plastic board. When the legs are irradiated alternately with light, the device moves like an inchworm with a speed of 100μm/min.

In pursuit of thick film type photostrictive actuators for space structure applications, in collaboration with researchers at Jet Propulsion Laboratory we investigated the optimal range of sample thickness and surface roughness dependence of photostriction. We have found that 30 μm thick PLZT films exhibit the maximum photovoltaic phenomenon [14].

3 ACTUATOR DESIGNS

Two of the most popular actuator designs are multilayers and bimorphs. The multilayer, in which roughly 100 thin piezoelectric/electrostrictive ceramic sheets are stacked together, has advantages in low driving voltage (100V), quick response (10μsec), high generative force (100kgf) and high electromechanical coupling. But the displacement in the range of 10μm is not sufficient for some applications. This contrasts with the bimorph, consisting of multiple piezoelectric and elastic plates bonded together to generate a large bending displacement of several hundred μm, but the response (1msec) and the generative force (100gf) are low.

A multilayer actuator with interdigital internal electrodes has been developed by Tokin [15]. In contrast to the conventional electrode configuration, line electrodes are printed on piezoelectric green sheets, and are stacked so that alternationg electrode lines are displaced by one-half pitch (see Fig.3). This actuator generates motions at right angles to the stacking direction using the longitudinal piezoelectric effect. Long ceramic actuators up to 74 mm in length are manufactured.

A three-dimensional positioning actuators with a stacked structure has been proposed by PI Ceramic (Fig.4), in which shear strain is utilized to generate x and y displacements [16].

A monomorph device has been developed to replace the conventional bimorphs, with simpler structure and manufacturing process. The principle is a superposed effect of piezoelectricity and semiconductivity [17]. The contact between a semiconductor and a metal (Schottky barrier) causes non-uniform distribution of the electric field, even in a compositionally uniform ceramic. Suppose that the ceramic

possesses also piezoelectricity, only one side of a ceramic plate tends to contract, leading to a bending deformation in total. A monomorph plate with 30mm in length and 0.5 mm in thickness can generate 200μm tip displacement, in equal magnitude of that of the conventional bimorphs. The "rainbow" actuator by Aura Ceramics [18] is a modification of the above-mentioned semiconductive piezoelectric monomorphs, where half of the piezoelectric plate is reduced so as to make a thick semiconductive electrode to cause a bend.

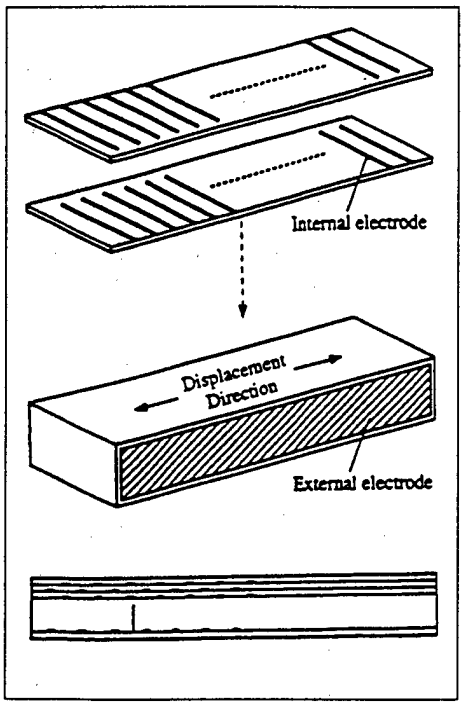


Fig.3 Structure of an internal interdigital electrode actuator.

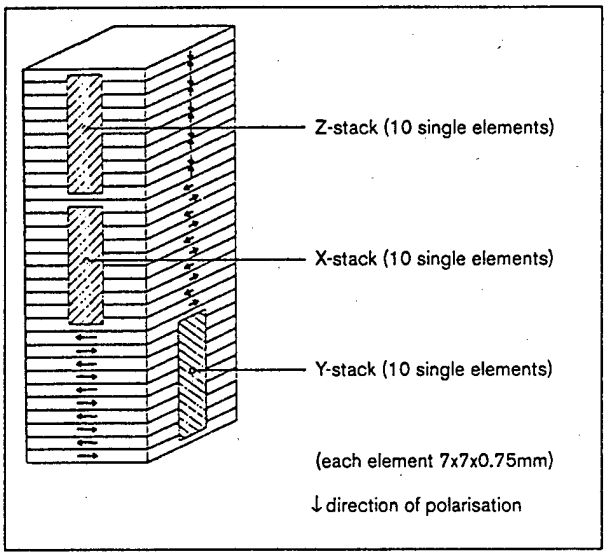


Fig.4 3D controllable multilayer piezoelectric actuator.

A composite actuator structure called the "moonie" has been developed at Penn State to provide characteristics intermediate between the multilayer and bimorph actuators; this transducer exhibits an order of magnitude larger displacement than the multilayer, and much larger generative force with quicker response than the bimorph [19,20]. Figure 5 shows the displacement characteristics for a Moonie, a modified version, and a Cymbal. A Cymbal with a thickness 1-2 mm and a diameter 12 mm can generate a displacement up to 100 μm. This new compact actuator has been applied to make a miniaturized laser beam scanner.

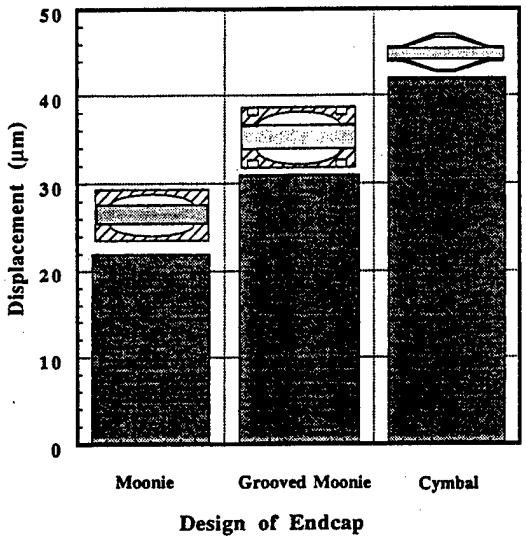


Fig.5 Comparison of the displacement levels for different designs of the endcap in Moonies/Cymbals.

Table I Difference in the ceramic actuator developments among USA, Japan and Europe.

	U.S.	Japan	Europe
TARGET	Military-oriented product	Mass-consumer product	Lab-equipment product
CATEGORY	Vibration suppressor	Micro-motor Positioner	Micro-motor Positioner Vibration suppressor
APPLICATION FIELD	Space structure Military vehicle	Office equipment Camera Precision machine Automobile	Lab stage/stepper Airplane Automobile Hydraulic system
ACTUATOR SIZE	Up-sizing (30 cm)	Down-sizing (1 cm)	Intermediate size (10 cm)
MAJOR MANUFAC-TURERS	AVX/Kyocera Morgan Matroc Itek Opt. Systems Burleigh AlliedSignal	Tokin Corporation NEC Hitachi Metal Mitsui Chemical Canon Seiko Instruments	Philips Siemens Hoechst CeramTec Ferroperm Physik Instrumente

4 DEVICE APPLICATIONS

Table I compares the difference in the ceramic actuator developments among USA, Japan and Europe. The details will be described in this section.

4.1 USA

The target of the development is mainly for military-oriented applications such as vibration suppression in space structures and military vehicles. Notice the up-sizing trend of the actuators for these purposes.

A typical example is found in a space truss structure proposed by Jet Propulsion Laboratory [21]. A stacked PMN actuator was installed at each truss nodal point and functioned actively so that unnecessary mechanical vibration was suppressed immediately. A "hubble" telescope has also been proposed using multilayer PMN electrostrictive actuators to control the phase of the incident light wave in the field of optical information processing (Fig.6)[22]. The PMN electrostrictor provided superior adjustment of the telescope image because of negligible strain hysteresis.

Passive dampler application is another smart usage of piezoelectrics. Mechanical noise vibration is radically suppressed by the converted electric energy dissipation through Joule heat when a suitable resistance, equal to an impedance of the piezoelectric element $1/\omega C$, is connected to the piezo-element [23]. Piezoceramic:carbon black:polymer composites are promising useful designs for practical application. The damping time constant change with volume percentage of the carbon black, which determines the resistance. The minimum time constant (i.e. quickest damping) was obtained at 6 % of carbon black, where a drastic electric conductivity change was observed (percolation threshold) [24].

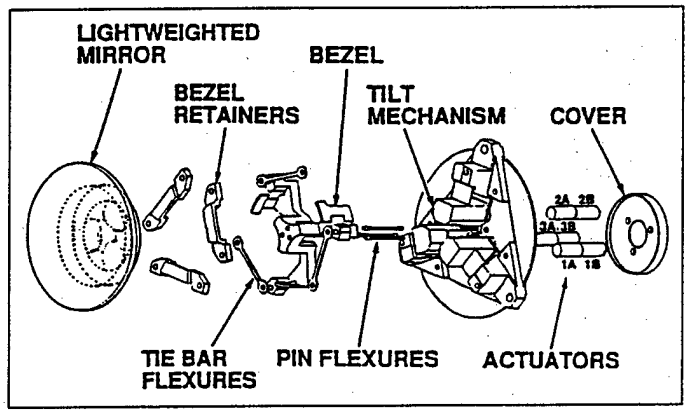


Fig.6 Hubble telescope using PMN electrostrictive actuators.

4.2 Japan

Japanese industries seek to develop mass-consumer products, and the categories are only limited to mini-motor and positioner areas, aiming at the applications to office equipment and cameras/video cameras. In that sense, tiny actuators smaller than 1cm are the main focus.

A dot matrix printer is the first widely-commercialized product using ceramic actuators. Each character formed by such a printer is composed of a 24 x 24 dot matrix. A printing ribbon is subsequently impacted by a multiwire array. A sketch of the printer head appears in Fig.7(a) [25]. The printing element is composed of a multilayer piezoelectric device, in which 100 thin ceramic sheets 100μm in thickness are stacked, together with a sophisticated magnification mechanism (Fig.7(b)). The magnification unit is based on a monolithic hinged lever with a magnification of 30, resulting in an amplified displacement of 0.5 mm and an energy transfer efficiency greater than 50%. A piezoelectric camera shutter is currently the largest production quantity item. A piece of piezoelectric bimorph can open and close the shutter in a milli-second through a mechanical wing mechanism [26]. Piezoelectric gyro-sensors are now widely used to detect the noise motion of a handy video camera. Figure 8 shows a Tokin's cylinder type gyroscope [27]. Among the 6 electrode strips, two of them are used to excite total vibration and the other two pairs of electrode are used to detect the Corioli's force or the rotational acceleration cause by the hand motion. By using the gyro signal, the image vibration can be compensated electrically on a monitor display.

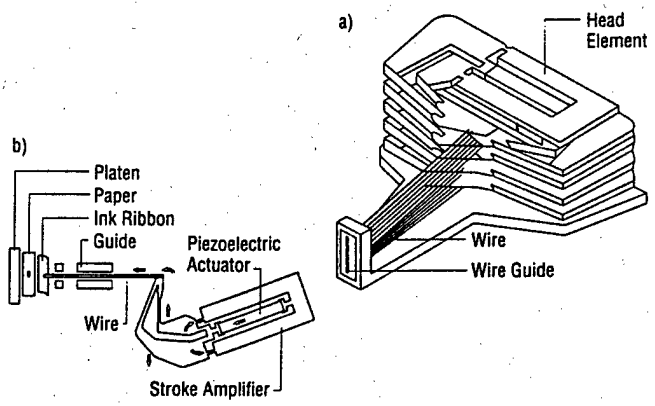


Fig.7 Structure of a printer head (a), and a differential-type piezoelectric printer-head element (b).

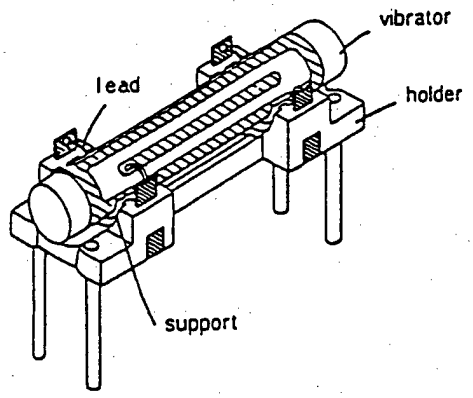


Fig.8 Piezo-ceramic cylinder vibratory gyroscope.

Efforts have been made to develop high-power ultrasonic vibrators as replacements for conventional electromagnetic motors. The ultrasonic motor is characterized by "low speed and high torque," which is contrasted with "high speed and low torque" of the electromagnetic motors. Two categories are being investigated in Japan for ultrasonic motors: a standing-wave type and a propagating-wave type.

The standing-wave type is sometimes referred to as a vibratory-coupler type or a "woodpecker" type, where a vibratory piece is connected to a piezoelectric driver and the tip portion generates flat-elliptical movement. Attached to a rotor or a slider, the vibratory piece provides intermittent rotational torque or thrust. The standing-wave type has , in general, high efficiency, but lack of control in both clockwise and counterclockwise directions is a problem. An ultrasonic linear motor equipped with a multilayer piezoelectric actuator and fork-shaped metallic legs has been developed as shown in Fig.9 [28]. Since there is a slight difference in the mechanical resonance frequency between the two legs, the phase difference between the bending vibrations of both legs can be controlled by changing the drive frequency. The walking slider moves in a way similar to a horse using its fore and hind legs when trotting. A trial motor 20 x 20 x 5 mm^3 in dimension exhibited a maximum speed of 20 cm/s and a maximum thrust of 0.2 kgf with a maximum efficiency of 20%, when driven at 98kHz of 6V (actual power = 0.7 W). This motor has been employed in a precision X-Y stage.

By comparison, the propagating-wave type (a surface-wave or "surfing" type) combines two standing waves with a 90 degree phase difference both in time and in space, and is controllable in both rotational directions (Fig.10) [29]. By means of the traveling elastic wave induced by the thin piezoelectric ring, a ring-type slider in contact with the "rippled" surface of the elastic body bonded onto the piezoelectric is driven in both directions by exchanging the sine and cosine voltage inputs. Another advantage is its thin design, which makes it suitable for installation in cameras as an automatic focusing device. 80 % of the exchange lenses in Canon's "EOS" camera series have already been replaced by the ultrasonic motor mechanism.

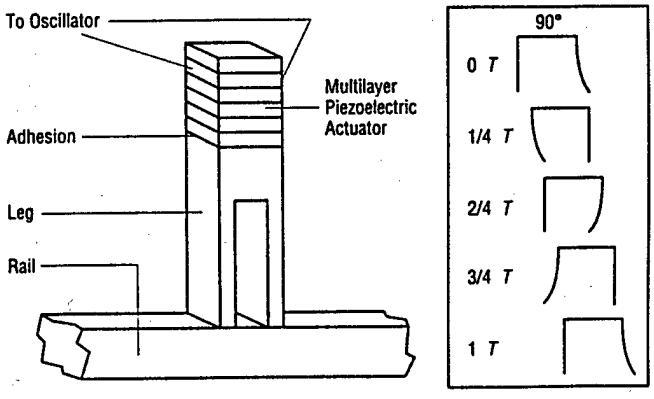


Fig.9 Ultrasonic linear motor of a vibratory coupler type.

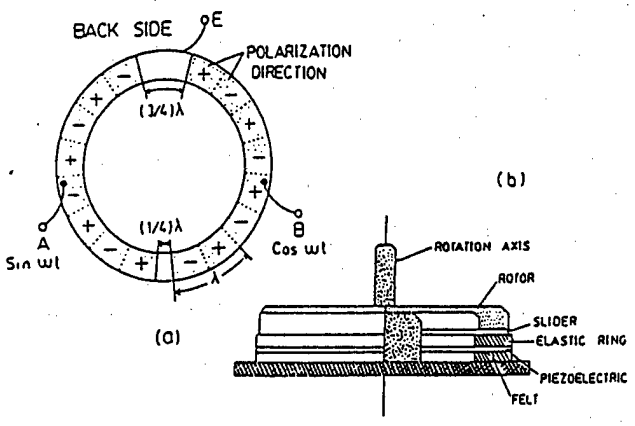


Fig.10 Design of the surface wave type motor (a), and its electrode configuration (b).

4.3 Europe

Ceramic actuator development has started relatively recently in Europe, and the research topics diverges very widely. However, the current focus by major manufacturers is probably put on lab-equipment products such as lab-stages and steppers with sophisticatedly complicated structures.

Figure 11 shows a walking piezo motor with 4 multilayer actuators [30]. Shorter two are used to function as clamplers and longer two provide the proceeding distance in an inchworm mechanism.

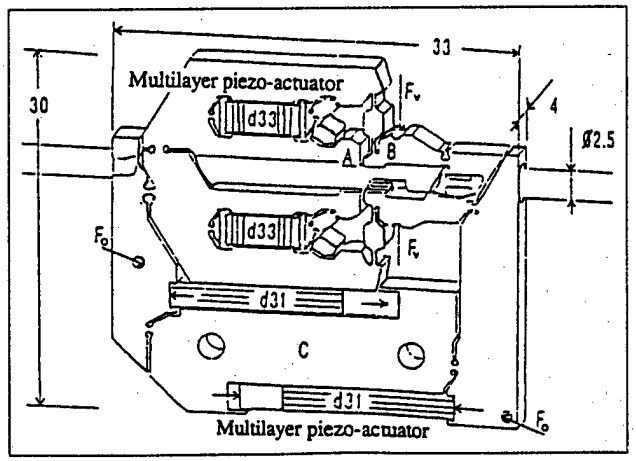


Fig.11 Walking piezo motor.

5 FUTURE OF CERAMIC ACTUATORS

5.1 Market of Piezoelectric Actuators

20 years have passed since the intensive development of piezoelectric actuators began in Japan, then spreaded worldwidely. Presently, the focus has been shifted to practical device applications.

The market in USA is limited to military and defense applications, and it is difficult to estimate the sales amount. The current needs from Navy are smart submarine skins,

hydrophone actuators, prop noise cancellation etc., and smart aircraft skins from Air Force, while Army requires hilicopter rotor twisting, aeroservoelastic control and cabin noise/seat vibration cancellation.

The European situation is still too early to calculate the market size, because most of the manufacturing is a prototyping stage sometimes under the government support.

On the contrary in Japan, ink-jet printers (Epson), piezoelectric shutters (Minolta Camera) and automatic focusing mechanisms (Canon) in cemeras, dot-matrix printers (NEC) and part-feeders (Sanki) are now commercialized and mass-produced by tens of thousands of pieces per month. During the commercialization, new designs and drive-control techniques of the ceramic actuators have been mainly developed in the past few years. A number of patent disclosures have been found particularly in NEC, TOTO Corporation, Matsushita Electric, Brother Industry, Toyota Motors, Tokin, Hitachi Metal, Toshiba etc.

5.2 Future Research Trend

Future research trends will be divided into two ways: up-sizing in space structures and down-sizing in office equipment. Further down-sizing will also be required in medical diagnostic applications such as blood test kits and surgical catheters. Piezoelectric thin films campatible with silicon technology will be much focused in micro-electromechanical systems. An ultrasonic rotary motor as tiny as 2 mm in diameter fabricated on a silicon membrane is a good example [31].

One ceramic multilayer component actuator proposed by Mitsui Chemical is very suggestive for predicting the future trend. Figure 12 shows the electrode pattern [32]. Only by the external connection, a combined vibration of the longitudinal L_1 and bending B_2 modes can be excited.

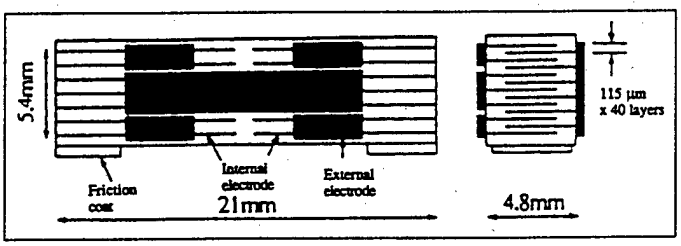


Fig.12 Multilayer ceramic simple linear motor (Mitsui Chemical).

The Penn State University has developed a compact ultrasonic rotory motor as tiny as 3 mm in diameter. As shown in Fig. 13, the stator consists basically of two piezoelectric rings and a metal ring with "windmill" shaped fingers bonded together, so as to generate a coupled vibration of radial and bending types on a finger [33]. Since the component number and the fabrication process were minimized, the fabrication price would be decreased remarkably, and it would be adaptive to the disposable usage. When driven at 160 kHz, the maximum revolution 2000rpm and the maximum torque 0.8mN·m were obtained for a 5 mm motor. Notice that even the drive of the motor is intermittent, the output rotation becomes very smooth because of the inertia of the rotor. Figure 14 shows motor characteristics plotted as a function of motor size for "windmill" motors.

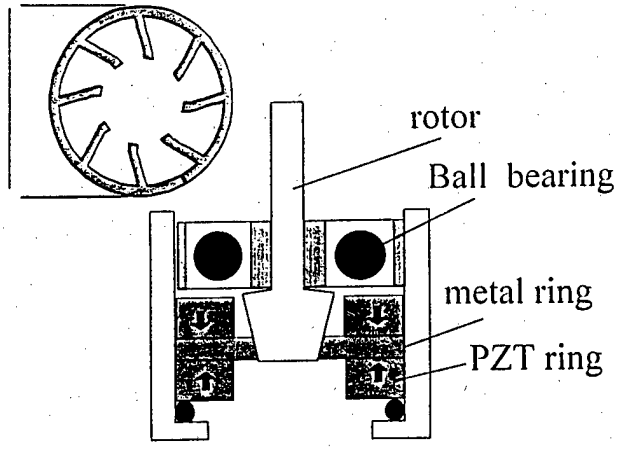


Fig.13 Compact ultrasonic motor with a "windmill"-shaped torsional coupler.

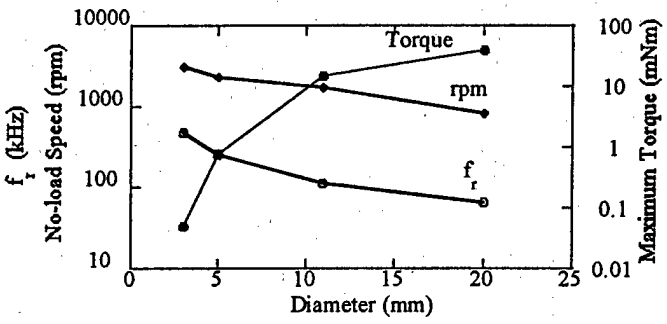


Fig.14 Radial mode resonance frequency, no-load speed and starting torque vs. diameter of the stator. Speed and torque were measured at 15.7 V.

With expanding the application field of ceramic actuators, the durability/reliability issue becomes more important. The final goal is, of course, to develop much tougher actuator ceramics mechanically and electrically. However, the reliability can be improved significantly if the destruction symptom of the actuator is monitored.

Safety systems or health monitoring systems have been proposed with two feedback mechanisms: position feedback which can compensate the position drift and the hysteresis, and breakdown detection feedback which can stop the actuator system safely without causing any serious damages onto the work, e.g. in a lathe machine [34]. Acoustic emission and

internal potential measurements, and resistance monitoring of a strain-gauge type internal electrode embedded in a piezo-actuator under a cyclic electric field drive are good predictors for the life time [35].

Future research and development should focus on superior systems ecologically (i.e. fit for human!) as well as technologically. Safety systems, which can monitor the fatigue or the destruction symptom of materials/devices, and stop the equipment safely without causing serious problems, will be desired.

REFERENCES

[1] K.Uchino, Piezoelectric/Electrostrictive Actuators, Morikita Publishing, Tokyo 1986

[2] K.Uchino, Bull.Am.Ceram.Soc., **65**(4), 647 (1986)

[3] K.Uchino, MRS Bull., **18**(4), 42 (1993)

[4] K.Uchino, Proc. 4th Int'l Conf. Electronic Ceramics & Appl., p.179(1994)

[5] J.Kuwata, K.Uchino and S.Nomura, Ferroelectrics, **37**, 579 (1981)

[6] J.Kuwata, K.Uchino and S.Nomura, Jpn.J.Appl.Phys., **21**, 1298 (1982)

[7] K.Yanagiwawa, H.Kanai and Y.Yamashita, Jpn.J.Appl. Phys., **34**, 536 (1995)

[8] S.E.Park and T.R.Shrout, Mat.Res.Innovt., **1**, 20 (1997)

[9] X.H.Du, J.Zheng, U.Belegundu and K.Uchino, J.Appl. Phys.Lett., **72**, 2421 (1998)

[10] K.Uchino and S.Nomura, Ferroelectrics, **50**(1), 191 (1983)

[11] A.Furuta, K.Y.Oh and K.Uchino, Sensors and Mater., **3**(4), 205 (1992)

[12] K.Uchino, Mat.Res.Innovat., **1**, 163 (1997)

[13] K.Uchino, J.Rob.Mech., **1**(2), 124 (1989)

[14] P.Poosanaas, K.Tonooka and K.Uchino, J.Mechatronics [in press]

[15] J.Ohashi, Y.Fuda and T.Ohno, Jpn.J.Appl.Phys., **32**, 2412 (1993)

[16] A.Banner and F.Moller, Proc. 4th. Int'l Conf. New Actuators, AXON Tech.Consult.GmbH, p.128 (1995)

[17] K.Uchino, M.Yoshizaki, K.Kasai, H.Yamamura, N. Sakai and H.Asakura, Jpn.J.Appl.Phys., **26**(7), 1046 (1987)

[18] Aura Ceramics, Inc., Catalogue "Rainbow"

[19] Y.Sugawara, K.Onitsuka, S.Yoshikawa, Q.C.Xu, R.E.Newnham and K.Uchino, J.Am.Ceram.Soc., **75**(4), 996 (1992)

[20] A.Dogan, K.Uchino and R.E.Newnham, IEEE Trans. UFFC, **44**,597 (1997)

[21] J.T.Dorsey, T.R.Sutter and K.C.Wu, Proc. 3rd Int'l Conf. Adaptive Structures, p.352 (1992)

[22] B.Wada, JPL Document D-10659, p.23 (1993)

[23] K.Uchino and T.Ishii, J.Jpn.Ceram.Soc., **96**(8), 863 (1988)

[24] Y.Suzuki, K.Uchino,H.Gouda,M.Sumita,R.E.Newnham and A.R.Ramachandran, J.Jpn.Ceram.Soc., **99** (11), 1135 (1991)

[25] T.Yano, I.Fukui, E.Sato, O.Inui and Y.Miyazaki, Proc. Electr. & Commun.Soc., p.1-156 (Spring,1984)

[26] Y.Tanaka, Handbook on New Actuators for Precision Control, Fuji Technosystem, p.764 (1994)

[27] Tokin Corporation, Catalogue "Ceramic Gyro"

[28] M.Tohda, S.Ichikawa, K.Uchino and K.Kato, Ferroelectrics, **93**, 287 (1989)

[29] Y.Akiyama (Editor), Ultrasonic Motors/Actuators, Triceps, Tokyo 1986

[30] M.P.Koster, Proc. 4th Int'l Conf. New Actuators, Germany, p.144 (1994)

[31] A.M.Flyn, L.S.Tavrow, S.F.Bart, R.A.Brooks, D.J. Ehrlich, K.R.Udayakumar and L.E.Cross, J. Microelectro-mechanical Systems, **1**, 44 (1992)

[32] H.Saigo, 15th.Symp.Ultrasonic Electronics, No.PB-46, p.253 (Nov.1994)

[33] B.Koc and K.Uchino, IEEE int'l. Ultrasonic Symp., YY-6, Sendai, Japan (Oct.1998)

[34] K.Uchino, J.Industrial Education Soc. Jpn., **40**, 28 (1992)

[35] K.Uchino and H.Aburatani, Proc. 2nd Int'l Conf. Intelligent Materials, p.1248 (1994)

Chemical Processing and Properties of Functional Ceramics

Shin-ichi Hirano, Toshinobu Yogo, Wataru Sakamoto, Ko-ichi Kikuta, Kazumi Kato, Yoshikuni Takeichi, Yasushi Araki, Masahiro Saitoh, Satoru Ogasahara, Tetsuya Kohigashi, Yasuhiro Ito, Kazuyuki Suzuki and Hiroyuki Ukai

Dept. of Applied Chemistry, Nagoya University, Furo-cho, Chikusa-ku, Nagoya, 464-8603, Japan

Abstract:

Functional ceramic films have been receiving great attention because of their potentials for emerging applications, which include integrated sensors, actuators and other devices responding to magnetic, electric, optic and stress fields. Many methods, such as liquid phase epitaxial growth, chemical vapor deposition, molecular beam epitaxial growth, sputtering, laser ablation and chemical solution deposition, have been developed to fabricate thin films with desired properties. Among these methods, the chemical solution deposition method has the advantages of good homogeneity, ease of compositional control, low temperature processing, and large area and versatile shaping with integrated functionalities over vacuum deposition techniques. This paper reviews a part of the authors' results on the chemical processing of some epitaxial ferroelectric, pyroelectric, and piezoelectric films as well as nonlinear optic films. In addition, the processing and properties of nano-sized functional ceramic particles/organic hybrids is presented as an example of novel and promising materials, which are expected to create a emerging area.

1. Introduction

Recently, functional ceramics have been receiving a great deal of attention in the advanced technologies. The studies on processing of ferroelectric, piezoelectric and non-linear optic films have given significant opportunities for developing miniaturized devices in emerging areas.

Systems of $LiNbO_3$, $Pb(Zr,Ti)O_3$ (PZT) and $K(Ta,Nb)O_3$ (KTN) have large electromechanical coupling coefficient, and pyroelectric and electro-optic properties. Thin films with preferred orientation have mainly been fabricated by physical deposition methods and chemical vapor deposition method. On the other hand, the chemical solution deposition (CSD) process has the advantages of feasible control of composition, homogeneity, and shape.[1-14]

Nano-sized functional ceramic particles/organic hybrids have recently been developed as a new family of materials.[15-19] The conventional bending of fine dielectric or magnetic particles into polymer causes the particle agglomeration, leading to the degradation of the properties. The authors have developed a novel method to fabricate the hybrids based on the in-situ nucleation and growth of dielectric particles in an organic matrix below 100°C through the reaction control of designed metallo-organic molecules with combination of the polymerization.

This paper reviews the processing and properties of epitaxial films of $LiNbO_3$, PZT and KTN as well as a novel functional material of $PbTiO_3$/organic hybrids though the chemical solutions.

2. Processing Scheme of thin films

Figure 1 illustrates the general flow diagram for the preparation of electronic ceramics by chemical processing through metal alkoxide solutions. The formation of the intermediate compound, e.g. complex alkoxide, has been mentioned elsewhere in terms of homogeneous solution. The partial hydrolysis of the solution is most critical to manipulate the nature of the precursor chemistry.[12]

The chemical bonds and the coordination state of

1999 INTERNATIONAL SYMPOSIUM ON
MICROMECHATRONICS AND HUMAN SCIENCE
0-7803-5790-6/99/ $10.00 ©1999 IEEE.

alkoxides were analyzed by FT-IR, NMR, UV spectroscopy and gas chromatography (GC). The viscosity and density of the precursor alkoxide solutions were measured with a rotational viscometer and a pycnometer. Alkoxy-derived films were prepared on substrates by a dip-coating method or a spin coating method and then heat-treated in a mixture gas flow of water vapor and oxygen to promote crystallization and the release of carbonates.

The crystallization process of alkoxy-derived films was analyzed by XRD, TEM and FT-IR. Morphologies and structures of film and substrate interfaces were analyzed by Auger electron spectroscopy, Rutherford back scattering, and microscopic observations.

D-E hysteresis loops of films were measured using a modified Sawyer-Tower circuit. Refractive indices were determined by ellipsometry.

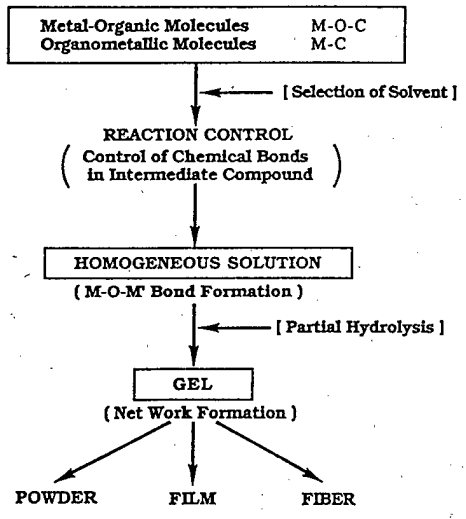


Fig.1 CSD processing of electronic ceramics

3. Ferroelectric and Non-linear $LiNbO_3$ Thin Films[1-7]

Figure 2 summarizes the key processing factors to synthesize stoichiometric epitaxial $LiNbO_3$ films at low temperature (below 500°C). Lithium ethoxide is reacted with niobium ethoxide for 24h, which was followed by FT-IR spectra and NMR spectra[1]. This chemical coordination of ions in a double alkoxide was also confirmed by Eichorst et al.[20].

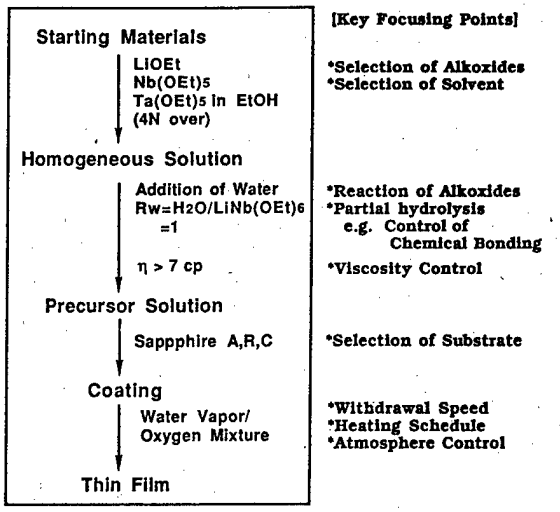


Fig.2 Key processing parameters for the processing of $LiNbO_3$ films

The amount of water addition for the partial hydrolysis influences strongly the crystallization of films. The addition of an equivalent mole of water to $LiNb(OC_2H_5)_6$ and heat treatment of alkoxy-derived films in flow of water vapor and oxygen mixture were found to enhance the crystallization and avoid carbonate formation.

The crystalline films were fabricated above 250°C on various substrates, such as sapphire and Si. The typical linear relationship could be observed between logarithm of withdrawal speed and logarithm of film thickness as crystallized for one dip-cycle. By repeating the dip-coating procedure, the thickness of crystallized films increased lineally without any distinct interface between layers.

Films on sapphire indicated highly preferred orientation at 400°C according to the sapphire orientation, such as (001), (100) and (012). The films carefully crystallized on sapphire substrates exhibited

the epitaxial feature as confirmed by RHEED and X-ray pole figure profile. However, films on Si substrates were polycrystalline. Auger electron spectroscopy and Rutherford back scattering data showed clearly the uniform composition and the sharp interface between film and substrate. No significant interdiffusion of ions was detected.

The authors also have developed the methods to pattern $LiNbO_3$ waveguides using a chemically modified precursor, which is sensible to UV light. The epitaxial films of $LiNbO_3$ processed at 500°C on sapphire substrates exhibit the characters of waveguides and second harmonic wave generation, which lead to the new electro-optic devices.[21,22]

4. $Pb(Zr,Ti)O_3$[7,10,12] and $(Pb,La)TiO_3$[23] Films

Recently, increased focus has been placed in processing ferroelectric $Pb(Ti,Zr)O_3$ (PZT) and $(Pb,La)TiO_3$ thin films. The processing of these thin films with desired perovskite structure has been required, because ferroelectric properties are influenced by the presence of a competing pyrochlore phase. The development of perovskite structure is more difficult in thin films integrated on substrates in comparison with the amorphous powders.

$Pb(Zr,Ti)O_3$ perovskite films have been successfully crystallized on various substrates such as MgO, $SrTiO_3$, and $Pt/Ti/SiO_2/Si$. Figure 3 summarizes the processing conditions of PZT thin films. The Zr and Ti ions located in B site of perovskite structure have to be coordinated in solution prior to the reaction with lead acetate anhydrate in order to form the perovskite films at low temperatures. Lead acetate anhydrate was selected because it is superior to other chemicals in effect to stabilize the precursor solution. The annealing of alkoxy-derived films in flow of water vapor and oxygen was found to be effective on the low temperature development and the preferred orientation of perovskite films. The films were crystallized into perovskite phase on $SrTiO_3$ substrate at 450°C.

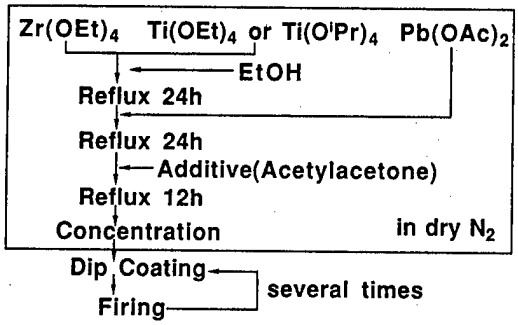


Fig.3 Scheme for processing of alkoxy-derived PZT films

Figure 4 shows XRD profiles of $Pb(Zr_{0.53}Ti_{0.47})O_3$ films on $Pt/Ti/SiO_2/Si$ substrate. The films, when properly crystallized, exhibit the typical ferroelectric hysteresis and a dielectric constant of about 500 at 100kHz at room temperature. Figure 5 summarizes the properties of the films crystallized at 600°C on passivated Si substrates. The permittivity increases from 50 to 500 with increasing thickness from 0.1 to 1.5 μm. The films have quite uniform and small grain size. The increase with film thickness corresponds to the increase in grain size of PZT.[10]

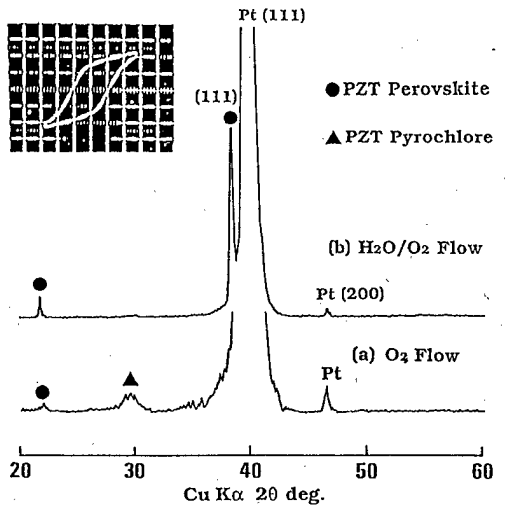


Fig.4 XRD profiles and D-E hysteresis curve of PZT (Zr:Ti=53:47) thin films on substrate ($Pt/Ti/SiO_2/Si$) crystallized at 600°C

[Condition of calcinations: (a) O_2 flow (2) H_2O/O_2 flow]

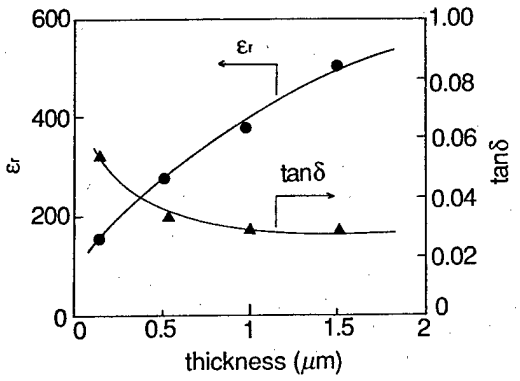


Fig.5 Change of dielectric constant and tanδ at 100 kHz for PZT films with film thickness

Lanthanum modified lead titanate ($Pb_{1-1.5x}La_xTiO_3$, PLT) has been receiving great attention for pyroelectric sensors, nonvolatile memories and large variety of electro-optic devices because of its excellent pyroelectric, ferroelectric and electro-optic properties. The properties of PLT can be controlled by the amount of lanthanum doping. Recently, the demand for thin film processing has increased for integrated-device development. (100) or (001) highly oriented PLT thin films are expected to give a large figure of merit and exhibit several excellent properties compared with other materials because of its polarization without poling treatment.

Highly oriented $Pb_{0.85}La_{0.1}TiO_3$ films were successfully synthesized on $LaNiO_3/SrTiO_3/MgO(100)$ substrates through metallo-organics. A homogeneous and stable PLT precursor solution was prepared from lead acetate, lanthanum isopropoxide and titanium ethoxide in ethanol. PLT precursor was stabilized by the coordination of acetylacetonate group to metals. Perovskite $Pb_{0.85}La_{0.1}TiO_3$ thin films with (100) or (001) preferred orientation were successfully synthesized on $LaNiO_3/SrTiO_3/MgO(100)$ substrates above 400°C. The orientation of the PLT film was improved markedly by using a $SrTiO_3$ thin film as a buffer layer between $LaNiO_3$ film and MgO substrate. PLT thin films on $LaNiO_3/SrTiO_3/MgO(100)$ substrates showed a typical P-E hysteresis. The dielectric constant of the film was about 600 at 25°C. The Curie temperature of the film was found to be at around 270°C.[23]

5. $K(Ta,Nb)O_3$ (KTN) Films[12-14]

Potassium ethoxide, tantalum ethoxide and niobium ethoxide were used as starting materials. A certain amount ratio of tantalum ethoxide and niobium ethoxide was reacted in absolute ethanol to coordinate metal bondings in B-site of perovskite structure. Then a stoichiometric ratio of potassium ethoxide solution was added to react at refluxing temperature for 24 h.

The changes of coordination states in a KTN original precursor and partially hydrolyzed precursor were followed by NMR and FT-IR measurements. In the ^{13}C NMR spectra, bridging metal-oxygen bonds in the original precursor diminished to break-up, indicating that the condensation-polymerization reaction of metal alkoxides takes place. The behavior was also confirmed in FT-IR spectra.

An MgO (100) plate was chosen as a substrate because of the similar oxygen packing with KTN (100). XRD profiles of the KTN thin films crystallized at 675°C are shown in Fig.6. The formation of pyrochlore phase was observed after heat treatment without flow of water vapor (Fig.6(a)). A mixture of water vapor and oxygen gas during calcinations has a pronounced effect on the elimination of remaining organic components, leading to the formation of the preferred orientation of the perovskite phase (100) as shown in Fig.6(b), as observed in $LiNbO_3$ processing. Continuing the water vapor treatment hinders the further formation of the perovskite phase during the crystallization process, which might be attributable to potassium reacting with the hydroxy group and disturbing the network of the oxygen-metal bond at 675°C.

KTN65 (Ta/Nb = 65/35), KTN50 (Ta/Nb = 50/50), and KTN35 (Ta/Nb = 35/65) films were crystallized at 700°C on Pt(100)/MgO(100) substrates. The dielectric

measurements were conducted on 1.0-μm-thick KTN films. Figure 7 shows the variation in the dielectric constant as a function of temperature for the KTN50 film on Pt(100)/MgO(100) substrate. The maximum dielectric constant is observed at around 0°C at 1 kHz with a broad transition. The dielectric constant also depends upon the frequency. The transition range is shifted to higher temperature with increasing frequency from 1 kHz to 1 MHz. This result indicates a diffuse transition from a ferroelectric to a paraelectric phase. The broad peak is due to the stress in the films. Films having low stresses showed properties close to those of single crystals. However, films having large stresses showed broad peaks in the dielectric constant verses temperature curves with a diffuse phase transition.[14]

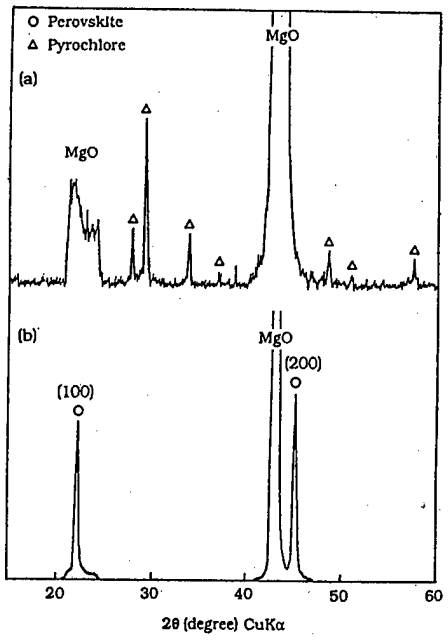


Fig.6 XRD profiles of $KTa_{0.65}Nb_{0.35}O_3$ thin films on MgO(100) substrates crystallized at 675°C after calcinations through (a) oxygen at 300°C and (b) oxygen/water vapor at 300°C

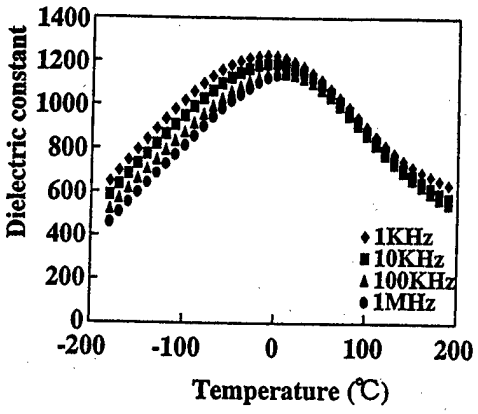


Fig.7 Changes of dielectric constant for KTN50 films with temperature measured from 1 kHz to 1MHz

6. Functional Fine Ceramic Particles/Polymer Hybrids

Inorganic/organic hybrids are expected to have novel features as well as the combined characters of each component. The conventional mixing of particles into organics usually causes the particle agglomeration due to the van der Waals force, leading to the degradation of the properties. The authors have developed a novel method to synthesize magnetic oxides or $BaTiO_3$ particles/organic hybrids through the reaction control of the designed precursor from modified titanium and barium alkoxide below 100°C.[15-18]

Tetragonal $PbTiO_3$ (PT) of perovskite structure is one of the ferroelectric and piezoelectric materials with attractive properties. Crystalline $PbTiO_3$ particles can be synthesized at 470°C from the precursor of lead acetate and titanium alkoxide. Usually, the heat treatment above 400°C is required to prepare crystallized $PbTiO_3$ particles. The authors discovered the crystallization of $PbTiO_3$ particles directly into perovskite phase below 100°C in organic matrix to form a hybrid.[19] Figure 8 shows the processing scheme for the preparation of hybrids. The fabrication of $PbTiO_3$/organic hybrids was carried out according to the scheme shown in Fig.9. Lead methacrylate and titanium

isopropoxide were weighed to be a molar ratio of 1.0 and dissolved in absolute methanol. The mixture was refluxed at 65°C for 24 h producing a clear PT precursor solution. The PT precursor is analyzed to comprise a complex alkoxide, $Pb[Ti(OR)_n(methacryl)]$. The solution was hydrolyzed with CO_2-free water, followed by the evaporation to afford a solid product, which was sealed with 2,2'-azobis (isobutyronitrile) (AIBN) and methanol under vacuum in a glass tube after freezing-melting treatments in order to remove oxygen and polymerized at 100°C. The solid hybrid was obtained after removal of solvent by drying under vacuumat room temperature.

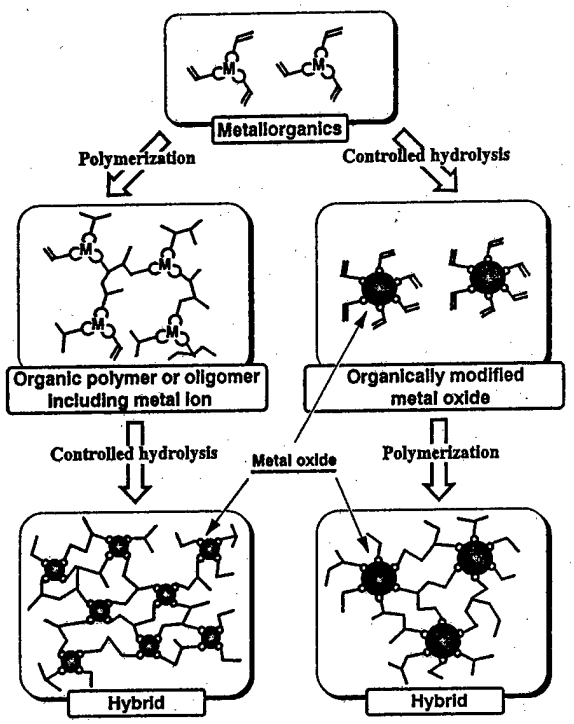


Fig.8 Chemical processing scheme of hybrids

The hybrid films were prepared from the hybrid powder by pressing between electrically heated planes at about 170°C. Crystalline perovskite $PbTiO_3$ particles/organic hybrids behave to be dielectric and respond to the applied electric field as an electrorheological fluid. The selected area electron diffraction and the Raman spectra of the oxide particles confirm to be crystalline tetragonal $PbTiO_3$ particles. The ratio of Pb to Ti was found to be 1:1 by the EDX analysis. The dielectric constant of a hybrid film, prepared from the $PbTiO_3$ precursor hydrolyzed with 30 equiv. water followed by polymerization at 100°C for 24h, is 5.2 at 10kHz at room temperature, which is higher than that of poly(methylmethacrylate) (PMMA) as the matrix. The hybrid in silicone oil suspension behave as the typical electrorheological fluid as shown in Fig.10, which affords a novel modified ceramic material in the emerging areas.

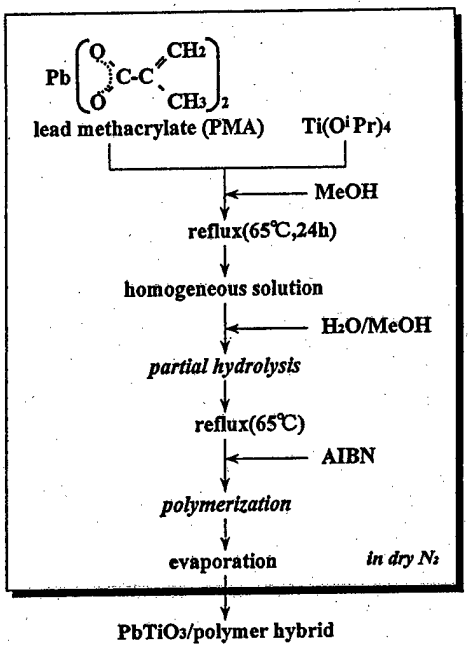


Fig.9 Processing of $PbTiO_3$/polymer hybrid

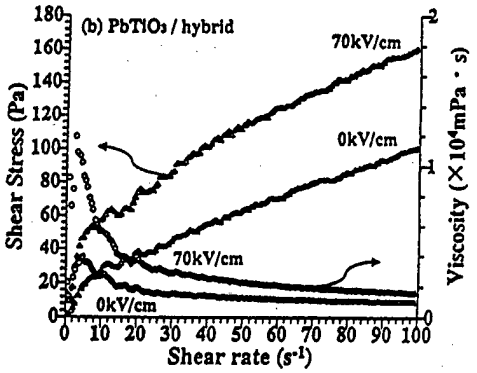


Fig.10 Shear stress and viscosity changes as a function of shear rate on $PbTiO_3$/hybrid

7. Conclusions

The concept described in this paper can be applied to the processing of functional ceramics with controlled characters and orientations at relatively low temperatures. The crystallization of films can be promoted by the reaction control of designed metal alkoxides in intermediate state and then the pre-heat treatment of alkoxy-derived films in flow of water vapor and oxygen gas mixture. The chemical processing does realize a promising route to synthesize functional ceramic films, which leads to the integration of functionalities.

The newly developed method provides novel inorganic/organic hybrids below 100°C through the reaction control of designed metallo-organic molecules with combination of the polymerization, which creates the future strategy of the new material families.

REFERENCES

[1] S. Hirano and K Kato, "Synthesis of $LiNbO_3$ by Hydrolysis of Metal Alkoxides", Advanced Ceramic Materials, **2** 142-145 (1987).

[2] S. Hirano and K Kato, "Formation of $LiNbO_3$ Films by Hydrolysis of Metal Alkoxides", J. Non-Crystalline Solid, **100** 538-541 (1988).

[3] S. Hirano and K Kato, "Preparation of Crystalline $LiNbO_3$ Films with Preferred Orientation by Hydrolysis of Metal", Advanced Ceramic Materials, **3** 503-506 (1988).

[4] S. Hirano and K Kato, "Preparation of Crystalline $LiNb_xTa_{1-x}O_3$ ($0<x<1$) Films from Metal Alkoxide Solutions", Bull. Chem. Soc. Jpn., **62** 429-434 (1989).

[5] S. Hirano and K Kato, "Processing of Crystalline $LiNbO_3$ Films with Preferred Orientation through An Organometal", Solid State Ionics, **32/33** 765-770 (1989)

[6] S. Hirano and K Kato, "Processing of Crystalline $Li(Nb,Ta)O_3$ Films with Preferred Orientation through Metal Alkoxide", Processing Science of Advanced Ceramics, Mater. Res. Soc. Symp. Proc., **155** 181-190 (1989).

[7] S. Hirano, T. Yogo, K. Kikuta, K. Kato, W. Sakamoto and S. Ogasawara, "Sol-Gel Processing and Characterization of Ferroelectric Films", Ceram. Trans., **25** 19-32 (1992).

[8] S. Hirano, T. Yogo, K. Kikuta, T. Morishita and Y. Ito, "Preparation of Potassium Tantalate Niobate by Sol-Gel Method", J. Am. Ceram. Soc., **75** 1701-1704 (1992).

[9] S. Hirano, T. Yogo, K. Kikuta, H. Urahata, Y. Isobe, T. Morishita, K. Ogiso and Y. Ito, "Chemical Processing of Ferroelectric Niobates Epitaxial Films", Mater. Res. Soc. Symp. Proc., **271** 331-338 (1992).

[10] S. Hirano, T. Yogo, K. Kikuta, Y. Araki, M. Saitoh and S. Ogasahara, "Synthesis of Highly Oriented Lead Zirconate-Lead Titanate Film Using Metallo-organics", J. Am. Ceram. Soc., **75** 2785-2789 (1992).

[11] S. Hirano, T. Yogo, K. Kikuta, Y. Isobe and S. Ono, "Study of Crystallization of $LiNbO_3$ Films from Metal Alkoxides", J. Mater. Sci., **28** 4188-4192 (1993).

[12] S. Hirano, T. Yogo and K. Kikuta, "Processing of Better Ferroelectric Films Through Chemistry", Third Euro-Ceramics, **2** 685-698 (1993) (Edited by P. Duran and J. F. Ferrandez).

[13] T. Yogo, K. Kikuta, Y. Ito and S. Hirano, "Synthesis of Highly Oriented $K(Ta,Nb)O_3$

(Ta:Nb=65:35) Film Using Metal Alkoxides", J. Am. Ceram. Soc., **78** 2175-2179 (1995).

[14] K. Suzuki, W. Sakamoto, T. Yogo and S. Hirano, "Processing of Oriented $K(Ta,Nb)O_3$ Films Using Chemical Solution Deposition", J. Am. Ceram. Soc., **82** 1463-1466 (1999).

[15] T. Yogo, K. Kikuta, S. Yamada and S. Hirano, "Synthesis of Barium Titanate/Polymer Composites from Metal Alkoxide", J. Sol-Gel Sci. and Tech., **2** 175-179 (1994).

[16] S. Hirano, T. Yogo, K. Kikuta and S. Yamada, "Processing and Propertiesof Barium Titanate/Polymer Hybrid Materials by Sol-Gel Method", Ceram. Trans., **68** 131-140 (1996).

[17] T. Yogo, T. Nakamura, K. Kikuta, W. Sakamoto and S. Hirano, "Synthesis of α-Fe_2O_3 Particle/Origomer Hybrid Material", J. Mater. Res., **11**, 475-482, (1996).

[18] T. Yogo, T. Nakamura, W. Sakamoto and S. Hirano, "Synthesis of Magnetic Particle/Organic Hybrid from Metalorganic Compounds", J. Mater. Res., **14**, 2855-2860, (1999).

[19] T. Yogo, H. Ukai, W. Sakamoto and S. Hirano, "Synthesis of $PbTiO_3$/Organic Hybrid from Metal-Organics", J. Mater. Res., in press.

[20] D. J. Eichost, D. A. Payne, S. R. Wilson and K. E. Howard, "Crystal Structure of LiNb(OCH2CH3)6: A Precursor for Lithium Niobate Ceramics", Inorg. Chem., **29** 1458-1459 (1990).

[21] T. Yogo, Y. Takeichi, K. Kikuta and S. Hirano, "Ultraviolet Patterning of Alkoxy-Derived Lithium Niobate Film", J. Am. Ceram. Soc., **78** 1649-1652 (1995).

[22] S. Hirano, T. Yogo, K. Kikuta, W. Sakamoto and Y. Takeichi, "Processing and Ultraviolet Patterning of $LiNbO_3$ Epitaxal Films from Metallorganic Precursors", Mater. Sci. and Eng. **B41** 117-122 (1996).

[23] W. Sakamoto, S. Yada, T. Kohigashi, K. Kikuta, T. Yogo and S. Hirano, "Synthesis of Highly Oriented $(Pb_{0.85}La_{0.1})TiO_3$ Thin Films by Chemical Solution Deposition Method", Ceram. Trans., **83** 331-337 (1998).

Integrated Sample Preparation Systems for Miniaturized Biochemical Analysis

A. Bruno Frazier[1,2], Ian Papautsky[2], Thayne L. Edwards[2], Bruce K. Gale[3]
[1]School of Electrical & Computer Engineering, Georgia Institute of Technology
777 Atlantic Drive, Atlanta GA 30332-0250
[2]Department of Bioengineering, University of Utah
50 S. Central Campus Drive, Room 2480, University of Utah, Salt Lake City, Utah 84112
[3]Department of Biomedical Engineering
Louisiana Tech University, Ruston, LA 71272
Phone & Fax: (404) 894-2030, E-mail: Bruno.Frazier@ece.gatech.edu

ABSTRACT

This work is focused on the development of miniaturized formats for integrated biochemical sample preparation. The formats discussed in this work include micromachined pipette arrays, a micro thermal field flow fractionation system, and a micro electrical field flow fractionation system. The micromachined pipette arrays are used for macro scale manipulation of pL - μL volumes of samples / reagents and for interfacing with micro scale biochemical analysis systems. The micro thermal field flow fractionation system is a chromatographic separation technique for fractionating samples based on the heat capacity, thermal conductivity and size of the particles. The micro electrical field flow fractionation system fractionates samples based on the size and zeta potential of the sample constituents. Electrical and thermal micro FFF systems are capable of separating samples with constituents in the diameter range from approximately 1 nm to 1 μm . In each case, the need for mechatronics technologies is demonstrated for manipulation and placement of the biochemical samples being delivered to/from these preparation systems.

INTRODUCTION

The miniaturization of biochemical analysis systems has been a topic of growing interest over the past decade. During this time, a large majority of the technical effort has been invested in the development of the primary separation (or amplification) component of the various analysis systems such as the micro columns used in the miniaturized chromatographic systems (e.g. electrophoresis, gas chromatography, liquid chromatography) or the chambers used for miniaturized polymerase chain reaction (PCR) systems. Less efforts have been directed toward the development of technologies for micro scale sample preparation (with the exception of PCR). Sample preparation technologies include methods for purifying, manipulating, interfacing, amplifying, and chemically modifying sub-micro liter volumes of samples for analysis in a miniaturized format. While each of these technologies is available in a macro scale format, most have not been available on the micro scale until recently. During the past two to three years, there has been a significant increase in the worldwide efforts to improve the technology base for integrated miniaturized sample preparation. These efforts have resulted in integrated systems for purifying and sorting samples, manipulating samples, interfacing samples and modular analysis system components, and sample amplification [1].

In this paper, we will focus on the use of micro systems fabrication technologies for the development of three different micro systems for sample preparation. The three systems include: a) micro electrical field flow fractionation; b) micro thermal field flow fractionation; and c) micromachined pipette array technology.

MICROMACHINED PIPETTE ARRAY SAMPLE DELIVERY SYSTEM

The micromachined pipette array (MPA) sample delivery system relies on microscale pipettes for highly-parallel sample loading of pL to μL volumes. A schematic diagram of an array of such micromachined pipettes is shown in Figure 1. The MPA is an array of microchannels extended off the substrate. Each microchannel, or pipette, has an input port etched through the substrate and an output at the free end. The

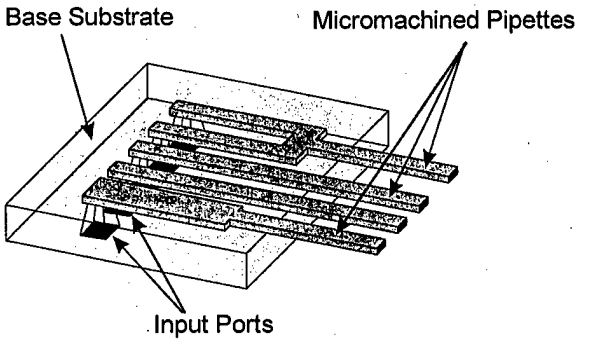


Figure 1. Schematic diagram a micromachined pipette array.

1999 INTERNATIONAL SYMPOSIUM ON
MICROMECHATRONICS AND HUMAN SCIENCE
0-7803-5790-6/99/ $10.00 ©1999 IEEE.

process used to fabricate the MPA has been described in detail elsewhere [1,2,3,4]. The MPA provides a micromachined interface between the macroscale sample preparation formats and the microscale analysis systems. There are many advantages to the micromachined pipettes, including the ability to transfer precise volumes of samples in the sub-μL range, the ability to handle samples/reagents in a highly parallel fashion by manipulating hundreds of samples/reagents simultaneously, and the compatibility with the size dimensions (center-to-center spacing) of the microscale biological/chemical analysis systems.

In addition to the use as a passive element for sample handling, the MPA can be used for multiple operations (passive and active). One example is the use of the MPA for mixing of multiple reagents, samples, and/or catalysts prior to loading onto a miniaturized biochemical analysis device, which is accomplished by joining several inputs into a single output (see Figure 1). The MPA can also be used for parallel loading of the same samples/reagents onto highly parallel microscale analysis systems by distributing a single input into several outputs.

System Components and Operation

The micromachined pipette array sample delivery system is composed of several major components that are connected together to create a complete system. As mentioned earlier, a MPA is used to precisely dispense sub-μL samples in a highly parallel fashion. A pump is used as a pressure source during dispensing of samples, while a machined interface and Teflon™ tubing are used to connect the pump to a MPA.

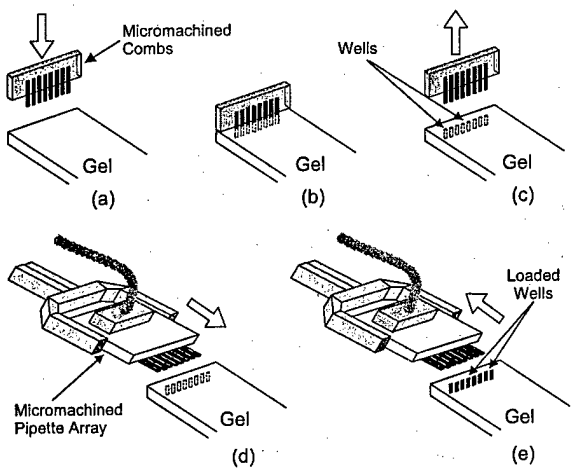


Figure 2. Schematic representation illustrating the use of the MPA in the high lane density slab gel electrophoresis. (a) Insert micromachined combs into prepared gel; (b) allow gel to polymerize; (c) remove micromachined combs forming wells in the gel; (d) load micromachined pipette arrays with sample and align with wells in the gel; (e) load samples onto the gel using syringe pump.

The pipette arrays can be operated in two modes, depending on application. In the first mode, termed precision dispensing, samples are loaded into individual pipettes through the free ends by capillary action. The inner dimensions of the individual pipettes precisely control the sample volume actually drawn. The samples loaded into the individual pipettes may be the same if a single source is used, or may be different in the case of a high-density titer plate. If a titer plate is used, the center-to-center spacing of the MPA must be the same as that of wells on the plate. Once the pipettes are loaded, a constant pressure is applied at the input ports until the samples are dispensed through the free end. The described method of sample manipulation is preferred when only small quantities of sample are available (e.g., genetic material) or when moving samples from one microscale analysis system to another.

In the second mode, termed continuous dispensing, a reservoir of buffer, sample, or a reagent is placed between a MPA and a pump. Continuous pressure applied by the pump is used to drive the solution into the pipettes through the backside input ports. Once solution is inside the pipettes, additional pressure results in a continuous flow from the pipettes via the free ends. The actual volume of the buffer solution dispensed is determined by the solution flow rate and the duration of the dispensing operation. In this case, the pipette inner dimensions are directly proportional to the flow rate through the pipette, nut do not determine the dispensed volume directly. The continuous dispensing mode is typically used when loading buffer solutions or reagents onto the microscale analysis systems. However, this mode may also be used for batch loading of samples onto multiple analysis systems.

Application to Agarose Gel Electrophoresis

The general methodology for using micromachined pipettes to enable high-density agarose gel electrophoresis is the same as that of a conventional gel electrophoresis process and involves three basic steps: gel preparation and sample loading, separation, and visualization of results. The last two steps in the process are identical to their conventional counterparts. Following preparation and sample loading, gels are placed in a buffer solution in a constant electric field and DNA fragments are separated. The gels are visualized using ethidium bromide dye under a UV light source.

The first step, gel preparation and sample loading, however, is different. While agarose gel is prepared as normal, the sample loading relies on micromachined combs and micromachined pipettes. The general technique is schematically shown in Figure 2. The approach involves five basic steps. Initially, the

agarose gel solution is mixed and poured into the form (Figure 2a). Next, the micromachined combs are inserted into the gel to form wells (Figure 2b). The teeth of the micromachined combs are spaced at the same center-to-center spacing as the pipettes of the MPA that will be used to load DNA samples. The teeth width and height are matched with the outside dimensions of the micromachined pipettes. The micromachined combs are necessary since the combs fabricated using the conventional machining methods are incapable of forming clean wells at close center-to-center spacing. The currently used "macromachined" combs have center-to-center spacing of 1.9 mm. While combs with smaller center-to-center spacing can be machined, the roughness of these combs is too high, which results in gels being ripped during well formation. The micromachined combs, on the other hand, are formed by microelectroforming and have very smooth surfaces, with relative roughness on the order of 0.00028. The process used to fabricate micromachined combs has been described in detail elsewhere [2]. The electrophoretic gel is allowed to polymerize micromachined combs inserted. Once gel is formed, micromachined combs are removed exposing the formed wells (Figure 2c). The DNA samples are loaded onto the gel by first loading the MPA using capillary action. Once samples are inside the micromachined pipettes, the MPA are visually aligned with wells in the gel (Figure 2d) and samples are dispensed in parallel (Figure 2e).

Using the described methodology, a 0.8% agarose electrophoretic mini-gel (7 cm × 10 cm) was prepared by first dissolving 0.56 g of agarose in 70 mL of 1× TBE buffer. This was accomplished by first heating approximately 70 mL of 1× TBE in a flask in a microwave for 2-3 min until agarose dissolves. Additional 1× TBE buffer was then added to the flask to yield to the total volume of 70 mL. The mixture was allowed to cool for approximately 5-10 min and was the poured into a plastic form. The micromachined combs were applied and the gel was allowed to sit for 30-40 min in order to completely set. Once agarose was polymerized, the micromachined combs were removed from the gel.

The DNA samples (1 kb ladder) were initially loaded into the MPA by capillary action by placing ends of the pipettes into a titer dish well containing the sample. During this process, the pipette array was disconnected from the syringe pump so that there was no backpressure. The DNA samples were dispensed onto the agarose gel by first aligning ends of loaded pipettes with wells formed by micromachined combs. A controllable syringe pump produced the buffer flow. Initially, the MPA was positioned so that the tips were just inside the wells. During dispensing, the MPA was gradually moved away from the gel, thus allowing to fill the wells. The buffer flow was stopped once the samples were transferred and the MPA tips have cleared the top of the wells. A photograph of the gel loading setup is shown in Figure 3.

Following sample loading, the agarose gels were for 2 hours at 7 V/cm (i.e. 70 mV of total electric potential). Micro-gel separations performed to date include those with lane center-to-center spacing of 1 mm, 500 μm, and 250 μm. The conventional center-to-center

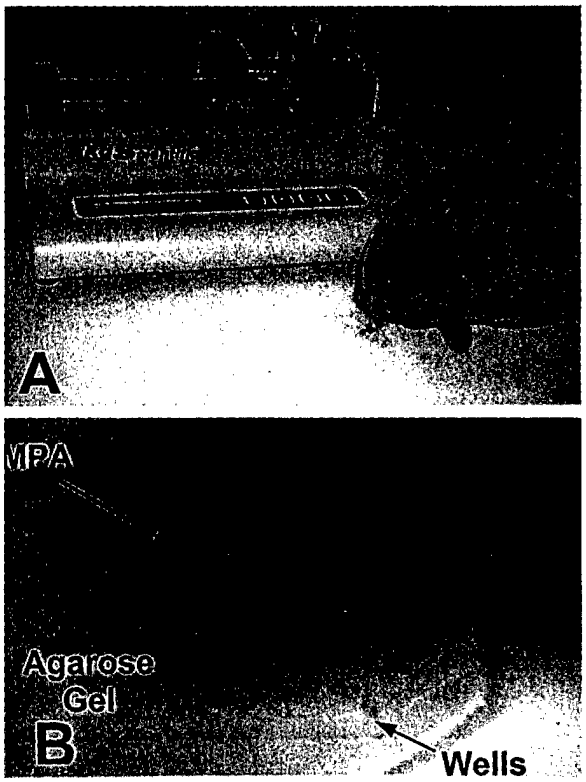


Figure 3. A. A photograph of the gel loading setup. The MPA loaded by capillary action are aligned with wells in the gel. Samples are dispensed using a syringe pump. **B.** A photograph of the micro-gel and the MPA during sample loading.

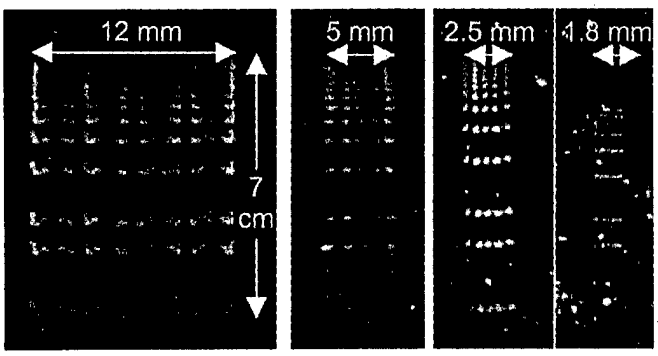


Figure 4. Photographs of slab gel separations of 1kB DNA ladder in mini-gel (left) and micro-gels with 1 mm, 500μm, and 250 μm lane spacing.

spacing of lanes on the mini-gel is 6 mm. Sample volumes of 0.5 μL are used in the micro-gels, while the mini-gels use the typical 5 μL volumes. The ten-fold reduction in sample size results in a nearly 55% reduction in intensity from approximately 119 counts to approximately 54 counts when gels are visualized using the fluorescent dye ethidium bromide staining dye under UV light following a separation. The signal intensity, however, is still very well measurable using state-of-the art low-light CCD imaging systems.

Photographs of gels taken under UV light following a separation are shown in Figure 4. The micro-gel separations can be seen clearly and are comparable to the mini-gel separation. The number of theoretical plates of the micro-gel separations is approximately 11,300 for 1 mm center-to-center spacing, 12,200 for 500 μm spacing, and 21,500 for 250 μm spacing. This corresponds to the 52%, 65%, and 190% increase, respectively, as compared to the mini-gel system (~7,400). The resolution is increased from 3.13 for the mini-gel system to 4.13, 4.28, and 5.34 for the corresponding micro-gel. Since the total length of the 2-hr separations is approximately 7 cm, the plate heights are calculated to be on the order of 10.4 μm for the mini-gel system and 6.4 μm, 6.1 μm, and 2.6 μm for the micro-systems. This means that the micro-gel system can perform separations in nearly half to a quarter the distance (i.e. time) of the mini-gel system.

MICROMACHINED THERMAL FIELD-FLOW FRACTIONATION (μ-TFFF)

TFFF is an elution separation technique similar to chromatography except the separation field is normal to the sample and carrier flow. TFFF utilizes thermal diffusion as the separation field instead of the gel, liquid, or column packing found in chromatographic separations. This field is accomplished by a temperature gradient across the channel. A schematic of the TFFF system is shown in Figure 5. Separation of the suspended particles are performed in a solvent carrier such as methanol, THF, acetonitrile, or DMSO. Many solvents have been used and there have been studies shown how these solvents affect separation characteristics [5]. Water is not typically used as a carrier fluid unless an electrolyte has been added. The particles in the solvent react to the temperature gradient by diffusing toward the cold wall. Higher molecular weight particles react more to the thermal gradient and are compacted more tightly against the cold wall than do lower molecular weight particles. Because of the laminar velocity profile of the carrier, samples that compact less will have a higher average velocity than the samples that compact more. The difference in average velocity results in the spatial and temporal particle separation at the output of the TFFF channel. [6]

The TFFF system has some unique characteristics making it more suitable for some separations than some conventional systems. In TFFF, the separation field is applied normal to the separation. The resolution requirement in the direction of separation is no longer needed, which means lower field strength, lower power consumption demands, and shorter separation times. TFFF also has the advantage of elution techniques, in that the samples are collected in fractions at given times. As a result, very pure samples can be obtained. [6]

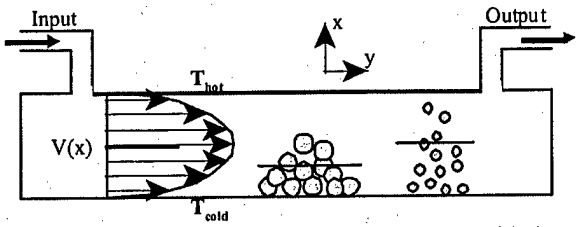


Figure 5. Schematic of a thermal field-flow fractionation (TFFF) channel.

In order for a separation in a TFFF channel to occur, there must be: 1, a difference in molecular weight or diameter of the samples; 2, a sample selective perturbation of the samples toward one wall; and 3, a laminar velocity profile that results in a different average velocity of each constituent of the sample [7].

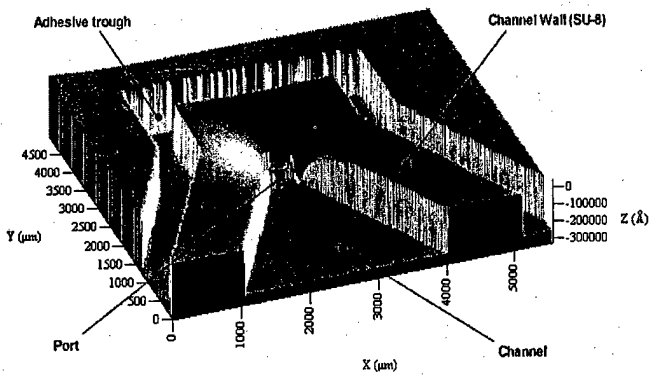


Figure 6. Profile of one end of μ-TFFF

The channel height is a critical parameter is the spatial resolution of two eluting samples. The channel height is inversely proportional to this resolution. Current systems have channel widths of about 127μm [7]. Micromachining technologies allow accurate and precise definition of channels of very small size. The channels fabricated for the μ-TFFF device are approximately 25μm. Smaller channels are achievable. As a result, higher resolution separations can be performed which means faster separations and more pure samples.

TFFF Experimental Methods

The μ-TFFF system was fabricated with an n-type, [100], single side polished, silicon wafer using common micromachining processes. A silicon dioxide (SiO_2) mask was thermally grown at 1200EC to approximately 1μm thick on the surface. Photolithographic techniques were used to define the input/output ports in the photoresist on the backside of the wafer. The SiO_2 mask was etched using a buffered HF solution. The ports were then anisotropically etched through the silicon wafer in 10% KOH at 90EC.

The SiO_2 was left on the wafer as an electrical insulating layer for the heaters. Titanium (Ti) was sputtered onto the backside of the wafer to about 1000Δ and patterned to define the resistive heater.

A negative photosensitive epoxy (SU-8) was spun on the wafer to a thickness of 25μm. The channel was defined in the SU-8 by UV exposure and developing, Figure 6. Heat treatment of the channel walls ensured a strong bond and durability when exposed to the carrier fluid, which is typically an organic solvent.

A glass microscope slide was adhered to the top of the SU-8 to complete the channel. After completing the fabrication of the μ-TFFF separation channel, the complete system was assembled (e.g. fluid interconnections, power supply, flow meters, detector, and fraction collector) and tested.

Using the μ-TFFF device fabricated as described in this paper, the total plate height was determined as a function of flow velocity for an unretained sample. DI water was used as the carrier and the sample was pure acetone. The flow rate of water was set by the pump. The flow rates used were 2.0, 1.75, 1.5,1.25, and 1.0 mL/hr. An acetone sample, 0.2μL, was injected into the input port at time zero for each flow rate. A detector measured the absorbance with respect to a sample of DI water. Data were collected with a computer.

The retention of polystyrene (PS) spheres was then tested in the system, since separation is based on the difference in retention for different sized particles. Although water is not typically used for TFFF separations because of the difficulty in performing separations in this medium, DI water was used to demonstrate the ability of the μ-TFFF system. The flow rate was set to 1.5 mL/hr to minimize the plate height. A temperature gradient of 40°C ($T_{hot\ wall}$=70°C, $T_{cold\ wall}$=30°C) was set up using the integrated heater and an external heat sink. A 0.2μL sample of PS spheres (394 nm) was injected into the system.

Micro TFFF Results

One end of a fabricated channel and port is shown in Figure 6. The channel height has been reduced from 127μm (macro-TFFF system) [7] to 50μm (μ-TFFF). A power of only 10 W was required to achieve a 20EC temperature difference across the channel. This power is more than 1000 times lower than that reported for a typical macro-scale TFFF channel. Plate height

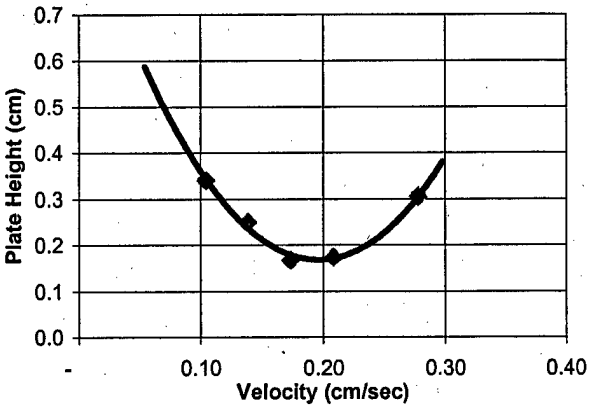


Figure 7. Plate height as a function of flow velocity. This result is typical of such a channel.

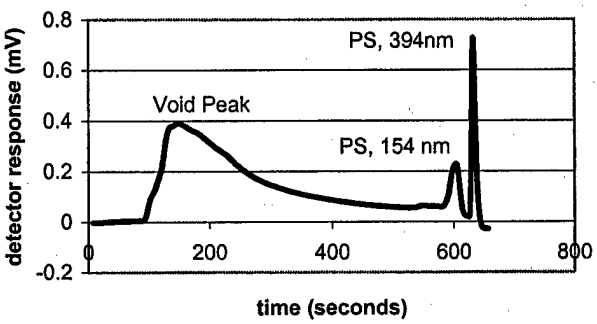


Figure 8. Retention of PS, 394nm spheres and separation with and unknown size PS impurity.

was determined as a function of average carrier velocity and compared with results from the μ-EFFF system [8] and TFFF theoretical results. The plate height curve is shown in Figure 7. The μ-TFFF plate height characteristics follow the curves that are found in the μ-EFFF channel as well as the theoretical curve for the TFFF system. The data are of lower magnitude than the sum of plate heights reported for retained polystyrene samples (MW_n:154k, 392k, and 735k). The temperature gradient was 30EC and toluene is the carrier. The channel dimension is 0.025cm × 1.2cm × 305cm. [9]

The PS-394 sample retention results are found in Figure 8. Three peaks appeared as a result of the test. The first peak is the void peak which contains unretained impurities. The sample was apparently not a pure 394nm PS sample. The other peak that showed up was an impurity of unknown size. This result indicated the effectiveness of the μ-TFFF system in purifying samples in preparation for further processing.

MICROMACHINED ELECTRICAL FIELD- FLOW FRACTIONATION

Another system with significant potential in the area of sample preparation with which we have been working is the micromachined electrical field- flow fractionation system (μ-EFFF). Electrical

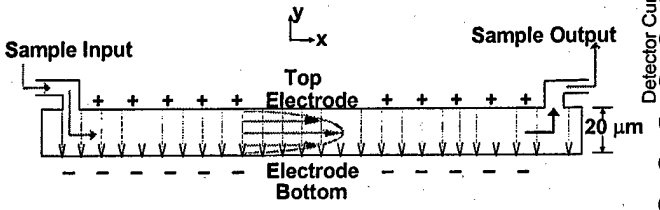


Figure 9. Schematic diagram of the operating principle for the EFFF system.

Field-Flow Fractionation is a particle separation technique that relies on an electric field perpendicular to the direction of flow and separation as shown in Figure 9. The separations are performed in a low-viscosity liquid (typically an aqueous buffer solution) which is pumped through the separation channel. EFFF controls the relative velocity of particles by forcing particles towards the wall of the channel. Particles with high charge density pack closer to the wall and move more slowly compared to particles of lower charge density that form a more diffuse cloud and move more quickly through the channel.

The channels for the miniaturized EFFF system are shown schematically in Figure 10 and are fabricated

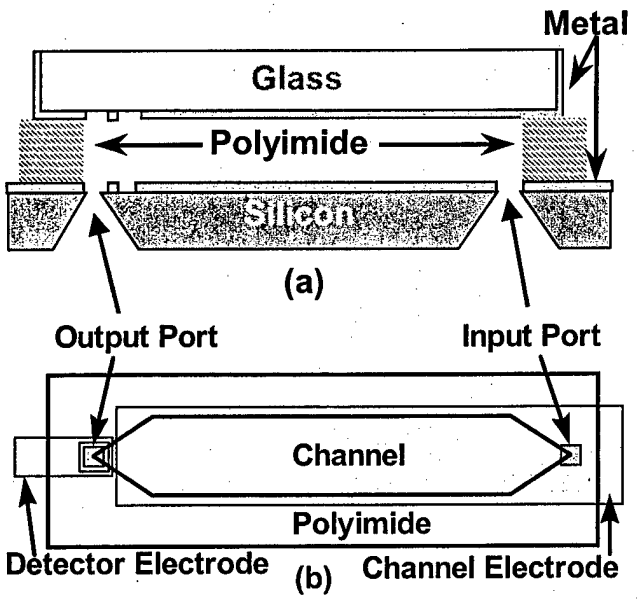


Figure 5. Schematic of channel and detector layout (a) Side view of channel (b) Top view of channel

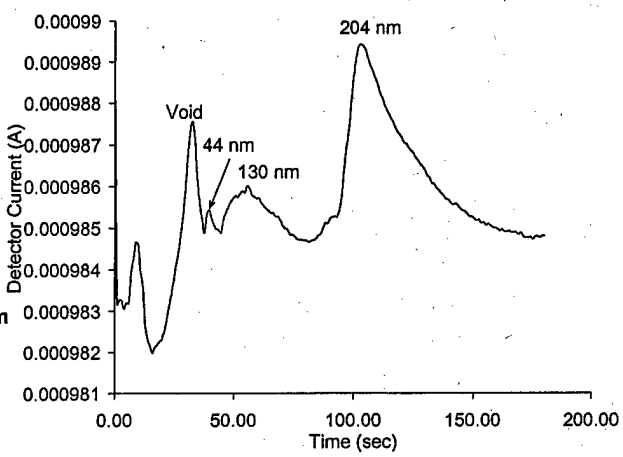


Figure 11. Separations of 44, 130, and 204 nm polystyrene particles with on-chip AC mode detector showing steadily increasing diameter of eluting particles. Voltage was 1.6 V, flow rate was 0.3 mL/hr and current was 27 μA.

by bonding a silicon substrate and a glass substrate together around a photolithographically defined polyimide spacer. Both substrates have metal thin films on their surface, which are patterned to define the electrodes for the channel and an electrical impedance detector. The input and output ports are fabricated in the silicon substrate using KOH etching and are 200 μm square on the interior of the channel and about 1 mm square on the external face of the silicon substrate. The channel dimensions are typically about 6 cm long, 1-6

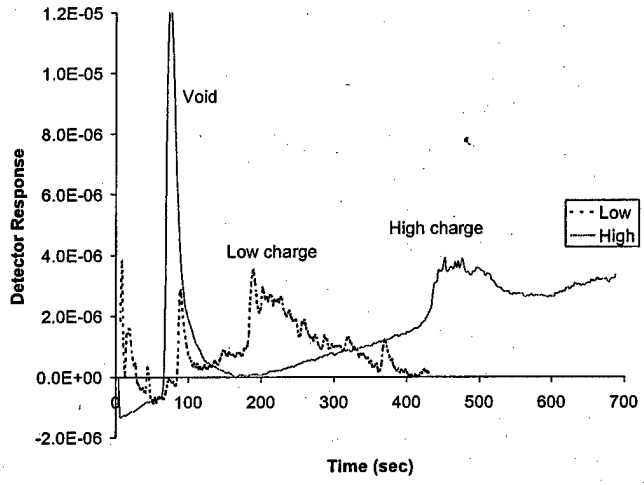


Figure 12. Fractograms of particles with the same diameter, but differing levels of carboxylation. The run labeled "low" had a lower density of COOH groups on the surface and a correspondingly lower surface charge, so the particles eluted sooner than did those with a greater surface charge, labeled by "high".

mm wide, and 10-50 μm in height. Fabrication and other information about the system have been reported previously [310]. The system also has an integrated electrical impedance detector that has been incorporated at the exit end of the channel [4,5,11,12].

One of the main advantages associated with EFFF is that it is an elution method that allows for the collection of fractions at the exit to the system. Thus, EFFF, which separates by particle size and charge, can produce a monodisperse sample for later analysis using another system. EFFF has an additional advantage in that it is a very gentle separation method and is suitable for cells, liposomes, micelles, fragile proteins, and other delicate structures and polymers. Particles ranging in size from about 5 nm up to about 1 μm in diameter are separable using a micromachined EFFF (μ-EFFF) system. Combining EFFF on a chip with other analysis systems would provide the opportunity for performance of a sample purification or separation step using EFFF and then, by simply redirecting the flow at appropriate intervals, allowing the analysis to continue in an orthogonal direction, using another system, or in a parallel direction using a similar system.

Micro EFFF Results

The μ-EFFF system has been demonstrated with a range of polymers as well as a few biological samples of interest. A typical separation is shown in Figure 11. In this figure, a high-speed separation of a three component mixture of polystyrene samples was accomplished. As demonstrated here, EFFF separates particles of similar material based entirely on the particle size. Thus a polydisperse sample would show up as a wide peak on the x-axis with each slice in time or volume representing a monodisperse sample. Accordingly, collection of a small volume of sample at a given location provides a well-defined, monodisperse sample for further analysis.

The micromachined EFFF system also has the ability to separate identically sized particles based entirely on electrophoretic mobility. In this case, the particles of lower charge will elute before particles with a higher charge as shown in Figure 12. The μ-EFFF would then also be available to prepare samples that differ only by surface charge characteristics.

A biologically valuable separation of this type was demonstrated in the μ-EFFF system when particles with adsorbed proteins were differentially retained from those without any adsorbed protein. The results of such an analysis are presented in Figure 13. An analysis of this type is very useful in biocompatibility and protein adsorption studies. Since particles with and without protein are retained differentially, particles with adsorbed proteins could be collected for later analysis, assuming they were the particles of interest. In addition, the wide peak for the particles with attached proteins indicates

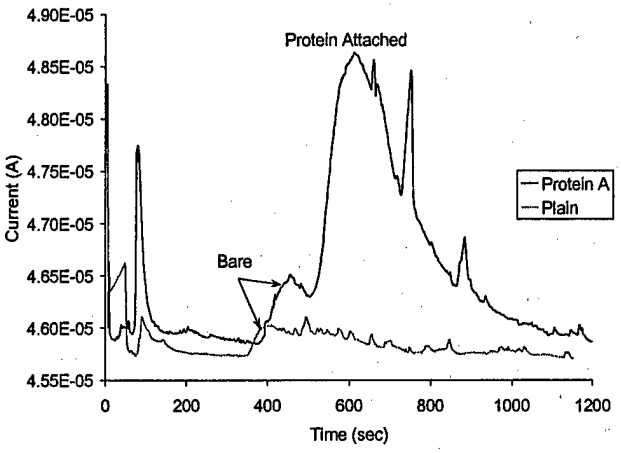


Figure 13. Fractograms of showing differential retention between bare particles and particles with attached proteins.

that there is a variation across the peak that corresponds to the amount of protein adsorbed to the particle. Thus, if particles were required to have a minimum level of protein attached to the particle, particles towards the end of the elution peak could be collected, or if a uniform number of attached proteins was required, a thin slice of the peak could be collected to create a monodisperse sample for later analysis.

EFFF also has the ability to retain a wide variety of particles contained in a single sample, such as a blood sample. Blood analysis is one of the most common medical procedures and the retention of a blood sample is demonstrated in Figure 14. While the cells found in blood are much too large to be significantly retained in a μ-EFFF system, the proteins and other

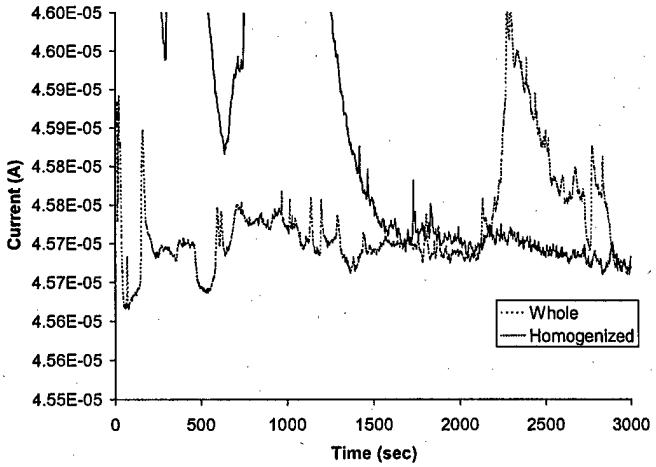


Figure 14. Comparison of whole blood and homogenized blood retained in the μ-ElFFF system focusing on the whole blood fractogram. Notice there is continual elution of particles during most of the run, but a strong peak appears near the end of the run in a range where no elution in the homogenized sample occurred.

particles found in blood are quite easily retained. Thus, the cells could be separated from the smaller particles, or the smaller particles can be collected for later analysis. In Figure 6, the same blood sample is shown for two different runs. In the first run, the retention of the whole blood is shown. The second run shows a sample that was homogenized in an ultrasonic bath. The homogenized sample shows the retention of the cell contents that were not present in the whole blood sample. In both cases, after the elution time is determined for the particle type of interest a fraction of that sample could be collected for later analysis. Thus, μ-EFFF demonstrates its ability to function as a sample preparation system for a wide range of analytes and particles of interest.

CONCLUSION

In this work, three miniaturized formats are discussed for integrated biochemical sample preparation. In each of the cases, mechatronics related technologies are needed in order to increase the degree of automation associated with the sample preparation system as well as the degree of automation associated with the overall miniaturized biochemical analysis system (with sample preparation as one of the sub-systems). Methods are needed for precise manipulation and placement of samples being delivered from and delivered to the micro scale sample preparation systems.

REFERENCES

[1] Handbook of Microlithography, Micromachining, and Microfabrication, Editor: J. Rai-Choudhury, SPIE Press, Vol. 2, Chapter 1, 1997.

[2] I. Papautsky, J. Brazzle, H. Swerdlow, and A. B. Frazier, "A low temperature, IC compatible process for fabricating surface micromachined metallic microchannels," *IEEE J. Microelectromech. Syst.*, vol. 7, no. 2, pp. 267-273, 1998.

[3] I. Papautsky, J. Brazzle, H. Swerdlow, and A. B. Frazier, "Micromachined pipette arrays," *in Proc. 19th International Conference of the IEEE Engineering in Medicine and Biology Society (EMBS '97)*, Chicago, IL, Oct. 30 - Nov. 2, pp. 2281-2284, 1997.

[4] Ian Papautsky, John Brazzle, Timothy Ameel, and A. Bruno Frazier, "Parallel fluid manipulation using micromachined pipette arrays," in *Proc. SPIE Micro Fluidic Devices and Systems*, Santa Clara, CA, Sep. 21-24, pp. 104-114, 1998.

[5] Sisson, R.M., Giddings, J.C. Nov. 15, 1994. *Effects of solvent composition on polymer retention in TFFF.* Analytical Chem., 66, pp. 4043-4053.

[6] Caldwell, K.D. *1987. Field-flow fractionation of biological materials.* Dept. of Bioengineering, University of Utah.

[7] Lou. J.Z. March 1994. *Studies on the theory and applications of polymer separation by thermal field-flow fractionation.* Ph.D. Thesis, University of Utah, Salt Lake City, Utah. p. 37.

[8] Gale, B.K., Frazier, A.B., Caldwell, K.D., *Characterization. of a μ-EFFF system*, MEMS '97, pp. 119-124.

[9] Hovingh, M.E., Thompson, G.H., Giddings, J.C. Feb. 1970. *Column parameters in TFFF.* Analytical chem., 42, pp. 195-120.

[10] B. K. Gale, K. D. Caldwell, and A. B. Frazier, "A Micromachined Electrical Field- Flow Fractionation System," *IEEE Tran. on Biomedical Engineering*, vol. 45, no. 12, pp. 1459-1469, 1998.

[11] B. K. Gale, K. D. Caldwell, and A. B. Frazier, "Electrical conductivity particle detector for use in biological and chemical micro-analysis systems," in *Proc. SPIE Symposium on Micromachining and Microfabrication: Micro Fluidic Devices and Systems,* 1998, pp. 230-242.

[12]B. K. Gale and A. B. Frazier, " Electrical impedance-spectroscopy particle detector for use in microanalysis systems," in *Proc. SPIE Symposium on Micromachining and Microfabrication: Micro Fluidic Devices and Systems,* 1998.

Mechatronic Micro Devices

Frank Michel[1], *Wolfgang Ehrfeld*

Institut für Mikrotechnik Mainz GmbH (IMM)

Carl-Zeiss-Strasse 18-20, D-55129 Mainz

Germany

Abstract:

Nowadays, novel trends can be observed in micro system technology: Micro systems more and more develop into stand-alone devices for multi-purpose applications, and they do not only comprise detector elements but really interact mechanically by micro actuators with their surroundings. A modular concept especially for high performance actuators which proved to be a main prerequisite for these developments is illustrated in the contribution.

With dimensions of a few millimeters, piezo-driven valves and membrane pumps overcome fluid pressures of 1,000 hPa. Electromagnetic motors generate torques of 7 to 100 µNm which are multiplied by adapted micro gears.

Gear motors serve as a key unit for high force micro positioning systems or micro gear pumps which are first examples for the device level.

With the integration of electronics and optics the actuator performance can considerably be increased by establishing a feedback control and the systems become really micro mechatronic devices. Additionally, interface components like electrical and fiber-optical connectors with pitches as small as 250 µm, special gears and miniaturized clamping structures enable the implementation of complex optical fiber networks, micro robots or chemical micro reactors from these mechatronic devices in a construction kit.

A wide range of 3D-micro fabrication techniques, from design and simulation, micro spark erosion (µ-EDM) for the prototypes to mass technologies like LIGA including injection molding, allows a fast commercialization into "micro product lines" and will round the circle of the considerations on the mechatronic micro devices.

1 INTRODUCTION

Meanwhile, micro systems are widely used in all domains of our daily life but they are hardly recognized. This is due to the fact that most of them are integrated into mass-products and specialized for the one application they are developed for. Airbag sensors in passenger vehicles or laser heads in CD players illuminate that fact impressively. Another example are print heads of ink jet printers which only work in the specified printers and use only one type of fluid – ink. On the other hand ink printer heads are at least stand-alone micro devices in the geometrical sense. And they interact, like more and more modern micro systems do, with their surroundings. The mechanical or fluidic interaction is executed by small but powerful actuators. Chosen from a huge variety of physical principles, nowadays piezo-electric and electromagnetic actuators have found industrial use. Those actuators are mostly fabricated in a hybrid concept by combining advanced 3D micro fabrication methods with assembly and interconnection techniques. At IMM, they are manufactured as components for universal use in order to increase both production output and application fields. Finally, multi-purpose components subsequently lead to multi-purpose micro devices.

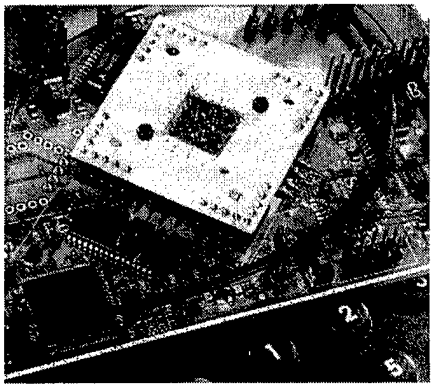


Fig. 1.1: 4 x 4 fiber-optical matrix switch to be used for monomode fibers

A typical example is shown in Fig. 1.1. This 4 x 4 fiber-optical switch which contains 16 micro actuators [1] can flexibly be applied in high speed computers, communication networks and even in automobiles, where electrical cable harnesses are increasingly replaced by fiber-optical nets.

The contribution will follow the described modular concept starting with universal actuator components and actuation units developed at IMM. Via intelligent and stand-alone mechatronic devices it leads to complex micro systems where the modules can be rearranged and interact via mechanical, electrical, optical and fluidic interfaces. In Germany, a standardization of microproducts and interfaces has been started by applying this modular concept [2].

[1] phone +49 6131 990-178, fax +49 6131 990-205, email michel@imm-mainz.de, http://www.imm-mainz.de

1999 INTERNATIONAL SYMPOSIUM ON
MICROMECHATRONICS AND HUMAN SCIENCE
0-7803-5790-6/99/ $10.00 ©1999 IEEE.

2 ACTUATOR COMPONENTS

2.1 Micro valves

At present, there is a continuously growing demand for miniaturized valves in a wide range of applications: Valves in cold gas jet systems applied for space applications need to be lightweight and should deliver an ultra-short response time. Valves for printing devices or for chemical micro reactors must be small and cheap because a high number of valves has to be arranged in large arrays.

A promising approach which solves the mentioned requirements is shown in Fig. 2.1 [3]. In closed state, a ruby ball, which is commercially available down to a diameter of 300 µm, is pushed against the valve seat by the fluid pressure. To open the valve, the ball is flung into the valve cavity by hitting the valve seat with a piezo stack. When piezo actuation is finished, gas pressure of up to 2,000 hPa pushes the ball back in less than 1 ms.

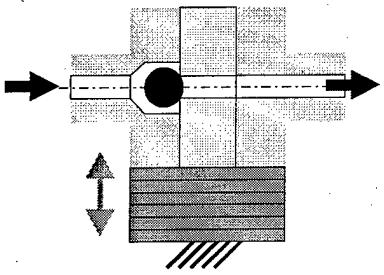


Fig. 2.1: Principle of a micro "ball valve"

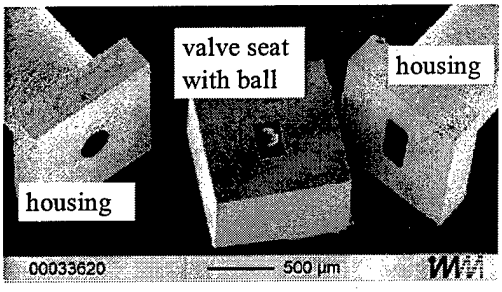


Fig. 2.2: Components of the micro valve

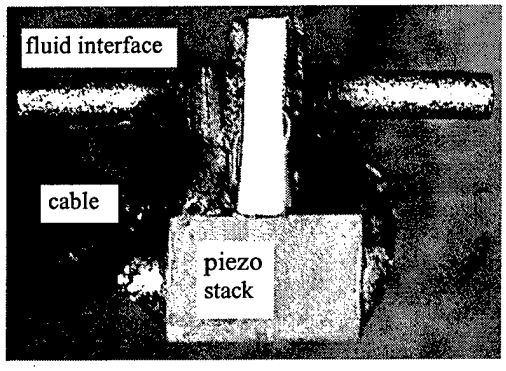


Fig. 2.3: Assembled micro valve

Valve prototypes were successfully realized with different ball diameters. The valve seats were made of silicon by Advanced Silicon Etching in a wafer process. For the machining of the housings a combination of micro die sinking and wire EDM was used which allows a series production in steel (Fig. 2.2). Fig. 2.3 shows an assembled valve.

2.2 Membrane pumps

Micro membrane pumps are attractive means for drug dosing in medicine, reagent delivery in chemical applications or adhesive dispensing in semiconductor industry. Furthermore, new application fields arise for dosing of lubricants for machine tool bearings or with pump arrays for high-throughput screening in chemical analysis.

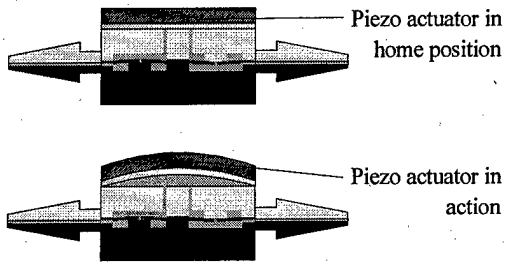


Fig. 2.4: Principle of the micro membrane pump

Pumps suitable for the mentioned specifications and working according to the simple principle shown in Fig. 2.4 were realized by silicon machining in many places. However, costs remain considerably high due to the large lateral size of 10 to 20 mm. Cost-efficient series production was achieved by switching to polymers like PC, PEEK or COC. Top and bottom part, which are injection molded, and membrane foils with 2 µm thickness are connected hermetically by laser welding. Finally, the bimorph piezo plate is glued onto the outer foil.

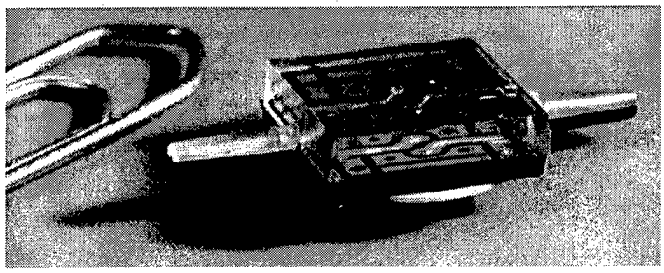


Fig. 2.5: Membrane pump with plastic parts. Size: 12 x 12 x 3 mm³

The self-filling membrane pump is already commercially available [4]. Maximal pressure and maximal flow rate are

- up to 2,000 hPa and 400 µl/min for water,
- up to 500 hPa, down to -350 hPa (vacuum) and up to 3,500 µl/min for air.

Oil has been delivered up to a viscosity of 220 mm²/s.

2.3 Electromagnetic motors

High precision motors with millimeter size have become a key element for minimal-invasive diagnostics and surgery as well as for miniaturized scanners in datacom or positioning drives e.g. for micro robots and hand held consumer devices. The rapid commercialization of miniaturized electromagnetic motors illustrates the urgent need for those motors but also the improved possibilities in micro technology to fabricate them. Four years ago the smallest motors amounted to 8 mm in diameter, except smaller low cost motors for pager devices. At present, a well-stepped product line (Fig. 2.6) is offered down to a motor with 1.9 mm in diameter which was developed in cooperation with Dr. Fritz Faulhaber GmbH & Co. KG in Schönaich, Germany

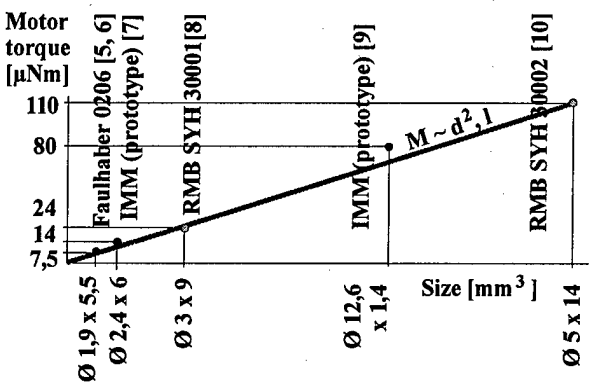


Fig. 2.6: Commercially available electromagnetic micro motors

All longish motors [5, 6, 7] are constructed in a similiar way: A diametrically magnetized rare-earth magnet in the rotor follows the rotary field of a three-phase winding which is fixed in a soft magnetic housing tube (Fig. 2.7).

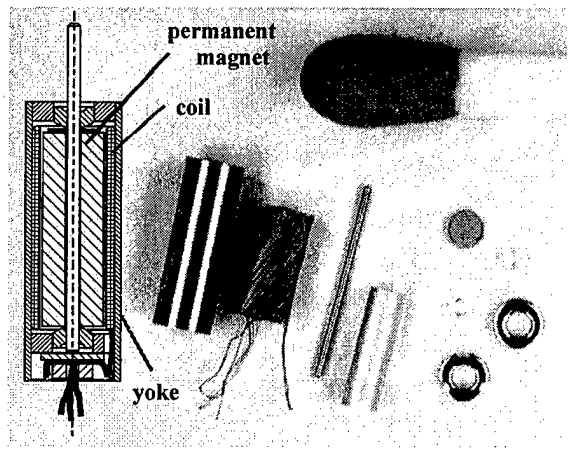


Fig. 2.7: 1.9 mm motor. Principle and components

In addition to the longish types a penny shaped electromagnetic motor as thin as 1.4 mm was developed ([8], Fig. 2.8). The rotor contains 8 permanent magnets and a soft magnetic return yoke which encloses the flat coil array in the stator.

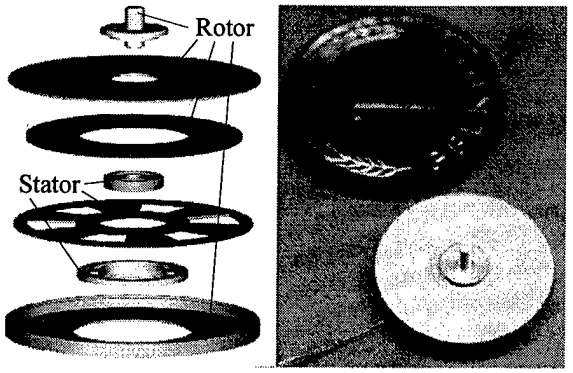


Fig. 2.8: Construction and realization of the "Penny motor"

Magnetic field simulation has turned out to be a key element to speed up the development and to improve motor behavior. Fig. 2.9 shows the magnetic flux inside the Penny motor which is concentrated in the yoke and crosses permanent magnet, axial air gap and coil. The magnetic simulation carried out with the software program ANSYS shows how the ball bearing can be pre-stressed by an additional softmagnetic ring in the stator in order to avoid yaw motion of the rotor axle. Furthermore, a magnetic scatter field hardly appears.

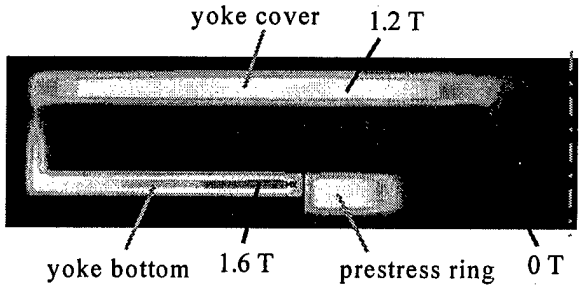


Fig. 2.9: Penny motor. Simulation of the magnetic field

For series fabrication of the motor, precision engineering technologies are combined with micro techniques which are advantageous for coil arrays, electrical interconnection and encoders.

Due to the very small radii extremely high accelerations and rotation velocities up to 100,000 rpm in continuous operation are reached. The motor torque scales almost directly to the volume and ranges from 7 to 110 µNm (see also Fig. 2.6).

2.4 Reduction gears for gear motors

In order to adapt the high speed of the micro motors to the industrial requirements of 100 to 5,000 rpm and in order to increase output torque considerably, miniaturized reduction gears with similar sizes and shapes are needed. In the contribution suitable gears for the 1.9 mm and the Penny motor are introduced:

The development of a gear with 1.9 mm diameter started by choosing a planetary gear type suitable for miniaturization. A special variant of a Wolfrom's gear shown in Fig. 2.10. contains only five parts: a sun wheel as input, three planet wheels without additional bearing and two ring wheels [9]. The tooth numbers of the ring wheels differ by three which causes a slow relative motion between the ring wheels. A careful profile correction guarantees that both ring wheels are in exact contact with the planets. One of the ring wheels is fixed to the housing, the other one serves as output.

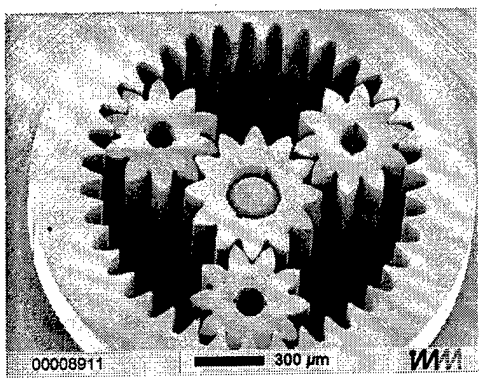


Fig. 2.10: Wolfrom's gear made by LIGA. Material: PMMA (resist). Gear modulus: 38 µm. Gear ratio: 47

Although prototypes of the Wolfrom's gear were successfully realized, for series production another gear type was chosen due its modular construction, the better gear efficiency and an easier assembly: the simple planetary gear. The realized gear (Fig. 2.11) is a three stages gear and contains plastic parts fabricated by LIGA technique (Fig. 2.12, [5]). For mass production a through-going batch process was developed where hundreds of gear components are molded simultaneously in a wafer-like magazine. Each stage is assembled separately. The gear, which was developed together with Dr. Fritz Faulhaber GmbH & Co. KG and is commercially available, may deliver an output torque of up to 300 µNm in short-time and 150 µNm in continuous operation.

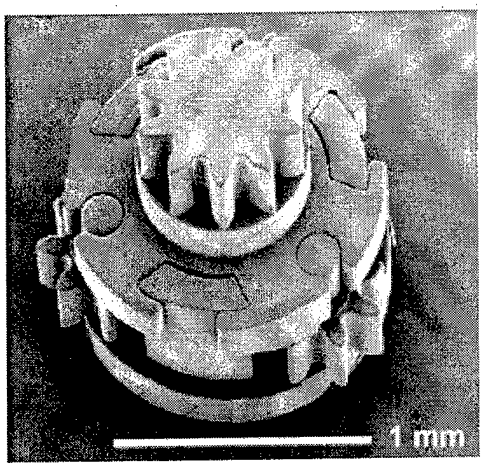


Fig. 2.11: Stage of the simple planetary gear. Parts are made of POM by LIGA incl. injection molding. Gear modulus: 55 µm. Gear stage ratio: 3.6

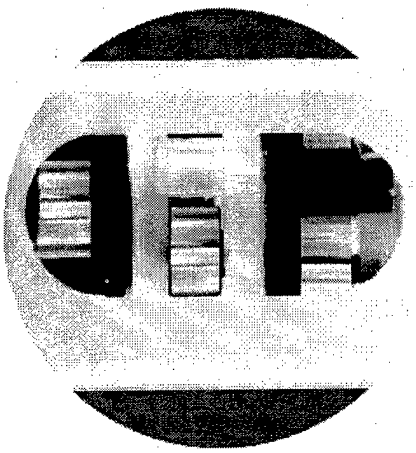


Fig. 2.12: Three-stage planetary gear with housing opened for visualization. 17 plastic parts, steel shaft and brass bearing for output. Gear size: Ø 1.9 x 4 mm³. Gear ratio: 47

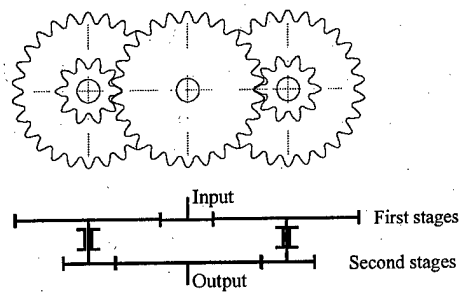


Fig. 2.13: Principle of a two-train spur gear

Gears for positioning tasks should hardly exhibit backlash. Consequently, a two-train spur gear with almost zero backlash was developed. Its working principle is shown in Fig. 2.13. Because of its rectangular cross-section and the lack of radial forces onto input and output shaft the two-train spur gear was applied in a linear positioning system (see section 3.2) to transmit the motor motion to a miniaturized spindle (Fig. 2.14, [6]).

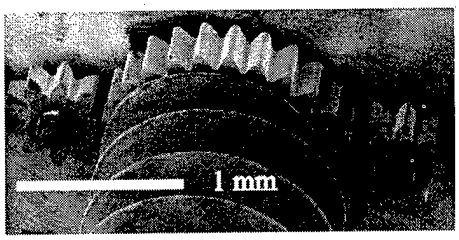


Fig 2.14: Second stages of the two-train spur gear. NiFe wheels made by LIGA. Gear modulus: 55µm. Whole gear ratio: 7

The Penny motor (see Section 3.3) with its flat shape is perfectly suited to miniaturized rotary positioning systems, if a flat gear with high gear ratio and zero backlash is integrated. Therefore, the harmonic drive with dynamic spline as output proves to be an excellent solution but extremely difficult to miniaturize. By realizing the wave generator by a simple planetary gear with two flexible planets the overall diameter

could be kept as small as 8 mm and a gear ratio of 505 – in one stage – could be achieved. High aspect LIGA technique turned out to be the prerequisite to realize the prototype shown in Fig. 2.15, which is illustrated impressively especially by the flex spline. Its inner and outer toothing have moduli of 34 µm and 35 µm respectively. While the tooth width is as high as 1 mm the ring, thickness amounts to only 40 µm. That means an aspect ratio of 25 is achieved.

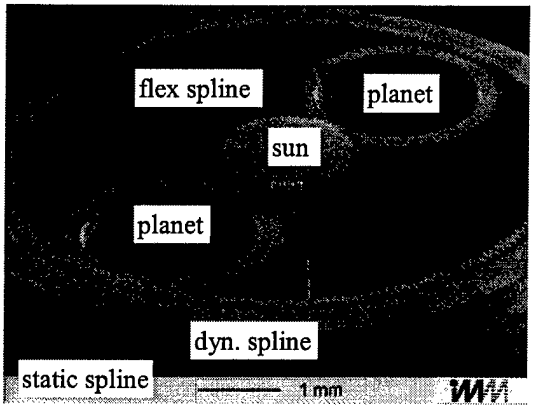


Fig. 2.15: Micro harmonic drive.
NiFe wheels made by LIGA. Gear moduli: 34 µm and 35 µm respectively.
Gear size: Ø 8 x 1 mm². Gear ratio: 505

The described examples show that miniaturization of reduction gears down to millimeter size can be achieved by applying 3D micro technologies, especially LIGA technique. The development may be executed step-wise by using high aspect ratio lithography and electroplating steps for prototypes and, eventually, injection molding for series production.

3 ACTUATOR DEVICES

3.1 Gear pumps

The same procedure occurs at the development of micro gear pumps where motor, gear and fluidic elements are combined to small micro devices as shown in Fig. 3.4. Fig. 3.1 demonstrates mechanisms to transport high viscous fluids even with solid particles by the roll off of two gear wheels. The pump with the oval wheels provides a larger pump room which increases flow rate and allows a higher size of solid particles or a more careful delivery of sensitive fluids like blood.

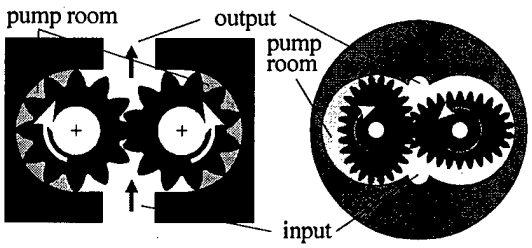


Fig. 3.1: Principles for micro gear pumps with an external gear pair

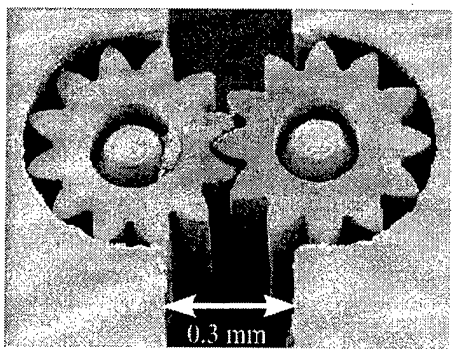


Fig. 3.2: Demonstrator of a gear pump with circular wheels Ø 0,6 x 0,5 mm²

A prototype of the circular pump has been realized by using LIGA wheels with a modulus of 38 µm and a brass housing which was conventionally milled (Fig. 3.2, [4]). Tests of the circular gear pump show a linear relationship between flow rate and rotary speed of the wheels, while pressure hardly has an influence on the flow rate. For a mixture of glycerin and water a maximum flow rate of 170 µl/min could be achieved at 2250 rpm up to a pressure of 1,000 hPa. The pressure was limited by the motor power. Depressions at the axial cavity faces, which lead to considerable axial gaps between housing and wheels, turned out to be the significant factor for further improvements. For that reason, the LIGA technique was also used for the housing, which is shown, together with two oval gears, in Fig. 3.3. Furthermore, the gear height was increased to 2 mm while keeping the axle base at 1 mm. In a next step injection molding of housing and wheels is prepared.

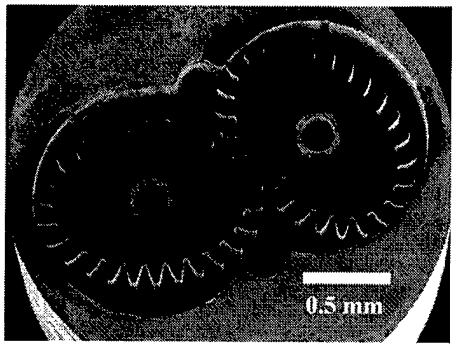


Fig. 3.3.: Gear pump with oval wheels made of NiFe by LIGA.
Gear size: Ø 0.9 to 1.3 x 2 mm². Gear modulus 40 µm

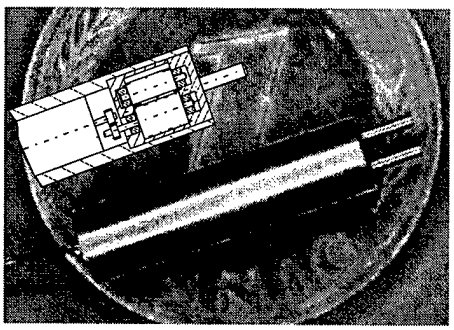


Fig. 3.4: Oval gear pump. Demonstrator Ø 3,4 x 11 mm² with micro motor

3.2 Miniaturized linear positioning systems

Miniaturized linear positioning systems have turned out to be a basic unit for an ultra-wide range of applications. Examples are robots and grippers for the production and handling of semiconductors and optical fibers, means for positioning, adjusting, focussing or zooming of lenses or fiber-optics in datacom, telecom or consumer products and the manipulation of cells and tools in medicine and biology. Besides required overall dimensions in the centimeter range and smaller, typically such devices have to provide a quick and precise travel over a positioning range of some centimeters and against forces up to 1 N. Additionally, they must fit to the rather low prices of the systems they will be integrated into.

Chosen from various principles like piezoelectric, pneumatic, and hydraulic actuators or electromagnetic linear motors the following arrangement proves to suit best to the mentioned requirements: a modular construction with rotary motor, gear and a unit to transmit the motion to a slider, which is guided in a housing. Following this concept, two prototypes of miniaturized linear positioning devices have been developed:

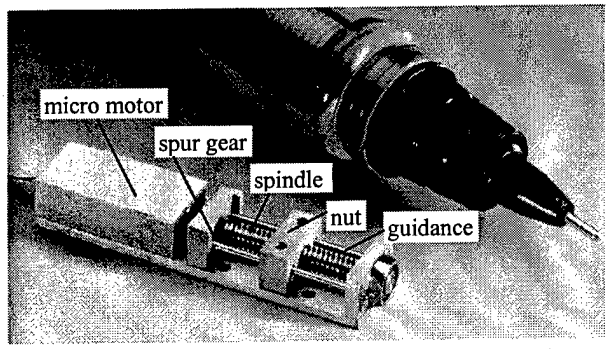


Fig. 3.5: Open loop controlled linear stage compared to a pen

The linear stage shown in Fig. 3.5 [6] contains a micro motor (Fig. 2.7), a two-train spur gear (Fig. 2.14) and a miniaturized spindle which drives a friction guided nut. Spindle-nut drive and guidance are fabricated mechanically. Compared to the small size of 24 x 5 x 3.5 mm³ the performance (travel range 7.5 mm, speed up to 10 mm/s, forces up to 0.15 N) is respectable. Although backlash hardly appears in gear and spindle-nut drive the positioning deviation amounts to a rather high value of ±20 µm due to the open loop control.

Consequently, the micro positioning device in Fig. 3.6 which was developed for the company Festo AG & Co. in Germany obtains a close loop control including a linear encoder which directly gauges the slider motion ([10], see Section 3.3). By applying modules like the micro motor (Fig. 2.7) and planetary gear (Fig. 2.12) and ultra-precise fabrication of steel slider and housing by wire EDM, the performance was considerably increased (40 x 6 x 4 mm³ overall size, 20 mm travel range with a velocity of up to 40 mm/s, a force of up to 0.75 N and an accuracy of ±5 µm).

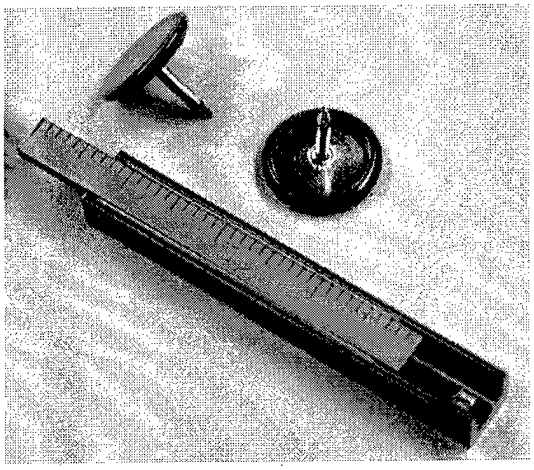


Fig. 3.6: Micro positioning device with close loop control compared to two thumbtacks

3.3 Integration of electronics and optics

In the beginning, all described mechanical and fluidic modules have been connected via long wires and tubes to external control units which have often come up to show-box size. However, performance and application field can incredibly be enlarged by integrating electronics and optics which establishes mechatronic micro devices. First experiences have led to an unexpected result: The development of a special ASIC often turns out to be the second choice. By a slight redesign of the mechanical and fluidic construction, standard electronics can be applied which reduces costs considerably.

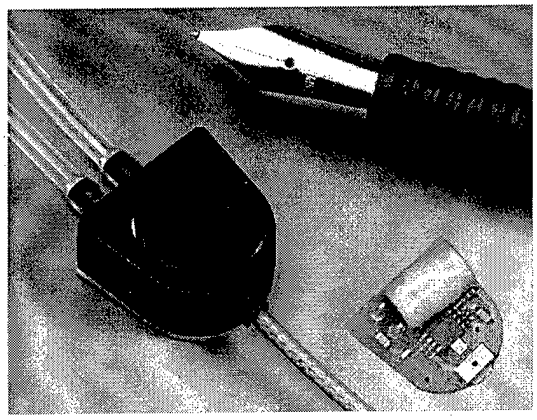


Fig. 3.7: Membrane pump with integrated electronics compared to a fountain pen

The piezo actuator of the membrane pump shown in Fig. 2.5 was provided with the required signal of +330 V to –90 V by a high voltage cable which has caused a lot of problems especially in medical application. Consequently, a miniaturized PCB assembled with standard components has been developed which could be integrated into the redesigned membrane pump shown in Fig. 3.7.

A similar development occurs for motor control. By switching from sinusoidal to square signal the controller PCB of the Penny motor (Fig. 2.8) could be shrunk to motor, i.e. penny size (Fig. 3.8). In the next step, COB technique and the integration of magnetic sensors will allow both to integrate the controller into the motor and to increase performance considerably by the implementation of a close loop control.

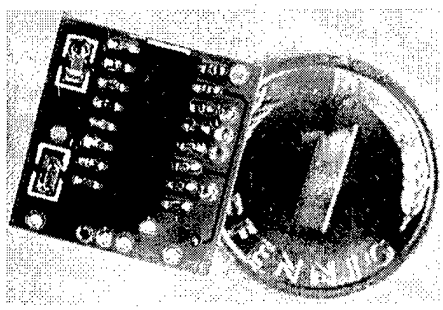


Fig. 3.8: Square signal control unit for the Penny motor. Size: 13 x 13 mm²

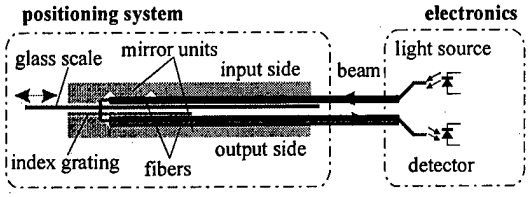


Fig. 3.9: Principle for a miniaturized optical encoder

In order to integrate a linear measuring system into the miniaturized positioning device shown in Fig. 3.6 an incremental optical encoder working with transilluminating IR light was developed [10]. By locating the laser diodes and photo detectors outside the stage (Fig. 3.9) the cross-section of the sensor head amounts to only 1.2 x 1.3 mm². The sensor head contains glass scale and index grating (5 µm lines and spaces, thickness of 100 µm) and two mirror units (Fig. 3.10). Sensor head and control unit are connected via four optical fibers which avoids electrical noise or disturbing signals from other sources. The resolution of 2.5 µm, which is achieved by counting the crossovers of the two sinusoidal signals, can considerably be improved by an electronic interpolation.

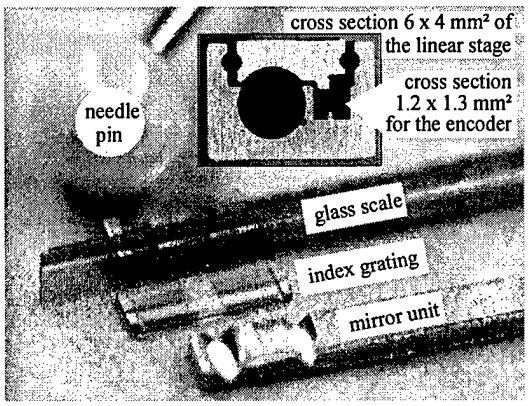


Fig. 3.10: Components of the sensor head of the optical encoder

4 INTERFACES

In order to connect micro modules or devices to more complex systems, miniaturized electrical, optical mechanical, and fluidic interfaces are an inalienable prerequisite.

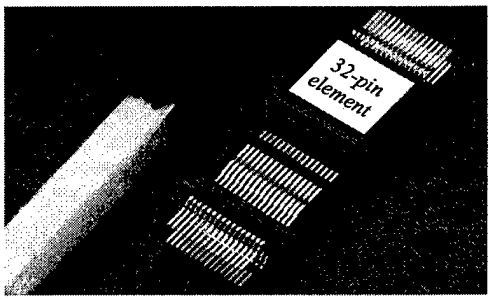


Fig. 4.1: Electrical connector with a pitch of 250 µm. 32 pins. 2 x 5 x 9 mm³

The electrical 250 µm pitch connector in Fig. 4.1, which was developed in close cooperation with Siemens Electromechanical Components GmbH & Co. KG in Speyer, Germany, provides extraordinary means both for the interconnection of small devices like micro robots by the single connectors and of large PCBs by the system unit shown in Fig. 4.2. The float mounting of eight separate connectors, which provides the system unit with 256 pins, allows a working temperature from -30 to +125°C. With a density of 3.2 pins/mm² for the single connector and 1.6 pins/mm² for the system unit, a reliable two-point contact, which permits a current up to 250 mA at 25°C, a break-down voltage as high as 650 V (AC) and 750 V (DC) resp., and, last but not least, an excellent HF behavior allowing signal frequencies up to the GHz range, the 250 µm pitch connector stands at the leading edge of electrical micro pitch connectors. Fabricated by technologies like injection molding suitable for mass production the 250 µm pitch connector could establish a standard for the electrical interface of mechatronic micro devices.

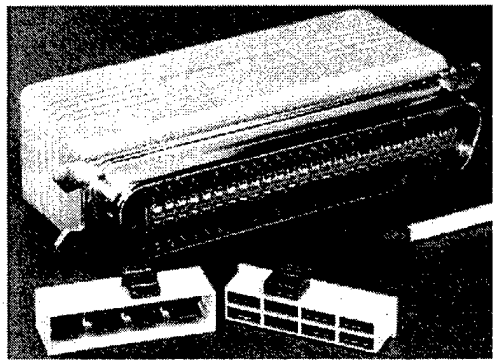


Fig. 4.2: System unit compared to a common SCSI-connector. Size: 25 x 6.4 x 9 mm³. 256 pins formed by eight 32-pin elements

The same pitch of 250 µm was established for fiber optics. The ferrule for 12 multi- or single-mode fibers (Fig. 4.3) is just being commercialized and can also be coupled with hybrid units e.g. for light sources or detectors. The ferrule may serve as an optical interface e.g. for the linear encoder.

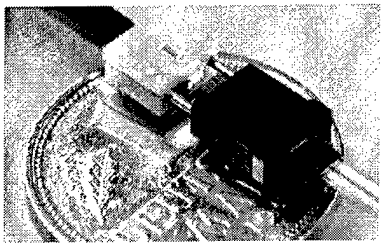


Fig. 4.3: Ferrule for 12 single-mode fibers together with a processing device

Mechanical interfaces have hardly been developed because actuators capable to interact mechanically with their surroundings have just come to market (Section 2.3). According to first experiences in micro robotics [6] gears may better serve as mechanical interfaces than micro "couplings" like polymer tubes. Although gears from precision mechanics like spur gears, crown gears (Fig. 4.4) or belt drives cause friction losses of 5 to 20 µNm, rotary motion has successfully been coupled between robot modules and transmitted over distances of several millimeters or even between twisted shafts.

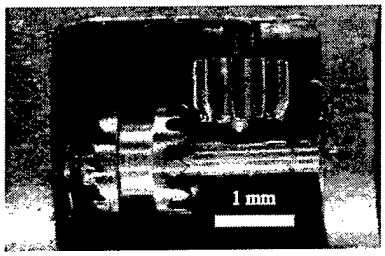


Fig. 4.4: Crown gear in a micro racing car

In order to mount modules of chemical micro reactors together like children's LEGO bricks, an easy-to-handle clamping interface has been developed including direct fluid couplings (Fig. 5.1). Standardization is just as much needed as for miniaturized electrical, optical, and mechanical interfaces.

5 SUMMARY AND OUTLOOK

While fiber-optical networks, including a large variety of mechatronic devices like MUX, DEMUX, connectors, and switches, already encompass the whole world, micro mechatronic systems for fluidic and mechanical purposes are still at their beginnings.

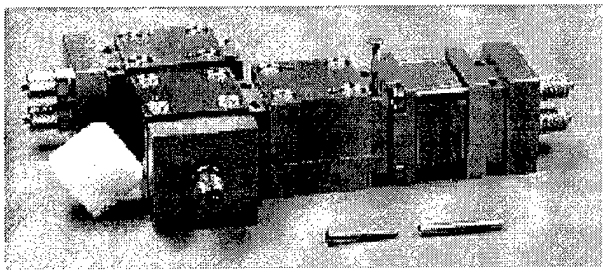


Fig. 5.1: Modular chemical micro reactor compared to a sugar cube

A construction kit for chemical micro reactors (Fig. 5.1) with mixers, heat exchangers, valve arrays and pumps is a first fluidic micro system already realized. This concept of a flexible fab with a daily interchange of the reactor modules may change the face of chemistry and pharmacy in near future.

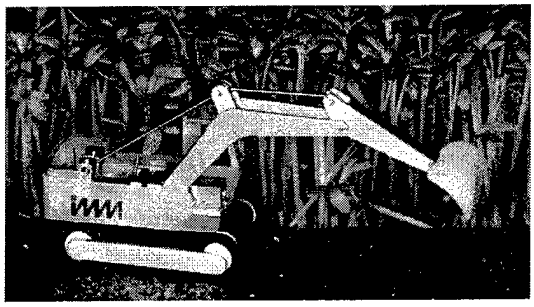


Fig. 5.2: Micro digger, 63 mm long, compared to garden-cress

An approach to mechanical systems are micro robots. A funny example shown in Fig. 5.2 contains 3 motors, 2 planetary gears, a spur gear and a linear stage as standard components.

An intensified commercialization of electrical, optical, mechanical and fluidic micro components and a quick definition and standardization of the interfaces is going to accelerate the development of complex mechatronic micro systems.

6 REFERENCES

[1] J. Hoßfeld, W. Ehrfeld, M. Neumeier, S. Sigloch: Polymeric micromechanical switches. Proc of MOEMS'99. pp. 92-99, Mainz (D), Aug 1999

[2] V. Großer, M. Schünemann, B. Michel, H. Reichl: A design and production framework for modular microsystems. To be published at Proc. of MHS'99, Nagoya (J), Nov. 1999.

[3] DE 3835788 C2.

[4] O. Soerensen, K. Drese, W. Ehrfeld, H.-J. Hartmann: Micromachined Flow Handling Components – Micropumps. To be published at Proc. of Chemical Microsensors and Applications II, SPIE Vol. 3857, Boston (MA), Sept. 1999.

[5] U. Berg, M. Begemann, B. Hagemann, K.-P. Kämper, F. Michel, C. Thürigen, L. Weber, Th. Wittig: Series Production and testing of a micromotor, Proc. of Actuator'98, pp 552-555, Bremen (D), June 1998.

[6] F. Michel, W. Ehrfeld, U. Berg, R. Degen, F. Schmitz: Electromagnetic driving units for complex microrobotic systems. Proc. Microrobotics and Micromanipulation. pp. 93-101, SPIE Vol. 3519. Boston (MA), 1998.

[7] Data sheets of High Precision Motor SYH30001 and SYH50002. RMB SA, Biel (CH), Sept. 1997.

[8] M. Nienhaus, W. Ehrfeld, H.-D. Stölting, F. Michel, S. Kleen, S. Hardt, F. Schmitz, T. Stange: Design and realization of a penny-shaped micromotor. Proc. of Design, Test, and Microfabrication of MEMS and MOEMS. pp. 592-600, SPIE Vol. 360 Part 2, Paris, 1999.

[9] C. Thürigen, W. Ehrfeld, B. Hagemann, H. Lehr, F. Michel: Development, fabrication and testing of a multi-stage micro gear system. Proc. of Tribology issues and opportunities in MEMS, pp. 397-402, Columbus (OH), November 1997, Kluwer Academic Publishers, 1998.

[10] R. Degen, U. Berg, G. Broerkens, W. Ehrfeld, F. Michel, M. Neumeier: Ultra small micro positioning system for high force, high velocity and long travel range with a built-in linear encoder. Proc. of MOEMS'99, pp. 113-119. Mainz (D), Aug. 1999.

Invited Lectures

Challenge to Micro/Nanomanipulation Using Atomic Force Microscope

Hideki Hashimoto and Metin Sitti
Institute of Industrial Science, University of Tokyo
Roppongi, 7-22-1, Minato-ku, Tokyo, 106-8558, Japan

Abstract — With the improving micro/nanotechnologies recently, micro/nanomanipulation technology has also become indispensable where such technology is in its early infancy. Thus, this presentation focuses on using Atomic Force Microscope (AFM) as a promising sensory robotic tool for challenging micro/nanomanipulation applications. AFM probe is proposed to be utilized as a mechanically contact pushing manipulator, and force and topology sensor. The focused task is the 2-D pushing of micro/nanometer size particles on a substrate in ambient conditions. Thus, the modeling of interaction forces and dynamics during pushing operation is analyzed for understanding the nano scale physical phenomenon which is different from macro robotics physics. Experiments of 2-D precise positioning of micro/nano gold-coated particles are reported. The results show that latex particles can be positioned on silicon substrates successfully, and AFM probe can be a promising sensory manipulator.

1 Introduction

Nanotechnology which aims at the ideal miniaturization of devices and machines down to atomic and molecular sizes has been a recent hot topic as a promising high-technology for the forthcoming century. By precise control of atoms, molecules or nano scale objects, new sensors and man-made materials, tera-byte capacity memories, micro scale robots/machines, DNA-computers, quantum devices, micro scale distributed intelligence system devices with integrated sensors, actuators and communication tools, etc. would be possible within the near future. However, for new nanotechnology products, still there are many challenges to be solved, and nano manipulation is one of the important challnges at the nano world. This kind of research is still immature since the physical and chemical phenomenon at this scale has not been completely understood, intelligent automatic precision manipulation strategies are not developed, and the specific tools for the specific applications have not been defined/designed clearly. Thus, the purpose of this paper is to propose an Atomic Force Microscope (AFM)-based force controlled pushing system with physical analysis of the manipulation tool (AFM tip) and micro/nano scale object physical interaction for 2-D positioning and assembly of micro/nanoparticles.

AFM is a 3-D atomic resolution microscope which uses the interatomic force measurement principle for helding the topology images. Its mechanicsm is mechanical, and can be applied to imaging of all types of particles/samples which are fully or semi-fixed on a substrate with homogenous surface stiffness and adhesion force properties. Changing its function from only imaging to both imaging and manipulation, new challenging problems are introduced. At first, the particles on substrates should be *semi-fixed* in order to be able to move them. The solution to this problem could be using non-contact mode AFM imaging for not moving the particles during imaging as proposed by [1]. However, the selection of the absorption chemicals is a difficult issue depending on the type of the substrate and particle (for Au particles, Silane is used for Si subtrates, and Ploy-L-Lysine for mica substrates [2]). Next, the mechanism of interatomic forces and dynamics should be understood for precise positioning of the particles [3]. However, the micro/nano mechanics for this kind of application has not been developed completely. Moreover, real-time monitoring of the manipulation process is almost impossible. Since the same tool is used as either the imaging or manipulation tool at an instant, imaging is not possible during pushing operation. As one approach to this problem, researchers scan the area, where the target particle is, before and after the manipulation [4], [5], [6], [7], [8]. Thus, by using some fixed reference features, the new relative position of the particle is obtained from the images. However, this imaging is still off-line and the problems during pushing cannot be understood by this way. On the other hand, the other way is utilizing the force feedback information during pushing for reliable manipulation [9], [10], [11]. Another approach may be using using high-resolution external Scanning Electron Microscope imaging while this can be done only in vacuum environments, tip and particle can be obscured, and only some specific particles can be imaged by this way.

In this paper, possible solutions are proposed for the above challenging problems of AFM-based pushing. Force and dynamics modeling of the pushing operation, using real-time force feedback instead of real-time visual feedback or another external microscope during pushing,

1999 INTERNATIONAL SYMPOSIUM ON
MICROMECHATRONICS AND HUMAN SCIENCE
0-7803-5790-6/99/ $10.00 ©1999 IEEE.

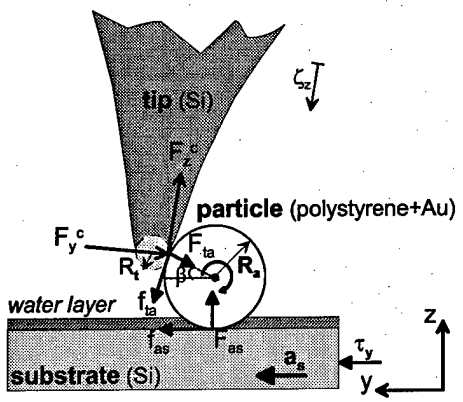


Figure 1: Positioning of the nano particles by the AFM tip contact pushing.

and using non-contact (tapping) imaging mode for imaging and contact-mode for pushing are to be realized. A home-made AFM system with piezoresistive detection is constructed, and simulation and experimental results are compared for gold-coated latex particle pushing applications.

2 Physical Modeling of 2-D Nano Particle Manipulation

In this paper, gold-coated latex particles absorbed on silicon substrates are to be pushed using a silicon fabricated AFM cantilever tip in ambient conditions as shown in Figure 1.

2.1 Manipulation Strategy

AFM-based pushing is realized by the motion steps as shown in Figure 2.

- $A \rightarrow B$ (*auto-parking*): the tip is automatically moved at z-direction until detecting the contact by the substrate by measuring the cantilever deflection (absolute tip-substate distance is not known initially), and retracted back to a predetermined parking position,
- $B \rightarrow C$ (*auto-particle contact detection*): the tip is moved along the substrate until detecting the particle by cantilever deflection detection, and then stopped,
- $C \rightarrow D$: pushing the particle for a desired distance by moving the tip or the substrate with a constant speed,
- $D \rightarrow E$: after completing the pushing operation, retracting back to the initial height.

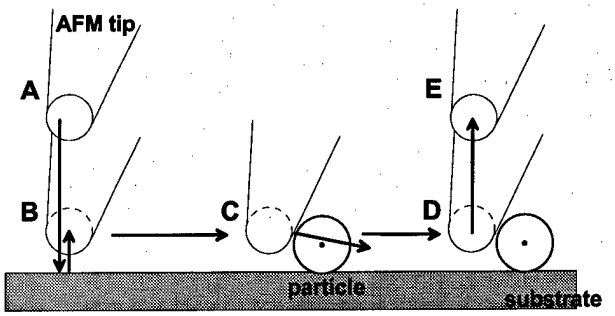


Figure 2: AFM-based particle pushing strategy.

2.2 Interaction Forces in Air

The interatomic force $F_z(t)$ between the AFM tip and elactic sample which is perpendicular to the cantilever is attractive or repulsive. Gravitational forces are relatively very small, and therefore negligible. These forces should be understood in order to control them for precise manipulation and interpret the cantilever deflection curves. A typical deflection curve of the cantilever depending on the tip-sample distance is shown in Figure 3 for a silicon AFM tip and silicon flat sample. The main components of the interatomic forces are van der Waals, capillary, electrostatic and indentation/repulsive forces. These forces are to be analyzed for modeling the tip-sample interaction. As the notation, the (-) force means the attractive and (+) do repulsive forces.

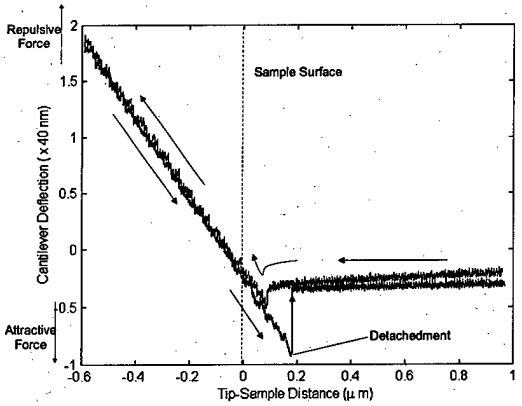


Figure 3: The typical cantilever deflection, i.e. interatomic force, and tip-sample distance relation.

2.2.1 Van der Waals Forces

It exists for every material in every environmental condition (like the gravitational force in the macro world), and depends on the object geometry, material type and relative distance. Assuming the interaction of the spherical cantilever tip with a spherical absorbate/particle, the exact additive solution becomes as [12]:

$$F_{vdw}^{ta}(h) = -\frac{H(h+r_+)}{3}\left\{\frac{2R_aR_t}{h^2(h+2r_+)^2} + \frac{2R_aR_t}{((h+r_+)^2-r_-^2)^2} + \frac{1}{h(h+2r^+)} - \frac{1}{(h+r^+)^2-r_-^2}\right\}, \quad (1)$$

where $r_+ = R_t + R_a$, $r_- = R_t - R_a$, R_t and R_a are the tip and particle radius respectively, $h = h(t)$ is the tip-particle distance, and H is the Hamacker constant. In most cases, $h >> R_a$ kind of assumption is made for micro particles, but for the nanoparticles, exact solution would be more proper. Since there is always a liquid (water) layer on the sample in air conditions, $H = \{(H_{tip} - H_{liquid})(H_{particle} - H_{liquid})\}^{1/2}$ [13]. For the particle-substrate interaction, van der Waals force becomes as:

$$F_{vdw}^{as}(h) = -\frac{H}{6}\{\frac{R_a}{h^2} + \frac{R_a}{(h+2R_a)^2} - \frac{1}{h} + ln\frac{1}{(h+2R_a)}\} \ . \quad (2)$$

2.2.2 Capillary Forces

For the capillary force between the tip and particle, including solid-solid adhesion force $F_{s-s}^{ta} = 2\pi\tilde{R}\gamma_{SL}$,

$$F_{cap}^{ta}(h) = -\frac{2\pi\tilde{R}\gamma_L}{1 + \frac{h-a_0}{2r_1}}u(h-L) - F_{s-s}^{ta} \ , \quad (3)$$

where $\tilde{R} = R_t R_a/(R_t + R_a)$ using the Derjaguin approximation, r_1 is the meniscus curvature radius (r_1 can be approximated as $r_1 \approx -0.54/log(P/P_s)(nm)$ using Kelvin equation [13] assuming a water layer at $20C^o$ where P/P_s is the relative humidity ratio), $L = L_l$ during approaching and $L = \delta$ during retraction where $L_l \approx 2r_1$ is the thickness of the water layer, and δ is the breaking length of the meniscus which is determined by the JKR contact mechanics modeling as $\delta = 0.132(6\pi\tilde{R}^{1/2}\gamma_L/K)^{2/3}$ where $1/K = [(1-\nu_t^2)/E_t + (1-\nu_a^2)/E_a]$, and E_t and E_a are the Young modulus, and ν_t and ν_s are the Poison's coefficients of the tip and particle respectively. γ_L is the liquid surface energy (for water $\gamma_L = 72mJ/m^2$), and γ_{SL} is the surface energy between solid-liquid interface. Often $\gamma_L > \gamma_{SL}$, and the F_{s-s} force can be ignored.

For the particle and substrate, i.e. F_{cap}^{as}, above equations are changed such that $\tilde{R} \to R_a$, $F_{s-s}^{ta} \to F_{s-s}^{as}$, and $\gamma_L \to 2\gamma_L$ where $F_{s-s}^{ta} = F_{s-s}^{as}$ in our case.

2.2.3 Electrostatic Forces

Grounding a (semi)conducting substrate such as Si, Au or HOPG, the electrostatic forces are reduced. However, in the case of polystyrene latex particles, there are charges trapped around the perimeter of the particles, and during pushing or contact, triboelectrification introduces local charges. Since the particles are not picked up, the electrostatic force between the particle and substrate is not important. But, after pushing, the charge on the particle is transfered to the tip which can cause an electrostatic force between the particle and tip (then particles can stick to the tip during retraction which is observed in some cases experimentally). As solution to this problem, the latex particles are coated with Au, and by grounding all the substrate and particles, electrostatic forces can be negligible. However, still a model for the electrostatic forces is desirable for general cases.

It is assumed that the all objects are free of charge at the beginning. But, after contacting with the objects, contact electrification and triboelectrification occurs, and forces due to these charges should be computed.

For the work functions of ϕ_1 and ϕ_2 of two surfaces, resulting voltage difference is $U = (\phi_1 - \phi_2)/e$ where $e = 1.6 \times 10^{-19}$ C is the e^- charge. Then the electrostatic force becomes as:

$$F_{el}(h) = -\frac{\epsilon_0 U^2 S}{2h^2} \ , \quad (4)$$

where ϵ_0 is the permittivity, and S is the shared area. For the tip-particle interaction, $S = 4\pi\tilde{R}r_1$, and $U = 0.25$ V for gold-coated particle surface and silicon tip. For the gold-coated particle and silicon substrate, $S = 4\pi R_a r_1$, and $U = 0.5$ V. Then for $R_t = 30$ nm, $R_a = 250$ nm, $r_1 = 1.7$ nm, and $h < 10$ nm, F_{el}^{ta} is in the order of 10s of pN which can be almost neglected.

2.2.4 Indentation/Repulsive Forces

Since the contact area between the particle and tip is very small, only the deformation between the particle and substrate along the z-axes is considered [14]. Assuming still in the range of continuum mechanics, JKR contact model [15] is selected for approximate contact area prediction. Adding the short-ranged adhesion forces, for spherical tip and flat surface, JKR model results in the following equations:

$$P_z = Ka^3/R_a - \sqrt{3\pi\omega K a^3}$$
$$\delta = a^2/R_a - 2/3\sqrt{3\pi\omega a/K}$$
$$a^3 = R_a/K(P_z + 3\pi R_a\omega + \sqrt{6\pi R_a\omega P_z + (3\pi R_a\omega)^2}) \quad (5)$$

where P_z is the applied load along the z-axes, ω is the adhesion energy, and a is the contact radius.

2.2.5 Frictional Forces

During pushing, the friction between the particle and substrate plays an important role. The definition of the friction at the micro/nano scale can be given as:

$$f_{as} = \mu_{as}(A_{as} + F_l^{as}) \ , \quad (6)$$

where $A_{as} = 4\pi R_a\gamma_L$ is the adhesion force, and F_l^{as} is the external load. Also, there is a friction between the tip and particle such that

$$f_{ta} = \mu_{ta}(A_{ta} + F_l^{ta}) \ , \quad (7)$$

with $A_{ta} = 2\pi\tilde{R}\gamma_L$.

2.3 Sample Preparation

Preparation of dispersed nanoparticles is a challenging issue, and JEOL Co. particles which are dispersed with

a scattering gun on a silicon substrate is utilized for the experiments.

As the design issue, the above forces should be checked for the selected particle and substrate geometry and material type, and environmental conditions such that:

- during tip-particle approach and separation, the adhesion forces should not result in sticking of the particles to the tip,
- static frictional forces should be smaller than the applied load in order to be able to move a particle.

More detailed analysis results in following conditions for helding above features:

$$R_a > 0.5\tilde{R}sin\beta \ , \tag{8}$$

$$\mu_{as}^s \geq \frac{\tilde{R}cos\beta}{2R_a} = \frac{cos\beta}{2(1+R_a/R_t)} \ . \tag{9}$$

where μ_{as}^s is the static friction coefficient for particle-substrate interaction. First equality is always correct which shows the advantage of the sharp parabolic (spherical) tip apex structure. For the second one μ_{as}^s is calculated depending on R_a where $R_t = 30\ nm$ is fixed in our system. For $R_a = 10\ nm$, $\mu_{as}^s \geq 0.014$, and for $R_a = 1000\ nm$, $\mu_{as}^s \geq 0.35$. Here, μ_s cannot be selected arbitrarily since then the particle may not be pushed. For reducing this problem, μ_{as}^s should be selected as $\mu_{as}^s \approx cos\beta/2(1 + R_a/R_t)$, and a stiff cantilever should be used for enough pushing load.

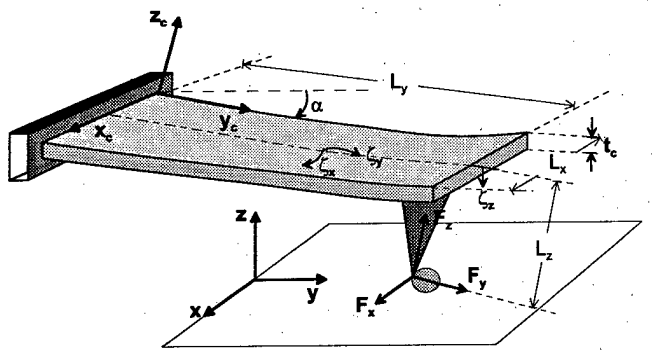


Figure 4: Cantilever bending along x-y-z axis during pushing nano objects.

2.4 Cantilever Dynamics and Position Control

Denoting the deflections along the x, y and z axis as ζ_x, ζ_y and ζ_z respectively as shown in Figure 4, the deflection vector is defined as $\zeta = [\zeta_x\ \zeta_y\ \zeta_z]^T$. Taking the force vector as $\mathbf{F} = [F_x\ F_y\ F_z]^T$, and assuming the cantilever with the normal stiffness of k_c is tilted by an angle of α along the x-axes, the deflection is determined by the forces as follows [16]:

$$\zeta = \mathbf{CF}$$

$$\mathbf{C} = \frac{1}{k_c}\begin{bmatrix} c_1 & 0 & 0 \\ 0 & c_2 & c_3 \\ 0 & c_3 & 1 \end{bmatrix} \tag{10}$$

where $c_1 = 2L_z^2/L_y^2 + t_c^2/L_x^2$, $c_2 = 3L_z^2/L_y^2$, $c_3 = 3L_z/(2L_y)$, L_x, $L_y and\ L_z$ are the cantilever lengths along the x-y-z axis, and t_c is the cantilever thickness. Thus, the important point is, the cantilever cannot be modeled as three decoupled springs for an accurate modeling where y and z axis are coupled. Using our piezoresistive deflection measurement system [?], [?] only ζ_z can be measured (also ζ_x can be measured if the optical detection method is utilized which is our future work). Then, the measured deflection corresponds to:

$$\zeta_z = (c_3F_y + F_z)/k_c \ . \tag{11}$$

Thus, the lateral force of F_y has also affect on ζ_z. Assuming the change of the normal force is negligible during the pushing operation, the change in F_y, i.e. ΔF_y, can be computed as:

$$\Delta F_y = k_c\Delta\zeta_z/c_3 \ . \tag{12}$$

This means that the F_y frictional force component corresponding to the applied pushing load can be observed from ζ_z directly.

Piezoelectric XYZ actuators are utilized for atomic resolution positioning. These actuators have hystheresis and drift problems depending on the motion duration and range, and temperature changes. For imaging, since xy motion consists of scanning with specified constant range, actuators can be calibrated off-line using laser interferometry, and these calibration data are then can be used for accurate scanning (in the case of commercial AFMs). However, in manipulation tasks, the tip moves on arbitrary user-defined or automatic points in a given range; thus, open-loop control is almost not reliable. Therefore, the best is to integrate high resolution sensors such as capacitive, strain gauge, LVDT, or optical sensors to motion axes for closed-loop control. In our system, a Physick Instrumente XYZ closed-loop stage (P-762.3L) with 10 nm resolution, 0.1 % hystheresis error and 100μm range in all axes is utilized. The dynamics of the stage along the y-axes can be given as [17]:

$$\frac{1}{\omega_y^2}\ddot{y}_s + \frac{1}{\omega_y Q_y}\dot{y}_s + y_s = \tau_y - f_{as} \ , \tag{13}$$

where $\omega_y = 2\pi f_y$, $f_y = \sqrt{k_y/m_s}/(2\pi) = 250\ Hz$ is the y-stage resonant frequency with m_s and k_y are the stage and sample total mass and k_y is the y-axes stage stiffness, $Q_y = 20$ is the amplification factor, y_s denotes the sample y-axes position, and τ_y is the stage driving force.

2.5 Pushing Mechanism

For simplifying the notations and graphs, the particle is assumed to be pushed along y-axis where same notation

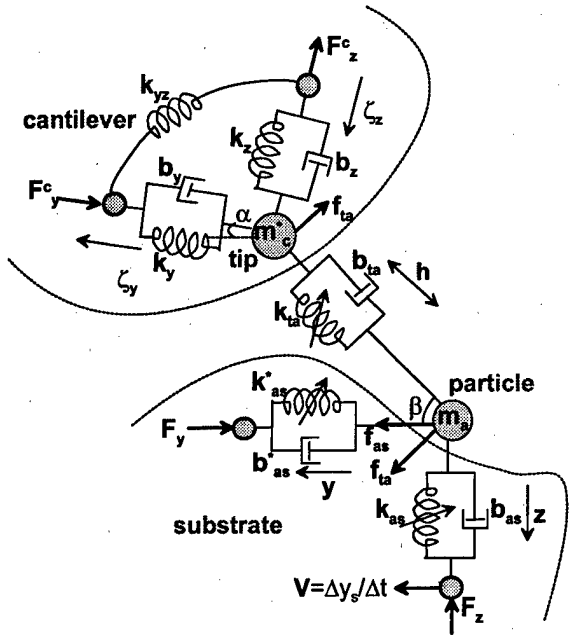


Figure 5: Point-mass model of the contact pushing mechanism along the y-axes.

and models can be extended to the x-y motion case directly. The interacting forces during pushing are shown in Figure 5. The parameters shown in the model are given as follows: $k_z = k_c$, $k_y = k_c/c_2$, $k_{xy} = k_c/c_3$, $b_z = b_y = 2\pi f_r m_c^*/Q_c$ where f_r is the cantilever resonant frequency and Q_c is the quality factor in air, $m_c^* = k_z/(4\pi^2 f_r)$ is the cantilever effective mass, m_a is the particle mass, $V = dy_s/dt$ is the *constant* y-stage speed, h is the tip-particle indentation depth, $k_{as}^* = 8R_a G^*$ with $G^* = ((2-\nu_a)/G_a + (2-\nu_s)/G_s)^{-1}$ where G_a and G_s are the shear modulus for the particle and substrate respectively, $k_{ta} = -\partial F_{ta}/\partial h$, b_{ta} is the tip-particle damping term which is negligible, $k_{as} = -\partial F_{as}/\partial z$, b_{as} is the particle-substrate damping, $k_{as}^* = 0.85 k_{as}$ [18], and $b_{as}^* \approx 0$.

During the pushing operation, there are two main phases: static friction and kinetic friction regions. At the beginning, due to the satic friction, the particle and tip follow the stage motion along y-axes until to the point where the applied cantilever load exceeds the static friction between the particle and substrate. In this region following equations are held at the equilibrium points assuming a slow motion:

$$\begin{aligned} f_{as} &= F_y^c cos\alpha + F_z^c sin\alpha \ , \\ f_{as} &= \mu_{as}^s(y)(F_{as} + A_{as}) \ , \\ F_{as} &= F_y^c sin\alpha - F_z^c cos\alpha \ , \\ F_y^c &= k_y y cos\alpha \ , \\ F_z^c &= k_z y sin\alpha \ , \\ F_y &= k_{as}^* y \ . \end{aligned} \tag{14}$$

Here, $\zeta_y \approx y cos\alpha$, $\zeta_z \approx y sin\alpha$, $y = y_s$, $z = \delta$ from the JKR model using Eq. (5) with $P_z = F_{as}$. At the shearing point $y = y^*$, $f_{as} = \mu_{as}^s(F_{as}(y^*) + A_{as}) = F_y(y^*)cos\alpha + F_z(y^*)sin\alpha$. Then y^* can be computed as

$$y^* = \frac{\mu_{as}^s 4\pi R_a \gamma_L}{k_y cos^2\alpha + k_z sin^2\alpha - \mu_{as}^s sin\alpha cos\alpha (k_y - k_z)} \ . \tag{15}$$

From this relation, the condition for enabling the particle pushing can be given as $y^* \geq 0$ which means that $\mu_{as}^s \leq (k_y cot\alpha + k_z tan\alpha)/(k_y - k_z)$. For example, for $\alpha = 15^o$, $k_z = 8\ N/m$ and $k_y = 1427\ N/m$, $\mu_{as}^s \leq 3.45$. Connecting this equality with Eq. (9):

$$\frac{cos\beta}{2(1+R_a/R_t)} \leq \mu_{as}^s \leq \frac{k_y cot\alpha + k_z tan\alpha}{k_y - k_z} \ . \tag{16}$$

After the particle is separated from the substrate surface, following cases may occur: pure sliding, stick-slip motion and rolling. The case of sliding is analyzed in [19].

3 Force-Controlled Pushing

Using the real-time ζ_z feedback during pushing, following force-controlled pushing strategies can be proposed: z-position , xy-position, or xyz-position controlled pushing. The z-position and xy-position controlled pushing control schemes are shown in Figure 6 and 7 respectively. The main design variable is the reference force and (x_r, y_r) position values. For a 2-D pushing-based positioning (x_r, y_r) is selected as $(x(0), y(0))$ where $x(0)$ and $y(0)$ are the after automatic contact detection particle (x, y) position since the stage and particle move, and the cantilever tip behaves as the stopper. z-position control could be needed if the surface is not flat, and a constant normal force control can compensate these types of errors. For this purpose, F_z^* should be selected by the user by getting a trial pushing force data. Here, the H_z and H_{xy} functions transform the deflection and position data to tip-particle distance (h), or the particle position (x_a, y_a) feedback such that:

$$H_{xy} = \begin{cases} (x,y) = (x_s, y_s) \ , & \text{if } t \leq t^*; \\ (x,y) = (x^o, y^o) \ , & \text{otherwise.} \end{cases} \tag{17}$$

Here, (x_s, y_s) is the stage xy-position, t^* is the particle-substrate separation instant, and (x^o, y^o) is the tip-particle pushing settling xy-position. t^* can be detected experimentally in real-time by observing ζ_z such that if ζ_z has a peak at time t, then $t^* = t$. However, (x^o, y^o) cannot be measured directly, and needed to be estimated from the pushing model. For example, using the previous models, y^o can be observed in the Figure 8 where x^o can be observed in the same way. However, depending on the special parameters, the behaviour of the (x, y) could be also periodic motion, which can be observed in the model and experiments. In this case, the mean of the periodic function can be used as the (x, y) information.

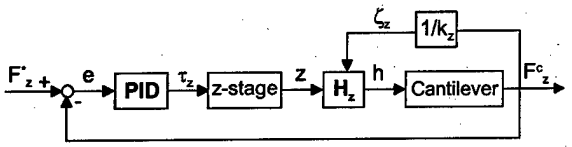


Figure 6: Force-controlled z-positioning.

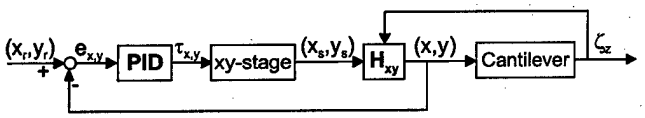


Figure 7: Force-controlled xy-positioning during particle pushing.

4 System Setup

For conducting experiments, a home-made open-structure AFM system with Virtual Reality (VR) graphics display and haptic device is utilized [20]. The photo of the home made open-structure AFM system is shown in Figure 10. Piezoresistive cantilevers where the cantilever has a doped silicon layer which changes its resistance due to the deflection moment are utilized. These type of cantilevers can be the future micro-robot grippers as the integrated sensor probes. Only the ζ_z is measurable with the present system. As the user interface, a graphics display as can be seen in Figure 9 which we call as VR Nano Visulator integrated with a 1-DOF haptic device is constructed. In the graphics display, scanned AFM images, and real-time cantilever tip position (spherical ball in the figure) are displayed. Using the haptic device, z-position of the tip can be controlled by the user with a real-time bilateral force feedback control. Thus, even there are positioning errors due to the piezoelectric stage on the visual display, the force-feedback enhances these types of errors.

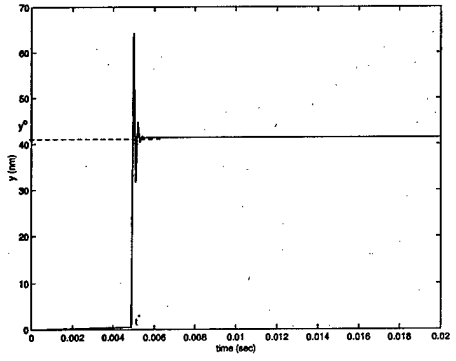


Figure 8: The settling of the y position of the particle during pushing.

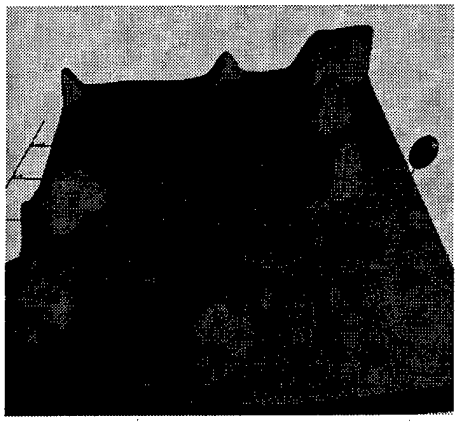


Figure 9: VR Nano Visulator display of 242 nm radius gold-coated latex nanoparticles during manipulation (spherical ball represents the AFM tip).

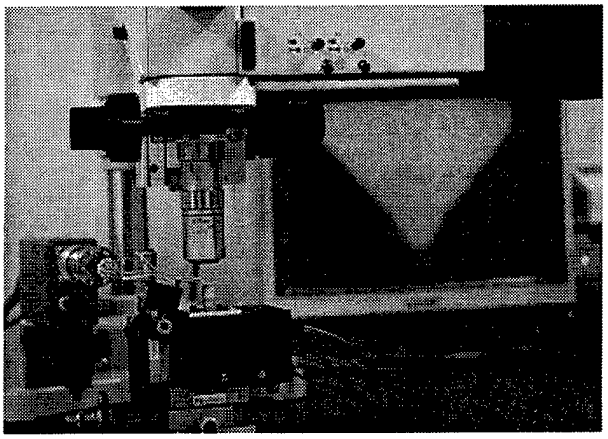


Figure 10: Home made open structure AFM system photo with piezoresistive cantilever and top-view optical microscope.

5 Experiments

As the first experiment, the contact point detection is tested. The cantilever parameters are $R_t = 30\ nm$, and $k_c = 8\ N/m$, $L_x = 50\ \mu m$, $L_y = 155\ \mu m$, and $L_z = 6.5\ \mu m$. The motion speed is around $V = 2\ \mu m/sec$ with $\Delta = 0.1\ \mu m$ steps. During the particle-tip contact as can be seen in Figure 11, $-0.2\ V$ is the no deflection line where around the 43^{th} step of motion the particle contacts and bends until to $-1.5\ V$ which is the ζ_{set} for automatic contact detection. At this point stage stops moving.

As the pushing experiment, 0.5 μm radius gold-coated latex particles are pushed in a task-based control user interface. The optical microscope images of an pushed particle example is given in Figure 12. During pushing, ζ_z measurement can be seen from the Figure 13. From the

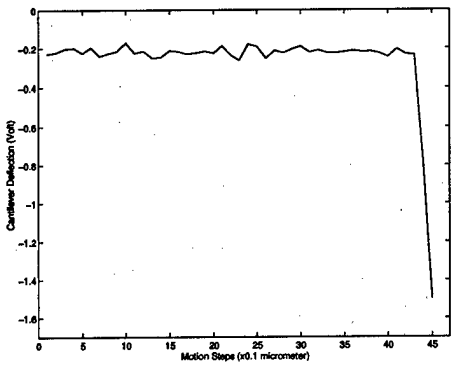


Figure 11: The cantilever deflection during automatic contact detection.

deflection data the pushing behavior of the particle can be estimated as *pure sliding*. Moving the substrate along the *y-axis*, the point **A** is the *contact point*, **B** is the *shearing point* where the particle is detached from the substrate by overcoming the static friction, and starts to slide afterwards, and **C** is the sliding region end point.

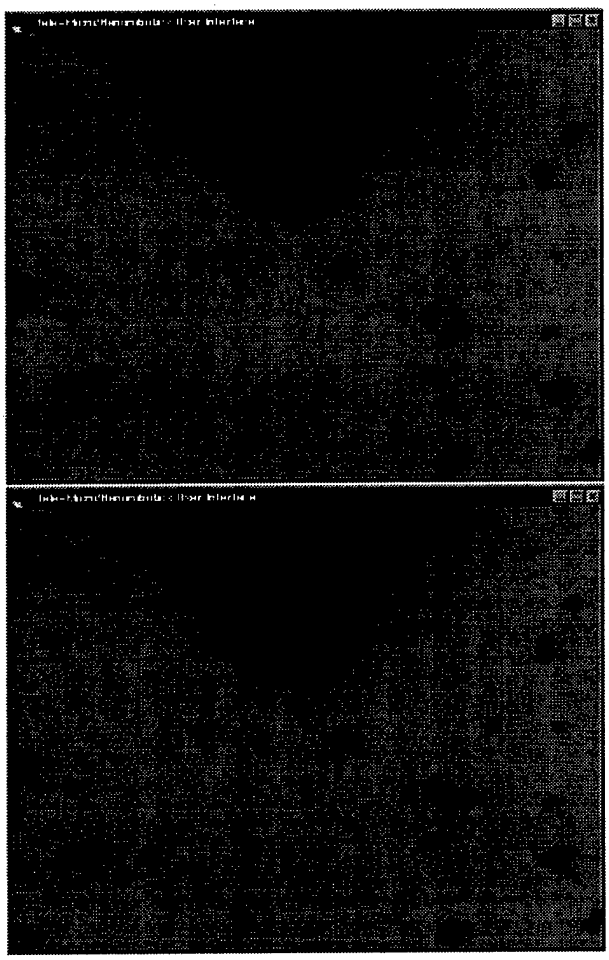


Figure 12: Pushing a 0.5 μm radius latex particle where the initial (upper image) and final positions (lower image) are shown using the high-resolution optical microscope top-view images.

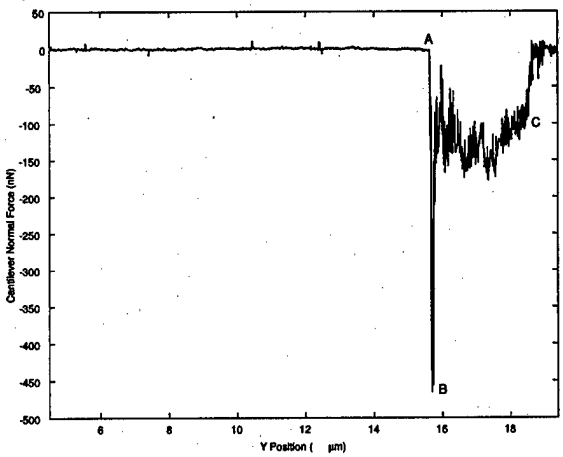


Figure 13: The cantilever normal interaction force data during pushing.

6 Conclusion

In this paper, utilizing AFM as a micro/nanomanipulation tool has been proposed. Modeling and control of the AFM cantilever tip and particle interaction has been realized for moving particles with sizes less than 3 μm on a silicon substrate in 2-D. Particle manipulation experiments are realized, and it is shown that the system can be utilized in 2-D micro/nanoparticle assembling. As the future work, the manipulation operations will be realized in a liquid environment where the capillary and electrostatic forces are reduced. Also, 3-D manipulation is aimed where more than one cantilevers or adhesive liquids can be used.

Fine particle aasembly systems with precise mechanical manipulation capability would enable a powerful tool for future *man-made* materials and devices. However, still there are many challenging problems such as 3-D manipulation, fast, repeatable and reliable automatic manipulation control, micro/nanophysics-based and compact new gripper design and fabrication, real-time monitoring at the nano scale, and etc. 3-D manipulation is aimed at pick-and-place manipulation, where the gripper design, position control and visual and force sensing are important problems. This work introduces the concept of self-sensing grippers which can be doubled, and utilized as mechanical grippers with visual and force sensing capabilities. For the automatic control, intelligent strategies integrated with real-time visual and/or force feedback should be developed. Finally, only mechanical contact manipulation would be limited for functional material and device fabrication, and it should be integrated with other chemical or physical methods such as self-assembly or laser trapping.

References

[1] D. Schafer, R. Reifenberger, A. Patil, and R. Andres, "Fabrication of two-dimensional arrays of nanometric-size clusters with the atomic force microscopy," *App. Physics Letters*, vol. 66, pp. 1012–1014, Feb. 1995.

[2] T. R. Ramachandran, C. Baur, and et al., "Direct and controlled manipulation of nanometer-sized particles using the non-contact atomic force microscope," *Nanotechnology*, vol. 9, pp. 237–245, 1998.

[3] R. Resch, C. Baur, and et al., "Manipulation of nano particles using dynamic force microscopy: Simulation and experiments," *App. Phys. A*, vol. 67, pp. 265–271, Sept. 1998.

[4] C. Baur, A. Bugaciv, and et al., "Nanoparticle manipulation by mechanical pushing: Underlying phenomena and real-time monitoring," *Nanotechnology*, vol. 9, pp. 360–364, 1998.

[5] T. Junno, K. Deppert, L. Montelius, and L. Samuelson, "Controlled manipulation of nanoparticles with an atomic force microscopy," *App. Physics Letters*, vol. 66, pp. 3627–3629, June 1995.

[6] M. R. Falvo, S. Washburn, and et al., "Manipulation of individual viruses: Friction and mechanical properties," *Biophysical Journal*, vol. 72, pp. 1369–1403, March 1997.

[7] L. T. Hansen, A. Kuhle, and et al., "A technique for positioning nanoparticles using an atomic force microscope," *Nanotechnology*, vol. 9, pp. 337–343, 1998.

[8] M. Sitti, "Teleoperated 2-d micro/nanomanipulation using atomic force microscope," *Ph.D. Thesis*, Dept. of Electrical Engineering, University of Tokyo, Tokyo, Sept. 1999.

[9] M. Sitti and H. Hashimoto, "Teleoperated nano scale object manipulation," in *Recent Advances on Mechatronics*, pp. 322–335, ed. by O. Kaynak, S. Tosunoglu and M.J. Ang, Springer Verlag Pub., Singapore, 1999.

[10] M. Sitti and H. Hashimoto, "Two-dimensional fine particle positioning using a piezoresistive cantilever as a micro/nano-manipulator," in *Proc. of the IEEE Int. Conf. on Robotics and Automation*, pp. 2729–2735, Detroit, May 1999.

[11] M. Sitti and H. Hashimoto, "Tele-nanorobotics using atomic force microscope," in *Proc. of the IEEE/RSJ Int. Conf. on Intelligent Robots and Systems*, pp. 1739–1746, Canada, Oct. 1998.

[12] F. Arai, D. Ando, and T. Fukuda, "Micro manipulation based on micro physics: Strategy based on attractive force reduction and stress measurement," in *Proc. of the IEEE Int. Conf. on Robotics and Automation*, pp. 236–241, 1995.

[13] J. Israelachvili, *Intermolecular and Surface Forces*. Academic Press, 1992.

[14] M. Sitti, S. Horiguchi, and H. Hashimoto, "Tele-touch feedback of surfaces at the micro/nano scale: Modeling and experiments," in *Proc. of the IEEE/RSJ Int. Conf. on Intelligent Robots and Systems*, Korea, Oct. 1999 (to be published).

[15] D. Sarid, J. P. Hunt, R. K. Workman, and et al., "The role of adhesion in tapping-mode atomic force microscopy," *Appl. Phys. A*, no. 66, pp. 283–286, 1998.

[16] J. Colchero, E. Meyer, and O. Marti, "Friction on atomic scale," *Handbook of Micro/Nano Tribology, Second Ed., CRC Press*, pp. 273–333, 1999.

[17] F. J. Giessibl and B. M. Trafas, "Piezoresistive cantilevers utilized for scanning tunneling and scanning force microscope in ultrahigh vacuum," *Rev. Sci. Instrum.*, vol. 65, pp. 1923–1929, June 1994.

[18] M. Tortonese, R. C. Barrett, and C. F. Quate, "Atomic resolution with an atomic force microscope using piezoresistive detection," *App. Physics Letters*, vol. 62, pp. 834–836, Feb. 1993.

[19] T. R. Hicks and P. D. Atherton, *The Nano Positioning Book*. Queensgate Inst. Ltd., 1997.

[20] U. Rabe, J. Turner, and W. Arnord, "Analysis of the high-frequency response of atomic force microscope cantilevers," *Appl Phys. A*, vol. 66, pp. 277–282, 1998.

[21] M. Sitti and H. Hashimoto, "Force-controlled pushing of nanoparticles using afm," in *Proc. of the IEEE/ASME Int. Conf. on Advanced Intelligent Mechatronics*, pp. 13–20, Sept. 1999.

[22] M. Sitti and H. Hashimoto, "Tele-nanorobotics using atomic force microscope as a manipulator and sensor," *Advanced Robotics Journal*, Invited Session on IROS'98, Fall 1999 (to be published).

Preparation and Properties of Carbon Nanotubes

Yahachi Saito

Department of Electrical and Electronic Engineering,
Mie University, Tsu 514-8507, Japan

Abstract:
Carbon nanotubes exhibit extraordinary mechanical and electronic properties. In this report, synthesis of carbon nanotubes (multiwalled and single-wall) by an electric arc discharge is first mentioned, and then their unique structures and properties are briefly reviewed. Field emission of electrons from nanotube tips, which are now attracting considerable attentions as a promising application of carbon nanotubes, is also demonstrated.

1. INTRODUCTION

Carbon nanotubes are hollow cylinders with diameters ranging from 1 nm to 50 nm and length over 10 μm. They consist of only carbon atoms and can be thought of as a graphite sheet that has been rolled into a seamless cylinder [1]. There are two kinds of nanotubes; One is a single-wall nanotube (SWNT) that is made up of a single layer of graphite ("graphene" sheet) [2-4] as shown in Fig. 1, and the other is a multiwall nanotube (MWNT) that consists of multiple shells [1].

Nanotubes have aroused great interest recently because of their unique physical properties, which span a wide range from structural to electronic. For example, nanotubes have a light weight and high elastic modulus, and thus they are predicted to the strongest fibers that can be made [5]. Their high strength is accompanied by their ability to buckle in a reversible manner. When the nanotube is bent, it doe not fracture but buckles like a rubber hose [6,7]. Then, carbon nanotubes, especially SWNTs, possess the exceptional electronic properties; they can be metallic or semimetallic, depending on the geometry how a graphene sheet is rolled up into a tube (i.e., diameter and chiral angle) [8-11]. Quantum properties of electron transports along nanotubes have been revealed recently [12-16].

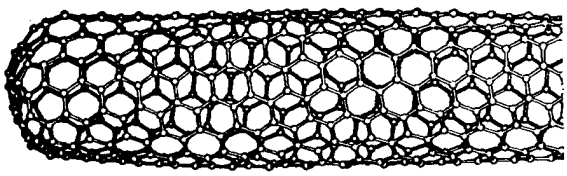


Fig. 1. Structure models of nanotubes a SWNT.

Due to these extreme properties, nanotubes are under investigation toward several applications including electron field emitters [17-24], probes of scanning-type microscopes [25,26], gas (such as hydrogen) storage materials [27,28], and electrode materials of secondary batteries and capacitors [29]. Among these proposed applications, field emission electron sources would be industrially the most promising and are nearly within reach of practical use.

2. GROWTH AND STRUCTURES OF CARBON NANOTUBES

Carbon nanotubes are produced by either electric arc discharge between carbon electrodes or laser vaporization of a carbon target. The synthesis method described here is restricted to the arc discharge technique. The details of the arc evaporation have been described in our previous publication [30]. For the laser ablation method, readers should consult Ref. [31].

2.1 Arc Discharge Method

A direct current (DC) arc is almost exclusively used because the DC arc is amenable and provides us with high yield of nanotubes though an alternative current (AC) arc can evaporate carbon electrodes. Both an anode and a cathode are made of graphite rods for producing MWNTs, while metal-containing carbon anodes are used for synthesizing SWNTs.

Carbon electrodes are evaporated in a buffer gas (usually helium) at a desired pressure (200 Torr to 600 Torr for helium gas). Since the anode surface is heated to higher temperature (~4000K) than the cathode surface (~3500K), the anode is selectively consumed in the arc. The position of the anode tip can be adjusted from outside of vacuum with a translation-motion feedthrough in order to maintain the proper spacing (about 1 mm) between the electrodes.

Approximately half of the evaporated carbon condenses on the tip of the cathode, forming a cylindrical hard deposit. The remaining vapor condenses in a gas phase, forming soot, which finally piles up on the inner walls of the reaction chamber and also around the root of the cylindrical hard deposit on the cathode. Hereafter, we call the first cylindrical deposit on the cathode as "cylindrical deposit", the second one "chamber soot", and the last one "cathode soot".

2.2 Single-Wall Nanotubes

The diameter of SWNTs ranges from 0.7 nm to about 3 nm. The smallest diameter corresponds to that of C_{60}

1999 INTERNATIONAL SYMPOSIUM ON
MICROMECHATRONICS AND HUMAN SCIENCE
0-7803-5790-6/99/ $10.00 ©1999 IEEE.

molecules. Metal catalysts are necessary to synthesize SWNTs for both the arc discharge and the laser vaporization methods. Typical catalysts for synthesizing SWNTs are listed in Table 1. The yield of SWNTs depends strongly on buffer gas and its pressure as well as catalysts. SWNTs are obtained in the chamber soot and the cathode soot, instead of the cylindrical hard deposit, being in contrast with MWNTs.

At the best synthesis condition, SWNTs occupy 50 - 70 % of carbon atoms in crude soot for both the arc discharge and the laser ablation. When the density of SWNTs in soot is high (>~50 %) as this image shows, tubes coagulate in parallel with each other through van der Waals forces and form bundles (called "ropes"). SWNTs in a bundle are closely packed in a triangular lattice.

Studies on growth patterns and morphologies of SWNTs revealed that SWNTs were growing from surfaces of metallic (catalyst) particles [32,33] and the free tips of SWNTs were closed by hemispherical caps [4, 32,33].

Table 1. Typical catalysts commonly used for synthesizing SWNTs.

Metal	Production method
Co	Arc
Ni	Arc
Fe-Ni	Arc and Laser
Co-Ni	Laser
Rh-Pt	Arc
Ni-Y	Arc

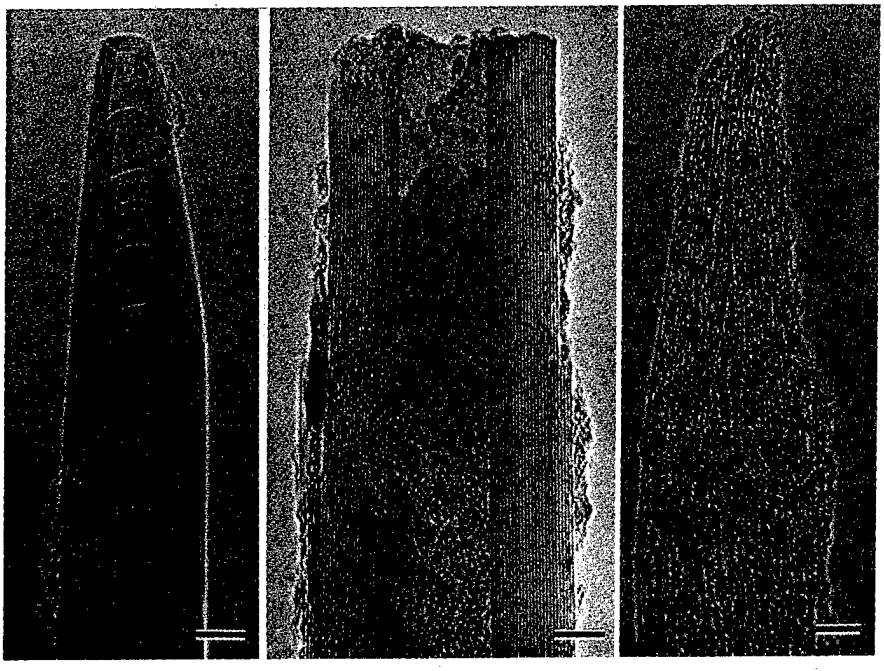
2.3 Multiwall Nanotubes

For the production of MWNTs, pure carbon is evaporated mainly in helium gas. Hydrogen gas can also be employed as working gas. In the latter case, "clean" MWNTs are produced (i.e., the amount of byproducts such as carbon nanoparticles is very small [34]), though the total amount of MWNTs is smaller than that obtained in helium.

2.3.1 Preparation in helium gas

For the production of nanotubes in helium gas, the arc discharge is carried out in the gas of at least 200 Torr, below which nanotubes are barely formed. A multiwall nanotube consists of graphene sheets stacked in a concentric way. The number of sheets ranges from 2 to about 40. The diameters of MWNTs are in a range from 4 to 50 nm, and the lengths are over 10 μm. MWNTs contain relatively large cavities (the diameter being 3 – 10 nm) in their center.

Both ends of a MWNT are capped by graphitic layers; the number of layers being the same as that for the sidewall of a tube, as shouwn in Fig. 2(a). The caps have polyhedral shapes with sharp corners, at which pentagons (five-member rings) are believed to be located. Pentagons have to be introduced into the hexagon network for the graphene sheet to make a closure, like C_{60} fullerenes. Curvatures of a graphene sheet concentrate around the pentagons, so the portions where a pentagon exists extrude like corners of a polyhedron whereas other places without pentagons are flat. Tips of MWNTs show various shapes depending on how six pentagons are introduced into the hexagon network.



(a) (b) (c)

Fig. 2. TEM images of tips of the four kinds of carbon nanotubes. (a) Pristine MWNT with a capped end, (b) MWNT with an open end, and (c) bundle of purified SWNTs. Scale bars show 5 nm.

The interlayer spacings between rolled graphene sheets are 0.344 nm in average [35], being a few percent wider than the ideal graphite value (0.3354 nm). Since MWNTs produced by arc discharge consist of nested graphene cylinders, they are very stiff (see the next section) and are straight over their length.

2.3.2 Preparation in hydrogen gas

Pressures of hydrogen employed for the MWNT production are typically in a range from 50 to 200 Torr, being in contrast to the case of helium gas. On the surface of the cathode deposit, a deep-black, sooty area is found. This soot consists mainly of MWNTs, i.e., the amount of accompanying nanoparticles is very small. Figure 3 shows a scanning electron microscope (SEM) image of the surface of the black, sooty area. The thickness of the layer containing "clean" MWNTs is very thin, approximately 0.1 mm. Under this layer, MWNTs also exist though nanoparticles and large carbon particles are the majorities.

Figure 4 (a) shows typical TEM images of pristine MWNTs produced by hydrogen arc. A hollow channel in the nanotube center is extremely narrow; the smallest diameter of the innermost layer is about 0.7 nm. Strictly speaking, these "nanotubes" synthesized in the hydrogen arc are not "tubes" but "rods" (or "fibers") because of the absence of central cavities. Therefore, we call these nanoscale graphitic fibers "nanografibers".

Another structural character of nanografibers grown in hydrogen is found in tips of nanotubes; partially broken or etched graphene sheets are sometimes observed at tips as shown in Fig. 4 (b). The structural defects at the nanotube tips possibly reflect reactivity of curved graphene sheets at the tips (due to stress around pentagons) with hydrogen atoms or ions during nanotube growth. This high reactivity of curved graphene sheets may be responsible for the low population of nanoparticles (which are considered to be made up of three-dimensionally curved graphene sheets) in the hydrogen arc.



Fig. 3. SEM images of nanografibers produced by hydrogen arc.

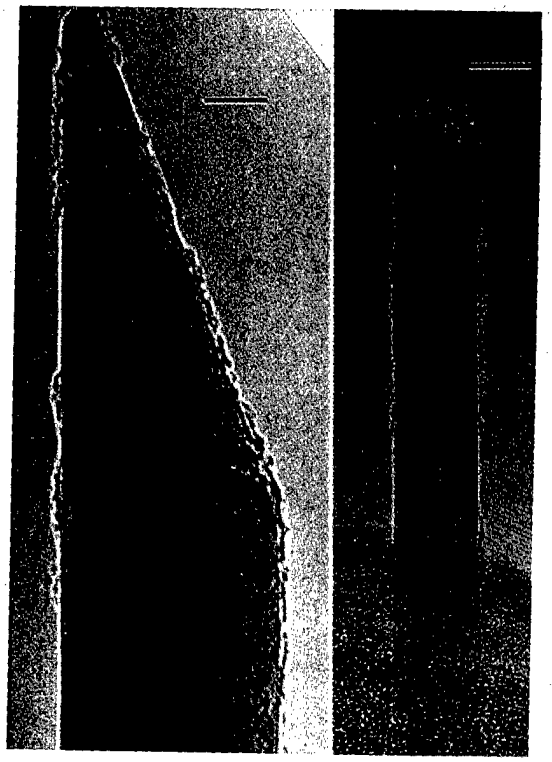


Fig. 4. TEM images of nanografibers, exhibiting (a) an extremely narrow channel in its center (the diameter of the innermost layer is 0.7 nm) and (b) a partially broken tip (the outer graphitic layers are disordered). Scale bars show 10 nm.

2.4. Purification of Nanotubes

MWNTs are produced together with other forms of carbon, mainly polyhedral nanoparticles. For SWNTs, amorphous carbon as well as metal particles which were used as catalysts for synthesizing SWNTs are included in crude samples. These carbon debris and metallic impurities have to be removed for exploring physical and chemical properties of nanotubes that are sensitive to impurities. Purification of MWNTs [36-38] and SWNTs [39,40] has been tried by oxidation, centrifugation, filtration, acid treatment and so on.

3. MECHANICAL PROPERTIES

Since the basal-plane elastic modulus of graphite is the largest of any other known materials, carbon nanotubes which are formed by seamlessly rolling graphitic sheets are predicted to be extraordinary stiff and strong. In fact, these expectations are demonstrated experimentally by TEM [5] and atomic force microscope (AFM) measurement [7]. In a

small-strain limit, Young's moduli of isolated MWNTs were found in a range from 0.40 TPa to 4.15 TPa (1.8 TPa in average) [5]. Their high stiffness, coupled with their low density, implies that the nanotube might be useful as nanoscale mechanical parts. Theoretical estimates predict that SWNTs might have a Young's modulus of the order of 5 TPa [5].

The most distinguished mechanical property of nanotubes is their unusual strength in large-strain region. MWNTs can be bent repeatedly through large angles (up to ~110°) without undergoing catastrophic fracture, despite the occurrence of kinks [6,7], as shown schematically in Fig. 5 [41]. Nanotubes are remarkably flexible and resilient.

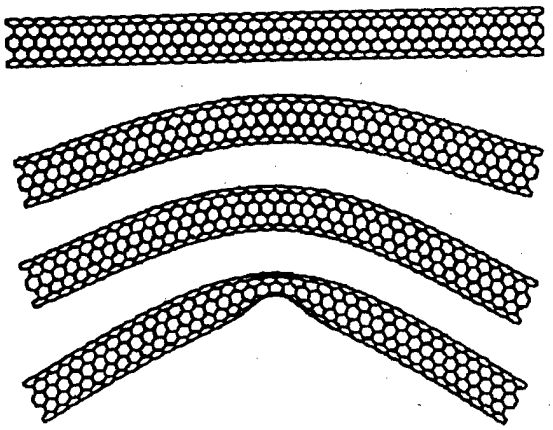


Fig. 5. Structures of bent nanotubes calculated by Rochefort et al. [42] The bending angles are (from the top) 0°, 30°, 45° and 60°.

4. ELECTRONIC PROPERTIES

Carbon nanotubes are predicted to be metallic or semiconductive depending on their diameter and the helicity (wrapping angle) of the hexagonal lattice. A slight change in the winding of hexagons along the tube drastically changes their conductive properties. Recently, the presence of metallic and semiconductive SWNTs has been experimentally verified by scanning tunneling microscopy (STM) [12,13] and also by resonant Raman scattering spectroscopy [42]. In the STM, the tunneling current is recorded as a function of the voltage between a STM tip and a nanotube. The observed tunneling conductance is a direct measure of the local electronic density of states (DOS) of the nanotube. Figure 6 displays a measured and a calculated DOS for a semimetallic SWNT [12], showing a remarkable agreement between them. Spike-like peaks observed in the DOS (called "van Hove singularity") are characteristic of one-dimensional materials.

By using resonant Raman scattering, the electronic energies between two van Hove singular points above and below the Fermi level are measured. The diameters of SWNTs can be precisely measured from the observed Raman scattering originating from the so-called "breathing mode" (radial vibration characteristic of nanotubes). The diameter dependence of the electronic energies between two van Hove singular points substantiated the presence of metallic and semiconduting tubes [42].

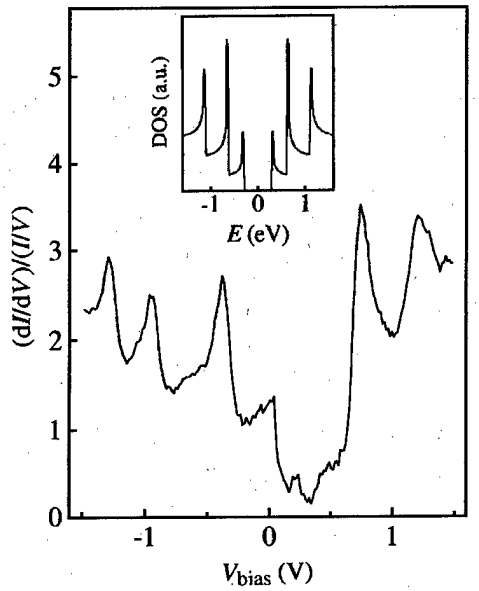


Fig. 6. Experimental tunneling conductance and theoretical DOS (inset) of a SWNT [15].

5. ELECTRON EMISSION FROM NANOTUBES

When a high electric field on the order of 10^7 V/cm is applied on a solid surface with a negative electrical potential, electrons inside the solid are emitted into vacuum by the quantum mechanical tunneling effect. This phenomenon is called field emission of electrons. Such an extremely high field can be obtain on a sharp tip of a very thin needle, because electric fields concentrate at the sharp points. The carbon nanotubes possess the following properties favorable for field emitters: (1) needle-like shape with a sharp tip, (2) high chemical stability, (3) high mechanical strength, and (4) high thermal stability. In 1995, field emission (FE) from an isolated single MWNT was first reported by Rinzler et al. [17], and FE from a MWNT film was reported by de Heer et al. [18]. We have studied emission properties using field emission microscopy (FEM) [19,43-45], and then applied nanotubes as cold electron sources in display devices [20,21,24].

5.1. FEM Study of Nanotubes

Four kinds of carbon nanotubes were employed as field emitters; (1) as-grown MWNTs prepared in the helium arc (hereafter, called "pristine MWNTs"), (2) as-grown MWNTs

in hydrogen ("nanografibers"), (3) purified MWNTs with open ends ("purified MWNTs" or "open MWNTs"), and (4) purified SWNTs. Tips of the respective nanotubes are shown in Figs. 2 and 4. Tips of pristine MWNTs are capped by graphitic layers (Fig. 8 (a)) while purified MWNTs that were obtained after oxidation have open tips (Fig. 8 (b)). Purified SWNTs form bundles, each of which consists of roughly 100 nanotubes (Fig. 8 (c)).

A bulk bundle of respective nanotubes for FEM study was fixed on the apex of a hairpin-shaped wire of tungsten (0.2 mm in diameter) using conductive paste. The emitter tip of the nanotubes was positioned 60 mm in front of an anode screen with a 1-mm probe hole. Field emission patterns could be observed on the anode screen on which phosphor was spread. Behind the probe hole was a Faraday cup, and electron current emitted from a restricted region of an emitter could be measured. The acceptance half angle of the probe hole was 17 mrad. Details of the tip preparation and FEM apparatus were described in our previous publications [19, 43, 44].

Both pristine MWNTs and bundles of SWNTs gave emission patterns consisting of a number of bright solid spots that originated respectively from individual MWNTs and from bundles of SWNTs [43,44]. On the other hand, emission patterns from open MWNTs showed "doughnut-like" annular bright rings [21]. A black spot in the central region (i.e., the absence of electrons in the core of an electron beam) corresponds to a cavity of nanotube.

We can measure emission current from a single nanotube by using the probe hole on an anode screen. Emission current accepted by the probe hole, I_p, was measured as a function of voltage applied to the tip (V). The I_p -V characteristics for the four kinds of nanotubes are shown in Fig. 7.

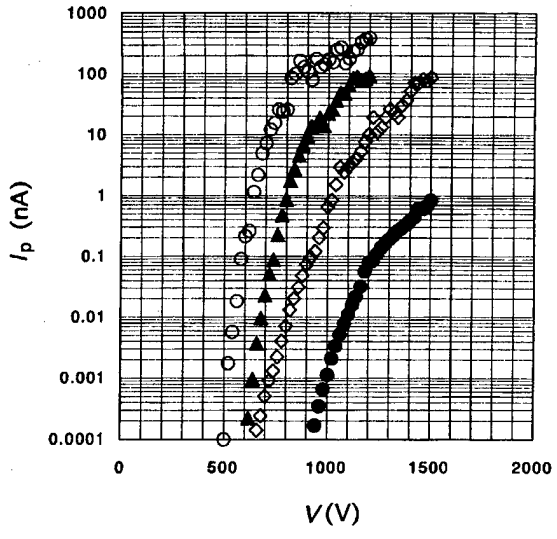


Fig. 7. Current vs. voltage characteristics for a pristine (●), a nanografiber (◇), an open MWNT (○), and a bundle of SWNTs (▲). Current (I_p) was measured with the 1 mm probe hole.

Threshold voltage and maximum current density are summarized in Table 2 for the four kinds of nanotubes. The open MWNTs begin to emit electrons at the lowest tip voltage and sustained the highest current density. Nanografibers grown in hydrogen give higher current than ordinary MWNTs (i.e., pristine MWNTs grown in helium). This is caused mainly by the cleanliness of nanografiber samples (i.e., less byproduct) and partially by the structural defects on nanografiber tips which have a lower work function.

Table 2. Field emission properties of a pristine MWNT, an open MWNT, a nanografiber and a bundle of SWNTs. The emission current was measured the 1-mm probe hole on the anode. The distance between the nanotubes and the anode was 60 mm.

Carbon nanotubes	Threshold voltage* (V)	Maximum current density ($\times 10^6$ A/cm^2)
pristine MWNT	900-1000	0.1-1
open MWNT	500-600	10-100
nanografiber	700-800	~ 1
SWNTs	600-700	~ 10

* Onset voltages represent tip voltages at which currents measured by the probe hole exceed 0.1 pA.

5.2. Nanotube-Based Display Devices

Developing the field emission study, we experimentally fabricated field emission display (FED) elements in collaboration with Ise Electronics Corp. FEDs that we employed for examining the performance of nanotube field emitters are CRT (cathode-ray tube)-type lighting elements [20].

Figure 8 shows a longitudinal cross section of a CRT lighting bulb with a nanotube cold cathode. Nanotubes we used were MWNTs produced by arc discharge. In our first trial fabrication, fibrous materials containing abundant MWNTs were directly glued onto a stainless steel plate by using conductive paste. Subsequently, several methods were examined to fix nanotubes on the cathode surface, and the screen printing technique was found to be the most effective for industrial application [21].

The nanotube cathode is covered with a grid electrode; the spacing between the cathode and the grid ($d_{T\text{-}G}$) is 0.2 - 1.0 mm. The phosphor screen is printed on the inner surface of a front glass and backed by a thin aluminum film. After sealing the vacuum tube, getter material was flashed to attain high vacuum on the order of 10^{-6} Pa.

The cathode was grounded (0 V), and the control grid was biased to a positive voltage. For $d_{T\text{-}G}$ = 0.2 mm, current density on the cathode was ca. 25 mA/cm^2 at an average field strength of 2 V/μm.

A high voltage (typically 10 kV) was applied to the anode to accelerate electrons, which excite the phosphor screen. Luminance of the phosphor screens was intense

enough for practical use; e.g., 6.3×10^4 cd/m^2 for green light (ZnS:Cu, Al for green phosphor) at an anode current of 200 μA, which is two times more intense than that of commercially available conventional thermionic CRT lighting elements which are operated at 100 μA. The light emission efficiency was ca. 60 lm/W for green light. A lifetime test showed that the nanotube cathode had a life of over 10,000 hours.

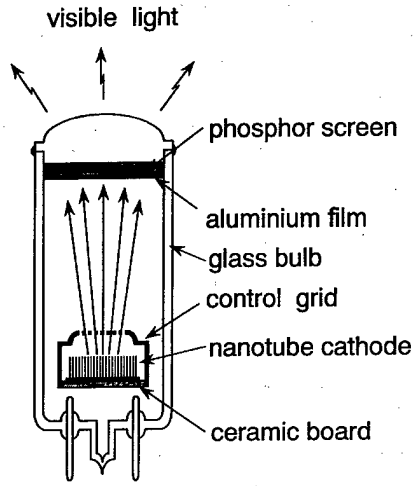


Fig. 8. Structure of a CRT-type lighting element with a nanotube cold cathode.

6. CONCLUDING REMARKS

One possible future direction of nanotube research, on which we have not mentioned here so much because of the limited space, is the exploration of so-called molecular electronics. The device integration can be raised to the ultimate scale because of the small size of molecular elements. Recently, the first prototype field-effect transistor with only one SWNT was demonstrated [46]. There is still much more to explore for developing integrated devices with many individual elements.

The future of nanotubes looks very bright. They are extremely versatile: They are strong, fine, light, conducting or semiconducting, inert and so forth. Fundamental science and applications of nanotubes are progressing rapidly, which are driven by this unique combination of properties.

REFERENCES

[1] S. Iijima, Nature **354** (1991) 56.
[2] S. Iijima and T. Ichihashi, Nature **363** (1993) 603.
[3] D. S. Bethune, C. H. Kiang, M. S. de Vries, G. Gorman, R. Savoy, J. Vazquez and R. Beyers, Nature **363** (1993) 605.
[4] Y. Saito, T. Yoshikawa, M. Okuda, N. Fujimoto, K. Sumiyama, K. Suzuki, A. Kasuya and Y. Nishina, J. Phys. Chem. Solid **54** (1993) 1849.
[5] M. M. J. Treacy, T. W. Ebbesen and J. M. Gibson, Nature **381** (1996) 678.
[6] S. Iijima, C. Brabec, A. Maiti and J. Bernholc, J. Chem. Phys. **104** (1996) 2089.
[7] M. R. Falvo, G. J. Clary, R. M. Taylor II, V. Chi, F. P. Brooks Jr., S. Washburn and R. Superfine, Nature **389** (1997) 582.
[8] J. M. Mintmire, B. I. Dunlap and C. T. White, Phys. Rev. Lett. **68** (1992) 631.
[9] N. Hamada, S. Sawada and A. Oshiyama, Phys. Rev. Lett. **68** (1992) 1579.
[10] R. Saito, M. Fujita, G. Dresselhaus and M. S. Dresselhaus, Appl. Phys. Lett. **60** (1992) 2204.
[11] K. Tanaka, K. Okahara, M. Okada and T. Yamabe, Chem. Phys. Lett. **191** (1992) 469.
[12] S. J. Tan, M. H. Devoret, H, Dai, A. Thess, R. E. Smalley, L. J. Greerligs and C. Dekker, Nature **386** (1997) 474.
[13] J. W. G. Wildoer, L. C. Venema, A. G. Rinzler, R. E. Smalley and C. Dekker, Nature **391** (1998) 59.
[14] T. W. Odom, J. –L Huang, P. Kim and C. M. Lieber, Nature **391** (1998) 62.
[15] S. Frank, P. Poncharal, Z. Ł. Wang, W. A. de Heer, Science **280** (1998) 1744.
[16] L. C. Venema, J. W. G. Wildoer, J. W. Janssen, S. J. Tans, H. L. J. T. Tuinstra, L. P. Kouwenhoven and C. Dekker, Science **283** (1999) 52.
[17] A. G. Rinzler, J. H. Hafner, P. Nikolaev, L. Lou, S. G. Kim, D. Tomanek, P. Nordlander, D. T. Colbert, and R. E. Smalley, Science **269** (1995) 1550.
[18] W. A. de Heer, A. Chatelain, and D. Ugarte, Science **270** (1995) 1179.
[19] Y. Saito, K. Hamaguchi, K. Hata, K. Uchida, Y. Tasaka, F. Ikazaki, M. Yumura, A. Kasuya, and Y. Nishina, Nature **389** (1997) 554.
[20] Y. Saito, S. Uemura, and K. Hamaguchi, Jpn. J. Appl. Phys. **37** (1998) L346.
[21] S. Uemura, T. Nagasako, J. Yotani, T. Shimojo and Y. Saito, Proc. SID 98, p.1052.
[22] Q. H. Wang, A. A. Setlur, J. M. Lauerhaas, J. Y. Dai, E. W. Seeling, and R. P. H. Chang, Appl. Phys. Lett. **72** (1998) 2912.
[23] W. B. Choi, D. S. Chung, S. H. Park and J. M. Kim, Proc. SID 99, p. 1134.
[24] S. Uemura, J. Yotani, T. Nagasako, Y. Saito and M. Yumura, Euro Display 99 (19th IDRC), Sept. 6-9, 1999.
[25] H. Dai, J. H. Hafner, A. G. Rinzler, D. T. Colbert and R. E. Smalley, Nature **384** (1996) 147.
[26] S. S. Wong, E. Joselevich, A. T. Woolley, C. L. Cheung and C. M. Lieber, Nature **394** (1998) 52.
[27] A. C. Dillon, K. M. Jones, T. A. Bekkedahl, C. H. Kiang, D. S. Bethune and M. J. Haben, Nature **386** (1997) 377.
[28] P. Chen, X. Wu, J. Lin and K. L. Tan, Science **285** (1999) 91.
[29] B. Gao, A. Kleinhammes, X. P. Tang, C. Bower, L. Fleming, Y. Wu and O. Zhou, Chem. Phys. Lett. (1999) in press.
[30] Y. Saito, New Diamond & Frontier Carbon Tech. **9** (1999) 1.
[31] A. Thess, R. Lee, P. Nikolaev, H. Dai, P. Petit, J. Robert, C. Xu, Y. H. Lee, S. G. Kim, A. G. Rinzler, D. T. Colbert, G. E. Scuseria, D. Tomanek, J. E. Fischer, and R. E. Smalley, Science **273** (1996) 483.
[32] Y. Saito, M. Okuda, M Tomita and T. Hayashi, Chem. Phys. Lett. **236** (1995) 419.
[33] Y. Saito, M. Okuda, N. Fujimoto, T. Yoshikawa, M. Tomita

and T. Hayashi, Jpn. J. Appl. Phys. **3 3** (1994) L526.
[34] X. K. Wang, X. W. Lin, V. P. Dravid, J. B. Ketterson and R. P. H. Chang: Appl. Phys. Lett. **6 6** (1995) 2430.
[35] Y. Saito, T. Yoshikawa, S. Bandow, M. Tomita and T. Hayashi: Phys. Rev. B **4 8** (1993) 1907.
[36] T. W. Ebbesen, P. M. Ajayan, H. Hiura and K. Tanigaki, Nature **3 6 7** (1994) 519.
[37] S. Bandow, J. Appl. Phys. **8 0** (1996) 1020.
[38] J. M. Bonard, T. Stora, J. P. Salvetat, F. Maier, T. Stoeckli, C. Duschl, W. A. de Heer and A. Chatelain, Adv. Mater. **9** (1997) 827.
[39] K. Tohji, T. Goto, H. Takahashi, Y. Shinoda, N. Shimizu, B. Jeyadevan, I. Matsuoka, Y. Saito, A. Kasuya, T. Ohsuna, K. Hiraga and Y. Nishina, Nature **3 8 3** (1996) 679.
[40] S. Bandow, A. M. Rao, K. A. Williams, A. Thess, R. E. Smalley and P. C. Eklund, J. Phys. Chem. B **1 0 1** (1997) 8839.
[41] A. Rochefort, D. R. Salahub and P. Avouris, Chem. Phys. Lett. **2 9 7** (1998) 45.
[42] M. Sugano, A. Kasuya, K. Tohji, Y. Saito and Y. Nishina, Chem. Phys. Lett. **2 9 2** (1998) 575.
[43] Y. Saito, K. Hamaguchi, T. Nishino, K. Hata, K. Tohji, A. Kasuya, and Y. Nishina, Jpn. J. Appl. Phys. **3 6** (1997) L1340.
[44] Y. Saito, K. Hamaguchi, S. Uemura, K. Uchida, Y. Tasaka, F. Ikazaki, M. Yumura, A. Kasuya, and Y. Nishina, Appl. Phys. A **6 7** (1998) 95.
[45] Y. Saito, K. Hamaguchi, K. Hata, K. Tohji, A. Kasuya, Y. Nishina, K. Uchida, Y. Tasaka, F. Ikazaki, and M. Yumura, Ultramicroscopy **7 3** (1998) 1.
[46] S. J. Tans, A. R. M. Verschueren, C. Dekker, Nature **3 9 3** (1998) 49.

Technical Session A-1

Micro / nano-manipulation and Control

Stochastic Dynamics of Molecular Machine
It's nanomachine which is based on Nyquist Theory

Hiroyuki MATSUURA[1)] *and Masahiro Nakano*[2)]

1) National Graduate Institute for Policy Studies

2-2, Wakamatsu-cho Sinzyuku-ku, Tokyo, 162-8677, Japan

2) University of Occupational and Environmental Health, Japan

1-1, Iseigaoka Yahatanishi-ku, Fukuoka, 807, Japan

Abstract :

A new model of actin myosin system named Stochastic Inclined Rods Model(SIRM), whose energy of motion is supplied from random noise(or thermal noise) and always moves to one direction, has been proposed. SIRM has a simple structure, which is composed of an inclined spring, a myosin head, and bundle of rods. In the SIRM, the energy of motion is supplied from random noise (or thermal noise) of water molecules generated through the heat energy of ATP hydrolysis. In an open and dissipative system, the myosin head works as a resonator of random noise, which accepts the energy through resonance. It is shown that the inclined rod and the spherical shape of G-actin are very important elements for the purpose of breaking the symmetry in the vibration of stochastic resonance(SR) and of generating a one directional motion. When the myosin head interacts with the spherical potential of G-actin, the trigonometric wave of stochastic resonance is distorted by the collision between the head and G-actin, and then it obliquely kicks the actin fiber by using the spring. It is thus shown that the inclined rod and the shape of the G-actin makes the SIRM move in one direction, even if the potentials between the myosin head and G-actin are perfectly symmetric.

1. INTRODUCTION

It is exciting and essential to study the problem of how a motor protein (actin myosin system) obtains an energy of movement and what mechanism makes myosin slide in one direction along actin filaments. H. E. Huxley, A. F. Huxley and R. M. Simmons proposed the rotating crossbridge model, which has been widely accepted in the past two decades and has been considered a standard model[1]-[2]. Nevertheless, extensive experimental efforts have failed to find evidence for a large conformational change in the myosin head during the force-generating process[3]-[4]. Moreover, T. Yanagida, A. Ishijima, and J. Finer, using a method of laser trapping, described a serious problem that ATP hydrolysis does not have a one-to-one correspondence with the rotation of the myosin head[5]. Due to the lack of evidence for the rotation of the myosin head, it is worthwhile to reconsider the old idea proposed by A. F. Huxley in 1957. The motor protein harnesses a considerable thermal energy that exists at physiological temperature to perform work [6].

In 1990, R. D. Vale and F. Oosawa proposed using Feynman's thermal ratchet model as an explanation for the muscle movement [7]. Following this work, there are many reports which discussed the relation between the muscle movement and stochastic resonance(SR) or thermal noise, which are related to many biological phenomena [8]-[11]. The explanation of [7] is, however, somewhat abstract from the view point of biology, and these proposed models are lacking in dynamic descriptions of the actin myosin interactions. Since 1991, we have tried to create a more definite picture of the actin myosin movement[12]-[14]. We pointed out the possibility that the muscle contraction utilizes SR, and estimated the magnitude of the power production generated by the actin myosin system based on the Langevin equation [15]-[17].

The main purpose of this paper is to propose a more concrete model which can describe the SR feature of the actin myosin system under thermally open system. We will show that 1) the actin myosin system can obtain sufficient energy from thermal noise through SR, and 2) SR allows the actin myosin system to move in one direction due to the structure of the inclined spring of the myosin head and due to the G-actin spheroid. We will add a comment that SIRM does not break the second law of thermodynamics.

1999 INTERNATIONAL SYMPOSIUM ON
MICROMECHATRONICS AND HUMAN SCIENCE
0-7803-5790-6/99/ $10.00 ©1999 IEEE.

2. OUR MODEL AND FORMULATION

The actin myosin system is an open dissipative system, whose energy is supplied from an external heat or energy source. The actin myosin system is essentially composed of three parts as shown in Fig.1: the myosin bundle(domain-2),the myosin rod which vibrates like a spring, and the myosin head(domain-1). A structural feature in the model is that the myosin rod is inclined, thus we called the model the Stochastic Inclined Rod Model(SIRM). The myosin head interacts with the G-actin of an actin filament(F-actin) through the intermolecular potential U_a. This potential indicates the repulsive force from the G-actin to the head. If the myosin head closely approaches the G-actin, then the head accepts the strong repulsion. This head is also subjected to an intermolecular potential U_S generated by the rod, which is approximately expressed as a spring vibrating like a harmonic oscillator. This potential represents the force which tries to keep the length of rod constant (its natural length) as a spring, therefore this potential always works to bring the head to its proper position. Domain-2, which consists of a bundle of many myosin filaments, plays the role of mother ship, gathering the generated force from each head, when domain-1 moves in one direction(Fig.1).

The equations of motion of domain-1 and domain-2 are obtained from the sum of the several related forces, the intermolecular potentials U_a, chemical binding potential U_S, and the random force from the water molecules. The equations of motion of the center of gravity (x, y) of domain-1 are

$$m\ddot{x} = -\frac{\partial}{\partial x}(U_a + U_S) + F_x(t) - \alpha_0 \dot{x} \qquad (1)$$

$$m\ddot{y} = -\frac{\partial}{\partial y}(U_a + U_S) + F_y(t) - \beta_0 \dot{y} \qquad (2)$$

With regard to the center of gravity (x_2, y_2) of domain-2, we set a similar equation:

$$M\ddot{x}_2 = -\frac{\partial U_S}{\partial x_2} + F_{x2}(t) - \eta \dot{x}_2 \qquad (3)$$

The variable y_2 is fixed at $y_2 = c$, since the myosin bundle does not significantly move along the y-direction compared to the x-direction. Here, $F_x(t)$, $F_y(t)$ and $F_{x2}(t)$ are fluctuations in the thermal noise [18-[19], and $\alpha_0 \dot{x}$, $\beta_0 \dot{y}$ and $\eta \dot{x}_{x2}$ are viscous drags in domain-1 and domain-2. The quantities M and m are the masses of domain-2 and domain-1, respectively. The intermolecular potentials, U_a and U_S and the random force from the water molecules are considered general ones, therefore, these equations are considered to include the typical (physical) features of the actin-myosin system. The system must be opened to the outer surroundings so that the SIRM continuously obtains the energy continuously from the energy source, and this prevents SIRM from breaking the second law of thermodynamics. The fluctuation force follows a fluctuation-dissipative relationship:

$$\langle F_a(t) \rangle = 0 \qquad (4)$$

$$\langle F_a(t) F_b(s) \rangle = 2k_B T \varsigma \delta_{ab} \delta(t-s) \qquad (5)$$

where $a, b = x, y$ or x_2 and x_2 and $\varsigma = \alpha_0, \beta_0, \eta$. We assume that the potential of the G-actin has a spherical shape since the shape of the G-actin is spherical as shown in Fig.1:

$$U_a = \sum_{j=1} U_a^0 \left(\sqrt{(x-x)^2 + (y-y)^2} - R \right)^{-n+1} \qquad (6)$$

where (x_j, y_j) denotes the center of the j-th G-actin glove, and R is its radius. The potential of the myosin rod is approximately expressed as follows:

$$U_S = A \exp\left(-\sqrt{(x-x_2)^2 + (y-y_2)^2} + L \right) + A \exp\left(\sqrt{(x-x_2)^2 + (y-y_2)^2} - L \right) + \frac{1}{2} K(\theta - \theta_0)^2 \qquad (7)$$

where K, L and θ are the spring constant, natural length of the spring and inclined angle $\theta = \{(x_2 - x)/y\}$. A is the strength of the replusive potential; this potential has the minimum at $(x-x_2)^2 + (y-y_2)^2 = L^2$ and $\theta = \theta_0$. Therefore, this potential indicates the force of the spring of the rod which tends to keep the myosin head at the minimum point. Here we emphasize that these potentials U_a, and U_S are symmetric along the x coordinate. As it will shown in a latter section, the rod breaks symmetry with the aid of the spherical shape of the G-actin and produces a one directional motion.

3. SIMPLEST EQUATION of SIRM

The main purpose of this paper is to show that there is a stochastic resonance(SR) between the actin myosin system and the thermal noise, and that SIRM moves in one direction by accepting energy from thermal noise. In order to show the existence of SR, we should solve the above equations. However, equations (from

Eq.(1) to Eq.(7)) are very complex and highly nonlinear, therefore we cannot obtain a strict analytical solution. The exact numerical solution will be shown in sec.4. In this section, for a clear analysis of the SIRM movement, we adopted a perturbative method. Following the perturbative method by Landau and Lifshitz[20], we consider only the truly essential part of the equations by neglecting the ineffective parts of the potentials. From Eq.(1) to Eq.(7), we set up the following simple equations for domain-1 and domain-2, where the j -th G-actin is the one nearest to domain-1:

$$m\ddot{x} = nU_a^0(x-x_j)^{-n} + F_x(t) - \alpha_0\dot{x} - 2K(x-x_2+L) \quad (8)$$

$$m\ddot{y} = nU_a^0(y-y_j)^{-n} + F_j(t) - \beta_0\dot{y} - 2K(y+L) \quad (9)$$

and for domain-2 which denotes the myosin bundle:

$$M\ddot{x}_2 = 2K(x-x_2+L) - \eta\dot{x}_2 + F_{x2}(t) \quad (10)$$

If we assume that the thermal noise contains all frequencies, one of the noise frequencies is express as $F_x(t)/m \to (f/m)\exp(i\gamma t)$, because the fluctuation $F(t)$ can be given in the following form using an operator $\hat{\rho}_a^j$:

$$F_a(t) \equiv \sqrt{\frac{k_B T\varsigma}{\pi}} \sum_j \hat{\rho}_a^j \exp(i\Omega_j t) \quad (11)$$

The operator expressions of the autocorrelation become

$$\left\langle F_a(t)F_b(t)\right\rangle = \frac{k_B T\varsigma}{\pi} \sum_{j,l} \delta_{a,b}\delta^{j,l} \left\langle \hat{\rho}_a^{j*}\hat{\rho}_b^l \right\rangle \times \exp i(\Omega^l s - \Omega^j t) \quad (12)$$

$$\left\langle \hat{\rho}_a^{j*}\rho_b^l \right\rangle = \delta_{a,b}\delta^{j,l}, \quad \left\langle \rho_a^{j*} \right\rangle = \left\langle \rho_b^l \right\rangle = 0 \quad (13)$$

Thus Eq.(8) gives us the following equation:

$$\ddot{\xi} + 2\lambda\dot{\xi} + \omega_0^2 = \frac{f}{m}\exp(i\gamma t) - \alpha\xi^2 - \beta^3 \quad (14)$$

where we rewrite the following quantities,

$$\xi \equiv x - x_2 + L, \xi_j \equiv x_j - x_2 + L, 2\lambda = \alpha_0/m$$

$$\omega_0^2 \equiv \frac{2K}{m} + \frac{n^2 U_a^0}{(-1)^{n-1} m\xi_j^{n+1}}$$

$$\alpha \equiv \frac{(-1)^{n-1} n^2 (n+1) U_a^2}{2m\xi_j^{n+2}}$$

$$\beta \equiv \frac{(-1)^{n-1} n^2 (n+1)(n+2) U_a^2}{3! m\xi_j^{n+3}} \quad (15)$$

Here we use the Taylor expansion for the intermolecular force of G-actin, and by ignoring $O(\xi^4)$, Eq.(14) is the so-called Duffing equation. In the following sections we attempt to determine the behavior of resonance using Eq.(14) on the basis of a perturbation method.

3.1 LINEAR SOLUTION

When the non-linear terms are zero in Eq.(14), the equation becomes the well-known linear damping equation. The solution is easily obtained:

$$\xi = a\, e^{-\lambda t}\cos(\omega_1 t + \sigma) + be^{-i(\gamma t+\delta)} \quad (16)$$

where the amplitude a and the phase σ are determined by the initial conditions, and the frequency ω, the amplitude b, and the phase δ are given as

$$\omega_1 = \sqrt{\omega_0^2 - \lambda^2}, b = f\Big/(m\sqrt{(\omega_0^2-\gamma^2)^2 + 4\lambda^2\gamma^2} \quad (17)$$

and

$$\tan\delta = (-2\lambda\gamma)/(\omega_0^2 - \lambda^2) \quad (18)$$

Thus the maximum amplitude b_m of the forced damping oscillator is given as

$$b_m = f\Big/m\sqrt{\left\{\gamma^2 + (2\lambda^2 - \omega_0^2)\right\}^2 + 4\lambda^2(\omega_0^2 - \lambda^2)} \le f\Big/2m\lambda\sqrt{\omega_0^2 - \lambda^2} \quad (19)$$

After a sufficient time, the damping terms of Eq.(16) go to zero, and only the oscillational term $be^{-i\gamma t}$ survives. Within this limit, the energy of domain-1 has a constant value which is determined by the amplitude b. In other words, this system always absorbs the same amount of energy that is consumed by friction or dissipation. Moreover, the average absorbed energy per unit time $I(\gamma)$ will be

$$I(\gamma) = 2\gamma^2\lambda m b^2 \quad (20)$$

Near the resonance point, the signal to noise ratio (S/N) is written as

$$(S/N) = 1/2m\omega_0\sqrt{\varepsilon^2 + \lambda^2} \quad (21)$$

by having a peak value at $\varepsilon = 0$, the peak value is:

$$1/2m\omega_0\lambda \quad (22)$$

hence $\gamma = \omega_0 + \varepsilon$, $\varepsilon \approx 0$. We emphasize that an energy flows into domain-1 from the surroundings through the resonance with noise even if the system is the simplest linear case, where the resonance frequency of noise is estimated as $\gamma = \sqrt{\omega_0^2 - 2\lambda^2}$.

3.2 DUFFING EQUATION

It is essential to know how SR occurs in domain-1. We then applied a perturbation to solve the non-linear equation(Eq.(14)). If the linear solution, Eq.(16), is a good approximation, the value of ε is small in $\gamma = \omega_0 + \varepsilon$, then we obtain the following approximate relation from Eq.(17).

$$b^2\left(\varepsilon^2 + \lambda^2\right) = f^2/4m^2\omega_0^2, \quad \tan\delta = \lambda/\varepsilon \qquad (23)$$

Since the proper frequency ω_p of domain-1 depends on its amplitude b, it is given by

$$\omega_p \approx \omega_0 + \kappa b^2 \qquad (24)$$

where κ is determined by the non-linear term in Eq.(14)[20]. Using Eq.(24), Eq.(23) is rewritten as

$$b^2\left\{\left(\varepsilon_0 - \kappa b^2\right)^2 + \lambda^2\right\} = f^2/4m^2\omega_p^2 \qquad (25)$$

where $\varepsilon_0 \equiv \gamma - \omega_0$, or

$$\varepsilon_0 \equiv \kappa b^2 \pm \sqrt{\left(f^2/2m\omega_0 b\right)^2 - \lambda^2} \qquad (26)$$

Since Eq.(25) is a cubic equation of b, the true amplitude of the forced vibration is given by the real roots of this equation(Fig.2). If the amplitude of noise b is small, Eq.(25) is approximately equal to Eq.(23). For this case, the shape of b as a function of ε_0 is shown in Fig.3. As the amplitude of noise f increases, the shape of b^2 gradually changes while it keeps the characteristic that this graph of b^2 has only one maximum.

Differentiating Eq.(25) with respect to ε_0, we can obtain the following relation with respect to the critical amplitude f_κ above which the b^2 value has three real roots:

$$\varepsilon_0^2 - 4\kappa b^2\varepsilon_0 + 3\kappa^2 b^4 + \lambda^2 = 0 \qquad (27)$$

and the maximum amplitude $b_{\max}$ is given by

$$b_{\max} = f/2m\lambda\omega_0 \qquad (28)$$

From Eq.(25) and Eq.(27), the critical amplitude f_κ is written as

$$f_\kappa^2 = 32m^2\omega_0^2\lambda^3/3\sqrt{3}|\kappa| \qquad (29)$$

If the noise amplitude $f \geq f_\kappa$, Eq.(25) has three real roots, which denotes a collapse in the function b^2 and has a kind of hysteresis loop. Moreover, Eq.(28) is similar to Eq.(22) for the linear case. Calculating the SN ratio using a computer, we find that the graph of the SN ratio always has one peak as shown in Fig.3, which indicates the existence of the resonance with noise. This is the so-called stochastic resonance (SR).

Generally, it is shown that the resonances are observed in descrete noise frequencies of $\gamma = m\omega_0/n$ for integer m and n [20]. If the thermal noise is composed of all frequencies just like white noise, SR never fails to occur between domain-1 and the noise. With an increase in the noise strength, the maximum of the SR amplitude shifts to the positive area of frequency ε_0.

From the view point of making an artificial micro-machine, we finally comment that the proposed SIRM model resembles the supersonic Langevin type motor though its size is larger than the SIRM, when stochastic resonators are replaced by piezoelectric elements.

4. MOTION OF DOMAIN-2

In this section, we will show that domain-2 accepts the energy which domain-1 supplies from the thermal noise through SR, and then domain-2 moves in one direction using the inclined rod. In this model, domain-2 follows Eq.(10):

$$M\ddot{x}_2 = 2K\xi - \eta\dot{x}_2 + F_{x2}(t) \qquad (30)$$

Since the collision between domain-1 and G-actin distorts the motion of SR from ξ to $\overline{\xi}$, the distorted motion $\overline{\xi}$ can be approximately given by which are damping terms (or dissipative ones). After a long time, the damping terms go to zero, then the motion of domain-2 is given by

$$x_2 = C_0 + \frac{A_1 t}{2\mu} + \frac{A_1 \sin\gamma t}{2\mu\gamma} - \frac{A_1(\mu\cos\gamma t + \gamma\sin\gamma t)}{2\mu(\mu^2+\gamma^2)},$$
$$\mu = \eta/M \qquad (31)$$

Clearly, the first term of Eq.(31) means the translational motion of domain-2, and the second and third terms are the vibrational mode of SR. It is clear that the equations (from Eq.(1) to Eq.(3) do not have an energy-source except for the thermal noise term $F(t)$. Domain-1 (myosin head) interacts with the thermal noise. When SR occurs between the spring and the noise, SR causes an energy transfer from the noise to domain-1. According to this model, the noise energy (i.e., the random motion of the water molecules) is not consumed by this energy transfer, since the heat energy due to ATP hydrolysis is supplied to the surroundings. The more important consequence is that the system does not break the second law of thermodynamics. We will provide more detailed discussions on non-breaking of the second law in sections 6. Since the heat energy is constantly supplied from ATP, domain-1 and the spring are kept vibrating by SR, and domain-1 constantly collides with G-actin.

The inclined spring of domain-1 then automatically contracts and can obliquely kick the G-actin in the same direction. This is possible because the G-actin has a spherical shape.

In this way, domain-2 (myosin bundle) always moves in one direction by accepting the energy from noise as shown in Eq.(31). Since domain-1 and domain-2 are connected by the spring, the myosin molecule(domain-1, domain-2 and rod) slides along the direction of the actin fiber.

5. NUMERICAL SOLUTION

We have shown by the perturbative method that the equation of motion is appropriate to describe SR and the movement of the actin myosin system. In order to strictly solve these equations(Eq.(1)-Eq.(7)), we adopted a numerical method instead of the perturbation. The numerical results are shown in Figs.4 and 5. In Fig.4, the displacement of the actin myosin system is shown. The straight line in Fig.4 shows the position of domain-2, though this trace has irregularities and randomness like Brownian particles, whose movement is a translational one as a whole. The displacement of domain-1 is denoted by the dashed line. It also moves forward along one direction. In Fig.5, the relative coordinate x_i between domain-1 and domain-2 is shown with a straight line, and the motion of domain-1 along the y coordinate is described by a dashed line.

The straight line, which means a stretching vibration of the spring (myosin rod), also has an irregularity as seen in Fig.4. As is shown with a dashed line, the collision between the G-actin and domain-1 distorts their relative motion from a trigonometric function. This trace of the motion is given by an accurate trigonometric function if there are no interactions or no collisions. Truly, the strain of the trigonometric function indicates that domain-1 obliquely kicks the G-actin or F-actin when the spring is stretched by the resonance vibration. As a conclusion, these results agree with the perturbative solutions, indicating that the method is proper in this case.

6. NYQUIST THEORY AND THERMODYNAMICS

We have discussed the mechanism and characteristics of the movement of the actin-myosin system due to the stochastic resonance. We are afraid that someone may insist that the system breaks the second law of thermodynamics. It is wrong to think that SIRM violates this law of thermodynamics. The reason is simply that the system is thermally open to the outer surroundings and it has a outer heat source of ATP.

The heat or energy consumed by SIRM is directly supplied from the surroundings (i.e., the thermal motions of water molecules), and the energy provided to the surroundings comes from the outer heat source or reservoir through a general energetic flow. The heat source is the energy due to the ATP hydrolysis in the case of SIRM. In the SIRM system, ATP supplies the heat energy and provides heat energy to the surrounding water molecules. ATP hydrolysis is irreversible chemical reaction and ATP is one of the heart resources. Water molecules surrounding SIRM have some temperature and heat energy which is named the near-surrounding heart resources(NSHR). SIRM system (or actin myosin system) is open to the outer-surroundings which is named the far macro-outer-surroundings(FMOS), and the energy generated from ATP hydrolysis flows out and dissipates from NSHR and SIRM to FMOS. Feynman showed from statistical discussions that the ratchets under an isothermal temperature cannot turn as a total since the ratchets turn to both sides with equal probability. This discussion is so famous that many people have the impression that a ratchet cannot move in isothermal heat both[21]. However, we should realize that

Feynman also showed in the same section, 46-2, that it can turn to one side if a load is suspended from the one side even in an isothermal bath. These Feynman's explanations mean that some kind of loads or bias sometimes, which are almost equal to thermal resources, break the heart balance or thermal equilibrium. In SIRM or actin myosin system, the actin fiber fastened to Z-membrane and the intermolecular forces between G-actin and myosin head are considered to be the loads or bias of Feynmans' thermal ratchets. Thus, SIRM or actin myosin system has four heart resources at least, i.e. ATP, load or bias, FMOS and NSHR. The other example which can work in the thermal equilibrium is an electric resistor. Nyquist theory was established in 1928 by two elegant papers, which were a theoretical paper and Johnson's experimental ones. The Nyquist theory holds in thermal equilibrium[22]. If a resistor produce electric fluctuations, these will produce a current which will generate heat. The heat produced in the resistor must exactly balanced the energy taken out of the fluctuation. According to Nyquist theory, we can take out a part of energy from the random noise in the surroundings. SIRM or actin myosin system never break the second law of thermodynamics, because of the existence of four

heart resources.

This is an example of Nyquist theory in mechanical nanomachine and the existence of four heart resources. From the view point of making an efficient nanomachine, our SIRM resemble the Langevin type supersonic motor, when stochastic resonators are replaced by piezoelectric elements.

7. SUMMARY

We have shown a new model(SIRM) for the actin and myosin system, and proposed a sliding mechanism for the actin myosin system, which is summarized as follows(Fig.6).

The myosin head interacts with thermal noise (i.e., the random motion of the water molecules), and resonance occurs between the myosin head and the noise, which is the so-called the stochastic resonance(SR). When SR occurs, the energy transfers from the random noise to the myosin head, then the myosin head and spring are made to vibrate. While the myosin head vibrates, it collides with a G-actin and obliquely kicks the G-actin sphere because the direction of the vibration is inclined against the line of the actin fibers. In this way, the myosin molecule obtains the propelling force along the direction of the actin fibers, while the component perpendicular to the fibers is canceled out in the average of the total force.

We should add additional explanations on the features of the proposed model. Although the potentials of the G-actin and the myosin head are completely symmetrical, the structure of the actin myosin system makes it possible to move asymmetrically. It should be stressed that the sphericity of the G-actin is very important to provide the oblique repulsion. If the potential of the G-actin fiber is completely flat, the repulsion is only perpendicular to the fiber and does not give the propelling force. This explanation of the breaking symmetry is very simple compared with other models, in which complicated asymmetric potentials are assumed.

On the other hand, we need not assume the other interactions between actin and the myosin head, neither a direct contact as a rigid body nor an asymmetric potential which is made by ATP hydrolysis[23]. In the SIRM model, ATP supplies the heat energy and provides heat energy to the surrounding water molecules. The movement does not break the second law of thermodynamics, because the actin-myosin system is open to the surroundings and the energy flows in from its surroundings.

We have shown the solutions of the SIRM's equations by two methods: a perturbative method and a numerical calculation. The perturbative method is successful enough to explain the qualitative characteristics of non-linearity of the actin myosin system.

Comparing its result with the numerical one, we found agreement in that the trigonometric function of the vibration is distorted by the collision between the myosin head and G-actin, which indicates the production of a strong force. In order to compare the model prediction to the experiment on muscle movement, we calculated the force, output-power and gliding speed using the analytic solution.

In our previous paper[12]-[17], we estimated the vibrational amplitude of the myosin head $A = 10^{-11}$ m, the spring constant of the rod $k = 10$ n/m, and the mass of myosin bundle $M = 10^{-16}$ kg. When the spring constant of SIRM is adopted as 10 N/m, the amplitude of resonating wave is estimated 10^{-11} m, and the value of resonating frequency is shown as 10^{16}rad/s. Under these conditions, we calculate the mechanical characteristics of SIRM and actin myosin system, i.e. maximum power, output of one myosin head, sliding velocity, OUTPUT/INPUT Ratio(O/I), and INPUT/SIZE Ratio(I/L). These calculated values are compared with the measurement's values of Yanagida's experiments(Fig.7). It is impressive that the prediction well agree with the experimental data. Presently, this agreement is obtained only in this model from among the models based on the fundamental equations.

Thus, utilizing the phenomenon stochastic resonance, an efficiency of SIRM can be improved in the same level as that of natural muscle. It is important to adopt stochastic resonance as one of the energy conversion mechanism for making nanomachines mimed biological machines and molecular ones, which are believed to have excellent mechanical efficiency for a long while.

8. REFERENCE

[1] Huxley H E: Science, 164, 1356 (1957).

[2] Huxley A F and Simmons R M: NATURE, 233, 533 (1971).

[3] Huxley H E and Hanson J: NATURE, 173, 973 (1954).

[4] Cooke R.: CRC Crit. Rev. Biochem., 21, 53 (1986).

[5] Yanagida T: Kagaku, 58, 477-485 (1988).

[6] Huxly A F: Prog. Biophys., 7, 255 (1957).

[7] Vale R D and Oosawa F: Advances in Biopysics. 26, 97-134 (1990).

[8]Kurt W and Frank M: Nature, 373, 33-36(1995).

[9] Collins J J, Chow C C and Imhoff T: NATURE, 376, 236-238(1995).

[10] Neiman A, Schimansky-Geier L: Physical Review Letter 72 (19), 2988-2991 (1994).

[11] Astumian R D and Martin B: Physical Review Letter, 72, 1766-1769 (1994).

[12] Fujimasa I, Matsuura H, Imachi K, et.al: Micromachine, Journal of Micomachine Society, 4(1), 33 (1991).

[13]Matsuura H, Fujimasa I, Chinzei T, et al.: Micromachine, Journal of Micromachine Society, 5(1), 21-26 (1992).

[14]Matsuura H, Fujimasa I, Nakano M, et al.: Micromachine, Journal of Micromachine Society, 7(1), 54-126 (1994).

[15] Matsuura H: Parity, Maruzen, 11, 11, 48-60 (1996).

[16] Matsuura H, and Nakano: Biomedical Fuzzy and Human Sciences, J. of Biomedical Fuzzy Systems Association, 3(1), 47-52 (1997).

[17] Matsuura H, Nakano M and Noda: Biomedical Fuzzy and Human Sciences, J. of Biomedical Fuzzy Systems Association, 4(1),23-31(1998)

[18] Uhelenbeck G E, Ornstein: Physical Review, 36, 823-841 (1930).

[19] Wang M C, Uhelenbeck G E : Review of Modern Physics, 17(2), 323-342 (1945).

[20] Landau L D and Lifshitzs E : Course of Theoretical Physics, Mechanics. 3rd ed. Butterworth Heinemann (1970).

[21] Feynman R, Leighton R and Sands R: Lectures on Physics, Addison-Wesley (1963).

[22] Nyquist, H : Phys. Rev., 32 (1928).

[23] Mitsui T and Oshima H: J. Muscle Res, Cell Motility, 6, 153-56,(1988)

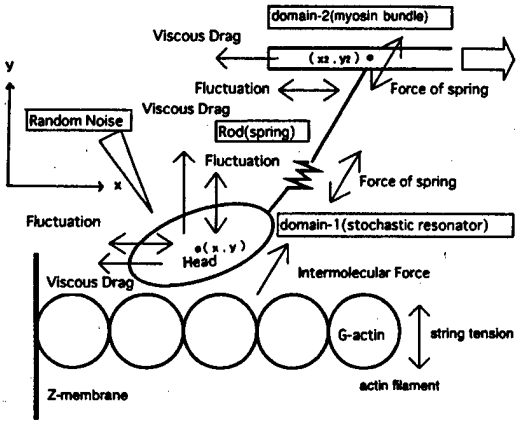


Fig.1 STRACTURE AND FORCE ACTING ON SIRM

The various forces acting on the SIRM are shown. $F_x(t)$ and $F_y(t)$: fluctuation acting on the head of SIRM, $\alpha_0\dot{x}$ $\beta_0\dot{y}$, and $\eta\chi_{x2}$: viscous drag, The head of SIRM (or myosin hea good resonator of random noise. There is an intermolecular force betw actin and the myosin head.

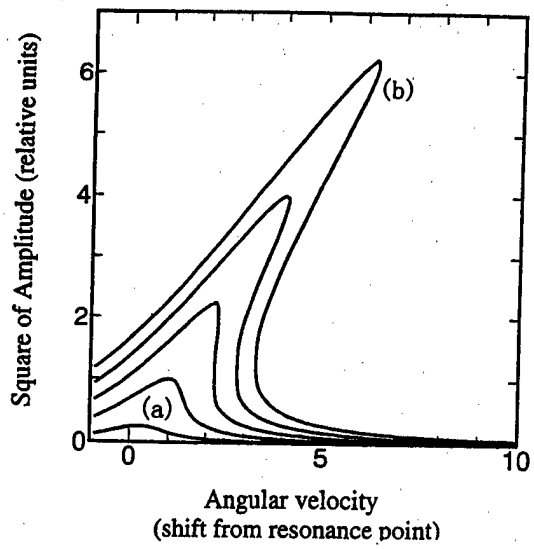


Fig.2 RESONANCE CURVE

This figure shows the relation between the square of the resonance amplitude b^2 and the shift from the resonance point, ε_0, which is the solution of Eq.(25). If the amplitude of noise f is so small as shown in case (a), the shape of b^2 becomes similar to the case of Eq.(14), which is the linear one. With increasing f, the shape of b^2 gradually changes by keeping the characteristics that b^2 has only one peak. In the case of a real actin myosin system, we think that the motion of equation satisfies $f \geq f_\kappa$ and has three real roots, which means an amplitude collapse and has a kind of hysteresis loop.

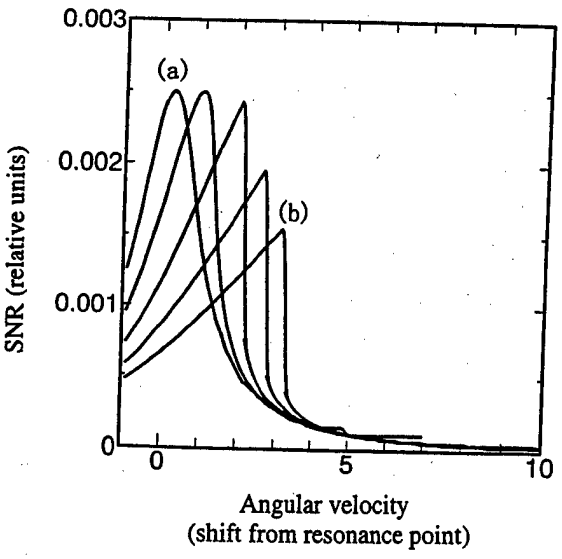


Fig.3 SIGNAL-TO-NOISE RATIO (S/N)

This figure shows the relation between S/N and the shift from the resonance point. As we saw in Fig.2, the shape of graph is similar to case (a), if $\varepsilon \approx 0$. By increasing the amplitude of noise f, the graphic shape of S/N approaches type (b). However, the S/N graph always has one peak, which truly shows the existence of SR.

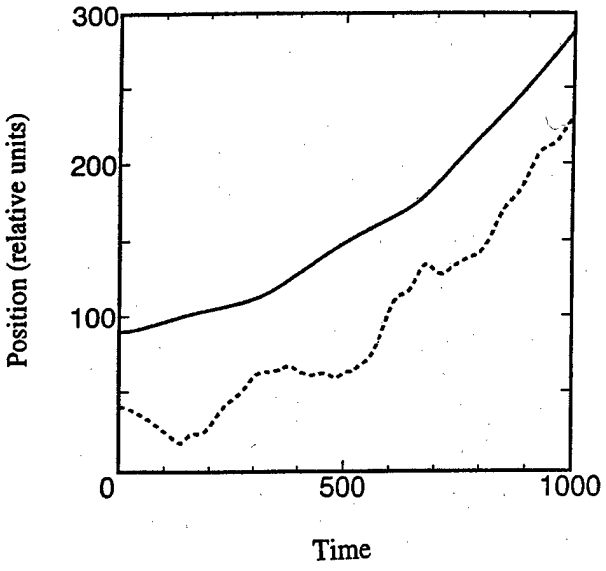


Fig.4 POSITION OF MYOSIN HEAD

The straight line shows the position of the myosin bundle (domain-2), and the displacement of the myosin head (domain-1) is described by the dashed line. We find that these domains, bound by the spring, move forward along one direction as a whole by having an irregular and randomness of motion like Brownian particles.

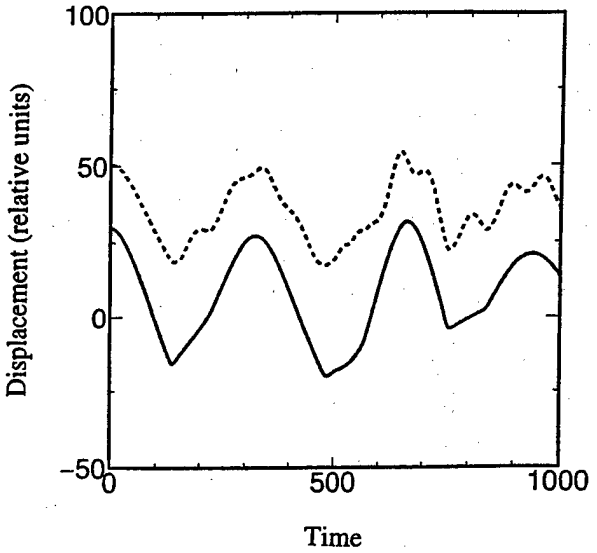


Fig.5 MOTION OF ROD AND MYOSIN HEAD

Straight line of x_i indicates the stretching motion of the myosin rod (spring). The displacement of the myosin head (domain-1) along the y coordinate is shown with dashed line. We find that the collision between the G-actin and domain-1 distorts the relative motion distort from an accurate trigonometric function.

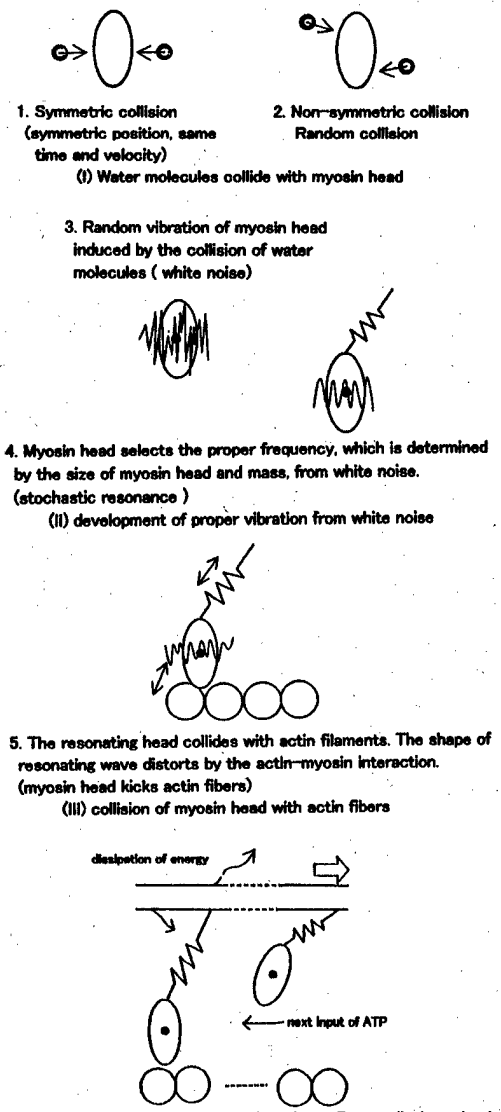


Fig.6 Actin-Myosin sliding process and energy supplement

	unit per one head	
	Actin Myosin	SIRM
Input of Energy : 33ATP (J/s)	10^{-18}	10^{-18}
[Mechanical Characteristics]		
maximum power (J/s)	$2.1X10^{-17}$	10^{-17}
output of one myosin head (N)	$3X10^{-12}$	$3\sim10X10^{-12}$
sliding velocity (m/s)	$7X10^{-6}$	10^{-6}
[Efficiency]		
O/I [N/(J/s)]	10^{6}	$10^{5}\sim10^{6}$
I/L [(J/s)/m]	10^{-12}	10^{-12}

Fig.7 CHARACTERISTICS OF SIRM AND ACTIN MYOSIN SYSTEM

Application of Atomic Force Microscopy to An Encoder

Masayuki SHIMODAIRA , Akihiro TORII , Akiteru UEDA
Dept. of Electrical Eng., Aichi Institute of Technology
1247 Yachigusa, Yakusa, Toyota 470-0392, Japan
Tel: +81 565 48 8121 ext. 2012
Fax: +81 565 48 0010
Email: torii@ee.aitech.ac.jp

Abstract :

Minute position measurement is needed in the field of precision engineering. We have proposed an encoder using the principle of the an atomic force microscopy (AFM), which is called the AFM encoder. Since the AFM realizes atomic scale resolution, an encoder having the atomic scale resolution will be realized. The AFM encoder is a multiple probe AFM. The deflections of AFM cantilevers are detected by a Michelson interferometer simultaneously. A line-focused red color semiconductor laser is used as a light source and a photodiode array is used as a detector. The periodicity of a crystal lattice, for example the highly oriented pyrolytic graphite, is used as the standard of displacement. The AFM cantilevers detect surface topography with atomic resolution and measure the displacement by using the detected signals. In this paper, two AFM cantilevers are used as the probes of the AFM encoder. An optical grating is used as a displacement standard and a pitch of the optical grating is 1.1 μm. Surface topography is obtained by two AFM cantilevers simultaneously.

1 Introduction

A linear encoder is an indispensable instrument for the precise positioning of many machines. The recent demand is about 10 nm or less. It is difficult for conventional encoders to meet the recent demand. The atomic force microscope (AFM) is capable of imaging surface topography with atomic scale resolution. It is mainly used for physical investigation of surface properties. In addition to the physical evaluation of the surface, some metorological applications have been proposed[1]-[3]. We have proposed the application of the AFM to an encoder, which is called an AFM encoder[4]. The feasibility of the AFM encoder was discussed. In our previous work, the optical beam deflection method was used to detect the deformation of the AFM cantilevers. Therefore the absolute values of the AFM cantilevers' deformations were not obtained.

In this paper, we proposed an AFM encoder using a Michelson interferometer and we manufacture a prototype. A line-focused red color semiconductor laser is used as a light source and a photodiode array is used as a detector. Two AFM cantilevers are used as probes of the AFM encoder. An optical grating is used as a sample and a pitch of the optical grating is 1.1 μm. The surface topography of the optical grating is detected by the AFM cantilevers. The deflections of the AFM cantilevers are simultaneously detected by Michelson interferometry and a surface topography of the optical grating are obtained by the detected signals. By using a Michelson interferometer, the deflections of the AFM cantilevers are measured with the standard of the wavelength of the light.

2 AFM Encoder

2.1 Principle

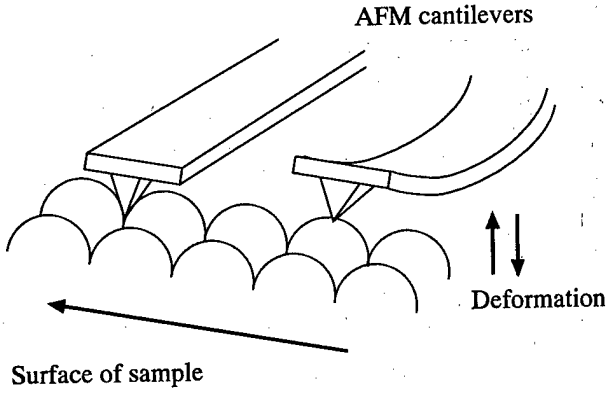


Figure 1: Schematic diagram

1999 INTERNATIONAL SYMPOSIUM ON
MICROMECHATRONICS AND HUMAN SCIENCE
0-7803-5790-6/99/ $10.00 ©1999 IEEE.

Figure 1 shows the principle of an AFM encoder. Two AFM cantilevers are used as probes of the AFM encoder. The periodicity of a crystal lattice, for example the highly oriented pyrolytic graphite, is used as a standard of the displacement. The AFM cantilevers are deformed by the periodic surface topography of the sample. The deformations of the AFM cantilevers are detected and the displacement is measured by the detected signals. The displacement is determined from the periodicity of the detected signals. The direction of the displacement is determined from the phase difference of the two detected signals. In this study, the deformation of the AFM cantilevers is detected by a Michelson interferometry.

2.2 Structure

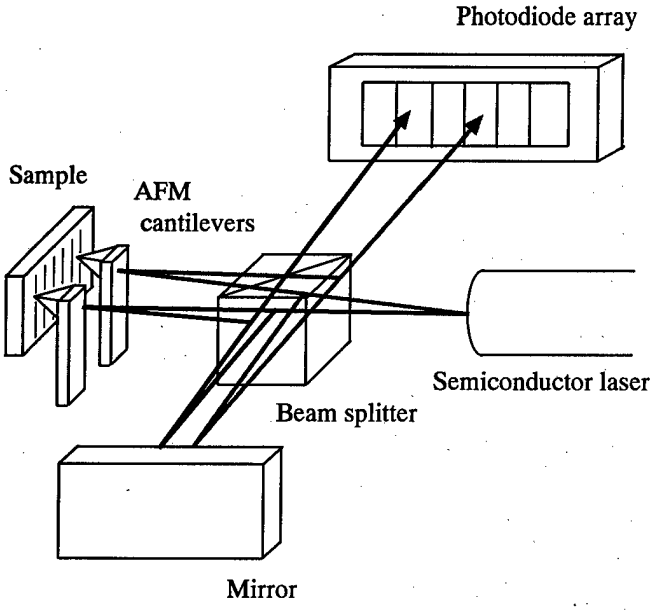


Figure 2: Schematic diagram of Michelson interferometer with two AFM cantilevers

Figure 2 shows the structure of the AFM encoder using Michelson interferometry. A line-focused red color semiconductor laser (MORITEX, SNF-501L-670-10, wavelength: 670 nm, laser power: 10 mW) is used as a light source and a photodiode array (Hamamatsu Photonics, S4112-38Q) is used as a detector. The laser beam is divided into an object beam and a reference beam by a beam splitter. The reference beam is reflected by a mirror and the object beam is reflected by the AFM cantilevers (OLYMPUS, OMCL-TR800PSA-2). These reflected beams are interfered by the beam splitter and detected by each element of the photodiode array. The sample stage is tripodical PZT (TOKIN, AE0203D08, size: 2 mm × 3 mm × 9 mm) stage. The optical grating is used as the sample.

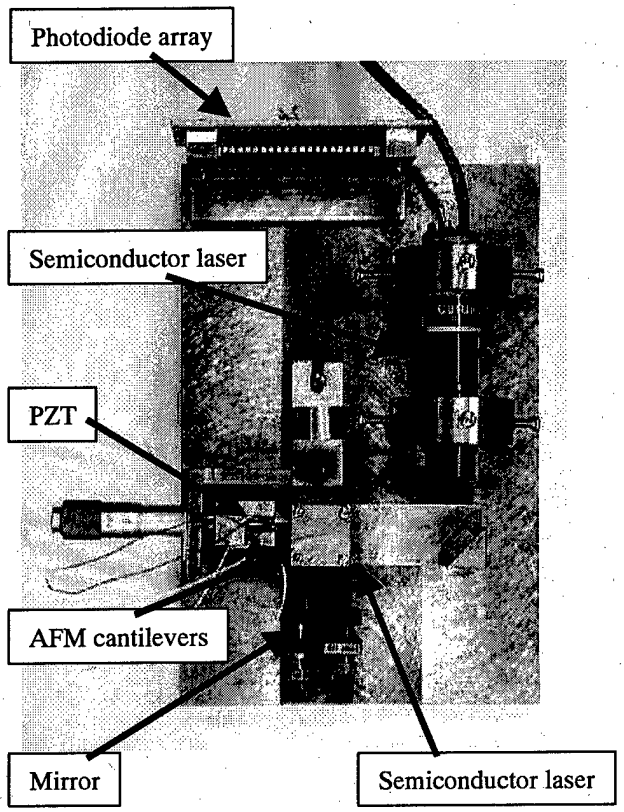


Figure 3: Prototype

Figure 3 shows the photograph of the AFM encoder manufactured. The size of the AFM encoder is 126 mm × 186 mm.

Figure 4 and 5 shows the electrical circuit and the signal processing of the AFM encoder. I/V converters, amplifiers and low-pass filters are connected in each element of the photodiode array.

3 Experiment

Figure 6 shows the schematic diagram of AFM cantilevers and an xyz-stage. Two AFM cantilevers are used as probes of the AFM encoder. In this experiment, an optical grating is used as a sample and the pitch of the optical grating is 1.1 μm. The optical grating is fixed on the sample stage. The sample stage uses the PZT tripod

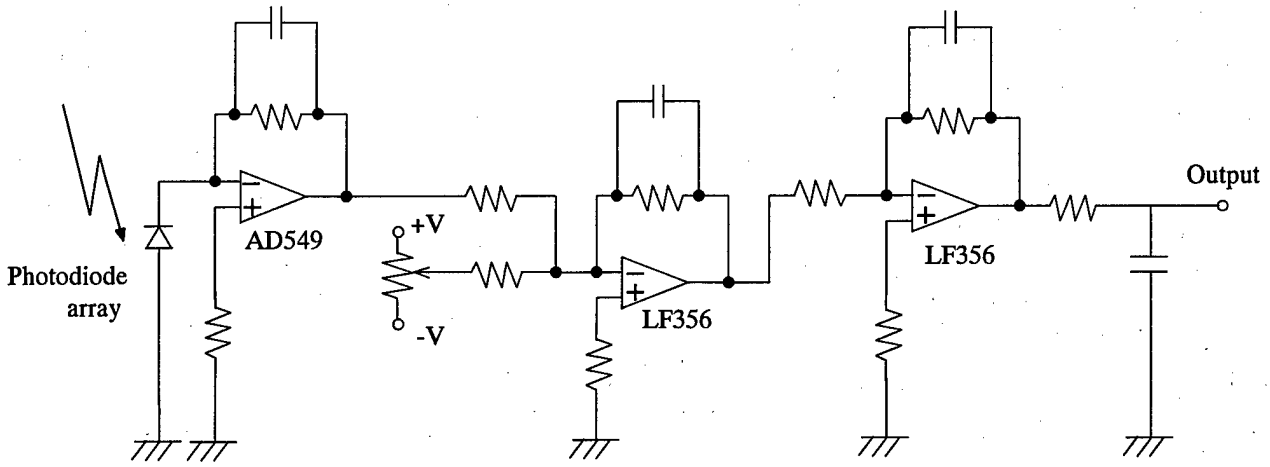


Figure 4: Electrical circuit

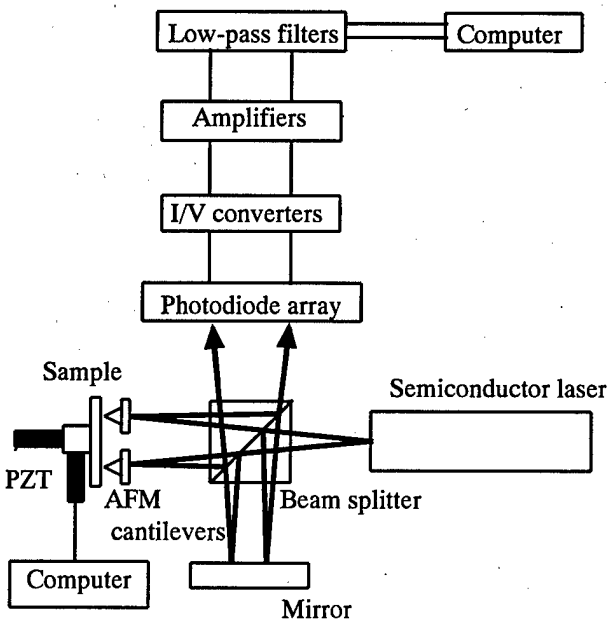


Figure 5: Signal processing

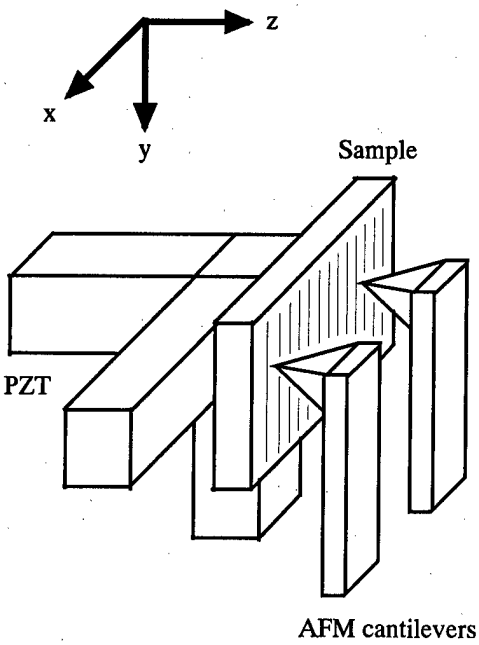


Figure 6: Schematic diagram of the AFM cantilevers and PZT stage

structure. The displacement of the sample is controlled with the PZT and the PZT is controlled by a control waveform. The Control waveform is made by a computer and applied to the PZT through a D/A board.

First, the PZT element is calibrated. The z-axis PZT is deformed by the applied voltage. The deformation of

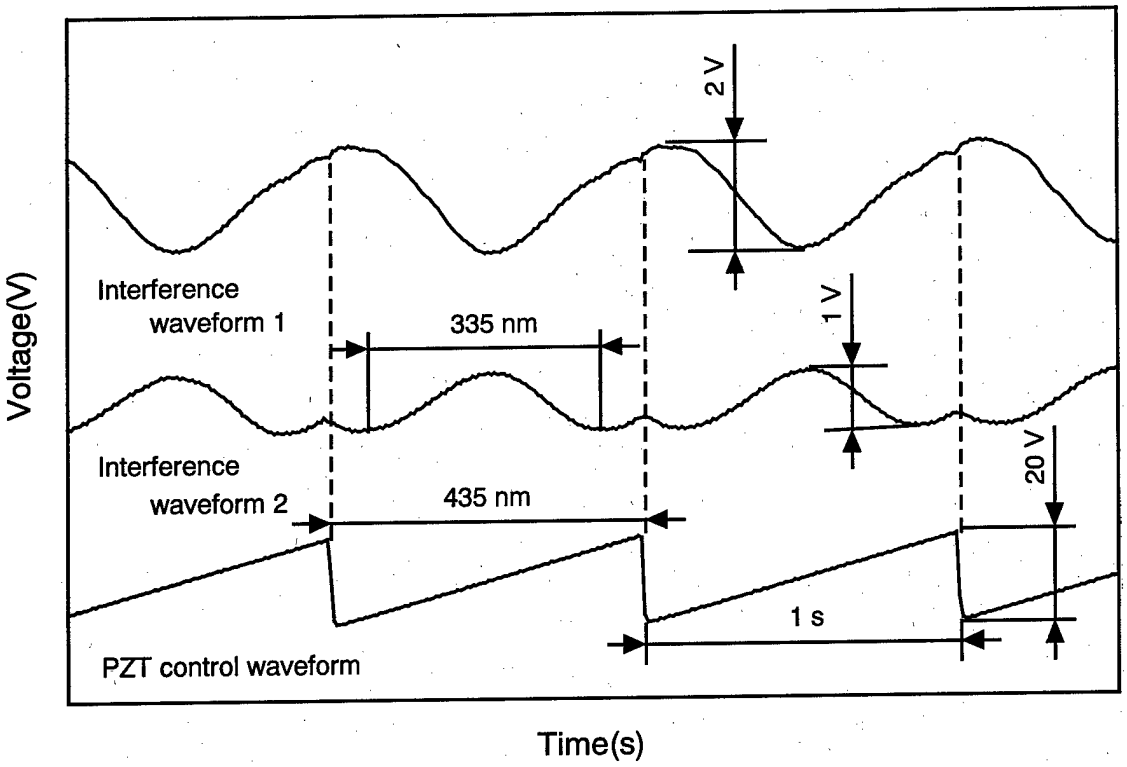


Figure 7: Waveform of detected signals and applied voltage to z-axis PZT

the PZT deflects two AFM cantilevers and the interference signals are obtained. The periodicity of the obtained signals are a half of the wavelength of the light source. Therefore, the PZT property is calibrated.

Next, the displacement measurement is carried out. The x-axis PZT is deformed by the applied voltage. An optical grating is used as a standard of the displacement measurement. The optical grating is 1.1 μm period. The deflections of the AFM cantilevers are simultaneously detected by the Michelson interferometer. The interference waveform to the deflections of the AFM cantilevers are drawn with the I/V converters, the amplifiers, the low-pass filters and an A/D board and processed to a computer.

4 Results and Discussion

We calibrate PZT deformation first. When the z-axis PZT is extended by an applied voltage, the AFM cantilevers are deformed by the interaction between the sample and the tip of the AFM cantilever. The deflections of the AFM cantilevers are measured by a Michelson interferometer.

Figure 7 shows the waveforms of the output voltage of the AFM encoder and the applied voltage to the z-axis PZT. The horizontal axis denotes the time, and the

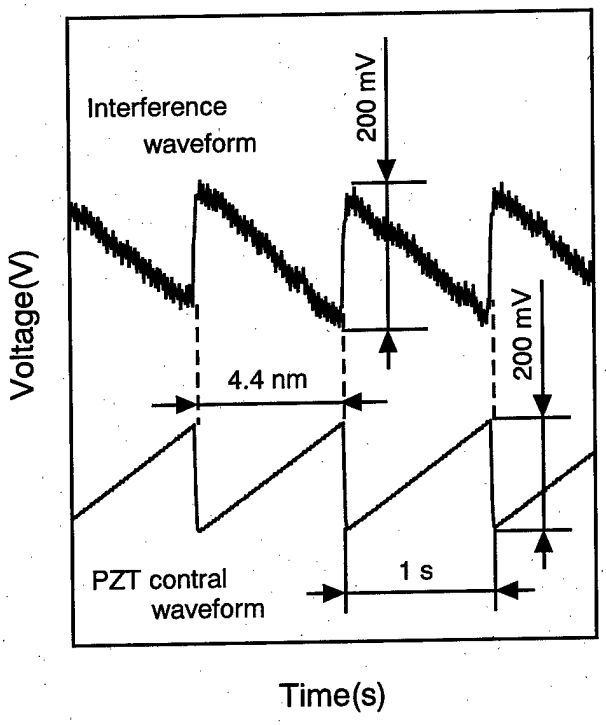


Figure 8: Waveform of detected signal and applied small voltage to z-axis PZT

vertical axis denotes the voltage. The detected signals

are 1.3 periods. Since the wavelength of the laser is 670 nm, the displacement of the PZT is 435 (= 1.3 × 670/2) nm. Therefore, the displacement of the PZT is 21.8 (= 435 nm / 20 V) nm/V.

Figure 8 shows the waveforms of the output voltage of the AFM encoder and the applied small voltage to the z-axis PZT. The horizontal axis denotes the time, and the vertical axis denotes the voltage. The displacement of the PZT is about 4.4 nm at the applied 200 mV, since the sensitivity of the PZT is 21.8 nm/V. Therefore, the heighest resolution of the detected signal is about 1 nm.

Encoding signals are obtained by using an optical grating with 1.1 μm pitch. the optical grating is attached on an xyz-stage and is displaced in the x-direction. Two AFM cantilevers are deformed according to surface topography of the optical grating. The Michelson interferometer using a line-focused laser beam is used to measure the deflections of the AFM cantilevers.

Figure 9 shows the waveforms of the AFM encoder and the applied voltage to the x-axis PZT. The horizontal axis denotes the time, and the vertical axis denotes the voltage. The applied waveform to the x-axis PZT is a sawtooth wave (frequency: 1 Hz, peak voltage: 60 V). The displacement of the x-axis PZT is about 1.3 μm at the applied 60 V, since the sensitivity of the PZT is 21.8 nm/V. Therefore, the displacement resolution of the detected signal is about 100 nm. Although the obtained signals include electrical noise, we can observe the signals with the 0.8 μm period. The periodicity of the signals are measured by the deformation of the x-axis PZT. The obtained period of the optical grating roughly corresponds to the nominal value(1.1 μm). The inclinations of the signals are considered to be caused by the slope of the sample surface. The difference between the nominal periodicity of the optical grating and the measured periodicity is caused by the difference of the z-axis and x-axis PZT deformations.

5 Summary

In this paper, we constructed an AFM encoder using a Michelson interferometer. An optical grating with 1 μm pitch was used as a displacement standard. Two AFM cantilevers were used as the probes of the AFM encoder. They were deformed by the surface topography of the displacement standard. In our developed encoder, the 1 nm resolution in z-axis was obtained. The periodical signals indicating surface topography is obtained. The 100 nm resolution in horizontal displacement was obtained.

Acknowledgement

Part of this work was financially supported by the Naito Research Grant.

References

[1] H. Kawakatsu, et al., "Crystalline Lattice for Metrological Applications and Positioning Control by a Dual Tunneling-Unit Scanning Tunneling Microscope ", J. Vac. Sci. Technol., B9, 2, (1991) 651

[2] Y. Li, et al., "Polystyrene Latex Particles as a Size Calibration for the Atomic Force Microscope", Rev. Sci. Instrum., 61, 12, (1991) 2630

[3] H. J. Mamin, et al., "Thermomechanical Writing with an Atomic Force Microscope Tip", Appl. Phys. Lett., 61, 8, (1992) 1003

[4] A. Torii, et al., "The Feasibility of a Precise Linear Displacement Encoder Using Multiple Probe Force Microscope", Int. J. of The Japan Society for Precision Engineering, 27, (1993) 367

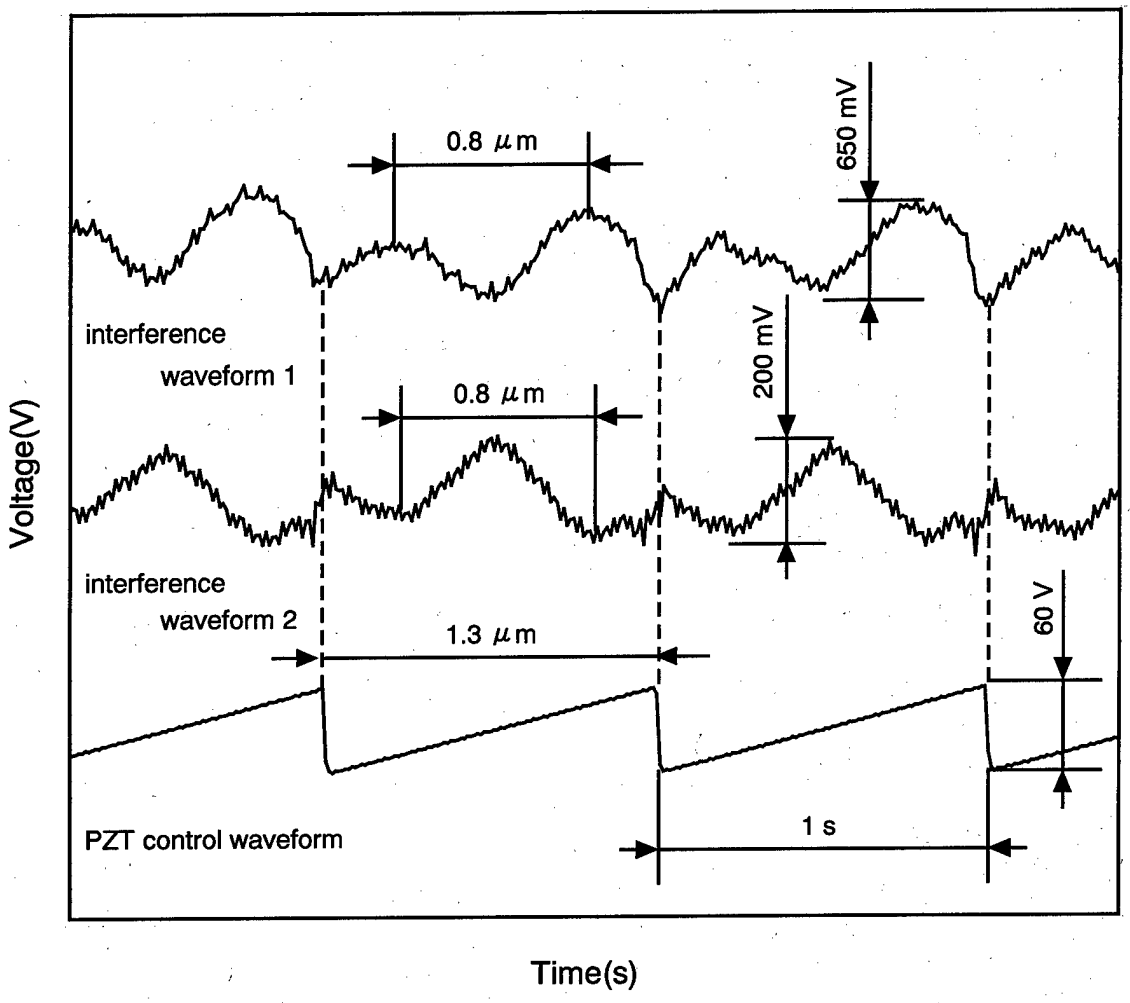


Figure 9: Waveform of detected signals and applied voltage to x-axis PZT

Contact Motion Control of a Micro Operation Hand

Tatsuya Nakamura, Yoshiyuki Kogure and Koichiro Shimamura

Dept. of Precision Engineering

Tokyo Metropolitan University

1-1 Minami-Ohsawa, Hachioji, Tokyo 192-0397

Japan

Abstract:

Force control is required in dexterous micro operation of small mechanical parts and biological objects. Our research aims at the development of micro operation hands. For this purpose a finger subsystem with a lever mechanism and magnetic actuators were developed and applied to contact motion task. In this paper, characteristics of the mechanism and actuators are analyzed and it is shown that some nonlinear terms deteriorate the positioning accuracy even in free motion. Friction apparently influences positioning accuracy in contact motion. A motion control system which compensates for these disturbances was designed and applied to drawing tasks of micro figures with the size less than 1 mm.

1 INTRODUCTION

Handling and machining of small parts are required in production of micro machines. Since various micro machine components such as micro sensors and actuators have been developed recently, the need of the means of production is increasing. Commercial micro manipulators can perform picking up, cutting and scratching operations. These operations might be sufficient for industrial inspections and bioengineering but are insufficient for production of micro machines.

Dexterous handling of mechanical parts or biological objects are investigated in several institutes[1,2]. Force control is required in contact motions even in a micro world and Arai et al. developed a micro force sensor and applied to operation of biological objects[3]. However the robot is position controlled. Our research aims at the development of a micro operation hand by which we can position a tool attached to the hand in the accuracy of several μ m and output force directly to an object [4,5,6].

For this purpose a finger subsystem with a lever mechanism and magnetic actuators were developed and applied to contact motion task. In this paper, characteristics of the mechanism and actuators are analyzed and it is shown that there are some nonlinear terms which deteriorate the positioning accuracy even in free motion. Friction apparently influences positioning accuracy in contact motion. A motion control system which compensates for these disturbances was designed and applied to drawing tasks of micro figures with the size less than 1 mm. A disturbance observer was used for the position control to cancel the disturbance. An open loop control was used for the force control since contact force corresponds to the coil current accurately because of the low friction of the mechanism. The experimental results show that disturbance observer is effective for disturbance rejection.

2 STRUCTURE OF ONE FINGER SUBSYSTEM

Fig.1 and Fig.2 show a structure of the one finger subsystem developed and its photograph, respectively. A finger is constrained with a three DOF lever mechanism and three motions of rotations around three joints are allowed.

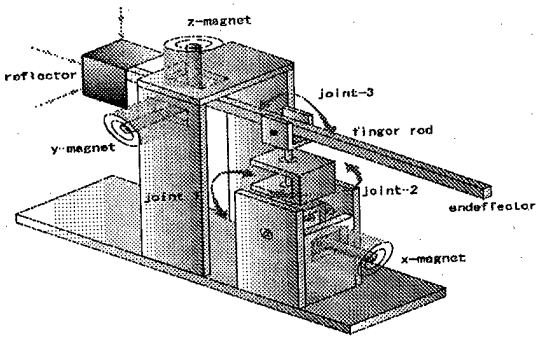


Fig.1 Structure of one finger subsystem

1999 INTERNATIONAL SYMPOSIUM ON
MICROMECHATRONICS AND HUMAN SCIENCE
0-7803-5790-6/99/ $10.00 ©1999 IEEE.

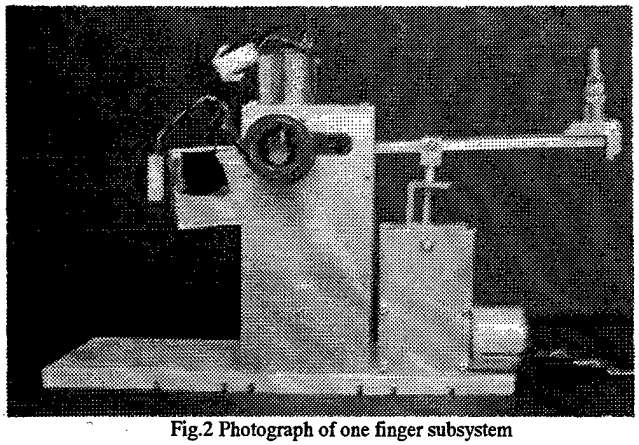


Fig.2 Photograph of one finger subsystem

Rotations around joint 1, 2 and 3 produce approximate straight line motions of the finger tip in x, y and z directions, respectively, due to the relatively longer lever compared with the size of the workspace. Three dimensional position (x, y, z) is measured at the opposite side of the finger with laser displacement sensors. Three permanent magnets are placed at this side. Each permanent magnet and a coil fixed in the environment produce a driving force of the finger in one direction.

The features of the subsystem are as follows: First, the lever mechanism is simple. For this reason, it is possible to form a small mechanism. Second, direct-drive actuators are used and the effect of joint friction is very small at the actuator position. For this reason, force control is carried out very easily. Third, since the mechanism is gravitationally balanced by attaching counter balances, the subsystem can be used as a finger of a macro robot.

Specifications of the finger subsystem are as follows:

[lever mechanism]

size:	L320 × H110 × W175 [mm]
weight:	1 [kg]
workspace:	5 × 5 × 5 [mm]

[sensor]

type:	Keyence LK-2000/LK-030
measurable range:	±5 [mm](analog output)
resolution:	1 [μm]
response:	512 [μs]

[magnetic actuator]

permanent magnet:	rare earth magnet with 0.8 [T]
size:	ϕ10 ×40 [mm]
size:	ϕ20 ×26 [mm]
force:	0.12 [kg f / A]
time constant:	1 [ms]

3 CHARACTERISTICS OF ACTUATOR

The actuator used in this study uses a pair of an air-core coil and a permanent magnet as shown in Fig.3. Characteristics of the actuator are analyzed in this section. Consider a multi-layer cylindrically wound coil. Let z be the distance from the center of the coil along the axis. Then the z-component H_z of the magnetic field **H** on the axis is given by Eq.(1)[7].

$$H_z(z) = \frac{nI}{2(a_2 - a_1)} \left\{ (b+z) \ln \frac{a_2 + \sqrt{a_2^2 + (b+z)^2}}{a_1 + \sqrt{a_1^2 + (b+z)^2}} + (b-z) \ln \frac{a_2 + \sqrt{a_2^2 + (b-z)^2}}{a_1 + \sqrt{a_1^2 + (b-z)^2}} \right\} \quad (1)$$

a_1: an inner diameter of the coil,

a_2: an outer diameter,

b: half length of the coil,

n: the number of windings per unit length,

I: coil current.

As the finger moves, the position of the pole of the permanent magnet relative to the coil changes. At this time, the magnetic field changes depending on the position in the air-core coil. For this reason, the magnetic force which arises by the pair of a permanent magnet and an air-core coil changes. In the control of the finger, a change of the driving force is a kind of disturbance when an ideal actuator model is used. Fig.4 shows the magnetic field inside the coil.

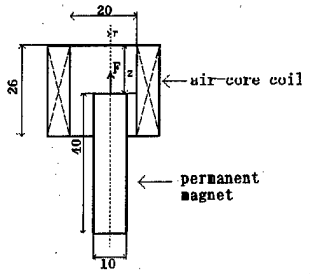


Fig.3 Configuration of a magnetic actuator

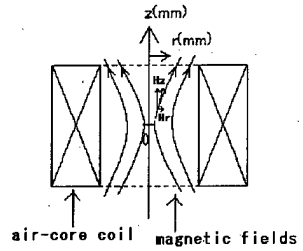


Fig.4 Magnetic field inside the air-core coil

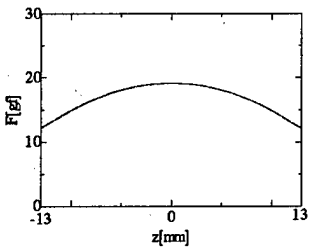


Fig.5 H_z on the z-axis (theory)

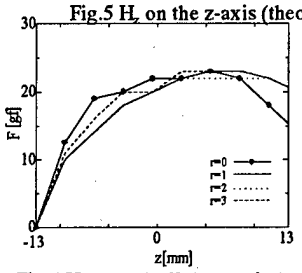


Fig.6 H_z on and off the z-axis (experiment)

The intensity of the magnetic field off the axis can be theoretically calculated using the magnetic equations inside core.

$$\text{Div } \mathbf{H} = 0 \tag{2}$$

$$\text{Curl } \mathbf{H} = 0 \tag{3}$$

From Eq.(3), **H** is a potential field with axis symmetry. Radial and axial components, H_r and H_z, are obtained from Eq.(2) by using a potential function approximated up to the second order with respect to a radial distance r in its Taylor series expansion.

$$H_z(r,z) = H_z(0,z) - \frac{1}{4}r^2\left(\frac{\partial^2 H_z}{\partial z^2}\right)(0,z) \tag{4}$$

$$H_r(r,z) = -\frac{1}{2}r\left(\frac{\partial H_z}{\partial z}\right)(0,z) \tag{5}$$

Where H_r and H_z are r and z components of magnetic field **H**. To verify the equations magnetic force along z axis was calculated and compared with the measurement. Magnetization of the permanent magnet and coil current were assumed to be 0.8[T] and 0.2[A] respectively. The results are shown in Fig.5, 6. Theory and measurement give similar results but the z-values which gives a maximum magnetic force are different. The reason for this is that the effect of the pole of the other side of the permanent magnet is not taken into consideration in the theory.

4 CHARACTERISTICS OF MECHANISM

A model shown in Fig.7 is used to derive kinematics and dynamics of the lever mechanism. The model consists of two links. The first link rotates around the first joint G1 fixed in the environment The second finger link is connected to the tip of the link through a 2-DOF joint G2. The figure shows that the mechanism is gravitationally balanced when the center of gravity of the whole links and joints is at point G1 and the center of gravity of the finger link is at point G2.

Let x-y-z be a reference coordinate frame and ξ-η-ζ be a coordinate frame fixed to the finger. The relation between x-y-z frame and ξ-η-ζ frame is expressed in terms of angles θ_1, θ_2 and θ_3:

θ_1: angle between the first link and the z-axis.

θ_2: rotational angle around z-axis.

θ_3:rotational angle around η axis.

θ_1 determines the position of the supporting point of the finger link, while θ_2 and θ_3 determine the orientation of the finger link.

Kinematics of the mechanism is given by the following equations:

$$x = a\sin\theta_1 + b\cos\theta_2\cos\theta_3 \tag{6}$$

$$y = b\sin\theta_2\cos\theta_3 \tag{7}$$

$$z = a\cos\theta_1 - b\sin\theta_3 \tag{8}$$

where x, y and z are the coordinates of the tip of the finger link.

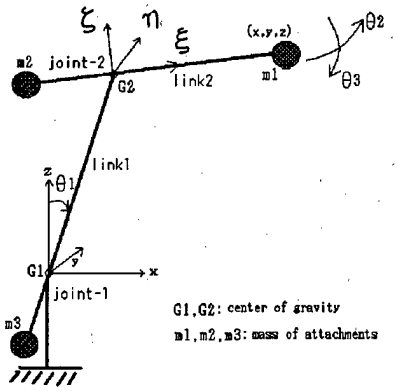


Fig. 7 Modeling of the mechanism

Dynamics of the mechanism is divided into two parts. The first part is the rotation around the first joint. Since the joint is fixed the following equation of motion is obtained.

$$m_{1y} = I_1\ddot{\theta}_1 \tag{9}$$

I_1 is an inertial moment of the first link and constant because joint G2 is assumed to be the center of gravity of the finger link and m_{1y} is a torque produced mainly by the magnetic actuator for x motion and contact forces in case of contact motion. Rotational equations of motion of the finger link are derived by using Euler formulation as follows:

$\mathbf{m}_2 = I_2 \, d\omega_2/dt + \omega_2 \times I_2\omega_2$ (10)

where I_2 is an inertial matrix of the finger link, $\mathbf{m}_2$ is a torque vector produced by the magnetic actuators for y and z motions and contact forces in case of contact motion, and ω_2 is an angular velocity vector of the link. Generally I_2 is not a diagonal matrix due to the tool attached to the finger tip.

It can be shown that these attachments produce centrifugal and Coriolis forces even if the center of gravity is located at joint G2. We can show this by expanding the vector equation (10) into each coordinate component.

$$\begin{aligned} m_\xi &= I_{\xi\xi}\dot{\omega}_\xi + (I_{\zeta\zeta} - I_{\eta\eta})\omega_\eta\omega_\zeta + I_{\xi\eta}(\dot{\omega}_\eta - \omega_\zeta\omega_\xi) \\ &\quad + I_{\xi\zeta}(\dot{\omega}_\zeta + \omega_\xi\omega_\eta) + I_{\eta\zeta}(\omega_\eta^2 - \omega_\zeta^2) \\ m_\eta &= I_{\eta\eta}\dot{\omega}_\eta + (I_{\xi\xi} - I_{\zeta\zeta})\omega_\zeta\omega_\xi + I_{\eta\zeta}(\dot{\omega}_\zeta - \omega_\xi\omega_\eta) \\ &\quad + I_{\xi\eta}(\dot{\omega}_\xi + \omega_\eta\omega_\zeta) + I_{\zeta\xi}(\omega_\zeta^2 - \omega_\xi^2) \\ m_\zeta &= I_{\zeta\zeta}\dot{\omega}_\zeta + (I_{\eta\eta} - I_{\xi\xi})\omega_\xi\omega_\eta + I_{\zeta\xi}(\dot{\omega}_\xi - \omega_\eta\omega_\zeta) \\ &\quad + I_{\eta\zeta}(\dot{\omega}_\eta + \omega_\zeta\omega_\xi) + I_{\xi\eta}(\omega_\xi^2 - \omega_\eta^2) \end{aligned} \quad (11)$$

where

$$\omega_\xi = \sin\theta_3\dot{\theta}_2 \quad (12)$$

$$\omega_\eta = \dot{\theta}_3 \quad (13)$$

$$\omega_\zeta = \cos\theta_3\dot{\theta}_2 \quad (14)$$

Thus centrifugal and Coriolis forces are disturbances even in case of free motion when an ideal decoupled model used in the control system. Obviously, contact forces are large unknown disturbances in contact motion and difficult to reject the disturbances when actuator forces are not large like magnetic actuators .

5 DISTURBANCE OBSERVER

A hybrid position and force control is used for the contact motion control. However the force control is simply an open loop control since the coil current is proportional to the normal force applied to an object, while position control suffers from disturbances such as friction. As pointed out in the previous sections, it also suffer from modeling error when a linear controller like PID is used. Recently, disturbance observer is known for its robustness against disturbance and modeling error, and it is implemented in various motion controls. For these reasons, we applied disturbance observer for the position control of our micro operation hand.

Assume that the x, y and z motions of the endeffector are decoupled. Since the mechanical time constant is longer than electrical constant, the endeffector motion in one direction is formulated as follows:

$$\frac{dv}{dt} = \frac{p'q'}{R'}u - f_{dis} \quad (15)$$

where u is a control, f_{dis} is a disturbance, and p', q' and R' are nominal values of system parameters p, q and R:

p: amplification rate of the amplifier

q: force constant of the actuator

R: resistance of the coil

The principle of disturbance observers is stated as follows: "If $\dot{v}$ and u are known values, we can estimate the disturbance from Eq.(15). Then, by adding the corresponding value to u we can cancel the disturbance[8]." In our system, velocity v is not measured thus $\dot{v}$ has to be estimated from the displacement, say x, where

$$v = \dot{x} \quad (16)$$

Fig.8 describes this principle in the form of block diagram., where a low pass filter

$$\frac{ab}{(s+a)(s+b)} \quad (17)$$

is added to reject noises. However, Fig.8 is not desirable since derivative operations are included. But Fig.8 can be converted to the diagram as shown in Fig,9 which contain no derivative operation.

The reference u' of the control can be determined by PID.

$u' = K_p(x_d - x) + K_i \int (x_d - x)dt + K_d(v_d - v)$

where K_p, K_i and K_d are PID gains, and x_d and v_d are desired values of x and v.

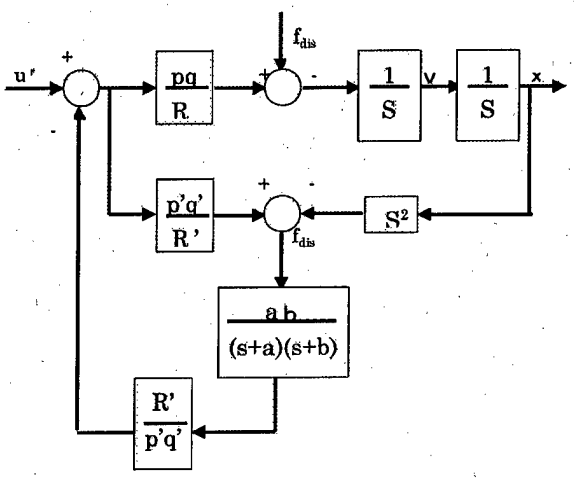


Fig.8 Disturbance observer with derivative operation

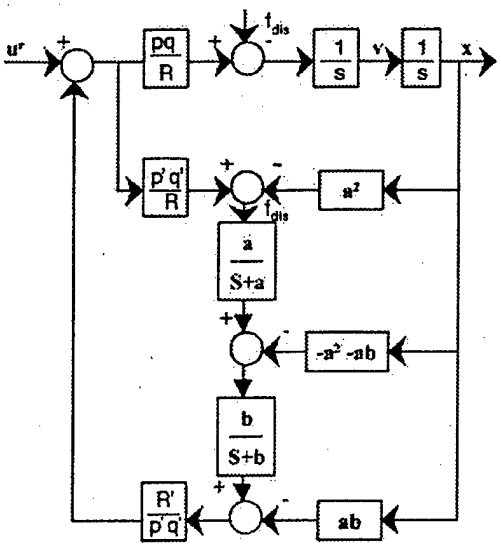


Fig.9 Disturbance observer without derivative operation

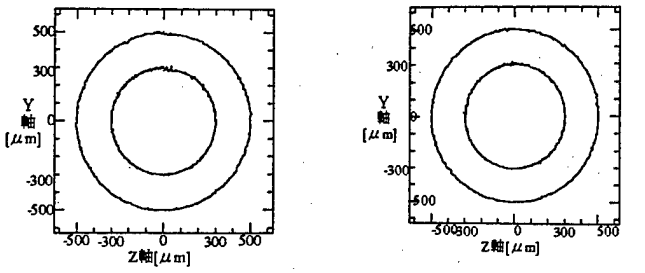
6 EXPERIMENT

In the experiments, the laser displacement sensor was fixed with a fixture placed in the environment and detects the distance between the sensor and the target on the finger link. A pencil and a counter balance were attached to the other side of the heavy permanent magnets. The total weight of the finger link is 120 [gf] including the weights of permanent magnets, the counter balance and the pencil.

Using this experimental setup, the effectiveness of the disturbance observer was experimentally investigated by drawing small circles in the air in case of free motion and on a paper placed in case of contact motion. In both cases, the circles are parallel to the x-y plane. In free motion, x, y and z are position controlled. In contact motion, x and y are position controlled, and the force in z-direction is open-controlled. The discrete-time form of the controller described above was derived by approximation and implemented on a computer. Sampling time of 5 [ms] was used. This value is related with the resolution of the measurement and the derivative operation of the PID control law.

6.1 Free motion

Fig. 10 shows the trajectories formed from the data of the laser displacement sensor outputs where references are circles with radii of 300 and 500 [μm] and the operational time T=13.6[s]. In this figure, (a) results in case of without disturbance observer and (b) with disturbance observer are shown. Comparing these figures significant differences can not be observed. On the other hand , Fig. 11 shows the results with T=0.72 [s]. In this case, the non-linearity of the actuator and the dynamics can not be cancelled with the integral operation of PID. So the result without disturbance observer deviates from the reference circle.



(a) without disturbance observer (b) with disturbance observer

Fig.10 Experimental results in free motion (T=13.6)

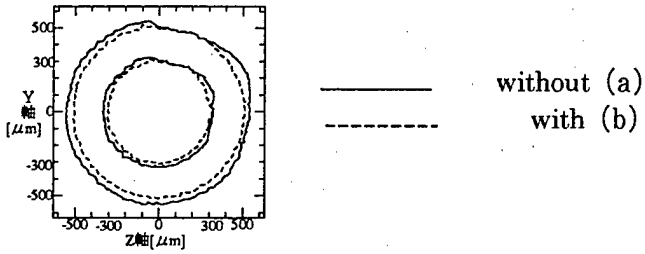


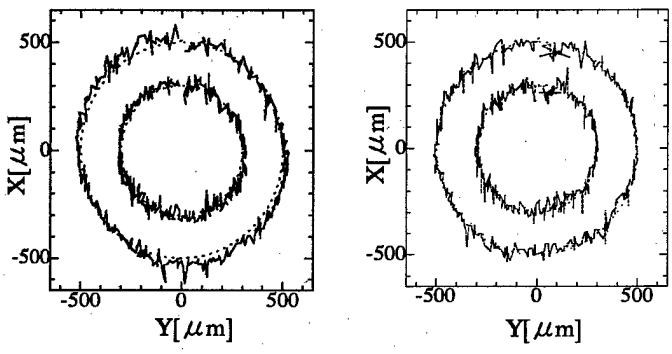
Fig.11 Experimental results in free motion (T=0.72)

6.2 Contact motion

Fig.12 shows the results in contact motion where references are circles of radii 300 and 500 [μm] a and T= 13.6 [s]. Force enough to draw circles on the paper was applied to the z-direction. The applied force was 24 [gf]. (a) is the results without disturbance observer and (b) is the ones with disturbance observer. Both results show the stick-slip motions of the endeffector. However the results with disturbance observer show smaller stick-slip motions. This tendency is obvious from the graph of y(t) in the straight line contact motion with applied force of 100[gf] as shown in Fig. 13.

Moreover, Fig.11 shows that the results without disturbance observer deviate from the reference circle but the results with disturbance observer are on the reference circles in average.

Fig.14 shows actually drawn micro circles with radius of 500[μm] on a paper. Drawn pictures are distorted a little due to some calibration errors.



(a) without disturbance observer (b) with disturbance observer

Fig.12 Experimental results in contact motion (T= 13.6)

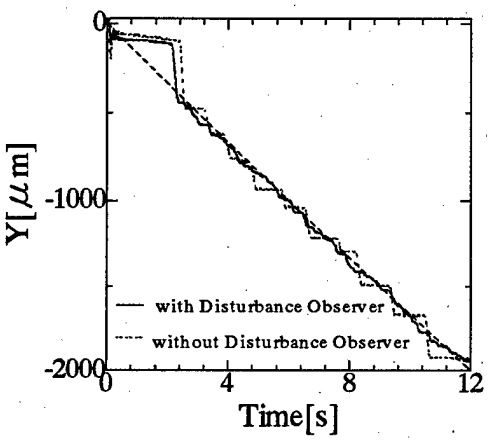


Fig.13 y(t) in the experiment of straight line contact motion

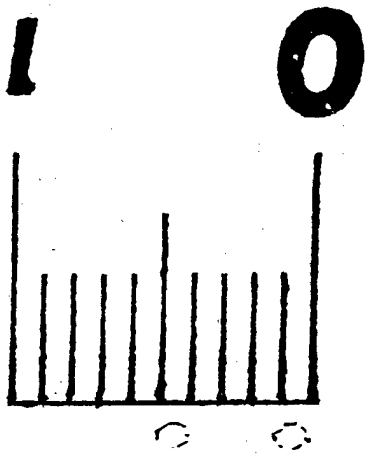


Fig.14 Drawn micro circles on apaper

7 CONCLUSION

This paper proposed a micro operation hand. A finger subsystem with a lever mechanism and magnetic actuators are designed and made in trial. Characteristics of the mechanism and actuators are analyzed and it was shown that there are some nonlinear terms which deteriorate the positioning accuracy even in a free motion. Friction apparently influences positioning accuracy in a contact motion. A motion control system which compensates for these disturbances was designed and applied to drawing tasks of micro figures with the size less than 1 mm. A disturbance observer was used for the position control to cancel the disturbance. An open loop control was used for the force control since contact force corresponds to the coil current accurately because of the low friction of the mechanism. The experimental results show that disturbance observer is effective for disturbance rejection.

In this paper force control was restricted to one direction but force control in any direction remains as future works. Also, the improvement of contact motion control is necessary to apply this system to the practical use.

REFERENCES

[1]T.Sato, K.Koyano, M.Nakano and Y. Hatamura: "Novel Manipulator for Micro Object Handling as Interface between Micro and Human World", IROS '93, pp.1674-1681, 1993

[2]M.C.Carrozza, P.Dario, A.Menciassi and A.Feno, "Manipulating Biological and Mechanical Micro-Objects Using LIGA-Microfabricated End-Effectors", ICRA '98, pp.1811-1816, 1998

[3]F.Arai, T.Sugiyama, A. Kawaji, P. Luangjarmekorn, T. Fukuda and K. Itoigawa, RSJ'99, pp.469-470, 1999-

[4]T.Nakamura and M.B. Khamesee, "Prototype Mechanism for Three-Dimensional Levitated Movement of a Small Magnet", IEEE/ASME Trans. on Mechatronics, Vol. 2, No.1, pp.41-50, 1997

[5]T.Nakamura and I.Ando," Design of Micro-Hand with Two Magnetic Levitated Fingers", MHS'97, pp.137-142,1997

[6]T.Nakamura, Y. Mori, Y. Kogure, H. Akamatsu, "Feasibility Study of Magnetically Leviated Micro Hand for Machining and Assembly", MHS'98, pp.189-194,1998

[7]T. Kono: Applied Electro Magnetism, Byhukan, 1991

[8]K. Ohnishi et al. "Microprocessor-Controlled DC Motor for Lord Insensitive Position Servo System", IEEE Trans. On Ind. Elec. Vol. IE-34, pp.44-49 (1987)

3D Bio-Micromanipulation (Bilateral Control System Using Micro Tri-axial Force Sensor)

Fumihito Arai*, Tomohiko Sugiyama*, Poom Luangjarmekorn*, Akiko Kawaji*, Toshio Fukuda, Kouichi Itoigawa***, and Atsushi Maeda*****

* Department of Micro System Engineering, Nagoya University
Furo-cho, Chikusa-ku, Nagoya 464-8603, JAPAN, *http://www.mein.nagoya-u.ac.jp*
** Center for Cooperative Research in Advanced Sci. & Tech., Nagoya University
*** Tokai Rika Co., LTD., Oguchi, Niwa-gun, Aichi 480-0195, JAPAN

Abstract

Recently, it is demanded to manipulate a small biological object, such as an embryo, cell, and microbe. Bio-micromanipulation is important for Biology and Bio-engineering field. However, it is very difficult, since the object is very small, kept in the liquid, and observed by the optical microscope. The image of the microscope is two dimensional, so it is hard to manipulate the target in the 3D space. The object is fragile, so it is hard to manipulate safely. To improve the manipulation works, here we propose the viewpoint selection method in the VR space, and a new bilateral control system to improve manipulation of the micro object under the microscope.

1. Introduction

Recently, dexterous micromanipulation of small biological objects, such as a cell (Ex. animal cell 10 - 100 μm) in high speed is demanded. Bio-micromanipulation is important for Biology and Bioengineering field. However, it is very difficult, since the object is very small, kept in the liquid.

Most of the cases, operators manage to manipulate the biological objects by the micromanipulators with the two-dimensional image from the optical microscope[1,2,3]. However, most work is carried out in the three dimensional space. So, operation of the micromanipulator is quite difficult and hard. It takes time to do such works.

From these points of view, three-dimensional high speed micromanipulation is needed[4,5]. In this paper, we focus on the contact type micromanipulation in the liquid. We designed and made a contact type micromanipulation system, which has a 3DOF narrow range positioning system on a 3 DOF wide range positioning system. To improve the manipulation of the micro object, we propose the 3D bio-micromanipulation system. The key technologies of this system are written as follows.

(1) 3D free viewpoint selection in the VR simulator
(2) Bilateral control system using the multi-axial micro force sensor and precise positioning of the micromanipulator

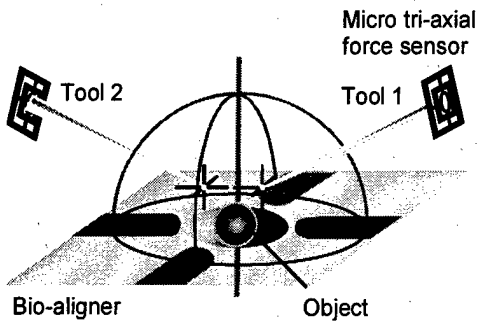
The image of the microscope is two dimensional, so it is hard to manipulate the target in the 3D space. Depth of focus is very narrow. To expand the image in depth direction, we linked the VR space and the actual working space based on the precise 3D calibration technique. There has been reported on the VR navigation for the micromanipulation[6], however, previous works didn't consider the matching between the VR space and the real space. We realized less than 3 μm as absolute positioning accuracy of the micromanipulator within 100 μm^3 working range[7]. It is enough for the cell manipulation works. Based on this achievement, we can match the VR space and the real operation space.

The object is fragile, so it is hard to manipulate it safely. We developed a micro tri-axial force sensor, which can be installed near the tip of the endeffector[8]. The chip size is small (4.5mm$\times$5.0mm$\times$0.525mm), which is the smallest tri-axial force sensor in the world. Using this micro force sensor, we designed a new bilateral control system. Desired position of the micromanipulator is given by the master manipulator. The force measured by the micro force sensor is fed back to the master manipulator. The prototype sensor has good accuracy, however, each output of the micro tri-axial force sensor interferes. The coupling between each output of the sensor degrades the position control of the micromanipulator. So, here we propose a new bilateral control system. Conventional bilateral system for micromanipulation uses a single-axis force sensor[9]. Therefore, there was no need to consider the coupling effect to the control system. In our system, position control is highly regarded. We employed the parallel type bilateral control method[10]. The slave manipulator is actuated by the PZT actuators, so it has fast response. Thus we can increase the position feedback gain of the slave side to reduce the position error caused by the coupling.

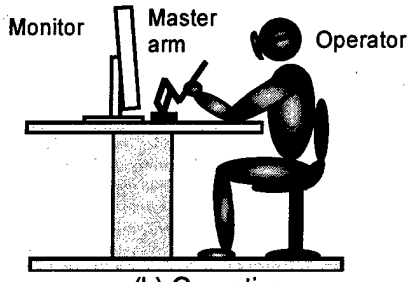
2. Three-Dimensional Micromanipulation System

In the case of biological application, most of the

1999 INTERNATIONAL SYMPOSIUM ON
MICROMECHATRONICS AND HUMAN SCIENCE
0-7803-5790-6/99/ $10.00 ©1999 IEEE.



(a) Visual Information



(b) Operation

Fig. 1 Concept of the 3D Bio-micromanipulation

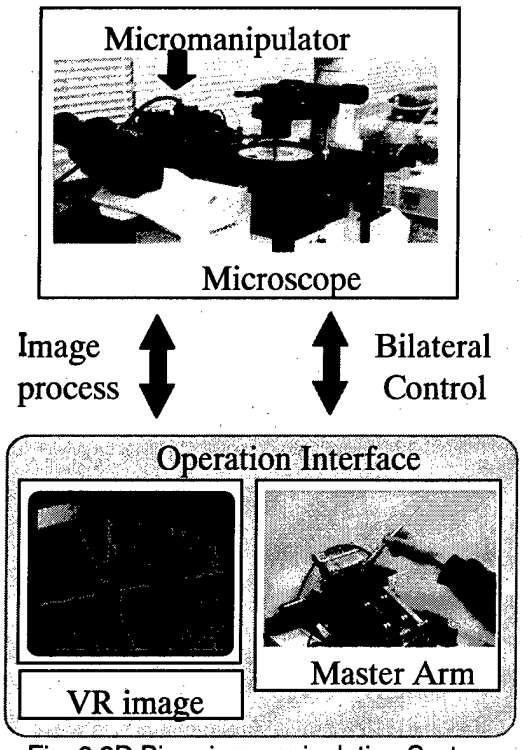
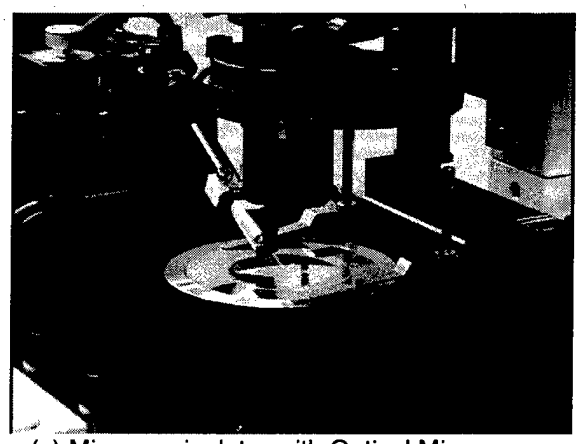


Fig. 2 3D Bio-micromanipulation System

objects are kept in the liquid, and observed by the optical microscope. If the size of the object is bigger than about 10 μm, contact type manipulation is suitable. Here we focus on the contact type micromanipulation in the liquid.

As an example of the contact tasks in the liquid, anatomical operations such as nuclear transplantation and electrophysiological inspection are considered.

Figures 1 and 2 show a new 3D bio-micromanipulation system integrated with the real time Virtual Reality simulator. Figure 3 shows a micromanipulator which has a 3DOF narrow range positioning system on a 3 DOF wide range positioning system and a micro tri-axial force sensor. The narrow range stage is actuated by the three PZT actuators. Position of each axes (x, y and z) is measured by the magnetic sensor. Mobile range of each xyz axes is 100 μm, and has absolute position accuracy of 40nm by the closed loop position feedback along each axis. The resonance frequency of the narrow range stage is about 300 Hz. We can control the position of this stage very fast compared with the human motion. The wide range stage is actuated by the three stepping motors. Mobile range of each axes(x, y and z) is 25 mm. Step resolution of the stepping motor is 26nm(lead: 1mm, 0.0094 deg/pulse). Position of each axes is measured by the linear scale. Resolution of this linear scale is less than 26nm.


(a) Micromanipulator with Optical Microscope

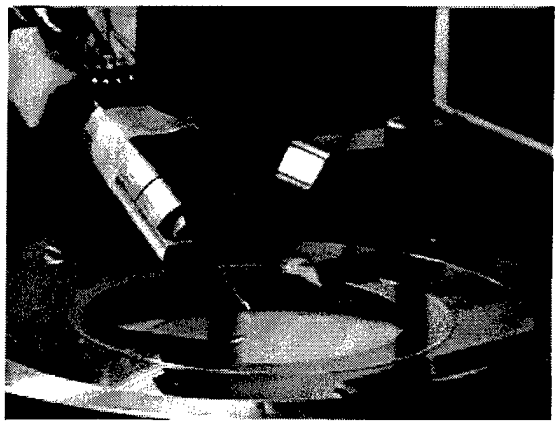

(b) Micro Tri-axial Force Sensor at the Tip

Fig. 3 3DOF Micromanipulator

A micro tri-axial force sensor is installed near the tip of the endeffector[8]. The chip size is small (4.5mm × 5.0mm × 0.525mm). The spring coefficient of the sensor is estimated as 1600 N/m. If we install a glass tool (weight: 67 mg), the resonance frequency of the sensor tip is estimated as 6300 Hz. It is bigger than the resonance frequency of the narrow range xyz stage(300 Hz), so we can operate the micromanipulator fast.

We have reported basic strategies to improve the operability[4,5,8]. In this paper, we focus on a 3D free viewpoint selection and a new bilateral control system.

3. Operation Improvement by Viewpoint Selection

3.1 Classification of the Viewpoint Selection

The size of the target is micrometer order, and the microscope is inevitable. To improve operation under the microscope, we need to control orientation of the target as well as the tool and to select the viewpoint properly. Orientation of the target is controlled by the bio-aligner[11]. Here we propose a free viewpoint selection method.

The microscope can be classified into the positive type and the inverted type. Most of the cases, the relative positional relation between the optic axis and the observation object is fixed. To improve the operation, we classified the viewpoint selection method as follows.

(1) Change the relative positional relation between the microscope optic axis and the object
(2) Construct the three-dimensional VR model of the environment including the object, and carry out the viewpoint change in the virtual space

Here the first approach is difficult to realize in the system with the marketed microscope. We classified the second method as follows.

(A) Classification by the display speed
a. Construction of the VR space in the off line and operation planning in the VR space

In this case, a viewpoint is selected freely and trajectory planning is easy. However, the work is weak in the environmental change, since there is no real-time modification.

b. Real-time construction of the VR space and real-time operation in the VR space

In this case, a viewpoint is selected freely. It is resistant to the environmental change, since the task is real-time.

(B) Classification by strength and weakness of the depth sensation from the display
a. Stereo view

In this case, although it is possible to obtain the depth feel, time and labor depend on the system performance in calculation. And the system becomes complicated and expensive.

b.3D computer graphics and local coordinate display

In this case, the depth information is easy to be obtained from local coordinate system displayed in the image. The visual display system becomes simple.

Figure 4 shows those classification. Region A in Fig. 4 is the most desirable case, since the display speed is real-time with the depth sensation. (A)–a is easy to achieve, because calculation is simple, but it is not robust. For the depth sensation, stereo view is desirable. On the other hand, the depth information is easy to be obtained by the support line of the coordinate system at the object and the tool tip in the 3D image. In this sense, (B)-b is practical. So, we integrate (A)-b and (B)-b and propose the viewpoint change strategy.

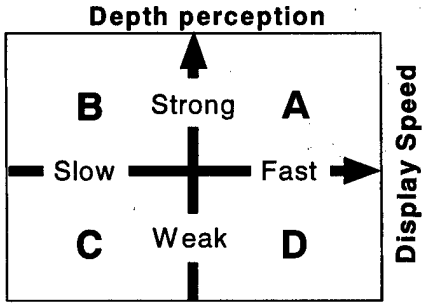


Fig. 4 Classification of the VR Space

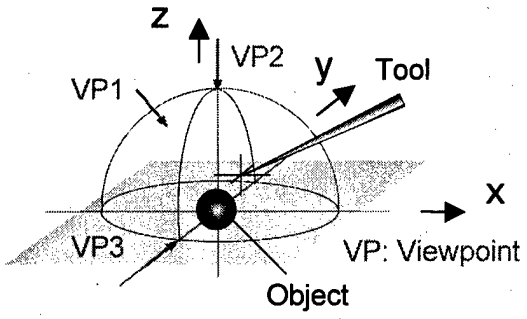


Fig. 5 Viewpoint Selection Strategy

3.2 Strategy of the Viewpoint Selection

The flow until the tool contacts the object is shown in Fig. 5 with the coordinate system.

(1) Viewpoint 1: We carry out the generous access to the object using the image, which is useful for us to grasp the spatial relative position relation between the object and the tool. Figure 6 shows the monitor image from the viewpoint 1(SGI Octane).

(2) Viewpoint 2: We are the conditions that the allowance of the distance was given to the z axial direction, and the relative position (xy coordinates) in watching the object and the tool from the top is adjusted. Figure 7 shows the monitor image from the viewpoint 2.

(3) Viewpoint 3: We select the viewpoint from the lateral direction, and adjust the z axial direction. Figure 8 shows

the monitor image from the viewpoint 3.
(4) We repeat the viewpoints 2 and 3, if it is necessary.

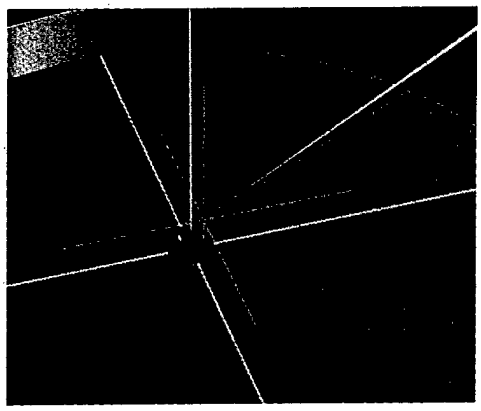


Fig. 6 Viewpoint 1

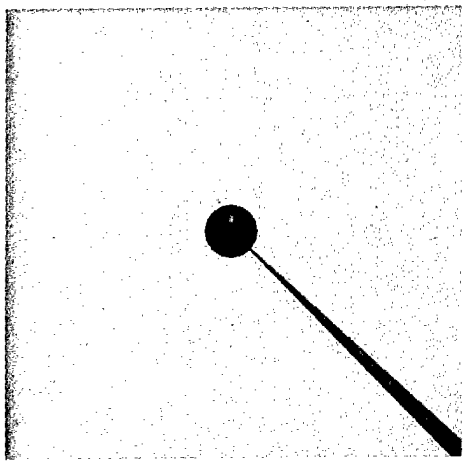


Fig. 7 Viewpoint 2

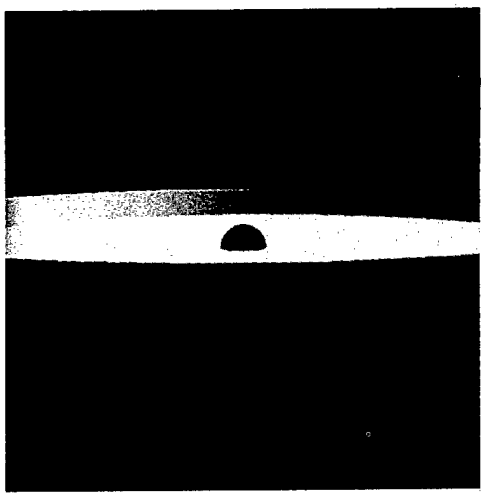


Fig. 8 Viewpoint 3

In this way, we can improve the operability of the micromanipulation task by the free viewpoint selection. We take the matching between operation direction of the master manipulator and motion direction of the micromanipulator. The sure operation can be expected, if the teleoperation is done with this VR space, and if the system in which the calibration was taken is used. We confirmed the absolute accuracy of less than 3 μm as a positioning capability of the narrow range stage [7]. It is enough for the cell manipulation.

4. Bilateral Control of the Micromanipulator

4.1 System Configuration

To improve the operation of the micromanipulator, the bilateral control is important. We have developed a micro tri-axial force sensor, which can be set near the tip of the micromanipulator as shown in Fig. 3 (b). Here we propose a new bilateral control system using this micro sensor. The system consists of the micromanipulator, master manipulator, and the 3D VR simulator as shown in Fig. 2. The micromanipulator has a 3DOF narrow range stage driven by the PZT actuators. The response of the stage is very fast compared with the human motion.

The master manipulator has 3DOF with the 6DOF force & torque sensor, which is set between the master manipulator and the operation grip. The operator grasps this grip on the master to control the micromanipulator as shown in Fig. 9. If the operator apply force on it, then the force sensor measures force and torque on it. Based on this configuration, we can design the force reflection bilateral control system.

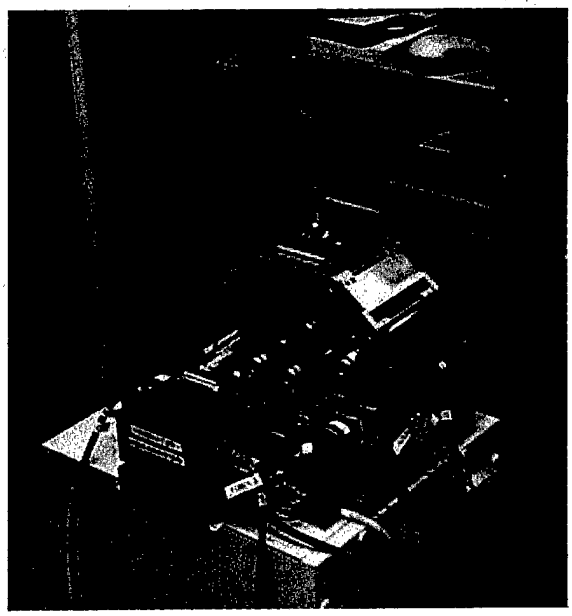


Fig. 9 Master Manipulator

4.2 New Bilateral Control System

Force measured by the micro tri-axial force sensor is fed back to the master manipulator by the appropriate scale. This sensor has good accuracy, however, each outputs of this sensor interferes. We eliminated the coupling by the force sensor calibration as much as possible. However, it is not perfect. The coupling between each outputs of the sensor degrades the position control of the micromanipulator. So, here we propose a new bilateral control system. Conventional bilateral system for micromanipulation uses a single-axis force sensor[9]. Therefore, there was no need to consider the coupling effect to the control system. In our system, position control is highly regarded. The position command from the master manipulator must be precisely controlled at designated magnification.

We employed the parallel type bilateral control method[10]. The block diagram of this controller is written in Fig. 10. For simple explanation, here we suppose a 1 DOF system modeled by the following.

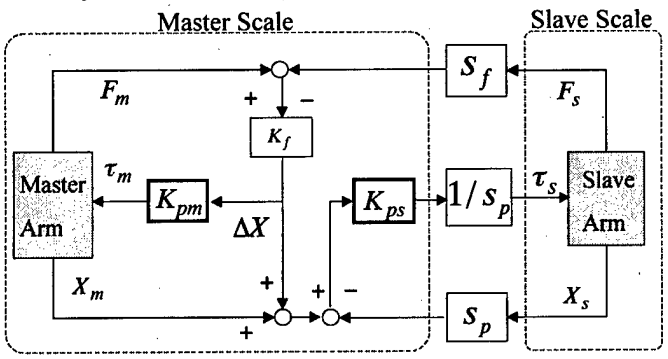


Fig. 10 Block Diagram of the Bilateral Control System

$$\tau_m + F_m = M_m\ddot{X}_m + B_m\dot{X}_m \qquad (1)$$

$$\tau_s - F_s = M_s\ddot{X}_s + B_s\dot{X}_s \qquad (2)$$

where

τ_m, τ_s: control input to the master and control input to the slave manipulator

F_m, F_s: force to the master by the operator and force to the object by the slave

X_m, X_s: position of the master manipulator and position of the slave manipulator

Control input to the system is given as follows.

$$\tau_m = K_{pm}\Delta X \qquad (3)$$

$$\tau_s = \frac{1}{s_p}K_{ps}(X_m + \Delta X - s_pX_s) \qquad (4)$$

$$\Delta X = K_f(F_m - s_fF_s) \qquad (5)$$

where

ΔX: desired position change

S_f, S_p: force scale and position scale

K_{pm}, K_{ps}: position feedback gain of the master and position feedback gain of the slave

K_f: force feedback gain

With this control rule, force of the master F_m and deviation between position of the master and the slave $X_m - s_pX_s$ are written as follows.

$$F_m = \frac{K_{pm}K_f}{1+K_{pm}K_f}s_fF_s + \frac{1}{1+K_{pm}K_f}(M_m\ddot{X}_m + B_m\dot{X}_m) \qquad (6)$$

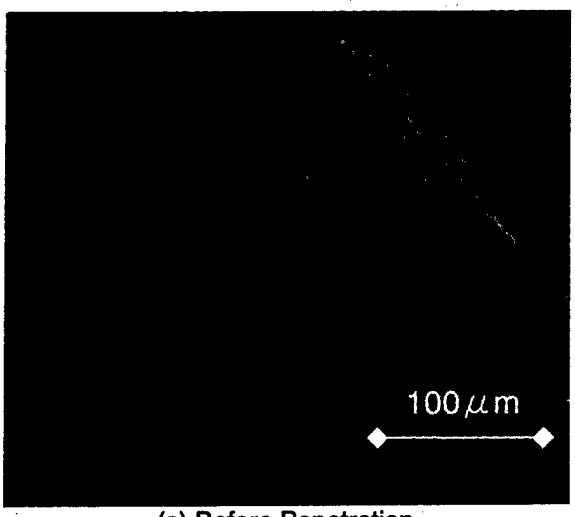
$$X_m - s_pX_s = \frac{1}{K_{ps}}s_p\{(M_m\ddot{X}_m + B_m\dot{X}_m) + F_s\} - K_f(F_m - s_fF_s) \qquad (7)$$

In eq. (6), if we set a large feedback gain to let $K_{pm}K_f \to \infty$, then $F_m \to S_fF_s$ and the master force follows the slave force. Moreover, in eq. (7), if we set $K_{ps} \to \infty$, then $X_m - S_pX_s \to 0$ and the slave position follows the master position.

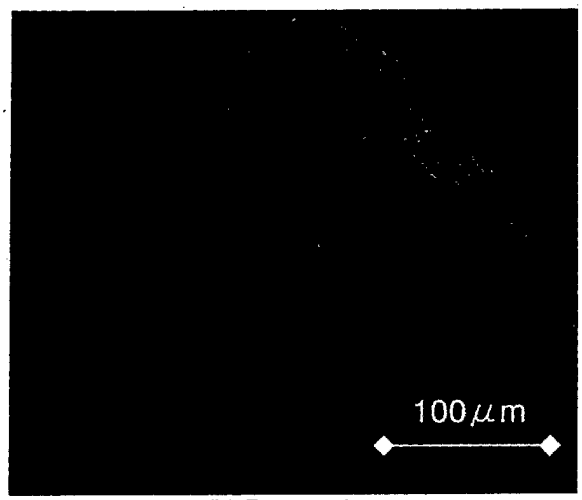
The proposed system divides the position feedback gain of the master and the slave, thus each gains is set independently. Even if the dynamics of the master manipulator is large and impossible to set large K_{pm} from the stability problem, we can set large K_{ps}, since the slave manipulator is driven by the PZT actuators, which have quick response compared with the human motion. Base on this configuration, we can reduce the force coupling effect to the positional deviation and increase the stability margin. It is very important to keep good performance in position control of the micromanipulator, since the operator performs the tasks while seeing the image of the tool and the target.

4.3 Experiment Results

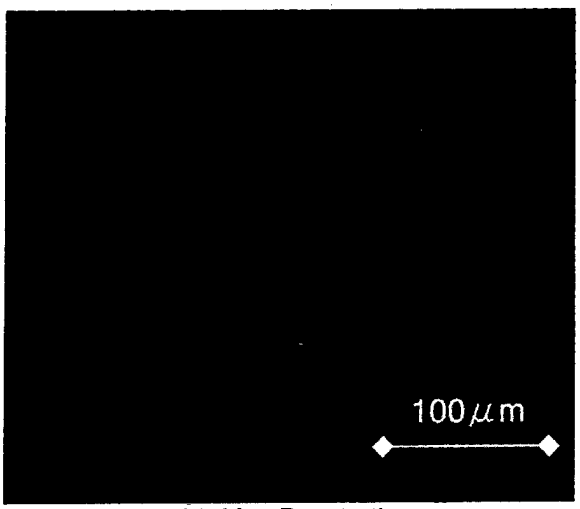
Here we tested the proposed bilateral control system. A glass pipette is set perpendicular to the micro force sensor on the micromanipulator as shown in Figs. 3 (b) and 11. The target is a plant cell of an onion. The target is set on the glass plate and observed by the inverted microscope. We observed it by the 10 times objective lens. Angle between the glass plate and the glass pipette is 23 degrees (Fig. 11). We used 1DOF of the 3DOF master manipulator and controlled the 3DOF narrow range positioning system toward the tool direction x_s. The operator controlled the master manipulator to penetrate the onion cell by the glass pipette. The position scale is set 400, and the force scale is set 1000 in our bilateral control system. Figure 12 shows the image of the optical microscope.



(a) Before Penetration



(b) Penetration



(c) After Penetration

Fig. 12 Onion Cell and the Glass Pipette

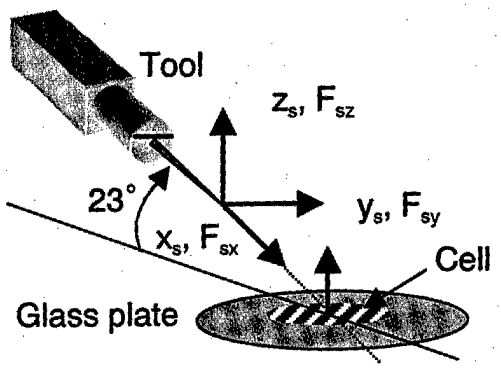
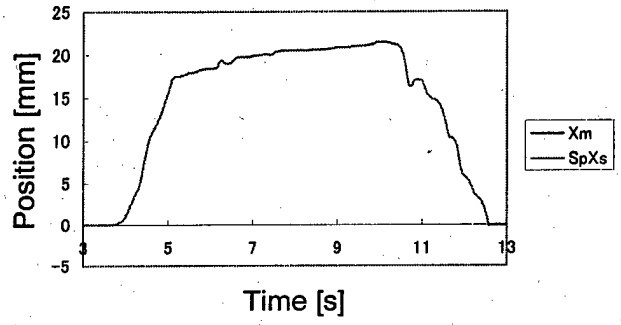
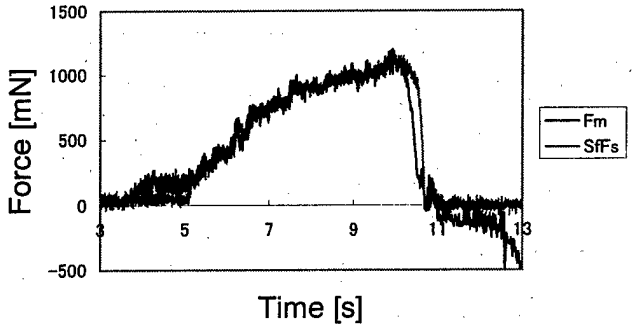


Fig. 11 Coordinate System of the Tool Tip



$S_p = 400$

(a) Position of the Master and the Slave



$S_f = 1000$

(b) Force of the Master and the Slave

$K_f = 0.0001, K_{pm} = 150, K_{ps} = 2.5$

Fig.13 Experimental Result of Bilateral Control

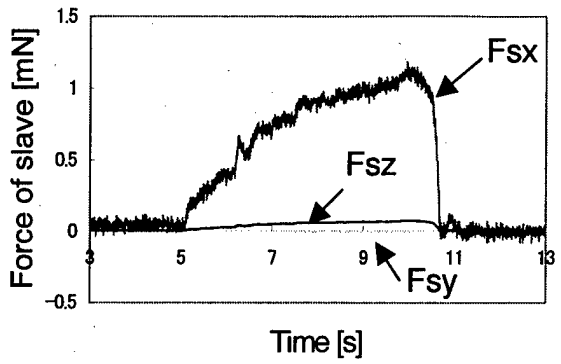


Fig.14 Output of the Micro Tri-axial Force Sensor

Figure 13 shows the experiment results of the bilateral control on the proposed system. Here the position and force of the slave is expanded at designated magnification. By increasing the position feedback gain of the slave manipulator, we can Improve the position following of the slave. The position control error between the master and the slave is almost zero. There was small force error, but it was not serious for practical use. Figure 14 shows 3 outputs of the micro force sensor (Fsx, Fsy, Fsz). The coordinate system of the force sensor is shown in Fig. 11. Fsx is the force component to the axial direction of the tool. It has good accuracy to evaluate the stiffness of the cell. There was a slight output in Fsz, since the tool was pushed towards the tool direction, which is inclined 23 degrees from the glass plate. The output in Fsy is almost zero since the tool is not moved to the horizontal direction. In this example, the coupling of the force sensor was not serious. This sensor has good accuracy in Fsy and Fsz direction compared with that in Fsx direction. In our future, we plan to evaluate this system for 3D micromanipulation.

5. Conclusions

Here we focused on the contact type bio-micromanipulation in the liquid and introduced basic strategies to improve the bio-micromanipulation. We developed the 3D bio-micromanipulation system. To improve the manipulation works, we proposed the viewpoint selection strategy in the VR space, and the new bilateral control system to improve micromanipulation tasks under the microscope.

We can improve the operability by the free viewpoint selection strategy. It is effective, since our method is based on the 3D calibration[7] with absolute accuracy less than 3 μm. We also improved the position control of the teleoperated micromanipulator. The micro tri-axial force sensor is useful to measure precise force information less than mN. It was installed in the bilateral control system without problem. We can move the tool in high speed without apparent mechanical vibration of the force sensor. We pushed the plant cell and were able to feel the strength of the cell.

In our future, we plan to evaluate the coupling effect of the force sensor in the 3D position control of the slave manipulator.

Acknowledgement

This research work was supported in part by a grant from NEDO (New Energy and Industrial Technology Development Organization), Japan.

References

[1] I. Pappas, A. Codourey: " Visual Control of a Microrobot Operating under a Microscope", Proc. IEEE/RSJ Int. Conf. on Intelligent Robotics and Systems, VOL. 2, pp. 993-1000, 1996.

[2] B. Vikramaditya and B.J. Nelson: " Visually Guided Microassembly Using Optical Microscopes and Active Vision Techniques ", Proc. IEEE Int'l Conf. on Robotics and Automation, Vol. 4, p.3172-3177, 1997.

[3] T. Tanikawa, T. Arai, and Y. Hashimoto: " Development of Vision System for Two-Fingered Micro manipulation", Proc. IEEE/RSJ Int. Conf. on Intelligent Robotics and Systems, VOL. 2, pp. 1051-1056, 1997.

[4] F. Arai, et al.: "Bio-Micro-Manipulation (New Direction for Operation Improvement)", Proc. of IEEE/RSJ Int. Conf. Intelligent Robots and Systems (IROS), VOL. 3, 1997, pp.1300-1305.

[5] F. Arai, et al.: " 3D Micromanipulation System under Microscope ", IEEE Proc. MHS'98, 1998, p.127-134

[6] A. Sulzmann, et al.: " Virtual Reality and High Accurate Vision Feedback as Key Information for Micro Robot Telemanipulation", SPIE, Proc. Microrobotics: Components and Applications, Vol. 2906, Boston, p.38-57, 1996

[7] A. Kawaji, F. Arai, et al.:" Calibration for Contact Type Micromanipulation", Proc. of IEEE/RSJ Int. Conf. Intelligent Robots and Systems (IROS), 1999 (To be published)

[8] F. Arai et al.:" Micro Tri-axial Force Sensor for 3D Bio-Micromanipulation", Proc. IEEE ICRA'99, Detroit, 1999, pp.2744-2749

[9] T. Fukuda, K. Tanie, and T. Mitsuoka: "A Study on Control of a Micromanipulator", Proc. of Micro Robots and Teleoperators Workshop, Hyannis, MA, Nov. 1987

[10] T. Miyazaki, S. Hagihara: "Parallel Control Method for a Bilateral Master-Slave manipulator", J. Robotics Society of Japan, Vol. 7, No. 5, 1989, pp.446-452(in Japanese)

[11] F. Arai, T. Kasugai, T. Fukuda:"3D Position and Orientation Control Method of Micro Object by Dielectrophoresis", IEEE Proc. MHS'98, 1998, p.149-154

A Model for Operating Spherical Micro Objects

Quan Zhou[a], *Pasi Kallio*[a], *Fumihito Arai*[b], *Toshio Fukuda*[b] *and Heikki N. Koivo*[c]

[a]Tampere University of Technology, Automation and Control Institute, P.O. Box 692, 33101 Tampere, Finland;
Email: quan@ae.tut.fi, kallio@ae.tut.fi

[b]Nagoya University, Dept. of Micro System Engineering, Furo-cho, Chikusa-ku, Nagoya 464-8603, Japan
arai@mein.nagoya-u.ac.jp, fukuda@mein.nagoya-u.ac.jp

[c]Helsinki University of Technology, Control Engineering Laboratory, P.O. Box 3000, 02015TKK, Finland;
Email: Heikki.Koivo@hut.fi

Abstract:

This paper addresses one of the important topics in micro assembly - the micro operation modeling - which is essential for planning of micro assembly. The modeling method combines constraint based rigid body modeling method and micro domain forces. A model for manipulating spherical micro objects is presented here as an application of the method. Simulation results of pushing operation are presented. The modeling method is applicable to more complicated objects and can be used as a part of a virtual environment.

1. INTRODUCTION

With the progress of microsystem technology, the demands for microsystem modeling and simulation increase substantially. One topic in microsystem modeling is to study the interactions of micro parts, which is very important for such tasks as assembly of micro electromechanical devices. The task in the interaction studies is how to deal with the specific phenomena in the micro world caused by the so-called scaling effect - dominant physical quantities in the micro world are different from those in the macro world. For example, van der Walls forces, electrostatic forces and other adhesion forces play more important roles than gravitational and inertial forces.

Work related to micro forces and micro manipulations has been carried out by many groups. For example, Arai, et. al. have studied attractive forces and handling strategies in micromanipulation [1]; Feddema et. al. have done initial studies on the effects on van der Waals forces and electrostatic force in micro assembly [2]; Zhou, et. al. have theoretically and experimentally studied adhesion forces between sphere and plane under different material and environment conditions [3]; Saito, et. al. have researched precise pick and place operations for micro objects under SEM [4]; Sitti et. al. have developed a micro/nano manipulation system with one dimensional force measurement [5]; Zesch, et. al. have done research on the pushing control of micro parts [6], etc.

Those works give a broad view and a rather deep insight into the problems in micro operations and possible ways to handle them. To study operations in the micro world further, we still need to understand the dynamic behaviors in the micro world. Experimental study of dynamics in the micro world is still difficult due to the limited measurement technology. However, such knowledge can be gained through modeling and simulation. The currently available knowledge about van der Walls forces, electrostatic forces and other adhesion forces facilitates the modeling of micro operations at a reasonable realistic level. Such a model also lays ground for further development of a virtual environment that can be used in micro operation research, planning of micro assembly and development of force-reflective control strategy in microtelemanipulation, for example.

This paper presents a model for manipulating spherical micro objects. Operations are assumed to be performed in a dry environment. The method is based on dynamics of rigid bodies, and it takes into account dominant micro world forces such as van der Waals forces and electrostatic forces. In section 2, the modeling methods will be discussed. Section 3 describes the formulation of a dynamic model. Section 4 presents the simulation results. Section 5 concludes the paper.

2. METHODS

There are many different kinds of phenomena in micro operation environment, some of them are difficult to determine and some are even not well understood. For example, the adhesion of micro objects and surface, either dry or wet; the friction in the micro environment, where a thin liquid layer may play a role; the contact electrification; charge stored in dielectrics; inconsistency of surface roughness, etc. The objective of this work is to build a dynamic model including micro domain forces. However, the model will not address all above mentioned phenomena due to the lacking knowledge.

Another consideration is the computational speed. To model the dynamics in physical details, we have to model bodies as deformable, since no real rigid body exists. The deformation also exists when a body contacts another body or a surface [7][8]. Different from static models, transitions in interactions have to be modelled. Finite element method is obviously a method closer to the physical reality. However, their

1999 INTERNATIONAL SYMPOSIUM ON
MICROMECHATRONICS AND HUMAN SCIENCE
0-7803-5790-6/99/ $10.00 ©1999 IEEE.

complexity hinders a model being used in realtime applications. Moreover, the detailed deformation models of bodies in micro world normally are restricted to some simple cases and are not as general as required for simulating the dynamics. One of the future goals is to construct a virtual environment. Thus, a model having fast algorithms is more suitable for this purpose. Rigid body modeling method fits the requirement.

In modeling of rigid bodies, all bodies are regarded as rigid (incompressible) and their motions are normally bounded. The main tasks in dynamic rigid body simulation are detecting contacts and predicting the accelerations and contact forces of rigid bodies in contact under friction. The governing equations and constraints of rigid body modeling are the Newton-Euler equations of motions, unilateral (inequality) and bilateral (equality) constraints, contact condition and maximum work principle.

Many methods for modeling of rigid bodies dynamics in contact condition have been developed, e.g., applying complementarity theory and pivoting method [9][10]; impulse-based simulation which models all type of contacts including colliding, rolling, sliding and resting through a series of collision impulses between objects in contact [11]; or using penalty based method which gives a spring constant for the small interpenetration between two contact bodies [12]. The tasks in rigid body modeling include: contact point detection; modeling of contact forces at each contact points; modeling of transition between contact states.

Currently we use the complementarity theory based rigid body modeling method following the work of Stewart and Trinkle [10], Sauer and Schömer [13], and including van der Waals forces and electrostatic forces. The model also assumes that the environment is dry, such that the surface tension force can be neglected. This assumption can be relaxed in the future. Other assumptions include: the tool is a rode with a half sphere head; all contact normals are well-defined; the surfaces have a roughness of ε; the collision at low speed is assumed to be dissipative; the charges (if exist) are uniformly distributed.

3. Model Formulation

In this section we present the rigid body dynamic formulation of the micro operation model. The problem under study is illustrated in Fig. 1. An illustration of forces in the configuration is shown in Fig. 2. The friction forces are omitted here, but they will be presented in a latter part of this section.

The motion of rigid bodies is described by generalized coordinates vector $\boldsymbol{q}$, velocity $\boldsymbol{u}$ and acceleration $\dot{\boldsymbol{u}}$, where $\boldsymbol{u} = \dot{\boldsymbol{q}}$. If the generalized mass matrix is $\boldsymbol{M}(\boldsymbol{q})$, the model can be formulated as:

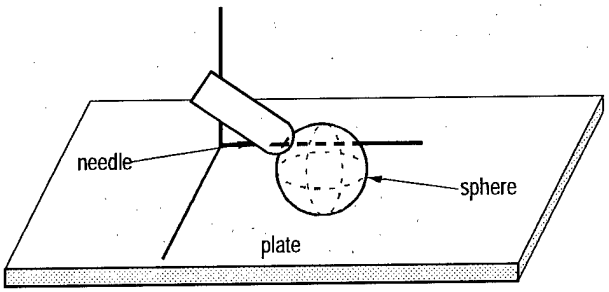
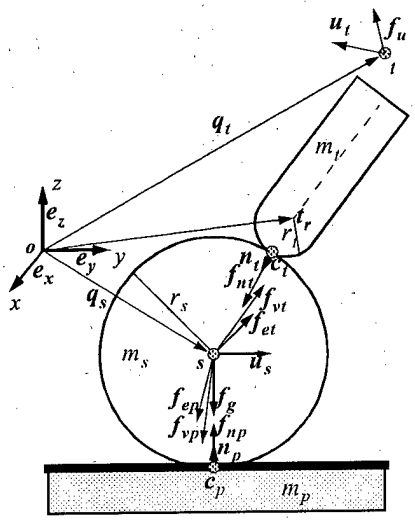


Figure 1: The problem under study.



where

m_s, m_t are the masses of the sphere and the tool; r_s, r_t are the radiuses of the sphere and the tool respectively; s, t are the centres of mass of the sphere and the tool; t_r is the reference point of the tool; $\boldsymbol{q}_s$, $\boldsymbol{u}_s$ are generalized coordinates and velocity of the sphere, where $\boldsymbol{q}_s = \left[\boldsymbol{p}_s^T\ \theta_s^T\right]^T$, $\boldsymbol{u}_s = \left[\boldsymbol{v}_s^T\ \omega_s^T\right]^T$, $\boldsymbol{p}_s$, θ_s, $\boldsymbol{v}_s$ and ω_s are position, angle, velocity and angular velocity of the sphere;
$\boldsymbol{q}_t$, $\boldsymbol{u}_t$ are generalized coordinates and velocity of the tool, where $\boldsymbol{q}_t = \left[\boldsymbol{p}_t^T\ \theta_t^T\right]^T$, $\boldsymbol{u}_t = \left[\boldsymbol{v}_t^T\ \omega_t^T\right]^T$, $\boldsymbol{p}_t$, θ_t, $\boldsymbol{v}_t$ and ω_t are position, angle, velocity and angular velocity of the tool;
$\boldsymbol{c}_t$, $\boldsymbol{c}_p$ are contact points between sphere and tool and between sphere and plane respectively (both may disappear); $\boldsymbol{n}_s$, $\boldsymbol{n}_t$ are normal vectors at the contact points; $\boldsymbol{f}_{nt}$ is the normal force between the sphere and the tool; $\boldsymbol{f}_{et}$ is the electrostatic force between the sphere and the tool; $\boldsymbol{f}_{vt}$ is the van der Waals force between the sphere and the tool; $\boldsymbol{f}_{np}$ is the normal force between the sphere and the plane; $\boldsymbol{f}_{ep}$ is the electrostatic force between the sphere and the plane; $\boldsymbol{f}_{vp}$ is the van der Waals force between the sphere and the plane; $\boldsymbol{f}_g$ is the gravitational force of the sphere; $\boldsymbol{f}_u$ is the force applied by the user.

Figure 2: The force configuration in frictionless case.

$$M(q)\frac{du}{dt} = k(q, u, t) + \psi(t)\nabla f(q) \quad (1)$$

where $\psi(t)$ are contact forces, $f(q) \geq 0$ are the unilateral constraints and $k(q, u, t)$ are external forces.

In the problem under study, the plane is unmovable. If we assume the angle of the tool is fixed, the mass matrix is:

$$M = \begin{bmatrix} m_t E & & & \\ & i_t E & & \\ & & m_s E & \\ & & & \frac{2m_s r_s^2}{5} E \end{bmatrix} \quad (2)$$

where $E = \begin{bmatrix} 1 & & \\ & 1 & \\ & & 1 \end{bmatrix}$ and $i_t = \infty$.

3.1 The External Forces

The external forces include gravitational force, van der Waals forces and electrostatic forces respectively:

$$k(q, u, t) = \begin{bmatrix} f_t(q, u, t) & \\ & f_s(q, u, t) \end{bmatrix} \quad (3)$$

where f_t and f_s are generalized external forces applied on the tool and the sphere:

$$f_t(q, u, t) = -f_{vt}(q) - f_{et}(q) + f_u(t) \quad (4)$$

$$f_s(q, u, t) = f_g(q) + f_{vt}(q) + f_{vp}(q) + f_{et}(q) + f_{ep}(q) \quad (5)$$

If vectors e_x, e_y and e_z are the unit vectors corresponding x, y, z axis in the general coordination system, we have

$$f_g(q) = -mg \cdot e_z \quad (6)$$

The non-retarded van der Waals force between two spheres [14] is computed using the equation following the concepts in Fig. 3:

$$F_{vdw} = \frac{Hdr_1r_2}{3}\left[\frac{8r_1^2r_2^2 - (d^2 - (r_1 + r_2)^2)(d^2 - (r_1 - r_2)^2)}{(d^2 - (r_1 + r_2)^2)^2(d^2 - (r_1 - r_2)^2)^2}\right] \quad (7)$$

where $H = \pi^2 n^2 \lambda$ is the Hamaker constant having the value in the range $0.4 \times 10^{-19} J - 4 \times 10^{-19} J$. Similarly, the force between a sphere and a plane is:

$$F_{vdw} = \frac{2Hr_1^3}{3\delta^2(\delta + 2r_1)^2} \quad (8)$$

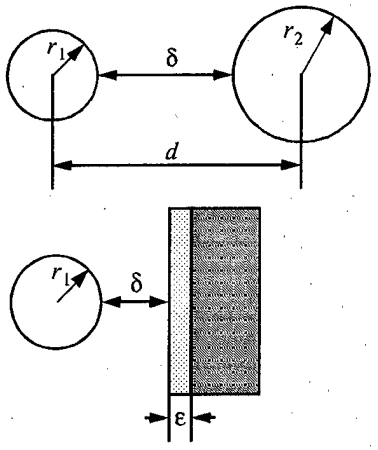


Figure 3: Notation for sphere-sphere and sphere-plane relation.

In the case of surface roughness ε, the modified van der Waals force is [1]:

$$F_{vdwr} = \left(\frac{\delta}{\delta + \varepsilon/2}\right)^2 F_{vdw} \quad (9)$$

When approximating the van der Waals force between the sphere and the tool using (7), we have:

$$f_{vt}(q) = -\frac{Hdr_sr_t}{3} \cdot n_t \left[\frac{8r_s^2r_t^2 - (d^2 - (r_s + r_t)^2)(d^2 - (r_s - r_t)^2)}{(d^2 - (r_s + r_t)^2)^2(d^2 - (r_s - r_t)^2)^2}\right] \quad (10)$$

where $d = |p_s - t_r|$ and n_t is the normal vector at the contact point c_t. Similarly, the van der Waals forces between the sphere and the plane can be computed using (8) and (9):

$$f_{vp}(q) = -\left(\frac{\delta}{\delta + \varepsilon/2}\right)^2 \frac{2Hr_s^3}{3\delta^2(\delta + 2r_s)^2} \cdot n_p \quad (11)$$

where $\delta = |p_s - c_p|$ and n_p is the normal vector at the contact point c_p.

For the electrostatic forces, here we only consider classical Coulomb forces. However, it will be very interesting to formulate the electrostatic forces in a more detailed way in the future. In the simplest case, we can use the point charge assumption, i.e., the sphere having a charge Q_s at its centre, and the tool having a charge Q_t at its tip centre t_r, the electrostatic force between the sphere and the tool can be estimated for this simple case by:

$$f_{et}(q) = \frac{Q_sQ_t}{4\pi\varepsilon_0\varepsilon|p_s - t_r|^2} \cdot n_t \quad (12)$$

where $\varepsilon_0 = 8.854 \times 10^{-12} C^2 J^{-1} m^{-1}$ is the permittivity of free space, ε is the relative permittivity or dielectric constant of the medium.

3.2 The Contact Forces

The contact forces include the normal forces and the friction forces. The friction forces obey the Coulomb law, i.e.:

$$f_t = \mu f_n \text{ if sliding} \tag{13}$$

$$f_t \le \mu f_n \text{ if not sliding} \tag{14}$$

However, such formulation requires solving a nonlinear complementarity problem for (1). In order to obtain a linear complementarity problem, the friction cone is discretized using a number of direction vectors. The friction cone at the contact point between the tool and the sphere is shown in Fig. 4. For detailed discussion of friction cone, refer to [10]. In the following discussion, we assume that two contacts exist, as shown in Fig. 2. The formulation of a single contact is simply a reduced version.

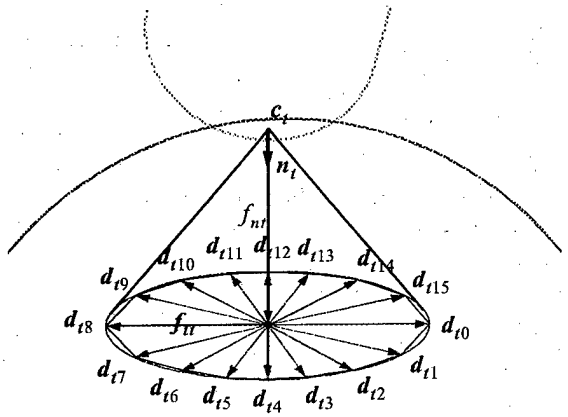


Figure 4: The friction cone.

In addition to the normal vector n_t, two tangential vectors t_{t1} and t_{t2} are defined that perpendicular to each other. Thus, the friction cone at the contact point c_t is discretized with a number of k direction vectors d_{ti}, $i = 0 \ldots k-1$:

$$D_t = [d_{t0}, \ldots, d_{tk-1}] \tag{15}$$

$$d_{ti} = \cos(2\pi i/k)t_{t1} + \sin(2\pi i/k)t_{t2} \tag{16}$$

By introducing a friction weighting vector $\beta_t = [\beta_{t0}, \ldots, \beta_{tk}]^T$, the friction force becomes $D_t\beta_t$. Similarly we have n_p, D_p and β_p for the contact point between the sphere and the plate. Let f_{np}, f_{nt} be the magnitude of normal forces f_{np} and f_{nt}, and introducing

$$N = \begin{bmatrix} n_p & \\ & n_t \end{bmatrix}, f_n = \begin{bmatrix} f_{np} \\ f_{nt} \end{bmatrix}, D = \begin{bmatrix} D_p & \\ & D_t \end{bmatrix}, \beta = \begin{bmatrix} \beta_p \\ \beta_t \end{bmatrix} \tag{17}$$

the contact force can be formulated as:

$$\psi(t) = Nf_n + D\beta \tag{18}$$

where f_n and β are unknowns.

3.3 Contact Condition

The contact forces are related to the contact points. A contact condition matrix is required to apply contact forces to the corresponding objects. The contact condition matrices are:

$$J_f = \begin{bmatrix} 0 & -E \\ 0 & -r^x_{tct} \\ E & E \\ r^x_{scp} & r^x_{sct} \end{bmatrix} \text{ and } J_v = \begin{bmatrix} 0 & -E \\ 0 & r^x_{tct} \\ E & E \\ -r^x_{scp} & -r^x_{sct} \end{bmatrix} \tag{19}$$

where r^x_{tct}, r^x_{scp} and r^x_{sct} are skew-symmetric matrices to translate contact forces to moments of force and angular velocities to velocities, which have the form:

$$r^x(r) = \begin{bmatrix} 0 & -r_3 & r_2 \\ r_3 & 0 & -r_1 \\ -r_2 & r_1 & 0 \end{bmatrix} \text{ and } r^x(r) \cdot f = r \times f \tag{20}$$

and $r_{scp} = c_p - s$, $r_{sct} = c_t - s$ and $r_{tct} = c_t - t$.

3.4 LCP Formulation

One of the possible formulations of the Linear Complementarity Problem (LCP) is the following [15]:

Given $M \in \mathbf{R}^{n \times n}$ *and* $q \in \mathbf{R}^n$, *find* $w, z \in \mathbf{R}^n$ *such that*

$$w, z \ge 0,\ w = q + Mz,\ z^T w = 0 \tag{21}$$

or show that no such w and z exist.

By using the notion of the contact condition matrix and Euler's approximation, we can rewrite equation (1) in discrete form as:

$$M(q)(u(n+1) - u(n))/h = J_f(q)\psi(t) + k(q, u, t) \tag{22}$$

where h is the sampling period. The constraints are expressed using the following complementarity conditions:

$$e\lambda + D^T J_v^T u(n+1) \ge 0,\ \beta \ge 0 \tag{23}$$

$$\mu f_n - e^T\beta \ge 0,\ \lambda \ge 0 \tag{24}$$

$$N^T J_v^T u(n+1) - \zeta/h \ge 0,\ f_n \ge 0 \tag{25}$$

where $e \in \mathbf{R}^{kn_c \times n_c}$ is a $n_c \times n_c$ diagonal matrix of $[1, \ldots, 1]^T$ in $\mathbf{R}^k$ and n_c is the number of contacts, $\mu \in \mathbf{R}^{n_c \times n_c}$ is the friction coefficient diagonal matrix, $\lambda \in \mathbf{R}^{n_c \times 1}$ has no physical meaning, in most cases it is an approximation of the magnitudes of the relative contact velocities, $\zeta \in \mathbf{R}^{n_c \times 1}$ are the estimated distances between the contact points. The conditions (23) and (24) describe the Coulomb friction law and the condition (25) describes the contact condition. The equation of motion can also be written as:

$$u(n+1) = u(n) + h\, M(q)^{-1}(J_f(q)\psi(t) + k(q, u, t)) \tag{26}$$

$$q(n+1) = q(n) + h\,u(n+1) \tag{27}$$

By replacing $u(n+1)$ in (23) and (25) using (26) and rearranging, we have the following LCP-formulation:

$$\begin{bmatrix} D^T J_v^T M^{-1} J_f D & D^T J_v^T M^{-1} J_f N & e \\ N^T J_v^T M^{-1} J_f D & N^T J_v^T M^{-1} J_f N & 0 \\ -e^T & \mu & 0 \end{bmatrix} \begin{bmatrix} h\beta \\ h f_n \\ \lambda \end{bmatrix} + \begin{bmatrix} D^T J_v^T (u(n) + hM^{-1}k) \\ N^T J_v^T (u(n) + hM^{-1}k) - \zeta/h \\ 0 \end{bmatrix} \geq 0 \tag{28}$$

$$\text{complementary to } \begin{bmatrix} h\beta \\ h f_n \\ \lambda \end{bmatrix} \geq 0 \tag{29}$$

The above LCP problem can then be solved by Lemke algorithm [15]. Due to the scope of this paper, the LCP formulation presented here is rather brief. Further details can be found in [10] and [13].

3.5 Collision

Collision is a continuous process physically. When two bodies collide, there is a compression phase during which materials accumulate elastic energy and a restitution phase during which some of this energy is returned to kinetic energy, as the bodies rebound off each other. In the rigid body model, the process of collision is ignored since the collision can happen in a infinitesimal period. The process is normally approximated using e.g., the Newton's model or the Poission's model of impact.

In the case of frictionless collision, the result of the impact can be easily computed out based on rigid body dynamic equations and the restitution coefficient. If the speeds of two colliding bodies at the contact point before collision are u_a^0 and u_b^0 for body a and b respectively, then the speeds of the two bodies at the contact point after collision are:

$$u_a^1 = u_a^0 + (E/m_a - r_a^x I_a^{-1} r_a^x) n P \tag{30}$$

where $r_a^x = r^x(r_a)$ and r_a is the vector from the centre of mass of body a to the contact point, n is the normal vector at the contact point, m_a and I_a are the mass and the inertial moment of the body a respectively, and P is the magnitude of impulse which can be computed by

$$P = -\frac{(1+e)(n \cdot (u_a^0 - u_b^0))}{\frac{1}{m_a} + \frac{1}{m_b} - (n \cdot r_a^x I_a^{-1} r_a^x n + n \cdot r_b^x I_b^{-1} r_b^x n)} \tag{31}$$

where $e \in [0, 1]$ is the coefficient of restitution.

The model of collision can include friction as well, e.g., Mirtich's frictional collision algorithm which integrates the collision process vs. the relative normal velocity v_n such that the effect of friction to final velocity can be determined [11]. The rigid body assumption is also maintained. However, the algorithm is quite complicated comparing to the above one.

3.6 Roll Resistance

Currently the rolling resistance is modelled using a rolling friction in addition to the friction force in $\psi(t)$. A unified formulation can be developed in the future. The rolling resistance is modelled using the friction law [16]:

$$f_{rf} = -\mu_r f_n v/|v| \tag{32}$$

where μ_r is the rolling friction coefficient, f_n is the normal force at contact point, v is the velocity of the object at tangential direction.

3.7 Modelling Procedure

The algorithm to solve the micro operation model is generally similar to other types of rigid body modeling tasks. The modeling procedure can be summarized as in the following:

detect contacts

if the contact conditions are changed,

modify the system matrices, update system parameters

solve contact forces subject to constraints and external forces

update the system states

Due to the simple shape of objects in the current model, contact detection is rather easy. An advanced contact detection algorithm will be required when objects have complicated shapes.

4. SIMULATION

This section presents the simulation results of pushing a micro sphere. The material of the sphere, tool and the plate is assumed to be silicon dioxide. The radius of the sphere is $2.0 \times 10^{-5} m$ and the end of the tool having radius of $1.0 \times 10^{-5} m$, the surface roughness is assumed to be $1.0 \times 10^{-10} m$, the friction coefficient between sphere/tool and sphere/plate is $\mu = 0.3$, the rolling resistance coefficient is $\mu_r = 0.1$. The sphere is initially at rest on the plate and the tool is $1.0 \times 10^{-5} m$ above the plate. The tool is moving in x direction at velocity $1.0 \times 10^{-6} m/s$ from $t = 0ms$ towards the sphere and reaches the sphere at $t = 100ms$. At $t = 200ms$ the tool is pulled back by an external force. The sampling period of simulation is $h = 1.0 \times 10^{-3} s$.

Two simulations are performed. The collisions are assumed dissipative in both cases. In the first case, no micro domain force is present. In the second case, van der Waals forces are present. Fig. 5 shows the pushing force and relative distance between the tool and the micro sphere when there is no micro

domain force. The force during pushing is caused by the inertial force, rolling and sliding friction forces. The magnitude of the force is in the order of one hundred pico Newtons. This is due to the small mass of the sphere which is about $7.7 \times 10^{-11} kg$. Fig. 6 and Fig. 7 show the force, relative distance between the tool and the sphere, displacements and velocities of the tool and sphere when van der Waals forces are present. In this case, the pushing force is much larger. It is in the order of tens of nano Newtons. Here non-retard van der Waals force law is used and $H = 1.5 \times 10^{-19} J$. The large pushing force is result of the larger sphere/plate and sphere/ tool contact forces caused by the van der Waals forces. It is also noticeable that the sphere does not move due to the attraction force between the sphere and the tool before the tool reaches the sphere. The reason is the large rolling resistance caused by the van der Waals forces between the sphere and the plate.

The small absolute value of the parameters, which are not far from the floating point relative accuracy 2.2×10^{-16} can cause problems in the current model. Furthermore, van der Waals forces change rapidly when two objects come close to each other. In certain cases convergence difficulties may occur.

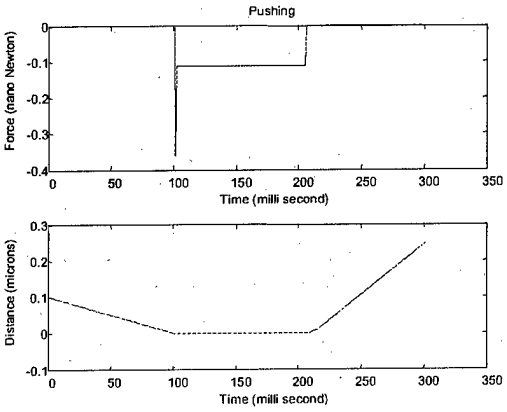


Figure 5: Force and relative distance when no micro domain force presents.

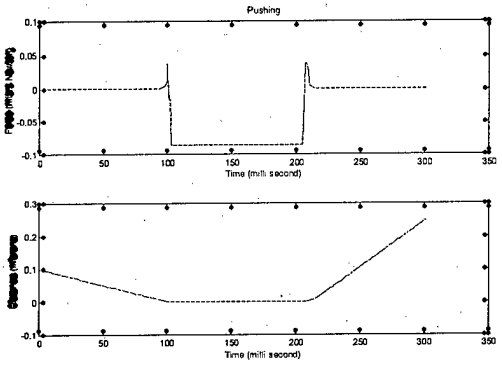


Figure 6: Force and relative distance when van der Waals forces present.

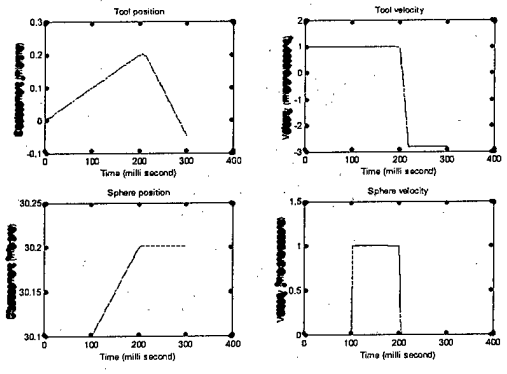


Figure 7: Displacement and velocity of the tool and the sphere when van der Waals forces present.

5. Conclusions and Discussion

This paper has presented a model for manipulating spherical micro object based on rigid body dynamics and micro domain forces. The model has taken into account dominant forces in micro world including van der Waals forces and electrostatic forces. Constraint based approach has been applied to compute the contact forces. This approach describes the multiple contacts in a single linear complementarity problem which can be solved using Lemke algorithm. The model is presented in the context of dry micro operation. Pushing of micro sphere has been simulated in two case: without micro domain forces and with van der Waals forces. The pushing force is much larger when van der Waals forces is present.

The current model lays ground for further development of micro operation modeling. Future work includes integrating more detailed micro force laws including liquid bridge forces and unified rolling resistance law into the model, developing an advanced contact detect algorithm and collision model. The model will be applied to various operations and objects having more complicated shapes, and integrated into a virtual environment with haptic human interface.

Acknowledgements

The authors wish to thank the National Technology Agency of Finland (TEKES) and the Academy of Finland for funding the project.

REFERENCES

[1] F. Arai, D. Ando, T. Fukuda, Y. Nododa and t. Oota, "Micro Manipulation Based on Micro Physics - Strategy Based on Attractive Force Reduction and Stress Measurement", *IEEE/ RSJ Int. Workshop on Intelligent Robots and Systems*, Vol. 2, pp. 263 - 241, Pittsburgh, PA. 1995.

[2] J.T. Feddema, P. Xavier, and R. Brown, "Assembly Planning at the Micro Scale", *IEEE International Conference on Robotics and Automation, ICRA'98*, Workshop 4: Precision Manipulation at Micro and Nano Scale, pp. 56 - 69, Leuven, Belgium, 1998.

[3] Y. Zhou and B.J. Nelson, "Adhesion Force Modeling and Measurement for Micromanipulation", in *Microrobotics and Micromanipulation, Proceeding of SPIE*, Armin Sulzmann, Bradley J. Nelson, Editors, Vol. 3519, pp. 169 - 180, Boston, USA, 1998.

[4] S. Saito, H. Miyazaki and T. Sato, "Pick and Place Operation of Micro Object with High Reliability and Precision based on Micro Physics under SEM", *Proceeding of the 1999 IEEE International Conference on Robotics and Automation, ICRA'99*, pp. 2736 - 2743, Detroit, Michigan, USA, May 1999.

[5] M. Sitti and H. Hashimoto, "Tele-Nanorobotics Using Atomic Force Microscope", *Proceeding of the 1998 IEEE/RSJ International Conference on Intelligent Robots and Systems, IROS'98*, pp. 1739 - 1746, Victoria, B.C, Canada, 1998.

[6] W. Zesch and R.S. Fearing, "Alignment of Microparts Using Force Controlled Pushing", in *Microrobotics and Micromanipulation, Proceeding of SPIE*, Armin Sulzmann, Bradley J. Nelson, Editors, Vol. 3519, pp. 148 - 156, Boston, USA, 1998.

[7] J. Israelachvili, *Intermolecular and Surface Forces*, Academic Press, London, 1992.

[8] D. Maugis, "Adhesion of Spheres: The JKR-DMT Transition Using a Dugdale Model", *Journal of Colloid and Interface Science*, Vol. 150, No. 1, April 1992.

[9] D. Baraff, *Dynamic Simulation of Non-Penetrating Rigid Bodies*, Ph.D. thesis, Cornell University, 1992.

[10] D.E. Stewart and J.C. Trinkle, "An implicit time-stepping scheme for rigid body dynamics with inelastic collisions and Coulomb friction", *Internat. J. Numer. Methods Engineering.* 39(15):2673-2691, 1996.

[11] B. V. Mirtich, *Impulse-based Dynamic Simulation of Rigid Body Systems*, Ph. D. thesis, University of California at Berkeley, 1996.

[12] A. Joukhadar, A. Deguet and C. Laugier, "A Collision Model for Rigid and Deformable Bodies", *Proceeding of the 1998 IEEE International Conference on Robotics and Automation, ICRA'98*, pp. 982 - 988, Leuven, Belgium, 1998.

[13] J. Sauer and E. Schömer, "A Constraint-Based Approach to Rigid Body Dynamics for Virtual Reality Applications", VRST'98, pp. 153 - 162, Taipei, Taiwan, 1998.

[14] H.C. Hamaker, "The London-van der Waals Attraction Between Spherical Particles", *Physica IV*, No. 10, pp. 1058 - 1072, November 1937.

[15] R.W. Cottle, J.-S. Pang and R.E. Stone, *The Linear complementarity Problem*, Academic Press, Boston, San Diego, New York, 1992.

[16] A.D. Lewis, R.M. Murray, "Variational Principles for Constrained Systems: Theory and Experiment", *International Journal of Nonlinear Mechanics*, 1995.

Technical Session A-2

Microfabrication, Material, and Property I

Study on Fabrication of Sub-Micron Structures for MEMS Using Deep X-Ray Lithography

Hiroshi Ueno, Nobuyoshi Nishi and Susumu Sugiyama
Faculty of Science and Engineering, Ritsumeikan University
1-1-1 Noji-Higashi, Kusatsu, Shiga 525-8577, Japan
phone: +81-77-561-2845, facsimile: +81-77-561-2845, e-mail: sme20034@se.ritsumei.ac.jp

Abstract:

It is necessary for practical MEMS with high performance to be fabricated microstructures with sub-micron widths and gaps (lines and spaces). In sub-micron deep X-ray lithography, one of the most crucial considerations is the fabrication of an X-ray mask with thick X-ray absorbers having sub-micron width. An X-ray mask, composed of 1 μm-thick Au with a 0.6 μm line width and a 0.2 μm space as absorbers, 2 μm-thick SiC with 240 MPa of tensile stress as a membrane and 625 μm-thick Si as a frame, was fabricated. A procedure for the fabrication process of the X-ray mask that obtains the smallest deformation of the X-ray absorbers, was adopted. On the other hand, in order to reduce the influence of Fresnel diffraction on lithography accuracy, a PMMA resist was polymerized without residual stress, which had been the main cause of a warp in the substrate, by controlling of the polymerization process. As a result, a sub-micron PMMA structure with 0.23 μm-minimum width and 15 μm height was fabricated by deep X-ray lithography.

1. INTRODUCTION

Fabrication techniques for microstructures with high aspect ratio, such as the LIGA process, deep RIE and so on, are attracting attention because the microstructures with high aspect ratio are expected to be applied to high power micro-actuators driven by low voltage and high sensitivity microsensors. As the results of our previous work using the LIGA process, microstructures with aspect ratio of 100, corresponding to 2 μm-width and 200 μm-height, were fabricated [1] and actuation of a wobble motor with aspect ratio of 50, corresponding to 2 μm-minimum gap and 100 μm height, was confirmed [2]. The results of another study reported that microstructures with the feature size of 1 μm and 100 μm height were able to be fabricated [3].

It is necessary for practical microelectro-mechanical systems (MEMS) with high performance to be fabricated microstructures with sub-micron widths and gaps (lines and spaces) for the following reasons: Microstructures with gaps less than 0.2 μm can decrease driving voltage of electrostatic micro-actuators to less than 15V [2,4]. Microstructures with widths and gaps (lines and spaces) less than 0.2 μm can be applied to Bragg grating having $\lambda/4$ pitch of visible light for optical communication devices.

In this paper, we present the fabrication of sub-micron structures with high aspect ratio for practical and high performance MEMS using deep X-ray lithography.

2. RESOLUTION

Two important factors, that influence the accuracy of X-ray lithography, are the creation of photoelectrons and Fresnel diffraction [5]. The influence of the creation of photoelectrons will be increased at shorter wavelengths. However, it has been reported that the creation of photoelectrons did not the influence accuracy of the X-ray lithography [6]. On the other hand, the influence of Fresnel diffraction will be increased at longer wavelengths. The resolution limit owing to Fresnel diffraction, R_d, is given by

$$R_d = 1.5(\lambda \cdot G/2)^{1/2}, \qquad (1)$$

where λ and G are wavelength and the gap between an X-ray absorber and a PMMA resist. In order to fabricate sub-micron microstructures, the values of λ or G must be reduced.

In our experiment, deep X-ray lithography is carried out using the LIGA beamline of synchrotron radiation (SR) light

1999 INTERNATIONAL SYMPOSIUM ON
MICROMECHATRONICS AND HUMAN SCIENCE
0-7803-5790-6/99/ $10.00 ©1999 IEEE.

source, "AURORA", at Ritsumeikan University. The beamline is composed of a 200 μm-thick layer of Be and a 50 μm-thick layer of Kapton as band-pass filters. Critical wavelength and wavelength range at the beamline are 0.4 nm and from 0.15 nm to 0.8 nm [7]. The wavelength range has the smallest influence on the X-ray lithography resolution [5]. Therefore, the gap must be controlled precisely in order to fabricate the sub-micron microstructures. Figure 1 shows the influence of Fresnel diffraction on resolution under different gaps at 0.4 nm. It was found that the gap must be set at less than 0.2 μm for the sub-micron deep X-ray lithography.

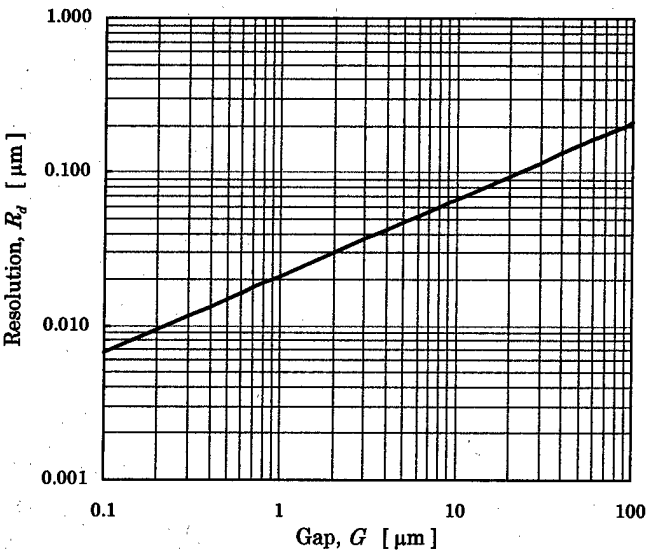


Fig. 1. Influence of Fresnel diffraction on resolution.

3. DEEP X-RAY LITHOGRAPHY

3.1 X-Ray Mask Design

As shown in Fig. 2, an X-ray mask for deep X-ray lithography is composed of an X-ray absorber, a membrane and a frame. Table 1 shows the important requirements for the X-ray mask. Based on the requirements, Au, SiC and Si were selected as the X-ray absorber, the membrane and the frame respectively and the thicknesses of SiC and Si were decided at 2 μm and 625 μm. The required thickness of Au X-ray absorbers was obtained in the following procedure.

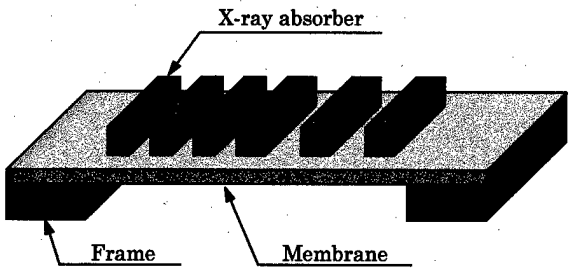


Fig. 2. Structure of an X-ray mask for deep X-ray lithography.

A beam spectrum of the AURORA is converted into an X-ray energy spectrum, e_0, per unit time. Exposure energy, E, at the terminal of the beamline for LIGA is given by

$$E = \int e d\lambda = \int \left[e_0 \times \exp\left\{ -\left(x_{Be}\mu_{Be} + x_{Ka}\mu_{Ka} \right) \right\} \right] d\lambda , \qquad (2)$$

where e is a spectrum of X-ray energy at the terminal of the beamline. x_{Be} (μm) and x_{Ka} (μm) are the thickness of Be and Kapton, which are 200 μm and 50 μm respectively. μ_{Be} (μm^{-1}) and μ_{Ka} (μm^{-1}) are the absorption coefficients of Be and Kapton. Transmitted energies of the X-rays through the membrane, E_M, and through the absorber, E_A, can be expressed as

$$E_M = \int \left[e \times \exp\left(-x_{SiC}\mu_{SiC} \right) \right] d\lambda , \qquad (3)$$

$$E_A = \int \left[e \times \exp\left\{ -\left(x_{SiC}\mu_{SiC} + x_{Au}\mu_{Au} \right) \right\} \right] d\lambda , \qquad (4)$$

where x_{SiC} (μm) and x_{Au} (μm) are the thicknesses of SiC and Au. μ_{SiC} (μm^{-1}) and μ_{Au} (μm^{-1}) are the absorption coefficients of SiC and Au. Contrast, C, is defined a ratio of E_M to E_A;

$$C = \frac{E_M}{E_A} . \qquad (5)$$

Table 1. Important requirements for an X-ray mask for deep X-ray lithography.

high absorption against X-rays
high accuracy of the pattern
high transparency against X-rays
high optical transparency
moderate tensile stress
high Young's modulus
high mechanical strength

In order to fabricate microstructures with a high aspect ratio, a large value of C is required. Figure 3 shows the required contrast, C, versus a lithography depth using the X-ray mask with a membrane of 2 μm-thick SiC. This result shows that C is required to be 5.5 for X-ray lithography of a 20 μm-thick PMMA resist. Figure 4 shows the required Au thickness versus a lithography depth using the X-ray mask. It was found that an Au X-ray absorber of 1 μm-thickness was required to fabricate a 20 μm-thick PMMA resist.

3.2 X-Ray Mask Fabrication

In sub-micron deep X-ray lithography, one of the most crucial considerations is the fabrication of an X-ray mask with thick X-ray absorbers. The designed X-ray mask is composed of 1 μm-thick Au as an X-ray absorber, 2 μm-thick SiC as a membrane and 625 μm-thick Si as a frame. The combination of the absorber of 1 μm-thick Au and the membrane of 2 μm-thick SiC gives a contrast of about 5.5 which is enough for the deep X-ray lithography of a 20 μm-thick PMMA resist using the energy spectrum produced by the AURORA.

Figure 5 shows a procedure for a fabrication process of an X-ray mask for sub-micron deep X-ray lithography. This fabrication process was adopted as it is the procedure which obtains the smallest deformation of X-ray absorbers. After SiC etching on reverse side by reactive ion etching (RIE), a membrane was formed by KOH etching (a). A metal seed

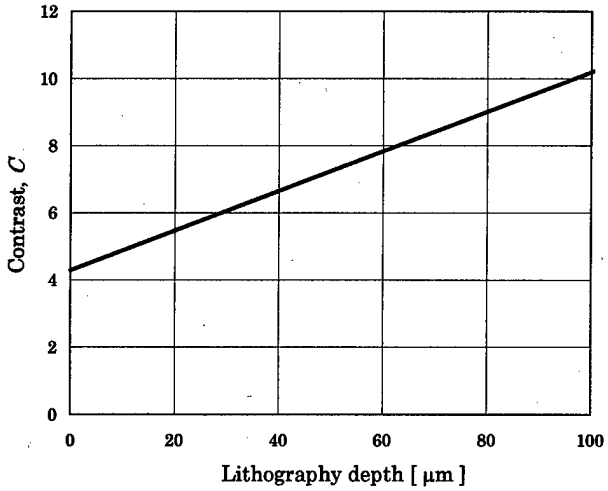


Fig. 3. Required Contrast, C, versus lithography depth.

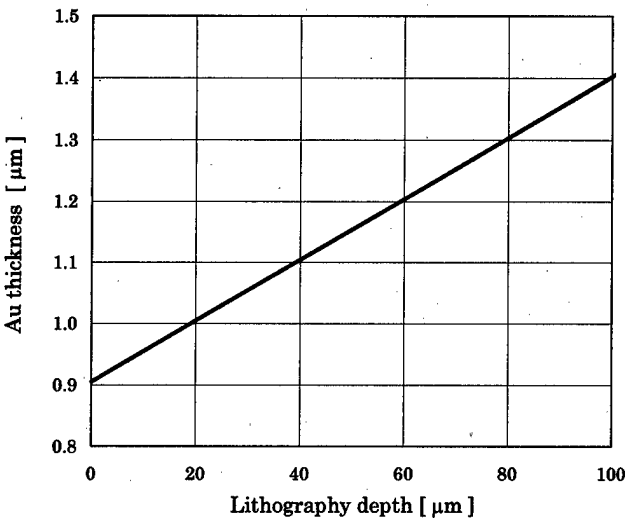


Fig. 4. Required Au thickness versus lithography depth.

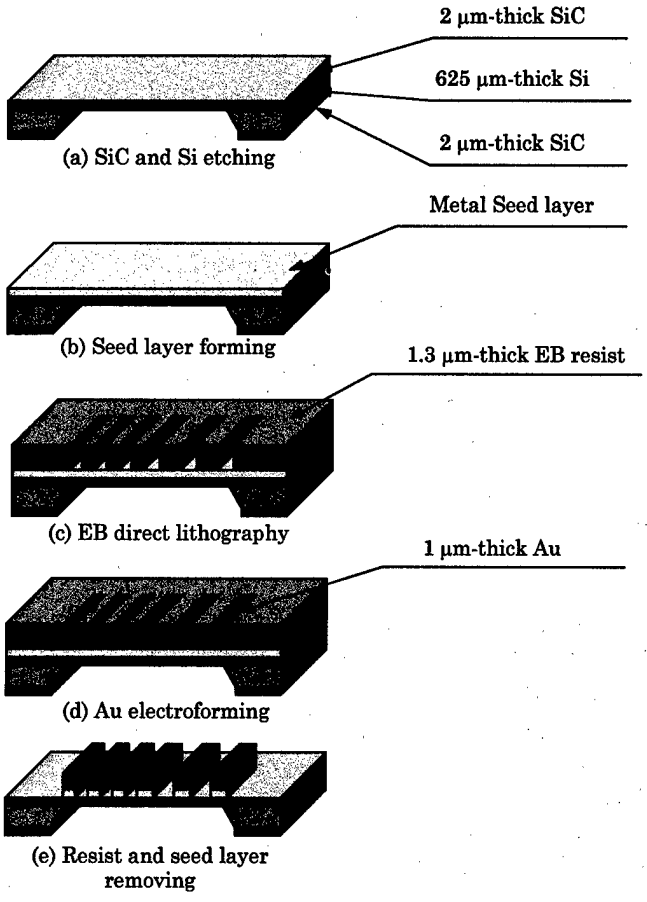


Fig. 5. Proceduer of fabrication process of an X-ray mask for sub-micron deep X-ray lithography.

layer for Au electroforming was formed on the upper side by vacuum evaporation (b). Sub-micron structures of electron beam (EB) resist as molds was formed by EB direct lithography (c). After Au electroforming (d), the EB resist structures and the metal seed layer were removed by wet etching using an organic solution and an acid solution (e).

Figure 6 shows an SEM photograph of fabricated X-ray absorbers with 0.6 μm line width, 0.2 μm space and 1 μm thickness. Although these absorbers have a slope of about 84° , it may not matter for deep X-ray lithography accuracy because it was reported that deep X-ray lithography accuracy was not influenced by absorbers with a slope of 82° [8]. The X-ray mask with a maximum membrane size of 60 mm × 30 mm can be fabricated. The membrane stress is 240 MPa of tensile stress.

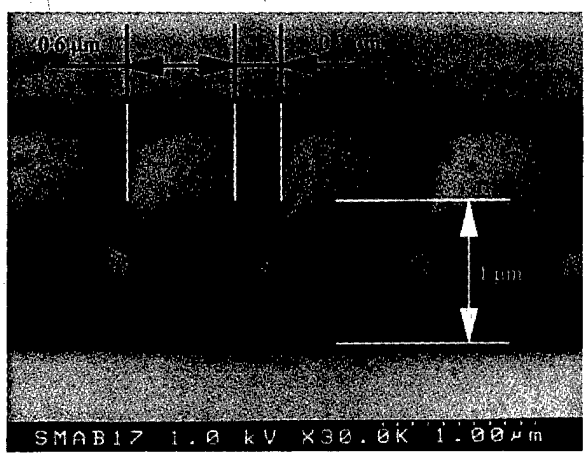


Fig. 6. SEM photograph of sub-micron X-ray absorber fabricated by Au electroforming after EB direct lithography.

3.3 Resist Forming

As shown in Fig.1, the gap between the X-ray mask and the PMMA resist must be set less than 0.2 μm for sub-micron deep X-ray lithography. However, there is a problem where a warp forms in a Si substrate by reason of residual stress of a PMMA resist which is generated by a high polymerization temperature and a difference of thermal expansion coefficients between Si (3.6×10^{-6} /℃) and PMMA (75.0×10^{-6} /℃).

A curvature radius, κ , of a warp in a Si substrate and residual stress of a PMMA resist, σ_P , are given by

$$\kappa = \frac{6E_p E_{Si} t_p t_{Si} t(\alpha_p - \alpha_{Si})}{(E_p t_p{}^3 + E_{Si} t_{Si}{}^3)(E_p t_p + E_{Si} t_{Si}) + 3E_p E_{Si} t_p t_{Si} t^2} \times \Delta T ,$$

$$\sigma_P \cong -\frac{E_p t_p{}^3 + E_{Si} t_{Si}{}^3}{6 t_p t}, \quad (6), (7)$$

where E_P and E_{Si} are Young's modulus of PMMA and Si, t is the total thickness of Si and PMMA resist, t_P and t_{Si} are the thickness of PMMA resist and Si, α_P and α_{Si} are the thermal expansion coefficients of PMMA and Si, and ΔT is temperature change.

Figure 7 shows the residual stress of PMMA versus different polymerization temperature. These experimental values are similar to the calculated results. Based on these results, a PMMA resist was polymerized without residual stress, which was the main cause of the warp in the substrate,

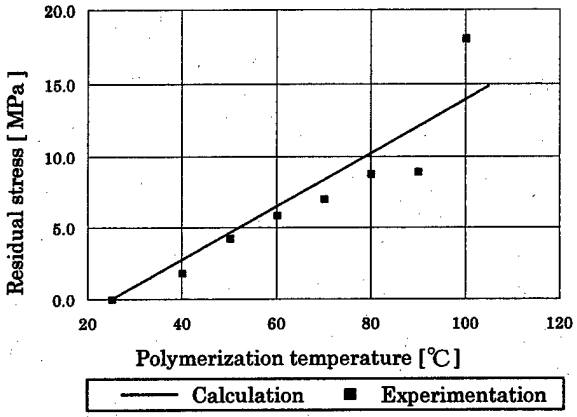


Fig. 7. Residual stress of PMMA versus different polymerization temperature.

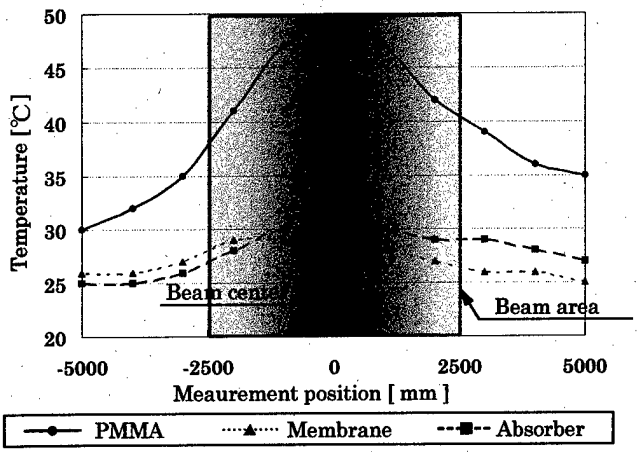


Fig. 8. Surface temperature profiles of a PMMA reist, a SiC membrane and an Au absorbers under the SR irradiation.

by controlling the temperature of the polymerization process.

3.4 Lithography

In order to fabricate sub-micron structures, the deformation of the X-ray absorber, the membrane and the resist due to heat generation under SR X-ray irradiation must be taken into consideration. Figure 8 shows the profiles of the surface temperature of an Au X-ray absorber, a SiC membrane and a PMMA resist in He at 1 atm under SR irradiation. An increase of 5 ℃ of the surface temperature of the Au X-ray absorber and the SiC membrane was indicated. In calculation, the maximum stress of the Au X-ray absorber and the SiC membrane is a compressive stress of 5 MPa. However, this is not a problem as the stress is compensated by the tensile stress of 240 MPa in the SiC membrane. On the other hand, the surface temperature of the PMMA resist indicated an increase of 25 ℃. In calculation, the maximum stress of the PMMA resist is a compressive stress of 6 MPa. This stress may be the main cause of a warp in the substrate and deformation of the PMMA resist. However, this stress can be reduced by repetition of short time exposure or cooling down the substrate.

As a result, a sub-micron PMMA structure with 0.23 μm-minimum width and 15 μm height was fabricated by deep X-ray lithography as shown in Fig. 8. This result shows that structures with sub-micron widths and gaps for practical and high performance MEMS can be fabricated by deep X-ray lithography. In particular, sub-micron PMMA structures fabricated by the deep X-ray lithography are expected to be applicable to optical communication devices because PMMA is characterized by a high permeability to visible light.

4. CONCLUSIONS

An X-ray mask, which is composed of 1 μm-thick Au as absorbers, 2 μm-thick SiC as a membrane and 625 μm-thick Si as a frame, was fabricated. A fabrication process of the X-ray mask, which obtains the smallest deformation of X-ray absorbers, was adopted. The X-ray mask has the X-ray absorbers with 0.6 μm line width and 0.2 μm space. The membrane stress of the X-ray mask is 240 MPa of tensile stress, which compensates the stress caused by heat generation under SR irradiation. In order to reduce the influence of

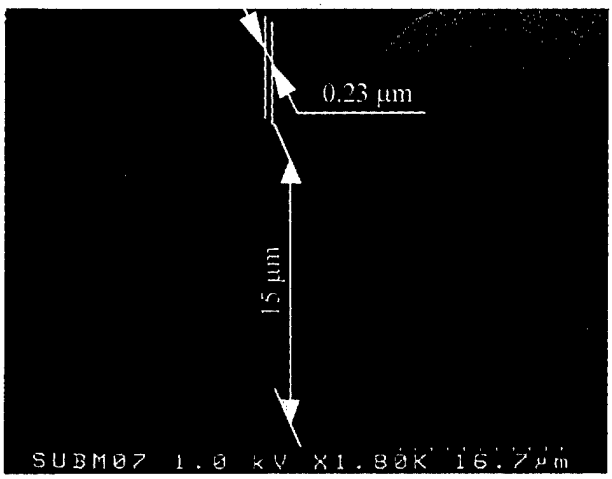


Fig. 9. SEM photograph of a sub-micron PMMA structure fabricated by the deep X-ray lithography.

Fresnel diffraction on the accuracy of the X-ray lithography, the PMMA resist was polymerized without residual stress, which was the main cause of a warp in the substrate, by controlling of polymerization process. As a result, a sub-micron PMMA structure with 0.23 μm-minimum width and 15 μm height was fabricated by the deep X-ray lithography.

These results are expected to be applicable to the manufacturing of practical and high performance MEMS devices. In future work, we intend to develop optimum conditions of sub-micron deep X-ray lithography and to fabricate practical and high performance MEMS devices.

ACKNOWLEDGEMENT

The authors would like to thank A. Kurikawa and H. Horiuchi at HOYA Corporation for supplying of SiC substrates.

REFERENCES

[1] Hiroshi Ueno, Makoto Hosaka, Osamu Tabata, Satoshi Konishi and Susumu Sugiyama, "X-ray Mask with SiC Membrane for LIGA Process", T. IEE Japan, Vol.119-E, No.4, 1999, pp. 229-235.

[2] Ryoji Kondo, Shinsuke Takimoto, Kenichiro Suzuki and Susumu Sugiyama, "High Aspect Ratio Electrostatic Micro Actuators Using LIGA Process", HARMST'99, 1999, pp.138-139.

[3] M. W. Borner, M. Kohl, F.J. Pantenburg, W. Bacher, H. Hein, and W.K. Schomburg, "Sub-Micron LIGA Process for Movable Microstructures", Microelectronic Engineering, 30, 1996, pp. 505-508.

[4] A. Azzam Yasseen, Chein-Hung Wu, Christian A. Zorman, and Mehran

Mehregany, "Fabrication and Testing of Surface Micromachined Silicon Carbide Micromotors", MEMS'99, 1999, pp. 644-649.

[5] W. Ehrfeld and H. Lehr, "Deep X-ray Lithography for the Production of three-dimensional Microstructures from Metals", Polymers and Ceramics: Radiation Phys. Chem., Vol.45, 1995, pp. 349-365.

[6] F. J. Pantenburg and J. Mohr, "Influence of secondary effects on the structure quality in deep X-ray lithography", Nuclear Instruments and Methods in Physics Research B 97, 1995, pp. 551-556.

[7] S. Sugiyama, Y. Zhang, H. Ueno, M. Hosaka, T. Fujimoto, R. Maeda and T. Tanaka, "A Compact SR beamline for Fabrication of High Aspect Ratio MEMS Microparts", MHS'96, 1996, pp. 79-84.

[8] M. Gentili, E. Di Fabrizio, L. Grella, M. Baciocchi, L. Mastrogiacomo, R. Maggiora, J. Xiao and F. Cerrina, "Fabrication of controlled slope attenuated phase-shift x-ray masks for 250 nm synchrotron lithography", J. Vac. Sci. Technol. B 12(6), Nov/Dec 1994, pp.3954-3958.

3-Dimensional Micromachining of PTFE Using Synchrotron Radiation Direct Photo-Etching

Nobuyoshi Nishi, Takanori Katoh, Hiroshi Ueno, Satoshi Konishi and Susumu Sugiyama*
Faculty of Science and Engineering, Ritsumeikan University
1-1-1 Noji-Higashi, Kusatu, Shiga 525-8577, Japan
phone: +81-77-561-2845, facsimile: +81-77-561-2845, e-mail: rm104950@se.ritsumei.ac.jp
*Sumitomo Heavy Industries, Ltd. 2-1-1 Yatocho, Tanashi, Tokyo 188-8585, Japan

Abstract:

In order to fabricate highly functional microdevices for MEMS, three-dimensional (3D) micromachining that can form certain round or curved structures is required. Recently, a high aspect ratio micromachining process using synchrotron radiation (SR) direct photo-etching of polymers without any process gases, the so called TIEGA (Teflon included etching galvanicforming), has been developed. The etching rate is of the order of 10-100 μm / min. Therefore, the processing for a 1000 μm-depth microstructure takes about 10 minutes, much shorter than that required for the deep X-ray lithography (LIGA) process. Moreover, it is free from problems of sticking due to the surface tension of the developer, the rinsing process etc., as SR etching is a completely dry process. Due to the high processing speed and smoothness of the etched surfaces, SR etching might have a potential for 3D micromachining by combining a scanning stage with a high degree of freedom. It is expected that microstructures formed by SR etching will be applied not only to highly functional microdevices, but also in the biomedical field, due to the material characters of PTFE. In this paper, we propose SR etching as a new approach to form 3D microstructures of PTFE and describe results of preliminary experiments for 3D micromachining.

1. INTRODUCTION

Three-dimensional (3D) microstructures with well-defined curved and inclined surfaces are of great interest for current microparts applications including mechanical, optical and electronics devices and subsystems. Several approaches to meet such requirements have been performed. Fabrication technologies such as the multi-mask process and the gray-tone lithography process [1, 2], have been utilized to realize 3D microstructures. Deep X-ray lithography (DXL) in the LIGA process has been tested in forming high aspect ratio 3D microstructures using sequential planar formation of individual levels [3], or moving mask technology to control a side-wall inclination of PMMA [4]. These processes require several or modulated masks for LIGA and elegant feedback systems, resulting in expensive and complicated processes. Moreover, serious problems of sticking, such as that due to the surface tension of the developer, occur in wet processes. The ideal method for 3D microfabrication is direct writing to be able to form any microstructure without using masks. The SR etching in the TIEGA (Teflon included etching galvanicforming) [5] process might meet these requirements.

TIEGA is a new process that fabricates microstructures using polymers like PTFE (polytetrafluoroethylene, Teflon) by etching directly in a vacuum using synchrotron radiation (SR). PTFE may be one of the most suitable materials for microparts in many fields, because of its thermostability, resistance to chemicals and its very low adhesion. However it has been difficult so far making microparts with a structural accuracy of some tens of microns and a structural height of some hundreds of microns, using PTFE. SR etching has overcome these difficulties, resulting in the possible micromachining of these materials. Metal structures with a high aspect ratio were also able be fabricated, as achieved in the LIGA process.

Here we will describe our study for 3D micromachining using SR etching, and discuss the potential of SR direct writing using our technology.

2. TIEGA PROCESS

2.1 Direct Photo-Etching Using SR Light

Recently, micromachining tasks have been approached with surface micromachining, LIGA etc. It has usually been a combination of lithography with etching technology. However, it is difficult for more complex microstructures with

1999 INTERNATIONAL SYMPOSIUM ON
MICROMECHATRONICS AND HUMAN SCIENCE
0-7803-5790-6/99/ $10.00 ©1999 IEEE.

round or curved surfaces to be fabricated with lithography and wet etching. Degradation of material surfaces by bombardment of ions and plasma cannot be avoided in dry etching processes like reactive ion etching (RIE). On the other hand, these problems can be avoided using the SR etching process, which is based on non-thermal photochemical reaction induced by SR irradiation. The decomposition of PTFE by SR proceeds via the scission of C-C bonds due to absorption of high-energy photons. As a result of this process, saturated fluorocarbons are evolved during irradiation by SR, which does not occur in the thermal decomposition of PTFE [6]. It is worth mentioning that the SR etching can be made available using SR X-rays extracted by filters. Thus X-ray lithography technology (such as using X-ray masks and processing under a He atmosphere) can be simply applied to SR etching.

2.2 Principle Process

The principle process steps for the fabrication of microstructure by TIEGA is shown in Fig. 1.

①,② The absorber patterns on an X-ray mask are transferred onto a thick PTFE layer (200-1000 μm) on the metallic substrate by SR etching. The exposed regions of the PTFE are selectively etched. The unexposed regions, covered during irradiation by the absorbers of the mask, form the primary microstructure.

This microstructure may be the end product of the process.

③ Metallic microstructure is formed by filling the PTFE mold with metal by electroforming.

④ The PTFE mold on the metallic substrate is removed by SR etching without mask, in another process, direct removing of the PTFE mold can be achieved by taking advantage of the non-adhesion character of PTFE to metal.

⑤,⑥ Metallic mold inserts are used in the molding process to produce secondary polymer microstructure.

SR etching, as in X-ray lithography, can fabricate high aspect ratio microstructures. Moreover SR etching is free from problems of sticking due to the surface tension of water etc., because it is a completely dry process. Because the etching rate is very fast using white SR light, SR etching can fabricate high aspect ratio microstructures with evenness of the etched surfaces in a short time. Therefore, SR etching might have a potential to fabricate microstructures with curved sur-

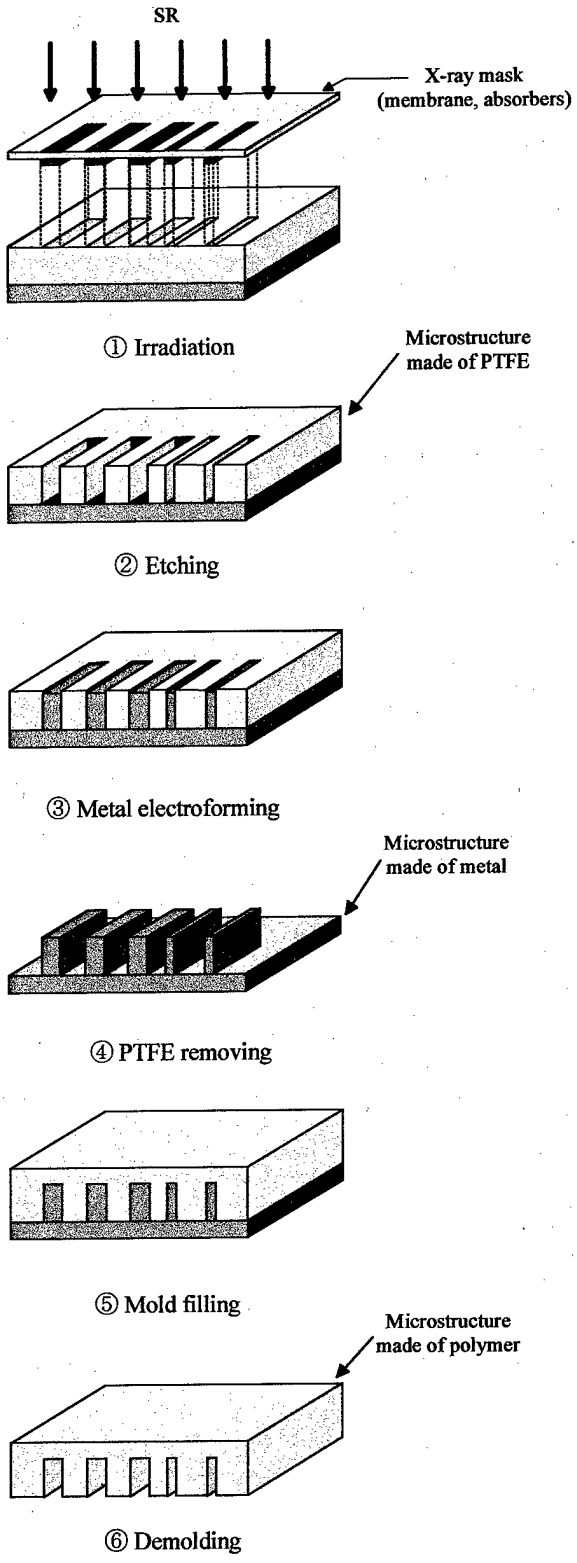


Fig. 1. Principle process steps for the fabrication of microstructure by TIEGA.

faces by combining the scanning stage with high degree of freedom.

3. FABRICATION

3.1 Preliminary Experiment

The TIEGA experiments in this paper were performed using two beam lines of the compact SR source "AURORA" in the SR center of Ritsumeikan University. One is the BL-6 for LIGA process and the other is the BL-14 for SR-stimulated processes including TIEGA. Exposure can be done at a wavelength range between 0.15 to 0.73 nm under a He atmosphere of 1 atm [7] at the BL-6, and 0.15 to 2.7 nm in a vacuum at the BL-14, respectively. The comparison between the BL-6 and the BL-14 is shown in table 1 and the spectra of the BL-6 and the BL-14 are shown in Fig. 2.

The first experiment was carried out to fabricate PTFE microstructure with line and space (L&S) (L: 100 μm, S: 200 μm) patterns using the metal mask at the BL-6. The average roughness of the utilized commercial polished sheets of PTFE was 248 nm. Figure 3 shows the PTFE microstructure fabricated in this condition. The depth of this microstructure was 100 μm, the etching rate was 0.8 μm / min and the side-wall taper-ratio was 0.04. The roughness of the side-walls and the irradiated surfaces are as shown in the figure. The average roughness of the irradiated surfaces was 3480 nm.

These results indicate that the etching rate severely influences the surface morphologies or roughness of PTFE irradiated by SR. The saturated fluorocarbons evolved by SR may be repolymerized at the PTFE surfaces in the case of a low etching rate. As for the desorption rate of saturated fluorocarbons, a higher PTFE temperature during processing resulted in a higher etching rate. So it is possible to make smooth surfaces of PTFE by using a higher etching rate while heating the PTFE [6]. Figure 4 shows the PTFE microstructure that was fabricated at 200 ℃ by using a heater attached to the rear of the PTFE. The depth of this microstructure was 180 μm, the etching rate was 6 μm / min and the side-wall taper-ratio was 0.016. Repolymerization at the PTFE surfaces could be controlled and a smooth surface with a roughness of 450 nm was obtained.

The PTFE microstructure that was fabricated with the BL-14 is shown in Fig. 5. The depth of this microstructure was

Table 1. Comparison between the BL-6 and the BL-14.

Beam line	BL-6	BL-14
Energy range (eV)	2000-10000	50-10000
wave length (nm)	0.15-0.73	0.15-2.7
Distance between SR and samples (m)	3	4

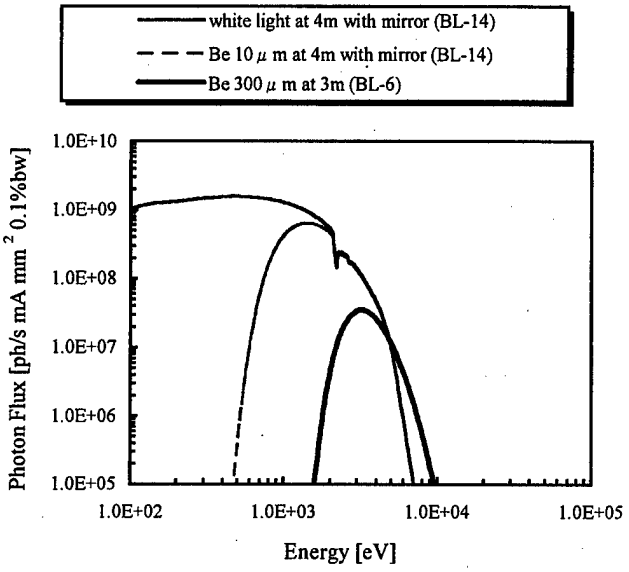


Fig. 2. Spectra of the BL-6 for LIGA and the BL14 for SR-stimulated process including TIEGA.



Fig. 3. SEM image of microstructure made of PTFE created by SR etching at room temperature with the BL-6.

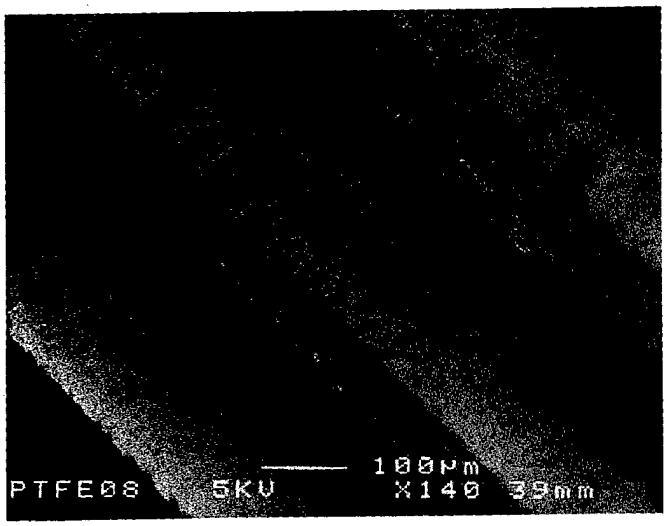


Fig. 4. SEM image of microstructure made of PTFE created by SR etching at 200 ℃ with the BL-6.

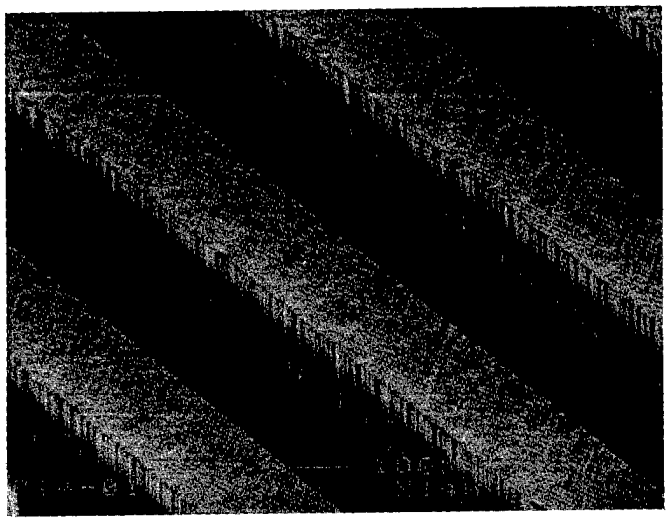


Fig. 5. SEM image of microstructure made of PTFE created by SR etching with the BL-14.

120 μm, the etching rate was 100 μm / min and the side-wall taper-ratio was 0.006. Moreover the irradiation surfaces achieved a very flat roughness of 110 nm. This is less than the roughness of PTFE without irradiation. Table 2 shows these preliminary experimental results.

3.2 Fabricated Microparts with the BL-14

Figure 6 shows the PTFE microstructure with 500 μm-depth, 20 μm-width in minimum and maximum aspect ratio of 25. The quality of the microstructure made by the SR etching process looks fairly good compared to that made by the LIGA process. The surface roughness of the side-wall was 100 nm and the side-wall taper-ratio was a small 0.006 in the irradiated part. PTFE patterns of less than 10 μm and maximum aspect ratio of 75 were successfully fabricated by using the BL-14 [5].

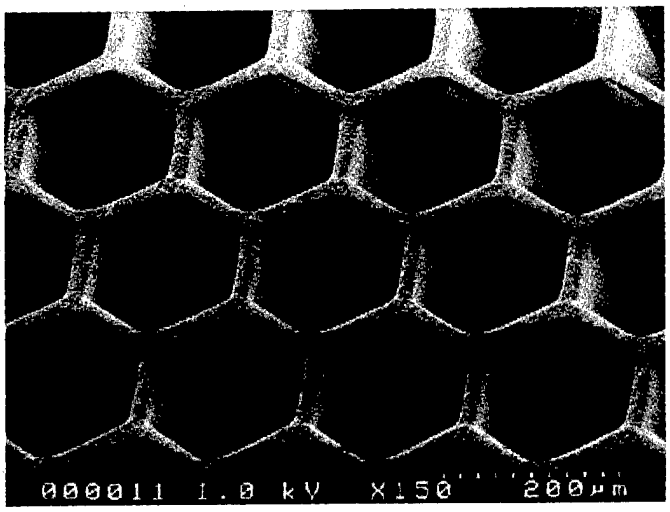


Fig. 6. SEM image of microstructure made of PTFE created by SR etching with the BL-14.

Table 2. The results of SR etching using metal mask with the BL-6 and the BL-14.

Beam Line	BL-6	BL-6	BL-14
Enviroment	He atmosphere	He atmosphere	Vacuum (10^{-5} Torr)
Sumple temperature (℃)	25	200	200
Etching rate (μm / min)	0.8	6	60
Roughness (nm)	3480	450	110
Taper-ratio	4 / 100	1.6 / 100	0.6 / 100

3.3 3D Micromachining

In order to carry out 3D micromachining of PTFE by SR etching, an atmospheric pressure for processing can be adopted from a practical point of view despite the low etching rate. Under atmospheric pressure, there is no limitation of materials in the stage and the mechanical systems. It is also easy to handle masks and the material for fabrication. So, 3D micromachining with the BL-6 was performed without using any masks as a result of the preliminary experiments. Figure 7 shows a schematic diagram of the experimental set up for direct etching. In order to carry out direct writing, the stage with the fixed PTFE was installed at a slant of 15 degrees against the X-rays, so it was possible to rotate and irradiate the PTFE. A curved surface was formed on the surface of the PTFE by SR etching with X-rays through the pin hole mask with a diameter of 80 μm with a rotating stage. Figure 8 shows a result of 3D micromachining created in PTFE with a turning radius of 300 μm. A surface profile of this structure measured by stylus plofilometer is shown in Fig. 9. However, deformation of a large area of the PTFE sheet occurred as the heater heated a greater area than required. This had an influence on precision and the heater's size and wiring had an influence on the degree of freedom of the scanning stage. Local heating using a microheater-tip with a collimator for SR attached to the end of the nozzle will be an alternative method for heating during processing without deformation. We will test the microheater-tip to reduce the tolerance of the processing in the future.

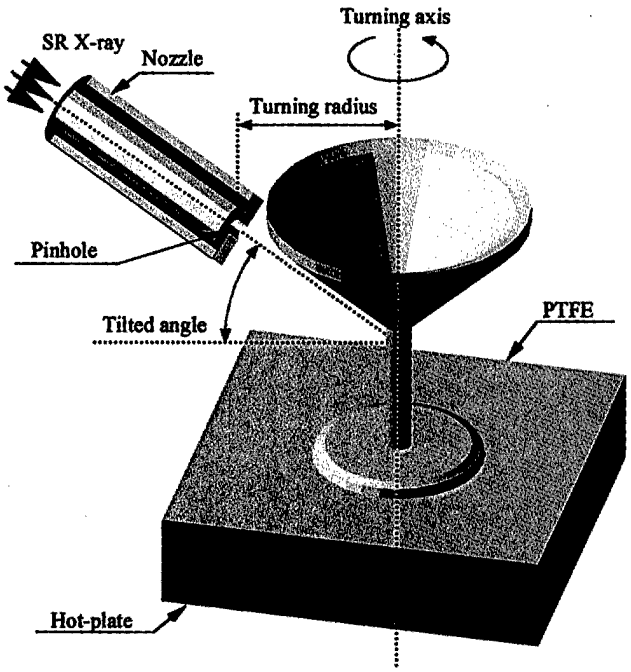


Fig. 7. Schematic diagram of experimental set up for direct writing.



Fig. 8. SEM image of 3D structure created in PTFE surface.

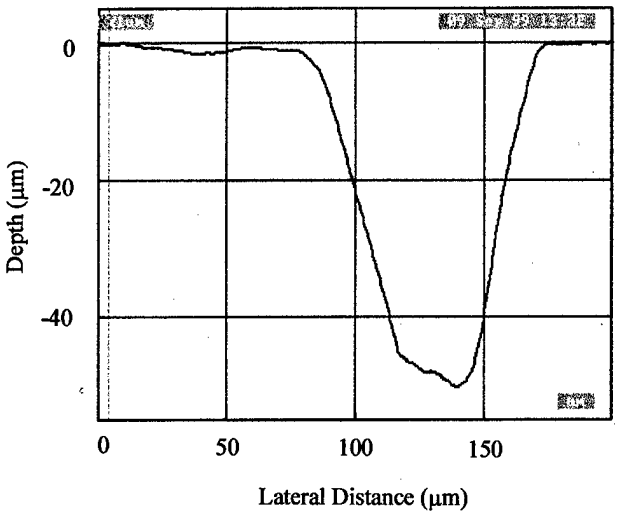


Fig. 9. Surface profile of the 3D structure in Fig. 8.

4. CONCLUSIONS

In this paper, rapid 3D micromachining technology based on SR etching without using any masks was proposed. The experiments were carried out with the BL-6 in which X-rays of the wavelength of 0.15 to 0.73 nm were exposed in a He atmosphere, and with the BL-14 in which white SR light of the wavelength of 0.15 to 2.7 nm was exposed in a vacuum using the compact SR source "AURORA". The PTFE sheet that was used in this experiment was of a surface roughness of 248 nm. As for the experiments with the BL-6, the etching rate was 0.8 μm / min, the side-wall taper-ratio was 0.04 and the irradiated surface roughness was 3480 nm. Adding the heating process to the PTFE, the etching rate was 6 μm / min, the side-wall taper-ratio was 0.016 and the irradiated surface roughness was 450 nm. We confirmed the effects of the desorption speed of saturated fluorocarbons for the surface morphologies. Using the BL-14, an etching rate of 100 μm / min, a side-wall taper-ratio of 0.006 and a surface roughness of 110 nm were achieved. As for 3D micromachining, the preliminary experiment for the fabrication of curved structures of PTFE was successful. The potential for 3D direct writing using SR etching was discussed.

REFERENCE

[1] S. Nicolas, Eurosensors XI, 1997, pp. 1271-1274.

[2] K. Reimer, H. J. Quenzer, M. Jürss, and B. Wagner, SPIE Vol. 3008, 1997, pp. 279-288.

[3] T. Hirata, H.Hein, T. Akashi, and J. Mohr, to be presented Micromachining and Microfabrication '99.

[4] O. Tabata, K. Terasoma, N. Agawa and K. Yamamoto, MEMS '99, 1999, pp. 252-256.

[5] Takanori Katoh, "Microfabrication Process Using Synchrotron Radiation Exicited Photodecomposition", Journal of the Japan Society for Precision Engineering Vol. 64, No. 7, 1998, pp. 1008-1011.

[6] T. katoh and Y. Zhang, "Synchrotron radiation direct photo-etching of polymers and crystals for microfabrication", Journal of Synchrotron Radiation Vol. 5, 1998, pp. 1153-1156.

[7] S. Sugiyama, Y. Zhang, H. Ueno, M. Hosaka, T. Fujimoto, R. Maeda, and T. Tanaka, "A Compact SR beamline for Fabrication of High Aspect ratio MEMS Microparts", MHS'96, 1996, pp. 79-84.

Mechanical and Electrical Characteristics of Poly-silicon Film Deposited by New LPCVD Using Lamp Heating

Tetsuo UEDA

Fine-gas Equipment Engineering Dept., Central Engineering Co., Ltd.
5272-4 Oaza Okiube, Ube, Yamaguchi 755-0001
JAPAN

Katsutoshi KURIBAYASHI

Faculty of Engineering, Yamaguchi University
2-16-1 Tokiwadai, Ube, Yamaguchi 755-8611
JAPAN

Satoru HASEGAWA

Mita works, Mitsubishi Electric Corporation
2-3-33 Miwa, Mita, Hyougo 669-1513
JAPAN

Abstract:

The newly developed LPCVD apparatus using lamp heating was shown[1] valid for obtaining the same poly-silicon film for micromachine as that produced by the conventional LPCVD apparatus, by analysing the metallurgical properties of the poly-silicon film deposited by the new LPCVD apparatus. However, when producing a micro machine using the poly-silicon film deposited with this apparatus, it is necessary to know the mechanical and electrical characteristics of this film. Therefore, this report describes the analysis of Young's modulus, resistivity and gage factor of the poly-silicon deposited by the new LPCVD apparatus.

1. Introduction

Among mechanical characteristics of the poly-silicon thin film, Young's modulus, an elastic modulus, is an important characteristic[2] that relates to the sensitivity of various micro sensors of acceleration and pressure and the displacements of an electrostatic type comb actuator, etc. There are a variety of methods of measuring Young's modulus of these thin films such as a tensile test[3], bending test[4][5], bulge method[6][7], Raman scattering method[8] and nano-indentation method[9], etc. However, these methods are often used for thin films of 1μm or less in thickness and have the problems for measuring Young's modulus of thick poly-silicon films deposited by this LPCVD apparatus using lamp heating. Next among electrical characteristics of the poly-silicon thin film, the piezoresistance effect and gage factor after doping impurity material in the poly-silicon thin film are major properties for an electro static actuator and force sensor[10]~[16].

Therefore, in this study we have proposed a new bending test method suited to measurement of Young's modulus of this thick-film poly-silicon and measured Young's modulus of poly-silicon film deposited by the LPCVD apparatus using that mesurement method. The electrical properties of resistivity[10][13][14][16][17] and gage factor[10]~[16] of the poly-silicon deposited by the new LPCVD and diffused by boron impurity, were analysed.

2. New mesurement method of Young's modulus of the poly-silicon and the results

2-1 Principle of the new measurement method

The new measurement method of Young's modulas for the poly-silicon film is as follows. First, the bending profile of the Si substrate with the poly-silicon film deposited by the new LPCVD is obtained experimentally by loading the weight to the end of test piece. Next the bending profile is approximated numerically by the non-linear equation of dynamical model of cantilever beam, by adjusting the parameter of the Young's modulas in the non-linear equation. The program for the simulation model for this measurement was created using Matlab of Cybernet, Inc.

2-2 New measurement method

The method for measuring Young's modulus used in this experiment uses a cantilever-state large transformation bending test method. The load is applied using the following method. First, a test piece is attached to a fixation base with a rotational axis as shown in (1) in Fig.1. Then, a mass is

1999 INTERNATIONAL SYMPOSIUM ON
MICROMECHATRONICS AND HUMAN SCIENCE
0-7803-5790-6/99/ $10.00 ©1999 IEEE.

attached to it in the same direction as the poly-silicon test piece is hung and then the mass is set free. From this state, the test piece is turned clockwise around the test piece mounting axis by 20 degrees at a time and the deformation of the test piece at that time is read along the length of the test piece using a video camera and TV monitor. This operation is repeated until either the angle of rotation becomes 90 degrees or the test piece is destroyed. We measured the shape of the test piece using an optical microscope.

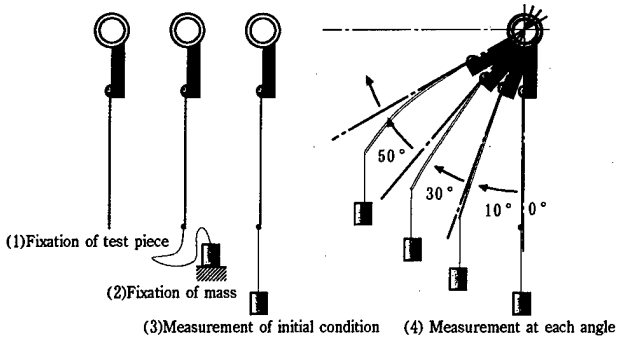


Fig.1 Principle of measurement

2-3 Test pieces

The thickness of the poly-silicon deposited using the LPCVD apparatus using lamp heating distributes due to a heating temperature distribution on substrate. A colorized pattern of its surface properties can also be distinguished by the unaided eye[1].

To measure Young's modulus using the above measurement method, it is necessary to get the test piece in a size of 1 mm wide and 12 mm long. However, the poly-silicon film is deposited on a 15 mm x 20 mm substrate, and it has a thickness distribution as mentioned above[1]. Since there was no other way, we decided to get roughly the test piece from 15 mm x 20 mm to 1 mm x 12 mm as shown in Fig.2. We used the extraction method as follows.

(1) The substrate used is an n-type Si substrate in a size of 15 mm x 20 mm and thickness of 600 μm with a 0.5 μm thick SiO2 deposited on it. Poly-silicon is deposited for one hour using the LPCVD apparatus using lamp heating.

(2) After poly-silicon is deposited, Ti-Ni, which serves as a mask for the RIE apparatus, is deposited 1.0 μm using sputtering apparatus. Then, to shape the test piece pattern on Ti-Ni, OMR-83, a negative type photo-resist, is applied and the test piece pattern is patterned on the resist.

(3) The patterned substrate is dipped in a mixture of HF and HNO_3 ($HF:HNO_3:H_2O=1:9:10$) for 30 seconds and Ti-Ni outside the resist is subjected to wet etching and the shape of the test piece is formed. Then, the substrate etched with the desired pattern is subjected to etching for 10 minutes using the RIE apparatus, subjected to anisotropic etching until it reaches the depth of the SiO2 layer.

(4) The etched substrate is dipped in a mixture of HF and NH_4F ($HF:NH_4F=1:5$) for 24 hours or more at a room temperature and the SiO2 layer between poly-silicon layers is subjected to wet etching and then the test piece is released.

The test piece produced has a strap-like form of 1.0 mm wide and 12.0 mm long and the thickness varies depending on the test piece, but is within the range of 10 to 20 μm.

As seen in Fig.2, this results in a film thickness distribution along the length of the test piece and also a distribution in the width direction. However, since the film thickness in the width direction is as narrow as 1 mm compared with the length direction, and so we decided to admit averaged simulation results and conducted a simulation considering that there is a thickness distribution only in the length direction. The film quality is also considered to have a concentric distribution, but we decided to leave this for later discussions. Table 1 shows the conditions to create each test piece using the CVD apparatus using lamp heating. As is clear from this, we did our best to keep the same conditions to create each test piece, but it is unavoidable to have some differences for reasons related to reproducibility of the apparatus.

Table 1 Condition of Poly-Si film deposited with each test piece

		a	b , c	d , e
Temperature of deposition	°C	825	805	835
Pressure of gas	Pa	67	67	67
Deposition time	minute	60	60	60

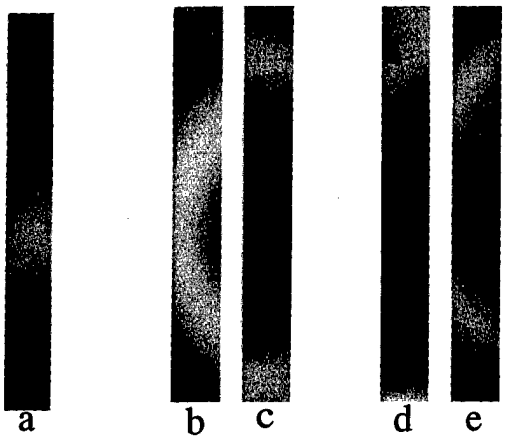


Fig.2 The test pieces which were used for the experiment

2-4 Simulation model

The simulation model used in this study was obtained theoretically from a dynamic model in Fig.3 as follows:

There is a relation between the curvature of a neutral plane and bending moment M as shown in equation (1).

$$\frac{M}{EI_z}=\frac{-\frac{d^2y}{dx^2}}{\{1+(\frac{dy}{dx})^2\}^{\frac{3}{2}}} \quad \cdots\cdots \quad (1)$$

Where, E: Young's modulus; Iz = 1/12bh³: geometrical moment of inertia; b: test piece width; h: test piece thickness. The test piece is a cantilever, fixed at one end and free at the other. Thus, supposing the mounting section of the test piece is a point at coordinate 0, the mounting stand surface is placed on the x-axis and the direction perpendicular to this is set on the y-axis as shown in Fig.3. Then, the boundary condition is slope dy/dx=0, deflection y=0 when x=0. No matter how the test piece is bent, its length L is constant and thus binding condition equation (2) is established.

$$L=\int_0^{X_{max}} \sqrt{1+(dy/dx)^2}\ dx \quad \cdots\cdots (2)$$

However, since this bending test is conducted with the test piece inclined as shown in Fig.3, bending moment M is expressed as follows:

$$M=mg\{(X_{max}-x)\sin\theta-(Y_{max}-y)\cos\theta\} \quad \cdots\cdots (3)$$

Substituting M in (3) into (1) results in equation (4) below.

$$\frac{d^2y}{dx^2}=-\frac{mg}{EI_z}\{(X_{max}-x)\sin\theta-(Y_{max}-y)\cos\theta\}\{1+(\frac{dy}{dx})^2\}^{\frac{3}{2}} \quad \cdots\cdots (4)$$

These equations (2) and (4) are the basic equations of cantilever large transformation. However, equation (4) is a non-linear equation, and so it is not possible to find an analytical solution. Thus, in this study, we used a Runge-Kutta method to do numerical calculations. Before calculations, coordinates Xmax and Ymax at the end point are not known. Therefore, calculations were performed presuming Xmax and Ymax and when the results coincided with the hypothesized Xmax and Ymax, we adopted the result as a numerical solution of (4).

With the theory above alone, it would be possible to conduct bending tests of a test piece with a linear shape with a uniform surface on both sides. But the poly-silicon test piece used in the experiment has an uneven surface on one side and residual stress causes the test piece to have a bent shape from the beginning. Therefore, in order to incorporate this information into simulation, we decided to express it as a function using the following method. To examine the surface shape with variations of the uneven thickness described above, we observed and measured the sides of the test piece using an optical microscope. We used 3 to 5 measuring points along the length of the test piece. We approximated these measuring points using a quartic polynomial and calculated it by means of a least square method, expressing thickness h as a function of coordinate S along the length of the test piece. The warpage of the substrate due to residual stress of the latter was obtained by accurately measuring the shape of the test piece without load using the same measurement method and approximated by means of a cubic polynomial likewise and calculated using the least square method, expressing the deflection of the test piece as a function of coordinate S along the length of the test piece. It would be impossible to obtain correct Young's modulus without considering these two functions, and so we decided to add these two test piece conditions to the simulation in addition to equations (2) and (3).

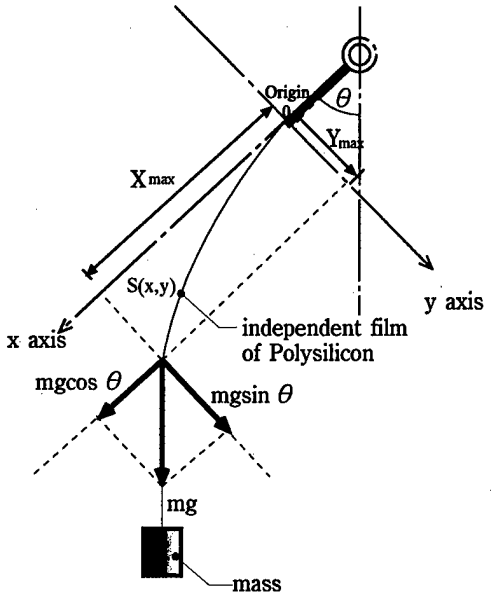


Fig.3 Dynamical model of the experiment

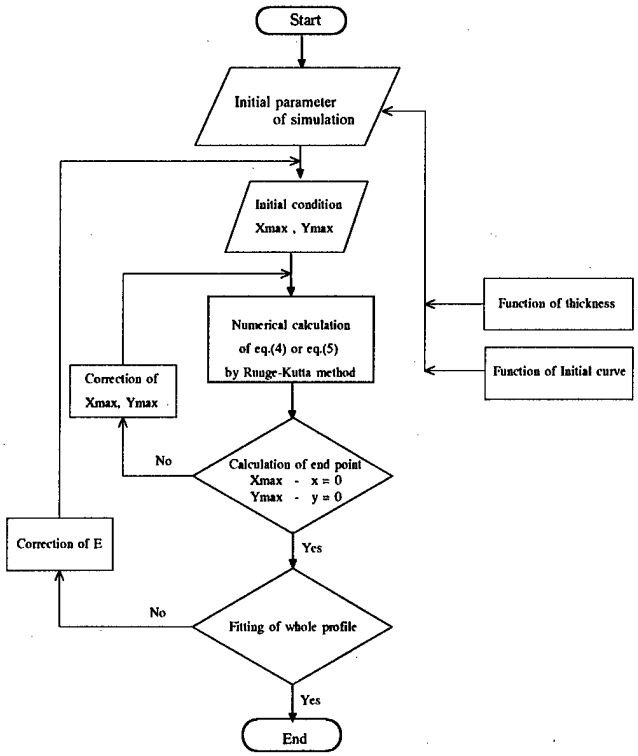


Fig.4 Simulation flow chart

This simulation was calculated based on a simulation flow

as shown in Fig.4. The simulation initial values are the mass of the weight (measured value), width of the test piece (measured value), distance from a fixed end to the other end of the test piece (measured value), angle (measured value), initial value of Xmax (hypothetical value), initial value of Ymax (hypothetical value) and initial value of Young's modulus (hypothetical value). Due to a two-point boundary value problem as mentioned above, this simulation performs calculations to find the end point (Xmax, Ymax) then tries to match the experiment measurement profiles while changing Young's modulus.

2-5 Measurement results

After verifying the validity of the measurement method above using a Si single crystal test piece with uniform characteristics, we measured Young's modulus of a poly-silicon film deposited by this CVD apparatus using this measurement method.

Fig.5 shows a relationship between Young's modulus and measurement angles. The average and standard deviation of the total measured value of Young's modulus of poly-silicon are 121.4 ± 7.1 GPa.

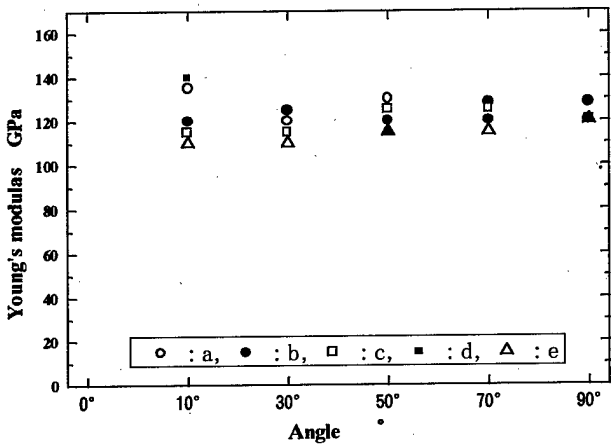


Fig.5 Relation between bending angle and Young's modulas

When attention is given to the differences in the average value between test pieces, some of theses differences possibly reflect the differences in the lots in which test pieces were created and the differences in the film quality at the points where the test pieces were collected. But we cannot find any tendency. Moreover, if we also take into account the fact that there is an error of the measurement method itself of ± 4.5 GPa in standard deviation, we can say that there is no significant difference in Young's modulus between test pieces in this measurement method and under the poly-silicon test piece creation conditions. Therefore, it is reasonable to conclude that Young's modulus of poly-silicon obtained within the accuracy given in the experiment is virtually constant.

3. Diffusion characteristics of boron impurity in poly-Si film

The boron diffusion was applied to the poly-Si film deposited by this LPCVD apparatus using lamp heating. The the two-stage diffusion method consisting of the predeposition (diffusion at the constant concentration of surface impurity) and the drive-in (removal of impurity source, adjustment of resistivity by the rearrangement of impurity is used) .

3-1. Diffusion method

Table 2 shows the condition of deposition to the poly-Si film deposited by the LPCVD apparatus using lamp heating. And Table 3 shows the condition of boron diffusion to the poly-Si film deposited by the LPCVD apparatus using lamp heating. The deposition applied to the same 20×30mm Si substrate as shown in previous report.

The boron diffusion are carried out by followings.

(1) Apply a diffusion agent polyboron film (PBF 6R-10, manufactured by Tokyo Ohka Kogyo Co., Ltd.) onto poly-Si film using a spinner.

(2) Anneal it at 600° C for 30 minutes.

(3) Increase the temperature of the tube to over 800° C to let boron in the diffusion agent diffuse into the inside of poly-Si film (predeposition).

(4) After the tube cooled down, remove the substrate from the tube and wash it with 46% HF to remove the remaining polyboron film.

(5) Again heat it at 1100° C for 83 minutes and rearrange the boron introduced in poly-Si film (drive-in).

But above heat proceses are heated using hot wall type heater.

Table 2 Deposition conditions of Poly-Si film as test piece

Temperature of deposition	850 °C
Pressure of gas	67 Pa
Deposition time	60 minutes

Table 3 Boron diffusion conditions into the Poly-Si

Pre-deposition time	144 minutes
Pre-deposition temperature	1000 °C
Drive in time	83 minutes
Drive in temperature	1100 °C

3-2. Measurement method of the depth of boron diffusion

For the measurement of the depth of diffusion in a substrate which received the boron diffusion, the staining method was used. In this method, a substrate which received the boron diffusion is immersed in a mixture of HF and a small amount of HNO_3 to stain the part where the diffusion of boron took place. The following is its procedure:

(1) Using a driller for the thickness measurement of thin film, make a spherical hollow with a diameter of about 1 mm and a depth of several μm on the boron-doped poly-Si substrate so that the diffusion layer can be seen as a fault in the hollow.

(2) Immerse the entire substrate in staining liquid (46% HF : 60%HNO_3 = 10 : 1) for 3.0 seconds to stain the diffused section of fault black.

(3) Measure the depth of stained diffused section by microscope.

Thus, the diffusion depth of poly-Si was measured.

3-3. Measurement results of the depth of boron diffusion

The film thickness of poly-Si film deposited by the LPCVD apparatus using lamp heating is concentrically distributed because there is a distribution regarding its heating temperature. Some surface characteristics are also visually observable as a concentric-circle pattern[7]. This pattern was drawn as shown in Fig.6 by personal computer. This time, by referring to five types(A,B,D,F,G) shown in Fig.6, the surface condition of test specimens was evaluated. Here, the classification symbols correspond to those of Fig.4 in the previous report[7]. The symbols ⊗ in Fig.6 shows mesurement point of diffused thickness.

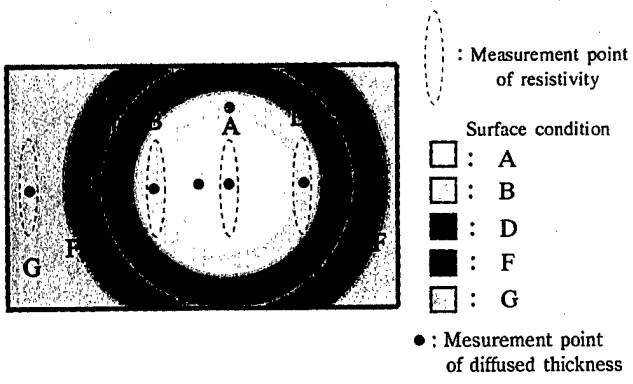


Fig.6 Schematic view of surface of Poly-Si deposited and the measurement points of diffusion depth (condition of deposition : 850° C, 67Pa, 40sccm<SiH$_4$(10%)/Ar:N_2= 1:1>)

Fig.7 shows the relationship between the thickness of poly-Si and the depth of diffusion and the surface condition which was obtained from the above measurement results. The same figure also contains the measurement results of n-type single-crystal silicon of the upper surface (100) which was given the diffusion treatment in the same condition.

Here, the average value was calculated from the data collected at three points - the central point of doped silicon substrate(20×30mm) and the two other points which were respectively located 5mm from the central point in the lateral longitudinal direction. The individual data collected at the three points fell within ±0.5 μm from the average. From these measurement results it was confirmed that the diffusion rate in poly-Si film was slower than that in n-type single-crystal silicon substrate. Meanwhile, among the diffusion rates classified by the individual surface condition the higher was observed in the surface condition B,D. This is considered to have been due to the fact that as the shape of granular structure in the surface condition B was large and round[7] and there was relatively large space, impurities were easily able to penetrate into the structure.

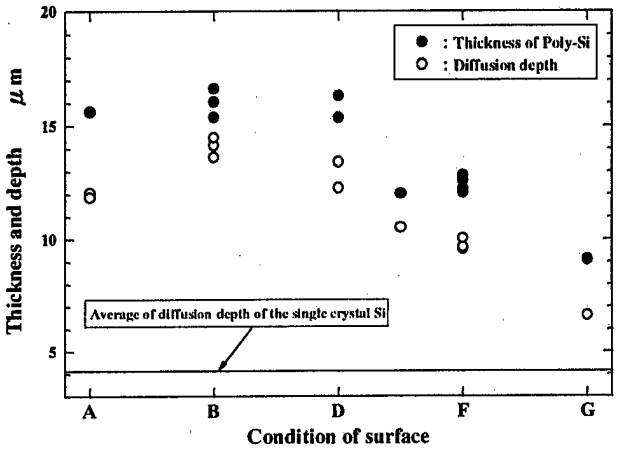


Fig.7 Thicness of diffusion for each surface condition

4. Electrical resistivity

4-1. Measurement method

The resistivity of the boron doped poly-Si film was measured by the four point probe method. The resistivity ρ Ω·cm of thin film can be calculated by the next equation[8] under supplying a certain level of electrical current to this four point probe equipment.

$$\rho = \frac{V}{I} \cdot \omega \cdot F\left(\frac{\omega}{S}\right) \cdot \frac{\pi}{\ln 2}$$

Here, the individual terms have the following meanings - V: voltage [V], I: current [A], ω: thickness of object to be measured [cm], S: distance between probes [cm], and F (ω/S): correction term. In this study, the thickness of object to be measured is the depth of diffusion. The correction term F (ω/S) is determined by both the distance between probes and the thickness of object to be measured and approaches 1 with the decrease in the magnitude of ω/S. In the case of measuring apparatus used this time, the distance between probes was S=1.0 mm and the maximum depth of diffusion was ω=14.5μm as shown in Fig.7. As ω/S=0.0145 was obtained in the measurement of this time, it could be assumed that F (ω/S)=1. Using the above-mentioned method and conditions, the resistivity of poly-Si film was measured.

4-2. Measurement results

For this measurement, the same specimen as used for the measurement of diffusion depth was used and its surface condition was evaluated by referring to five types shown in Fig.6. The mesurements points are showed in Fig.6. Fig.8 shows the relationship between the surface condition obtained and the resistivity of poly-Si. This figure also contains the measurement results of n-type single-crystal silicon doped under the same conditions. The diffusion-depth value of n-type single-crystal silicon is the average of the data collected at three points - the central point of doped silicon substrate and the two other points which were respectively located 5 mm from the central point in the lateral longitudinal direction.

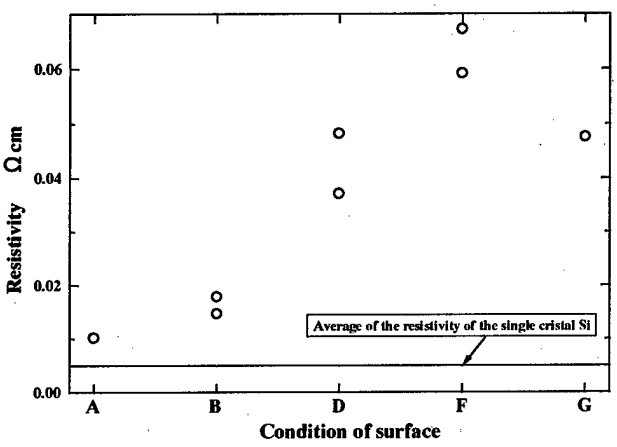


Fig.8 Relation between condition of surface and resistivity

From these measurement results, it was confirmed that the resistivity reached the lowest level in the surface condition A and then gradually increased toward surrounding area. And compared with the measurement results of n-type single-crystal silicon doped under the same conditions, those of poly-Si are 2 - 14 times higher. The tendency that the resistivities gradually increased toward surrounding area can be explained by the following way. As this CVD apparatus produces the concentric-circle temperature distribution as its charcteristic, center A was highest temperature and the temperature that have a characteristics of upside 凸 parabollic gradually decreased toward surrounding area[1]. There are differences in cristal shape of surface of poly-Si film deposited by this LPCVD apparatus and cristal shape of center of deposited film was large and round rather than surrounding area[1]. Accordingly, it is considered that surface cristal structure of center of poly-Si film deposited had wide gap and there was tendency that impurities were easily able to penetrate into the structure. So,when poly-Si was diffused with boron, density of inpurities at center of poly-Si film was higher. As a result, the value of resistivity was low, because resistivity was depend on density of impurities.

The resistivities of the semiconductor which boron impurities (P type impurities) were diffused were reported as within 2Ωcm in case of impurities addition of normal density and within 0.05Ωcm in case of impurities addition of high density. The measurement values of this time are range from about 0.001 to 0.007Ωcm, all the measured values of resistivity in every surface condition were confirmed to be sufficiently usable.

5. Gage factor

5-1. Measurement method

For this measurement, the bending test shown in Fig.9 was used. Here, the test specimen used for the bending test is not single poly-Si film but a test specimen with Si-substrate. Thus, the magnitude in the deformation of test specimen is very small. For this test, poly-Si film which was doped under the conditions shown in Table 3 was used.

The gage factor is defined as the rate of change in resistance per unit strain, and the rate of change in resistance $\Delta R/R$ caused by strain is given by the following equation:

$$\Delta R/R = K\varepsilon \quad \cdots\cdots \quad (5)$$

where, K is the gage factor and ε is the strain. That is, to calculate the gage factor K, it is necessary to find $\Delta R/R$ and ε. Here in this study, these values were found according to the following manner. That is, first of all, the resistance R was measured by connecting a code to two electrodes of test specimen as shown in Fig.10. The increment of resistance ΔR was obtained by installing the same test specimen as shown in Fig.9, loading 50g weights one after another, measuring the resulting resistance values and calculating the difference between the resistance value when no load was added and those individual resulting resistance values. Next, about the measurement of strain, it is necessary to use a high-precision measuring instrument for measurement of a small degree of deformation of test specimen. To calculate the strain without using such instruments, we supposed that test pieces as shown in Fig.9 are one side beam, the strain value between the two electrodes are calculated by the moments. Its basic equation is as follows.

$$\varepsilon = \frac{b/2}{EIz} M = \frac{b/2}{EIz} mgx \quad \cdots\cdots (6)$$

Here, the individual terms have the following meanings - b: thickness of test pieces, Iz : geometrical moment of inertia ($Iz = 1/12 \cdot w \cdot b^3$ <w : width of testpieces>), E: Young's modulus of Si of test pieces, mg : test load, x : coordinates of position which measured from point of load. The concrete values of parameter are b =610μm, E=130GPa, m=0,50,100,・・・g.

In the measurement of ε by experiment, as left parameter R and ΔRof equation (5) are measured value of average between the two electrodes, it is necessary to set value of average between the two electrodes to its correspondence strain of right parameter of equation (5). So the value of strain should take a mean value too, but we paid attention to a linear function of position coordinate X and calculated the strain value of by equation (6) as the strain value at the middle point between the two electrodes are mean value.

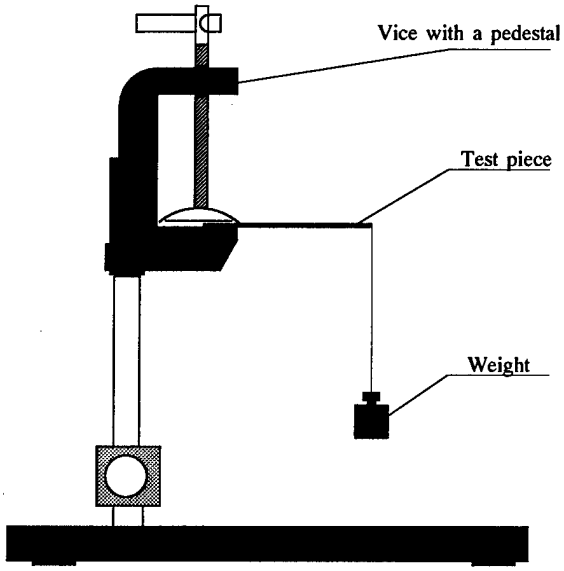
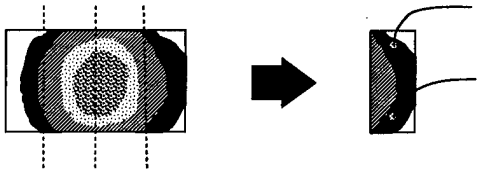


Fig.9 Schematic diagram for the experiment of gage factor of Boron doped Poly-Si



(1) Test pieces cut with a part of broken line.

(2) Connecting codes to both ends of test piece for measuring electrical resistance

Fig. 10 Test piece for the gage ratio measurement

5-2. Measurement condition

To analyze whether the gage factor changes depending on the difference in the surface condition as shown in Fig.6, for the measurement, under three different conditions of deposition (by the LPCVD apparatus using lamp heating, pressure: 67 Pa, flow: 40 sccm <SiH_4(10%)/Ar:N_2=1:1>, deposition time: 1 hour, and deposition temperature: 785, 805 and 910° C), three poly-Si film substrates were prepared. From these substrates, 2,4,3 pieces each different number by cutting, a total of 9 test pieces were prepared. And these test pieces were sorted according surface condition, A:2 pieces, D:3 pieces, F:2 pieces, G:2 pieces. Each test pieces was cut out of Si substrate by scratching the substrate from its back using a glass cutter for Si substrate.

The load was increased from zero by adding 50g weights one by one until the test pieces breaks while measuring the electrical resistance value whenever the weight was increased by the addition of new weight.

5-3. Measurement results

Fig.11 shows the distribution of gage factor classified by the surface condition which was obtained from these measurement results using the above-mentioned method. Here, the horizontal line shown in Fig.11 is the measurement results of gage factor of the n-type single-crystal Si of upper surface (100) with the crystal orientation<110> in the longitudinal direction doped under the same condition as that of poly-Si film.

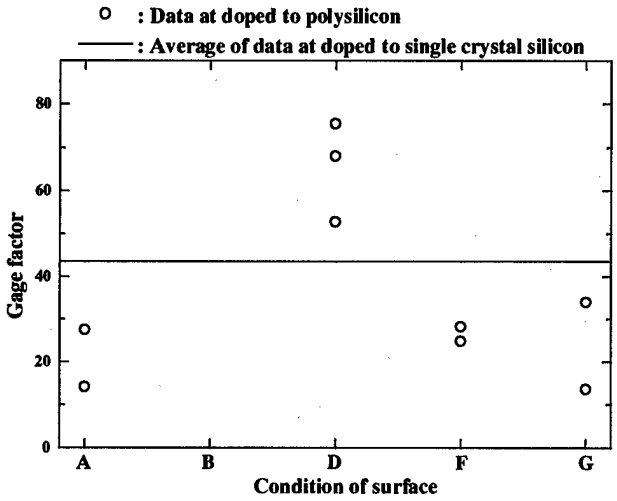


Fig.11 Relation between condition of surface and gage factor

The gage factor of silicon semiconductors used for the conventional sensors[10] ranges from 4 to 187 [20]. Therefore, it was confirmed from the above-mentioned measurement results that making sensors based on the piezoresistance effect of doped poly-Si film prepared from this CVD apparatus was highly feasible. Especially, a test specimen with the surface condition D was found to be more sensitive than n-type single-crystal Si of upper surface (100) with the crystal orientation <110> in the longitudinal direction doped under the same condition and its surface shape was also smoother than the latter, indicating that the poly-Si film with the surface condition D was quite suitable for the preparation of micromachines.

6. Conclusions

From the experiment results, what we discovered about the prototype LPCVD apparatus using lamp heating and the poly-silicon film deposited therewith are as follows:

(1) The new measurement method of Young's modulus was shown useful for the thick poly-silicon film.

(2) We could confirm that poly-silicon deposited using this apparatus was capable of depositing poly-silicon films with mostly uniform Young's modulus, and its value expressed in average value and standard deviation is 121.4 $\pm$ 7.1 GPa.

(3) The resistivity of boron-doped poly-Si was found to fall within a range of 0.01 - 0.07 Ωcm.

(4) The gage factor of boron-doped poly-Si was found to fall within a range of 10 - 80.

References

1) Tetsuo Ueda, et al., Production of Prototype of New LPCVD Using Lamp Heating and Its Study of Characteristics, Journal of the Japan Society for Precision Engineering, Vol.65, No.2, 1999, pp.214-218 [in Japanese]

2) Shogo Esashi, Hiroyuki Fujita, et al., Micro-machining and micro-mechatronics, Baifukan, pp.73-97 [in Japanese]

3) W.N.Sharp et al., Measurements of Young's modulus, Poisson's ratio, and tensile strength of polysilicon, Proc. Micro Electro Mechanical Systems, 1997, pp.424-429

4) Zenya Nakano, et al., Three-point bending test of fine materials, The Japan Society of Mechanical Engineers 70th annual conference, Vol.B (1992), pp.519-521 [in Japanese]

5) Kenjiro Komai, et al., Production of prototype of fine material mechanical characteristics evaluation & testing equipment and evaluation of fracture characteristics of single crystal fine elements, Japan Society of Mechanical Engineers collected papers A, Vol.60, No.569 (1994), pp.52-589 [in Japanese]

6) M.G.Allen, M.Mahragany, R.THowe, and S.D.Senturia, Microfabricated structures for the in situ measurement of residual stress, Young's modulus, and ultimate strain of thin films, Appl. Phys. Lott., 51-427 (1967), pp.241-343

7) O.Tabata et al., Mechanical property measurement of thin films using load-deflection of composite rectangular membrane, Proc. Micro Electro Mechanical Systems, 1989, pp.152-156 [in Japanese]

8) Thin film manufacturing application handbook, supervised by Shun'ichi Yokota, NTS [in Japanese]

9) F.R.Brotzen, "Mechanical testing of thin films", International Materials Reviews, 1944 Vol.39 No.1, pp.24-454

10) LE BERRE M, KLEIMANN P, SEMMACHE B, BARB IER D, PINARD P, Electrical and piezoresistive characterization of boron - doped LPCVD polycrystalline silicon under rapid thermal annealing., Sens Actuators, Vol.54,No.1/3,pp700-703,1996

11) FRENCH P J, EVANS A G R, Piezoresistance in polysilicon and its applications to strain gauges.,Solid - State Electron, Vol.32,No.1,pp1-10,1989

12) M. Misawa, H. Yonehisa, Y. Kurokochi and S. Suyama: The piezoresistance effect of silicon thin film, Research Report of Nagano Prefecture Precision Industrial Research Institute, No. 4 (1990), pp.95-98, 1991 [in Japanese]

13) Characteristics of semiconductor gauges and their handling, Kyowa Giho, No. 386, p.2878, 2882, 1990 [in Japanese]

14) SCHUBERT D, JENSCHKE W, UHLIG T, SCHMIDT F M, Piezoresistive properties of polycrystalline and crystalline silicon films., Sens Actuators (Lausanne),Vol.11,No.2 pp145-155,1987

15) S. Yamazaki, S. Yamazaki, M. Nakao, K. Uemura, Y. Konuma and T. Honma: Polycrystal silicon thin-film piezoresistance device, in the proceedings for "Basics and Application of Sensors" symposium, Vol. 5th, p.39-40, 1985 [in Japanese]

16) H. Tsukioka and Y. Konuma: Electrical characteristics of poly-Si thin film prepared by CVD method and its application to detection devices, Technical Research Report of Institute of Electronics and Communication Engineers of Japan, Vol. 80, No. 169, p.39, 1980 [in Japanese]

17) T.I.Kamins, "Resistivity of LPCVD Polycrystalline-Silicon Films", J.Electrochem, Soc:Solid-State Science and Tecchnology, Vol.126,No.5, pp.833-837, 1979

18) K.Shouno, "Physical engineering experimentation 2, Semiconductor Technology(vol.1)", Tokyo university publisher, pp100-105, 1979 [in Japanese]

19) S.Tokumaru, "The newest semiconductor guide with illustration" ,Seibundou shinkousya, pp5, 1997 [in Japanese]

20) BETHE K, Sensoren mit Duennfilm Dehnungsmesstreifen aus metallischen und halbleitenden materialien.,ITG Fachber,Vol.79,pp168-176,1982

Evaluation of Strength Property of HAp-Tyranno Fiber Composite by Flexural Test and Process of Sintering Condition

Kazuo YAGI, Masataka TOKUDA, Keijou SUZUKI*, Hiroshi YOSHIDOME**

Tokyo Metropolitan University of Health Sciences,
7-2-10, Higashiogu, Arakawa-ku, Tokyo
*Mie University, 1515, Kamihama, Tsu, 514, Mie

ABSTRACT

Hydroxyapatite(HAp) has been used as the implant material because it's similar to the bone for the components and its bioactive characters. But it's lack of enough mechanical strength, for example, bending strength and elastic. Therefore, in order to improve those characters of HAp, we have been tried that composed for HAp and Tyranno fiber. Take into consideration of sintering condition, HAp-Tyranno fiber composite gave the 3-point bending test, and evaluated the several property. On the other, on the method of sintering called Hot Press tried and compared with the former one. We found that, Hot Press got better result than the former. However, sufficient data don't get yet, we need to get the one further. After this, considerable problem is the influence of the boundary between HAp and Tyranno fiber for the condition of high temperature.

Key Words: **Bioceramics, Hydroxyapatite, HAp-Tyranno fiber composite, Bending test of hydroxyapatite, Method of Hot Press**

1. INTRODUCTION

Bone organization is one of the important support mechanisms for the human body, and it is decided that the loss leads to a serious functional disorder. When a bone loss in the extensive territory was brought about by the tumor of the bone and the external injury due to the traffic accident, the more better methods that make up for these loss can select the way of the self-bone transplant or the same kind bone transplant, but their methods often needs large quantity of bone. Therefore, from the viewpoint of morality and immunology they still have many problems. So recently, the development of various implant materials called bioceramics that aimed at the recovery of function of the living body is done. Especially, HAp (Hydroxyapatite) has a high affinity for the living body, and combined with the bone directly, and it can compose artificially. Moreover, it is superior to affinity with the skin and soft organization, and attracts the attention of hard organization substitutive material inside the living body. But, generally speaking, the mechanical strength of HAp is poorer than precise bone, it is difficult to use HAp only. So, HAp is used as the material of artificial bone by coating it in titanium alloy and so on, but this method has various problems that when it is filled up in the living body, the exfoliation with HAp and titanium base material, and the metal ion begins to melt by the body liquid are raised.

So, we use Tyranno fiber (manufactured by Ube Industries, (co Ltd.)) that inorganic fiber material without using the metal material as the way of reinforcing HAp in our laboratory. Tyranno fiber is the Si-Ti-C-O inorganic fiber and it has a very excellent character in the mechanical strength, light weight. And it is considered that Tyranno fiber is superior to the characteristic of heat-resisting and oxidization-resisting, being suitable for sintering with HAp at the high temperature.

We tried to make the material composite by composed to Tyranno-fiber and HAp that should be necessary for the artificial bone material, mechanical strength (improvement of bending strength, improvement of brittle fracture) and bio-compatibility and the safety that it faces a living body.

2. THE PREPARATION OF HAP-TYRANNO FIBER COMPOSITE OF SPECIMEN (I)

As the way of composing HAp, wet process that a large-scale device is unnecessary and it's to operate comparatively easily adopted. With keeping 40℃ for liquid temperature, stirring the hydroxide calcium (manufactured by Nakarai-Techs. Co,Ltd.) water solution of 1.5mol/l, and dropping gradually phosphoric acid (manufactured by Wako Pure Medicine Industry) water solution of 1.0mol/l in that, and made suspension of pH8. The chemical reaction formula is shown in the equation (1).

$$Ca(OH)_2+H_3PO_4 \rightarrow Ca_{10}(PO_4)_6(OH)_2 \quad (1)$$

1999 INTERNATIONAL SYMPOSIUM ON MICROMECHATRONICS AND HUMAN SCIENCE
0-7803-5790-6/99/ $10.00 ©1999 IEEE.

After composition was finished, a white HAp deposit was ripening for one day, and washing due to centrifugal machine, dryness, smashed with ball-mill. And, HAp powder that the particle diameter is 10μm or less was completed by the process. Tyranno-fiber used 1mm chopped fiber for short type fiber. It decentralized by supersonic wave washer in the pure water, and HAp powder and Tyranno-fiber were set up in the fiber volume content rate 5%. After that, the sample was mixed by wet ball-mill method, and drying, and made the HAp-Tyranno fiber composite powder.

A preparation process here is shown in Fig.1.

This time, the composite powder was set up in various sintering conditions (for instance, sintering temperature, sintering holding time, sintering atmosphere), and sintered using the tube-fireplace to rise at the speed 5K/min, and to reduce at the speed 1K/min. The specimen of a square of pillar-shaped about 46×6×4mm was made by grinding a surface with sandpaper to final #1000.

3. THE PREPARATION OF HAP-TYRANNO FIBER COMPOSITE OF SPECIMEN (II)

As new sintering method to get higher precision, it is added, sintering by the hot press (FVHP-R-50, FRET-60 (manufactured by Fuji Electric Wave Industry)) that can be carried out at the same time pressurization and sintering. It practiced the pressurization sintering by using the composite powder that it was made in the method shown with Fig.1. As for the establishment condition and so on, it is mentioned later.

After sintering, separated as the specimen of a square of pillar-shaped about 40×4×3mm, and made the specimen of HAp-Tyranno fiber composite by grinding a surface to the final #800.

4. EXPERIMENT METHOD

As a strength characteristic test of the HAp-Tyranno fiber composite specimen, 3-points bending test was performed by using test machine(small all-around test machine of low speed load pattern (TENSILON-II-20 (manufactured by Boldwin, Co. Ltd.))). An establishment condition was made 35mm at the distance between the marked points, 2mm/min at cross head speed, and the load value when the specimen was ruptured was measured. The value of the bending stress σ [MPa] of this case was calculated by using the next equation(2) that used the theory of material dynamics. The parts of 3-point bending test showed Fig.2.

$$\sigma = \frac{3Pl}{2wt^2} \qquad (2)$$

Where P [N] is the maximum load when the specimen was broken, l [=35mm] is the distance

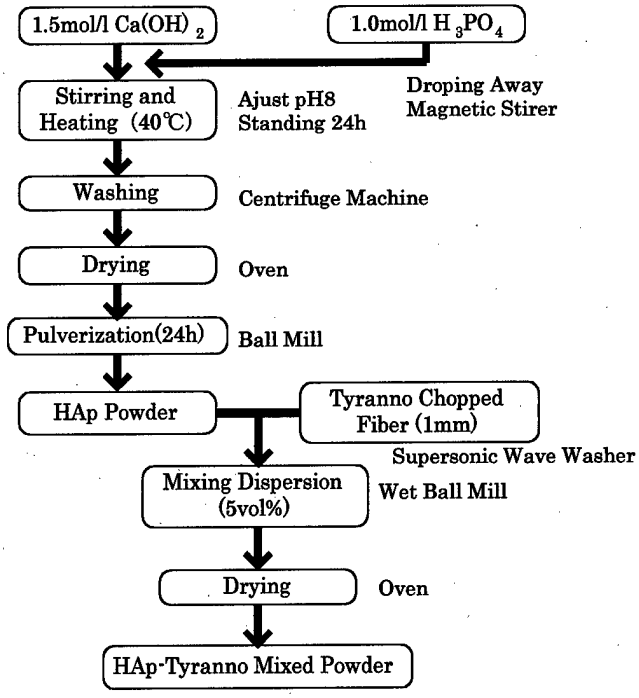


Fig.1 The process of how to making HAp-Tyranno fiber composite mixed powder

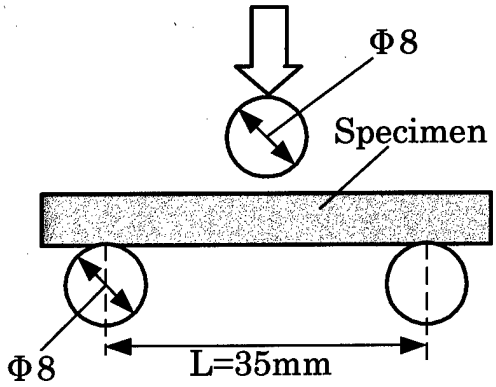


Fig.2 The parts of 3-point bending test and the specimen of HAp-Tyranno fiber composite

between the marked points, w [mm] is the width of the specimen, t [mm] is the thickness of the specimen. Furthermore, about deformation the load condition was put with y [mm], and about deformation rate D [%] was defined like the next equation(3). Take into consideration the thickness of the specimen, and using the value of the dimension-less, and the state of the destruction action was judged.

$$D = \frac{y}{t} \times 100 \qquad (3)$$

And, the rupture surface after the test was observed by using scanning electron microscope (SEM). We considered that the relations about bending strength and the destruction action, because observed the progress of sintering condition with HAp and Tyranno-fiber and minute structure.

5. RESULT AND CONSIDERATION (I)

The result of the test is shown in Table.1 and Fig.3～Fig.6.

Table.1 shows the data on the maximum bending stress to get by bending test of the specimen sintered in the air condition. It was understood from these results that bending strength is raised as much as the specimen made on the condition whose sintering temperature is high and sintering keeping time is long.

In Fig.3, from the result of Table.1, shown in the result of the pore ratio that it is thought to the index of precision in sintering. It is showed here that the specimen of sintering keeping time at 5-hours. From the result, it is understood that the precise makes progress as the strength is higher. Hence, it can understand that the precise of sintering is occupied as a big factor of the strength.

Fig.4 is shown the relations (D- σ curve) between bending stress σ [MPa] and displacement ratio D [%] on each sintering condition. This curve is analyzed the state of the destruction action until the specimen is ruptured. It is shown the specimen of sintering keeping times at 5 hours, too. The area surrounded by a curve can be thought that there is correlation with the destruction energy, and the destruction energy is increase that sintering temperature is risen.

However, the result of the gentle destruction action one of the purposes of this study was not shown. So, SEM photographs is shown in Fig.5, Fig.6. The thing seems to be a round pillar is Tyranno fiber. From the figure of this photograph, the progress condition of precision can be judged by sintering temperature is risen. And, it is understood that the deterioration of Tyranno fiber caused by sintering temperature is risen, too. About this cause, it is thought the Tyranno fiber was deteriorated by the oxidation (or corrosion) at the high temperature sintering. As the improvement measure of this problem is considerable to the change of sintering atmosphere (vacuum or un-active gas (N2)) and so on. This is shown in the following.

Table.1 The result of the bending strength

	1 hour	5 hours
1173K	11.62 [MPa]	11.71 [MPa]
1373K	18.16 [MPa]	13.95 [MPa]
1573K	29.16 [MPa]	33.49 [MPa]

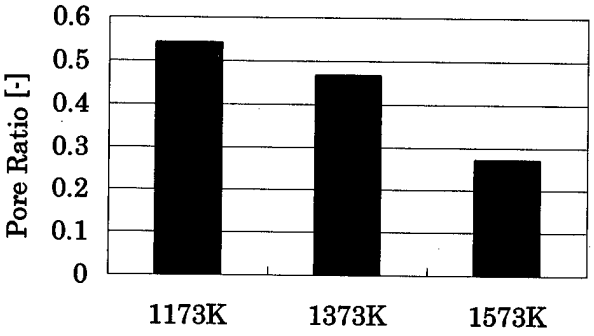


Fig.3 The relation of the sintering temperature to the pore ratio on keeping 5 hours

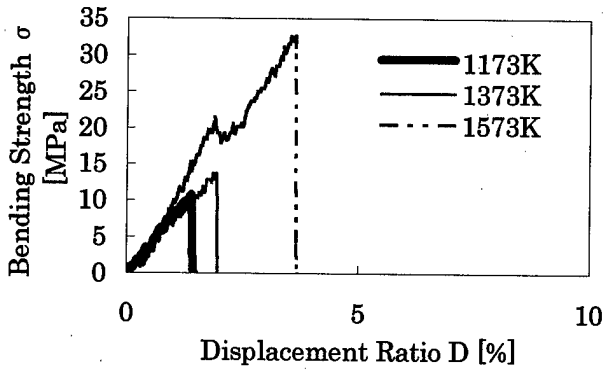


Fig.4 The relation of the bending strength to the displacement ratio on keeping 5 hours

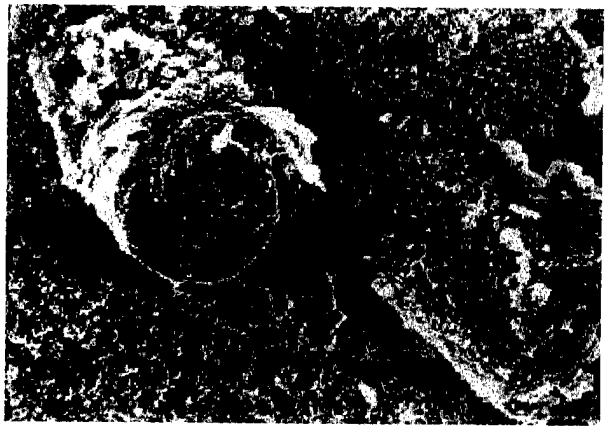


Fig.5 The photograph of HAp-Tyranno fiber composite keeping 5 hours at 1173K



Fig.6 The photograph of HAp-Tyranno fiber composite keeping 5 hours at 1573K

6. RESULT AND CONSIDERATION (II)

From the result until now, a result in the case of each sintering atmosphere at 1573K that the strength is especially increase is shown.

First, it's shown to each bending strength in Table.2, the pore ratio in Fig.7, and the D-σ curve in Fig.8. Compared with the air condition, it is understood that the strength, displacement ratio, and the energy of destruction is increase alike. And about the pore ratio, it is understood that the more precise gets to bring about this change. Compared with the case of the air condition, the precision progress in more short time in vacuum and N_2 gas atmosphere. And when sintering keeping time become long, the strength and the pore ratio tend to show the no good data.

However, the improvement of fragile destruction is still not to get, and the sample inside is observed by the SEM photograph in Fig.9, Fig.10. Compared with the air condition, the existence of the Tyranno fiber can be confirmed more clearly. Therefore it is considerable that there is a problem in boundary side between HAp and Tyranno fiber in the high temperature condition. There is a report that the surface of the Tyranno fiber deteriorated in the alkaline atmosphere and the strength is seen to decline, and it seems that the effect of fiber couldn't be enough.

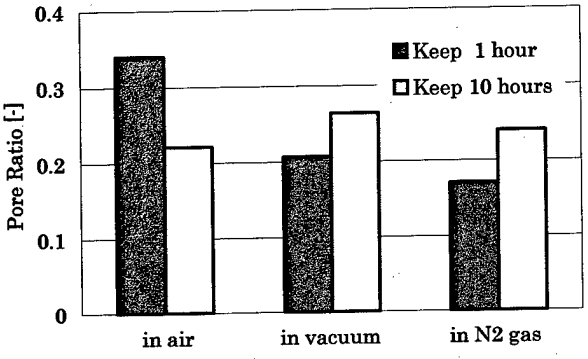


Fig.7 The relation of the sintering temperature to the pore ratio at 1573K

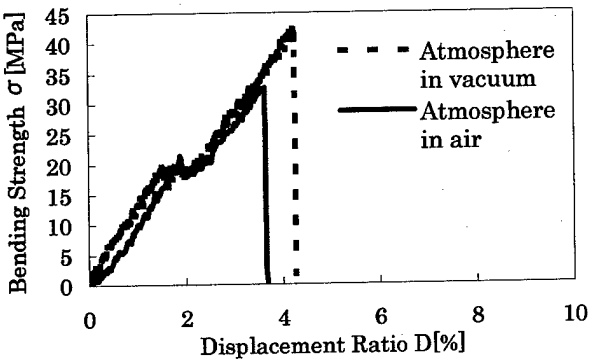


Fig.8 The relation of the bending strength to the displacement ratio on keeping 10 hours at 1573K

Table.2 The result of the bending strength

	1 hour	10 hours
In air	29.16 [MPa]	40.67 [MPa]
In vacuum	38.55 [MPa]	42.66 [MPa]
In N_2	40.10 [MPa]	40.10 [MPa]

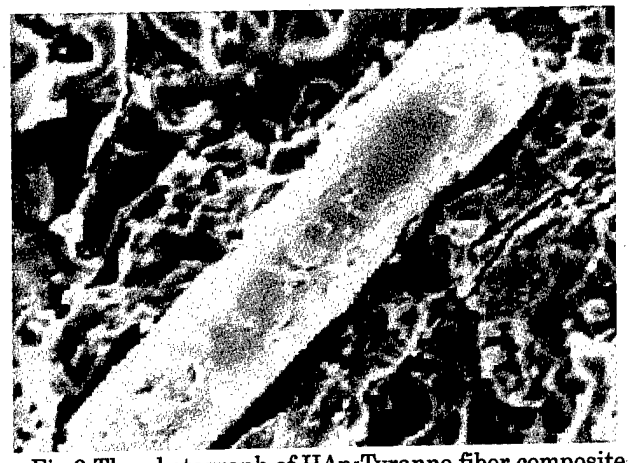


Fig.9 The photograph of HAp-Tyranno fiber composite keeping 10 hours at 1573K in air



Fig.10 The photograph of HAp-Tyranno fiber composite keeping 10 hours at 1573K in N_2 gas

7. RESULT AND CONSIDERATION (III)

A result about the specimen made by the hot press is shown in this chapter. First, it is written in the following about each condition.

Heat treatment with the hot press is severe condition to the viewpoint of both environment heat and pressure in comparison with sintering until now. The pattern for square of 50mm and 4 division made of the black lead was applied to BN spray and put the carbon seat of 0.2mm thickness that was further applied between the pattern and the sample to the same BN spray, and press the mixed powder. As the establishment condition, establish temperature (1173K, 1573K), rise temperature speed at 5K/min, and kept for 1 hour in fixed temperature, after that, cooled in furnace. The pressure was held to 30MPa at fixed temperature, after that as for the pressure with descending to 10MPa and holding temperature at 573K, and it

remove the pressure to restrain the occurrence of the crack. The atmosphere used Ar gas.

The result is shown in the following.

The D-σ curve is shown in Fig.11. As it was expected, maximum bending strength is increase with rise in sintering temperature, too. As for the destruction energy, it can be said to be increase in the same way. Especially, rise in the bending stress and the fracture energy at low temperature (1173 k) is remarkable. As for the pore ratio shows in Fig.12, it is understood that the ratio is much advance, and it greatly contribute to the progress of the sintering. So, we observed to the SEM photograph in Fig.13, Fig.14 to examine inside condition of the organization. Compared with the air condition, the save condition of the fiber was good, and could be more clearly. It is buffered the existence of the gas which contains Ca resolved and evolved from HAp by making Ar atmosphere, and was defended to deteriorate the surface of Tyranno fiber. Moreover, by having adopted hot press, it is greatly facilitated the precision of the organization, and stick more with the Tyranno fiber and HAp, and these causes thought to bring out the large advance of the strength and the fracture power.

However, a rupture curve showed in the brittleness-like fracture form. This is estimated that the fiber volume is not enough essential to a gentle fracture action may be shown so that there may be little rate of the complexed fiber toward the weight of HAp which becomes base material. In other words, the deficiency of the fiber volume is thought the maximum causes that couldn't produce the result to expect. From the result of the above and in consideration to being enough precision condition by 1573K, Tyranno fiber containing rate was made 25vol% from 5vol% to aim at the expression of the effect on a fiber clearly, and heat treatment by the hot press was done as 1373k sintering temperature.

The result is shown to following.

It was not brittleness-like fracture, but fracture progressed gently from the D-σ curve of Fig.15, and as the displacement ratio could get the value of beyond 15%. Compared with the specimen in air condition, bending strength rises greatly, and shows the ideal action having never seen. Even if it is related to the pore ratio, the highest value is shown about 15%. (It is shown in Fig.12.)

SEM photograph is shown in Fig.16. The imbalance site is seen about the sintering, and the decline of the sintering by increasing the fiber containing rate is seen, too. But a change in the fiber wasn't seen especially, and about fiber fracture surface observed that crack was producing in the various directions.

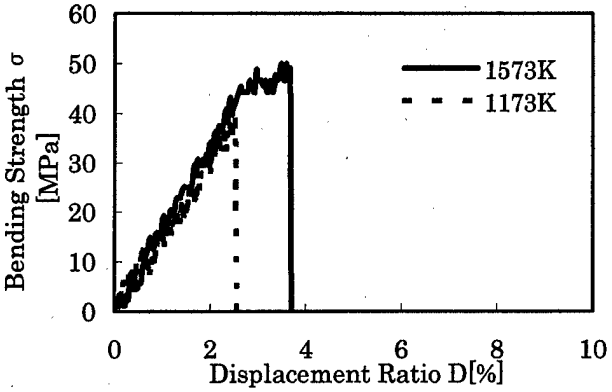


Fig.11 The relation of the bending strength to the displacement ratio on keeping 1 hour at hot press

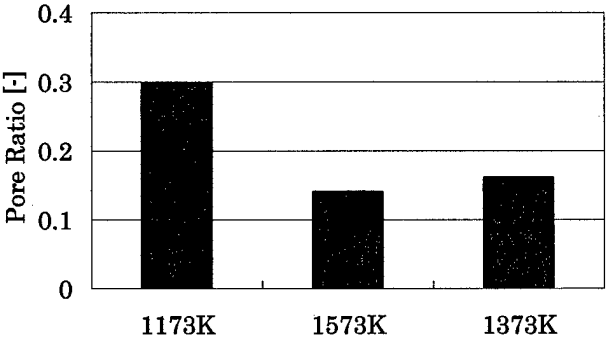


Fig.12 The relation of the sintering temperature to the pore ratio at hot press

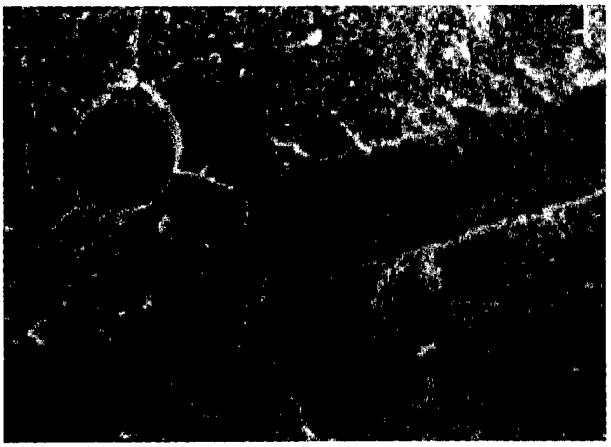


Fig.13 The photograph of HAp-Tyranno fiber composite to hot press at 1173K



Fig.14 The photograph of HAp-Tyranno fiber composite to hot press at 1573K

8. CONCLUTION

In this research, it was object to make composite materials complex by HAp and Tyranno fiber that have safety and hardness in the living body. Though it was stronger than the usual HAp-Tyranno staple fiber composite from the viewpoint of hardness, it is a future subject as for the improvement of the brittleness-like fracture action.

The way of sintering used hot press is given as a reform measure. Compared with the former results, it can exceed one about bending strength, pore ratio, and the gentle fracture action. But the data is not still enough, it seems that the problem is considered to the sintering temperature that fiber degradation isn't started from. As a result, this thing thought to proceed in the direction of the improvement as for the problem of the brittleness. And, you must take into consideration as for the change of the fiber containing rate in the mixing to make the effect of the fiber more remarkable. After this, we will be advanced the examination respectively about the grope of the optimum conditions.

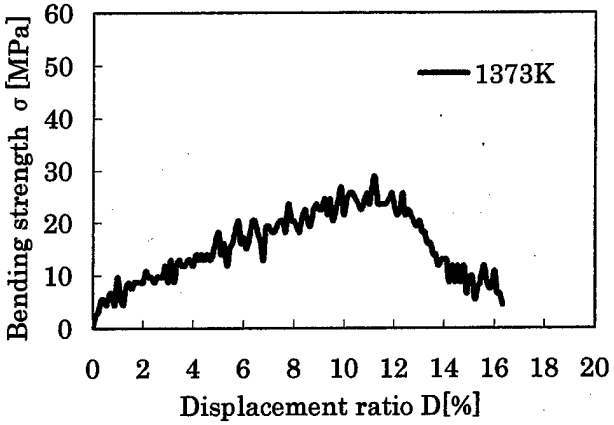


Fig.15 The relation of the bending strength to the displacement ratio on keeping 1 hour at hot press

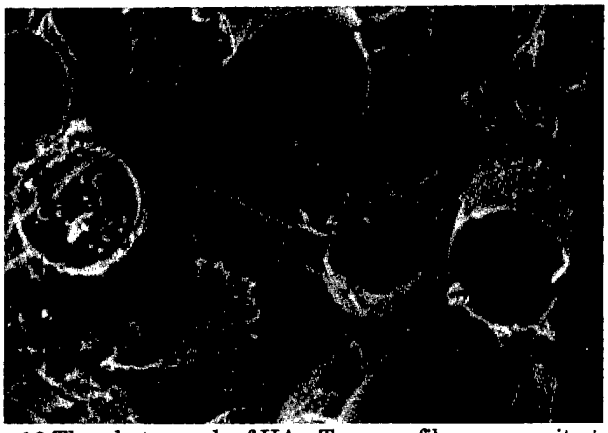


Fig.16 The photograph of HAp-Tyranno fiber composite to hot press at 1373K

REFERENCE LITERATURE

(1) K.YAGI, other, Evaluation of Strength Property of Hydroxyapatite (HAp) by Flexural Test and Process of Manufacturing HAp. Proc. of IMMM '97-pp.693-700. (1998)

(2) K.SUZUKI Master's Thesis
The Study of Material Design of HAp-Tyranno fiber Composite
Department of Mechanical Engineering
Mie-Univ. (1997)

(3) Y.KAGAWA, H.HATTA
Tailoring Ceramics Composites
Aguneshoufuusha(1990)

(4) M.SHIBUYA Fine Ceramics Report11-No.10-
Tyranno-Fiber And Tyranno-Fiber
Reinforced Composite (1993)

Design of Functional Hydrogel and Evaluation of its Material Properties

K.Yagi*, M.Tokuda, T.Yoshikawa** and Y.Ichiminami****

***Tokyo Metropolitan Univ. of Health Sciences,Japan,**
7-2-10 Higashiogu, Arakawaku, Tokyo, Japan
****Department of Mechanical Engineering, Mie University**
1515 Kamihama, Tsu 514, Japan

ABSTRACT

Recently, several chemo–mechanical functions of high molecular polymers were studied for the biomimetic properties, sensor and switch function, enormous actuator and output energies as possible candidates for energy transducers etc. So, Poly-Vinyl Alcohol (PVA) and Poly-Sodium-Acrylic-Acid (PAA - Na) were selected as Raw-materials from number of high molecules materials for making up new type gels、especially design of functional hydrogel. The reason why it is PVA gel is several kinds of properties with soft, strength, 3D meshes structure etc. and other PAA - Na gel were possessed of organic radical, ionization, polarize by electronics fields etc. For this PAV-PAA-Na hydrogel, tensile tests and swelling examination were carried out in wet condition. The microstructure of gels was observed by SEM. Many interesting results were found out, so swelling mechanism, various mechanical properties and microstructure of hydrogel was evaluated.

1.Introduction

High molecule hydrogel were very interesting material property that the form and materiality were made to change responds to the change in the outside environment with the osmosis(soak and pickle) solvent formation, temperature, electric field, others[1][2][3][4]. If it makes the most of such a character, the possibility of the application of gel as well as the machine element of active new soft material will spread out, and which it had fits sensor function to, it seemed that a usual machine equipped in complex mechanism and enormous element an unnecessary, too. By this research, high molecule hydrogel when it was applied as a function machine element, about the strength character which it thought about with the importance, it didn't depend on a chemical technique of the change of the material formation, and it was tried to improve control by the change of condition in preparation, and it was evaluated from the viewpoint of strength of materials. Test specimen material is excellent in the strength character in gel formation, and water contained rate was very high material of Poly Vinyl Alcohol(PVA), too:, it was high molecule hydrogel which added Poly Sodium Acrylic Acid to make PVA the mother material and to give the response of the ion origin. This gel was made by the way of freezing and fusing. The freezing temperature condition to make it mainly at -20°C, -50°C, -85°C, and by changing it ethanol solution was make to osmosis about the controlled and improved material, it was evaluated by tensile strength examination, the measurement of the change volume, inside micro structure observation by SEM, and so on from the strength and the structure[1][2][5][6][7].

2. Test specimen material and experiment method.

2-1 Test specimen material

As the test specimen material, in the mother material, Poly Vinyl Alcohol by using PVA (Povall: PVA-124H

1999 INTERNATIONAL SYMPOSIUM ON
MICROMECHATRONICS AND HUMAN SCIENCE
0-7803-5790-6/99/ $10.00 ©1999 IEEE.

manufactured by Kurare Co., Ltd., degree of polymerization 2500, degree of saponification 99.6mol per cent), for the response grant, Poly Sodium Acrylic Acid (degree of polymerization 2700 - 7500, manufactured by Wako pure medicine industry) was added. PVA was very high water contained rate of with more than 60-90% at the time of gel formation, and it was the material which 500% of the expansion rates were excellent about like maximum tensile strength examination 4MPa and material strength, too, again in comparison with other gel material. However, there was a little necessary of the consideration in PVA to secure a function because it was inferior to the response and the answer toward the outside stimulus. So, Poly Sodium Acrylic Acid was added by this research to make up for the environment answer character of PVA. There was Poly Sodium Acrylic Acid of condition contained in the high molecule chain, and it could give high response to gel of the ion origin along with dissociation of carboxyl radical that H was substituted for the a sodium. But, the rate of the addition was made at 25wt per cent toward PVA so that we might take the maintenance of the strength at the time of gel formation as example and besides comparatively high swelling rate might be shown because was inferior to the mechanical strength with Poly Sodium Acrylic Acid. And, Poly Sodium Acrylic Acid used by this research was the water solution of low viscosity, and it knows that it was the weight per cent concentration 18wt per cent by the mass measurement after freezing was dried as for it.

2-2 The preparation of the test specimen

First, the 30% Dimethyl Sulfoxide (DMSO) water solution with 20ml mixes powder-shaped PVA at the rate of 3g, and it was left for more than 24 hours, and solution and PVA were made to get used. DMSO was the polarity solvent of non-proton, and encourages the dispersion of PVA during the water, and had the function which made of turned to sol (solation) easy. But, DMSO was expelled from the inside of gel, and DMSO that it remained must take the mixed rate that an influence wasn't left into consideration after gel preparation was completed because the strength of formed gel was made to decline. As, the most suitable value of DMSO was applied 30% water solution in our laboratory.

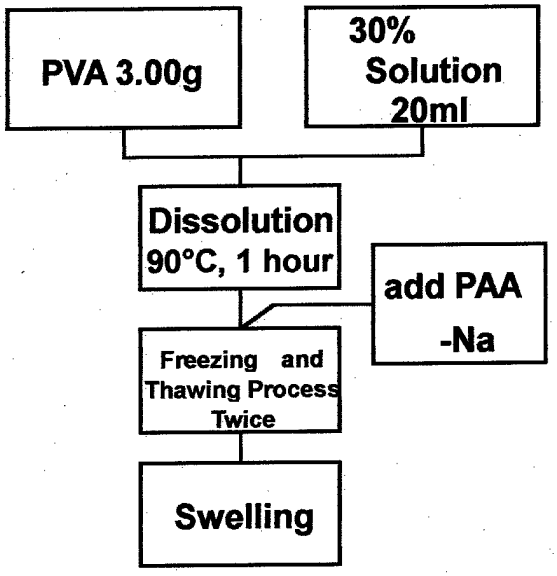


Fig.1 The flowchart producing PVA-PAA hydrogel

The next, prepared for DMSO water solution- PVA mixture was heated at 90°C for about 1 hour within hot water, and PVA was completely made turn to sol. Glass transfer temperature of PVA was at 85°C, and boiling point of the water at 100°C, as it decides heating temperature from a balance.

Poly Sodium Acrylic Acid was mixed with the proper quantity in this PVA-sol to be suitable for the ratio of the 25wt per cent, after it was stirred well, it was poured into the made pattern corresponding to the use, it was made to freeze rapidly in super-low temperature preservation refrigerator that was set up in advance at -85°C, -50°C and -20°C. After that, it was stored inside refrigerator which made inside temperature decrease in advance in each temperature, and hung for more than 12 hours, and made to do returning to the original temperature gradually. It was made up turn to gel at twice repetition in the treatment of

this rapid cooling, freezing, fusion and returning to the original temperature. And it was stuck, and mentioned later though treatment corresponding to the experiment use was given after it was picked out from the pattern.

The flowchart producing PVA-PAA-Na hydrogel of these operation processes was shown in the fig. 1.

The test specimen form for tensile strength examination

Poisson's ratio of gel was big in the same way as the rubber and so on, and shows very big deformation corresponding to the outside power. Therefore, only the space of standard line didn't become increase in the load together in tensile strength examination, the test machine installation part of the test specimen was greatly transformed in it, too, as for the stretch of sincerity and the stretch measured space of standard lines of the distance, it becomes the thing which was far easily. And, as for gel that generally to be osmosised a liquid, a surface was the condition that it slides easily by the solvent, if strong tightening isn't given, though it has danger which comes out at the time of the load and to go down, The pressure distribution which it is inappropriate for occurs due to the deformation of the tightening part place, and it may influence a rupture with mere flat board-shaped test specimen. So, dumbbell type test specimen which a fully big moreover three-dimensional thickness was given to was devised, and we made the section product of the test machine installation part place in comparison with the section product of the space of standard lines. By this form, against the deformation space of standard lines, it could be done fully small that the influence of the deformation in the load in the test machine installation part place, and besides, it became possible that enough conclusion in the case of the test machine installation was given. (Fig.2)

As for the test specimen which did Tensile strength examination, though volume swelling (or, contraction) of gel was formed by the test machine installation by the solvent osmosis treatment, the thing made by the pattern of the completely same form was being used. Moreover, this pattern copied the male type which began to cut down by the good plaster of blocking as a female type, and it was taken, and a skin film applied waterproof paints to that surface and made.

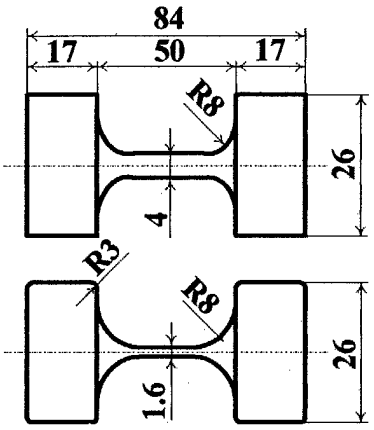


Fig.2 Design of Specimen for Tensile Test

2-3. Tensile strength examination

And after rapping the test specimen to freeze in dumbbell type and which was made at -85°C, -50°C and -20°C, it made water substitute for 3-4 days during the water to get rid of the influence of DMSO. For this time, the sample was preserved with being stirred during the water by starer, and water was divided into several times, and exchanged for the fresh distilled water.

The sample was preserved in ethanol solution made in 0-100% of the concentration after fully swelling with during the water and the change in the volume disappeared and reached the balance condition. It was made to preserve for more than two days as for this operation as well until a change in the volume disappears with dividing it into several times so that the solvent permeating the sample fully and replacing a solvent with the fresh solution.

The sample which the treatment of these varieties was

given to, it was pulled until been ruptured with cross head speed 20mm /min, and it got stress and strain curve.

2-4. The observation of the inside micro structure

It was observed by SEM how the inside micro structure of gel changed by the freezing temperature condition in the preparation and the permeating of solvent condition. An observation sample used the part of the head of the test specimen for Tensile strength examination. The thing which put notch in advance was soaked in liquid nitrogen directly, and it was made to divide the sample, and it deals with freezing dryness. After that, a gold ion was coated on the surface of the sample, and an observation sample was made.

3. Experiment result and consideration

3-1. The change in the inside structure of gel by the solvent formation

The change in maximum Tensile strength by ethanol concentration was compared in freezing temperature in the preparation from the result of Tensile strength examination which could get it and illustrated (Fig. 3).

The vertical axis took maximum Tensile strength, and took the concentration of ethanol solution which was permeated in the side shaft.

As for the material as well made in which freezing temperature, maximum Tensile strength increases caused by the increase in ethanol concentration. Generally it was greatly raised before and after be permeated ethanol concentration 60%, and the increase tendency of this strength showed the strength value of about 10 times in comparison with condition of the pure water was permeated and more of the ethanol was permeated at 90% over.

Furthermore, when it tried to compare it by freezing temperature in the preparation, the material made at -50°C under by the extreme low temperature of shows the strength of 3 times and more in comparison with the thing made at -20°C, it was recognized as at -85°C with the sample of preparation that it had the value of about 10 times was higher at -20°C than the sample of preparation in 30%-50 % of ethanol concentration.

Generally, though the big difference of maximum Tensile strength isn't admitted which were made to freeze the materials at -85°C and -50°C, in the range of the neighborhood was very small by 30% ethanol solution concentration about the sample made at -85°C, strength value, the tendency that it was raised peculiarly almost appears even on about 1MPa from 0.2MPa, such the phenomenon wasn't recognized in the material which was made to froze at -50°C. As for the increase in such strength which appeared in the case of the material which was made to froze at -85°C, correlation with the volume phase transfer phenomenon of gel is predicted.

Suppose a preparation condition was unified, as for deciding the strength character of high molecule gel which was high solvent content of material and porous, being the strength of every combination that shape creates the bridge structure of gel and structure's own flexibility was considered. In other words, now put system condition balance reach gel inside, dynamics-interaction of the high molecule and the solvent, the degree of crowding of the high molecule, it depends on the form of conformation of the high molecule chain's own and so on greatly, and considers that the strength character of gel was decided.

For example, an interaction with the gravitation which was strength to the high molecule chain and the space of the solvent such as an electron and a cation works, and besides, if the force of repulsion which the space of the same quality solvent has acts, the solvent particle attracts high molecules strongly, and it will strengthen gel's own bridge structure.

And, because a high molecule chain had very complicated conformation, if the density of the high molecule chain inside gel rises, showing big effect due to the friction of the high molecule chains toward the outside power was considered, and combination in the bridge point

will be a weak thing and if it was in the condition that conformation was greatly developed and it finishes growing.

When it was permeated the PVA hydrogel of the Poly Sodium Acrylic Acid addition in ethanol solution, the state that the inside microstructure changed remarkably was recognized from the SEM observation in this research. During the pure water which doesn't contain ethanol at all, with (Fig4, Fig6), though conformation of the high molecule chain is being developed into the condition that each fiber part that porous structure was made finishes combining it with each other from the viewpoint of pin point and finishes growing comparatively long, as ethanol concentration rises, and the fiber cohere or it adsorbs, and the little part of hole diameter appears, and such a territory goes into the whole area spreads out. In other words, the fibers being combined in the point and the point during the pure water change caused by the increase in the concentration in ethanol solution from the point from the line, the line to the combination of the surface.

The material of the research object was the material which had both parents water bases. PVA contains a water acid base (-OH) in quantity, and Poly Sodium Acrylic Acid exposes a sense base to the outer world further by dissociation of Na+ under the condition of carboxyl (-COO-) whose parents water character was high.

Therefore, the degree of dissolution was high under the conditions which many polarity solvents such as water exist in, and the degree of dissolution shows a tendency of decreasing under the conditions which many little organic solvents of the polarity exist in. In other words, under the condition where the water concentration of was permeated solvent was high, so that the high molecule chain might attract large quantities of polarity molecule in the circumference, which did extension long was taken in conformation, and the degree of hydrogel's own swelling becomes an extremely big thing. And, conformation becomes the condition which contracts small with organic solvent of ethanol concentration was an rises, and fibers neared to it further. And, it thought about dehydration action by ethanol with the thing that cohesion and adsorption of such a fiber was promoted, too. Let's guess that the change in such structure influences stress strain character of gel directly easily.

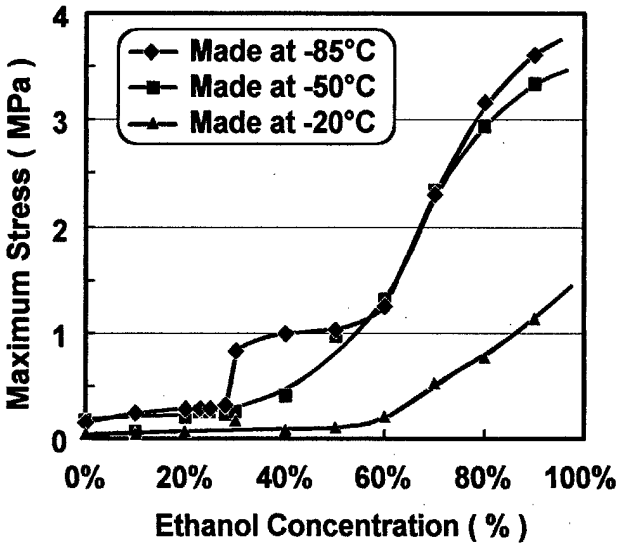


Fig3.Change of Maximum Stress

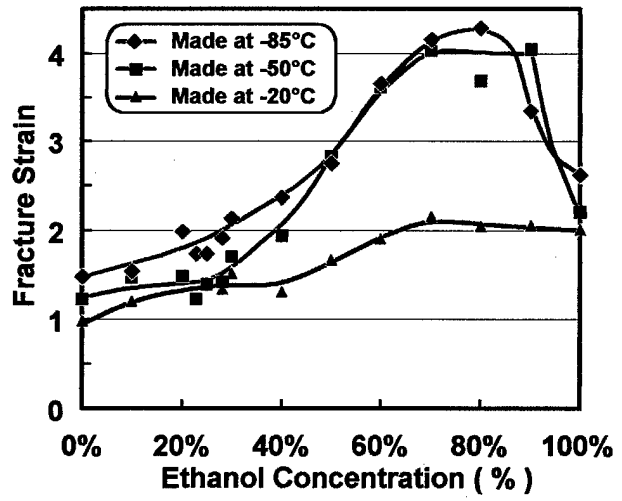


Fig4.Fracture Strain

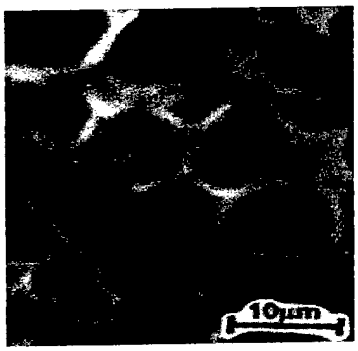


Fig 5. Made at –20℃ (soaked in D.W)

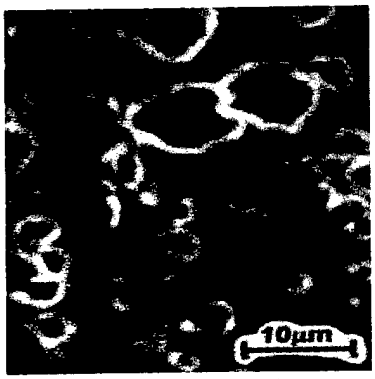


Fig.6 Made at –20℃ (soaked in Ethanol)

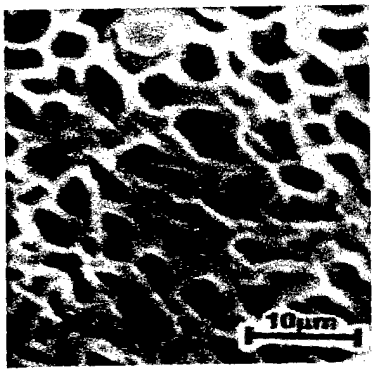


Fig.7 Made at –85℃ (soaked in D.W)



Fig.8 Made at –85℃ (soaked in Ethanol)

3-2. The change in the rupture strain toward concentration of immersion ethanol solution

The state of the transition of the rupture distortion along with ethanol solution concentration which had been permeated from the result of stress strain curve which could get it was compared in freezing temperature in the preparation, and the graph turned. (Fig.4) The vertical axis takes distortion in the rupture, and the side shaft is ethanol concentration of permeation solvent.

Rupture strain shows the tendency that it decreases after they increased caused by the increase in concentration of ethanol solution permeation and maximum value was shown.

In other words, however the expansion until it was ruptured became big, and the tendency that it was ruptured early gradually was recognized in 70%-80 % of ethanol concentration in the higher concentration than it.

Moreover, freezing temperature in the preparation was compared with the material that it was made of sample at -50°C in less than at -20°C, on the whole, it was small faces at the change of ethanol concentration, rupture strain doesn't show the big change that much, and only about 50% of the size of the preparation material at -85°C showed even the maximum department place of 70% of the concentration. The position of the rupture distortion actually changes in the concentration of concentration of ethanol solution permeation.

If the following was never refused specially, it decided to be stated about the material made in freezing temperature at -50°C and under that the character was shown remarkably. The value of rupture strain was changed low value →high value → low value, and maximum value in accordance with the increase in ethanol concentration. In other words, the sample was easy to be ruptured that swelling rate was too low with the sample whose swelling rate was high couldn't stand up to either of the big deformation. The former was probably because it was connected with the

destruction that the rupture of the bridge point created by the big load was directly broad because conformation which the high molecule chain inside gel expanded excessively was made.

And, even if there was the part of the expensive high molecule density that cohesion and adsorbed inside, the rate of such the territory faces was small in the whole, the destruction part which appeared first plays the part of notch, and thought with the benefit as well that destruction progresses at once due to big stress concentration. The latter was thought a rupture to be advanced due to the contraction on the other hand because conformation's own occupancy capacity of him was small and the contact of the high molecule chains in the slide deformation of the high molecule chain was lost toward about big deformation. Big expansion was decided to be assured under the condition located in the middle of these 2 phase for conformation which had enough spatial unevenness with the high molecule chain inside gel by the rupture toward the outside power to made suitable extent and friction occur.

3-3. Freezing temperature in the sample preparation and the strength property of gel

It would be "turn to remarkble and turn to clear" of the various nature if the influence of freezing temperature in the preparation toward the strength property of this research material was expressed with the word. In other words, as for which of the rise tendency of the strength that the material made with -50°C faces ethanol concentration, the rupture distortion as well, the ups and downs of the pattern were clearer than the material made with -20°C in Fig.3～ Fig.4. The response of the change in the strength property towarded concentration of ethanol solution impregnation of the material made at -20° C shows a tendency of being bad very much. It could be said that it depended on the change in micro structure of gel entirely about such the property changed by freezing temperature.

3-4. Descent temperature speed and micro structure of gel

The decline of freezing temperature could be considered to promote precision of the high molecule net from the result by the SEM observation Fig.5 , Fig7). Turning to the precision phenomenon of such reticulate structure will depend on the speed of the change in temperature in sol-gel transfer process.

Descent temperature speed was changed imitatively in our experiment by setting up temperature inside the low temperature preservation container(: high power of refrigerator) which keeps sol which was heated at the time of gel preparation and which it was made to dissolve. In other words, the heat way speed of around the unit time when the inside of sol was robbed was decided by sols temperature at 90°C just before the injection and the temperature of inside the freezer at -20°C , -50°C,-85°C, among the difference in temperature it. The more rapid temperature descent was decided to be put on sol by being thrown into the freezer held consequently further in the low temperature.

It thought that the speed of the temperature descent was given to it to prevent the water crystal from turning to fault in sol which was a water-high molecule. In other words, generally the crystal (ice particle) of the water congealed by being cooled faster and rapidly which was decided that it would be frozen in amorphously condition. These things make it predict that it becomes the thing that generally the distribution of the high molecule discharged outside the ice due to the solidification of the water dispersed very delicately. Conversely, if freezing proceeds slowly, as for the particle of the ice turns to fault, and the rates of turns to locally in spatially of increase as for the distribution of the high molecule. If the bridge of the high molecule chains due to volume swelling of the ice proceeds under the little condition of the rate of turn to locally spatial, the gel structure would be the precise thing in the uniformity as

well which decentralized minute hole not to lean as for it. In other words, it considers that increase in the speed of the temperature descent promotes turn to precise of the reticulate structure in hydrogel preparation by freezing-fusing method.

3-5. The prediction from swelling curve of the strength property of gel

You may think the swelling ratio of the swelling curve to express inside high molecule density from the viewpoint of reciprocal number in gel which was vesicular structure material. In other words, high molecule density increases if gel was shrinks and high molecule density decreases if the gels degree of swelling was high. Increase in the high molecule density had the correlation which was close to the strength property of gel with being natural.

But, the one related to the line shape by the fixed number couldn't actually exist between the high molecule density and the strength. In the condition whose density was high and that it shrinks, and the condition that low density was moistened, it lacks a limit of the bridge rupture which the existence of the frictional slide by the contact of the high molecule chains occurred in and which partly occurred, and effect will act only on the latter greatly, too

Therefore, experientially, in the same way as the movement frictional coefficient of the reverse proper tangent function type of the high molecule density, by the reverse proper tangent function type, it effect factor of lacks the limit when value decreases caused by the increase in the high molecule density, it thinks with the thing that strength can be predicted by taking advantage of the contact pressure of the high molecules which could get it from the high molecule density from the viewpoint of line shape.

Because it doesn't reach that various fixed numbers about swelling curve of gel are decided under the present condition, though a strength prediction by swelling curve couldn't be actually done, as for the possibility that the improvement of the strength could be done, it could explain as mentioned above due to the rise in the temperature descent speed in sol freezing caused by the decline of freezing temperature by the qualitative interpretation.

3-6. The influence on gel strain character by freezing temperature

It depended comparatively of the reticulate structure that it was turned to precise, and it could explain in the same way as for the strain property as well. If the reticulate structure of gel was very a fault, rupture was hastened by effect of cut and lacks, and effect of cut and lacks was declined, and effect on friction would rise in the substitute because a bridge point and the contact total area of the high molecule chains in the contraction become big if it was precise structure. In the case of the condition of swelling and contraction which, As for -20° C preparation material which became the condition that the density of the high molecule which was the inside organization of gel was low, and it works of cut and loss, and it guesses the rupture which generally occurred in a part of rupture by the outside power so big deformation could not stand. Therefore, it considers that the influence of ethanol concentration against the rupture strain becomes not clear in comparison with the material that it was made at -50°C in under.

4. Conclusion

By this research, the strength property which it thought about with the importance when high molecule hydrogel was applied as the function machine element, it wasn't based on the chemical technique such as the material formation change, it was tried to improve and control due to the decline of freezing temperature in method of turn to gel by the freezing and fusion, besides, it was carried out for the purpose of evaluating the strength character of gel from

the viewpoint of material dynamics. The following thing became clear as the result.

1. PVA hydrogel which added Poly Sodium Acrylic Acid 25% has the property which makes maximum tensil strength, rupture strain and swelling rate change remarkably corresponding to ethanol concentration which had been permeated from it 25% Poly Sodium Acrylic Acid
2. Inside reticulate structure turned to the precision with hydrogel that freezing was made by the way of fusing caused by the rise in the speed of the imitative temperature descent of the decline of freezing temperature.
3. Maximum tensil strength and rupture strain of this material improved greatly by reticulate structure turned to the precision.

The phenomenon of the change in volume of high molecule hydrogel was taken up so far by many researchers, though the possibility of the application was suggested, then the material of gel was often searched for further in search of the fast voluntary bigger deformation in many cases. In those, though very promising material exists as an active machine element, it was never almost applicable as a product due to the industry in the direction which had it so at present for the strength-like reliability. However, though it was the technique of the way of fusing which freezing was limited to as this research result, it was suggested that improvement was made like the strength of gel by the change of the condition in gel preparation. In other words, without looking for the combination of the material which both strength and function had been fitted to, it thought that the place of the application of gel material in the strength side a difficulty was expanded though a function was high while it knows at present by investigation's and taking it into consideration how the inside micro structure of gel changes by the preparation condition.

REFERENCE LITERATURE

(1)K. YAGI, T. Suzuki, T. Yoshikawa, others, Design of Functional Hydrogel Responding to the Environment and Evaluation of Its Material. Properties. Proc. of IMMM'97. pp.683-691, (1998.1),
(2)T. SUZUKI, Master's Thesis of Mie Univ., The Study of High Molecular Hydrogel Responding to the Enviroment and the Function. (1995)
(3)M. Kuriaki, K. Makamura and J. Mizutani, Kobunshi Ronbunshu, Vol.46 (1989), No.11, pp.739-743.
(4)M. Kuriaki and T. Hara, MEMBRANE, 8(1) (1983), pp.39-45.
(5)N. Tsunemoto, and M. Suzuki, Report of Mechanical Engineering Laboratory, Vol.48 (1994), No.5, pp.237-242.
(6)T. Shiga, Y. Hirose, A. Okada and T. Kurauchi, Kobunshi Ronbunshu, Vol.46 (1989), No.11, pp.709-713.
(7)Y. Ikada, et al, Report of the Poval committee, No. 89, pp.1-1o, (1987)

Technical Session B-1

Microrobot

Frequency Modulation Velocity Control of Multiple Cybernetic Actuators for Two-lead-wire Drive

Makoto Nokata and Koji Ikuta

Department of Micro System Engineering, School of Engineering, Nagoya University

Furo-cho, Chikusa-ku, Nagoya-shi, 464-8603 JAPAN
Tel:+81-52-789-5024, Fax:+81-52-789-5027 E-mail: ikuta@mech.nagoya-u.ac.jp

Abstract:

A new concept for an active endoscope with hyper redundancy has been already proposed. This medical tool called "Hyper Endoscope" for minimally invasive surgery is driven by miniature cybernetic actuators. A dynamic model of the cybernetic actuator, taking into account its piezoelectric effect, is proposed and its detailed performance analyzed. Based on the result, a new technique to minimize the number of lead wires is proposed and verified experimentally. FMVC (Frequency Modulation Velocity Control) with two lead wires as an analog control method has been perfected.

1 Introduction

The authors have already developed a laparoscopic surgical robot, the "Hyper Redundant Active Endoscope (Hyper Endoscope)", as shown in **Fig.1** [1] [2]. The outer diameter of the segment is 10 [mm] and the length is 50 [mm]. Each miniature active universal joint has two degrees of freedom and can be bent by a pair of miniature cybernetic actuators sliding along the segment. Total length of the present prototype is 250 [mm] and it has ten degrees of freedom. But any such mechanism, which is distributed with several micro actuators, increases in the number of lead wires as actuators are increased. This makes not only miniaturization but also any bending motion difficult.

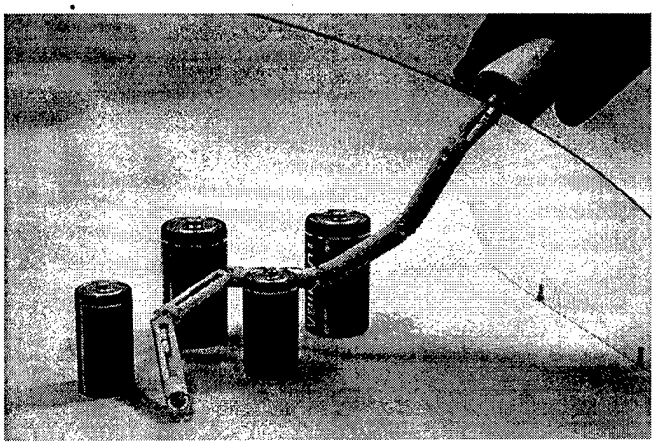


Fig.1 Prototype of Hyper Endoscope

In this paper, a new method for the minimum wire drive of multi micro actuators is proposed and verified.

2 Proposal of minimum wire drive by analog control method

It has been considered that both the digital control method and an analog one will be appropriate to the minimum wire drive of a multi-micro actuator system. The digital control method (**Fig.2**) proposed by K.Park, K.Minami and M.Esashi has three lead wires such as power supply line, ground line and control line [3]. This method has the advantage of easily increasing the number of actuators. But many decoder circuits must be put into the equipment, which makes the system weak. This is not always suitable for medical robots which demand reliability.

We propose the "analog control method for two lead wires" as shown in **Fig.3**. Multi-actuators, which have a different proper oscillation, are connected in parallel and controlled separately by tuning the frequency of the driving wave. This produces two-lead-wire drive control without a control line. In this method, there is a limit to a frequency band, so it is difficult to increase the number of actuators relative to the digital method. But with decoder circuits and many components unnecessary, this improves the reliability of the whole system dramatically.

The characteristics of the digital and analog methods are integrated as follows:

Digital method

three lead wires, many actuators, many components, complicated system

Analog method

two lead wires, a limit to the number of actuators, fewer components, simple system

There were some researches for wireless methods that use of analog vibration. One or several parts on the plate can be moved by vibrating a base plate horizontally or vertically (e.g. T.Yasuda et al. [4], D.Reznik et al. [5]). This

1999 INTERNATIONAL SYMPOSIUM ON
MICROMECHATRONICS AND HUMAN SCIENCE
0-7803-5790-6/99/ $10.00 ©1999 IEEE.

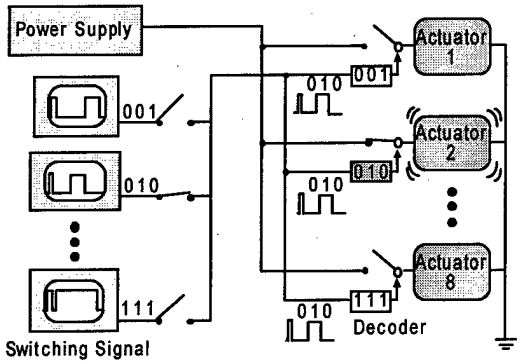


Fig.2 A digital method for reducing the number of wires

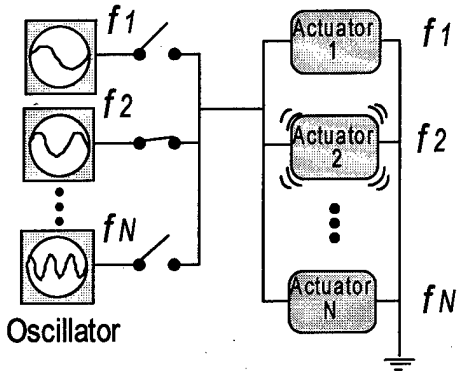


Fig.3 An analog method for reducing the number of wires

method cannot help vibrating the whole area which the parts move. The vibration is transmitted by the mechanical contact between plate and parts, so it produces a loss of energy and it is difficult to achieve precise operation of independent part. It is not suitable to drive miniature actuators for medical use.

A new requirement for the analog control method is an actuator which can have speed controlled by frequency modulation. The authors have already designed and developed a safe, small, lightweight and silent actuator called the "Cybernetic Actuator".

The basic concept of the Cybernetic Actuator was proposed by Tomovic and McGee in 1966 [6]. It is based on consideration of the human muscle system. It has four drive states, namely free, decreasing, increasing and locked. **Fig.4** shows the world's first Cybernetic Actuator we designed [7] [8]. Its dimension is 4x4x12[mm] and weight is only 1[g]. The miniature electromagnetic coil produces "clamping force" magnetically to control friction between the actuator and a guide rail made of steel. A miniature piezoelectric element (1x2x5[mm]) is used to produce "high frequency impact" for motion.

The motion characteristic of the actuator is determined by the inertial weight and the proper oscillation, one which

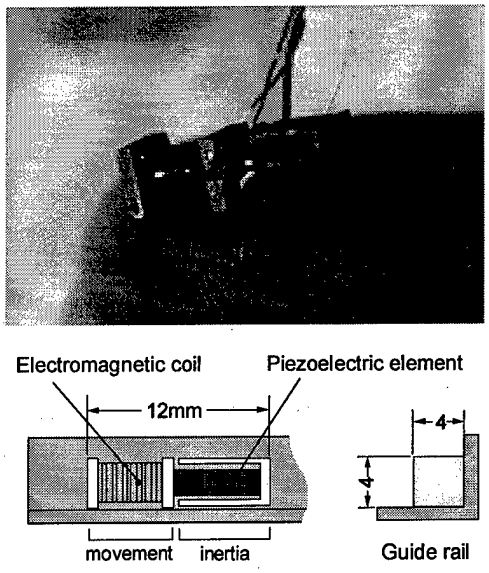


Fig.4 The Cybernetic actuator

is dependent on the field-effect of the piezoelectric element. As a result, the cybernetic actuator is the most suitable for the analog control method in order to realize a minimum wire drive.

So we studied the method of speed control by using frequency modulation. First, we tried to investigate the movement characteristic theoretically.

3 Characteristic analysis at high frequency

3.1 Proposal of a dynamic model

A piezoelectric impact drive such as that of a cybernetic actuator used to be analyzed by a "static model" with the law of conservation of momentum [9]. This model is used for positional adjustment equipment which has a weight from 200[g] to 1000[g] with a low-frequency impact drive, so it can deal only with heavy actuators. Our cybernetic actuator is small and lightweight, so it is difficult to resolve its detailed performance in a high-frequency band by using the static model.

We proposed a linear approximate dynamic model of the cybernetic actuator shown as **Fig.5**. This model consists of three components, namely movement, piezoelectric element and inertia. The parts in movement and inertia are deemed a material particles. The piezoelectric element is deemed an aspect of viscoelasticity. Frictional force is always produced against the direction of the moving part.

3.2 Introduction of piezoelectric effect

The merit of this model is that it takes into account the piezoelectric effect for detailed analysis. A piezoelectric effect means the phenomenon in which a dielectric polar-

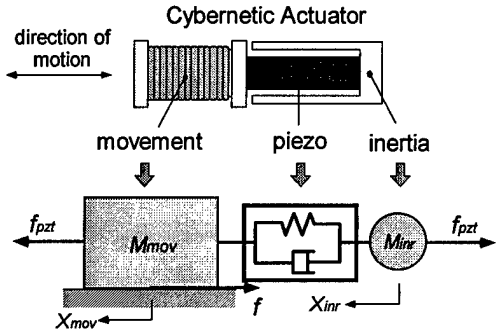


Fig.5 Dynamic model of cybernetic actuator

ization causes stress or strain by inputting voltage. This phenomenon can be expressed as a piezoelectric equation, eq.(1).

$$\epsilon_i = s_{ij}{}^E \sigma_j + d_{mi} E_m \tag{1}$$

ϵ_i : *strain*
E_m : *Electric field intensity* $[V/m]$
σ_j : *Stress* $[N/m^2]$
$s_{ij}{}^E$: *Inverse of Young modulus* $[m^2/N]$
d_{mi} : *Piezoelectric modulus* $[m/V]$

The attached symbols in eq.(1) are used for the expression of the multi-dimensional tensor with the piezoelectric phenomenon. The upper attached symbol is a parameter kept constant during the phase transition and the lower attached symbol is a piezoelectric axis of cause and result. Each axis of i, j, m(i, j=1,2,$\cdots$,6; m=1,2,3) shows the direction of strain, stress and the electrode surface. It takes into account the piezoelectric effect in the producible force of the piezoelectric element (f_{pzt} in Fig.5) .

This actuator uses a piezoelectric element that is layered only toward the direction of motion, so it produces the mode of a vertical vibration. As a result, it can be replaced eq.(1) with a simple equation, and the upper and lower attached symbols can be omitted. This equation also expresses a piezoelectric response against a force impinging from outside. In this paper, in order to deal with an inner force, the sign of the first member of a right side equation is used. From the above premises, eq.(1) simplified is shown as eq. (2).

$$\epsilon = -s\sigma + dE \tag{2}$$

Consequently, a producible stress by the piezoelectric effect is shown as follows.

$$\sigma = \frac{dE - \epsilon}{s} \tag{3}$$

A piezoelectric element has a high response (response speed: 0.1[msec]), so it is possible to consider that the target stress is produced at $\epsilon = 0$, with electric field intensity when $E = V/L$ (input voltage is V, distance between electrode plates is L). When the cross section of a piezoelectric element is A, the producible force of both of its edges is calculated as eq.(4) from eq.(3).

$$f_{pzt} = A\sigma = \frac{AdV/L}{s} \tag{4}$$

The motion equations of the inertial and moving parts can be expressed as eq.(5)(6). We can verify the dynamic performance of an actuator by solving these simultaneous equations.

$$M_{inr}\ddot{x}_{inr} + C(\dot{x}_{inr} - \dot{x}_{mov}) + K(x_{inr} - x_{mov}) = -f_{pzt} \tag{5}$$

$$M_{mov}\ddot{x}_{mov} + C(\dot{x}_{mov} - \dot{x}_{inr}) + K(x_{mov} - x_{inr}) = f_{pzt} - sgn(\dot{x}_{mov})f \tag{6}$$

$$sgn(x) = \begin{cases} +1 : x \geq 0 \\ -1 : x < 0 \end{cases} \tag{7}$$

x_k : **Displacement** f_{pzt} : **Force(piezo)**
C : **Coefficient of viscosity** M_k : **Mass**
K : **Modulus of elasticity** f : **Friction**
$(k = inr, mov)$

Table 1 Parameters of actuator

Young's modulus[N/m^2]	$1/s$	27×10^9
Mass(movement)[g]	M_{mov}	0.503
Mass(inertia)[g]	M_{inr}	0.353
Modulus of elasticity[N/m]	K	10.8×10^6
Cross section[mm^2]	A	2.0
Piezoelectric modulus[m/V]	d	66.7×10^{-9}
Piezo length[mm]	L	5.0
Friction[N]	f	1.2

3.3 Simulation result of a dynamic model

This simulation has solved the discrete eq.(5)(6). The viscosity is small, so it can be neglected. **Fig.6** shows the wave pattern input to the piezoelectric element and electromagnetic coil. In the voltage wave, the hysteresis of piezoelectric element has not been taken into account because the input electric field intensity is not high. Simulation parameters are shown in **Table 1**. The value of friction was measured by a load cell (KYOWA Electronic Instruments Co. LTD., LVS-1kA). It was used Young's and piezoelectric modulus provided from the manufacturer.

The simulation results of the displacement in which driving frequency is 20[kHz] are shown in **Fig.7**(4 cycles) and **Fig.8**(10 cycles). The results obtained show that high-frequency vibration increases inside the actuator by inputting the driving waves. It shows that the actuator oscillates at a high frequency and moves at a constant speed. As a result, it is clear that the cybernetic actuator is driven by mixing low vibration with the input wave pattern.

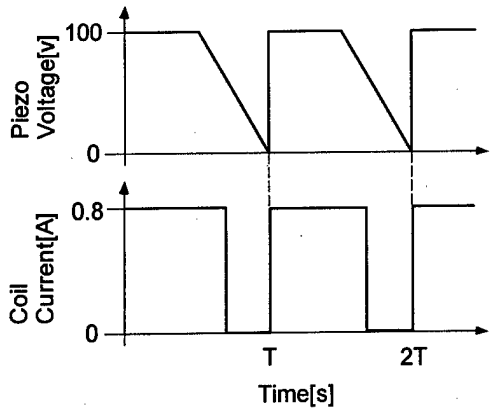


Fig.6 Input voltage and current pattern

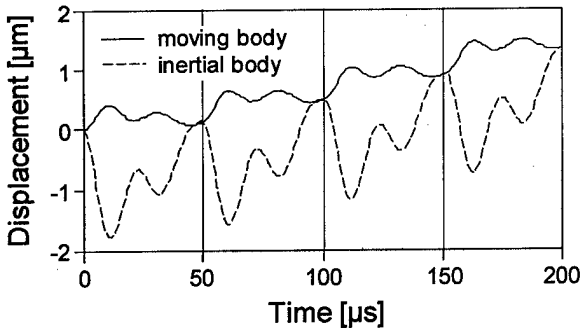


Fig.7 Result of simulation (4 cycles)

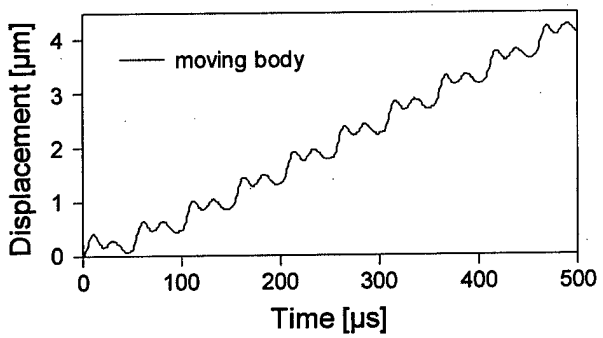


Fig.8 Result of simulation (movement part,10 cycles)

3.4 Comparison between measured values and simulation results

We verified the dynamic model by experimentation using the cybernetic actuator(**Fig.4**). The experimental equipment is shown in **Fig.9**. Driving wave patterns produced by a function generator (YOKOGAWA, AG2100A) were inputted and amplified by a voltage amplifier (NF ElECTRONIC INSTRUMENT, 4010) or a current amplifier (TAKASAGO LTD., BPS120-5). These waves were inputted to the piezoelectric element (NEC, size: $1 \times 2 \times 5$[mm]) and electromagnetic coil (ϕ 0.15, 30 turns). Measurements of the actuator's displacement were made using a laser sensor(KEYENCE,LB $-$ 02, LB $-$ 62). The same equipment was used for the following experimentation. **Fig.10** shows the comparison between the experimental values and the simulation results of actuator speed against various frequencies when the same wave is inputted. There is a little disagreement between each of the speed values. It is considered that the effect of the frequency dependence appeared to be sensitive because the cybernetic actuator is driven by mixing the input wave pattern with low vibration caused by the proper oscilla-

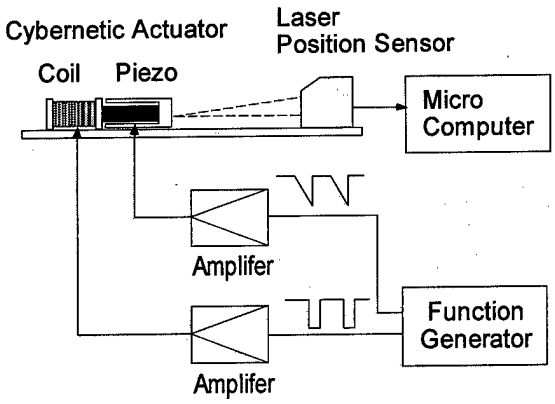


Fig.9 Experimental systems of driving cybernetic actuator

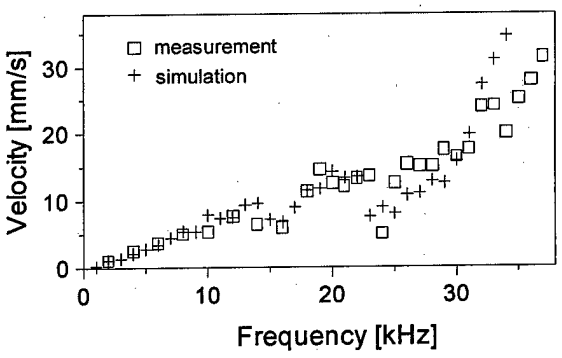


Fig.10 Comparison between measurement and simulation of moving part

tion of the actuator, friction of the rail, and so on. This is clear from the behavior of the moving and inertial parts. In a low-frequency range from 0 to 10[kHz], the simulation results of the dynamic model agree quite well with the experimental values of the static model. In the upper-frequency range, we can see the same tendency of speed as in the simulation results, so the validity of this model was verified. It will be useful for design and control of a cybernetic actuator.

From these results, our dynamic model made it clear that the performance of the actuator in motion is driven by piezoelectric impact in a wide-frequency band.

4 Frequency Modulation Velocity Control (FMVC)

4.1 Proposal for FMVC

The authors propose a new technique in order to minimize the number of lead wires for multi-micro actuators called the "Frequency Modulation Velocity Control (FMVC) ", which makes full use of frequency dependence on speed. The following experiment was conducted to verify the feasibility of this control method.

First, we tried to direct the inputting wave pattern to control not only speed but also the moving direction of the actuator by FMVC. **Fig.11**(broken line), which is a symmetrical wave used against **Fig.6**, was chosen as a driving wave. The magnetic clamp at 0.8[A] is kept in place in order to supply constant friction between the rail and actuator.

Fig.12 shows the relationship between the speed and driving frequency. Although other waves such as square, triangle and so on were examined, the authors selected the trapezoid wave (broken line in **Fig.11**) for the following reasons: (1)This wave produces high-impact force; (2)there is little rapid change and less load on the piezoelectric element; and (3)the self-vibration of the actuator is retained on part of the flat voltage wave. We consider this wave to be the most suitable one for FMVC.

4.2 Results of experiment for FMVC

The experiments were made by inputting the driving wave (broken line in **Fig.11**) to the cybernetic actuator. The actuator weight was 0.422[g](including the mass of the piezoelectric element). The same parameters as those in **Table 1** were used, too.

The measured speed values of the cybernetic actuator were shown on the simulation results of **Fig.12**. As a result, it was verified that speed could be controlled by tuning the driving frequency. In particular, it is possible to control the speed linearly in a frequency band from 6 to 10[kHz]. In addition, the negative speed, namely reverse motion, was confirmed at around 16[kHz]. The conventional method of changing the motion direction requires two types of driving waves for forward and reverse. It was ensured that the motion direction could be changed by FMVC, with the validity of the proposal method verified experimentally.

As a result, it was confirmed that the trapezoid wave pattern was a suitable wave for precisely controlling the speed of one cybernetic actuator. But when multi-actuators are driven on only two wires, there is a slight tendency that the high-frequency aspect, which is produced by the folding part of the trapezoid wave, will affect other actuators on the same wires.

So we chose a sine wave as shown in **Fig.11** (solid line) for the FMVC of multi-actuators, because there is no high-frequency aspect and the voltage power as the same as the trapezoid wave in the sine wave. Impact force is a little smaller, but the speed of the attracting inertial part is almost the same, so the same producible force can be expected.

5 Experiment on minimizing lead wires

In this section, we describe the experiment of minimizing lead wires for multi-actuators using a sine wave **Fig.11** (solid line) as a driving wave. Three cybernetic actuators with masses of were 0.353[g], 0.518[g], 0.683[g]

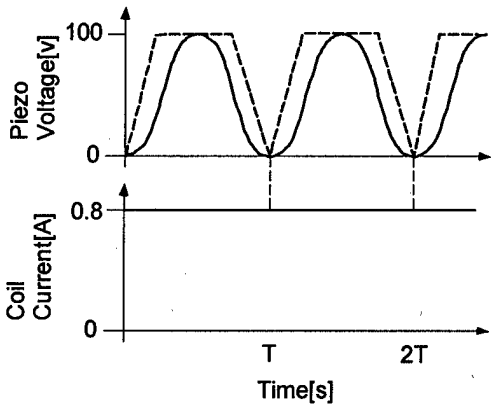


Fig.11 Input voltage and current pattern for FMVC

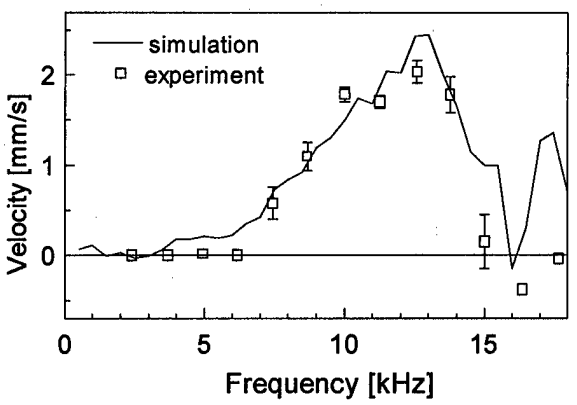


Fig.12 Comparison of simulation and experiment for frequency dependence of velocity

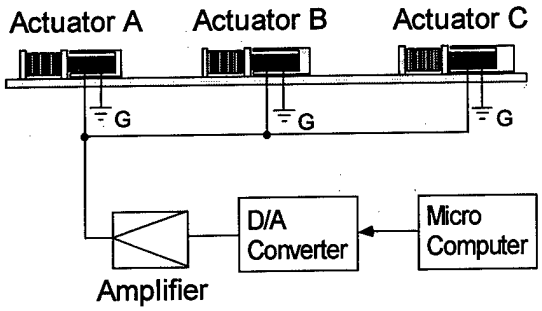


Fig.13 Experimental system of two-wire drive of multi-actuators

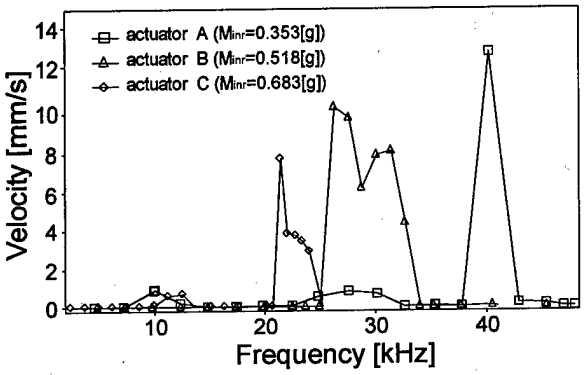


Fig.14 Experiment on minimum wire drive of multi-micro actuators(Analog method, moving part)

(named actuators A,B,C), were wired in parallel as shown in **Fig.13**. When driving waves with frequencies from 0 to 50[kHz] were inputted, speed of the moving part was measured.

The experimental values of the actuator's speed are shown in **Fig.14**. The results revealed the appearance of each speed peak in the frequency band of 38∼42[kHz](actuator A, mass: 0.353[g]), 25∼35[kHz] (actuator B, mass: 0.518 [g]) and 20∼25[kHz] (actuator C, mass: 0.683[g]). We were able to divide the band of the driving frequency. As a result, success has been attained in driving multi-actuators individually with only two wires.

Accordingly, it was verified that the minimum wire drive of multi-actuators could be realized by the analog control method using "FMVC". The optimum driving wave and precise control of speed are undergoing study now.

6 Conclusion

A new technique to minimize the number of lead wires for medical micro robots such as the "Hyper Endoscope" for minimally invasive surgery was proposed. A dynamic model of a cybernetic actuator, taking into account the piezoelectric effect was proposed, and detailed performance was analyzed. Frequency Modulation Velocity Control(FMVC) with two lead wires as an analog control method was invented and verified experimentally.

These results indicate the availability of FMVC not only for medical micro robots such as the Hyper Endoscope but also various other micro machines driven by actuators that use of vibration or resonance.

Acknowledgement

The authors would like to acknowledge the great help of Mr.N.Kanayama at Hiroshima University, Mr.S.Aritomi at Sumitomo Metal Industries Ltd. and Mr.H.Tahara at the Department of Construction in Kyushu.

References

[1] K.Ikuta, M.Nokata and S.Aritomi : "Biomedical Micro Robots Driven by Miniature Cybernetic Actuator," Proc. of IEEE International Workshop on Micro Electromechanical Systems (MEMS'94), pp.263-268, 1994.

[2] K.Ikuta, M.Nokata and S.Aritomi : "Hyper Redundant Active Endoscope for Minimally Invasive Surgery" , Journal of Robotics Society of Japan, Vol.16, No.4, pp.569-575, 1998 (in Japanese).

[3] K.Park, K.Minami and M.Esashi : "An integrated communication and control system for a multi-link active catheter", J.Micromech. Microeng. 6, pp.345-351, 1996.

[4] T.Yasuda, I.Shimoyama and H.Miura : "Microrobot Actuated by a Vibration Energy Fieled" , Technical Digest of Transducers'93, 1993.

[5] Dan Reznik and John Canny : "A Flat Rigid Plate is a Universal Planar Manipulator" , Prof. of IEEE International Conference on Robotics and Automation,pp.1471-1478, 1998.

[6] R.Tomovic, R.B.McGee, "A Finite State Approach to the Synthesis of Bioengineering Control System" , IEEE Trans on Human Factor in Electronics, Vol.7, No.2, pp.65, 1966.

[7] K.Ikuta, A.Kawahara and S.Yamazumi : "Miniature Cybernetic Actuators Using Piezoelectric Device," Proc. of IEEE International Workshop on Micro Electromechanical Systems(MEMS'91), pp.131-135, 1991.

[8] K.Ikuta, S.Aritomi and T.Kabashima : "Tiny Silent Linear Cybernetic Actuator Driven by Piezoelectric Device With Electromagnetic Clamp," Proc. of IEEE International Workshop on Micro Electromechanical Systems(MEMS'92), pp232-237, 1992.

[9] T.Higuchi et al. : Proc. of IEEE International Workshop on Micro Robot and Teleoperation, 1987.

[10] K.Ikuta and M.Nokata : "Minimum Wire Drive of Multi Micro Actuators" , Journal of Robotics Society of Japan, Vol.16, No.6, pp.791-797, 1998 (in Japanese).

[11] Koji IKUTA and Makoto NOKATA :"Two-Lead-Wire Drive for Multi-Micro Actuators," Proc. of the 1999 IEEE Robotics and Automation Conference (ICRA'99), pp.2378-2384, 1999.

LAMAlice : A nanorover for planetary exploration

M. Freese, M. Kaelin, J-M. Lehky, G. Caprari, T. Estier, R. Siegwart

EPFL (Swiss Federal Institute of Technology Lausanne)
Institute of Robotic Systems
EPFL, DMT-ISR, CH-1015 Lausanne
http://dmtwww.epfl.ch/isr/asl

ABSTRACT

Over the last years considerable efforts in miniaturisation have been made in autonomous robotics, especially in the domain of space missions in order to reduce costs and increase chances of success if using several robots. This has led us to imagine and realise a prototype of a nanorover which shows an example of what planetary exploration could look like in the future.

The robot is a four-wheel drive rover which is composed of two separate parts linked together with a flexible passive coupling (figure 1). This configuration allows a "push-pull" effect improving the overcoming of an obstacle and offers good gripping. The wheels are made of flexible blades radially fixed on the axis. On the one hand this permits the wheels to be rolled up for transport, on the other hand a smooth movement of the gravity centre is reached, which increases power efficiency of the obstacle overcome. The robot also presents a simple structure and it is possible to equip it with a passive sensor like a very low-power camera as well as with active sensors.

The power consumption is less than 50 mW which allows an operating time of roughly 20 hours with on-board batteries. *LAMAlice* is 11 cm long, 6 cm wide and 4 cm high and has a weight of 30 grams. The maximum speed is 1 cm/s and it overcomes steps of its own height.

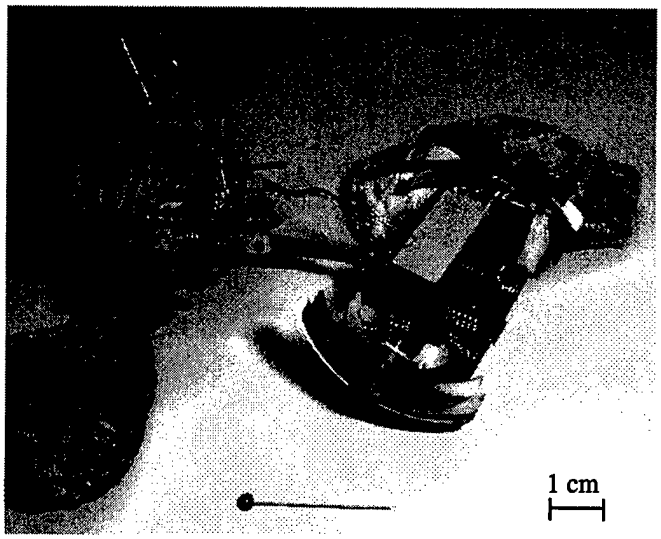


Figure 1: Nanorover *LAMAlice*

1. INTRODUCTION

Since more than one quarter century scientists and engineers occupied themselves with the design and improvement of robots used for planetary exploration. As space mission costs are extremely bound to the weight and volume of the payload, particular efforts have been made in miniaturisation [1], [6], [8]. This miniaturisation has taken advantage of recent developments in micro-technology and mobile robotics, and it is now possible to build tiny mobile robots, so called nanorovers, measuring only few centimetres and weighing less than a hundred grams.

Planetary exploration mainly consists in measuring chemical and physical data, classifying minerals, gathering of samples, searching for ice or microfossils on the surface. To achieve this, the robot has to be able to move around on the planetary surface which is not an easy task for the following reasons :
First, the environment contains plenty of obstacles which must either be avoided or overcome. The ability of moving straight until meeting an insurmountable obstacle is expressed by the mean free path, which depends on the dimension of the surrounding obstacles, their distribution, the robot's dimensions and its capability of overcoming obstacles [5]. Second, energy consumption for locomotion as well as for sensing, control, actuating and communication, has to be minimal, because of the very limited quantity of energy being able to be stored, carried or produced on the robot.
Finally, sensing and computing become difficult in these dimensions, therefore passive overcoming of obstacles is preferred.

Reliability is fundamental in space missions because of the impossibility of human intervention on the spot. Given the possibility of deploying several robots simultaneously, nanorovers increase the success rate of a mission because it is not terminated by the failure of one among them. It is conceivable to have many of these nanorovers cooperate and/or assist other robots by tracking them and so create a network of robots with a limited global control system. Moreover, nanorovers represent an almost negligible payload compared to the payloads planned for the Mars-missions of the next years and could be embarked as a secondary payload using whatever mass margin is left over at launch time.

1999 INTERNATIONAL SYMPOSIUM ON
MICROMECHATRONICS AND HUMAN SCIENCE
0-7803-5790-6/99/ $10.00 ©1999 IEEE.

It is also possible to use nanorovers as primary payload of a space probe for the exploration of Mars, the moons of gas giant planets, asteroids etc.
The development of a nanorover can take only a few months, much less than for a traditional rover. This permits to save development costs and space missions could be established in a shorter time.

At this point we want to briefly discuss some interesting examples of nanorovers. In the year 2001, the Japanese will send a spacecraft to an asteroid. On board, the MUSES-CN nanorover from JPL [1], will be the smallest rover ever used in a space mission. It is 20 cm long, weighs 1 kg and has a four-wheel drive articulated chassis, driven by small gear motors. Another nanorover, "Solette" [7], has been developed at the MIT Artificial Intelligence Laboratory. It has a mass of 30 g and is completely autonomous with its solar power system. Nevertheless, off-road behaviour is very limited.

In dimensions inferior to the MUSES-CN nanorover, off-road characteristics are difficult to maintain. It is a challenge to develop a passive locomotion system that keeps a high obstacle overcoming capacity in spite of reduced dimensions.

2. DESCRIPTION OF THE SYSTEM

Our goal was the conception of a nanorover for Mars-exploration. The considerations made above have given us the main criteria to be respected :

- Very small dimensions (around 1 dm^3) and weight (less than 100 g)
- Simple and reliable design
- Passive overcoming of obstacles and adaptation to the terrain
- Extremely low power consumption allowing a high energy autonomy

The development of *LAMAlice* was inspired of Alice [2], a tiny robot also developed at EPFL. Its dimensions are of only 23mm x 21mm x 16mm for a weight of 6 g and a power consumption of less than 10 mW. However, Alice, in its actual version, is not suited to move on uneven grounds.

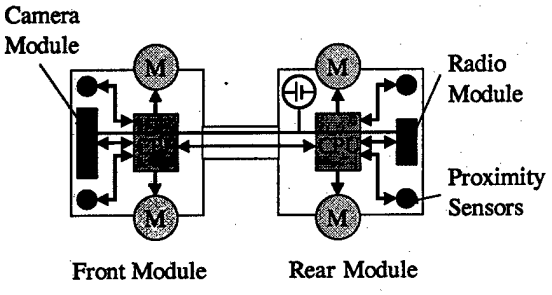


Figure 2: Bloc-scheme of *LAMAlice*

A total amount of roughly 600 hours was invested to realise a first prototype of the off-road nanorover: *LAMAlice* (figure 1 and figure 2).

LAMAlice is 11 cm long, 6 cm wide and 4 cm high, has a weight of about 30 grams and is powered by three button-batteries of 1.55 V (silver oxide) each.

2.1 Mechanical concept

LAMAlice is composed of two modules with two motorised wheels each. The modules are linked together with a passive coupling permitting torsion as well as horizontal flexion but avoiding vertical one. This configuration is advantageous as regards the adherence on the ground, due to the non hyper-static contact with the terrain. Another characteristic of such a system is the possibility of bending in place allowing almost a turning on the spot and so reducing the turning circle diameter to the minimum. During the surmounting of an obstacle the robot benefits from a "push-pull" effect :
first, the rear module helps the front module by pushing it, then, once the latter is on top of the obstacle, it helps by pulling the rear module up. The behaviour described above is strongly dependent on the type of the coupling. A simple solution is the use of a flexible blade as shown in figure 3.

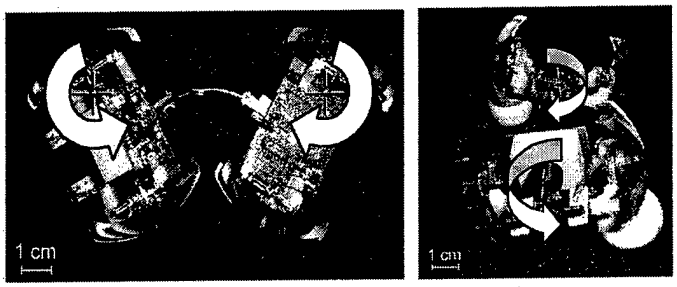


Figure 3: Horizontal flexion and torsion

Finally, the modularity of such a system permits to assemble more than two modules together and thus to realise a snake-like robot. It is evident that in such a case vertical flexion of the coupling is needed. By increasing the number of modules, the robot might be able to overcome higher obstacles, again benefiting from the "push-pull" effect. The number of modules used can be adjusted for specific environments. Furthermore, each module can execute individual tasks and carry out different measurements.

2.2 Wheels

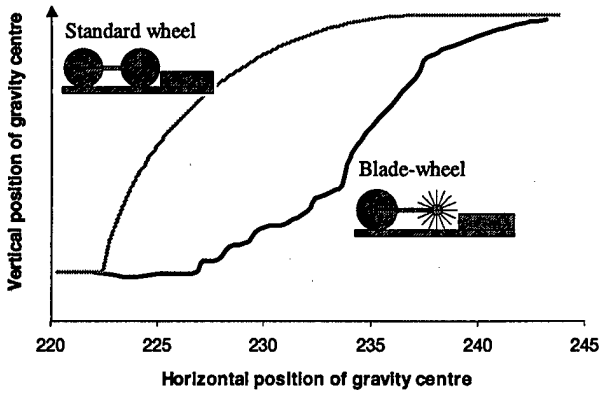
Space environments, presenting strong radiation and big temperature differences, impose severe constraints on the choice of materials. This is the main reason that tyres, commonly used on earth, are hardly suitable for space applications.

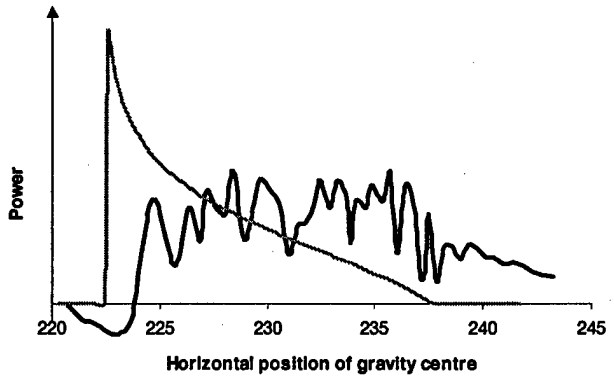
On our robot we introduced a novel concept, consisting in the use of wheels made of flexible stainless steel blades (figure 6). In comparison to a traditional wheel, this system has numerous advantages :

It has a low mass and presents a certain deformation possibility that increases adherence and thus improves terrain adaptation.

As a biologic inspiration, one may imagine a blade wheel as a multitude of arms and legs. Over a flat terrain this wheel has a walking behaviour and against obstacles it is a kind of climbing.

The elasticity provided by the blades can significantly enhance the overcoming of high obstacles and also offers better capability of surmounting overhanging obstacles than a traditional wheel. Additionally, the flexion of the blades adds a damping effect and also causes a smoother surmounting of the obstacle. Figures 4 and 5 show a simulation calculated with *Working Model®2D*. Two two-wheel-drive vehicles roll at constant speed towards a step. The first of them has standard wheels, the second a standard wheel at rear and a blade-wheel in front. Four rigid segments linked together by a rotational spring model a blade. Weight, wheel diameter and speed of both vehicles are identical. Figure 4 displays the position of gravity centre during the front wheel step overcome and figure 5 the matching total power consumption.





Figures 4 and 5: Step-overcoming : Standard wheel vs blade-wheel

We notice a smoother progression for the blade vehicle even if there are some oscillations which also appear in the power graph. The negative consumption at the beginning is the result of the polygon-shape of the blade-wheel on flat terrain. Compared to a standard wheel, the maximum power consumption is approximately reduced to the half. This is particularly important in the case of a power limited system (motor torque and supply current).

Another advantage of blade-wheels is that they can be folded for transportation of the robot and thus its volume can be even more reduced (figure 6).

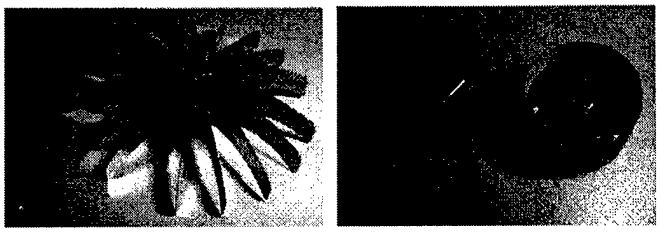


Figure 6: Opened and folded configuration of the blade-wheel

For the design of the blade-wheel, one has to consider the mass of the robot, the type of environment, the required stability and robustness. With an adapted shape of the blades the risk of flipping over can be reduced effectively. The number of blades fixed on the wheel depends on the terrain : The bigger the mean obstacle height (taking in account only obstacles smaller than the wheel diameter), the smaller the number of blades should be and vice versa. This is because a wheel with a high number of blades tends towards the behaviour of a traditional wheel, having good performance on flat ground (little sinking and reduced driving resistance). In the other case a low number of blades presents a better obstacle contact.

LAMAlice's wheels, only weighing 0.9 g for a diameter of 4 cm, are equipped with 16 stainless steel blades having a thickness of 50 µm.

The motors used on *LAMAlice* are swatch® watch-motors. They present very low power consumption (less than 10 mW) for a maximum torque of about 3 mNm at 3 rpm. The motor's weight is 1 g and its design allows a simple mounting onto the chassis.

2.3 Sensors

In order to permit autonomy of navigation and data gathering, it is necessary to equip the robot with sensors. Given the strongly restricted amount of available power for space applications, it is advantageous to use passive sensors. An example of a very low power sensor is the CMOS-camera (APS256D from the CSEM [3], [4]) mounted on the front

module, which has a power consumption of only a few milliwatts. The optics were chosen to have an opening angle of 50° and permit a focussed image for distances over 4 centimetres.
Four SIEMENS SFH 900 IR-proximity sensors, two on each module, were used for obstacle detection. Their range is of a few millimetres (at low power consumption), which is sufficient given the low speed of the rover.

2.4 Control and communication

Each module has a simple microcontroller (PIC16F84) permitting basic navigation, like detecting and avoiding obstacles as well as communication with a control unit. This communication consists in data transmission and command reception and is done by a radio transceiver.
The four motors being individually controlled, provide maximum liberty of action. Since the coupling between the two modules of the robot is passive, a differential drive of the motors will indirectly determine the bending of the coupling blade.
The navigation algorithm is limited by the processing capability and the sensors and allows a certain autonomous behaviour such as obstacle avoidance. To enhance the navigation abilities, radio communication permits assistance from the control unit which could be the lander.

3. Characteristics and Results

One might believe that a larger vehicle will always be able to surmount bigger obstacles than a smaller one, and so it is natural to believe that a larger vehicle is always better than a smaller one. However, for the rock distributions observed on Viking landing sites on Mars, this is not the case, since a smaller vehicle can fit between obstacles which a larger vehicle would have to overcome.

To check if our miniaturisation efforts for *LAMAlice* are justified we computed the mean free path (MFP) relative to the vehicle's turning circle diameter, using the calculation described in [5]. The results are shown in table 1 :

	Sojourner	*LAMAlice*
MFP of Viking landing site 1	9.6	15.1
MFP of Viking landing site 2	2	6.6
Mass of the robot [kg]	11.5	0.03
Volume of the folded robot [dm^3]	~45	~0.2

Table 1: Mean free path of Sojourner and *LAMAlice*

We notice that in comparison to Sojourner, *LAMAlice* is able to move further, relative to its turning circle diameter and therefore relative to its dimensions. Another interesting point is the fact that we could have packed more than 200 *LAMAlice* nanorovers instead of Sojourner in the Pathfinder lander !

A table with the main characteristics of *LAMAlice* is given below :

Dimensions [cm]	11x6x4
Front module weight [g]	15
Rear module weight [g]	14
Power consumption [mW]	~40
Autonomy [h]	~20
Maximum speed [cm/s]	1
Minimal Turning Circle Diameter [cm]	15
Maximum obstacle height [cm]	4
Maximum slope [°]	37

Table 2: Main characteristics of *LAMAlice*

4. Future Developments

Different improvements are presently under development and test phase. These concern essentially the coupling between the two modules as well as the blade-wheels :

With the current blade coupling, it is difficult to determine the relative positions of the modules and also to limit the horizontal flexion to a maximum value. A more sophisticated possibility solving these problems is represented in figure 7.

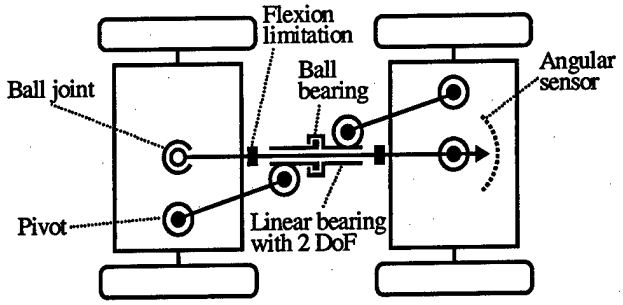


Figure 7 : Cinematic scheme of improved coupling

The blades provide excellent gripping, but there is an increased risk of sinking into the ground and therefore we have thought of another system (figure 8), which is supposed to keep the advantages of the current solution and additionally enhance soft ground performance.

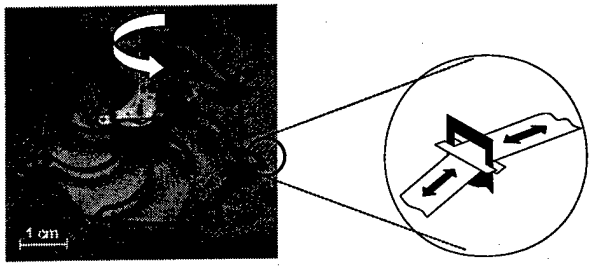


Figure 8: Alternative wheel design

5. CONCLUSIONS

We have seen the growing importance of nanorovers in space applications with their severe limitations concerning dimension and weight. In this paper, we have presented a simple two-module structure (upgradeable to even more modules) offering advantageous off-road characteristics. A novel concept was also the use of flexible blade-wheels providing high obstacle overcoming with torque limited low power systems. An interesting feature is the substantial volume reduction achieved by folding these wheels for transportation.

The work presented here is a step towards a new, simple and passive locomotion concept, which might be interesting for planetary exploration. Future work will have to confirm the performance of this concept.

REFERENCES

[1] B. Wilcox et al, "Nanorover Technology and MUSES-CN Mission", Proc. of i-SAIRAS, pp. 445-450, 1997

[2] G. Caprari, P. Balmer, R. Piguet, R. Siegwart, "The Autonomous Micro Robot "Alice": a platform for scientific and commercial applications", MHS'98, Int. Symp. on Micromechatronics and Human Science, Nagoya, Japan, November 25-28, 1998, p. 231-5

[3] M. Freese, M. Kaelin, J-M. Lehky, "*LAMAlice* Mini Mobile Robot for planetary exploration", Autonomous Systems Lab, Swiss Federal Institute of Technology, Personal communication, June 1999

[4] EM Microelectronic Marin SA, "APS256D Low Power CMOS Digital Video Camera With 256x256 Pixel Resolution", Preliminary Specifications, 1999

[5] B. Wilcox, A. Nasif, R. Welch, "Implications of Martian Rock Distributions on Rover Scaling", Planetary Society International Conference on Mobile Planetary Robots and Rover Roundup, Santa Monica CA, 1997

[6] R. Bertrand, R. Rieder, M. Van Winnendael, "European Tracked Micro-Robot for Planetary Surface Exploration", Proceedings of 5th ESA Workshop on Advanced Space Technologies for Robotics and Automation, ASTRA'98, The Netherlands, 1998

[7] The Rockettes, Solette, MIT AI Lab, Mars Rover, http://www.ai.mit.edu/projects/mars-rovers/rockettes.html

[8] R. Siegwart, M. Lauria, P.-A. Maeusli, M. Van Winnendael, "Design and Implementation of an Innovative Micro-Rover", Robotics 98, the 3rd Conference and Exposition on Robotics in Challenging Environments, Albuquerque, New Mexico, April 26-30, 1998

Development of an Artificial Fish Microrobot

Shuxiang GUO *1, *Toshio FUKUDA* *2 *and Keisuke OGURO* *3

*1 Dept. of Intelligent Mechanical Systems Eng'g, Kagawa University,
1-1 Saiwai-cho, Takamatsu, 760-8526, Kagawa JAPAN
Phone: +81-87-832-1672 Fax: +81-87-832-1658 E-mail: guo@eng.kagawa-u.ac.jp
*2 Dept. of Mechano-Informatics and System, Nagoya University
1 Furo-cho, Chikusa-ku, Nagoya 464-01, JAPAN
*3 Osaka National Research Institute, AIST, 1-8-31 Midorigaoka, Ikeda, Osaka 563, JAPAN

Abstract: It is our purpose to develop an underwater microrobot that has the characteristics of flexibility, driven by a low voltage, good response and safety in body. In this paper, we propose a new prototype model of an underwater microrobot utilizing ICPF (Ionic Conducting Polymer Film) actuator as the servo actuator. Biomimetic fish-like propulsion using ICPF actuator as a propulsion tail fin for a microrobot swimming structure in water or aqueous medium is developed. The overall size of the underwater microrobot prototype shaped as a boat is 40mm in length, 10mm in width and 2mm in thickness. There is a pair of fins. Characteristic of the underwater microrobot is measured by changing the frequency of input voltage from 0.1Hz to 5Hz. The experimental results indicate that the swimming speed of proposed underwater microrobot can be controlled by changing the frequency of input voltage.

1. INTRODUCTION

Intracavity intervention is expected to become increasingly popular in the medical practice, both for diagnosis and for surgery. As we know, many kinds of micro actuator such as an electrostatic actuator, a piezoelectric actuator, a giant magnetostrictive alloy (GMA) actuator, a shape memory alloy actuator, a polymer actuator and an optical actuator have been actively investigated for their potential applications to micro machine technologies. Recently many microrobots have been developed for various purposes due to the advances of the precise process technology, and further progress in this field is expected. One of the features that a microrobot has is a good possible advantage to work in a very small space. For instance, with medical technology a common application is to perform a delicate surgical operation supported by using micro machines thus avoiding unnecessary incisions. For an industrial application the use of microrobots is also proposed to maintain factory pipelines. As well as the medical case, the use of microrobots can help to avoid dismantling and reassembling. Microrobot can restrict their work to affected part or the breakdown spot and do not give unnecessary influence on their surroundings. Mother machine is the kind of robot that transports such microrobots and micro modules for accurate local work and operation in a very small space. In the medical field and in Industry application, a new type of fish-like microrobot that can swim smoothly in water or aqueous medium has urgently been demanded[1] [2]. The fish-like microrobot is one of the micro and miniature devices, which is installed with sensing and actuating elements. It can swim smoothly in water or aqueous medium such as use for in-pipe Inspection and microsurgery of blood vessel. Often time's nature can be the best source of learning tool to devise mechanical equivalents for the process of locomotion. As we know direct conversion of chemical to mechanical energy has been pursued by many scientists to date in order to achieve high efficiencies. Among various forms of locomotion forward swimming motion of a fish in water has been the subject of interest by both zoologists, marine biologists and engineers. The advantage of wavy motion of the swimming body as compared to mechanical propeller used in man-made swimming structures are numerous and can be attributed to its high efficiency of energy conversion noiseless propulsion and utilization of the energy of the surrounding medium. Mechanical swimming structures such as those that replicate undulatory motion by means of linkages and other interfacing parts face the same problems as propellers with low efficiencies and excessive thermal energy generation. Recently, several types of fish-like microrobot using SMA actuator, GMA actuator, PZT actuator and polymer actuator have been reported so far [3]--[8]. However there are some problems, such as compact structure, low response, leaking electric current, safety in water and so on. It is our purpose to develop a type of fish-like microrobot that can swim smoothly in water or aqueous medium. It has the characteristics of flexibility, driven by a low voltage, good response and safety in body. Biomimetic fish-like propulsion using ICPF actuator as a propulsion tail fin for an aunderwater microrobot swimming structure in water or aqueous medium is developed. ICPF actuator is made from the film of perfluorosulfonic acid polymer (Nafion 117, du Pont and company) chemically plated on it's both sides

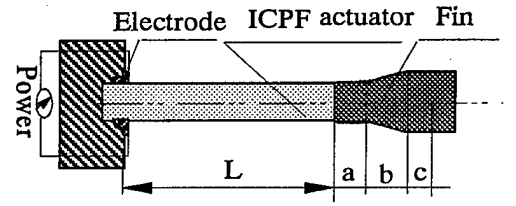
1999 INTERNATIONAL SYMPOSIUM ON
MICROMECHATRONICS AND HUMAN SCIENCE
0-7803-5790-6/99/ $10.00 ©1999 IEEE.

with platinum. In many points, ICPF actuator is superior to usual polymer gel actuator such as fast response, driven by low voltage (about 1.5V) in wet condition without electrolysis, safety in body and so on [9]. It is now possible to replicate the undulating motion of marine animals using ICPF actuator in a more direct way. This paper describes the new structure and motion mechanism of an underwater microrobot using **ICPF** actuator, and discusses the swimming possibility of the microrobot in water. Characteristic of the underwater microrobotis measured by changing the frequency of input voltage from 0.1Hz to 5Hz. The experimental results indicate that the swimming speed of the underwater microrobotcan be controlled by changing the frequency of voltage.

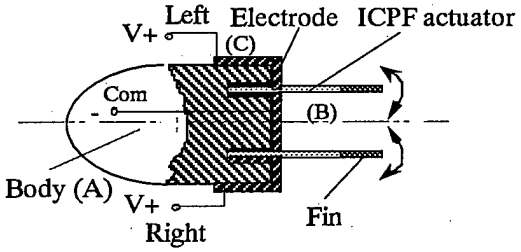
2. STRUCTURE OF MICROROBOT

2.1 Total Structure of the Microrobot

Fig.1 shows the basic structure of the developed underwater microrobot using ICPF actuator. This microrobot consists of the body made of wood material shaped as a boat (A), a pair of tail with a fin driven by ICPF actuator respectively(B) and the lead wires for supplying electric energy to ICPF actuator(C). ICPF actuators are installed in parallel structure for generating a large propulsive force. The fins are driven independently. The photo of the developed microrobot is shown in **Fig.2**.



(a) Structure of a Tail



(b) Total Structure

Fig.1 Structure of Microrobot

2.2 ICPF Actuator

ICPF actuator is made from the film of perfluorosulfonic acid polymer (Nafion 117, du Pont and company) chemically plated on it's both sides with platinum(one side is 0.003mm in thickness). It is known as an ion exchange membrane. It is a kind of high polymer gel actuator, works only in water and in wet condition. The ICPF is bent into anode side when the about 1.5v voltage is applied onto its surfaces. Displacement of the ICPF is proportional to the electrical voltage in put on its surface as the swelling of polymer gels. ICPF actuator (0.2*3*13mm) is cut in a strip to drive a fin for propulsion as shown in **Fig.1**.

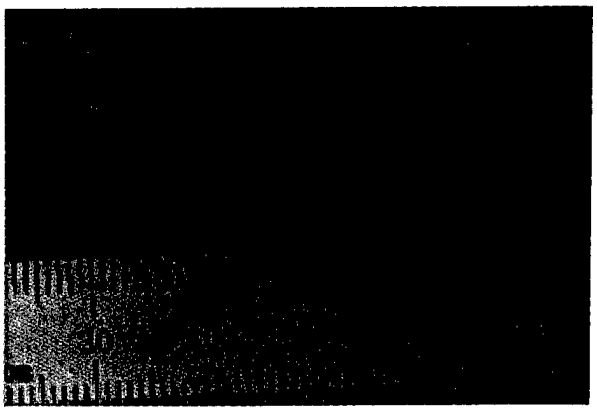


Fig.2 View of Developed Microrobot(10mm*40mm)

3. MOTION MECHANISM OF MICROROBOT

3.1 Theory of Fish Undulatory Motion (8)

According to the biomechanics theory, it is known that unlike carangiform mode of swimming where large undulatory motion near or at the fish tail takes place anguilliform (eel-like) mode of swimming involves most of the fish body in undulation or wavy motion. Rosen[8] was among the first to explain kinematics of motion of a simple carangiform fish through his observations using simple hydrodynamic forces and phenomenon. He described that creation and evolution of vortices generated by the forward half of the body (head and after head of the fish) is the main reason for its propulsion through water. The fish further uses these vortices by the last 2/3 of its body (after half) to propel itself forward by thrusting its body against the seemingly fixed vortices and utilizing their rotational energy. This is called "Vortex peg Hypothesis". The fish produces no net backward moving stream of water when swimming at constant speed. Only when the fish accelerates or turns around, a rearward current is created. The trail created by the fish is a system of large, slow spiraling vortices. They from a single row of vortices with direction of rotation reversing from one vortex to next. This row follows the path of the fish's head. The concave side of each flexural wave of the body of fish contains one vortex. All the main vortices are in line with and along the direction of travel of the fish. For a scaled fish, the mechanism of propulsion gets even more complex since the convex portion of the body in effect will have opened scales that act as small paddles on the side of the fish further pushing the vortices to propel the fish forward.

The net momentum of all forces for any swimming object must be zero. For a mechanically produced vortex, the pressure at the periphery is larger than ambient and higher at the center and we have the following equation for a water particle velocity at distance **r** from the center of the vortex rotating at **ω** rotational speed:

$$v = r\omega \tag{1}$$

Assuming mass of the spiral vortex residing in its arm (main body of vortex) just after fish passage and assuming mass of the arm depends only on its length **l**, thickness **h**, and span **b** of the fish's tail, thus the mass of vortex **m** is :

$$m = \frac{lbwh}{g} \tag{2}$$

where, w and g are weight density and acceleration of gravity respectively. Now assuming length **l** of each vortex is proportional only to amplitude of tail beat **a**, we get:

$$m = \frac{abwh}{g} \tag{3}$$

For a tail beat frequency **f**, and two vortices per beat, the number of vortices generated is **2f**, then the total mass of vortices generated per cycle of undulation is:

$$M = \frac{2fabwh}{g} \tag{4}$$

Assuming forward velocity of fish V, absolute speed of water dragged forward **v** and water speed relative to fish upon ejection **u** then:

$$u = kV \qquad k = cons\tan t \tag{5}$$

$$v = cV \qquad c = cons\tan t \tag{6}$$

The total fish velocity is then:

$$V_t = u - (V - v) = V(k + c - 1) \tag{7}$$

The thus force is then:

$$F = MV_t = \frac{2fabwhV(k + c - 1)}{g} \tag{8}$$

Assuming the drag force opposing the motion **D** is given by:

$$D = C_d w V_t^2 A/2g \tag{9}$$

where C_d is drag coefficient based on wetted surface area A. Setting drag and thrust equal we get:

$$V = \frac{4bh}{C_d A(k + c - 1)} fa \tag{10}$$

The above equation atates that fish forward velocity is proportional to product of tail beat frequency and amplitude of undulation. The constant of multiplication is dependent on fish geometry and fluid properties.

3.2 Motion Mechanism

The developed microrobot has two tails with a fin driven by the ICPF actuator respectively as shown in **Fig.1**. A pair of fins is offset in the distance d, and driven by electric voltage of f1 and f2 frequency independently as shown in **Fig.3**. A motion of a fin is described by combination of two kinds of motion, feathering and heaving(7). When proper phase difference appears between heaving and feathering, the fin generates an effective force as shown in **Fig.4**. The propulsive force is the sum of drag force vectors to the moving direction in equation (11). It can be realized by changing frequency f1, f2 of the electric voltage applied on the ICPF actuators that the moving motion in the directions(forward, right turn and left turn) as shown in **Table.1**.

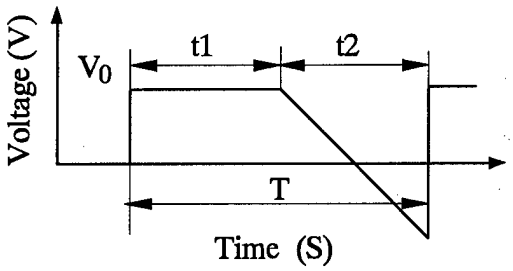


Fig.3 Driving Electric Voltage

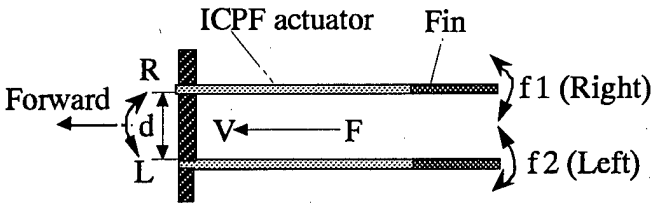


Fig.4 Mechanism of Microrobot Using ICPF Actuator

Table 1 Moving Motion of Microrobot

	Forward	Right Turn	Left Turn
Right ICPF Actuator frequency f1	f1 = f2	f1 > f2	f1 < f2
Left ICPF Actuator frequency f2			

$$Fd = -\frac{1}{2} C_d \rho A |V_h| V_h \tag{11}$$

Where C_d is drag coefficient based on wetted surface area A. **ρ** is the density of water.

4. CHARACTERISTIC MEASUREMENT

4.1 Measurement System

The electric voltage set onto the ICPF actuators can be controlled by a computer. The electrical current is measured by a galvanometer. The bending displacement of a fin at the point of the front end is measured by a laser displacement sensor. The bending amplitude of a fin can be obtained driven by an input voltage as shown in Fig.3. Measurement System is shown in **Fig.5**.

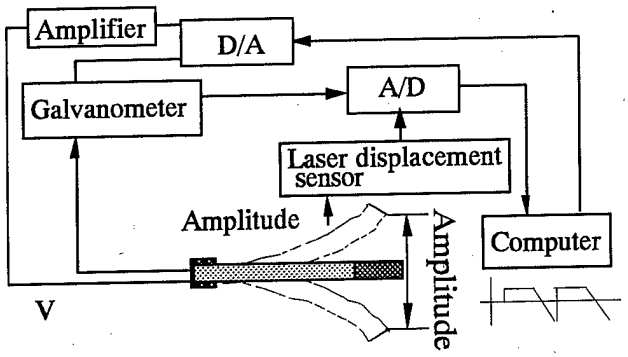


Fig.5 Measurement System

4.2 Characteristic of a Fin of Microrobot

By using the measurement system as shown in **Fig.5**, the following characteristics are measured. First, we measured the maximum displacement of a fin in the center point by changing the frequency of input voltage as shown in **Fig.3** in air. Second, the maximum current is also measured by changing the input voltage. The experimental results are shown in **Fig.6** and **Fig.7**. From these experimental results, it is known that the maximum displacement is in inverse proportion to the frequency of the input voltage, and the maximum current is nearly proportional to the input voltage respectively.

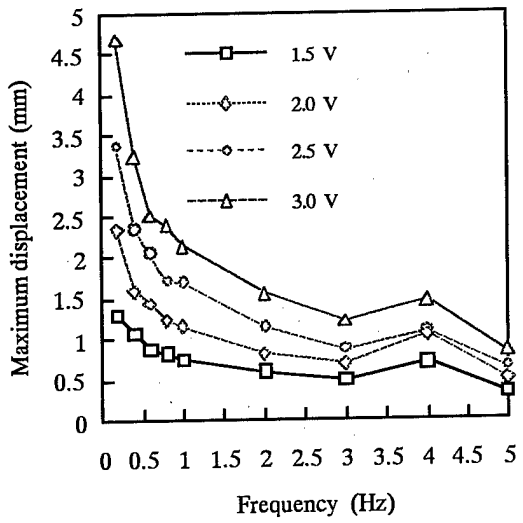


Fig.6 Maximum Displacement (In Air)

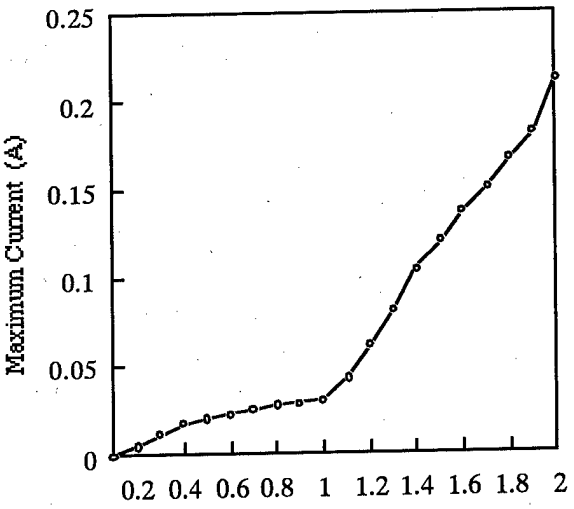


Fig.7 Maximum Electric Current (In Air)

5. MODEL OF FORCE CHARACTERISTIC

The Force characteristic of ICPF actuator is very important for application. It is hard to measure directly the force characteristic due to the characteristic of ICPF actuator. In this paper, we proposed a model for indirectly evaluating force characteristic.

5.1 Vertical module of elasticity (EI)

Fig.8 shows the measurement principle. ICPF actuator(L*w* t) is set up as a cantilever in wet condition. Equality distributed load q (weigh) and intensive load F are set on the ICPF actuator. The bending displacement at the position L' and force F are measured by laser sensor and electric balance respectively.

By using y' and F, the measurement EI is obtained shown in equation (12).

5.2 Model of Virtual Force

The model of virtual force is shown in **Fig.9**. The maximum displacement of the tip point is assumed as f_{max}. The virtual moment M_V and virtual force F_V are assumed on the ICPF actuator. If the bending displacement of M_V and F_V is equal to the maximum displacement of tip point f_{max}, the M_V and F_V are called virtual moment and virtual force respectively. So the M_V and F_V are obtained in equation (13).

$$\left.\begin{aligned} EI &= \frac{q L^4}{24 y'}\left[3 - 4\frac{L'}{L} + \left(\frac{L'}{L}\right)^4\right] - \frac{F L'^3}{3y'} \\ I &= \frac{w t^3}{12} \end{aligned}\right\} \qquad (12)$$

$$\left.\begin{aligned} F_v &= \frac{3EI f_{max}}{L^3} \\ M_v &= \frac{2EI f_{max}}{L^2} \end{aligned}\right\} \qquad (13)$$

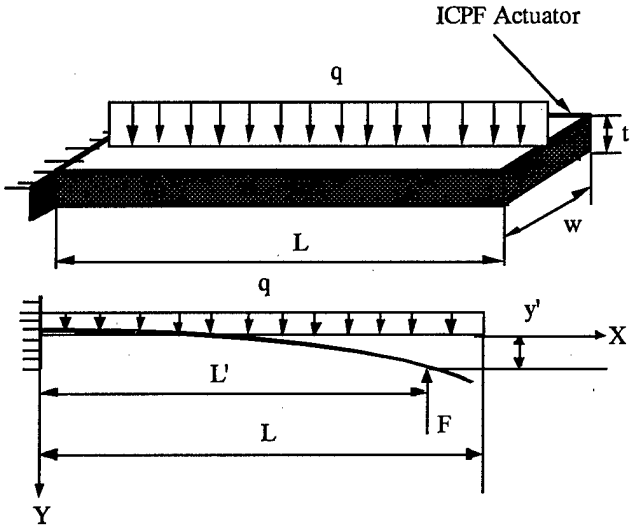


Fig.8 Measurement Principle of ICPF

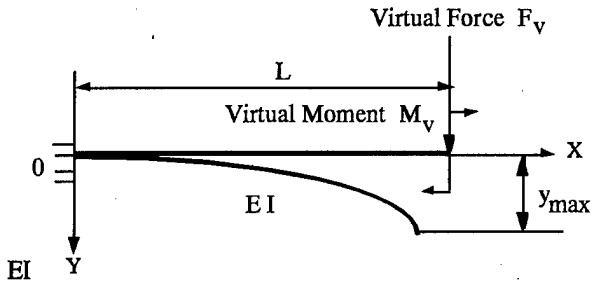


Fig.9 Model of Virtual Force

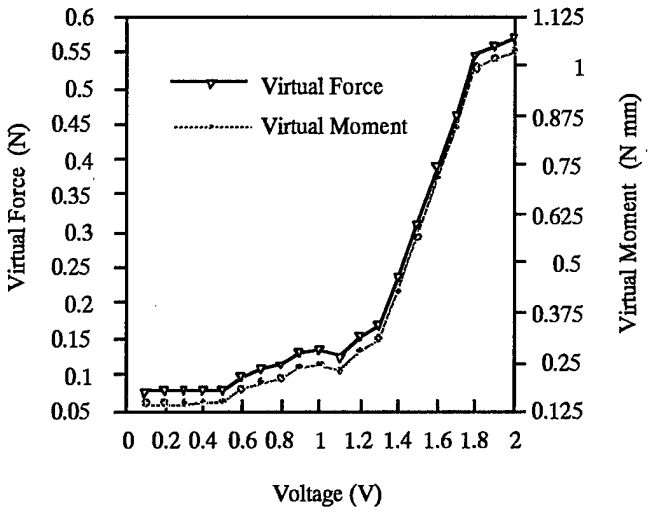


Fig.10 Calculation Results of Virtual Force

The maximum displacement f_{max} of ICPF actuator are measured by changing the voltage from 0.1V to 2V. By using the experimental results, we carried out the calculation of virtual moment M_V and virtual force F_V. The calculation results are shown in **Fig.10**. It is known that the maximum virtual force is 0.57 N.

Table 2 Specification of Prototype Microrobot

Size	10mm × 40mm
Weight	0.6g
Material	Wood
Actuator	ICPF Actuator (0.2 × 3 × 13mm)
Power Supply	Electricity (e.g. 2v, 0.14A)

6. PROTOTYPE FISH MICROROBOT

The prototype of developed microrobot using ICPF actuator is shown in **Fig.2**. The specification of the microrobot is 10mm in width and 40mm in length (body 15mm without tail) as shown in **Table 2**. The body of microrobot is mainly made of wood material for lightweight. In to verify the mechanism of the microrobot, we carry out the swimming experiments in water by changing the voltage frequency.

7. EXPERIMENTAL RESULTS

We made the swimming experiments of the prototype microrobot using a measurement system shown in **Fig.11**. The propulsive forces for various frequencies were measured using a laser displacement sensor, an electric balance and a copper beam. The copper beam is soft enough to be bent by the propulsive force. The electric balance is used for the force evaluation. We also measured the propulsion speed for various frequencies using a high speed camera. The average value of over 20 data is used as the final test data. By changing the frequency from 0.2Hz to 5Hz at 2.5 voltage input, the experimental results of average propulsive force, and average speed are shown in **Fig.12**. The experimental results show that the moving speed 1.34mm/s~5.35mm/s can be obtained by changing the voltage frequency.

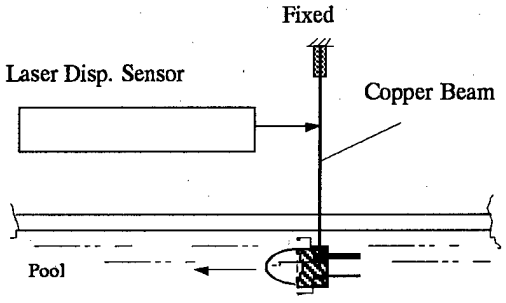


Fig.11 Measurement System of Propulsion

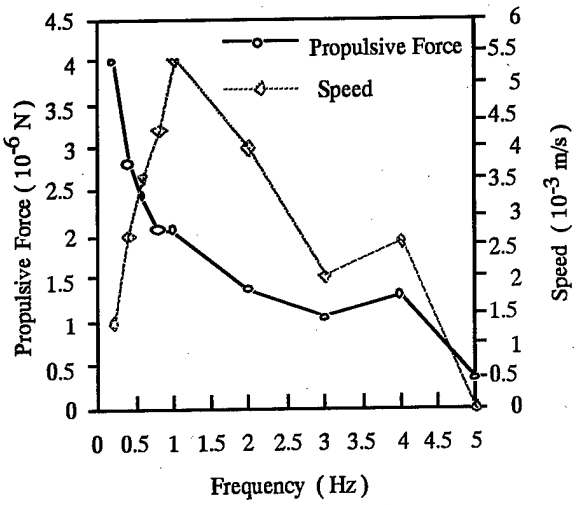


Fig.12 Experimental Results (2.5V)

8. CONCLUSIONS

In this paper, we propose a new prototype model of an underwater microrobot in water using **ICPF** actuator. It has two tails with a fin driven respectively. We also discussed the structure, motion mechanism, Characteristic of the microrobot is measured by changing the frequency of input voltage from 0.1Hz to 5Hz in water.

The research illustrates

(1) The structure of the underwater microrobot is effective.

(2) The swimming speed can be controlled by changing the voltage frequency.

(3)The moving motion in the directions (forward, right turn and left turn) can be realized by changing frequency f1, f2 of the electric voltage.

ACKNOWLEDGEMENTS

This study is supported by Research Foundation for the Electrotechnology of Chubu, and the Tateisi Science and Technology Foundation.

REFERENCES

[1] Proc. of the 1st IARP Workshop on Medical and Helthcare Robots, Ottawa, Canada, pp.789- 792, June 23 -24, 1988.

[2] Special session on Biorobotics, Proc. 12th IEES/EMBS Conf., Philadelphia, U.S.A., pp.1942-1943, November 1-4, 1990.

[3]Fukuda, Hosokai, Ohyama, Hashimoto and Arai, "Giant Magnetostrictive Alloy(GMA) Applications to Micro Mobile Robot as a Micro Actuator without Power Supply Cables", Proc. IEEE Conf. on MicroElectro Mechanical Systems, pp.210-215, Cincinaati, Ohio, May 1990.

[4]L. Fearing, "Micro Structures and Micro Actuator for Implementing Sub-millimeter Robots", Precision Sensors, Actuators and Systems (Kluwer Academic Publishers), pp.39-72, 1992.

[5] T. Fukuda, Hosokai et al, "Distributed Type of Actuator by Shape Memory Alloy and its Application to Underwater Mobile Robotic Mechanism", Proc. IEEE Conf. on Robotics and Automation, Vol.2, pp.1316-1332, Nara, Japan, Jan. 1991.

[6]Fukuda, Kawamoto, Arai and Matsuura, "Mechanism and Swimming Experiment of Micro Mobile Robot in Water", Proc. IEEE Con. on Robotics and Automation, Vol.1, pp.814-819, San Diego, California, May 1994.

[7]Fukuda, Kawamoto, Arai and Matsuura, "Steering Mechanism of Underwater Micro Mobile Robot", Proc. 1995 IEEE Con. on Robotics and Automation, Vol.1, pp.363-368, Nagoya, Japan, May 1995.

[8] M. Mojarrad and M. Shahinpoor, Biomimetic Robot Propulsion Using Polymeric Artificial Muscles, Proc. of 1997 IEEE International Conf. on Robotics and Automation, pp.2152-2157, New Mexico, USA, (1997)

[9] S. Guo, T. Fukuda, K. Kosuge, F. Arai, K. Oguro and M. Negoro, "Micro Catheter System with Active Guide Wire", Proceedings 1995 IEEE International Conference on Robotic and Automation, Vol.1, 79-84, Nagoya, JAPAN.

[10] Keisuke Oguro, Kinji Asaka and Hiroyasu Takenaka, "Polymer Film Actuator Driven by a Low Voltage", Proceedings of 4th International Symposium on Micro Machine and Human Science, pp. 39-40, JAPAN (1993).

[11] R.Kanno, A. Kurata, M. Hattori, S. Tadokoro and T. Takamori, "Characteristics and Modeling of ICPF Actuator -- 2nd Report: Frequency Characteristics ", Proceedings of JSME Annual Conference on Robotics and Mechatronics (ROBOMEC'94), pp. 1206-1209, Kobe, Japan 1994 (in Japanese).

[12] Y. Osada, H. Okuzaki and H. Hori: "A Polymer gel of electrically driven moiety", Nature, Vol. 355, pp. 242 - 244 (1992).

[13] R.McNeill Alexander, "Exploring Biomechanics Animals in Motion", 1992, W.H.Freeman and Company, pp.182-228.

[14] Y. Hirose, T. Shiga, A. Okada, T. Kurauchi, "Gel Actuators Driven by an Electric Field", Proc. of 3rd International Symposium on Micro Machine and Human Science, pp.21-26, 1992.

[15] Bone. Q, Marshall. N. B., "Biology of Fishes", Blackie and Son Limited, 1982.

[16] Maddock. L, Bone. Q et al , "Mechanics and Physiology of Animal Swimming", Cambridge University Press, 1994.

In-Pipe Wireless Micro Locomotive System

Hideaki NISHIKAWA, Takanari SASAYA, Takayuki SHIBATA, Takashi KANEKO,
Naoki MITUMOTO, Shinichirou KAWAKITA, and Nobuaki KAWAHARA

Research Laboratories, DENSO CORPORATION
500-1, Minamiyama, Komenoki, Nisshin, Aichi, 470-0111 JAPAN

Abstract

We have developed an in-pipe micro locomotive system. This system is composed of an outside host and a microrobot. The outside host supplies energy and transmits commands to the robot by using microwaves. The microrobot is 9.5 mm in diameter and 60 mm in length. The microrobot moves in a pipe of 10 mm diameter without wire. The microrobot consists of a microwave (RF) module used for energy supply and communication, a control circuit and a locomotive mechanism using a piezoelectric bimorph actuator. The RF module consists of a compact antenna, power divider, rectifying circuits, filter and communication MMIC. The antenna receives two frequencies of microwaves: 22 GHz for energy supply and 24 GHz for communication. The rectifying circuits convert the microwave into DC. The demanded energy of 480 mW is supplied via microwave. The control circuit drives the locomotive device and other devices installed in the robot by outside commands. The direction and speed of the system are also controlled by commands. The condition of the system is communicated between the robot and the outside host. The locomotive mechanism using a piezoelectric bimorph actuator moves according to inertia drive method.

1. Introduction

We have been developing a micromachine system for inspection on the inner surface of thermoconduction tubes of power plants under a Japanese national project. As the prototype of this system, we developed a wired in-pipe inspection micromachine that moves in a curved pipe and detects cracks in the pipe [1]. With a diameter of 5.8 mm and an overall length of 20 mm, the micromachine fits inside 8 mm piping and is inertia-driven [2] while searching for cracks in pipe walls using an eddy current sensor. The machine consists of an eddy current sensor, inertial mass, piezoelectric stacked actuator, base, radiation fin and three clamps. Wires are used for energy supply and signal monitoring of the eddy current sensor. Through development of the inspection micromachine, problems unique to microtechnology have been identified. One of the problems is wiring for the power supply and signal monitoring. Even if the diameter of the wire is as thin as 18 μm, the weight of the wire is heavy enough for the 1 g micromachine, and the hardness of the wire is hard enough for the machine. Therefore, the wireless system is strongly needed for micromachines, because the wire limits the movement of the machine. In our previous work, we have developed a wireless energy supply method utilizing microwave [3]. We also developed a 15 mm diameter in-pipe locomotive mechanism whose power was suplied from outside by microwave [4].

We are now developing an advanced wireless in-pipe inspection system shown in Figure 1. The system is designed to move in a pipe with a diameter of 10 mm, take pictures of the pipe walls, and transmit these images through a wireless communication system. To realize this system, a wireless energy supply system, wireless communication system, control circuits, and locomotive mechanism suitable for a wireless system are needed.

In this study, we developed a microwave energy supply system, microwave communication system, control circuits, and locomotive mechanism, and developed an in-pipe wireless micro locomotive system to verify the function of the devices.

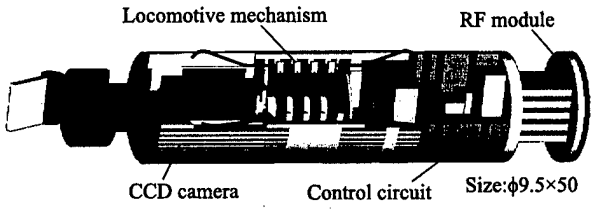


Fig.1 Wireless in-pipe inspection system.

2. System Configuration

The total system is composed of the outside host and in-pipe microrobot, as shown in Figure 2.

The host supplies microwave energy to the robot and communicates with the robot. For the wireless energy supply, we

1999 INTERNATIONAL SYMPOSIUM ON
MICROMECHATRONICS AND HUMAN SCIENCE
0-7803-5790-6/99/ $10.00 ©1999 IEEE.

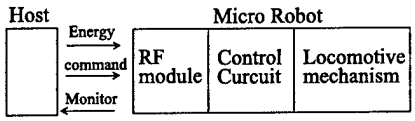


Fig.2 System configuration.

have proposed an in-pipe microwave energy supply and communication system for the microrobot. Microwaves are easily transmitted in a metal pipe, because metal pipe is regarded as a circular waveguide. Configuration of the host RF system is shown in Figure 3. Microwaves produced at the oscillator are amplified and conducted by the pipe. Microwaves are then received by an antenna attached to the microrobot within the pipe. The received microwave is converted to direct current and demodulated to the command signal at the RF module of the microrobot.

In this system, the pipe is regarded as a circular waveguide, and pipe diameter and frequency are closely related, as shown in Figure 4, and the transmitted frequency is classified into three states, as shown in Figure 4. These states are the cut-off area, TE_{11} mode area, and high mode area.

In the cut-off area, the microwave of lower frequency cannot transmit in the pipe. In the TE_{11} mode area, which is the dotted area in Figure 4, the microwave easily transmits in the pipe at a lower loss. In the high mode area, the microwave produces many high order modes and the transmitting loss is increased. For that reason we use TE_{11}, which is the dominant mode of the circular waveguide, as the microwave transmission mode. The transmission frequency is in the vicinity of 23 GHz in a pipe of 10 mm in diameter. At the developed system, microwaves are used not only for energy supply but also for communication. So we used 22 GHz for energy supply and 24 GHz for communication.

The microrobot consists of a RF module, control circuit, and locomotive mechanism.

The RF module receives two frequencies of microwaves: 22 GHz for energy supply and 24 GHz for communication.

The control circuit monitors the output voltage of the RF module and stabilizes its own output voltage. The control circuit generates saw-toothed wave voltage to drive the locomotive mechanism, and controls the direction and speed of the robot according to outside commands.

The locomotive mechanism is composed of a multi-layered piezoelectric bimorph actuator and is driven by saw-toothed wave voltage. The mechanism is driven by an inertial drive method [2].

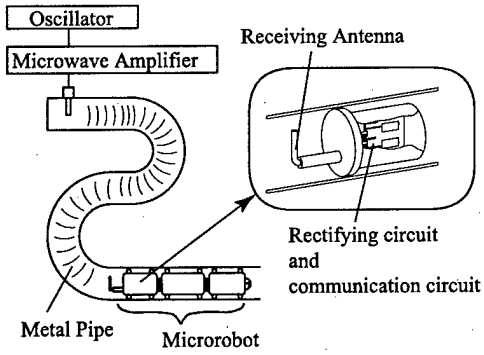


Fig.3 Configuration of host RF system.

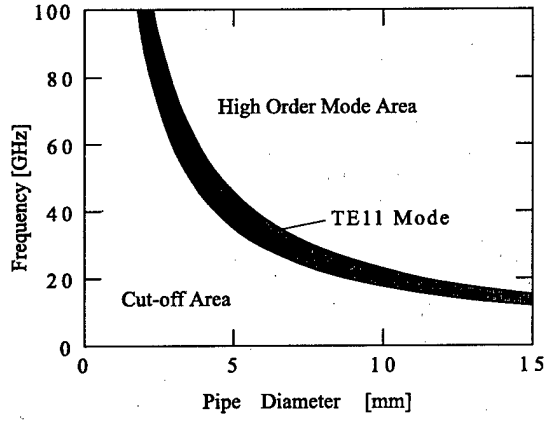


Fig.4 Relation of diameter and frequency.

3. Host

The host consists of a host computer and host RF. The host computer generates commands to control the microrobot, including speed and direction of the robot. Furthermore, the computer receives voltage data of the microrobot, displays the data, and controls the power of supplying microwaves. The host RF is described as the following.

3.1 Host RF

3.1.1 Energy supply

The actual transmitter of the host RF system is shown in Figure 5. In general, when a microwave of fixed frequency is transmitted in the pipe, a standing wave is produced between the coaxial waveguide adapter and the antenna attached to

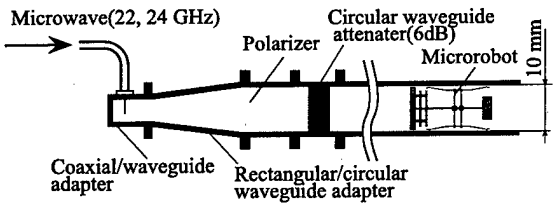


Fig.5 Configuration of microwave transmission system.

the microrobot. The received power fluctuates more than 10 dB and depends on the distance between the transmitter and the microrobot, because the microrobot moves in the pipe. In order to stabilize the received power, a 6 dB attenuator is placed to suppress the standing wave between the coaxial waveguide adapter and the microrobot. In addition to this, the frequency of the microwave is continuously swept between 21.5 and 22.5 GHz, so that the microwave does not stay at the resonance frequency. Moreover, a polarizer is placed to polarize the microwave in a circumferential direction so that the microrobot can receive steady power if it rotates in the pipe. Thus stable energy transmission is achieved. In addition, circumferential directions of two kinds of microwaves, for energy and for communication, are reversed to separate these microwaves.

3.1.2 Communication

Command data is transferred to the robot, in which the microwave is modulated by the amplitude shift keying method (ASK). Condition data is transferred from the robot by the phased shift keying method (PSK).

4. Microrobot

The microrobot consists of a RF module, control circuit, and locomotive mechanism.

4.1 RF module

The RF module consists of a stacked patch antenna, two rectifying circuits and a communication circuit. The antenna receives two frequencies of microwaves and isolates them. The rectifying circuit converts the microwave for energy supply (22 GHz) into direct current. The communication circuit receives the host command and answers the voltage condition of the robot.

4.1.1 Stacked patch antenna

The antenna consists of two patch antennas; one is for 22 GHz of energy supply and the other is for 24 GHz of communication. The antenna has a two-layered structure, as shown in Figure 6.

This antenna consists of a base and two antenna elements, which are three metal disks. The gap between the large antenna element and the base is air. The other gap is made of Teflon whose dielectric constant is about 6. The larger the dielectric constant of the antenna substrate becomes, the smaller the antenna and the narrower the band become. Therefore, we used Teflon for the communication antenna in order to reduce the size and to make the receiving band narrow. For the design of this antenna we carried out an electromagnetic analysis using the finite element method to optimize the element shape. The antenna is compact enough to be installed in the robot.

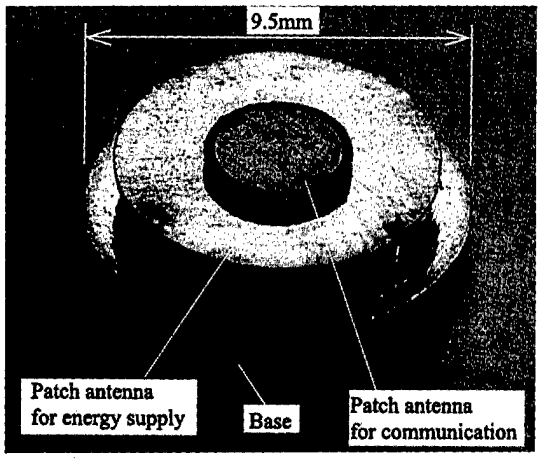


Fig.6 Stacked patch antenna.

4.1.2 Rectifying circuit

The rectifying circuits convert the microwave into DC. The rectifying circuit consists of a power divider and four GaAs MMIC rectifiers shown in Figure 7. The size of the circuit is 7 mm by 13 mm. The maximum converted energy of MMIC is 60 mW. As the demanded energy of the system is 480 mW, eight MMICs must be integrated in the system. The microwave is received at the antenna, distributed to the two rectifying circuits, distributed to four MMICs at the power divider, and supplied to the eight MMICs. The efficiency of the rectifying circuit is approximately 30%. To reduce the size of the circuit, we have designed the power divider and the circuits using computer electromagnetic analysis for optimization.

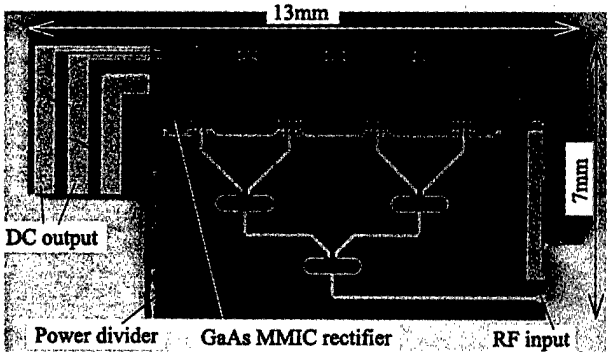


Fig.7 Rectifying circuit.

4.1.3 Communication circuit

The communication circuit receives commands from the host and transmits the voltage condition data to the host. The circuit consists of a filter and communication MMIC, as shown in Figure 8. The filter isolates the communication microwave from the energy microwave. The isolation of the filter is 20 dB.

The communication MMIC modulates and demodulates microwaves by the signal from the control LSI.

The size of the circuit is 7 mm by 13 mm. The communication bit rate is 2.5 megabits per second.

To realize a low-power consumption communication circuit, we adopted a transponder method for communication from the microrobot to the host. This method is generally used in an IC card reader system. The host transmits a carrier wave to the microrobot, and the communication circuit in the microrobot modulates and reflects the carrier wave. The strong point of this communication method is that the robot does not need a transmitter and that the power consumption of the communication is very low. Therefore, we believe this communication method is very suitable for microrobots.

The command data to the robot is modulated by the amplitude shift keying method (ASK). The condition data of the robot is modulated by the phased shift keying method (PSK). To demodulate the ASK signal, only a filter and one diode are required in the robot. Therefore, this method reduces the size of the communication circuit.

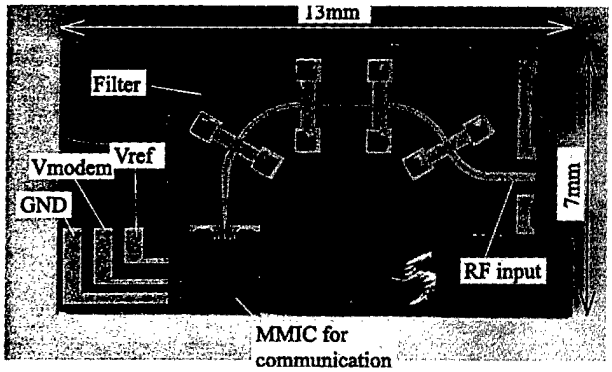


Fig.8 Communication circuit.

4.1.4 Structure of microwave module

The microwave module consists of the stacked patch antenna, two rectifying circuits for 3.3 V and 15 V, and a communication circuit. Although the size of each element is minimized, it is difficult to package them in conventional packaging as a plane structure, because the pipe diameter is small at 10 mm. For that reason, the elements are packaged in a three-dimensional structure shown in Figure 9. The two rectifying circuits and the communication circuit are mounted on a copper plate and vertically attached to the stacked patch antenna. Each circuit and antenna is connected by a coaxial cable and soldered to each other; each copper plate is soldered to the base of the antenna. The solder used in connecting the plate and the base has a low melting point to prevent a break in the connection between the coaxial cable and other elements.

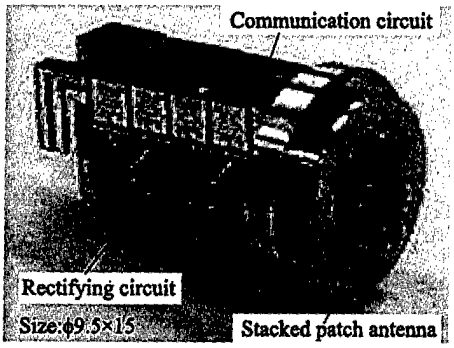


Fig.9 Structure of the microwave module.

4.2. Control circuit

The control circuit consists of a voltage regulator and voltage monitor, a system control gate-array, and a drive circuit of the locomotive mechanism. The voltage monitor detects the output voltage of the RF module and sends the data to the gate-array. The gate-array converts the data to digital and sends it to the RF module.

The gate-array also generates a timing signal to generate saw-toothed wave voltage for locomotion. The timing signal controls the direction and speed of the robot according to the host command.

4.2.1 Drive circuit of locomotive mechanism

The drive circuit generates saw-toothed wave voltage from DC voltage supplied from the voltage regulator. In order to make the circuit compact we developed a simple drive circuit shown in Figure 10. The circuit consists of four analog switches, two resistors, and a PZT actuator, which is used as a capacitor. In this circuit, the combination of the PZT actuator and resistors works for the CR circuit to generate saw-toothed wave voltage. The gate-array controls the switches, and generates forward and backward voltage as shown in Figure 11. This generation method is suitable for the microrobot because its power consumption is low.

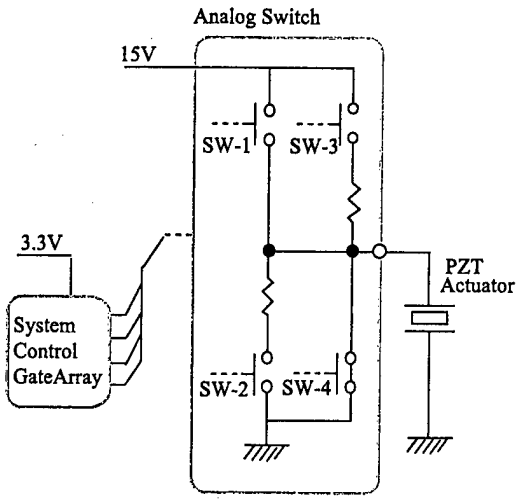


Fig.10 Drive circuit of the locomotive mechanism.

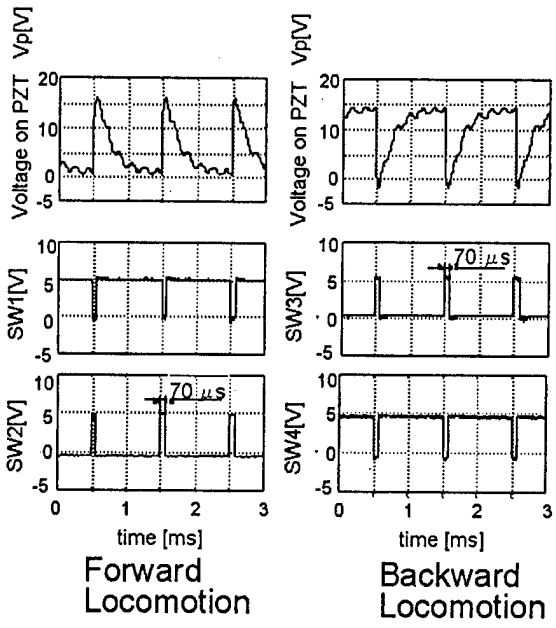


Fig.11 Saw-toothed wave voltage for locomotion.

4.2.2 Packaging of control circuit

Packaging is inevitable for the microrobot because the size of the robot is limited by the 10 mm diameter of the pipe. The total weight of the microrobot should be light because the power of the micro locomotive mechanism is limited. To realize a compact circuit, we used flip-chip assembly for the gate-array and the other eight LSIs, and they are packaged on a circuit board by the flip-chip assembly method.

The gate-array is made of 0.35 μm CMOS, the pad pitch is 120 μm, and the pad size is 88 μm. Stud bumps are formed on each pad of the bare chips. The bumps are bonded on a fine pitch six-layered printing circuit board (PCB) by using an anisotropic conducting paste (ACP). The chips are precisely aligned, mounted and heated on the PCB by a chip-bonding machine. ACP is composed of heat-hardening resin and many conductive particles. The advantages of using ACP are that the contacts between the bumps and the PCB are done by heating, and that stress between them is released.

4.3 Locomotive mechanism

The locomotive mechanism consists of a multi-layered piezoelectric bimorph actuator. The mechanism is driven by saw-toothed wave voltage and moves according to the inertia drive method.

4.3.1 Structure of locomotive mechanism

Power consumption of the actuator should be minimized, and in order to reduce the power consumption, we developed a new actuator whose displacement is larger compared with the piezoelectric stacked actuator [5].

The mechanism consists of an eight-layered bimorph, center shaft that connects each center of the bimorph, and four clamps that connect the edges of each bimorph shown as Figure 12 (eight-layered type). When the actuator is operated at 15 V, it deforms approximately 6 μm between the center shaft and the clamps.

The deformation behavior of each piezoelectric bimorph is shown in Figure 13. The piezoelectric bimorph consists of a metal plate and PZT, which is bonded on both sides of the plate.

In Figure 13, when an appropriate voltage is applied to the piezoelectric bimorph between the elastic plate and the surface electrodes, the upper PZT vertically expands and horizontally contracts; in contrast, the lower PZT horizontally expands and vertically contracts. As a result, the piezoelectric bimorph bends like the lower Figure 13. This mechanism enlarges the displacement of the actuator but reduces the gen-

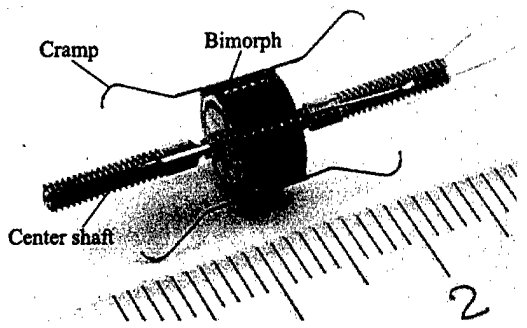


Fig.12 Developed locomotive mechanism using multi-layered PZT bimorph actuator.

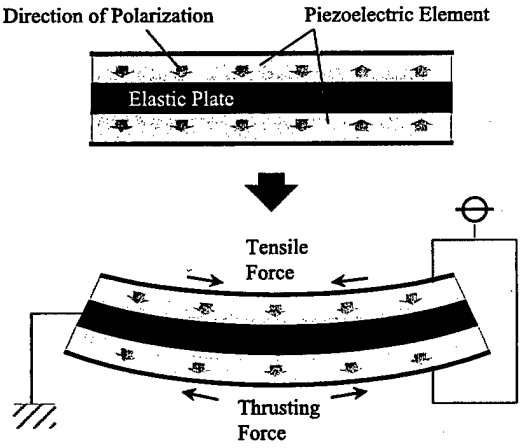


Fig.13 Deformation behavior of a piezoelectric bimorph (cross section).

erating force. Therefore, the actuator has a multi-layered structure that controls the generating force by the layer number.

4.3.2 Principle of locomotive mechanism

The principle of the locomotive mechanism is shown in Figure 14. The mechanism moves according to the inertia drive method. Initially, the locomotive device is suspended in tension to the pipe wall with clamps. The locomotive mechanism is driven by saw-toothed wave voltage. When the voltage is slowly increased, the actuator slowly deforms. The mass then moves upward, but the clamps do not move because the limiting frictional force between the clamps and the pipe wall exceeds the inertial force of the mass. When the voltage is quickly decreased, the actuator quickly recovers. The clamps then slip upward, but the mass does not slip because the inertial force of the mass exceeds the limiting frictional force between the clamps and the pipe wall. The combination of clamp slippage and mass movement creates an upward motion. In contrast, when the voltage is quickly increased and slowly decreased, the mechanism moves downward.

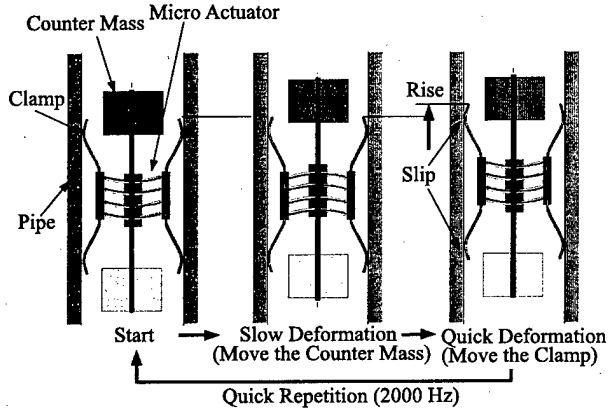


Fig.14 Principle of locomotive mechanism.

4.4 Developed microrobot

A prototype of the microrobot has been developed. The robot consists of a microwave module, control circuit, and locomotive device shown as Figure 15. The system receives microwaves of 480 mW and moves in a pipe 10 mm in diameter. The direction and speed of the system are controlled by outside commands. Table 1 summarizes the major specifications of the microrobot.

5. Conclusion

We developed an in-pipe wireless micro locomotive system consisting of a host and microrobot. The host transmits microwaves to the microrobot, and the microrobot moves in a 10 mm pipe without wire. To realize the microrobot, a RF module, control circuit and locomotive mechanism were developed. We will develop an advanced system, including CCD camera and wireless image transmission circuit, in collaboration with TOSHIBA and SANYO by the year 2001.

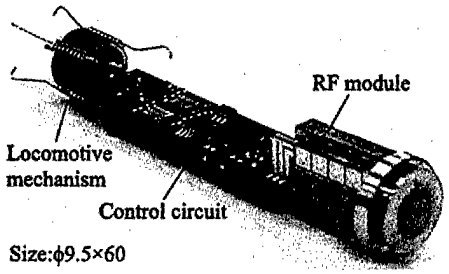


Fig.15 Developed microrobot.

Table 1 Major specifications.

Pipe Diameter	10 mm
Size of the Microrobot	ϕ9.5mm x 60mm
Microwave Frequency (Energy) (Communication)	21.5 GHz ~ 22.5 GHz 24 GHz
Transmission Loss	< 1dB / m
Type of Receving Antenna	Stacked pach anttena
Receiving Power	480 mW

Acknowledgment

A part of this work was performed under the management of the Micromachine Center as the Industrial Science and Technology Frontier Program (ISTF), Research and Development of Micromachine Technology of MITI, supported by the New Energy and Industrial Technology Development Organization (NEDO).

REFERENCES

[1] T. Idogaki, H. Kanayama, N. Ohya, H. Suzuki, and T. Hattori, "Characteristics of Piezoelectric Locomotive Mechanism for an In-Pipe Micro Inspection Machine", Proceedings of the 6th International Symposium on Micro Machine and Human Science, pp. 193-198, 1995, IEEE.

[2] T. Higuchi, M. Watanabe, and K. Kondou, "Precise positioner utilizing rapid deformations of a Piezoelectric Element", JSPE-54-11, pp. 2107-2112, 1988.

[3] T. Shibata, T. Sasaya, and N. Kawahara, "Microwave Energy Supply System for In-Pipe Micromachine", Proceedings of the 1998 International Symposium on Micromechatronics and Human Science, pp. 237-242, 1998, IEEE.

[4] T. Sasaya, T. Shibata and N. Kawahara, "In-Pipe Wireless Micro Robot", Transducers `99 Digest of Technical Papers Vol. 2, pp. 1058-1061, 1999.

[5] S. Kawakita, T. Isogai, N. Ohya, and N. Kawahara, "Multi-Layered Piezoelectric Bimorph Actuator", Proceedings of the 1997 International Symposium on Micromechatronics and Human Science, pp. 73-78, 1997, IEEE.

Screw Principle Microrobot Passing Steps in a Small Pipe

Toshiaki Yamaguchi
NEC Corporation, Production Technoplogy Development
3-484 Tsukagoshi Saiwai-ku Kawasaki, 210-8511
JAPAN

Yoshihito Kagawa, Iwao Hayashi, Nobuyuki Iwatsuki, Koichi Morikawa
Tokyo Institute of Technology, Faculty of Engineering
2-12-1 Ohokayama Meguro-ku Tokyo, 152-8552
JAPAN

and

Katsumi Nakamura
Kantool Giken Coporation
70-4 Kawaihontyo Asahi-ku Kawasaki, 241-0803
JAPAN

Abstract:
In order to pass the "screw principle microrobot", which the authors have proposed to inspect the inner wall of small pipes in plumblings, to pass a stepped portion automatically, a step climbing mechanism which does not require any special actuators nor motion control, is proposed. A prototype was designed to pass both concentric and eccentric steps at the junction between two pipes 100mm and 75mm in diameter. The running performance is experimentally examined for some pipes which have a step at different positions.

1. INTRODUCTION

Various pipes such as straight pipes, bend pipes, branches, and stepped pipes are used in the plublings of atomic power plants, chemical plants, and so on, and maintenance of these pipes is one of the very important issues to avoid disasters and to keep our daily life comfortable . For this reason, a screw principle microrobot which can automatically pass through the stepped portion is proposed in this paper, and a prototype of the microrobot was practically made to pass through the stepped portion between two pipes 75mm and 100mm in inner diamtere without any special actuators controlled from the outside. The running performaces of the prototype was also experimentally examined for eccentric and concentric steps at different positions between those two pipes.

2. SCREW PRINCIPLE MICROROBOT

Figure 1 shows the schematic diagram of the driving unit of the screw principle microrobot which the authors have proposed, and the principle of driving. The cylinder is the inner wall of a pipe. The tyres are mounted on the main body of the microrobot with an inclined angle against the center axis of the pipe, and are also pressed onto the inner wall. The tyres can rotate around their axles freely. Applying a driving torque to the main body of the microrobot as shown in the figure, the tyres roll spirally on the inner wall, and the microrobot moves forwards, as the result. If the microrobot is required to go back, a reverse driving torque is applied.

Figure 2 shows a practical driving method of the screw principle microrobot. The microrobot is composed of some driving units conneceted with each other with couplings. The driving torque is applied from the outside through a flexible wire. A CCD camera to watch the inner wall is mounted on the nose of the microrobot, and the

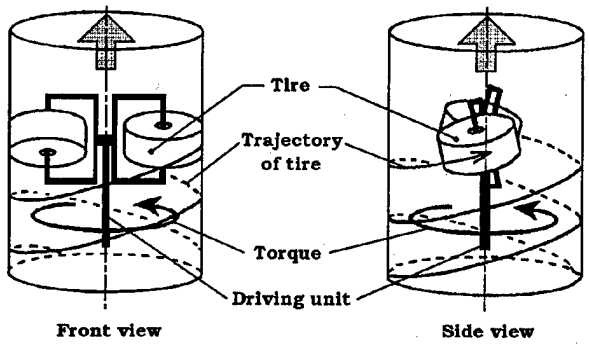


Fig.1 Schematic diagram of the driving unit of the "screw principle" micro robot

1999 INTERNATIONAL SYMPOSIUM ON
MICROMECHATRONICS AND HUMAN SCIENCE
0-7803-5790-6/99/ $10.00 ©1999 IEEE.

signal cables are connected to an external CRT through the inside of the flexible wire.

This microrobot has the following advantages:

(1) to move forward and backward only by rotating the main body.
(2) to be driven by a low driving torque since the driving unit istseld is a speed reduction mechanism.
(3) to increase a traction force easily by connecting many driving units
(4) to be able to stop and keep the position even in vertival pipes due to the function of selfrock since the inclined angle is small.

3. MECHANISM TO PASS THROUGH STEPPED PORTION

3.1 Specifications Required

Figure 3 shows the concentric and eccentric stepped portions at the junction between two pipes. The following performances are required for the screw principle microrobot to pass these stepped portion:

(1) to pass through the concentric and eccentric steps of 12.5mm and 25.0mm, respectively, with only one mechanism,
(2) to pass through without any special actuators,
(3) to pass through both at the forward and backward motion,
(4) to move apporximately 20m.

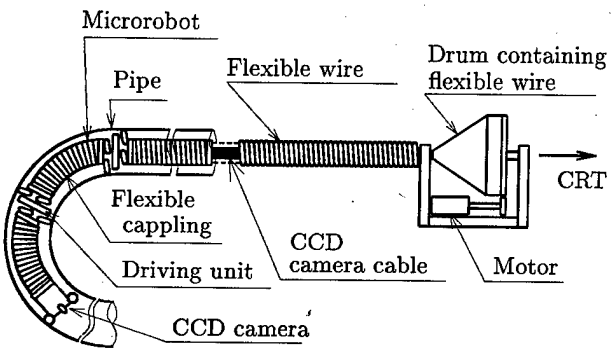


Fig.2 Practical driving method

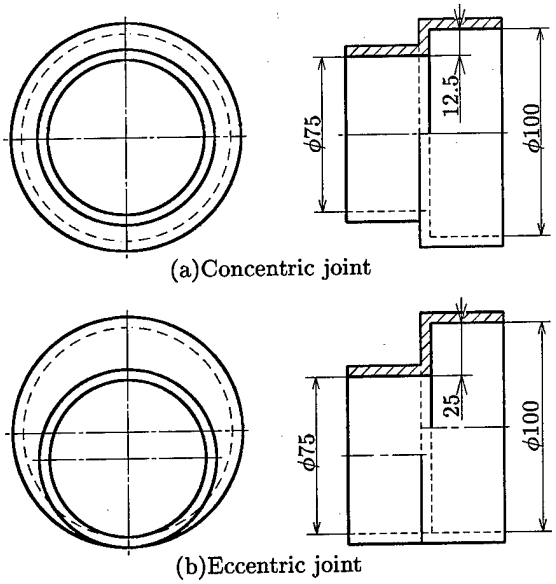


Fig.3 Concentric and eccentric steps (mm)

3.2 Basic Concept of Driving Unit

Figure 4 shows the schematic diagram of the driving unit which can pass through the stepped portions. The basic concepts are as follows:

(1) Two small tyres, which are mounted on an arm, climb the step half by half, since a large tyre is not be able to use from the restriction of space.
(2) The tyres are inclined with an angle, α, as shown in the figure to climb the steps easily.

The three arms with these two small tyres are mounted equally-spaced on the front and back disks of the main body, respectively. Also these arms are pressed onto the inner wall of pipes by a spring fixed at their roots.

(3) The construction is symmetrical in front and in the rear in order to climb both at the forward and backward motions.
(4) The arms for the forward and backward motions are connected with each other with a gear mechanism to prevent the arm for the backward motion from collising when the arm for the forward motion passes the steps.

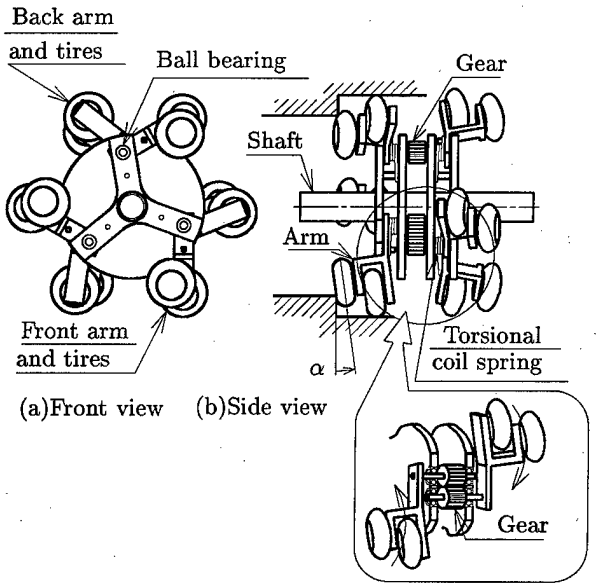


Fig.4 Driving unit climbing steps

Figure 5 shows the passing process of the driving unit based on the above concept. Figure 5(a) shows that the first half process where the inner tyre has climbed half the step; Figure 5(b) shows the second half process where the outer tyre is going to climb the remaining half; and Figure 5(c) shows the final stage where the driving unit runs in a smaller pipe after climbing the step.

4. Prototype of Driving Unit

Figure 6 shows the prototype of the driving unit based on the concept mentiond in Section. 3. The left and right figures show the front and side views, respectively. The outer diameter and length of the driving unit are approximaltely 110mm and 200mm, respectively, at the state that the coil springs mounted on the roots of the arms are free. The outer diameter, center diameter, and curcus diameter of the tyre are 14mm, 9mm, and 5mm, respectively.

5. Running Experiments

The experiments to pass the microrobot, which is composed of two driving units connected with each other with a coupling, through a step portion were conducted for the concentric and eccentric steps at the junction of two pipes 75mm and 100mm in diameter. The microrobot was driven by a driving shaft which was rotated by a motor. Also, the driving torque was meaured with a load cell which was mounted between the motor and the driving shaft.

Figure 7 shows one example of driving torques measured when the microrobot was going to climb the concentric step. In the figure, (1) is the value measured under the state that the microrobot was running in a pipe 100mm in inner diameter, (2) is the value measured under the state that the driving force was becoming lager and larger after the tyres had contacted the step, (3) is the value measured under the state that the tyres were climbing the step, and (4) is the value measured after the tyres had finished climbing. The three peaks observed in the period (3) appeared since the three tyres climbed the step one after another with a short interval after contacting the step.

Figure 8 shows one example of driving torques measured when the microrobot was going to climb the eccentric step. In the figure, (1) shows the state that the microrobot was running in a pipe 100mm in inner diameter. (2) shows

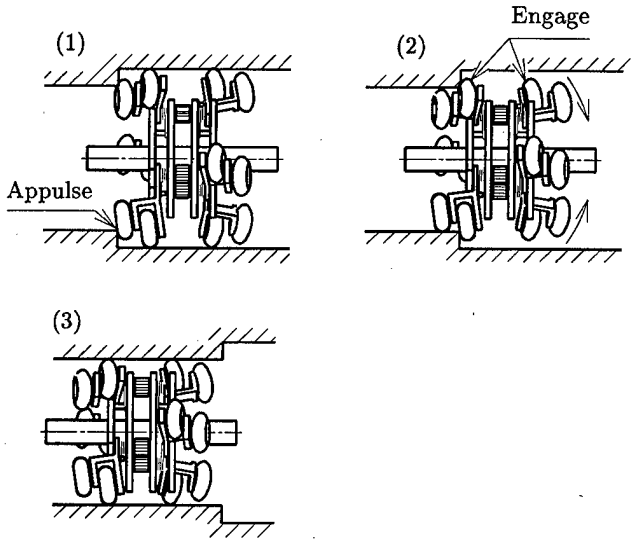


Fig.5 Climbing and passing processes of the driving unit

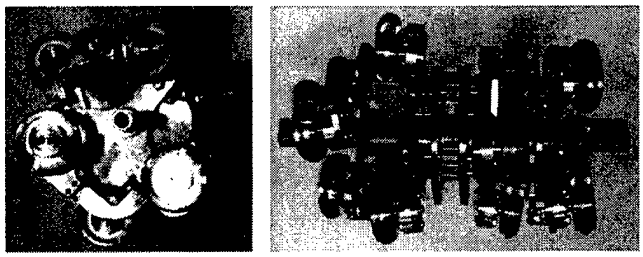


Fig.6 Prototype of driving unit

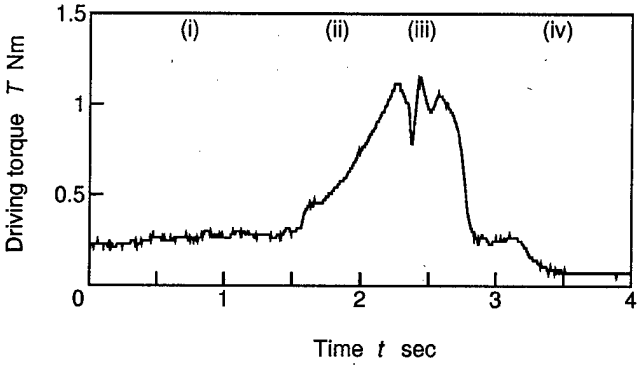


Fig.7 Driving torque measured for a concentric step

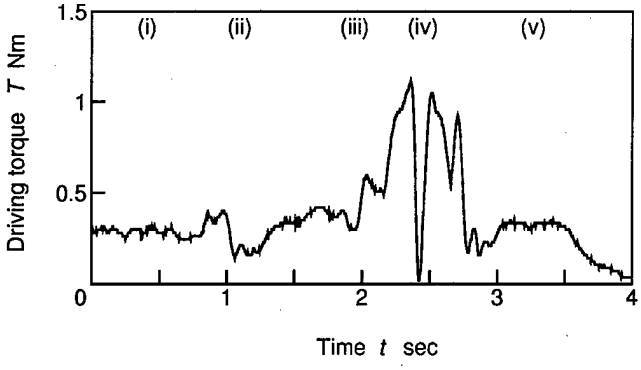


Fig.8 Driving torque measured for an eccentric step

the state that the inner tyres climbed the step. As seen in the region, the driving torque was small. This is becuase the force to press the tyres onto the inner wall was small since the angular displcements of coil springs were small. (3) shows the state that the driving torque was accumulated and was becoming large after the outer tyres contacted the step. (4) shows the instance that the outer tyres climbed the step. The large variations of driving torque are observed since the height of the step were different depending on the position to climb. (5) shows the state that the microrobot had climbed the step.

The long running experiments were next conducted by driving the microrobot with a flexible wire. Figure 9 shows one of the driving torques measured for the microrobot to pass a concentric step at a position 4m deep from the entrance of the pipe.In the figure, (1) shows the state that the microrobot was running in a pipe 100mm in inner diameter. (2) shows the state that the driving torque was accumulated and was becoming larger after the tyre contacted the step. (3) shows the state that the microrobot was running in a pipe 70 mm in inner diameter after passing the step.

Table 1 shows the driving torque which was purely required to climb the step; in other words, the value of driving torque which was obtained by subtracting the running torque from the peak value obtained when climbed the step. It is seen from this figure that the driving torque purely required to climb the step didn't changed evenif the position of the step was changed.

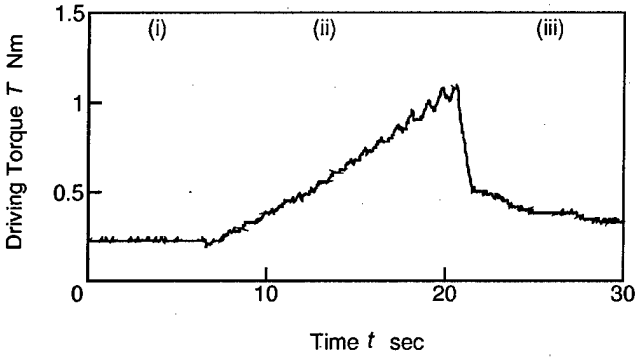


Fig.9 Measured driving torque for a step 4m apart from the entrance of the pipe

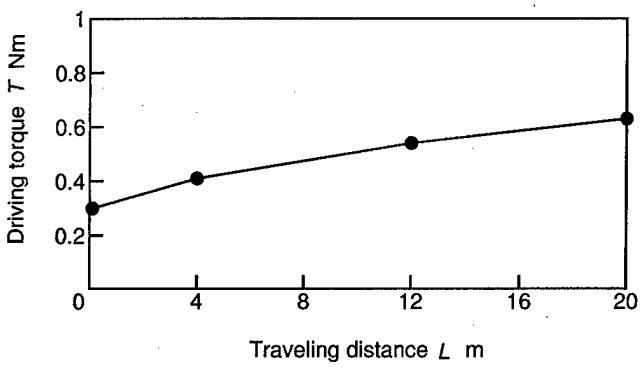


Fig.10 Driving torque for a long travel

Table 1 Maximum driving torque

Distance from the entrance m	Driving torque Nm		
	Concentric step	Eccentric step	Pipe (100mm)
0	0.92	1.02	0.14
4	0.88	0.82	0.22

Figure 10 finally shows the driving torque measured when the microrobot runned in a long pipe 70mm in inner diameter. From this figure it is seen that the driving torque increased as the running distance became longer. This is because the fricitional loss between the flexible wire and the inner wall of the pipe became larger as the running distance became longer. From this result it is noticed that the driving torque required to climb and pass the step at a distance is equal to the sum of the driving torque to run the distance of the pipe and the driving torque to climb the step.

6. Conclusions

The "screw principle" microrobot, which can climb and pass the concentric and eccentric steps at the junction, has been developed, and the followings have been obtained.

(1) The climbing mechanism with which the "screw principle" microrobot can climb and pass the concentric and eccentric steps at the junction has been proposed.

(2) The microrobot which can climb and pass the concentric and eccentric steps at the juntion of two pipes 75mm and 100mm in inner diameter have been worked out, and the running performances were experimetally examined.

References

[1] T. Morita et al., Development of mobile robot TOROVER III going up and down stairs, Journal of the Japan Society for Precision Engineering, Vol.60, No.10, 1495-1499 (1994) (in Japanes)

[2] T. Kagiwada et al., Robot Design for Stair Navigation, JSME International Journal Series C, Vol.39, No.3, (1996)

[3] Taguchi, Development of mobile robot moving on a rough land due to wheels with a leg, Proceedings of the third Symposium of the Japan Society of Robot Engieering, 61-66 (1993) (in Japanese).

Improvement of Characteristics of In-Pipe Micro Robot

Linzhi Sun Ping Sun Li Lian Xinjie Qin Zhenbang Gong

Dept. Of Precision Mechanical Eng., Shanghai University

Jiading(201800), Shanghai, P.R.China

E-mail: lzsun@online.sh.cn

Abstract:

This paper describes improvement of structure design based on previous study. The new micro robot with electromagnetic actuator possesses two opposite leg-sets mounting around main body instead of unidirectional mounting of old type. The moving speed characters of the new robot and other two small micro robots are studied. The new prototype can climb in *ϕ20mm* pipe forward or backward by applied voltage with different frequency.

Keywords: micro machine, In-pipe robot, electro-magnetic force

1. Introduction

The small pipe of diameter about *ϕ20mm* is widely used in industry, it is necessary to develop robot, which can climb into pipe to inspect and repair inside defects in order to prevent accident and to reduce economic loss.

Recent years, several micro robots or micro mechanisms in small pipe have been developed. It chiefly includes following kinds of actuator such as: earthworm type, screw friction drive type, PZT impact type, SMA type and some advanced achievement has been obtained. The diameter and length of the earthworm robot are *ϕ25×85mm*, walking speed are *2.2mm/s*, it was very slow and must be operated by air equipment[1]. The screw principle micro moving robot to be driven by slightly inclined friction wheels possesses *34-52mm/s* walking speed for straight and bent pipe and traction force of *12N*, but the length of its body are very long[2,]. The piezoelectric PZT actuator to generate driving force for the micro in-pipe machine has been actively studied by many researchers because of its high energy-efficiency and its quick time response A locomotive mechanism of *5.5mm* in diameter and *20mm* in length was developed with stack-type PZT actuator based on interaction of inertial impact force and friction force. It can move in *10mm* pipe at *6mm/s* velocity when the machine is operated by a serrated voltage[3]. A pin-type micro machine[4] and a new type locomotive mechanism[5] are developed with multi-layered bimorph piezoelectric element. It indicates better properties of moving speed and traction force as well as power consumption. Furthermore, some researchers are working on SMA actuator even if it has very low velocity.

Under the consideration of the advantages of electro-magnetic type actuator, we developed a micro robot based on electro-magnetic force. The first prototype of in-pipe micro robot possess main body size of *ϕ15×20mm* which can climb into horizontal or vertical pipe of diameter *ϕ20mm*. Power consumption of the micro robot is around *1.2watt* at speed of *6-8mm/s* even though it was a one direction moving mechanism[6].

This paper describes improvement of structure design of this type micro robot based on previous study.

2. Improvement of structure design

The configuration of our proposed electro-magnetic robot in small pipe is shown in figure 1-a. The main components of the robot include: a moving part m1 with inner plunger armature, an electro-magnet body m2, two sets of bronze pick feet mounting around these two parts and an elastic spring located between m1 and m2. These two sets of pick feet are orientated opposite to motion direction. When back and forth displacement generated by interaction of electromagnetic force and spring's elastic force is transferred to move the robots by means of the friction between thin bronze pick feet and inner surface of pipe. This prototype can be climbing in horizontal or in vertical direction at speed of 6-8mm/s when the small pipe is of diameter *ϕ20mm*[6].

1999 INTERNATIONAL SYMPOSIUM ON
MICROMECHATRONICS AND HUMAN SCIENCE
0-7803-5790-6/99/ $10.00 ©1999 IEEE.

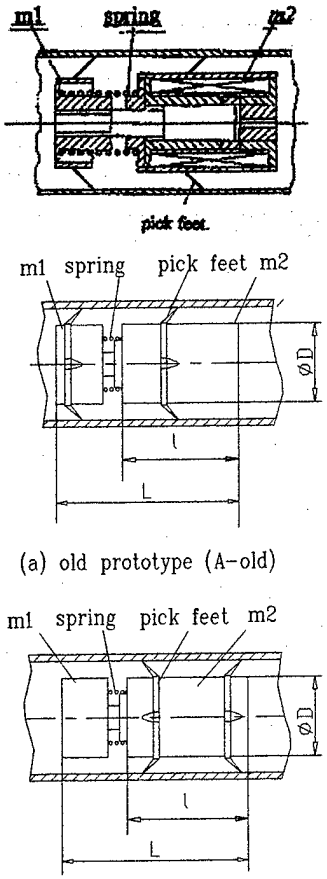


Fig. 1 Old and new prototype of micro robot

The moving principle of the old type structure is shown in author's paper[6]. It is obvious that the old prototype only can move forwards because it possess unidirectional leg-set, one leg-set is mounting on the counter mass 1, other leg-set is mounting on the main body separately.

For improving moving characters, several changes of structure design were done as follows.

2.1 Change of main body dimension

This structure change is for the purpose of reducing its weight and improving moving speed. As shown in table 1 the length of main body is changed from *20mm*(type A-old) to *14mm*(B-old), the weight is reduced from *19.5g* to *14g* even though its outside diameter D no changed. Other one robot changes its outside diameter from *ϕ15mm* to *ϕ11mm* with weight 9*g* (type C-old) but length is no changed.

Table 1. Design parameters

Type		A-old	B-old	C-old
Mass m1	*g*	5	5	5
Mass m2	*g*	19.5	14	9
Turns of coil	*N*	*2700*	1700	1060
Spring constant k	*N/cm*	9.21		4.78
Dimension of main body D×l	*mm*	*ϕ15×20*	*ϕ15×14*	*ϕ11×20*
Overall dimension D×L	*mm*	*ϕ15×30*	*ϕ15×22.5*	*ϕ11×26*
Total Weight	g	25	19	14
Leg-set mounting direction		Unidirectional	unidirectional	unidirectional

2.2 Change of leg-set on robot

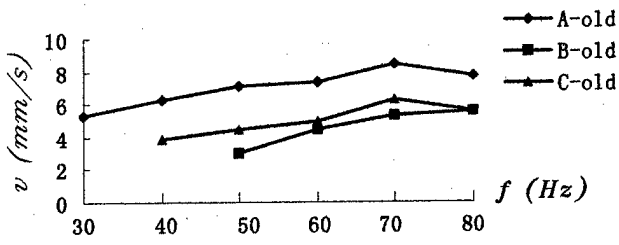
For the purpose to approach in both of forward and backward movement, the new structure design A-new is improved as shown in figure 1-b. That means to install all of the two leg-sets on main body with opposite pick feet instead of mounting on two moving parts m1 and m2 separately, and to increase the weight of counter mass m1 from *5g* to *15.2 g*. This is in order to generate bigger inertial impact force drive instead of pure friction driving between legs and tube surface.

Of course, it is obvious the moving principle for the new structure design should be changed because the leg-set on main body is different.

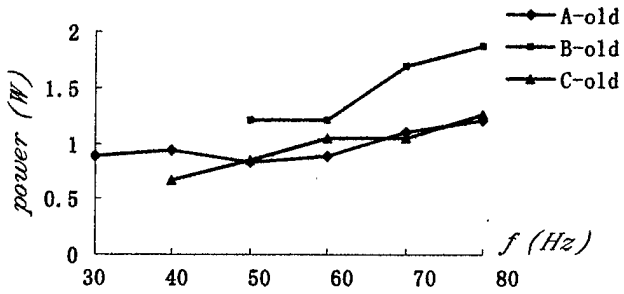
3. Characteristic experiment and moving principle analysis

3.1 Experiment of moving characters owing to reduce length of main body (type B-old) as well as reduce diameter of main body (type C-old) are as following.

The moving characters of three type A-old, B-old, C-old robots show in figure 2-a. It is obvious robot B-old can be moved forward at speed of *3.0-5.6mm/s* by frequency *50-80Hz*. Robot C-old can be moved at speed of *3.8-6.3 mm/s* by frequency *40 to 80Hz*. Its moving speed was lower than robot type A-old at speed of *5.3-8.4mm/s* by frequency *30-70Hz* separately. The power consumption of robot A-old and Robot C-old are lower than robot B-old in figure 2-b. The loss of power will be transferred to heat robot.



(a) Moving speed in relation frequency



(b) Power consumption in relation to frequency

Fig. 2 Moving speed and power consumption in relation to frequency

3.2 Experiment of the working clearance δ influence to moving characters

The working clearance δ is an important parameter in magnetic actuator. After determination of dimension of magnetic inner structure, the clearance δ affects to magnetic force directly and to step form of robot, therefore, involves in moving speed. We take the robot type C-old (*ϕ11×20mm*) to move into *ϕ20mm* pipe. The working clearance δ in relation to moving speed shows in figure 3. The prototype C-old possesses better result in moving speed at working clearance *0.1mm* than other clearances clearly.

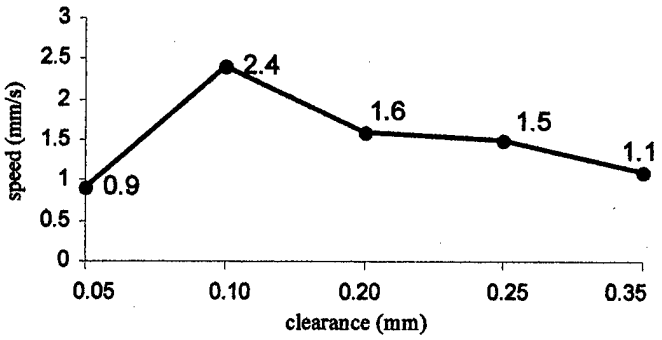
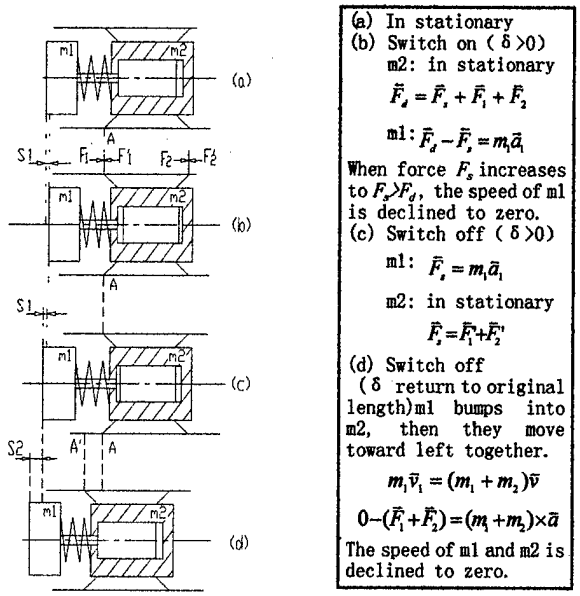


Fig. 3 Working clearance δ in relation to moving speed

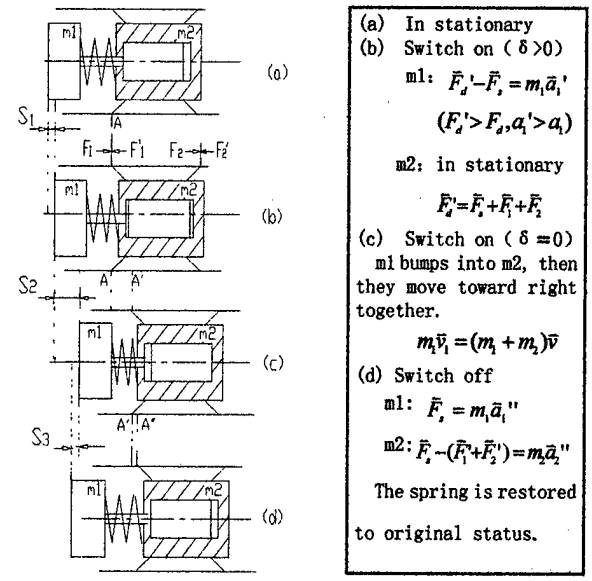
3.3 Experiment of moving characters by change of leg-set mounting on robot is as following.

The moving principle of the new structure design can be explained as figure 4.

When same testing equipment and electric instrument of previous study is used in experiment, after change of leg-set mounting on robot A-new, the result of the experiment for the new robot with main body dimension *ϕ15× 20mm* is shown in figure 5. It can be moved in *ϕ20mm* pipe in forward at moving speed *1.4 to6.2mm/s* by frequency *30-80Hz* and moved in backward at speed 0.9-5.0 *mm/s* by frequency *30-80Hz*. The applied voltage for backward movement is higher than for forward movement. The power consumption is also about 27% higher than old type.

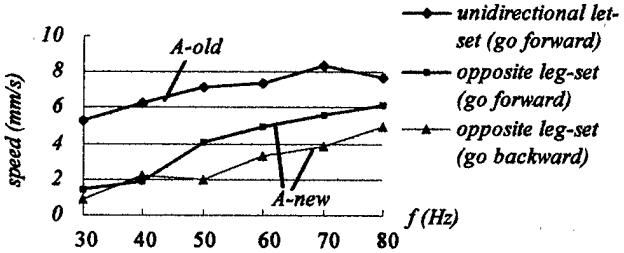


(a) forward movement

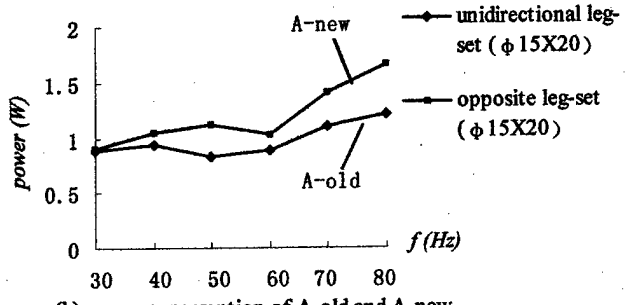


(b) backward movement

Fig. 4 Moving principle of new type robot A-new



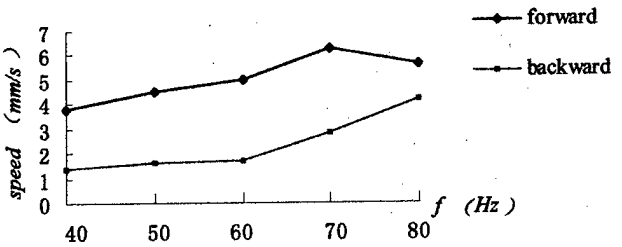
(a) moving speed of prototype A-old and A-new



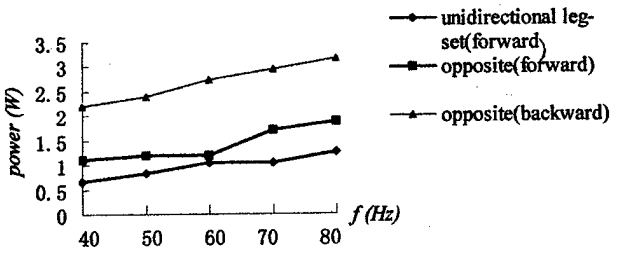
(b) power consumption of A-old and A-new

Fig. 5 Moving speed and power consumption of prototype A-old and A-new

A prototype of small diameter robot of main body ϕ *11×20mm*(Type C-new) with opposite leg-set on body is also experiment under same condition, the result is shown in figure 6. It is clearly that this one has similar result. This robot also can move in *20mm* pipe forwards and backwards, but the moving speed in backward is more slowly and the power consumption of opposite leg-set robot is about 50% larger than unidirectional leg-set robot C-old. Of course this power loss also transfers to heat.



(a) moving speed of opposite leg-set (C-new)



(b) power consumption of prototype C-new

Fig. 6 Moving speed and power consumption of prototype C-new

4. Conclusion

(1) Previous prototype micro robot based on magnetic force actuator only can be moved in small pipe forward. By means of change leg-set mounting on robot, the improved robot A-new or C-new can move both in forwards and backwards even though its backward moving speed lower than forward.

(2) The moving principle of the new type robot has been explained. This is due to generate bigger inertial impact force drive instead of pure friction driving between legs and tube surface, because counter mass m1 of the new magnetic actuator has bigger weight.

(3) By reducing dimension and weight of main body of robot it can improve moving characteristic of the electro-magnetic micro robot. It was shown in experiment that the smaller prototype C-new appears more smooth moving property even though its static magnet force was reduced.

(4) The electro-magnetic actuator appears a little power loss in high moving speed, especially, when it moves backward by higher applied voltage.

References

[1] Hayashi I, et al., "The running characteristics of a screw principle micro robot in a small bent pipe", Proc. of MHS'95

[2] Hayashi I, et al., "Micro moving Robotics", Proc. of MHS'98, p.41-50

[3] Idogaki T. et al., "Characteristics of piezoelectric locomotive mechanism for an in–pipe micro inspection machine". Proc. of MHS'95, p.193-198.

[4] Matsuoka T. et al, "Improvement of Micro Mobile Machine with Piezoelectric Driving Force Actuator", Proc. of MHS'95, p.211-217.

[5] Kawakita S, et al., "Multi-layered Piezoelectric Bimorph Actuator", Proc. of MHS'97, p.73-78.

[6] Sun Linzhi et al., "Micro Robot in Small Pipe with Electromagnetic Actuator", Proc. of MHS'98, p.243

Technical Session B-2

Microfabrication, Material, and Property II

The Design and Synthesis of Magnetic Ultra-fine Polysaccharide Particles

K.Yagi, M.Tokuda*,T.Kobayashi* and T.Kishita*

Tokyo Metropolitan University of Health Sciences,
7-2-10, Higashiogu, Arakawa-ku, Tokyo
*Mie University, 1515, Kamihama, Tsu, 514, Mie

Abstract

Magnetic iron oxide were synthesized by the initial materials of ferrous chloride ($FeCl_2$) and ferric chloride (Fe_2Cl_3) in Ar gas ambiance and at the same time, these magnetic iron oxide colloid particles were coated by Polysaccharides in solvent. How to make magnetite applied coprecipitation method again. Those were named to Polysaccharides magnetite (PSM) complex by us. PSM complex were synthesized by various conditions and several steps those were given as under. At first, the sample was measurement of Dynamic Light Scattering. Next, the influence of the polysaccharide to the saturation magnetization was examined. Third, a sample was observed with the transmission electron microscope. Last, it was tried to make a particle diameter small by decreasing polysaccharide molecular weight. As these results, particle diameter and saturation magnetization were possible to be controlled.

Key Words: Biomaterials, Material Design, Ultra-fine Particles, Polysaccharide - Iron oxide composite, Measurement of Dynamic Light Scattering

1. Introduction

Before aiming at the development of the new material, it can be said that it is full of much possibility about the size range of the sub micron unit. As the size becomes the sub-micron unit, the fine particle is in such cases as the stability of the crystal metamorphosis by the effect on volume and the effect on the surface, it is shown physically and chemical character in the solid of the fault particle of the cause hadn't property, and it knows that it has various peculiar action and the character.

Then, the magnetic material of ultra fine particle that made magnetic material the super-fine particle recently begins to be in the limelight. When it becomes the size that it is called the super-fine particle, the nature that is close to single domain structure or it is shown, and the magnetic material shows high holding magnetic force (: coercivity). The coercivity decreased, and ferromagnetism was lost at last, and characteristics as paramagnetism were shown when the ferromagnetic material such as iron and nickel were made up the super-fine particle again further little more than single domain structure. This is being called Super paramagnetizatism. (1) (2)

Magnetic moment which one particle has happens as for this because the direction can't be kept any more by the heat vibration energy. Super-paramagnetic material becomes very excellent soft magnetic material which therefore it doesn't have coercivity to, and it is being expected the birth of the new material which has a new function.

The magnetic fluid is the fluid that can see having magnetization in appearance with the colloid solution that decentralized magnetite, the fine particle of the ferromagnetic material such as iron, cobalt, nickel in water, hydrocarbon, solvent such as die-ester in the high density. (2)

As for the surface of the fine particle, the adsorption coat is done by surfactant such as oleic acid, even if gravity, usual centrifugal force, the magnetic power by the outside magnetic field, and so on act, solid liquid separation doesn't happen, and uniform dispersion is kept in it in the stability. Therefore the magnetic fluid is the fluid that have fits to the magnetism and the fluidity, and the various development of application which the character was used for is advanced.

It had been applied widely since application was proposed like engineering of the magnetic heat engine that used the magnetic fluid, the energy conversion device which temperature sensitive of magnetic fluid which had the characteristics that the change in the magnetization depended on temperature strongly were used for it, and the heat transport device by Rosensweigs. But, cohesion of those magnetic fine particles were prevented, the condition that decentralizes it in the solvent in the stability were kept, the protection film were formed in that surface, and it must draw the distance of the magnetic fine particles apart to the certain extent, and more development of the technology had been waited for.

That, this material that has the character with being a liquid of which has magnetism is used, and there is research to use in enhancement agent, the living body as the tracer, the diagnosis medium in the living body.
Because the grain diameter, being possible of the guidance due to the magnetism, the magnetic fine particle is very small and there are characteristics in the outside ratio of surface area is large. And, it pays attention to it, and decentralizes the magnetic fine particle in the solvent, and it is the research that it tries to use as the functional material in the living body.

But, there is a thing that has toxicity, too, and it isn't being taken into consideration as for the living body adaptability, and surfactant being use as the dispersion agent in the usual industry like magnetic fluid isn't suitable as the biomaterial. When therefore it thinks about application to the living body, the magnetic fine particle is safe toward the living body, and it is made to have the coat with the material that has affinity, and has

1999 INTERNATIONAL SYMPOSIUM ON
MICROMECHATRONICS AND HUMAN SCIENCE
0-7803-5790-6/99/ $10.00 ©1999 IEEE.

the need that decentralizes it as the colloid solution.
So this research to grapple, it was to make it apply the polysaccharide that it pay attention to it recently in the application to the biomaterial field as coating and composition material of the magnetic fine particle. Polysaccharides were high safety materials toward the living body, and moreover it was fully possible material to bear the part as the dispersion agent, the stable agent, the coat agent in water solution.

The water solubility polysaccharide which had magnetite (Fe_3O_4) of the magnetic oxidized iron and living body adaptability were chosen by this research to have living body adaptability and to hold the design of the new compound material which had magnetism and dispersion stability. Magnetite chosen as the core material was moved to the part of the magnetic, mucopolysaccharide and compound polysaccharide were used as the dispersion material of the non-magnetism as the outside shell coat material from the polysaccharide, and the composition of the materials were done. It decentralizes the fine particle in the solution, and these were thought that the part of preventing cohesion could be played so that it may contain the hydrophilic functional group during the composition sugar and chemistry may be adsorbed in the combination with the core. The sample made by this research could be placed on the function material that had multiple functions (magnetism, fluidity, living body adaptability) again as a really new material that didn't see the kind by now. And evaluation and measurement were done by this research about the character of the made material that examined how to make this new material, and it would be wanted to aim at the control of the magnetic character, the dispersion stability, the establishment of the preparation condition. [3]

2. The material and method

The polysaccharide coat magnetic super-fine particles synthesized in this research were magnetite (Fe_3O_4) as the core material, chondroitin sulfuric acid and hyaluronic acid were chosen as the outside shell coat material from mucopolysaccharide it thought to be safe toward the living body. How to make magnetite applied coprecipitation method again. The characteristics of this method were that it improved dispersion by doing compounding with the polysaccharide and composition of the magnetic fine particle at the same time. The chemical reaction-type to compose the magnetite colloid particle in the following was shown.[1]

$$FeCl_2 + 2FeCl_3 + 8NaOH \rightarrow Fe_3O_4 + NaCl + 4H_2O$$

The concrete way of making it was shown in the following. (Fig.1).

(1) Ferrous chloride ($FeCl_2$) and ferric chloride ($FeCl_3$) (: total iron quantity 14mmol) were dissolved in the water (100ml) which an authority added argon (Ar) gas for the prevention that it oxidizes to. On the other hand, polysaccharide was dissolved in the water, and heated to 70 degrees.

(2) It was added to the water solution (100m l) of the polysaccharide with stirring the iron chloride water solution. Sodium hydroxide (NaOH) was added at this time, and alkalinity was held. Then, pH holds the neighborhood of 7 in consideration of the living body adaptability.

PH in the preparation to improve how to make it and the relations of the progress time were shown in Fig.2. It explained here about the method 1 and the method 2. The method 1 added sodium hydroxide after it was composed to prevent the denaturation of the high molecule. And, the method 2 always kept pH of the sample solution under the alkaline condition. In other words, Sodium hydroxide was added in the solution before the composition because pH of the sample in the solution was alkaline condition that was suitable for the formation of magnetite. Next, pH was controlled with adding Mnochloroacetic acid ($CH_3ClCOOH$) of 3N to the solution, and reflux and it were heated for about 60 minutes at the high temperature, and the response were fully made to proceed. Some preparation conditions were taken into consideration on this occasion.

(3) Centrifugation was done after cooling, and it got rid of precipitates

(4) It dialyzes, and got rid of un-pure ions in the solution and so on. It could get Polysaccharides coat magnetic complexes (It was named with the Polysaccharides magnetic iron oxide complex following PSM.) here.

(5) And, it got the powder of the samples due to freeze-drying

3. Result

It was examined about the magnetic character and the influence on the average particle diameter by the difference in the amount of molecule of the polysaccharide that had the coat in the outside shell, as the master.

3.1 The measurement of the core particle diameter

The made samples were observed with transmission electron microscope (H-500; manufactured by Hitachi (Co.Ltd)). The size of the cores only was measured from now. (Fig.2)

3.2 The measurement of total iron concentration

The complete sample of total iron concentration was measured by the atomic absorption spectrometry device (manufactured by AA-855, Nippon Jarrell ash (Co.Ltd)).

3.3 The measurement of the whole particle diameter

These samples were the iron oxide minute particle and the complex of the polysaccharide, the particle diameter of the iron fine particles were found by the electron microscope, and the grain diameter of the whole which contains sugar were found by the dynamic light scattering (Rayleigh scattering) method. The measurement device used the dynamic light scattering measurement device (manufactured by DLS-7000; Ootsuka electronic (Co.Ltd.)).

3.4 Magnetic measurement

The saturation magnetization of around the unit mass were asked for magnetic hysteresis curve were drawn, and sweep did the outside magnetic field to 14kOe by using the vibration sample magnetometer (manufactured by VSM-5; Toei industry (Co.Ltd)) as the evaluation of the magnetic character of the sample. The measurement sample used the powdered that freeze-drying method could get further.

3.5 The measurement of the surface electric potential

The surface electric potential (: ζ , zeta potential) of the fine particle were measured and examined about the dispersion stability of the sample. The measurement

device used electrophorisis dynamic light scattering measurement device (manufactured by ELS-8000; Ootsuka electronic (Co.Ltd.)).

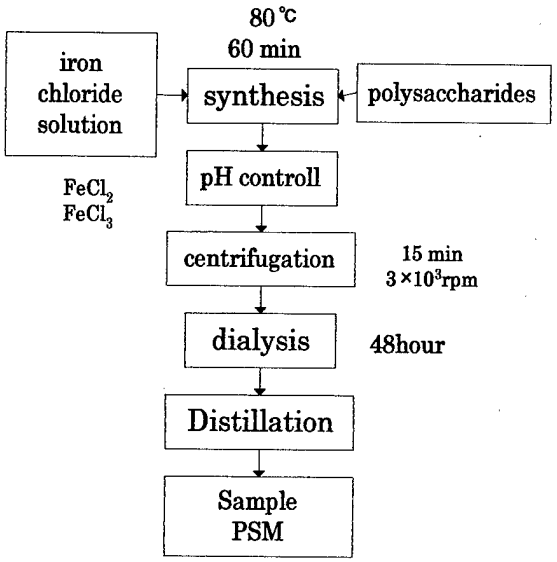


Fig.1 Preparation process

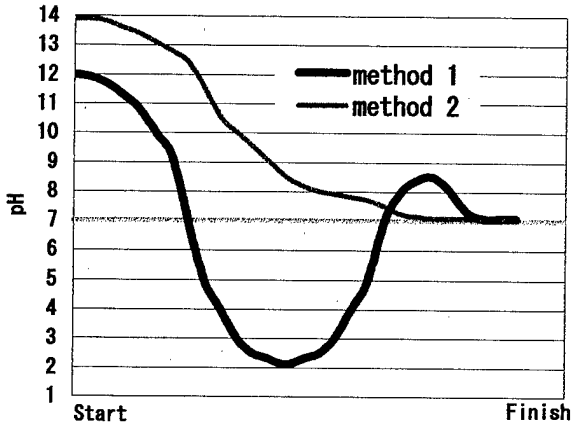


Fig.2 The relation of ph to passed time

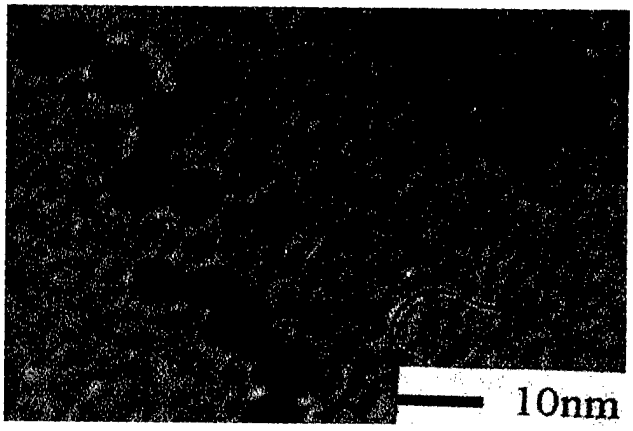


Fig.3 TEM Image of CSM

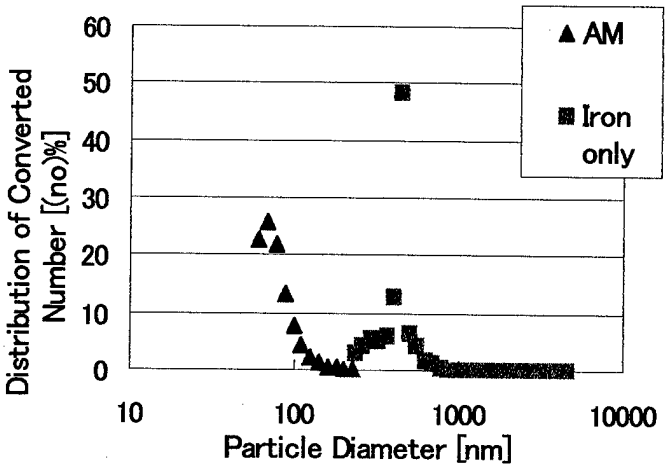


Fig.4 The relation of Distribution of Converted Number to Particle Diameter

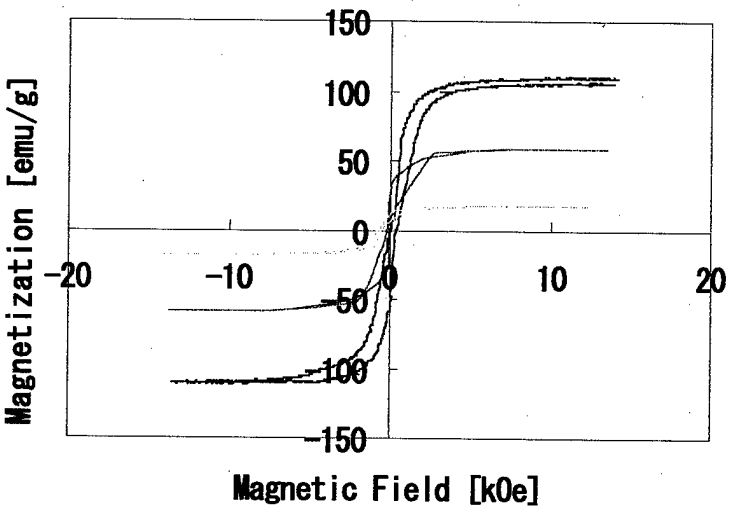


Fig.5 The relation of Magnetization to magnetic Field

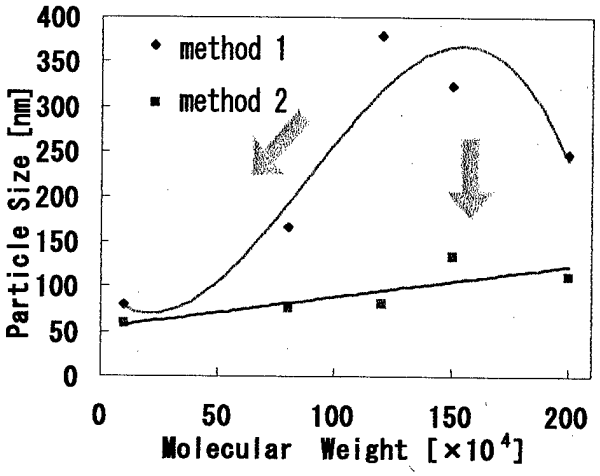


Fig.6 The relation of Particle size to Molecular Weight

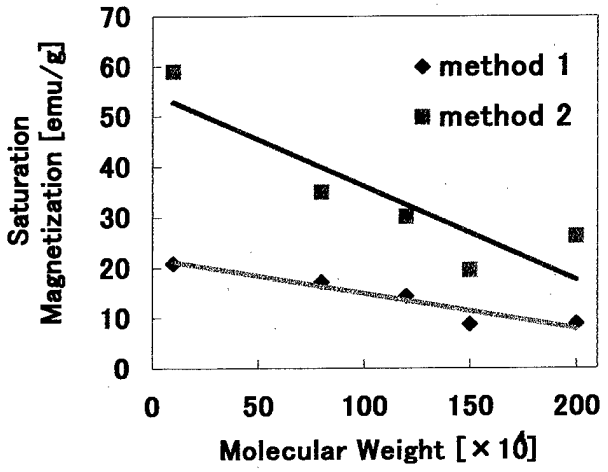


Fig.7 The relation of Saturation Magnetization to Molecular Weight

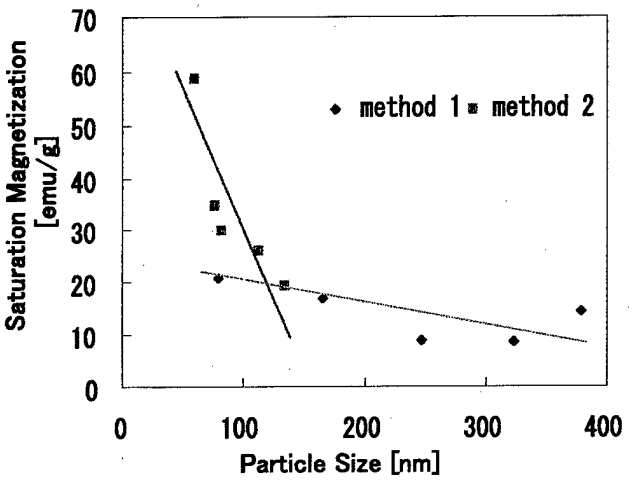


Fig.8 The relation of Saturation Magnetization to Particle Size

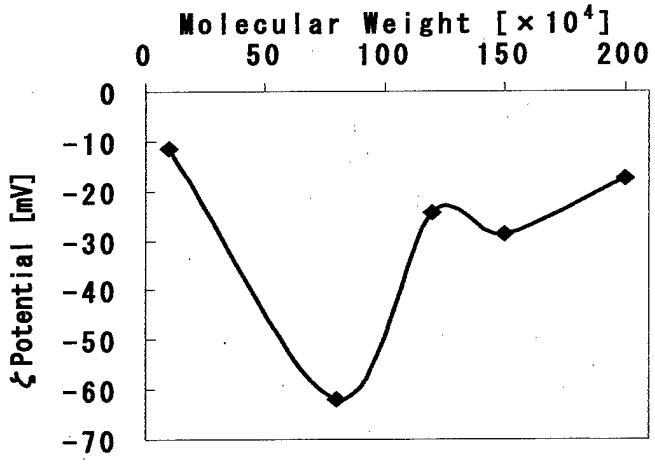


Fig.9 The relation of Potential to Molecular Weight

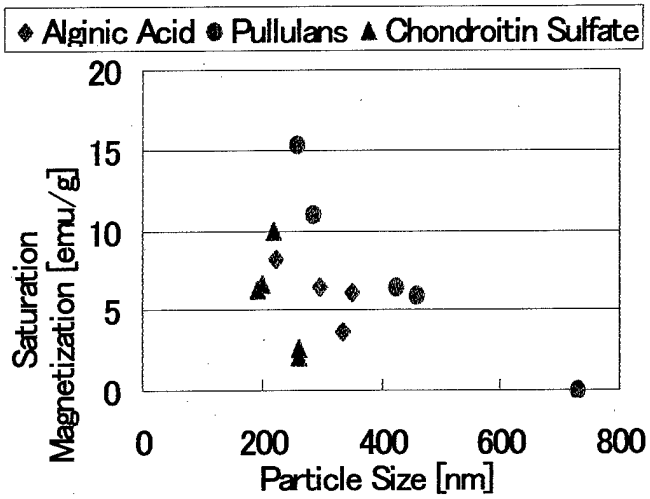


Fig.10 The relation of Saturation Magnetization to Particle Diameter

4. Consideration

Coprecipitation method was being used as the way of making magnetite to show it with Fig.2 by this research. As for the preparation condition of magnetite in coprecipitation method, it is desirable to be an alkaline territory. But, the change in pH was seen to compound the solution of iron chloride with the solution of the high molecule. (It was made a method 1.) So, to keep pH of the liquid for the mixture as much as possible in the alkaline territory, dropping the sodium hydroxide (NaOH) solution in the high molecule solution before the composition for the formation of magnetite gave only the necessary quantity, after that, the method (It was made the method 2.) that it was composed with the iron chloride solution was tried. With the method 1 that dropping did NaOH after the composition and the formation of magnetite was done, and the sample was made by the method 2 that dropping did NaOH in advance in the high molecule solution, and the comparison was done about the saturation magnetization of the sample and the average particle diameter. It was shown about the change in pH of the sample during the composition in Fig.2.

- Method 1: pH control is done, and magnetite was made after the iron chloride solution and polysaccharide solutions are synthesized because it has the possibility that denaturation happens in the polysaccharide that are an acid high molecule.
- Method 2: dropping does NaOH in advance in the multiple sugar solutions, and pH of the solution is always kept in the alkali, and magnetite is made and to do the formation of magnetite becomes the stable and the same.

The request for the magnetic character and the particle diameter distribution examined an influence on the character by the way of making it about the sample made by these two methods by this research. The measurement result was shown in Fig.7. It was compared with the method 1 from this figure, and the sample made in the method 2 could get the tendency that saturation magnetization rose. The formation of magnetite was done smoothly, and it was decided that more magnetite particles disperse in the polysaccharide compound magnetic colloid bodies, and it thought about this with the thing that saturation magnetization rose by the preparation by the method 2.

And, the measurement result of the particle diameter was shown in Fig.6. As for the particle diameter, the sample made in the method 2 showed the tendency of becoming small more than the sample made from now in the method 1. The action of haluronic acid that that pH during the composition was alkali was acid of mucopolysaccharides was held, and this was thought that the average particle diameter of the polysaccharide compound magnetic colloid bodies was being made small. But, the average particle diameter of the sample made in the method 1 was the smallest, and the average particle diameters of the sample made in the method 2 became 60 - 80 nm, too. And, it was found out that it wasn't unified in the range that the average particle diameter of the sample made in the method 2 was small. It could be said that composition in the alkaline territory was suitable from this thing about the polysaccharide compound magnetic colloid bodies.

The magnetic fine particle made with coprecipitation method were usually distributed in the size of about 1μm, and it settles in the water solvent as the result of the observation by the transmission electron microscope of Fig.3. Fine particle, as much as nuclear growth proceeds after the nuclear formation and the buoyancy of the particle becomes smaller than the gravity, this is because a particle becomes big, moreover, cohesion is brought about by the collision of the particle happening again by the brown movement and so on, and it settles to attract each other from having magnetism. But, the dispersion sample of the magnetic fine particle could get it, and the magnetic fine particle that therefore became the core were observed, and dispersion condition were observed in the polysaccharide compound magnetic colloid bodies.

First, after it dried this sample, observation by the electron microscope of the magnetic fine particle that becomes the core were done. The size of the particle could be confirmed from the result. These were thought to be the thing due to dryness though there were the place where bringing about cohesion were seen in the photograph. Moreover, the polysaccharide that it had the coat done by the sample outside shell weren't reflected as the photograph, and it were the photograph of only magnetite that were the core.

The magnetic fine particles (magnetite) that became the core of the samples were distributed in about the diameter 10 nm degree. It thought about this thing with the benefit that cohesion of the magnetic fine particle were prevented by polysaccharide had the coat in the particle. It made it possible that it dispersed in the water solution without the solid force of repulsion of the particle increasing and preventing mutual cohesion and causing precipitation by adsorbing on the surface of the fine particle that polysaccharide were cores. Single domain critical particle radius of magnetite was about 40 nm again, and it were proved that it were smaller than it in the particle diameter of this samples. It were understood that this sample were the material that shows super-paramagnetism from this thing as well. Therefore, as for our compound material, it were found out that the particle diameter of the core that were the magnetic fine particle were distributed in the range of about 10nm.

Fig.4 is the number conversion distribution of the particle diameter of the sample of only the magnetic minute particle which polysaccharide as the dispersion agent wasn't being used for and the sample which sugar (Alginic acid) was used for. It could confirm that a magnetic minute particle dispersed in the water solvent with the former as for the latter (magnetite only) though precipitation was seen as time passed. It was understood that polysaccharide functions as the dispersion agent from this thing and cohesion of magnetite, fault-macro-change were prevented and decentralizes it.

Fig.5.6.7.8.9s are saturation magnetization, a particle diameter and the graph that zeta potential were compared with the molar weight of the sugar (hyaluronic acid). The sample made by this research were the colloidal solution that tunica did magnetite by the polysaccharide, and thought to have magnetism. So, the curvilinear coordinates of magnetization were sought by using the vibration sample magnetometer to examine the magnetism character of the sample. The sample used for the measurement were made to freeze by using the liquid nitrogen, and it dried the sample had used for the measurement for more than 48 hours by the freeze drying machine, and it were eliminated fine particles in the moisture. Those fine particles were crammed so that there might not be the gap in the container of the cylinder type, and weight were measured and used for the magnetism measurement. Ni was used as the standard substance of the magnetism hardness, and calibration was done, and added the magnetization curve was drawn, and magnetic field was adjusted so that saturation magnetization might show 5 emu. Then, the measurement of the preparation sample was started.

Though the polysaccharide compound magnetism colloid body that it were made by our research acquires the multiple function that it had magnetic force and variance stability by compound with magnetite which were ferromagnetic substance, and the polysaccharide which were paramagnetic substance, but the saturation magnetization of around the unit mass showed the tendency of declining in comparison with the sample of magnetite chisel. In other words, it was the saturation magnetization of 109 emu/g with the sample of magnetite chisel with the sample made by this research though it was the biggest though the saturation magnetization of 59 emu/g was shown. As for this, though mixing of the polysaccharide (paramagnetic substance) which didn't just have magnetism was the cause, the sample was being made in the purpose of achieving it, and it was tried to reduce the decline of the saturation magnetization by compound with the polysaccharide due to the optimization such as a synthesis condition and magnetic force strengthening was tried by this research by this research.

Though super fine particle were made by used the different kind of sugars, the saturation magnetization of the sample made by the sugar of the large molecular weight were small, and the particle diameter showed the tendency of becoming large. Relative volume with the core increased the sugar whose molecular weight were large, and thought about this with the benefit that non-ferromagnetic area in the PSM particle component increased. Moreover, as for the zeta potential, though the difference in some wasn't seen by each sample, large ζ (zeta) potential were shown substantially, and it were found out that it dispersed in the stability in the water solvent.

Fig.8 was the graph that showed it about the

saturation magnetization and the relations of the particle diameter. Comparison were done about the saturation magnetization of the polysaccharide compound magnetism colloid body and the average particle diameter. The average particle diameter was sought from the measurement of the particle diameter distribution, and it sought saturation magnetization from the magnetization curve. The figure took the average of particle diameter in the x-axis and the saturation magnetization in the vertical axis. As for understanding it from this fructification that left approximate curve raise. In other words, as the average particle diameter became small, saturation magnetization showed the tendency of rising, and it was with the callosity. As the particle diameter becomes small, it considers that this is because the volume of polysaccharide (paramagnetic substance) to adsorb on magnetite decreases and the saturation magnetization of around the unit mass rises. It considers that strengthening of the magnetic force and the grain refining of the particle can go together from this thing in the polysaccharide compound magnetism colloid body.

Fig.9 was the graph which zeta potential in the different polysaccharide compound magnetism colloid body was compared with.

These polysaccharide compound magnetism colloid bodies were the functional material that had magnetism and variance stability at the same time. There was the sample which deposited in the sample as well that it dispersed by the preparation condition, and, there were the sample which produced due to the precipitation by the centrifugation, too. As for the variance stability, it is insufficiency by only seeing it and judging it. So, zeta potential was determined by this research as the index that showed the dispersibility of the colloidal particle. The examination can be done about the variance stability of the sample by this zeta potential. The zeta potential of the polysaccharide compound magnetism colloid body showed negative charge. This is because it decentralizes magnetite by the hyaluronic acid, and it is commonly said as the stability variance as much as -30～-80mV. The particle diameter became small in the sample whose molecular weight were small, and saturation magnetization showed the tendency of rising in the fructification until now. Then, it takes time to the aggregation, and considers that variance stability is high as much as a particle diameter is much smaller. The measurement samples were the high polymer bath of the made samples, and the polysaccharide chisel by used the hyaluronic acid. The molecular weight of the used hyaluronic acid showed it in the bottom table 1.

And, Fig.9 was the figure that took molecular weight in the x-axis and the zeta potential in the vertical axis. The zeta potential of the sample were compared with the zeta potential of the polysaccharide chisel from this figure, and it confirmed that it lowered. The polysaccharide compound magnetism colloid body produces by polysaccharide's adsorbing on magnetite in solution, and thinks about this more than the high polymer solution chisel with the benefit that aggregation became easy to do. And, it became to be peculiar the value that the zeta potential of the sample of the molecular weight 100,000 and 800,000 by the procedure 2. However though the average particle diameter of the sample of 100,000 was small and it was the sample whose saturation magnetization was the highest, it confirmed that it was produced gradually the precipitation in the sample tubing bottle and though zeta potential became the smallest with -11.4 mV. Though the particle diameter became small and saturation magnetization rose, it was found out that it couldn't always get variance stability at the same time as for the sample that decentralized magnetite with the polysaccharide whose molecular weight was small from this thing. The sample of the molecular weight 800,000 showed high zeta potential with -62 mV, and it was found out conversely about it that it dispersed in the stability. Moreover, it were distributed in -20 - -30 mV, and it could confirm that it dispersed in the stability as for the sample except for it
It were found out that it showed the tendency of being common with saturation magnetization became small as the particle diameter became large without being based on the sugar used as the dispersant in Fig.10. There are little things that the PSM particle diameter is big, and core of the contained magnetism area, and the saturation magnetization of around the unit mass is thought that it is small, too.

Hyaluronic acid(No)	Molecular Weight [$\times 10^4$] (Standard Value)	Molecular Weight [$\times 10^4$] (Test Value)
FCH-SU	60 under	10
FCH-80	60～100	79
FCH-120	100～140	126
FCH-150	140～180	142
FCH-200	180～220	204

Table.1: the molecular weight of the hyaluronic acid

5. Conclusion

It produces the aggregation and the fault turns, and deposits finally as for the magnetism particle which superparamagnetism is shown without variance occurring in the edge water solvent only in it. Not to lose the magnetism of the particle and to get the function of the material which flowability and bioadaptability were added to, it grappled with both the magnetic force and the control of the particle diameter, and polysaccharide compound magnetism particle was formed, when it established the synthesis procedure with the polysaccharide which is comparatively safe high polymer in the living body. It will be prepared for the material that made the uniform and the particle diameter smaller, and it must raise the variance stability of the PSM particle again from now on. Therefore the points of view are put in the adsorption condition of the magnetism particle and the organic high polymer, and it wants to advance research.

Reference literature

1. TAKETOMI, CHIKAKADO, Magnetism fluid-basis and application-, Nikkan Kogyo Sinbun
2. S.SAITO supervision, super-fine particle handbook, Fuji Techno. System
3. T.KOBAYASHI Master's Thesis, The Study of the magnetic character and the variance stability of the polysaccharide compound magnetism colloid, Department of Mechanical Engineering, Mie-Univ. (1998)

Study on XeF_2 Pulse Etching using Wagon Wheel Pattern

Koji Sugano and Osamu Tabata
Department of Mechanical Engineering
Ritsumeikan University
1-1-1 Noji-higashi, Kusatsu-shi, Shiga 525-8577
JAPAN

Abstract:
This paper reports the developed XeF_2 etching system and measured etching characteristics using a wagon wheel pattern. A pulse etching was used and an etching sequence was controlled by a computer. The etching rate was in proportion to the number of pulses and higher in the initial 15 seconds of etching than in the rest of the etching. The etching rates were 2.5 μm per pulse vertically and 2.0 μm per pulse laterally for pulse duration of 180 sec. The etching rate increased as the aperture width of the wagon wheel pattern increased. The measured ratio between the etch depth and the lateral undercut was 1.3. These etching characteristics were independent of crystal orientation.

1. INTRODUCTION

Etching of silicon (Si) by XeF_2 has great advantageous since it is isotropic dry etching and has great selectivity to most of the material used for MEMS devices such as aluminum, silicon dioxide (SiO_2), silicon nitride (Si_3N_4) and resist. Especially, XeF_2 etching has been expected to play important role for the surface micromachining using single crystal silicon (Si) or polycrystalline silicon (poly-Si) as a sacrificial layer material [1,2]. These materials have been used with anisotropic wet etching solutions such as KOH and TMAH. However, there have been a several problems during the Si or poly-Si sacrificial layer etching using KOH and TMAH as follows. (1) Etching rate decreases with etching time due to the diffusion effect of the solution, (2) Evolution of hydrogen bubbles during etching reaction damages the microstructures, (3) It is difficult to remove the residuals from the etched cavity and (4) It is difficult to prevent the sticking of the microstructures. These problems are expected to be solved using XeF_2 etching technique.

This paper reports the developed XeF_2 etching system and measured etching characteristics. Although the etching characteristics of XeF_2 have reported by P. B. Chu et. al. [3,4], etching rate dependencies on crystallographic direction of the silicon crystal has not been reported. We have clarified this using a wagon wheel pattern. Etching apparatus, experimental procedure and measured results are presented.

2. XeF_2 ETCHING MECHANISM

XeF_2 is a white solid at room temperature and pressure. It has a sublimation pressure of about 4 Torr at room temperature and form HF in the presence of H_2O. XeF_2 adsorbs and dissociates to Xenon (Xe) and fluorine (F) on the surface of silicon. Fluorine is the main etchant in silicon etching process and the XeF_2 molecule is a convenient source of fluorine atom. Therefore, XeF_2 had been used to study the interaction of fluorine species with silicon to reveal the fundamental physical and chemical mechanism of the Si etching process with fluorine [5]. The reaction equation for the Si and XeF_2 reaction is the following:

$$2XeF_2 + Si \rightarrow 2Xe + SiF_4$$

XeF_2 has high etching rate and reaction probabilities at room temperature. It requires no external energy sources or ion bombardment to etching silicon and exhibits high selectivity to many metals other than Ti and Mo [3,5].

3. ETCHING APPARATUS AND ETCHING SEQUENCE

Figure 1 and 2 show a schematic diagram and photograph of the developed etching apparatus, respectively. The etching apparatus

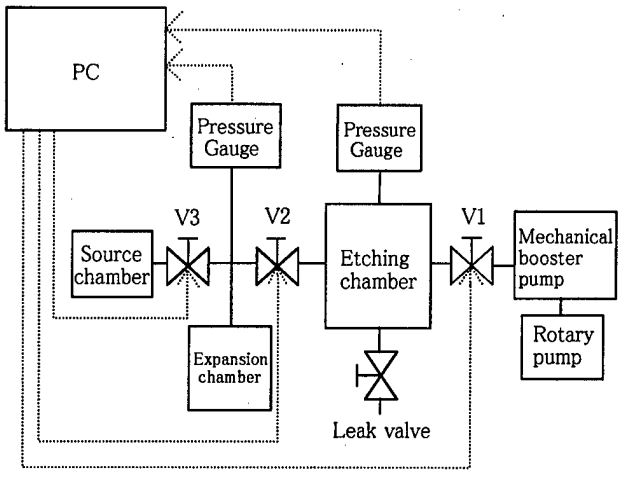


Fig. 1. A diagram of the developed etching apparatus. This etching sequence is controlled by the computer.

1999 INTERNATIONAL SYMPOSIUM ON
MICROMECHATRONICS AND HUMAN SCIENCE
0-7803-5790-6/99/ $10.00 ©1999 IEEE.

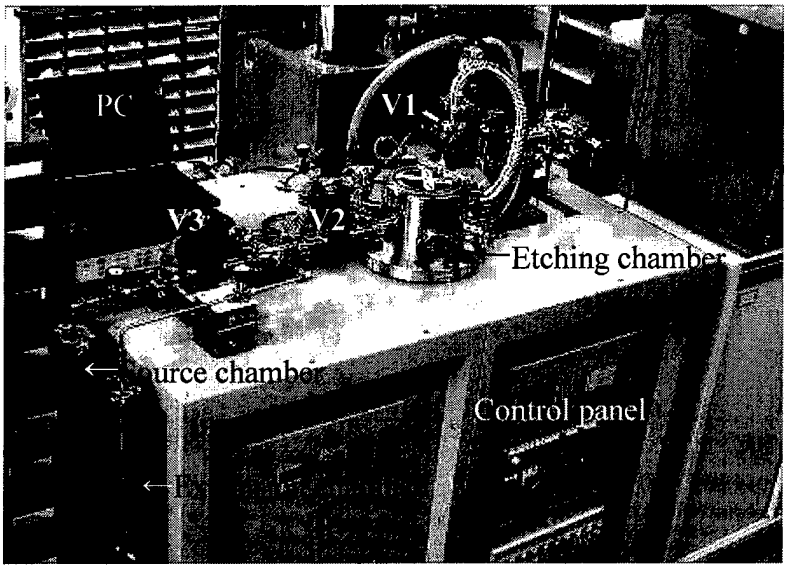


Fig. 2. A photograph of the developed etching apparatus.

consists of a XeF_2 source chamber, an etching chamber, an expansion chamber and two vacuum pumps, a rotary pump and a mechanical booster pump. The etching chamber and the expansion chamber have diaphragm pressure gauges. The expansion chamber that located between the source chamber and the etching chamber is used to charge the amount of XeF_2 gas source that will be used for pulse etching. The amount of the charged XeF_2 gas to the expansion chamber is measured precisely by the pressure and then injected into the etching chamber.

Figure 3 shows a change of pressure in the expansion chamber and the etching chamber during one pulse etching. First, the expansion chamber was filled with the XeF_2 gas charged from the source chamber. Once the designated pressures was reached, the charge was stopped and the evacuation at the etching chamber was stopped. Then XeF_2 gas in the expansion chamber was injected into the etching chamber and the etching begins. The starting pressure of the etching chamber is defined by the charged pressure of the expansion chamber, and a volume ratio between the expansion chamber and the etching chamber. The volume ratio is 12.7 since the volume of the expansion chamber and the etching chamber are 9519 cm^3 and 748 cm^3, respectively. After waiting for certain duration time allowing the etching reaction, the etching chamber and the expansion chamber were evacuated.

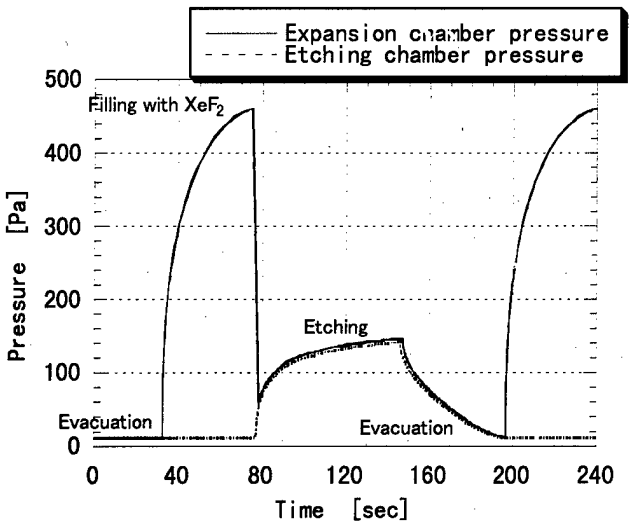


Fig. 3. Etching sequence

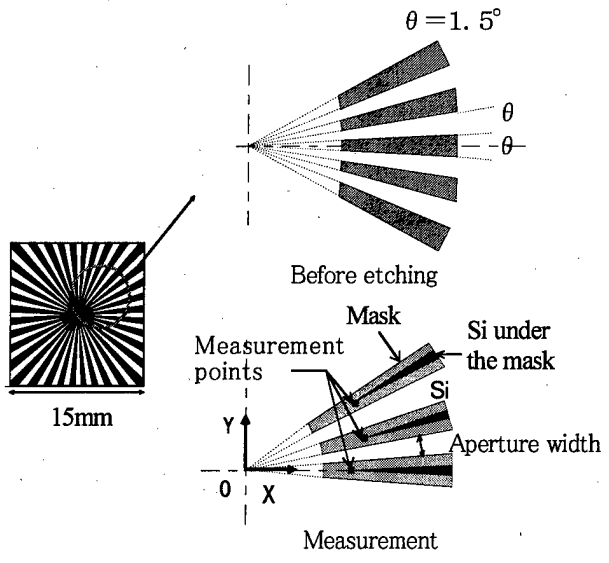


Fig. 4 Wagon wheel pattern used for measurement.

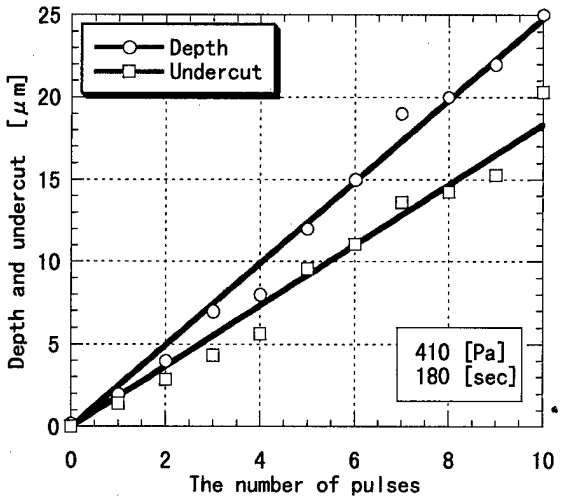


Fig. 5. Dependency of depth and undercut on the number of pulse with expansion chamber pressure of 410 [Pa] and etching time per pulse of 180 [sec].

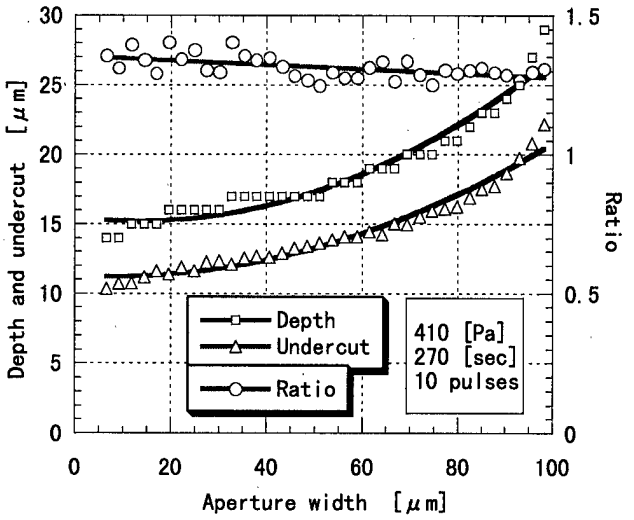


Fig. 7. Dependency of depth and undercut on the aperture width of wagon wheel pattern with expansion chamber pressure of 410 [Pa], etching time per pulse of 270 [sec] and the pulse number of 10.

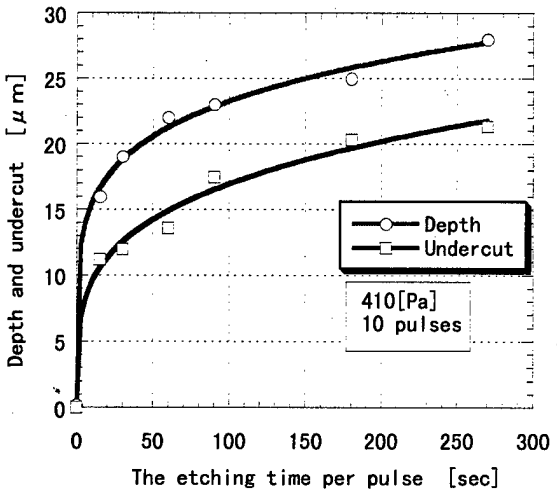


Fig. 6. Dependency of depth and undercut on the etching time per pulse with expansion chamber pressure of 410 [Pa] and the pulse number of 10.

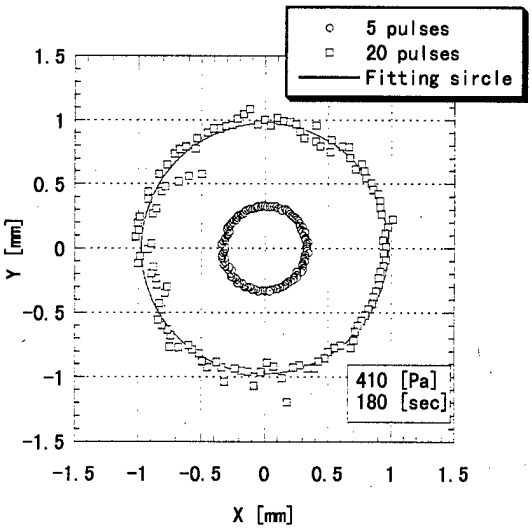


Fig. 8. Dependency of measured wagon wheel patterns etched by 5 and 20 pulses with pulse duration of 240 seconds. The solid lines indicate the least square fitted circles.

The above mentioned pulse etching sequence is controlled by a computer using three important valves, V_1, V_2 and V_3 of the etching apparatus.

1) V_3 is closed, V_1 and V_2 are opened. The etching chamber and the expansion chamber are evacuated.
2) V_2 is closed.
3) V_3 is opened and XeF_2 is sublimated into the expansion chamber until designated pressures are reached.
4) V_3 is closed.
5) V_2 is opened and XeF_2 gas is injected into the etching chamber.

After waiting for certain duration time allowing the etching reaction, the sequence is returned to 1).

4. EXPERIMENTS

The XeF2 etching characteristics of the developed etching apparatus were measured using a wagon wheel pattern formed on a (100) silicon wafer. LPCVD silicon nitride of 100 nm thickness was used as the etching mask layer. The nitride was patterned with RIE to prevent any etching of the silicon. Figure 4 schematically shows the wagon wheel pattern. The dimensions of the wagon wheel pattern before and after etching experiments are shown. The

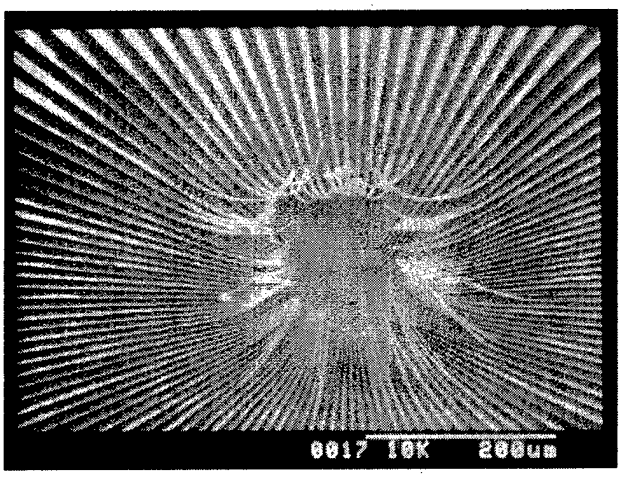


Fig. 9. A SEM photograph of the wagon wheel pattern etched with pulse duration of 180 seconds and the pulse number of 20.

depth and undercut were measured by optical microscope with X-Y stage. The etching rate dependencies on silicon crystal orientation was evaluated by measuring the coordinate of the measurement points shown in Fig. 4.

A sample was immersed in dilute HF before XeF_2 etching to remove the native SiO_2 on the sample surface. The XeF_2 etching experiments were carried out with expansion chamber pressure of 410 Pa and initial etching chamber pressure of 30 Pa.

5. RESULTS

An etching rate was found to depend on the number of pulses and the etching time per pulse. Figure 5 shows dependencies of an etching depth and an undercut on the number of pulses with pulse duration of 180 sec. The etching depth was in proportion to the number of pulses. The etching rates for depth and undercut were 2.5 μm per pulse and 1.8 μm per pulse, respectively.

Figure 6 shows dependencies of an etching depth and an undercut on etching time per pulse with pulse number of 10. Since the depth and undercut increases rapidly during initial 5 to 10 seconds, the etching rate in the depth and undercut decreases and became constant with increasing etching time. This saturation tendency in the depth and undercut was thought to be caused by the most part of the XeF_2 gas reacts in several seconds of the beginning.

Figure 7 shows dependencies of the etching depth and undercut on the aperture width of the wagon wheel pattern. The pulse duration of 270 seconds and the pulse number of 10 were used. The etching depth and undercut increased with increasing the aperture width of the wagon wheel pattern. The depth ranged from 29 to 14 μm and the undercut ranged from 22 to 10 μm as the aperture width decreases. The dependency of a ratio between the depth and undercut on the aperture width of the wagon wheel pattern is also shown in Fig.7. The ratio ranged from 1.25 to 1.40, because the etching rate in the depth direction is larger than that of undercut. From this dependency of etching rate on the pattern aperture, the etching rate is thought to be dominated by the diffusion of XeF_2 gas molecule than the reaction speed.

Measured wagon wheel patterns etched by 5 and 20 pulses with pulse duration of 240 seconds are shown in Fig. 8. The solid lines indicate the least square fitted circles. From these results, it was confirmed that the etching rate is independent of the crystal orientation and isotropic.

A SEM photograph of the wagon wheel pattern is shown in Fig. 9. This sample was etched with pulse duration of 180 seconds and the pulse number of 20, so the etched depth and undercut were 36 μm and 33.9 μm, respectively. Due to the internal stress distribution along the depth direction of the Si_3N_4 mask, released parts of the Si_3N_4 mask pattern was warped. Problems regarding sticking and breaking of the released Si_3N_4 mask pattern were not observed.

6. CONCLUSION

We have reported the measured characteristics of XeF_2 etching using the wagon wheel pattern. The etching depth was in proportion to the number of pulses. The most part of the XeF_2 gas reacts in several seconds of the beginning. The etching rate dependency on the crystal orientation indicates isotropy of the etching. From these experimental results, the etching rate is thought to be dominated by the diffusion of XeF_2 gas molecule than the reaction speed.

ACKNOWLEDGEMENTS

This research work was supported in part by grant from "NEDO".

REFERENCES

[1] Osamu Tabata, Keiichi Shimaoka, Ryouji Asahi and Susumu Sugiyama, "Micromachined Sensors Using Polysilicon Sacrificial Layer Etching Technology", Sensors and Materials, Vol. 8, No.1, pp.57-67, 1996.

[2] Osamu Tabata, "CAD for Silicon Anisotropic Etching -Effect of Etching Products and Diffusion-", Sensors and Materials, Vol. 10, No.7, pp.425-434, 1998.

[3] Patrick B.Chu, Jeffrey T.Chen, Richard Yeh, Gisela Lin, Jeff C.P. Huang, Brett A.Warneke, and Kristofer S.J.Pister, "Controlled Pulse-Etching with Xenon Difluoride", Int. Conf. Solid-State Sensors and actuators, Transducers'97, Vol.1, No.2, pp.665-668, 1997.

[4] Risaku Toda, Kazuyuki Minami, and Masayoshi Esahi, "Thin Beam Bulk Micromachining Based on RIE and Xenon

Beam Bulk Micromachining Based on RIE and Xenon Difluoride Silicon Etching", Int. Conf. Solid-State Sensors and actuators, Transducers'97, Vol.1, No.2, pp.671-674, 1997.

[5] H.F. Winter and J.W.Coburn, "The etching of silicon with XeF_2 vapor", Appl. Phys. Lett., Vol.34, No.1, pp.70-73, 1979.

Excimer Laser Processing in Nano-Technology

Y P Kathuria
Laser X Co. Ltd. Chiryu-shi Aichi-ken 472 Japan
Email: ypkathuria@aimnet.or.jp

Abstract:
In the emerging field of microelectronics, microrobotics and nano-electromechanical systems (NEMS) it is often desirable to fabricate sub um order structure of solid surfaces in various materials. Recently with the established technique of laser in science and industry, its application have become diversified in the nano- and micro- processing areas. Excimer laser operating in the u.v. region have been employed in various domains covering different spectrum of industrial applications. In all these processes, due to the short pulse width and different scale length of the beam interaction time with the material, various physical phenomenon are encountered that ultimately affects the structure development of the end product.The present paper describes a systematic study of *generating sub micron grating like structures* and underlines the different aspect on the quality and limitations of the fabricated structure. It further elaborate a few of the basic processes and explore the possibilties of current and new application areas.

Keywords: Excimer laser, sub-micron processing

1. INTRODUCTION

Nanometer patterning i.e creating a grating like structure has a number of applications, from optical waveguide coupler to nanoelectromechanical systems (NEMS), where they serves as nanocomponents that are assembled by the micro-orobotic technique to construct nanostructure. Besides that the rapid advancement in the telecommunication, data storage and micro-electronics needs the miniaturization and compactness of the various components in the submicron range. But as the feature size falls, the conventional techniques must be replaced by beam technology. With the unrelenting demand of ULSI technology in the lithograhy applications, the excimer laser is already replacing the conventional uv-sources, due to its inherrent advantage of shorter wavelength and higher resolution. Coupled with the advanced optical technique and unique property of shorter wavelength of the excimer laser operating in the uv region, it enables one to produce ultrafine submicron structures. Usually the excimer laser delivers a nanoseconds pulses, but when coupled with the dye laser or Ti-sapphire laser, they can deliver even the shorter pulses in the pico- or femto-seconds regime. These are very effective for generating high quality patterns, as the thermal diffusion length in this case is minimized. Table I show a few of the system combination with their application.

Table I

1. Conventional KrF / ArF excimer laser

Characteristics:
Wave length = 0.248μm /0.193μm
Pulse width = 16ns/23ns
PRR = 500Hz/20Hz

Applications:
Microlithography
Submicron or nm structuring by two beam beam interferometry or by laser etching of Si in Chlorine, GaAs in gaseous HBr+H2 and Pyrex glass in H2 etc

2. DFDL Dye laser coupled with KrF excimer laser

Characteristics:
Wave length = 0.248μm
Pulse width = 400fs
PRR = 500Hz

0-7803-5790-6/99/ $10.00 ©1999 IEEE.

Application:
Submicron or nm structure by interferomeric technique in polymide and creation of conducting lines thereof etc.

3. Ti-Sapphire laser coupled with KrF laser

Characteristics:
Wave length = 0.248μm
Pulse width = 500fs - 50ps
PRR = 100Hz

Applications:
Submicron or nm structure by interferomeric technique in polymide, semiconductor, metal and thin films etc. For example generation of nm grating structure in thin film of InOx, TaO2 or LiNbO3 for various applications such as waveguide coupler, planar waveguides, mask and opto-electronic devices.

This paper describe the various aspect of generation of grating like structures in the nanometer range with various applications in the micromachine technology.

2. TECHNIQUES

Excimer laser processing in the submicron processing can be carried out by the following two approaches:

2.1 Optical projection lithography

In this case the laser radiation is made to illuminate the appropriate object (mask), which is imaged on the substrate (wafer) with a large N.A. reflective optics. To achieve production throughput at dimension approaching the regime of X-rays and particle beam lithographies, a higher resolution optical projection lithography is required, which can be achieved by a combination of approaches [1]-[2]:

a: by increasing the N.A.
b: by shortening the wavelength
c: by inventing a photoresist material with nonlinear photoresponse /characteristics

A record resolution of 0.13μm lines and spacing can be achieved by using an excimer laser operating at 157nm and etching in chlorine.

2.2 Two beam interferometry

This technique typically employ the holographic arrangement with the objective of ablating the interference pattern of the polymer, glass, silicon and thin metal films. Keeping in view of the poor spatial coherence characteristic of the excimer laser, various types of configuration e.g. modified Mach-Zehnder[3] /Talbot[4] interferometer or mask projection technique of grating have been used to create such sub micron structures. Fig.1 show a novel set up developed recently [5]-[7] for such an application by using the uv femto second pulses in order to produce high quality structure with low thermal effects. The conventional excimer laser can produce the laser pulses in nanoseconds range. But by using it in conjuction with the Ti:Sapphire laser, it has become possible to generate the short pulses in the order of femto seconds operating at λ =0.248μm wavelength. In this case Ti:Sapphire laser (λ=0.745μm) is optimized to produce the 3rd harmonic signal, but it has appreciably low gain and the output energy is not sufficient for the material processing applications. To increase the gain, KrF - excimer laser (λ =0.248μm) is used as an amplifier. Although it is also possible to use dye laser to generate femto second pulses, but in that case the gain is not sufficient for the material processing applications.
These femto second uv radiation irradiate the grating mask which is imaged on the processing area by the Scwarzschild type reflective objective. When the +1 and -1 orders are recombined, the fringes are the same as the ideal phase mask and spaced by d/2, where d is the periodicity of the diffracting element. This period is independent of the wavelength and the set up could also be used for broad line width excimer laser [4].

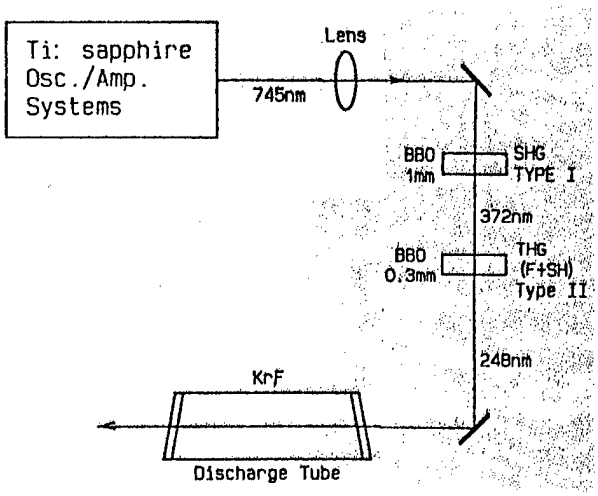


Fig.1A: Generation of λ=0.248μm fs pulses with [Ti -sapphire + KrF] laser [7]

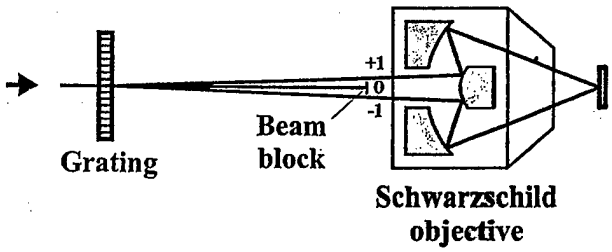


Fig.1B Material processing with grating mask projection [6].

3. DISCUSSION

Using the technique (2.2) various interesting results as shown in Fig.2 have been reported [8]-[9], to create the permamnent conductivity lines of the order of nm in polyimide, by excimer laser (λ=0.248μm) radiation. Actually in this case, laser irradiation above certain threshold of E = 20 mJ/cm2 produces localized cluster of carbons rich materials with average diameter ≅ 10nm. These clusters become connected and the electrical conductivity undergoes a metal-insulator percolative phase transition. The period of the interference pattern is 0.9μm with the width of the wire being about 0.5μm. Nitrogen is blown over the sample during irradiation, because it enhances the stability of the conducting material against degradation by chemical solvent or mechanical stress.

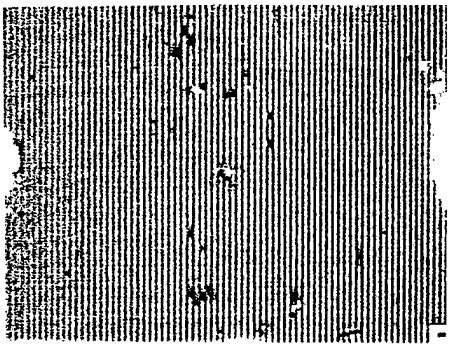


Fig.2: Optical micrograph of polyimide with conducting lines [9]

In another experiment, surface grating structure in the sub micron order have been produced [10] on a thick Cu-film and Si wafer. This is as shown in Fig.3. A smooth and homogeneous structure can be achieved over the whole area. The results have shown that the quality of pattern generated with the femto second pulse ablation is far superior than that with the nanosecond pulse ablation. At higher pulse width there is a broadening of the width due to the increased thermal effects.

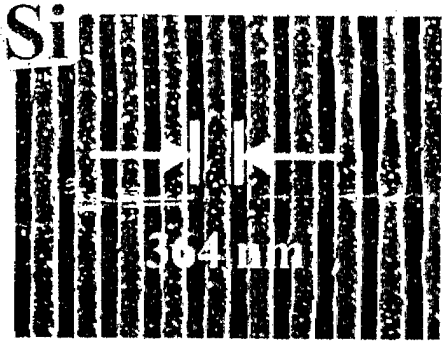


Fig.3: Sub micron periodic structure in Si [10].

4. CONCLUSION

The present report shows that the excimer laser processing is now becoming a viable technique in the nanaostructuring technology. The future generation of telecommunication, microelectronics, fiber optic and sensor waveguide applications shall expedite the use of this technolgy in nanometer electromechanical system (NEMS).

5. REFERENCES

[1] James H. rannon, 'Micropatterning of surfaces by excimer laser projection' J. Vac. Sci. Technol. pp1064-1071(1989).

[2] M. Rothschild and D. J. Ehrlich, 'A review of excimer laser projection lithography' J. Vac. Sci. Technol. pp.1-17(1988).

[3] S. Pissadakis, S. Mailis, L. Reekie, J. S. Wilkinson, R. W. Eason, N. A. Vainos, K. Moschovis and G. Kiriakidis, 'Permanent holographic recording in indium oxide thin films using 193 nm excimer laser' Appl. Physics pp.33-336(1999).

[4] P. E. Dyer, R. J. Farley, R.Giedl and D. M. Karnakis, 'Excimer laser ablation of polymers and glasses for grating fabrication' Appl. Surface Science pp. 537-549 (1996).

[5] F. Beinhorn, J. Ihlemann, P. Simon, G. Marowsky, B. Maisenhoelde, J. Edlinger, D. Neuschaefer and D. Anselmetti, 'Sub-micron grating formation in Ta2O waveguides by femtosecond uv-laser ablation' Appl. Surface Science pp107-110(1999).

[6] P. Simon, J. Ihlemann, 'Machining of submicron structures on metals and semiconductors by ultrashort uv laser pulses' Appl. Physics pp.505-508.

[7] O. Kittelman, J. Ringling, F. Noack, U. Stamm, J. Kleinschmidt and F. Voss, 'High repetition rate amplification of femtosecond pulses at 248nm and 193nm excimer amplifier module' Lambda Highlights No. 44.

[8] Harvey M. Phillips and Roland A. Sauerbrey, 'Excimer laser produced nanostructures in polymers' Optical Engg. pp.2424-2436(1993).

[9] H. M. Phillips, S. Wahl and R. Sauerbrey, 'Submicron electrically conducting wires produced in polyimide by ultraviolet laser radiation' Appl. Phys. Lett. 2572-2574(1993).

[10] P. Simon and J. Ihleman, 'UV-femto second pulse material processing' Laser Laboratory Goettingen e.V. Germany.

Movable Microstructures Made by Two-photon Three-dimensional Microfabrication

Shoji Maruo and Koji Ikuta
Department of Micro System Engineering, Nagoya University
Furo-cho, Chikusa-ku, Nagoya 464-8603, Japan

ABSTRACT:

Movable microstructures were made by the use of two-photon three-dimensional (3D) microfabrication with submicron resolution beyond the diffraction limit of light. In our method, movable microstructures are fabricated by fast scanning a focal point through the inside of the liquid photopolymerizable resin. Therefore, unlike silicon micromachining, neither sacrificial layers nor supporting parts are needed to produce movable mechanism. Furthermore truly three-dimensional movable parts, which have not been produced by silicon micromachining, are easy to make. This method is useful to make complicated 3D microfluidic systems, which include various movable device. In our experiment, a micro gear with a shaft was successfully fabricated within 7 minutes. The rapid fabrication makes mass production of 3D MEMS possible.

1. INTRODUCTION

In practical applications such as micro actuators, micro total analysis systems (μ-TAS) and micro optical devices, truly 3D microfabrication technology is required. Because the ability of 3D fabrication of conventional methods such as anisotropic etching and surface micromachining are not sufficient to fabricate complex microstructure. Even LIGA process, which can make microstructures with high aspect ratio, can not fabricate complicated microstructures with curved surface. Recently several truly 3D microfabrication technologies have been developed, for example microstereolithography like IH process [1] and Super-IH process [2, 3], two-photon microfabrication [4-7], 3D laser chemical vapor deposition [8], etc.

Moreover freely movable structure is necessary to construct various 3D microelectromechanical systems (MEMS). Therefore we demonstrated that a novel microstereolithography named Super-IH process enabled us to make freely movable structures [2, 3]. It is the most unique advantage of Super-IH process that sacrificial layers and supporting parts are not needed to make movable components unlike surface micromachining and LIGA process. This is because photopolymerizable resin is solidified only at the focus inside the resin by focusing a laser beam. In Super-IH process, the pinpoint inner solidification is obtained by the nonlinear response of the solidification reaction based on single-photon absorption.

In this paper, on the other hand, two-photon-absorbed photopolymerization, which we have already used for making 3D microstructures [4, 5], is applied to make freely movable microstructure. In two-photon process, the pinpoint inner solidification is achieved by using the nonlinear optical property of two-photon absorption. Consequently the resolution is expected to exceed the diffraction limit of light. Of course, two-photon microfabrication also provides us the advantages of microstereolithography. For instance, 3D parts are created directly from a 3D computer-aided design (CAD) model, and this leads to high flexibility of 3D modeling. The fast fabrication is of use for both rapid prototyping and mass production.

2. THREE-DIMENSIONAL MICROFABRICATION WITH A TWO-PHOTON PROCESS

2.1 Basic concept and advantages

Two-photon absorption is an optical nonlinear phenomenon that occurs in all materials at sufficiently high levels of irradiance when the combined energy of two photons matches the transition energy between the ground state and the excited state. The rate of two-photon absorption is proportional to the square of the incident light intensity. As a result, near infrared light is strongly absorbed only at the focal point, when it is focused inside the resin that normally absorbs ultraviolet light [5]. Owing to this feature, two-photon microfabrication enables us to make a 3D microstructure as shown in Figure 1. A pulsed near-infrared laser beam, which generates two-photon

1999 INTERNATIONAL SYMPOSIUM ON
MICROMECHATRONICS AND HUMAN SCIENCE
0-7803-5790-6/99/ $10.00 ©1999 IEEE.

absorption, is focused inside the resin. By scanning the focus along the shape of the structure, any 3D structure can be made. Unlike conventional stereolithography, layer-by-layer process is not required.

The use of two-photon absorption produces great advantages as follows:

1) **Submicron resolution**

The resolution is beyond the diffraction limit of light owing to the quadratic response of two-photon absorption on light intensity. In our current fabrication system, the lateral and depth resolutions attain to 0.36 μm and 1.0 μm, respectively.

2) **Large extent of 3D fabrication in depth**

The extent of the fabrication in depth is enlarged in comparison with that of Super-IH process, which is based on single-photon process. This is because the resin is transparent for the near infrared light without the focus where the intensity of light is extremely high, although the laser beam is attenuated by single-photon absorption in Super-IH process. As a result, near infrared light does not be attenuated, even it is focused in deep region of the resin.

3) **Ultra-fast fabrication**

The scanning speed of the laser beam is about tenfold faster than that of Super-IH process. In two-photon process, the resin does not solidified at out-of-focus positions basically. Therefore the resin can be solidified at high scanning speed of about 100 μm/s with high laser power of several ten mW. In Super-IH process, on the other hand, the speed is limited about 10 μm/s at most, since the laser power must be lowered so that the resin does not solidified in out-of-focus region.

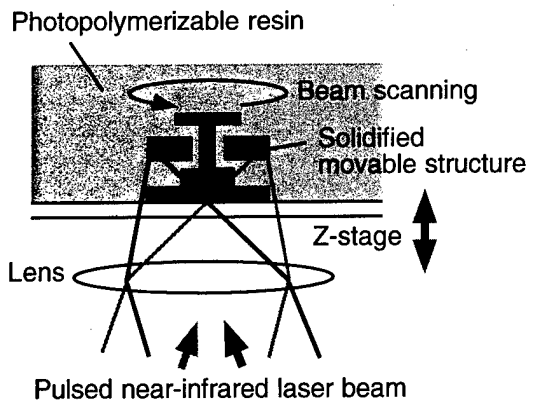


Fig. 1 Fabrication principle of two-photon 3D microfabrication

4) **Freely movable structure**

The pinpoint solidification inside the resin enables us to make a movable component without sacrificial layers nor supporting parts. Although the movable part is floating while the fabrication, it does not move around because of the high viscosity of the resin.

2.2 Fabrication process of freely movable structure by using two-photon microfabrication

Figure 2 (a)-(c) illustrate the fabrication process of freely movable micro gear as an example. After fabricating the shaft as shown in Fig. 2 (a), the stage supporting the resin is lowered to the position that the movable parts is fabricated (Fig. 2 (b)). The movable micro gear is also fabricated only by scanning the focus inside the resin (Fig. 2 (c)). The solidified movable part keeps still in the liquid resin owing to the high viscosity of the resin. After fabrication, the resultant structure is extracted by removing the unsolidified resin with ethanol.

2.3 Experimental setup

Figure 3 shows an optical system for two-photon 3D microfabrication. For generating two-photon absorption, a mode-locked Titanium Sapphire laser (wavelength: 710 nm, repetition: 82 MHz, pulse width: 130 fs) is used, because extremely high optical density is required for two-photon absorption. The beam from the laser is introduced into the galvano-scanner system to deflect its direction in two dimensions, and then is focused with an lens of high numerical aperture (N.A.: 1.3). As the beam scans laterally in the resin

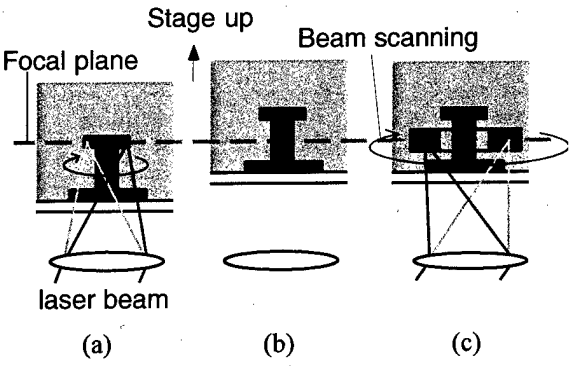


Fig. 2 Fabrication process of freely movable microstructure

and the stage supporting the resin was scanned vertically, any 3D structure can be formed in the resin.

The resin that we used is a mixture of urethane acrylate oligomers/monomers and photoinitiators. Figure 4 shows the absorption spectrum of this resin. As shown in Fig. 4, the resin is transparent at 710 nm which was the wavelength selected to generate two-photon absorption in our experiments. This means that the resin is not solidified by single-photon absorption at the wavelength of 710 nm. Therefore the resin is suitable for two-photon-initiated photopolymerization.

3. EXPERIMENTAL VERIFICATION

3.1 Fabrication of freely movable micro gears

In order to demonstrate the usefulness of our method, we made several micro gears with shafts at a time. Figures 5 (a), (b) show scanning electron microscopic (SEM) images of micro gears. The gear shown in Fig. 5 (a) fell on the base after washing out unsolidified resin. The incident laser power and scanning speed were 30 mW and 42 μm/s, respectively. The gears shown in Fig. 5 (b) were fabricated one by one. This results demonstrated high yield rate of our method. The fabrication time to make each gear was only 7 minutes. This indicates that our method is useful for mass production.

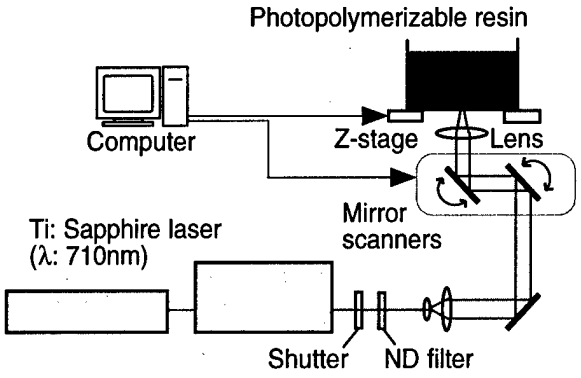


Fig. 3 Optical system for two-photon 3D microfabrication

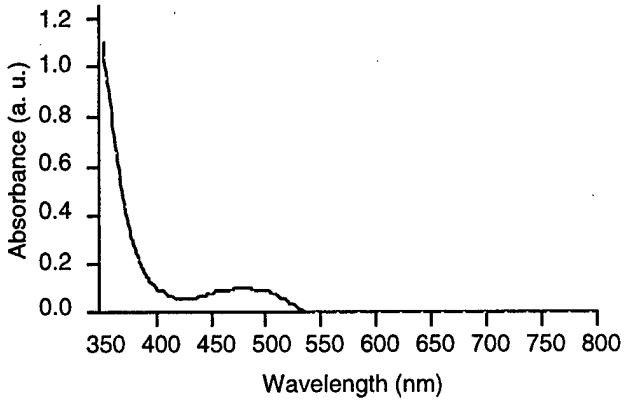
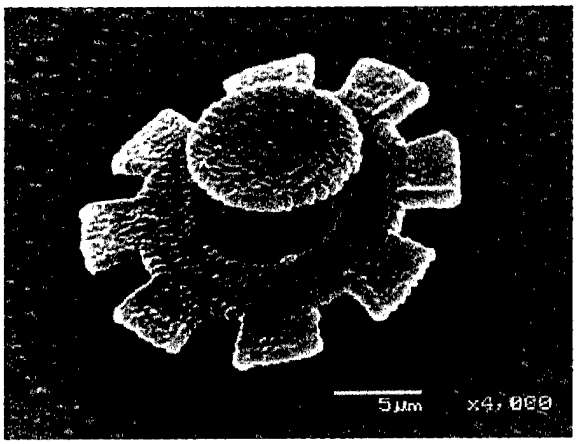
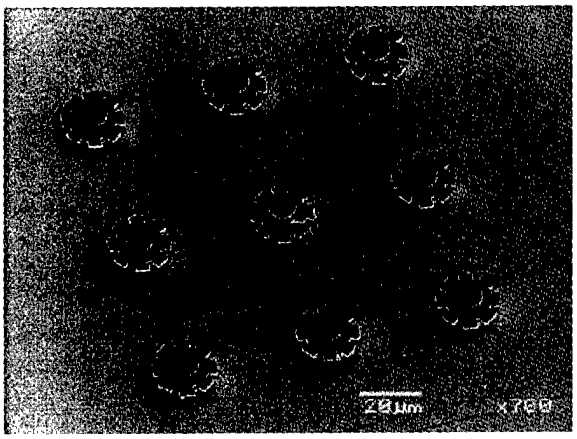


Fig. 4 Absorption spectrum of the resin that we used in our experiments



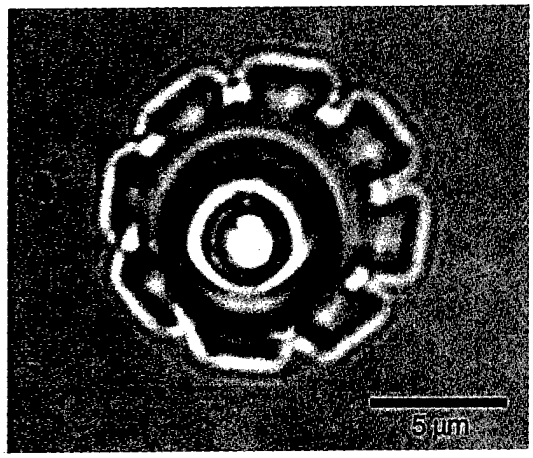
(a)



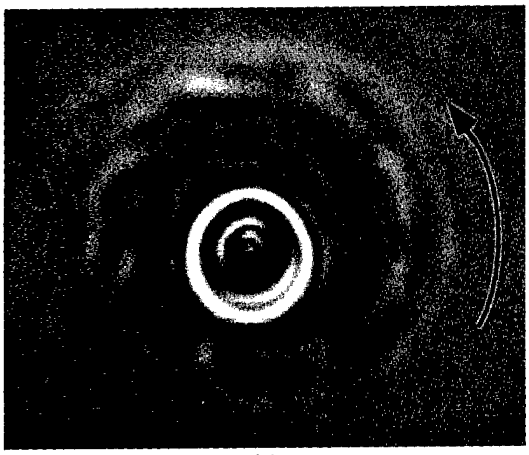
(b)

Fig. 5 Micro gear with shaft made by two-photon 3D microfabrication.
(a) Enlarged image of a micro gear (External diameter: 25 μm)
(b) A series of micro gears

We observed that a micro gear rotated during washing unsolidified resin with ethanol. Figures 6 (a), (b) show optical microscopic images of a micro gear during washing unsolidified resin with ethanol. The images were out of focus, because the



(b)



(a)

Fig. 6 Microscopic images of Micro gear rotating in ethanol.
(a) Micro gear kept still in the resin
(The external diameter of the gear was 12 μm)
(b) Micro gear rotating in the ethanol

gear was too high to be observed with optical microscope. The gear shown in Fig. 6 (a) stood still in ethanol. Fig. 6 (b) shows the gear rotated with ethanol. In this experiment, the rotative speed was about 84 rpm. We considered that the micro gear was rotated with the viscous drag force of the resin.

3.2 Lateral and depth resolution of our current fabrication system

The lateral and depth resolutions of our method were examined experimentally. As shown in Figures 7 (a), (b), in our experiments, the resin was solidified like a thread by scanning a focus. The width and depth of the solidified polymeric thread correspond to the lateral and depth resolution, respectively.

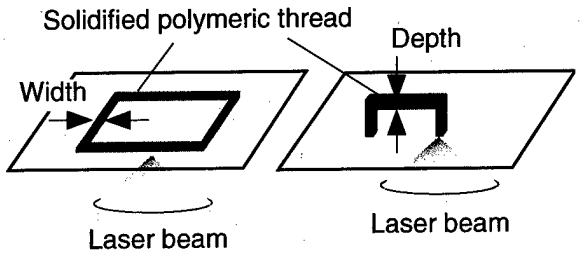


Fig. 7 Fabrication of polymeric threads in order to examine the lateral and depth resolution.
(a) The width of the thread corresponds to the lateral resolution
(b) The depth of the thread corresponds to the depth resolution

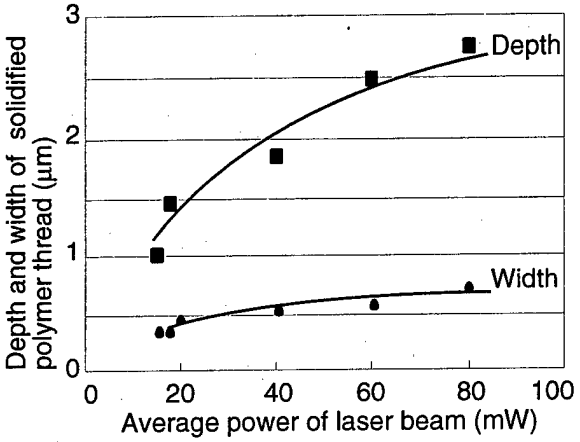


Fig. 8 Width and depth of solidified polymeric thread vs. average laser power.

Figure 8 shows dependence of width and depth on average laser power, while the scanning speed of the laser beam was kept 25 μm/s. Data was obtained by observing the resultant structures, which made by the methods shown in Fig. 7, with scanning electron microscope. The width did not exceed 1 μm, even if the average power of the laser beam was increased to 80 mW. The depth was also less than 3 μm. Therefore, two-photon microfabrication does not require accurate control of the laser power so as to attain submicron resolution unlike Super-IH process. The highest lateral and depth resolutions were 0.36 μm and 1.0 μm, respectively. The lateral resolution was beyond the diffraction limit of light at wavelength of 710 nm. Figures 9 (a), (b) show SEM images of the threads with the finest width and depth. Fig. 9 (a) shows a top left-hand

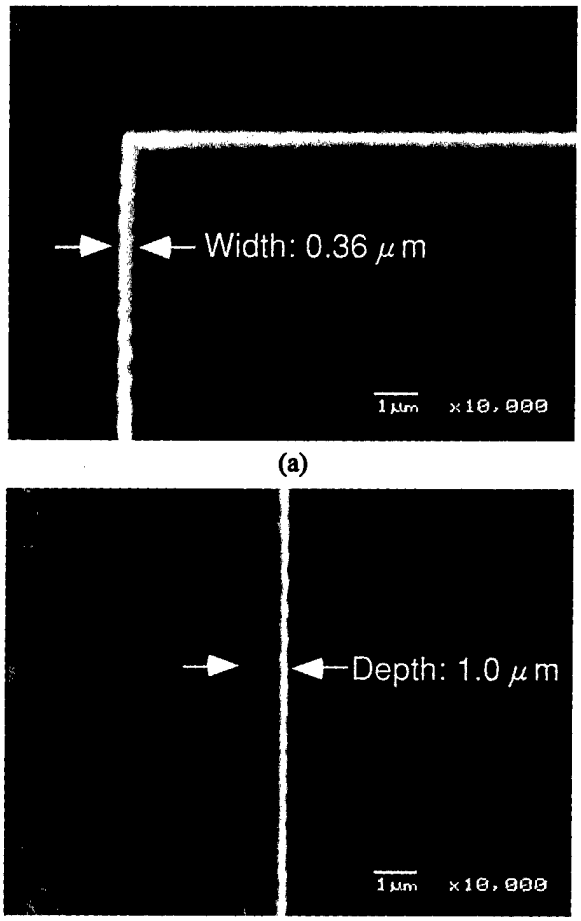


Fig. 9 SEM images of the finest polymeric threads
(a) A top left-hand corner of a square flame
(b) A thread fallen down on the base

corner of a square flame solidified with average laser power of 17.5 mW. The thread shown in Fig. 9 (b) fell down on the base after washing out unsolidified resin.

CONCLUSION

We demonstrated that two-photon 3D microfabrication was useful to make freely movable microstructure without sacrificial layer technique. A fabricated micro gear actually rotated in liquid. Such micro movable parts can be applied to various movable devices included in microfluidic systems. Moreover lateral and depth resolutions have attained to 0.36 μm and 1.0 μm, respectively. The submicron resolution is also useful to fabricate complicated 3D microchannels, which are required in microsystems such as Biochemical IC [9-11], DNA analysis, capillary electrophoresis, etc.

ACKNOWLEDGMENT

Authors would like to thank JSPS MIRAI KAITAKU project to support this research partially.

REFERENCE

[1] K. Ikuta and K. Hirowatari, "Real three dimensional micro fabrication using stereo lithography and metal molding," Proc. of IEEE International Workshop on Micro Electro Mechanical System (MEMS'93), 42-47 (1993).

[2] K. Ikuta, S. Maruo and S. Kojima, "New micro stereo lithography for freely movable 3D structure -Super IH process with submicron resolution -," Proceedings of the IEEE International Workshop on Micro Electro Mechanical Systems (MEMS'98), 290-295 (1998).

[3] S. Maruo and K. Ikuta, "New microstereolithography (Super-IH Process) to create 3D freely movable micromechanism without sacrificial layer technique," Proceedings of the 1998 international symposium on micromechatronics and human science (MHS'98), 115-120 (1998).

[4] S. Maruo, O. Nakamura and S. Kawata, "Three-dimensional microfabrication with two-photon absorbed photopolymerization," Optics Letters **22**, no.2, 132-134 (1997).

[5] S. Maruo and S. Kawata, "Two-photon-absorbed near-infrared photopolymerization for three-dimensional microfabrication," Journal of Microelectromechanical Systems 7, no. 4, 411-415 (1998).

[6] S. Maruo and K. Ikuta, "Two-photon three-dimensional microfabrication for the production of movable mechanism with 0.5 micrometer resolution," Proc. of 10th International Conference on Solid-State Sensors and Actuators (Transducers '99), 1232-1235 (1999).

[7] B. H. Cumpston, S. P. Ananthavel, S. Barlow, D. L. Dyer, J. E. Ehrlich, L. L. Erskine, A. A. Heikal, S. M. Kuebler, I. -Y. S. Lee, D. McCord-Maughon, J. Qin, H. Röckel, M.

Rumi, X. Wu, S. R. Marder and J. W. Perry, "Two-photon polymerization initiators for three-dimensional optical data strage and microfabrication," Nature **398**, 51-54 (1999).

[8] K. Williams, J. Maxwell, K. Larsson, M. Boman, "Freeform fabrication of functional microsolenoids, electromagnets and helical springs using high-pressure laser chemical vapor deposition," Proceedings of the IEEE International Workshop on Micro Electro Mechanical Systems (MEMS'99), 232-237 (1999).

[9] K. Ikuta, plenary talk paper, "3D micro integrated fluid system toward living LSI," Proc. of Fifth International Conference on Artificial Life (A-life V), 17-24 (1996).

[10] K. Ikuta, S. Maruo, Y. Fukaya and T. Fujisawa, "Biochemical IC chip toward cell free DNA protein synthesis," Proc. of the IEEE International Workshop on Micro Electro Mechanical Systems (MEMS'98), 131-136 (1998).

[11] K. Ikuta, S. Maruo, T. Fujisawa, T. Hasegawa, T. Adachi and Y. Nakatani, "Biochemical IC family for general micro chemical systems - Development of multiple concentrators, reactors and valve chips," Proc. of 10th International Conference on Solid-state Sensors and Actuators (Transducers '99), 1046-1049 (1999).

3D microstructuring of glass using electrochemical discharge machining (ECDM)

Valia Fascio, Rolf Wüthrich, Didier Viquerat, Hans Langen

Département de microtechnique. Institut des systèmes robotiques (DMT-ISR)
EPFL (Swiss Federal Institute of Technology Lausanne)
CH-1015 Lausanne EPFL, Switzerland.

Abstract :
3D micropattering is done in an electrolyte with electrodischarge assisted etching at the tool tip.
Reported are the influence of the percentage of sodium ions in the sample, the applied voltage and the distance between tool and glass sample, and the induced local composition modifications. SIMS analysis has shown the diffusion and extraction of sodium ions, dissolution of SiO_2^- and local substitution of Na^+ with H^+ ions.
The study of such aspects will contribute to the control of 3D microstructuring and to the local surface modification.

1. INTRODUCTION

The glass, due to its transparency and its chemical resistance, is often used in MEMS technology in combination with silicon wafers that have integrated mechanics and electronics (encapsulated accelerometers, pressure devices, fluid systems, etc).
ECDM is an alternative solution to the laser machining, the etching with HF or normal drilling and milling with special tools. On one hand, ECDM can offer a good surface quality if we compare with the laser technology, which is more flexible. On an other hand, deep and small structures can be obtained more easily than by etching with HF.
In this paper we will present the 3D high aspect ratio structuring of glass by electrochemical discharge machining (ECDM) technology.
The process can be described as following. The glass sample to be machined is dipped in an electrolyte solution together with two electrodes (cathode is machining tool). Applying a constant voltage between these electrodes, sparks are generated which erodes the glass. The process offers the advantage to obtain a small surface roughness and allows different kinds of structures, especially with high aspect ratios. Furthermore, we do not need any mask during the chemical attack, because the reaction occurs in the vicinity of the cathode and the size of the pattern is connected with the diameter of the cathode.
Few literature is available on glass machining with ECDM. The process is complex and the spark generation is not well known. Nevertheless, drilling holes in glass is not a new technology and was already applied in 1968 by Kurafuji et al. [1]. It has been reported that ECDM has a low efficiency and that there is a limit to the depth to which glass can be machined. Ghosh et al.[2], in 1995, found a theoretical model for the discharge phenomenon at the tool tip and estimated the critical voltage and the current required to initiate the discharge between the electrode and electrolyte. 3D micro structuring experiments using different types of actuators are reported by Langen et al. [3], where ECDM technology was used without feedback of any process parameters.

This paper presents the study of some ECDM parameters (the working distance d, the voltage V) on the machining characteristics, the changes in material composition in glass and the precision of machining (the gap and the resolution).

2. EXPERIMENTAL SET-UP AND ECDM PROCESS

To obtain more informations on the process parameters concerning machining precision, a tool holder was developed for EDCM machining by Wüthrich et al. [4]. The ECDM tool holder is composed of a mini voice coil motor used as actuator. Optical sensors are used for the measurement of the tool motion. The tool tip can be controlled in position control mode or in force control mode. Furthermore, the same tool tip will be used here to do measurements. The tool holder is fixed on the XYZ manipulator (see Fig. 1).
The tool electrode (the cathode) is a needle in stainless steel with a 0.6 mm diameter and the anode is a platinum foil. The tool tip motion is parallel to the Z-axis of the XYZ stage from Newport. The stage has a range of a few centimetres, a

1999 INTERNATIONAL SYMPOSIUM ON
MICROMECHATRONICS AND HUMAN SCIENCE
0-7803-5790-6/99/ $10.00 ©1999 IEEE.

resolution about 100 nm and is controlled from a Windows NT® platform.
The anode and the glass sample are fixed. We employ a rectified and regulated supply.
The substrate to be machined is dipped in NaOH-30% solution.

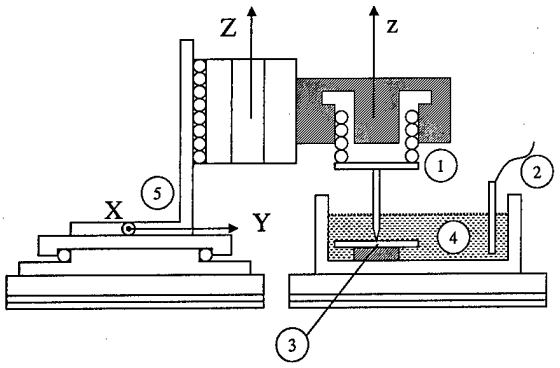


Figure 1 : The ECDM set-up: (1)- tool electrode with the holder mounted on a voice coil motor, (2) anode. (3) glass sample.(4) electrolyte (5) XYZ stage.

2.1. Thermal and chemical mechanisms

2.1.1. Spark generation

When the voltage is applied, H_2 bubbles are generated at the cathode and O_2 at the anode.
The two electrodes are separated form the solution by a gas film and sparks are generated through the bubbles around the cathode. The removal of glass takes place at the cathode, where discharges appear.
When the voltage increases, the spark generation becomes more important.
The erosion of the glass is not only thermal, due to the spark generation, but also chemical due to the chemical attack of the glass by the alkali solution.

2.1.2. Chemical reactions

The alkali attack is function of the pH and the temperature of the solution. The rate of alkali attack is multiplied by a factor two with an pH increase of one unit or a temperature increase of 10°C according to Mc Lellan et al.[5]. Due to the variations in temperature near the tool tip, it becomes difficult to control the etching rate as will be shown later.
The etching mechanism results in a smooth surface when the dissolution of the silicate is complete, otherwise a rough surface is produced.

The presence of ions like Ca^{2+}, Mg^{+} and Na^{+} in the composition increases also the rate of alkali attack, due to their high mobility.
The etching reaction of the glass is :

$$2\,NaOH + SiO_2 \rightarrow Na_2SiO_3 + H_2O$$

When etching occurs during the machining, we obtain the pattern like this shown on figure 2.

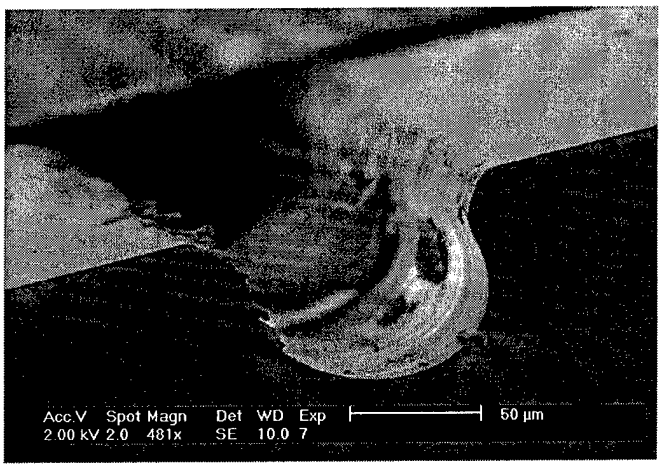


Figure 2: Microchannel machined in a borosilicate glass. The voltage applied was 30 V. The tool was positioned 50 µm under the surface of the glass. The profile has a width of 100 µm and a depth of 72 µm. The tool tip was in position control mode.

3. EXPERIMENTS

The aim of the first tests was to consider the parameters as the voltage applied between the electrodes and the working distance between the tool and the substrate and find the range of their values in order to control the quality of the surface and also the precision of the machining.

During these experiments, we machined a groove on the glass sample by changing the following parameters:

- The working distance d between –60 µm and 60 µm : If we consider the surface of the glass as 0, the position of the tool tip was between – 60 µm and 60 µm,
- The voltage applied V varied from 25 to 40 V,

Furthermore, different material compositions were chosen for the glass in order to study the contribution of mobile ions like Na^{+}. The results of surface quality measurement and machining depth are reported respectively in table 2 and Fig.4.
In order to start by studying the influence of the voltage, the working distance and the number of machining steps, we first used a soda-lime glass with a 14 % sodium concentration. It is important to precise the sodium concentration because Na^{+}

diffuses rapidly and accelerates the chemical attack together with Ca^{2+}, Mg^{2+} and K^{+}. The results of SIMS analysis are discussed later.

Our hypothesis is that the main mechanism during the machining is a chemical one, and consists in the extraction of sodium ions and the dissolution of the silicate. In order to obtain a good surface quality and to control the patterns designed, the chemical mechanisms should dominate the material removal due to the thermal cracking and spalling.

3.1. Discussion of the experimental results

Influence of the working distance

Experiments were done with working distances varying between –60 and 60 μm, where the tool tip was positionned respectively from 60 μm under the glass surface to 60 μm above the surface. The voltage was set to 30 V.
With working distances larger than 30 μm, the glass is not eroded. No transformation of the glass occurs because the removal depth of one step for 30 V was about 25 μm.
Between 0 and 30 μm, we could observe the pattern of the needle. For smaller working distances (d< 0 μm) the surface quality becomes better and the grooves are deeper. By scanning the machined groove, we could measure the machining depth m. The results are shown in the table 1. Even if the grooves are deeper, their width is always around 120 μm.

Working distance d (μm)	Machining depth m (μm)
0	5.5
- 20	39
- 60	118

Table 1 : Influence of the working distance d on the machining depth m

Furthermore, the pattern obtained depends on the duration of the machining. For example, when holes were drilled in the glass, best results in term of surface quality were obtained for the lowest working distances (the "negative" values). In this case, we did not observe any thermal deformation of the glass and the diameter was around 200 μm instead of 300 μm for the higher working distances. The diameter of the hole increases with the the duration of the machining.

Through these experiments, we could observe that the timing is not a minor problem during the machining and five seconds can change the pattern, we want to obtain, due to the increase of the electrolyte's temperature. Nevertheless to limit the timing problem, we could use a low working distance (d<0 μm).

Influence of the voltage

For a defined working distance, we observed that for a low voltage (below 25 V), the reaction is mainly an electrolytic one, we observed bubbles but the glass is not eroded. By increasing the voltage, the mechanism becomes chemical. For exemple, at 30 V, we obtained current peaks from 0.1 to 0.3 A. But for a voltage in the vicinity of 35-40 V, the current peaks are around 1 A.
Our results correspond with those obtained by Ghosh et al.[2]. They found that the critical voltage required to obtain a discharge between the electrode and the electrolyte in a NaOH-30% solution was between 20 and 30 V .
For 25 V, the removal depth is around 23 μm and for 30 V about 25 μm (see Fig.3). We can remark that for 30 V, less dispersion in the results occur than for 25 V. The standard deviation due to the fluctuation of the measures are respectively 2 μm for 30V and 4 μm for 25 V. We made the same experiments for 35 V and the dispersion in the results, due to the thermal cracking is much more important.
The dispersion in the results can be explained by the difficulty in controlling the H_2 film formation and the heat transfer in the vicinity of the tool tip.

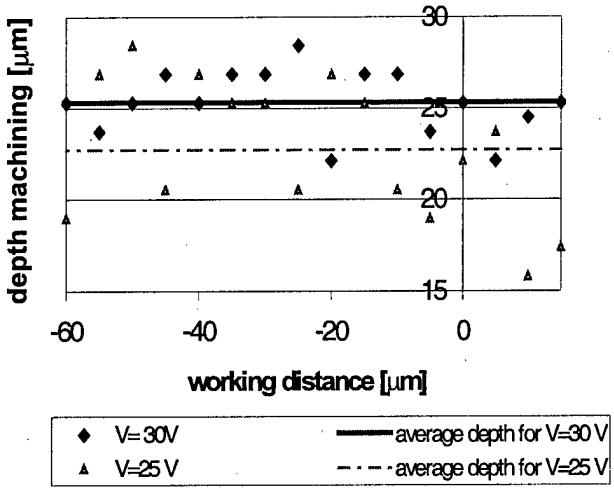


Figure 3: Influence of voltage applied for V=25 V and V=30 V

Influence of the number of machining steps

Multiple steps machining under different conditions is often applied to make a compromise between total machining time and resulting surface roughness. That is, rough machining steps and finishing machining are applied in a repetitive

manner where material removal is precisely defined or estimated. Due to the difficulty in controlling the hydrodynamic instabilities around the tool tip and its related heat transfer, the application of rough and finish machining is still under study. Preliminary experiments towards this direction are reported in [4].

Inflluence of the material composition

We used two glasses with a lower sodium percentage, we made the experiments in the optics of the 3D machining .
The first glass, called M, is a special glass, which has an intermediate sodium percentage (cf. table 2). By using this glass, when the voltage increases, the surface quality is better for 35 V and 40 V, we do not observe any thermal cracking in the pattern or the tip needle. When the working distance is higher than 15 µm, we do not obtain any results. For the borosilicate, the surface quality is excellent for 30 V. But, thermal cracking occurs at 40 V. The results are summarized in the table 2.

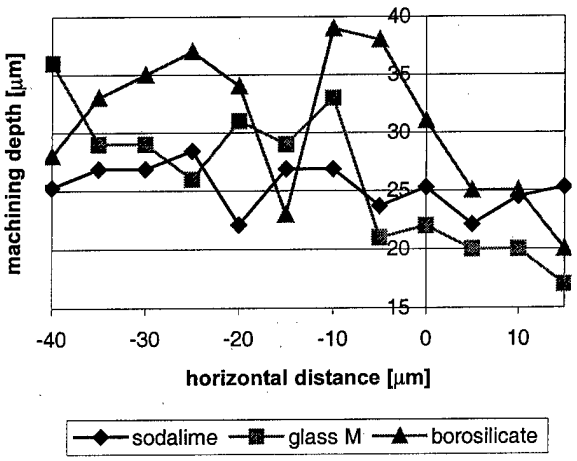


Figure 4: Influence of the glass composition on the machining depth for the tool tip in position control mode.

	Soda lime	Glass M	Borosilicate
% sodium	14	9	4
% SiO2	74	91	81
Other elements	MgO , CaO		B_2O_3, Al_2O_3
Surface quality	++	+	+++
Average machining depth *m* [µm] of one step (Average standard deviation [µm])	25 (2)	26(6)	30(6)

Table 2 : Chemical composition and surface quality of glasses

The standard deviation is important for the glass M and the borosilicate and equals to 6 µm. The sodalime gives the less important fluctuations.
For the borosilicate, the machining depth is higher than the corresponding values for the sodalime and the glass M. The surface quality is better for the sodalime and the borosilicate. The etching could be more important due to the presence of species, which can accelerate the chemical attack in this two glasses.

3.2. SIMS analysis

In order to determinate the influence of the voltage and of the working distance on the chemistry of the surface, SIMS analysis was done. The study was concentrated on the presence of sodium and silicate ions.

Firstly, we analysed the soda-lime sample machined with 30V and 40 V and with the same working distance 30 µm. These experiments were done in an early stage of the project, where no position feedback of the tool tip was applied.
As it could be expected the rate of sodium is much more important outside the groove than inside. We can make the same observation for Ca^{2+}, K^{+} and Mg^{+}.
The dissolution of the silicate can be observed. Its concentration is also less important in the groove than outside. Furthermore, an increased concentration of H^{+} species was observed in the groove.
The same results were observed for the sample machined with 40 V.

This analysis give indications on the chemical mechanisms that can occur and confirm in part our hypothesis on the machining mechanisms.

4. MACHINING EXAMPLES

The figure 5 shows the excellent surface quality we obtained after the study of the machining parameters detailed in the part 3.



Figure 5 : Groove machined in a borosilicate glass at 30V. the tool tip was in position control mode.

We machined with a voltage of 30 V and a working distance of –50 μm. An excellent surface quality was obtained.

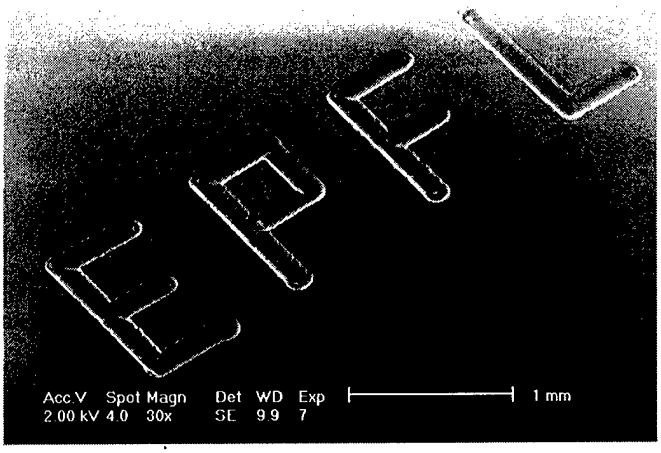


Figure 6 : Pattern machined in borosilicate at 30 V for a working distance equals to –60 μm. The tool's speed was constant at 0.05 mm/s. The tool tip was in position control mode.

On the figure 6 is shown a most complex structure, we machined. The voltage applied was 30 V and the working distance was – 60 μm. The figure 6 shows the potentials of the ECDM process for writing patterns in glass substrates. Moreover another advantage of the ECDM technology is that we can machine different section profiles, because the profile is connected to the shape of the tool holder. The use of different kind of microtools can be applied for machining much more complex shapes in the glass.

5. CONCLUSION

Our aim, in this paper was to present the newest investigations we made in the field of the ECDM machining. The influence of the voltage applied and of the working distance were studied in order to control the machining depth. The best surface qualities were obtained for 30 V and for "negative" working distances, using borosilicate but the resolution was about 6 μm. Using these results, we machined 3D structures. Although the machining step height can be estimated, the difficulty of controlling the process characteristics near the tool tip makes it difficult to obtain accurate machining depths and good surface qualities with high repeatability. This will remain a part of our study in the future. The results of some machining examples are very promising showing that ECDM technology has great potential for the prototyping of glass substrates for MEMS devices, like micro pumps or other fluidic micro systems.

ACKNOWLEDGEMENTS

It is a pleasure to thank Dr. Didier Leonard from the Laboratory of Metallurgical Chemistry (LMCH) and the CIME from the EPFL. We would thank the firm "Prime Verre" from Montpellier (France), which gave us the glass M. The research could not be conducted without the financial support of the Swiss Government.

REFERENCES

[1] H. Kurafuji and K. Suda, "Electrical Discharge Drilling of Glass-I", *Annals of the CIRP,* **16** (1968) 415

[2] I Basak and A. Ghosh, "Mechanism of Spark Generation during Electrochemical Discharge Machining: A Theoretical Model and Experimental Verification", *Journal of Material Processing Technology,* **62** (1996) 46-53

[3] H. Langen, J-M. Breguet, H. Bleuler, Ph. Renaud and T. Masuzawa, "Micro Electrochemical Discharge Machining of Glass", *International Journal of Electrical Machining*, **3** (1998) 65-69

[4] R. Wüthrich, V. Fascio, D. Viquerat, H. Langen, " In Situ Measurement and Micromachining of Glass", *International Symposium on Michromechatronics and Human Science (MHS'99)*

[5] G. W. McLellan and E.B. Shand, "Glass engineering handbook". Mc Graw-Hill book company.

In Situ Measurement and Micromachining of Glass

Rolf Wüthrich, Valia Fascio, Didier Viquerat, Hans Langen

Swiss Federal Institute of Technology
Département de microtechnique, Institut de systèmes robotiques
EPFL (Swiss Federal Institute of technology Lausanne)
CH-1015 Lausanne
Switzerland

Abstract:
Glass substrates were micromachined using electro chemical discharge machining. The developed tool holder allows to scan the substrate surface as well as machining it in a closed loop. The developed control algorithm for drilling holes allows to achieve relatively high machining speeds (up to 30 μm/s) and deep structures (up to 1 mm). Micro-channels up to a depth of 100 μm were machined in one step with a removal rate of $4.5 \cdot 10^5 \mu m^3/s$. Reported are some examples of machining micro-holes, micro-channels and modification of existing pattering.

1. INTRODUCTION

The glass is an important material in the field MEMS technology and often applied due to its transparency and its chemical resistance. It is often used in combination with silicon wafers that have integrated mechanics and electronics (encapsulated accelerometers, pressure devices, fluid systems, etc).
Normally conventional drilling or milling with special tools, laser machining or etching with HF is applied to structure the glass. Although a good surface roughness can obtained with the latter, the fabrication of devices with a variety of deep and small structures is more complex. Laser machining offers more flexibility but results in less surface quality.
In this paper we will present the 3D high aspect ratio structuring of glass by electrochemical discharge machining (ECDM) technology. For more functionality, an experimental set-up is proposed for parallel machining and measurement using micro tools. This technology has great potential for the prototyping of glass substrates for MEMS devices, like micro pumps or other fluidic micro systems.
The process can be described as following. The glass sample to be machined is dipped in an electrolyte solution together with two electrodes (cathode is machining tool). Applying a constant voltage between these electrodes, sparks are generated which erodes the glass. The process offers the advantage to obtain a small surface roughness and allows different kinds of structures, especially with high aspect ratios. Furthermore, no mask is needed during the chemical attack, because the reaction occurs in the vicinity of the cathode and the size of the pattern is connected with the diameter of the cathode.
Few literature is available on glass machining with ECDM. The process is complex and the spark generation is not well known. Nevertheless, drilling holes in glass is not a new technology and was already applied in 1968 by Kurafuji et al. [1]. It has been reported that ECDM has a low efficiency and that there is a limit to the depth to which glass can be machined. Ghosh et al. [2], in 1995, found a theoretical model for the discharge phenomenon at the tool tip and estimated the critical voltage and the current required to initiate the discharge between the electrode and electrolyte. 3D micro structuring experiments using different types of actuators are reported by Langen et al. [3], where ECDM technology was used without feedback of any process parameters.

This paper will report the development of a special tool holder. It enables the measurement of surface profiles direct after machining. If necessary, these surfaces could be corrected by a second machining step. Furthermore, for the first time, some structures have been machined in glass successfully by applying active control of some ECDM process parameters.

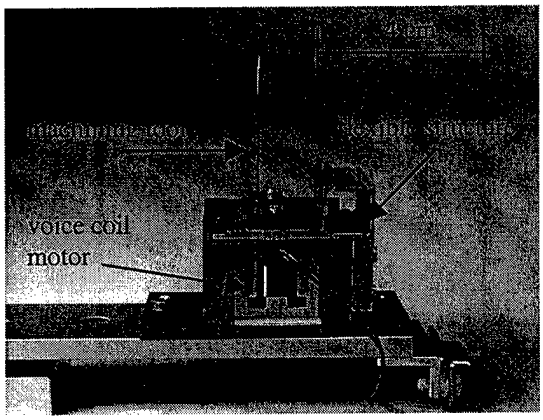


Figure 1 Realized ECDM tool holder. In the middle is the voice coil motor, on the top the machining tool fixed on the flexible structure.

1999 INTERNATIONAL SYMPOSIUM ON
MICROMECHATRONICS AND HUMAN SCIENCE
0-7803-5790-6/99/ $10.00 ©1999 IEEE.

2. ECDM TOOL HOLDER

To enable measurements on machined surface profiles a tool holder was developed. For the moment the same tool is used for doing measurement and machining as well, since tool wear during ECDMing can be neglected.

The ECDM tool holder (see Fig. 1) consists of a mini voice coil motor used as actuator, and of two small optical sensors for the measurement of the tool motion. A flexible structure acts as a spring and guides the motion of the voice coil. It is designed for controlling displacements of the machining tool in a range of 300 μm with an accuracy better than 1 μm. It can be used in three different ways. There are two control modes, and one measuring mode. The control modes are the closed loop mode which is used for the control of the position of the machining tool and the force sensor mode which is used for measuring, or controlling, the force during the machining process. The last one, that we call the scanning mode, is used for measuring surface profiles. The control modes are used during machining. It becomes possible to machine either at a defined tool height, or with a defined force.

2.1. Voice coil motor and flexible structure

The used mini voice coil motor is commercially available in the Swiss company ETEL SA. It is normally used in Die-bonding machines. Despite of his small size, it can produce a force up to 3 Newton (6 Newton during a short time). Other important proprieties are that these kinds of motors are fast and the motion is step free. Both are needed in the application of ECDM.
The flexible structure, which acts as a spring and guides the voice coil motor, was machined using wire electro-discharge machining (WEDM). Its stiffness is about 1000 N/m and it has a linear working range of ±150 μm.

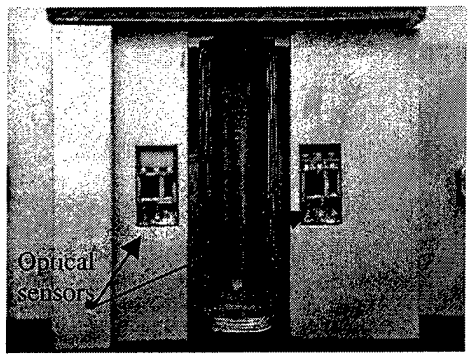


Figure 2 Two optical sensors mounted on the bottom of the device

2.2. Optical sensors

In order to measure the vertical displacement of the machining tool, the mean value of two optical sensors are used. These sensors are mounted between the base and the flexible structure (see Fig. 2). Each sensor has an LED and phototransistor combination that detects the reflected light on the flexible structure. The intensity of the reflected light is a measure for the distance between the target and the sensor. The LED and the phototransistor are mounted in the same package and are commercially available in SMD technology. With a well-designed readout electronic they show a linear response with high gain (about $3 \cdot 10^5$ V/m) in a range of ±150μm. The resolution of the sensors is about 100 nm.

2.3. Closed loop mode

The closed loop mode is realized by adding a controller. The input is the difference e between the set point w (desired tool position) and the measured position y by the optical sensors. The output u is the control current to drive the voice coil motor. We use a standard PID controller implemented on a DSP from Texas Instruments in a PC. The algorithm uses separate filtered derivation, and a antiwindup loop to avoid saturation of the actuator (see Fig. 3).

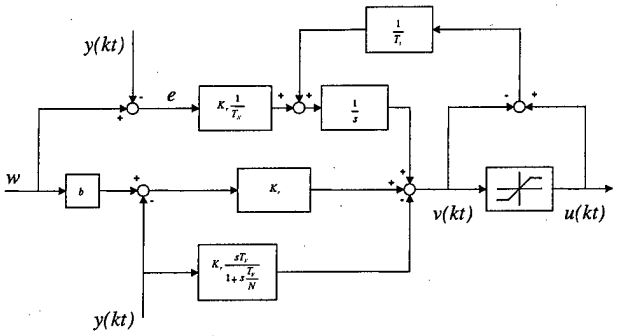


Figure 3 Flow chart of the implemented PID controller; w is the desired tool position, y the measured tool position by the optical sensors and u is the voice coil driving current.

In figure 4 a typical step input of the ECDM tool holder in closed loop is shown. The coordinate z is the displacement of the ECDM tool.

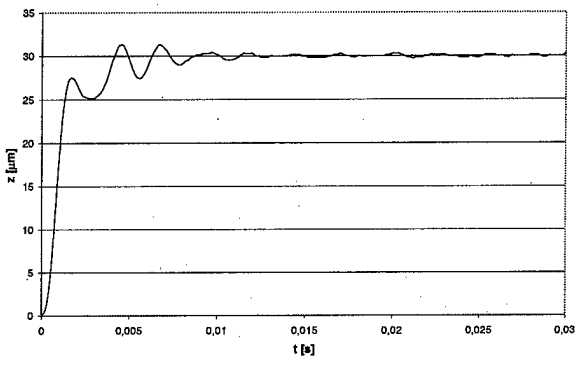


Figure 4 A typical step input of the ECDM tool holder; z is the displacement of the machining tool

In figure 5 a typical response of the device in closed loop when a constant external force is applied is shown. The voice coil generates the external force, by adding a constant offset current to the control current.
The value of 160 mN is a typical intensity of the force occurring during machining. These forces are probably due to the collapse of the hydrogen bubbles around the machining tool.

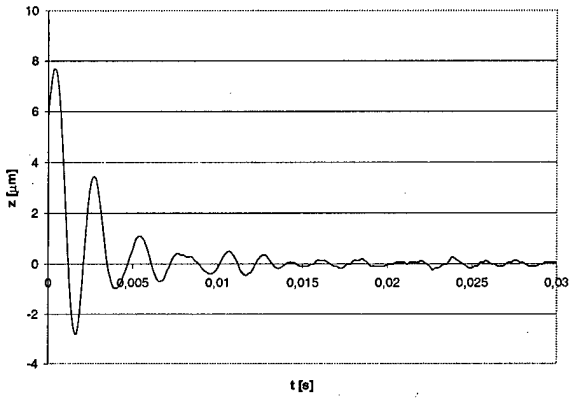


Figure 5 Response of the ECDM tool holder when a constant external force of 160 mN is applied; z is the displacement of the machining tool.

2.4. Force sensor mode

This mode is used in closed loop. The control current injected in the voice coil motor to keep the machining tool at constant height gives the measure of the force during machining. The device is able to see forces with a resolution of about 1 mN.

Using this mode we can monitor the evolution of the force applied on the tool during machining. We measured typical values about 100-200 mN. Another possibility is to control the applied force during machining. In this case the position of the tool is not fixed.

2.5. Scanning mode

This mode is used in open loop. Only the response of the optical sensors is used. The relatively high resolution of the sensors allows us to see small details in a scanned structure. The main limiting factor is the tool size. In order to keep contact between the machining tool and the surface during scanning, the voice coil applies a constant force (using a constant current).

3 SET-UP AND EXPERIMENTS

The used experimental set-up is shown on figure 6. The ECDM tool holder is fixed on a XYZ-stage from Newport. The stage has a range of a few centimetres, a resolution about 100 nm and is controlled from a Windows NT® platform.

The glass to be machined is dipped in a NaOH-30% solution. The tool, fixed on the ECDM tool holder, acts as cathode. The anode is a platinum foil. The electrodes are connected to a stabilised power supply which can be switched from the DSP used to control the ECDM tool holder. During machining a H_2 gas film is formed around the tool electrode.
As machining tool stainless steel needles were used with typical diameters of 0.6 mm or self made micro-tools in various materials (tungsten, stainless steel, copper) by using Wire Electro-Discharge Grinding on an extra developed prototype [4].

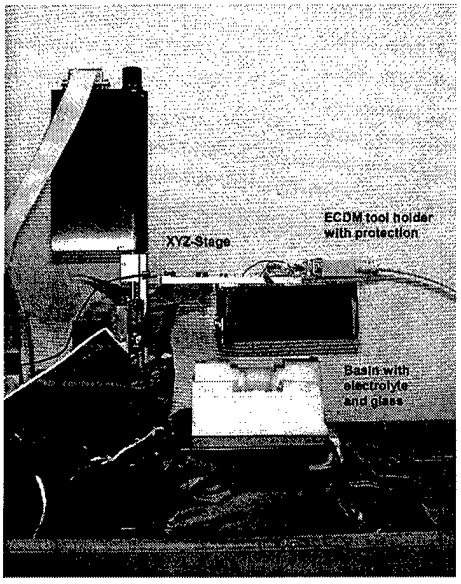


Figure 6 Experimental set-up with the ECDM tool holder mounted on a XYZ-stage

With this set-up it is possible to drill holes, machine channels like structures, and scan machined or existing patterns.

3.1. Drilling holes

Drilling holes is a good way to design machining control algorithms. With our algorithms we were able to drill holes with a depth up to 1mm and also through-holes. For this we used the combination of the motion of the Z stage and the ECDM tool holder. The Z stage gives a motion with constant velocity. During machining, the ECDM tool holder can very quickly adapt this motion by moving the machining tool in his working range. No rotation of the machining tool was used. We could achieve machining speeds up to 30 µm/s. This speed is a mean speed, as in the beginning the speed is very high, and then, when the hole becomes deeper, slows down. This is probably due to the fact that when the hole is deep, the electrolyte has more difficulty to circulate around the machining tool.

Drilling deep holes (>300 µm) presents three major difficulties. The first one is to maintain the flux of the

electrolyte around the machining tool. Once the hole is deep, the electrolyte has more and more difficulty to flow around the tool. Electrochemical attacks becomes harder to obtain. The machining process may stop. Linked to this problem is the increase of the temperature. As there is less electrolyte, the temperature increase faster and so may produce cracking of the glass and even break the complete glass sample. To avoid these problems our control algorithm regularly moves up the tool quickly in order to allow fresh electrolyte to flow into the machined hole.

The second difficulty is the increase of the temperature during the long machining time. This is particularly a problem when the machining speed is too slow. The glass may break. This was always observed for deep holes with too slow drilling speeds and especially in open loop system (simply pushing down slowly the machining tool).

The third difficulty is to avoid the increase of the hole diameter during machining. As the gas film occurs around the total surface of the machining tool, it normally happens that the hole becomes wider during drilling. One way to avoid this is to drill with high speed.

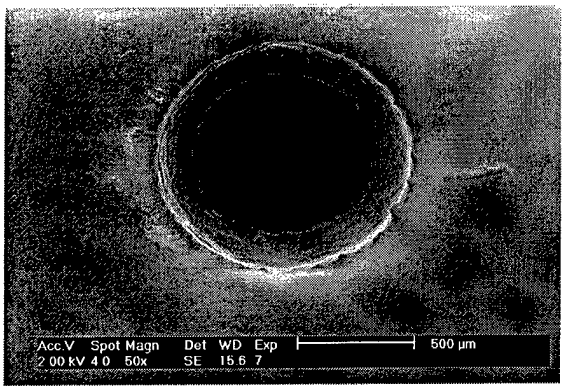


Figure 7 A trough-hole made with a cylindrical tool with 0.7 mm diameter in a borosilicate glass; the depth of the hole is 1 mm; active control on the machining force was applied. No cracking of the glass can be observed. The part were the tool entered the glass is shown. The applied voltage between the electrodes was 30 V.

On figure 7 a deep hole machined at 30 V in borosilicate glass is shown. The used tool was a cylinder with a diameter of 700 µm. The drilled hole has a diameter of 1109 µm. No thermal cracking of the glass can be observed. Force feedback was used with a certain threshold level.

3.2. Machining micro-channels

Using the ECDM tool holder in the closed loop mode, it is possible to machine channels with various depths and forms. This kind of structures are very interesting for fluid systems, like micro-pumps, micro-chemical sensor, etc.

In order to obtain a micro-channels of a defined depth, it is important to control the working distance between the machining tool and the glass surface. We have found that, depending on the applied voltage between the electrodes, the machining depth is about 25 µm as reported by Fascio et al. [5]. The tool holder is used to position the machining tool at the needed working distance from the glass which is computed using the desired channel depth and the known machining depth.

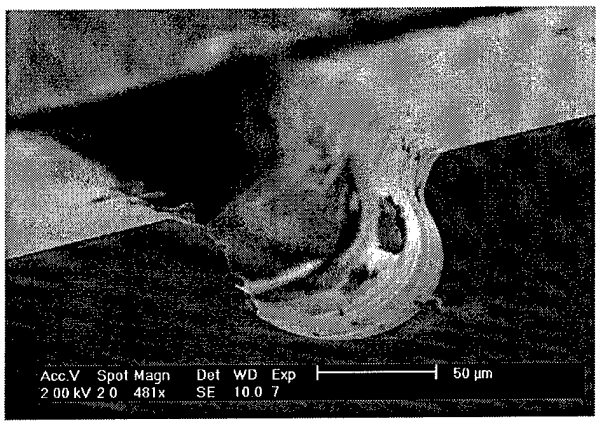


Figure 8 Profile of a machined channel in a Pyrex glass wafer with the tool from figure 9. The applied voltage between the electrodes was 30V; the machining tool was controlled 50 µm under the glass surface. The obtained mean depth is 72 µm

During machining of micro-channels no active control on ECDM parameters is applied. The tool motion in the XY plane is controlled by the XY-stage. During machining, a constant speed of 0.05mm/s was used. The tool holder had to control the position of the machining tool in Z direction.

Compared with drilling holes, local heating is less significant and the risk of glass cracking is not so great. The tool does never stay on the same place for a long time. This is the reason why it is possible to obtain good results also in a open loop machining. But the machining speed is not optimal.

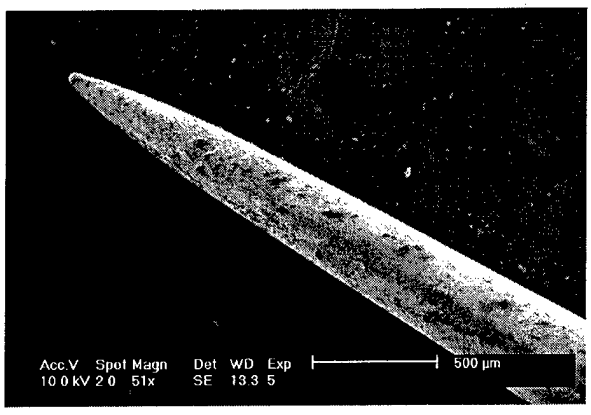


Figure 9 Needle used as an ECDM tool

Figure 8 shows an example of a machined micro-channel. It was machined in a Pyrex glass wafer at 30 V. The electrode tool holder controlled the position of the machining tool to be 50 µm under the glass surface. The used tool was the needle

shown in figure 9. The obtained channel mean depth is 72 μm and the width is 100 μm.

The obtained surface qualities are good. Figure 10 shows a zoom on a micro-channel machined in a borosilicate glass at 30 V. One major parameter that controls the surface quality is the applied voltage between the electrodes [5].

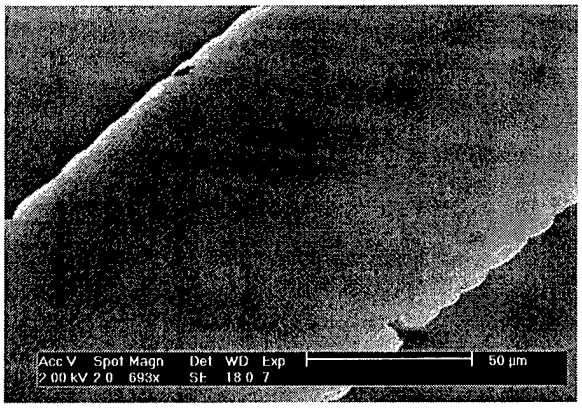


Figure 10 Zoom on a machined micro-channel in a borosilicate glass in one step. Machining at 30V. The excellent surface quality can be seen. The material removal rate was $4.5 \cdot 10^5$ μm³/s.

Using different machining tools allows getting different channel forms. Figure 11 shows the result obtained using a cylindrical tool with a diameter of 400 μm. The channel was machined in one step in a Pyrex glass wafer. The tool holder controlled the position of the machining tool at 50 μm under the glass surface. The obtained channel depth is 100 μm, and the channel width is 675 μm.

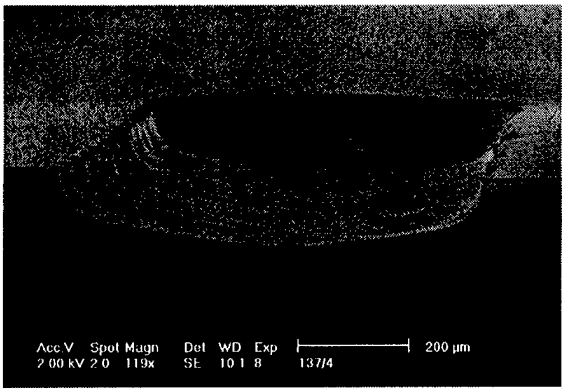


Figure 11 Profile of a machined channel in a Pyrex glass wafer with a cylindrical tool with a diameter of 400 μm. The applied voltage between the electrodes was 30 V; the machining tool was controlled 60 μm under the glass surface. The obtained mean depth is 100 μm, the width of the channel is 675 μm.

In figure 12 is shown an example of machining a more complex channel like structure. This structure was machined with a micro-tool machined using WEDG. The micro-tool, a small cylinder of 90 μm diameter and 150 μm length, was controlled to be 60 μm under the glass surface. The applied voltage was 30 V.

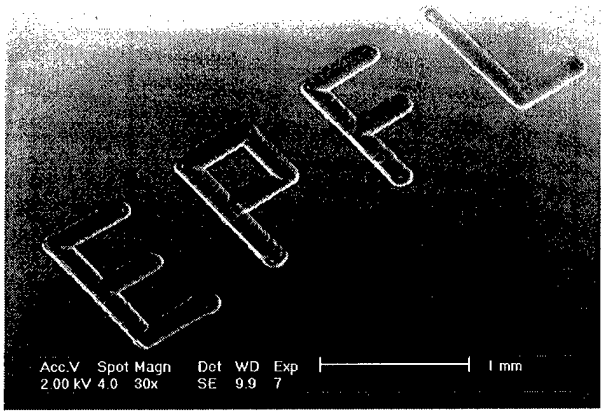


Figure 12 Example of a more complex channel like structure. The used micro-tool, a cylinder with a 90 μm diameter and 150 μm length, was controlled to be 60 μm under the glass surface at 30V. The structure was machined in one step with a machining speed of 0.05 mm/s.

One major problem that occurs during the machining of channels like structure is the control of a constant depth. This came from the fact that the machining depth is not constant. Although the initial profile was measured to correct glass alignment, still typical fluctuations of 5 μm were found.

3.3. Micro-pattern modification

It is not always possible to obtain directly the right shape (depth of a micro-channel for example). The developed tool holder allows to scan the obtained surface directly after machining. It becomes possible to do a second machining to correct the obtained surface.

In order to test the possibility of modifying in a controlled way a machined glass substrate we first machined a test structure in a Pyrex glass wafer. This structure is an array formed of ten micro-channels with a length of 1000 μm and spaced with 100 μm. The micro-channels were machined in one step. The desired depth of the channels was 110 μm.

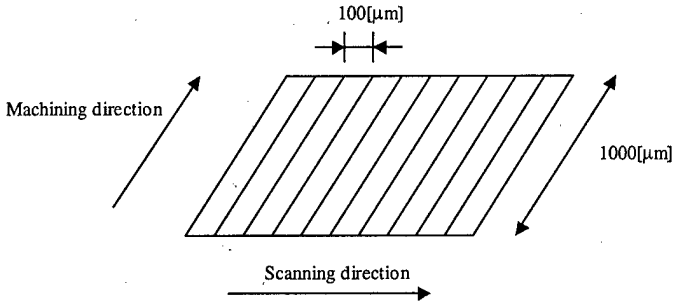


Figure 13 Machined array with the scan direction after machining

In a second step we scanned the obtained array perpendicularly to the micro-channels, in the middle of the

array. The tool holder measured every 10 μm the depth of the structure.

The obtained scan shows that in the middle, the structure is not totally flat. To obtain a flat surface at a depth of 110 μm a second machining was done in perpendicular direction with an additional material removal of 25 μm over a range of 600μm (see Fig. 15). As expected, a flatter surface with a mean depth of 110 μm was obtained.

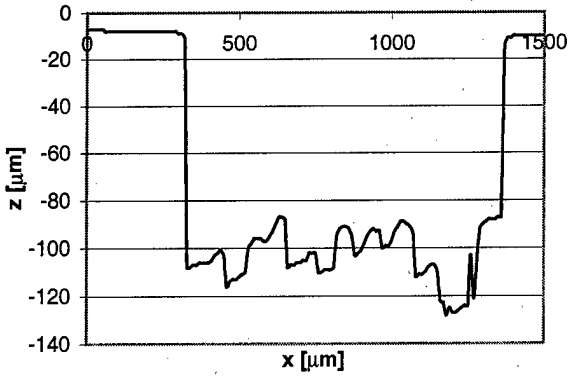


Figure 14 Scanned profile of the machined array according to figure 13. Every 10 μm a measurement was done.

In a third step we try to obtain a surface with a mean depth of 125 μm by advancing the tool by another 15 μm. In this case a surface with a mean depth of 140 μm was obtained. This is deeper than expected. This may be due to a bad control of the spark at the tip of the machining tool.

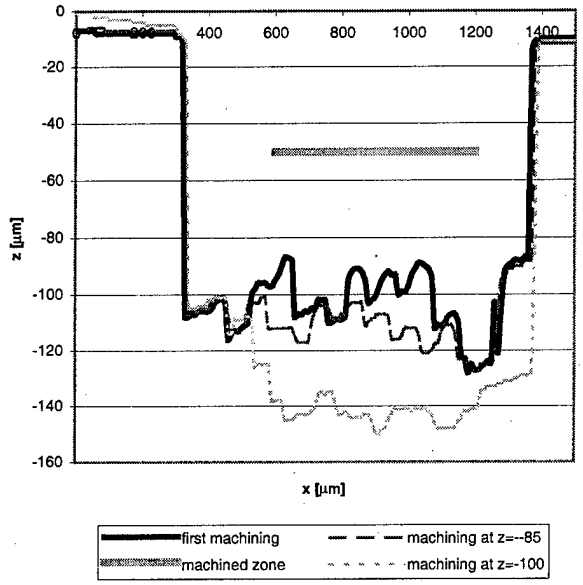


Figure 15 Profiles after a second and third machining step respectively at z=-85 μm and z=-100 μm, with z the tool position; the machining were done at 30 V. The goal was to obtain flat surfaces with a depth of 110 μm and 125 μm.

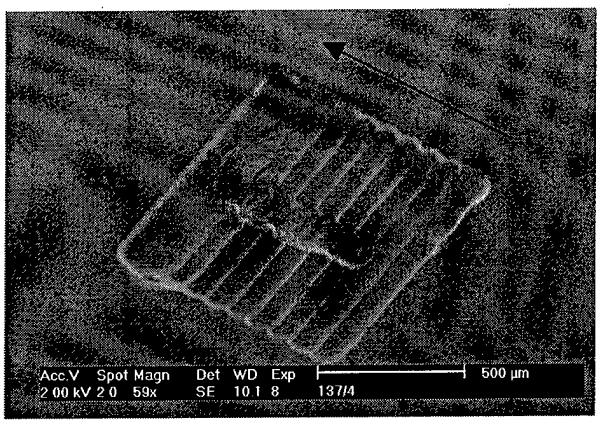


Figure 16 Machined structure in a Pyrex glass wafer, using measuring feedback. In the middle two other additional machining steps were done to correct the surface. The profiles are shown on figure 15. All machining were done at 30V.

4. CONCLUSION

A special ECDM tool holder was presented. It incorporates the possibility of measuring surface profiles directly after machining. Testing and developing control algorithms for electro chemical machining is possible using this device. An other possibility is to monitor the force applied on the machining tool during the process. Typical measured values are 100-200 mN. Several examples of structures machined in glass with this device using standard needles or WEDGed micro-tools were presented. Relatively high machining speed (up to 30 μm/s) were achieved. The possibility to machine deep holes (up to 1 mm) was demonstrated. The possibility to machine channel with a depth up to 100 μm in one step was shown. Typical removal rates of $4.5 \cdot 10^5$ $\mu m^3/s$ were achieved. The controlled modification using measurement feedback of a machined micro-structure in glass was also demonstrated. In all cases a good surface quality of the machined glass could be obtained. Because glass substrate are often used in micro devices, ECDM is a very promising technology to be used complementary to silicon micromachining.

ACKNOWLEDGEMENTS

The authors would like to thank Jurjen Zoethout for his helpful contribution in the choice of the optical sensors, Simon Henein for his help in designing the flexible structure. Part of this work was conducted under the sponsorship of the Fond National and MINAST (Swiss Priority Program in Micro and Nano System Technology) projects of the Swiss Government.

REFERENCES

[1] H. Kurafuji and K. Suda, "Electrical Discharge Drilling of Glass-I", *Annals of the CIRP,* **16** (1968) 415

[2] I. Basak and A. Ghosh, "Mechanism of Spark Generation during Electrochemical Discharge Machining: A Theoretical Model and Experimental Verification", *Journal of Material Processing Technology,* **62** (1996) 46-53

[3] H. Langen, J-M. Breguet, H. Bleuler, Ph. Renaud and T. Masuzawa, "Micro Electrochemical Discharge Machining of Glass", *International Journal of Electrical Machining*, **3** (1998) 65-69

[4] T. Masuzawa, M. Fujino, K. Kobayashi and T. Suzuki, "Wire Electro Discharge Grinding for Micromachining", *Annals of the CIRP*, **34,** 1(1985) 431

[5] V. Fascio, R. Wüthrich, D. Viquerat, H. Langen, „3D Microstructuring of Glass using Electrochemical Discharge Machining (ECDM)", *International Symposium on Michromechatronics and Human Science (MHS'99)*

Technical Session C-2

Microcomponents and Microdevices I

A Design and Production Framework for Modular Microsystems

Grosser, V.[1]; Schuenemann, M.[2]; Michel, B.[1]; Reichl, H.[1]

[1] Fraunhofer Institute for Reliability and Microintegration (IZM), Berlin, Gustav-Meyer-Allee 25, D-13355 Berlin, Germany
[2] Fraunhofer Institute for Manufacturing Engineering and Automation, Stuttgart, Nobelstraße 12, D-70569 Stuttgart, Germany

Abstract:

The trend to higher integration in microelectronics and the integration of micromechanical, microfluidic and microoptical components require new packaging solutions. So a highly flexible design and production framework for microsystems, suitable for mid-scale production at reasonable costs, was developed.

1. INTRODUCTION

The global trend for better energy efficiency, lower pollution, faster response time and decentralization of control functions mandates implementation of large volumes of miniaturized sensors, actuators and systems. For industrial branches like machinery and plant manufacturing, production control, power, the most important impact of highly miniaturized systems is expected to be in the area of smart autonomous control systems, self monitoring and self-diagnosis.

2. MODULAR DESIGN FRAMEWORK

The modular design and production framework consists of a supplier kit and an application kit. The modular framework also includes tools for design, fabrication and test of modules as well as of assembled smart microsystems.

The Figure 2 shows the structure of the supplier kit. This kit is based on a modular vertical integration technique. The conventional BGA was expanded to a *"top bottom ball grid array - TB-BGA"*. The advantage of TB-BGA is the enormous reduction of package size at the same pin count in connection with the possibility also to use the third dimension for the packaging. This area-configuration on the one hand reduces the requirements on printed wiring boards, on the other hand it allows the assembly of high pin count integrated circuits.

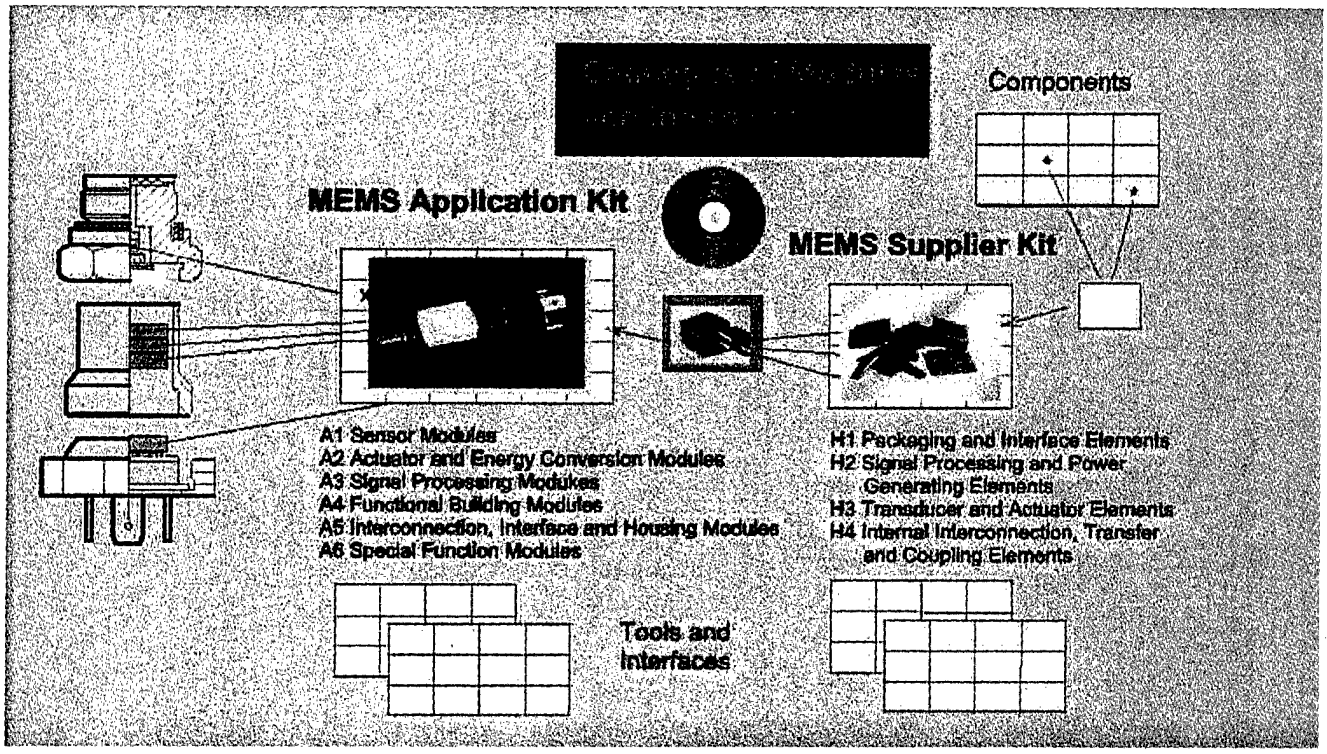


Figure 1: The Design and Production Framework of modular microsystems

0-7803-5790-6/99/ $10.00 ©1999 IEEE.

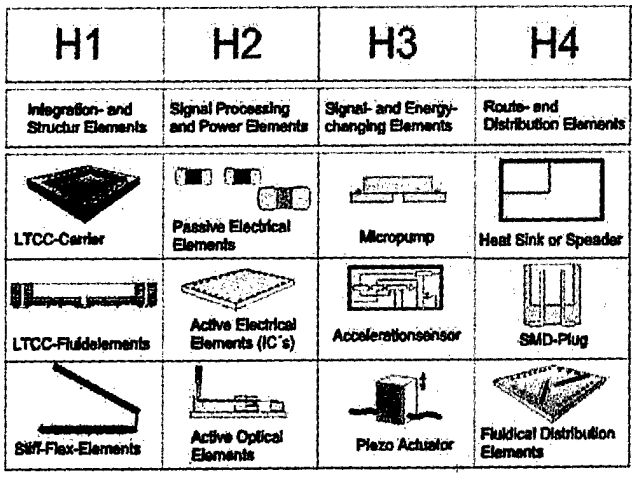


Figure 2: Structure of the supplier kit

In the supplier kit can be found different fabrication technologies:

- LTCC technology
- Stack-Pac technology
- Stiff-Flex technology and other

The following Figures 3 and 4 give an overview about some realized technologies at IZM.

As first demonstrators ceramic TB-BGA are being developed as single modules (SCM's) and multi chip modules (MCM's) as well. The modules will be mounted as intelligent sensors or transducers with micro controller, EEPROM and bus interfaces.

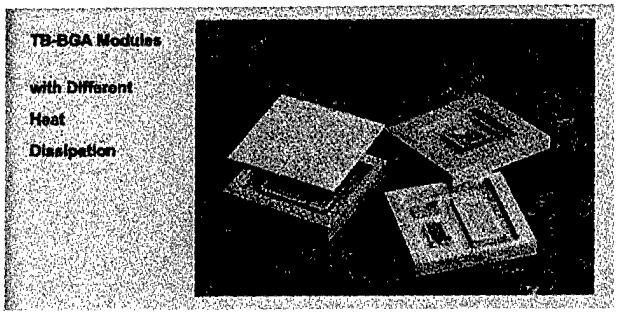


Figure 4: LTCC modules (SCM's and MCM's)

3. STANDARDIZATION AND INTERFACES

Standardization of packages and interfaces is a necessary precondition for modularization. This would allow for the combination of modules made from different materials and by different manufacturers. It is considered most important to define a standard which allows the combination of modules produced by different technologies. The Figure 5 shows the interfaces, defined in the framework.

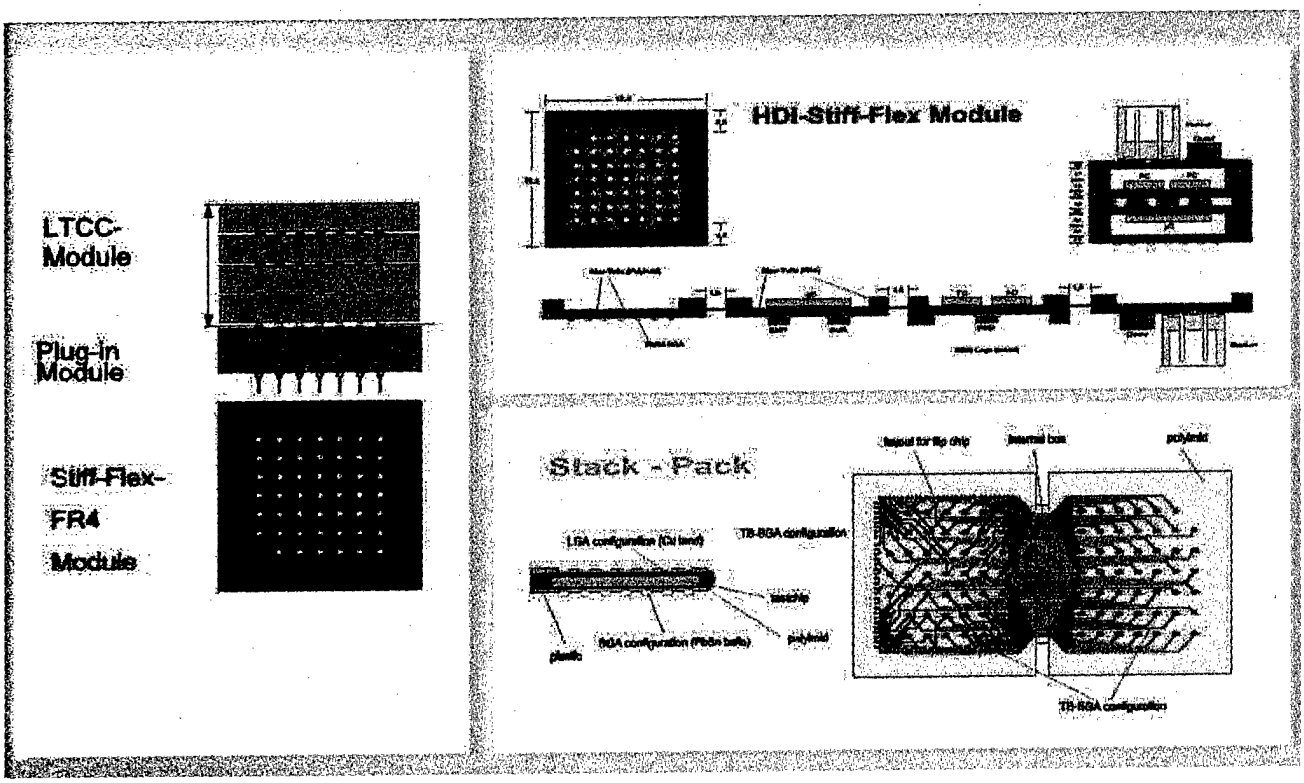


Figure 3: Different fabrication technologies

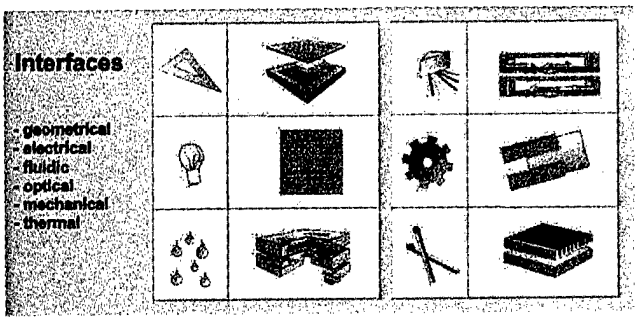


Figure 5: External and internal interfaces

All interfaces are described in detail and most of them are also manufactured and tested.

A second main part of standardization of modules is a bus system. In the framework an optical, a fluidic and a electrical bus were defined. The Figure 7 shows the whole bus system with all busses and the Figure 8 the arrangements for the vertical and the horizontal busses.

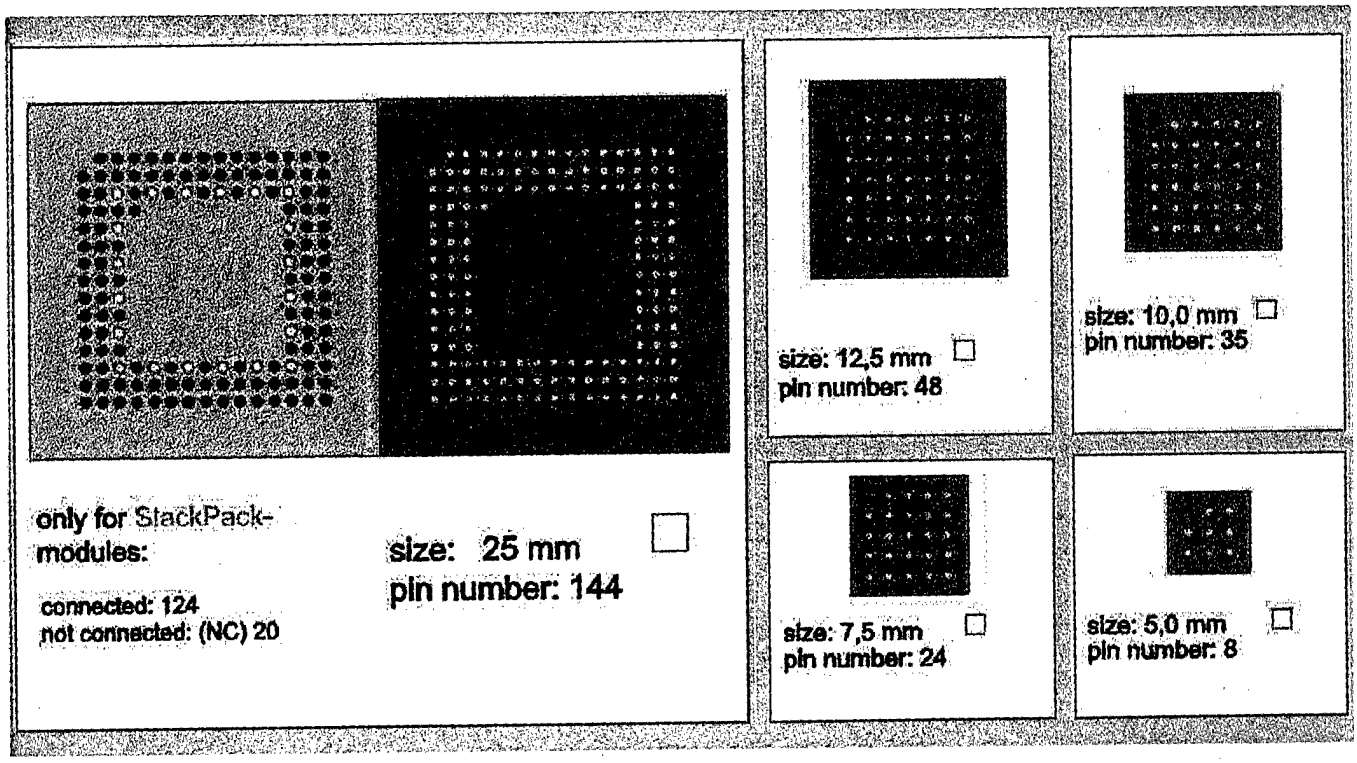


Figure 6: Geometrical and electrical interfaces

An example for geometrical and electrical interfaces gives Figure 6.

It is seen, that not in all dimensions, it is possible to connect all electrical pins. Depending on the design rules of different fabrication technologies the connected pin number for Stack - Pack modules is not in all sizes of the modules the same as in LTCC technology.

Fluidic interfaces and optical interfaces have already been developed. As an example, TB-BGA 17,5 feature an internal bus of 20 electrical and 8 microfluidic vias. They can be equipped with two vertical or two lateral fluid connectors, thus providing the opportunity to transport liquids or gases.

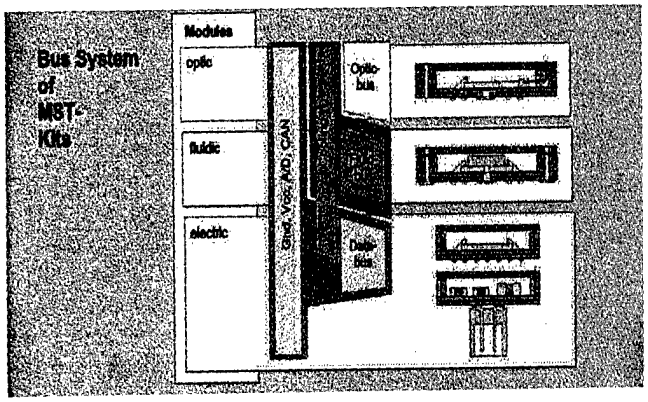


Figure 7: External and internal busses of the framework

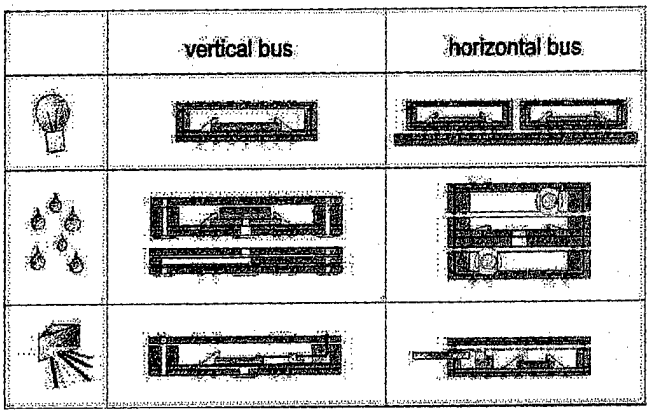


Figure 8: Vertical and horizontal busses

One of the main problems of stacked modules is the thermo-mechanical reliability (TMC - Thermo-Mechanical Compatibility). The thermal situation in a similar module or in the stack of modules depends among others on the power dissipation of the IC's, the used packaging materials (LTCC, FR4 etc.), the detailed manufacturing technology
of the modules and also on the module arrangement in the 3D stack. To describe the thermal situation and the design a thermal interface experimental and numerical analysis was done.

So the Figure 11 shows some cross sections of LTCC modules in connection with the thermal deformation by thermal loading. Such experimental results are used to optimize the parameters for FE calculation. The following Figure 12 demonstrates the FE results of a three TB-BGA stack with diffe-

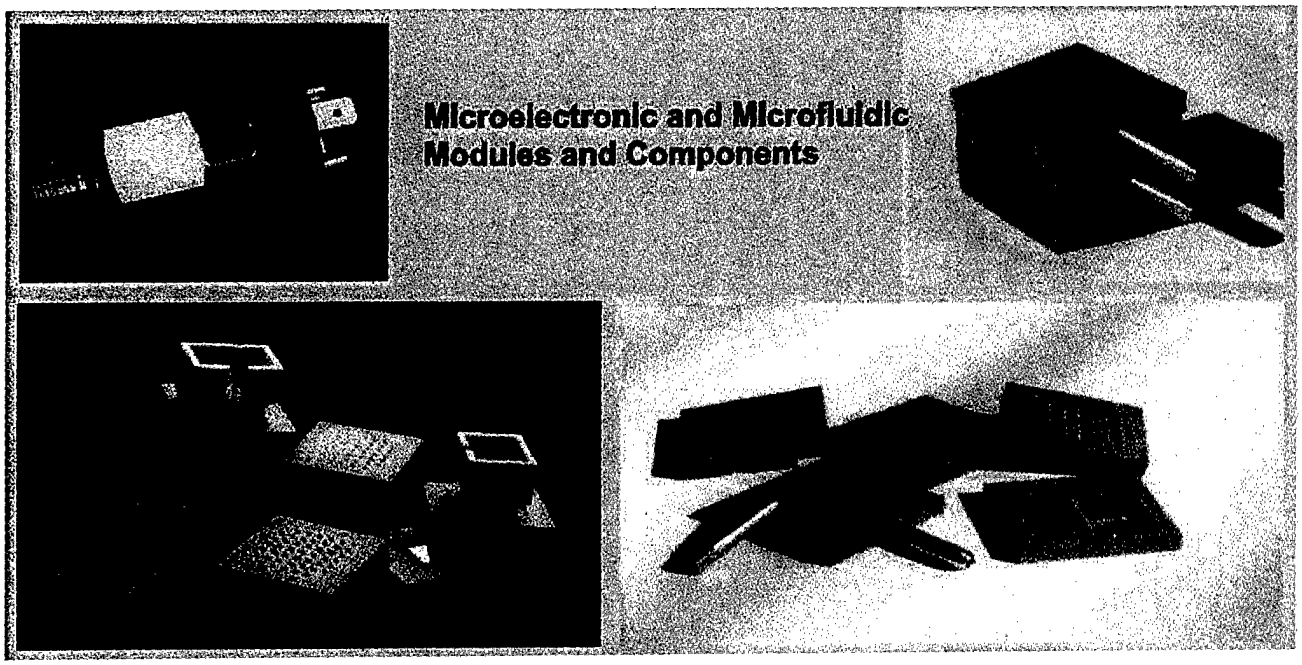


Figure 9: Available modules and components

The Figure 9 gives an overview about available microelectronic and microfluidic modules. In the lower part the components and at the bottom of the Figure first modular applications - a pressure and a flow sensor - are seen.

4. Reliability and Testing

To place the modular framework on the market testability and the reliability of all modules have to be proved. For that reason the methods of testing are also part of the framework. The Figure 10 shows special testboards. These boards are necessary for programming of the microelectronic modules and for electrical and functional tests of the separate modules and the stacked modular microsystems.

rent IC's inside. With the help of such FE modelling it is possible to describe the real temperature distribution and the heat transfer in 3D stacks and to define a general thermal interface.

5. Conclusion

The modular design and production framework has the potential to overcome present restrictions of the industrial application of microsystems. On one hand, the framework promotes the industrial application of modular microsystems by industries usually not familiar with microstructuring technologies. On the other hand, the modular approach enables the economically efficient design and medium-scale production of consumer-adapted smart microsystems.

Further development of homogeneous mechanical, optical, information, power supply and media interfaces are of outmost importance together with application examples for an industrial realization of the proposed design and production framework. The last Figure 13 shows with the arrangement for the functional test of modular sensors a first application.

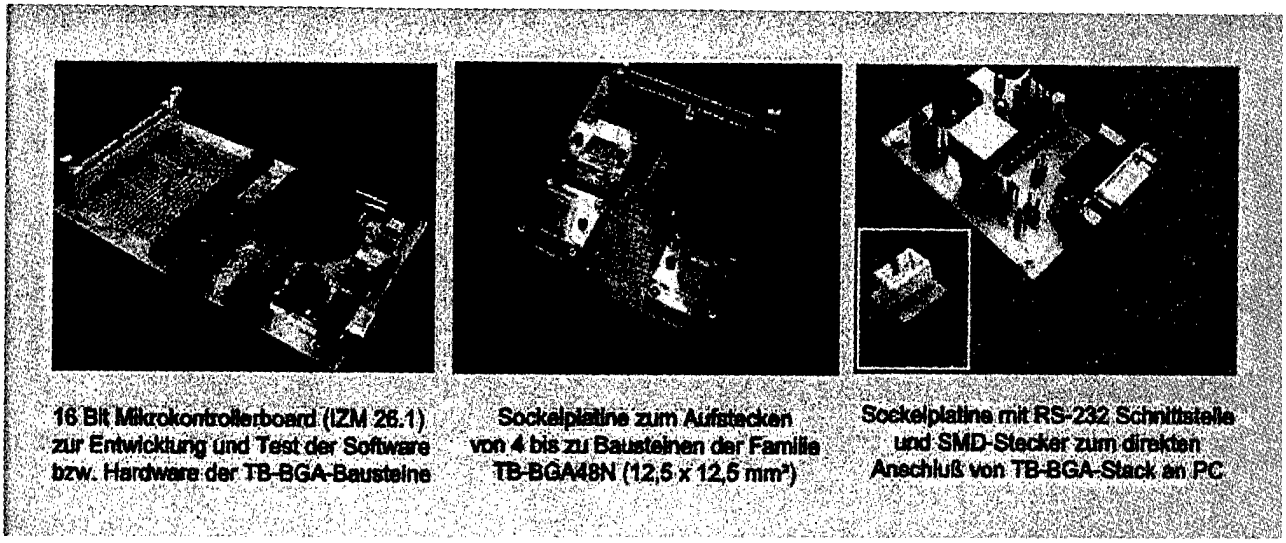


Figure 10: Testboards for modular microsystems

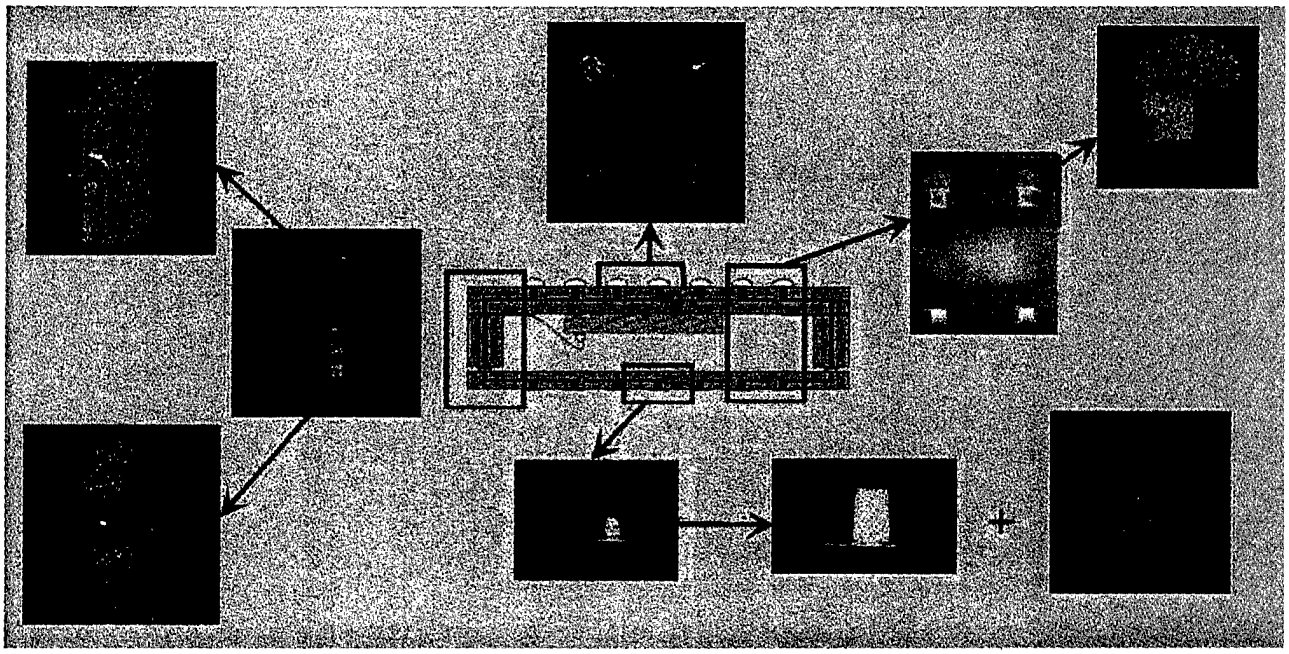


Figure 11: Several cross sections of a LTCC module

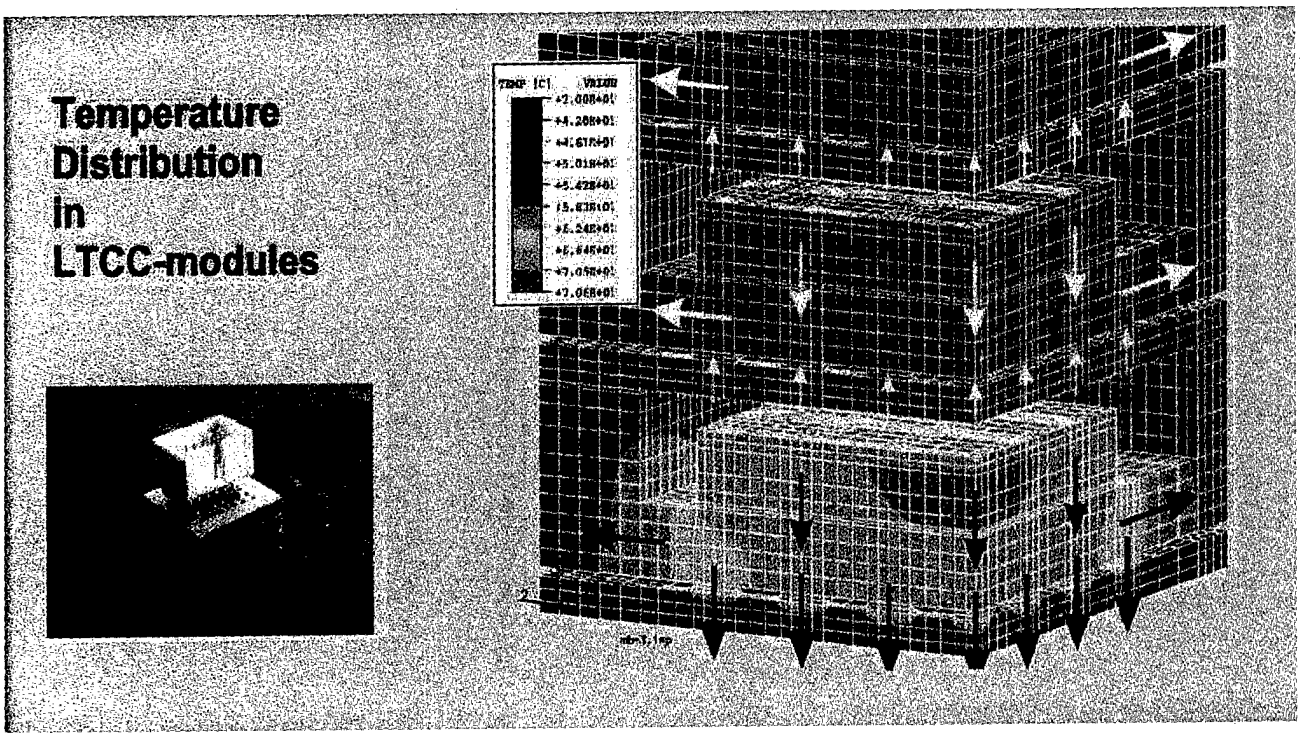


Figure 12: FE results of a 3D LTCC stack

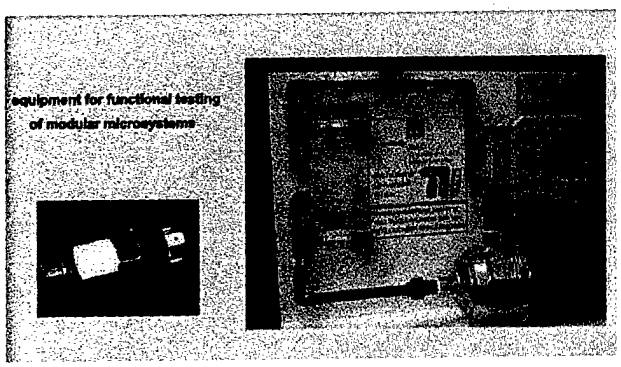


Figure 13: Equipment for functional testing of smart modular sensors

6. Acknowledgement

The authors would like to thank all the highly valuable information and discussion derived from partners from industry, laboratories and universities, too many to name them all, without this work would have been impossible. Funding was provided by the German Ministry BMB+F. In addition, we would like to thank K. Zimmer (VDMA Frankfurt), and H.Kergel (VDI/VDE-IT Teltow) for your support.

7. References

[1] Grosser, V.; Michel, B.; Leutenbauer, R.; Sommer, J.-P.: Reichl, H.; TB-BGA - Basic Elements for microsystem Packages. Proc. of Actuator'98, pp. 161-63.

[2] Leutenbauer, R.; Amiri Jam, K.; Sommer, J.-P.; Grosser, V.; Reichl, H.; Michel, B.: Thermo-mechanical Aspects of Modular Vertical Integration Techniques (TB-BGA). Proc. of MicroMat'97, pp. 1169-71.

Thermal Analysis of Fingerprint Sensor Having a Microheater Array

Ji-Song Han, Tadashi Kadowaki, Kazuo Sato, and Mitsuhiro Shikida

Department of Micro System Engineering, Nagoya University

Froh-cho, Chikusa-ku, Nagoya 464-8603, Japan

Abstract:

For the purpose of properties security, in particular of information systems, demands for portable fingerprint sensors are increasing. We proposed a new type of fingerprint sensor having an arrayed microheater, and successfully fabricated one-dimensional array of sensor elements on a silicon wafer using micromachining technologies. Electric resistance of each heater element is measured as signals of temperature difference between elements that are in contact or non-contact with ridges of the fingerprints.

In this paper, we analyzed thermal characteristics of our sensor device using computer modeling. Effects of the following parameters were investigated; cavity under heater, SiO_2 film between heater and sensor base, heater size, input power and pulse time duration applied to the heater, material properties contacting to sensor surface etc. We concluded that making cavities under the microheater elements and having SiO_2 film layer between heater element and sensor base both for the purpose of thermal insulation, is necessary to realize the performance of the proposed sensor system. From the simulation results, it was clarified that such a miniaturized heater element will work quite effective for detecting fingerprint patterns.

1. INTRODUCTION

The fingerprint is known to be the most representative biometric for authentication of individual persons, and various ID devices have been developed. Optical methods are now commonly used for detecting fingerprint for accessing personal computer, but optical system needs lots of elements, such as laser diode, photo diode, and prism etc., thus is not suitable for portable device. Micro Electro Mechanical Systems (MEMS) technology allows a new type of sensor having robustness in sensing and providing more portable systems with less production cost. We proposed a new type of fingerprint sensor and fabricated it by MEMS technologies. Using MEMS technologies, it is possible to produce many kinds of micro device with low cost, but before device design and development, work with computer modeling and calculation is necessary and useful. Computer modeling can reduce the total time to transfer a device concept into a commercial product, and thus reduces development time and cost. Device modeling also can help us working on advanced device concept to try out ideas, finding practical device configurations and getting estimates of device performances. This paper introduced the principle and fabrication process about our new type of fingerprint sensor device and discussed many kind of conditions for new device design with computer modeling software α-FLOW, and proposed some useful suggestions.

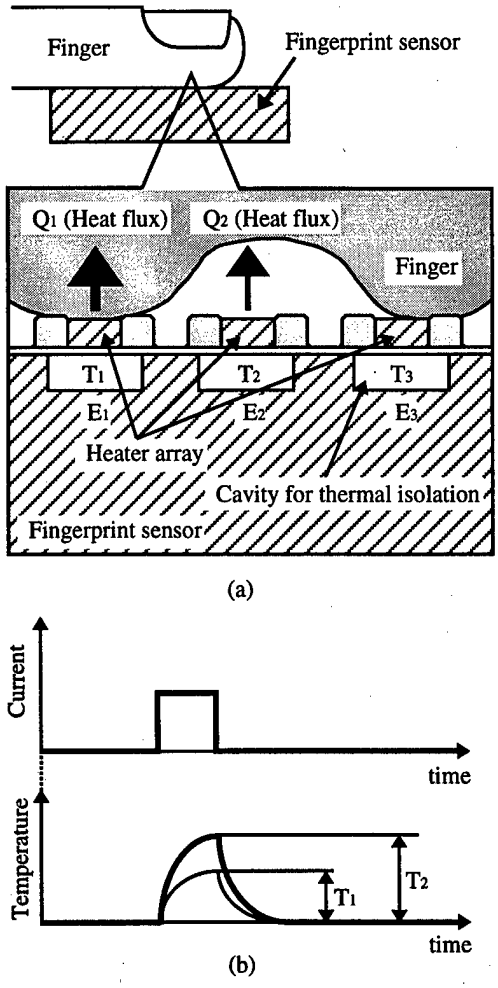


Fig. 1. Fingerprint sensor with an arrayed microheater.
(a) Device structure, (b) Sensing principle.

1999 INTERNATIONAL SYMPOSIUM ON
MICROMECHATRONICS AND HUMAN SCIENCE
0-7803-5790-6/99/ $10.00 ©1999 IEEE.

2. PRINCIPLE

The structure and the working principle of our device is schematically shown in Fig 1. It has an array of microheater elements. A cavity is formed under each heater element for enhancing heat insulation between the heater and substrate. When a fingertip is pressed to the device surface, heater element in contact with a ridge of human fingerprint (E1) shows less temperature rise than that which is facing a recess of fingerprint (E2), because the finger acts as a heat sink. When one applies a pulsed voltage to each element as shown in Fig. 1(b), element E1 shows less increase in temperature rise than element E2 as schematically shown in the Fig. 1(b). The proposed type of sensor has an advantage over the conventional type which has an array of CMOS gates for attachment/detachment sensing and inevitably containing problems such as stray capacitance and charges on a human body.

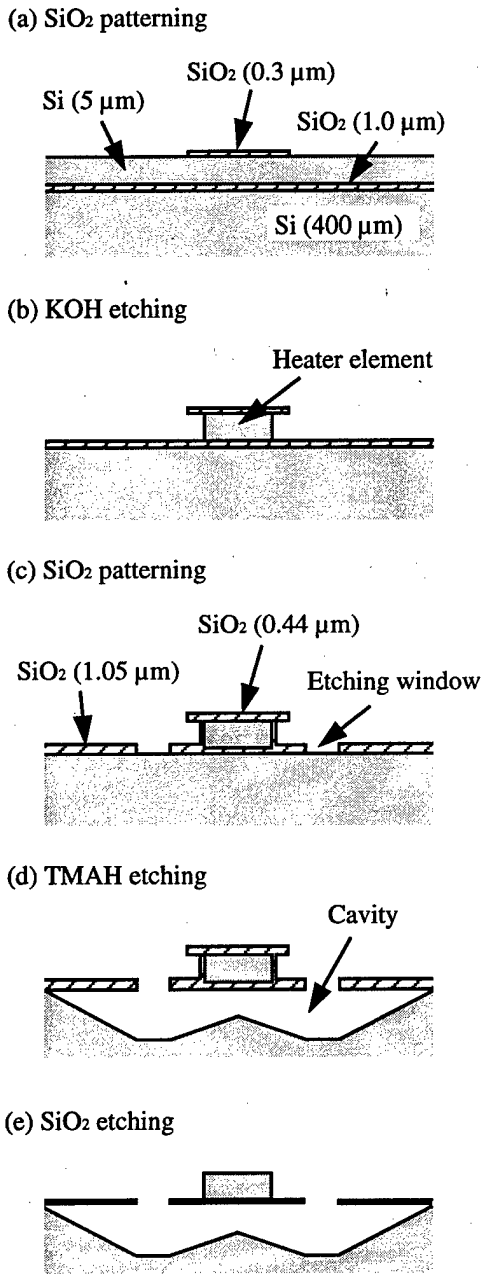


Fig. 2. Fabrication process of the fingerprint sensor element.

3. FABRICATION PROCESS

We have developed a fabrication process of the proposed device structure by using a SOI wafer as a starting material. The top silicon layer of the SOI is bonded to the substrate with 1 μm thick SiO_2 layer, and machined it to the thickness of 5.0 μm finally. The fabrication step is shown in Fig. 2. It is basically composed of two steps of wet etching. In the first step, we etched the top silicon layer to make a heater element in KOH solution. Then, the surface was protected with a thermal oxide film. The second TMAH wet etching was applied to form cavity under the heater element. We successfully fabricated an arrayed microelements (Fig. 3), whose minimum width, length and thickness are 20 μm, 40 μm and 5 μm, respectively. The minimum pitch distance of the heater elements is 80 μm. It satisfies in mechanical strength and the requirement to detect the fingerprint patterns.

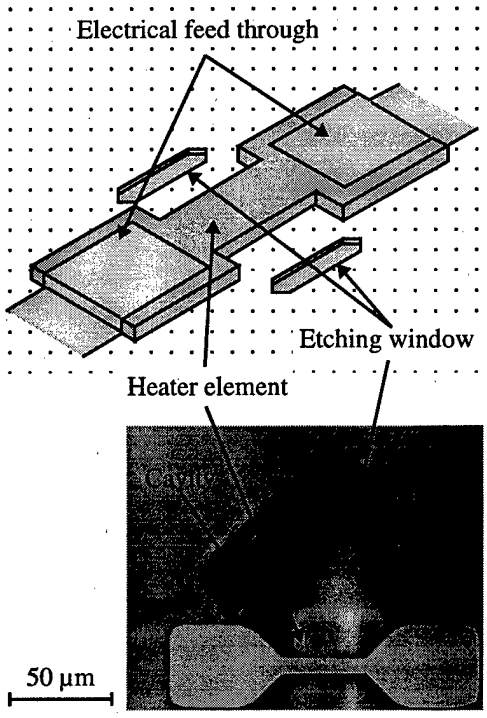


Fig. 3. Photograph of the fabricated microheater.

4. THERMAL ANALYSIS

(1) Temperature distribution characteristics on basic modeling

Figure. 4 shows our simplified fingerprint sensor modeling for computer calculation. It is one fourth of sensor element structure with vacuum cavity under heater; model surface is insulated with surroundings. Figure 5 shows the temperature distribution on heater element surface center-line along the length. Pulse time duration is in the range of zero to 1 ms. Figure 6 shows the temperature distribution on heater side-part centerline along width and Fig. 7 shows the depth temperature distribution on heater side-part center point B. Figure 8 shows the temperature at the center of heater plotted against different pulse time-duration. From Figs. 5~8, we can find the temperature distribution characteristics of sensor element. It is to say that the center point of heater surface has highest temperature, and widthwise have almost no temperature differences. SiO_2 film layer can make big temperature gradient, and the temperature at the center of the heater element shows good linear change with pulse time-duration.

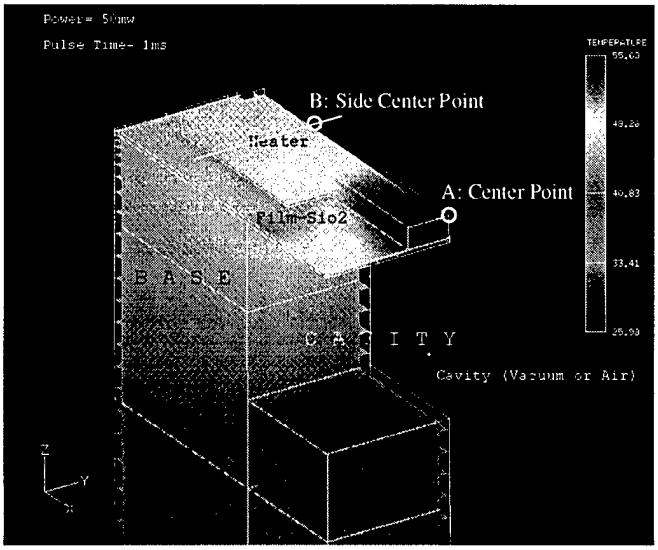


Fig. 4. Fingerprint sensor model.

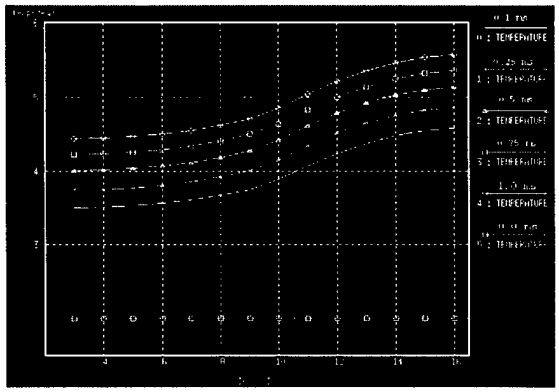


Fig. 5. Temperature distribution on heater surface.
(Centerline along length)

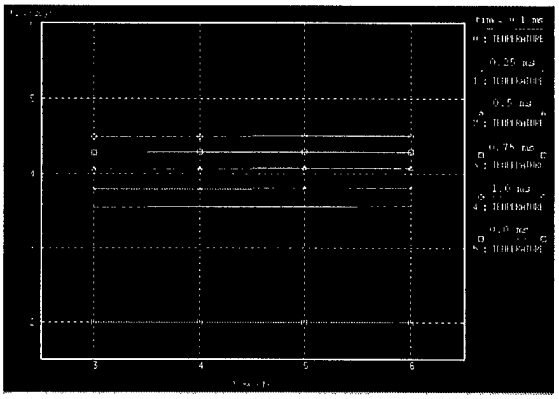


Fig. 6. Temperature distribution on heater side-part.
(Centerline along width)

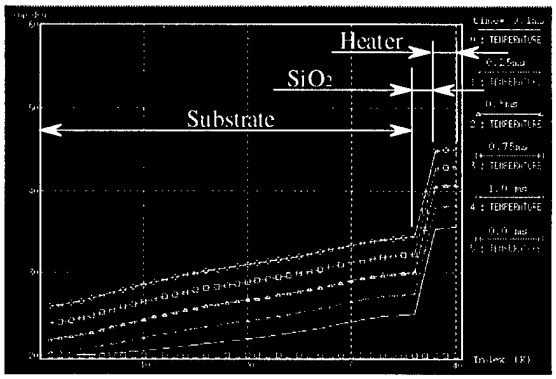


Fig. 7. Temperature distribution on heater side-part.
(Center point B along depth)

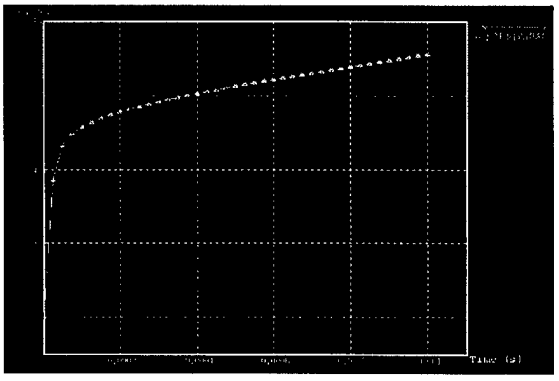


Fig. 8. Temperature at the center point A as a function of the pulse time duration.

(2) Effects of Cavity

As shown in Table 1 and Fig. 9, when the cavity is formed, temperature rise of the heater is remarkable compared to the case without cavity. Cavity raised the heater surface center temperature about 40 % than that of non-cavity structure in 50 mW input power and 1 ms pulse time duration in our simulation modeling. The cavity under the microheater element for the purpose of thermal insulation is effective.and there is almost no change on heater surface center temperature, when the cavity is in state of vacuum and full of air (See Fig. 10 for modeling).

(3) SiO_2-film Layer

From Table 2 and Fig. 11 it is understood that SiO_2-film layer also brings very good thermal insulation result. It raise the heater surface temperature about 30 % in the condition of 50 mW input power and 1 ms pulse-time with vacuum cavity under the heater and insulated with surroundings.

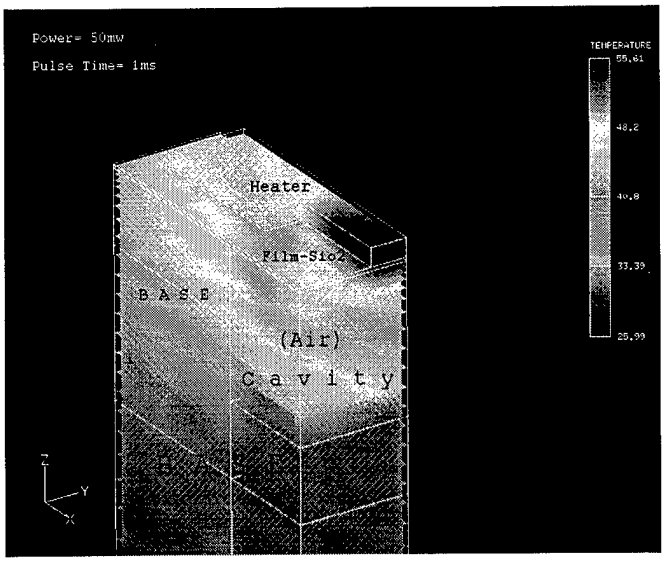


Fig. 10. Cavity (Air) and non-cavity.

Table 1. Cavity effect on the temperature Tmax of heater element.

Time (ms)	Tmax (vacuum)	Tmax (Air)	Tmax (non-cavity)
0.00	20.00	20.00	20.00
0.10	45.85	45.79	31.90
0.25	48.63	48.57	34.15
0.50	51.36	51.29	36.37
0.75	53.58	53.51	38.79
1.00	55.68	55.61	40.81

Table 2. SiO_2-film layer effect on the temperature of heater element.

Time (ms)	Tmax (SiO2-Film)	Tmax (without-SiO2/Film)
0.00	20.00	20.00
0.10	45.85	34.44
0.25	48.63	36.80
0.50	51.36	39.39
0.75	53.58	41.57
1.00	55.68	43.67

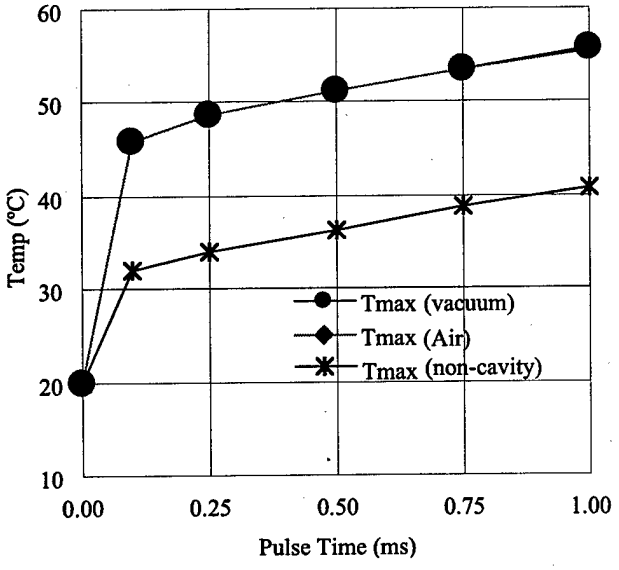


Fig. 9. Cavity effect.

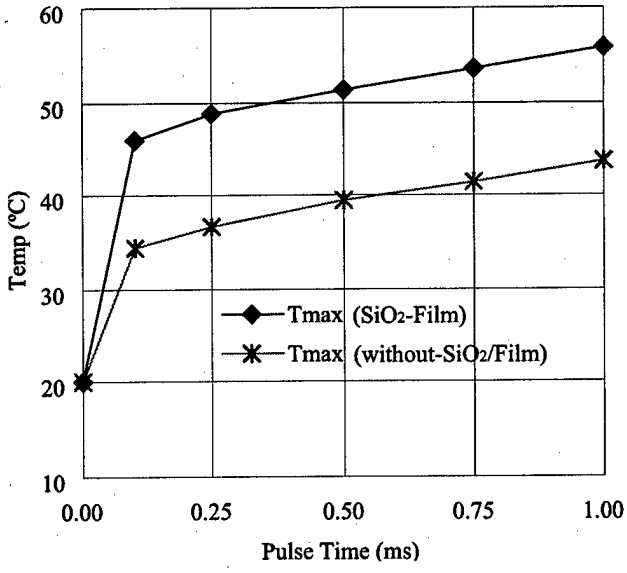


Fig. 11. SiO_2-film layer effect.

(4) Input Power Added To Heater Element

Figure 12 and 13 show the heater surface temperature with different input power by varying the pulse time duration. Even if pulse time duration is different, the relationship between the heater temperature and the input power is quite good linear. It means that when the temperature is set, the value relations between pulse-time duration and input power can be used to determine pulse width.

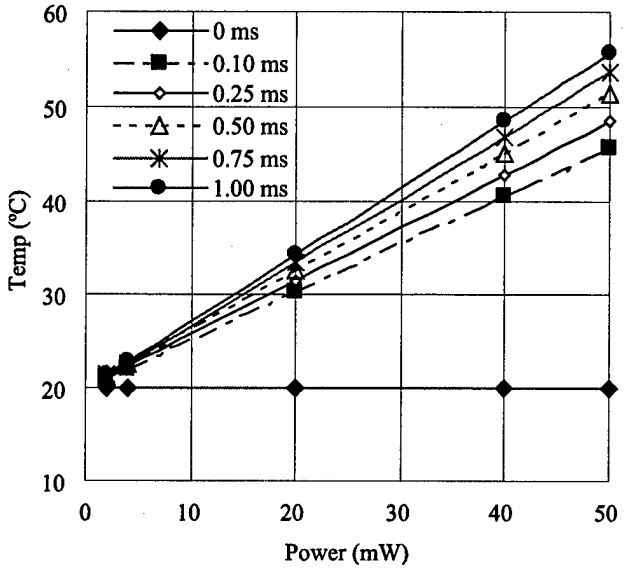


Fig. 12. Input power effect.

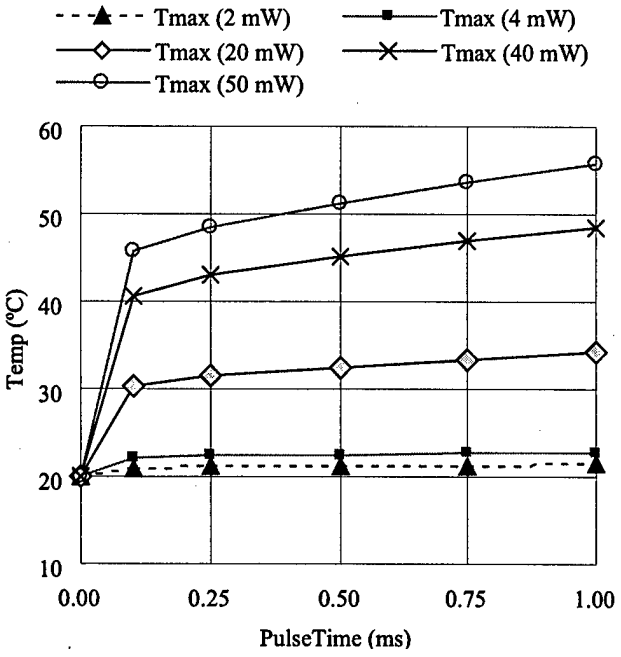


Fig. 13. Input power effect.

(5). Heater Size

From Fig. 14 we can know that at the conditions of the same pulse time duration and input power, the heater temperature is inversely proportional to heater element volume. We investigated two kinds of heater elements having same shape and different thickness. Thickness is 1 μm and 5 μm respectively. Input power is 50 mW. From Fig. 15 we can find that temperatures in the case of 50 mW input power applied to 5 μm thick heater and that of 20 mW input power applied to 1 μm thick heater are close to each other. It means that in order to get same temperature on heater element surface, small size heater ele-

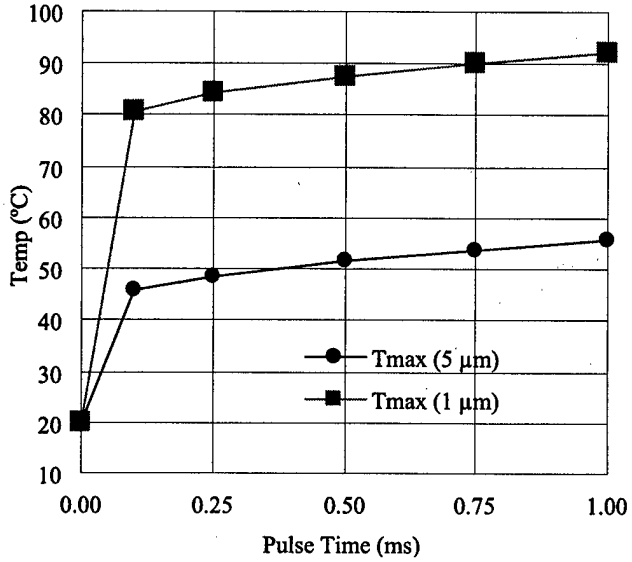


Fig. 14. Heater size effect.

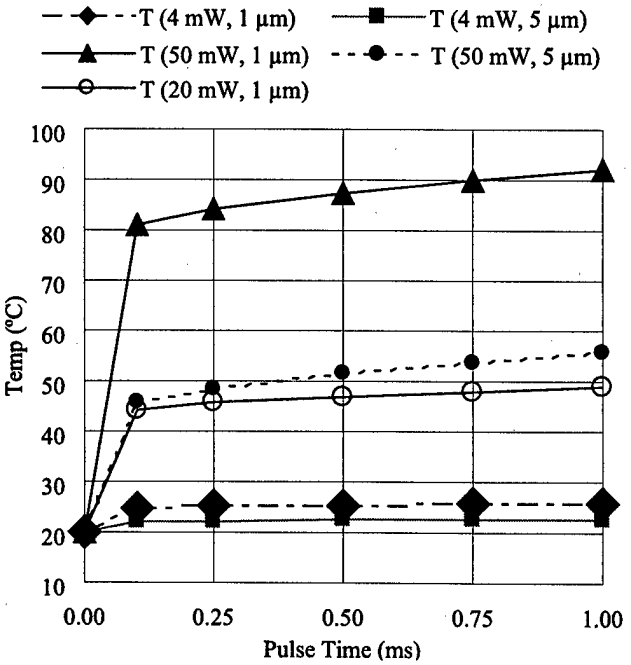


Fig. 15. Heater size and input power.

ment needs less input power. In other words, at the same conditions, small size heater element is much more sensitive.

(6) Effect of Material Properties Contacting To Sensor Surface

We investigated three kinds of contacting materials for the simulation of human fingerprint measurement (air, H_2O and leather). Table 3 and Figure 16 show a simplified fingerprint sensor modeling in touching state. Table 3 and Fig. 16 show the temperature at the center of the heater element, when the surface is in contact with air (this corresponds to valley of the fingerprint), H_2O or Leather (both corresponds to the ridge of the fingerprint). From Table 3 and Fig. 16, it is known that there exists enough temperature difference between valley (Air) and ridge (H_2O or leather) when they contact to heater surface, and the longer the pulse time duration, the bigger the temperature difference. In our simplified model, the temperature difference can reaches 12.5 °C between Air and leather, and 31.7 °C between Air and H_2O respectively, at the 1 ms pulse time duration and 50 ms input power. With another model (see Fig. 17, Table 4 and Fig. 18) found when the sensor base thickness decreases, the temperature difference will increase. For the high sensitivity of fingerprint sensor system, it will be better to reduce sensor base thickness and heater element size as can as possible.

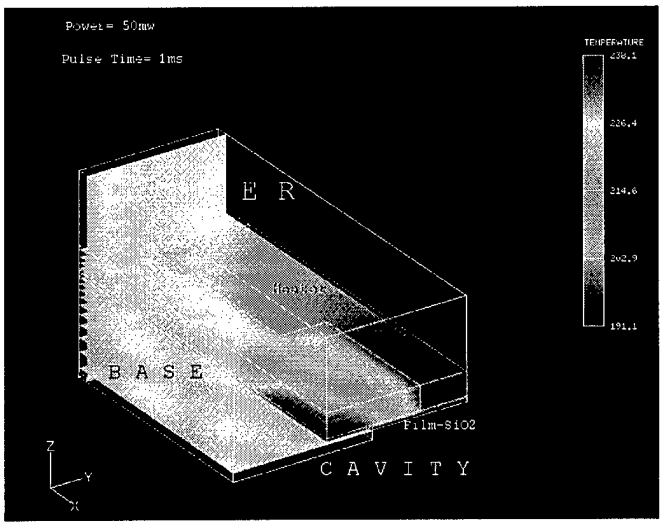


Fig. 17. Fingerprint sensor model
(With thinner size of base and finger).

Table 3. Material property effect.

Time (ms)	Tmax (Air)	Tmax (H2O)	Tmax (Leather)
0.00	20.00	20.00	20.00
0.25	57.49	46.93	53.68
0.50	74.12	57.19	67.76
0.75	90.73	66.67	81.45
1.00	107.30	75.61	94.84

Table 4. Thinner size model effect.

Time (ms)	Tmax (Air)	Tmax (H2O)	Tmax (Leather)
0.00	20.00	20.00	20.00
0.25	86.62	56.86	73.94
0.50	137.10	75.86	108.80
0.75	187.60	92.12	140.90
1.00	238.10	107.00	171.20

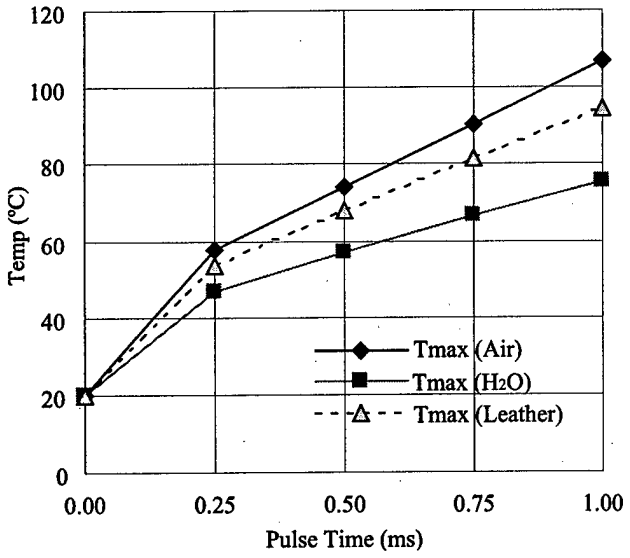


Fig. 16. Material property effect
(Materials contacting heater surface).

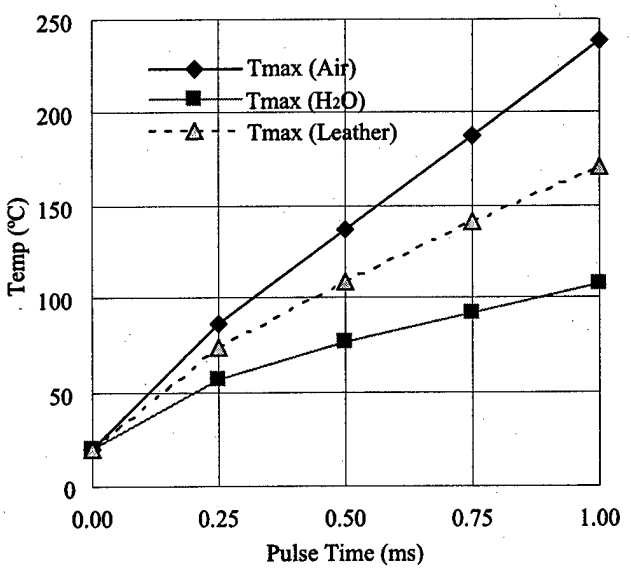


Fig. 18. Thinner size model effect.

(7) About α–FLOW

a-FLOW software system is developed by Fujitsu Japan, cooperated with numerous enterprises and university, through 4 years from Mar. 1988 to Mar. 1992 with 1.3 billion Japanese Yen. This project is supported by Tsuusansyou Japan.
a-FLOW system can make full use of super computer power. In hardware the analysis calculation is basically on super computer and man-machine inter face treatment is on workstations. It puts weight on three dimensional fluid analysis, and consist of following six independent analysis modelling, such as (a) Analysis for incompressible fluid, (b) Analysis for compressible fluid, (c) Analysis for incompressible fluid with free surface, (d) Analysis for flow including combustion and chemical reactions, (e) Analysis for heat conduction, (f) Analysis for material transference. Each analysis model and interface used the method of difference equation. We used the model of heat conduction analysis to analyze the thermal characteristics of our device.

5. CONCLUSION

We proposed a new type of fingerprint sensor device. The proposed device has an array of microheater elements thermally insulated from the substrate. We successfully fabricated an array of the sensor elements on the silicon wafer. After computer modeling calculation on this new type of fingerprint sensor with α-FLOW software, following results were clarified.
(1) Cavity under the microheater element is effective for thermal insulation, regardless the cavity is in vacuum or full of air.
(2) SiO_2-film layer acts as an insulation layer between heater and substrate effectively.
(3) Size minimization of heater element and substrate is very useful for system sensitivity.
(4) There are good linear relations between the heater temperature and the input power.
(5) Microheater arrayed fingerprint sensor can distinguish the fingerprint patterns effectively.

6. REFERENCES

[1] M. Kimura, et al., "Study on Ultraminiature Thermal Analysis Device with Micro-Air-Bridge Heater and a New Method for its Heating-rate Curve", J. IEE Japan, Vol. 119-E, No. 3, 1999, pp. 119-124.
[2] H. Baltes and O. Brand, "Micromachined Thermally Based CMOS Microsensors", Proc. Of IEEE, Vol. 86, No. 8, 1998, pp. 1660-1678.
[3] H. Wado and T. Yamamoto et al., "Analysis of heat transfer in micro-bridge heater", MM-99-6-12, Japan, pp. 1-4.
[4] S. Jung , et al., "Intelligent CMOS Fingerprint Sensors", Tech. Digest of Transducers'99, Vol.2, Sendai, Japan, Jun. 1999, pp. 966-969.

A New ID Acquiring Method for Personal Identification System with Fingerprint

Toshio FUKUDA*1, Fumihito ARAI*2, Jiro TSURUNO*3 and Kouichi ITOIGAWA*4

*1Center for Cooperative Reserch in Advanced Science & Technology, Nagoya University, Furo-cho 1, Chikusa-ku, Nagoya, 464-8603, JAPAN
*2Department of Micro System Engineering, Nagoya University, JAPAN
*3Department of Mechano-Infomatic & Systems, Nagoya University, JAPAN
*4Tokai Rika Co., LTD., 3-260 Toyota, Oguchi-cho Niwa-gun, Aichi, 480-0195, JAPAN

Abstract

Recently, more secure and more convenient personal identification system is needed in many places. Biometrics, such as a retina, voice, fingerprint etc···, is one of the solutions for these requests. We propose a new personal identification system, which uses fingerprint image and micro mechanical key. This system provides more convenient method for users and keeps high-level securities. This paper describes the system structure and hardware specifications. And we explain a fabrication method of these system components by MEMS techniques. At first, we simulated fabrication processes to make components of this system. Then we made a prototype of the Micro Mechanical Key.

1 INTRODUCTION

A large number of personal identification systems with using biometrics have already been produced by many companies. These systems are one of the solutions of the demand for more secure and more convenient systems. Especially, a fingerprint image is introduced into their systems because of its availability and its wide acknowledgement. These systems extracts some features, called minutiae, from captured fingerprint images. For example, the system records relative positions and orientation of its ridge ending and its ridge bifurcation [1]. Then the system considers the determined minutiae as a password of the conventional authentication systems. Then the security level of these systems becomes higher because users never forget their password and nobody can steal another person's password.

Some remarkable works have been achieved in this field. Especially, new fingerprint capturing sensors have been reported and produced from the various companies. The principles of fingerprint image sensors are, for example, optics, pressure[2], heat[3], and static capacitance[4] – [7]. This static capacitance type of sensors consists of many metal plate arrayed on the surface of the sensor with a thin dielectric layer. When the finger was contacted onto this sensor, this sensor measures the capacitance between each plate and the surface of fingerprint as the grounded plate of capacitor. Then the capacitance changes because of the distance between the finger and the sensor plate, which comes out by the ridges and the valleys. As a result, the fingerprint image can be detected by scanning these capacitances. Although this type of sensors are weak in the electrostatic discharge of human finger, it is a promising method for capturing fingerprint image.

We choose a fingerprint image as an authenticating factor because of the same reason. Here we introduce the optical method for acquiring fingerprint image to our system. The reason why we choose it is the high resistance for a chemical pollution and a stress from the finger. And there are some advantages for capturing fingerprint images clearly. We focus the total system performance for users availabillity, so we should adapt the most reliable method to capture it.

In the system constitution, the ID acquiring process for specification of the individual must be required. And this process spends most of time to access these systems. Although the technology which extracts ID from fingerprint images is also developed, it is greatly dependent on the processing of CPU that search the record from the big database. And from the point of countermeasure for "impersonation", it also makes the system huge.

So we propose a new method which can acquire the users ID and fingerprint images simultaneously in the personal identification system. Then, this system would

1999 INTERNATIONAL SYMPOSIUM ON
MICROMECHATRONICS AND HUMAN SCIENCE
0-7803-5790-6/99/ $10.00 ©1999 IEEE.

reduce the total time of authenticating the person.

Additionally, it is difficult to make a copy of fingerprint input device, because it is made by MEMS technique . This fact becomes the countermeasure for "impersonation".

2 SYSTEM STRUCTURE

Fingerprint input device shown in Fig.1 is the key device in this system. This device composes of a Multistage Prism and a Micro Mechanical Key and an image receiving equipment like a CCD.

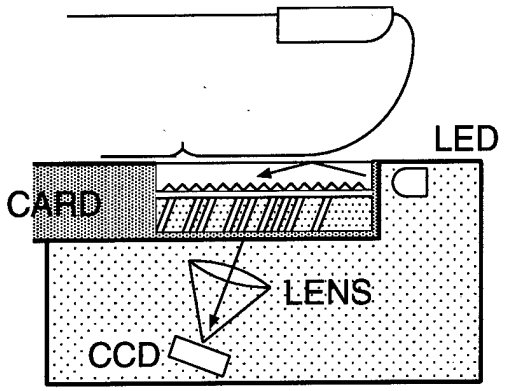


Fig.1 Fingerprint Input Device

The Micro Mechanical Key shown in Fig.2 has large number of oblique grooves with fixed angle. So it appears to be equal to the slit, which opened to the oblique direction. Therefore, this key does the role like the collimator where only the light from some directions passes. The Multistage Prism has an equal pitch to what the micro mechanical key has, and the perpendicular plane for the angle of the groove of Micro Mechanical Key.

The principle of this devices acquiring the fingerprint image is shown in the following.

When the finger was put on the upper surface of the prism, ridgelines of the fingerprint adheres to the prism, but valley lines do not. Then the reflected light from the ridge area decreases in comparison with that from the valley area, because the ridge absorbs the light. So, when the light is incident from the side of this prism, the light becomes a diffused reflected light in the prism inside, and a fingerprint image could be observed from the bottom side of the prism.

The case in which the upper surface of the prism was observed from the bottom side of the prism with large angle than the critical angle between a material of the prism and an air, a reflected light from the area of valley line becomes a total internal reflected light, then

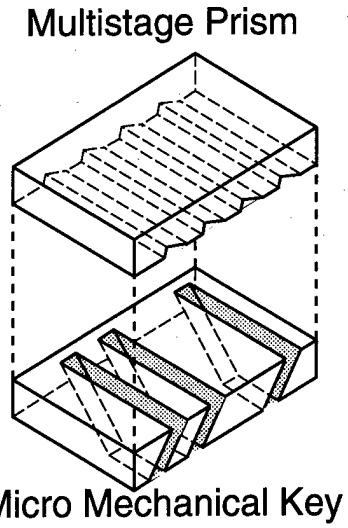


Fig.2 Micro Mechanical Key and Multistage Prism

the contrast of captured image improves. It is why an image receiving equipment was placed in the back lower.

The principle shown here is equal to the optical and conventional fingerprint image acquisition equipment. But we have placed Micro Mechanical Key between the prism and image receiving equipment. This Micro Mechanical Key affects like a shadow mask, then acquired image becomes an image shown in Fig.3.



Fig.3 Captured Fingerprint Image

We made the Micro Mechanical Key with a user's ID like a barcode. Then an acquired image contains both a fingerprint image as a password and a barcode as a user's ID. So it becomes possible that both information is acquired simultaneously. Of course, this Micro Mechanical Key must be small enough to get the minutiae of the fingerprint through this shadow mask.

It is well-known that a pitch of the human fingerprint is approximately 200–500 μm. So the width of the shadow mask should be held as 50–100 microns, since the minutiae of the fingerprint wouldn't be hidden. In Fig.3, the width of shadow mask is 50μm and the pitch is 100 μm. It is clear that this mask does not hide the minutiae of the fingerprint.

Figure 4 is a block diagram of image processing for authentication in this system.

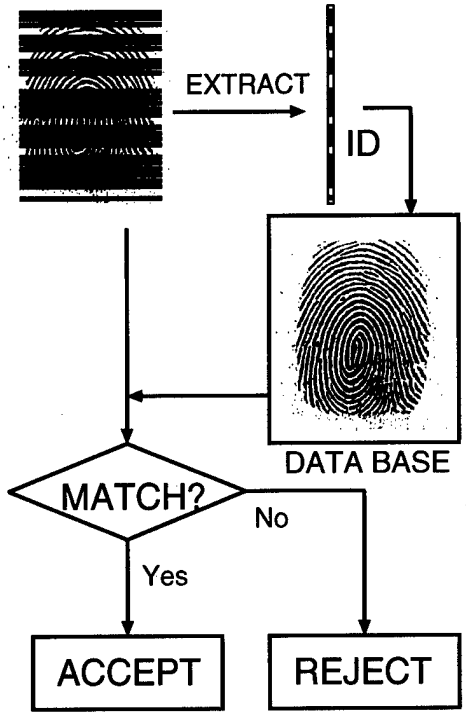


Fig.4 Block Diagram of Image Processing

User always brings this fingerprint-input device like a normal mechanical key or an IC card. Because this device was made for user's exclusive use. So we must devise a countermeasure for making a copy of that fingerprint-input device. We make a Micro Mechanical Key to be thick enough to be unable to make it easily.

Thickness of the Micro Mechanical Key would make an additional effect. It is because the direction of the light through this Micro Mechanical Key would be arranged in the same direction of this filter that the optical path length from the upper surface of the prism to the image receiving equipment would be shorten.

3 FABRICATION PROCESS

3.1 Micromechanical Key

In the previous section, we described that the width of the Micro Mechanical Key should be held as 50–100 microns so that it may not hide the minutiae of the fingerprint. Of course, this fingerprint input device, including Micro Mechanical Key and Multistage Prism, should be mass-produced. To satisfy these requests, it is suitable to be fabricated by MEMS technique.

Many papers had reported how to make a large number of micro deep grooves by an anisotropic etching [8]. But the grooves of this Micro Mechanical Key are tilted to a fixed angle. It is difficult to fabricate it by a former method or another method.

Then we thought up that we prepare the silicon wafer cut down from the ingot at the fixed angle shown in Fig.5, and that we can fabricate large number of oblique grooves with this special Si wafer by the process shown in Fig.6.

This special Si wafer was cut from a normal {110} Si ingot. The orientation flat must be cut to the direction of {112} and the rotation axes must agree with the direction of this orientation flat.

The optical mask must be designed that many windows like a slit is opened. Of course, we can design the windows' width, length and pitch, as we like. However we must align these narrow and long windows to be vertical to the edge of the orientation flat of the Si wafer.

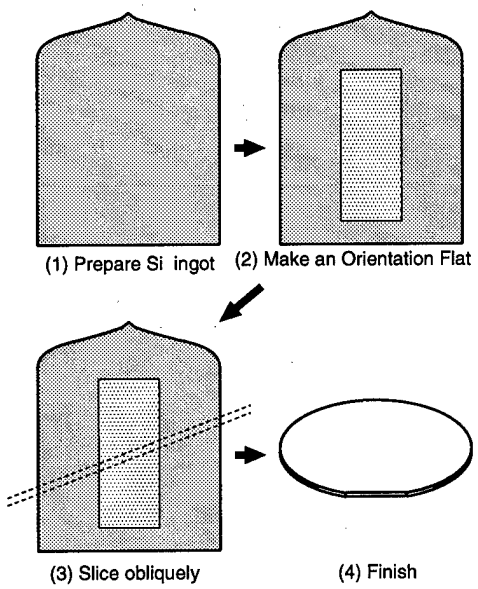


Fig.5 Making tilted Si wafer

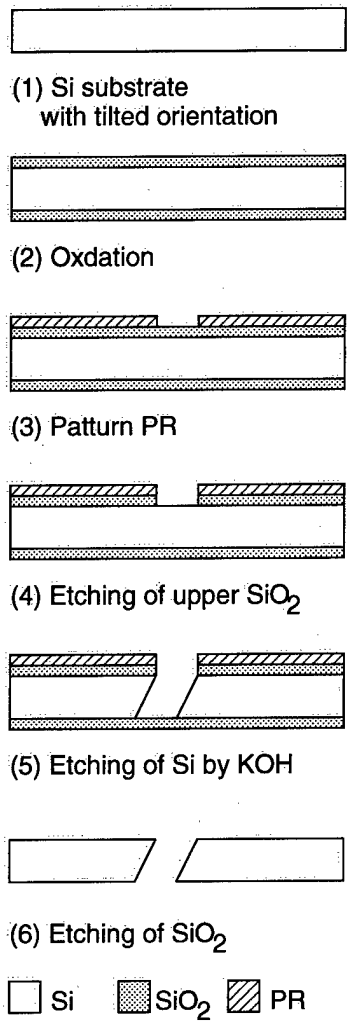


Fig.6 Fabrication Process of a Micromechanical Key

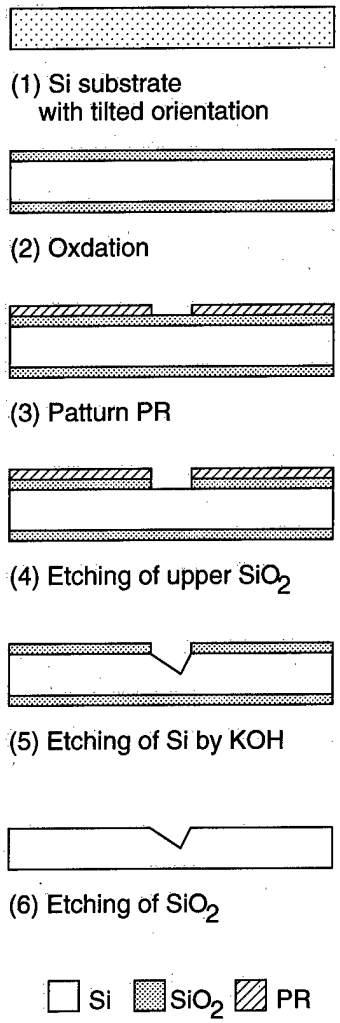


Fig.7 Fabrication Process of Multistage Prism

3.2 Multistage Prism

It seems easy to make this Multistage Prism. Probably, this prism may be made by cutting the flat glass plate. But this Multistage Prism should have the perpendicular plane for the angle of the Micro Mechanical Key. And it is suitable that the Multistage Prism has a pitch equal to the Micro Mechanical Key and a smooth plane enough to penetrate the light.

So we choose to make a mold from the Si wafer by the process shown in Fig.7, and cast the prism from this mold. Because, the {111} plane which exposes by anisotropic etching is smooth enough to satisfy that request, and the plane of required angle can be made at required pitch and required width.

To make this mold which has a smooth plane with specific angle, we also prepared a special Si wafer by the similar method shown in Fig.5. However, in this case, we cut the wafer from the {100} ingot, and its orientation flat is {110}, and the rotation axes is also {110}. The optical mask is prepared as well as that of the Micro Mechanical Key.

4 NUMERICAL SIMULATIONS

4.1 Parameters

We confirm our processes shown in the previous section with a numerical etching simulator MICROCAD[9]. This simulator can estimate an etched 3D shapes after fabrication processes in many situations. In particular, MICROCAD is good at an examination on Si wafers with various angles.

We had calculated a shape of Si wafer after etching under conditions listed below. Table 1 shows simulation parameters for the Micro Mechanical Key, and Table 2 shows those for the Multistage Prism. A rotation parameter and a direction of an orientation are defined in Fig.8. In the both simulations, the temperature of KOH is 85 degrees Celsius, and the concentration of KOH is 35 %.

Table 1 Simulation Parameters (Micro Mechanical Key)

Wafer Orientation	Z	< 110 >
Rotation Axis (Orientation Flat)	Y	< 112 >
Rotation Angle	θ [deg]	20
Etching Time	[min]	80
Optical Mask	[μm]	50 × 900
Si size	[μm]	1500 × 10000 × 500

Table 2 Simulation Parameters (Multistage Prism)

Wafer Orientation	Z	< 100 >
Rotation Axis (Orientation Flat)	Y	< 110 >
Rotation Angle	θ [deg]	35
Etching Time	[min]	10
Optical Mask	[μm]	50 × 600
Si size	[μm]	500 × 1000 × 200

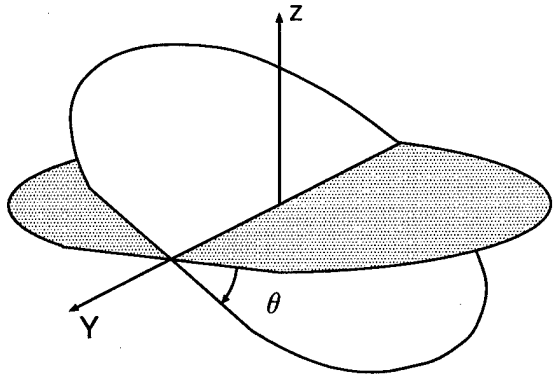


Fig.8 Difinition of the Rotation of the Silicon Wafer

4.2 Simulation Results

Figure 9 is the top view and cross section of the Si wafer after etching under the condition of Table 1. It is very clear to see that an oblique groove is made with a very little taper.

Figure 10 is the top view and cross section of simulation result under the condition of Table 2. It shows that the tilted plane of {111} appears.

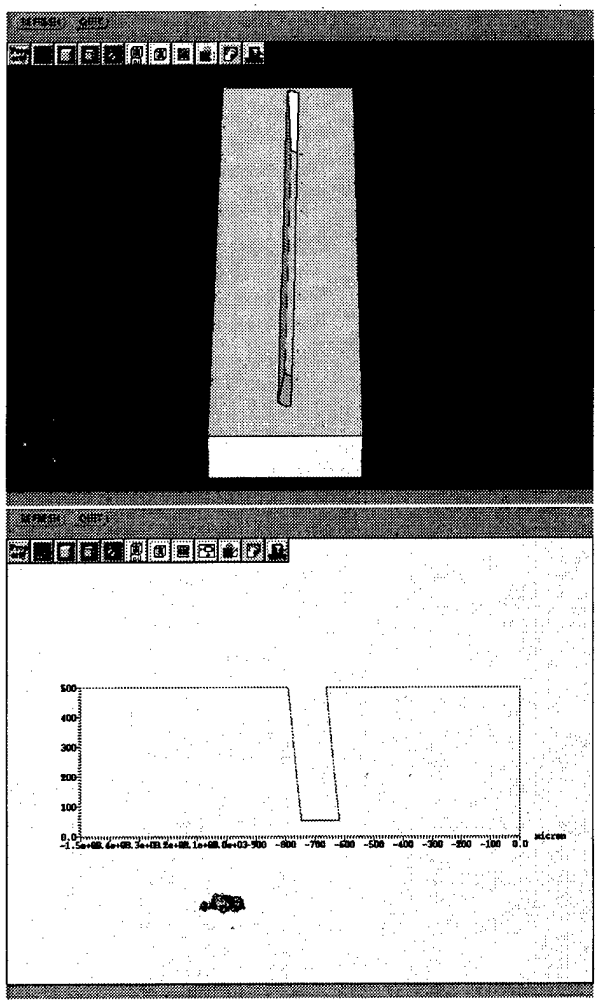


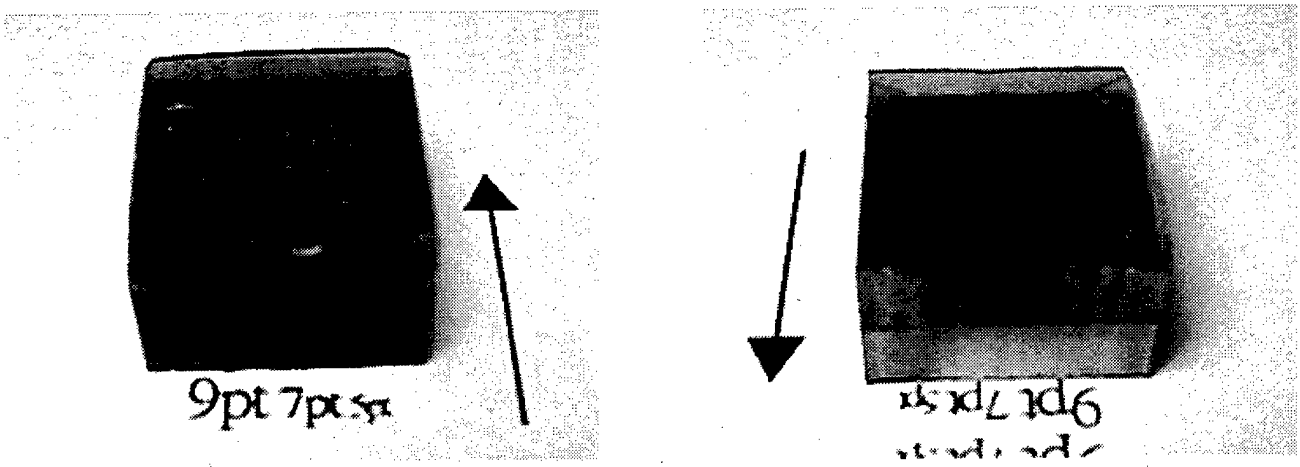
Fig.9 Simulation Result (Micro Mechanical Key)

Table 3 Properties of Si wafer

form method	CZ	Type	N
Orientation	{110}	Thichness [μm]	200
OF Direction	{112}	Rotation Angle[deg]	20

5 PROTOTYPE OF THE MICRO MECHANICAL KEY

We had tried to make a large number of oblique grooves for the Micro Mechanical Key with the special Si wafer, under the conditions shown in Table 1. The properties of Si wafer are shown in Table 3. Figure 4.2 is the photograph of the prototype of the Micro Mechanical Key. Figure 4.2(a), which was taken from the front side, shows that we can see the letters written under the Micro Mechanical Key. In Fig.4.2(b), which was taken from the back side, we can't see them. This fact indicates that the slit is open



(a) View from the front side (b) View from the back side

Fig.11 Prototype of the Micro Mechanical Key (width=70μm pitch=150μm)

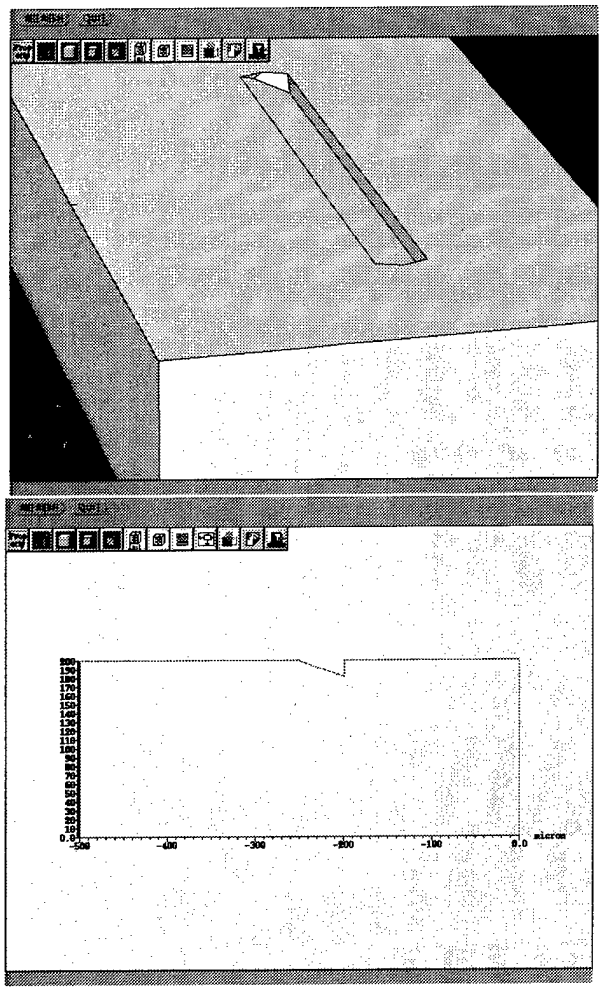


Fig.10 Simulation Result (Multistage Prism)

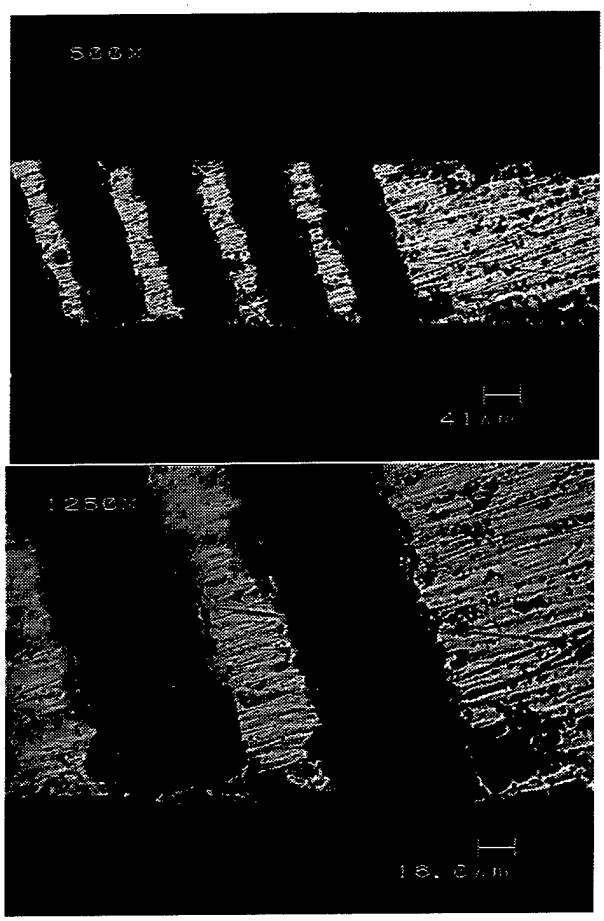


Fig.12 Cross Section of the Micro Mechanical Key (width=40 μm pitch=100μm)

to the fixed angle.

Figure 12 is the photograph of the cross section of the etched Si wafer. The conditions of etchant source are equal to the simulation parameters, and etching time is 110 min. It is clear that a large number of oblique grooves are made in the fixed angle.

In comparison with the simulation result, the effect of side etching appears little. Although a numerical error may affect the quantity of side etching, the final shape is almost the same.

6 CONCLUSIONS

We proposed a new ID acquiring method for personal identification system with fingerprint. This system consists of an optical filter, we call it Micro Mechanical Key, which has a large number of oblique grooves, and a Multistage Prism which has a large number of fixed plane.

We explained the micro fabrication processes to fabricate these components with a titled Si wafer. And we confirmed the effectiveness of the fabrication method by numerical simulation.

We tried to fabricate a prototype of the Micro Mechanical Key. We confirmed that a large number of oblique grooves were fabricated by the process we described.

ACKNOWLEDGEMENTS

This work was supported by a grant from the members of a joint research work on Micromechatoronics. We would like to thank all members and Chubu Science & Technology Center as a project manager.

References

[1] Lin Hong and Anil Jain, "Interrating Faces and Fingerprints for Personal Edentification," *IEEE Transactions on Pattern Analysis and Machine Intelligence*, vol. 20, no. 12, pp. 1295–1307, 1998.

[2] P.Rey, P.Chrvet, M.T.Delaye, S.Abou, and hassen, "A High Density Capasitive Pressure Sensor Array For Fingerprint Sensor Application," in *IEEE Transducers*, 1997, vol. 2, pp. 1453–1456.

[3] Thomson-CSF, *FCDEMO3BS: 500dpi 0.06" × 0.55" fingerprint liner sensor*, FingerChip Family Datasheet, July 1998.

[4] Tartagni and Guerrieri, "A 390dpi Live Fingerprint Imager Based on Feedback Capacitive Sensing Scheme," in *ISSCC Digest of Technical Papers*, 1997.

[5] D.Inglis, L.Manchanda, R.Comizzoli, A.Dickinson, E.Martin, S.Mendis, P.Silverman, G.Weber, and B.Ackland, "A 1.8V 250μW Direct-Contact 500 dpi Fingerprint Sensor," in *ISSCC Digest of Technical Papers*, 1998.

[6] Stefan Jung, Christofer Hierold, Thomas Scheiter, Paul Werner von Basse, Roland Thewes, Kael Goser, and Werner Weber, "INTELLIGENT CMOS FINGERPRINT SENSORS," in *IEEE Transducers*, Jun 1999, pp. 966–969.

[7] Satoshi Shigematsu, Hiroki Morimura, Yasuyuki Yanabe, and Katsuyuki Machida, "A 15×15mm^2 Single-Chip Fingerprint Sensor and Identifier using Pixel-Parallel Processing," in *ISSCC Digest of Technical Papers*, Feb 1999, pp. 138–139.

[8] A.I. Stoller, "The etching of deep vertical-walled patterns in silicon," in *RCA review*, 1970, vol. 31, pp. 271–275.

[9] Kazuo Asaumi, Yasuroh Iriye, and Kazuo Sato, "Anisotropic-Etching Process Simulation System MICROCAD Analyzing Complete 3D Etching Profiles of Single Crystal Silicon," in *Proc. of IEEE Micro Electro Mechanical Systems*, 1997, pp. 412–416.

A New Piezoresistive High Pressure Sensor Utilizing Combination of Three-Axis Normal Stress Components

Toshiyuki Toriyama, Kazuya Sawa, Yasutada Tanimoto and Susumu Sugiyama
Faculty of Science and Engineering, Ritsumeikan University
1-1-1, Noji-higashi, Kusatsu, Shiga, 525-8577 Japan
phone : +81-77-561-2845, facsimile : +81-77-561-2845, e-mail : ttv97012@se.ritsumei.ac.jp

Abstract:

A piezoresistive high pressure sensor utilizing a combination of three-axis normal stress components has been developed. Firstly, the principle, FEM analysis, fabrication and characteristics of a newly developed piezoresistive force sensor are briefly summarized. Secondly, the force sensor is adopted as the sensing unit of a high pressure sensor. The pressure sensor is composed of an embedded force sensor unit, a metal diaphragm and a metal case. Pressure is transmitted into force which is applied to piezoresistors on a sensor chip through a force transmission rod. Stresses in piezoresistors depend on the diameter, height and Young's modulus of the rod, and the diaphragm thickness of the sensor chip. In order to obtain large resistance changes in piezoresistors, the optimum combination of these parameters was investigated. A prototyped pressure sensor having an SUS630 stainless steel diaphragm of 10 mm-diameter and 1 mm-thickness was fabricated. An output voltage of more than 50 mV / 5 V at 150 MPa and a sensitivity temperature characteristic of 0.11 % F.S. / ℃ in the range from room temperature to 150 ℃ were realized.

1. INTRODUCTION

Semiconductor piezoresistive pressure sensors have been widely used in the field of industrial measurements, especially for high pressure measurement, where sensors having an oil-sealed dual-diaphragm or piezoresistors on a metal diaphragm, are used [1][2]. The structure and fabrication process of these sensors are complex and it is difficult to reduce cost and size.

It is expected that a low cost and miniature high pressure sensor will be developed for measuring internal pressure distribution, such as in an injection molding machine. For this purpose, a force sensor, used as a sensing unit of a metal diaphragm type high pressure sensor, has been developed. The pressure sensor can measure various ranges of pressure by changing the metal diaphragm thickness. Pressure is transmitted into force which is applied to the piezoresistors on sensor chip through the force transmission rod. Diffused p-type Si piezoresistors are used as force sensing elements. High sensitivity can be obtained by utilizing a combination of three-axis normal stress components in the piezoresistors. The relation between force sensor structure and output characteristics is investigated by FEM stress analysis. The output characteristics of the prototyped force sensor and high pressure sensor are reported.

2. FORCE SENSOR

2.1 Principle

Figure 1 shows a schematic for the force sensor structure. The force sensor is composed of a hemispherical head, a force transmission rod, a sensor chip containing a diaphragm and the piezoresistors, and a base plate.

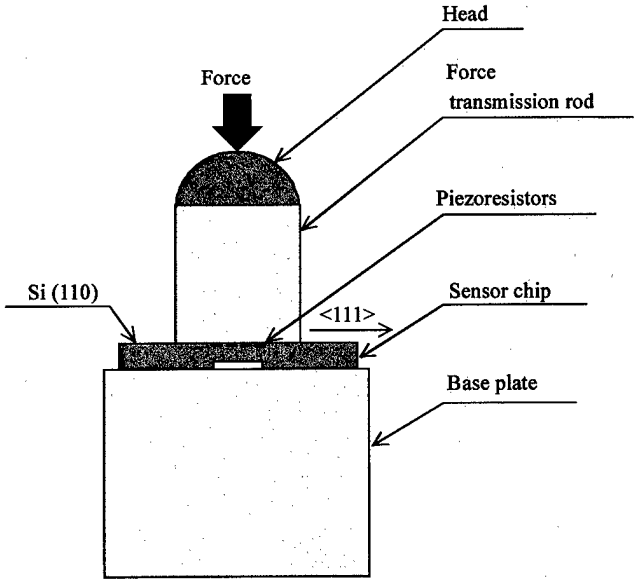


Fig. 1. Structure of the force sensor.

1999 INTERNATIONAL SYMPOSIUM ON
MICROMECHATRONICS AND HUMAN SCIENCE
0-7803-5790-6/99/ $10.00 ©1999 IEEE.

External applied force is transmitted into the diaphragm on sensor chip through the force transmission rod. As a consequence, resistance changes are induced in the piezoresistors on the diaphragm.

Figure 2 shows a schematic for the sensor chip structure. The substrate of the sensor chip is n-type (110) Si. A rectangular shaped diaphragm of $2000 \times 750\ \mu m^2$ is formed by using back side anisotropic etching. Four p-type Si piezoresistors are formed at the center (R_1 and R_4) and perimeter (R_2 and R_3) on the diaphragm along the $\langle 111 \rangle$ direction.

When stress is applied to a piezoresistor, resistance change $\Delta R/R$ is expressed as follows [3-5]:

$$\Delta R/R = \pi'_{11}\sigma_1 + \pi'_{12}\sigma_2 + \pi'_{13}\sigma_3 + \pi'_{14}\sigma_4 + \pi'_{15}\sigma_5 + \pi'_{16}\sigma_6 \qquad (1)$$

where, σ_1, σ_2 and σ_3 are the normal stress components. σ_4, σ_5 and σ_6 are the shear stress components. $\pi'_{11},\cdots,\pi'_{16}$ are the piezoresistive coefficients with respect to arbitrary directions. For cubic crystals, $\pi'_{11},\cdots,\pi'_{16}$ can be expressed in terms of the fundamental piezoresistive coefficients π_{11}, π_{12} and π_{44}. For the p-type Si, the absolute value of π_{44} is much larger than that for π_{11} and π_{12}. π'_{14}, π'_{15} and π'_{16} the components concerning shear stress, are equal to zero in this crystal direction. Therefore, Eq. (1) can be approximated as follows:

$$\Delta R/R = (1/3)\,\pi_{44}(2\sigma_1 - \sigma_2 - \sigma_3) \qquad (2)$$

Each piezoresistor is arranged into a full-bridge circuit (Fig.3). The resistance changes in the piezoresistors are transformed into change in voltage as Eq. (3):

$$V_{out} = \frac{1}{2}\left(\frac{\Delta R_p}{R_p} - \frac{\Delta R_c}{R_c}\right)V_{in} \qquad (3)$$

where V_{out} is the output voltage, V_{in} is the applied voltage, R_c are the resistances of the central piezoresistors (R_1 and R_4) and R_s are the resistances of the perimeter piezoresistors (R_2 and R_3). When the sign of σ_2 and σ_3 are opposite to that of σ_1, large resistance changes in piezoresistors can be obtained, since stress the effect in Eq. (2) becomes summational as follows: $|2\sigma_1|+|\sigma_2|+|\sigma_3|$. Also, in order to obtain large output voltage, the sign of resistance in the perimeter piezoresistors must be opposite to that in central piezoresistors, as shown in Eq. (3).

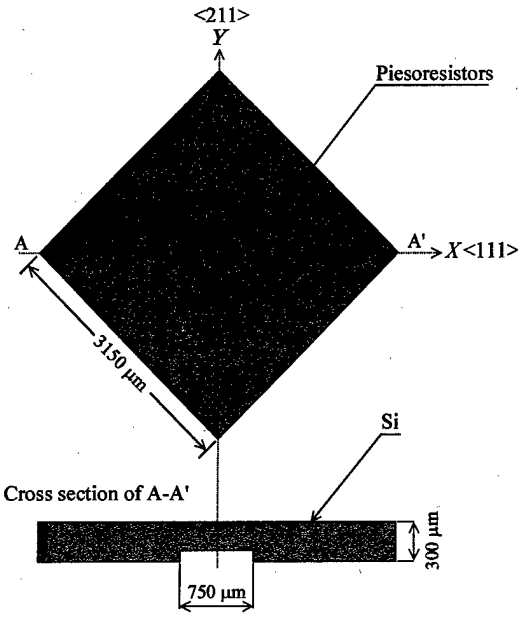


Fig. 2. Schematic of the sensor chip.

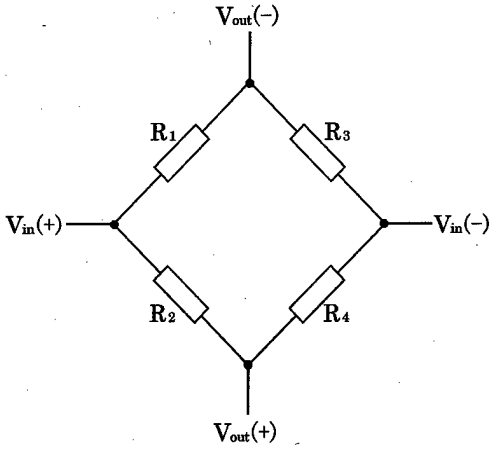


Fig. 3. Full bridge circuit.

2.2 FEM Stress Analysis

In order to estimate the output characteristics and optimum structural parameters, FEM stress analysis was carried out. The factors which control the output characteristics were assumed as follows:

(1) Young's modulus of the rod (E_r)
(2) Rod height (h)
(3) Rod diameter (d)
(4) Diaphragm thickness (t_d)
(5) Young's modulus of the base plate (E_p)
(6) Base plate thickness (t_p)

The variation of stresses in the piezoresistors were investigated by changing each factor in (1)-(6). As a result of analysis, a basic model was designed with the following specifications: E_r = 82 GPa, h = 2.0 mm, d = 1.5 mm, t_d = 200 μm, E_p = 82 GPa and t_p = 3.0 mm. Figure 4 shows the stress distributions on the diaphragm of the basic model along the X-axis when 150 N was applied to the center of the rod head. A mesh divided into 50 μm steps was adopted so that at least three nodes were included in each piezoresistor. The average stress values of each node were defined as stresses applied to the piezoresistors. From the result of FEM analysis, the shape and dimension of the sensor which can satisfy the above mentioned optimum combination of stress components were confirmed.

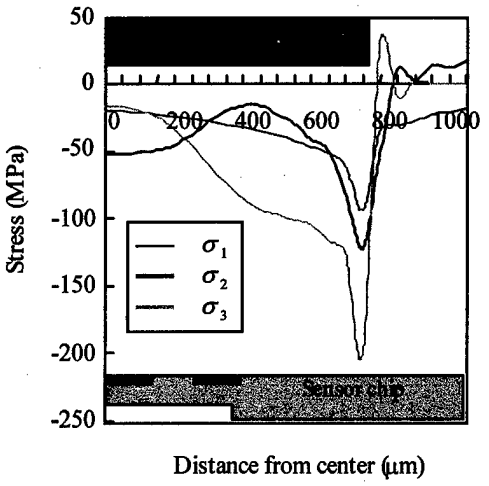


Fig. 4. FEM analysis.

2.3 Characteristics

Figure 5 shows the prototyped force sensor. The dimension of the prototyped force sensor was the same as the basic model. Glass (grade SW-3 : Iwaki Glass Co. Ltd.) was adopted as the material for the rod and the base plate. The coefficient of thermal expansion α of SW-3 ($\alpha = 3.4\times10^{-6}$ /℃) is close to that of Si ($\alpha = 2.3\times10^{-6}$ /℃) [6] and Young's modulus of SW-3 is 82GPa. Each part was bonded by an epoxy bonding agent.



Fig. 5. Prototyped force sensor.

In order to evaluate the characteristics of the force sensor, a compressive load up to 150 N was applied with a universal testing instrument (Instron Co. Ltd.). Temperature was also controlled by using a furnace associated with the universal testing instrument in the range from room temperature to 150 ℃. Then the resistance change in the four piezoresistors and the output voltage of the full-bridge circuit under applied voltage of 5 V were measured.

Figure 6 shows the resistance changes in piezoresistors versus applied load under room temperature. Figure 7 shows output voltage of the force sensor under room temperature. Figure 8 shows output change in the force sensor as a function

of temperature. Experimental values of resistance changes in piezoresistors were negative at the center (R_1, R_4) and positive at the perimeter (R_2, R_3). Under full scale load, i.e.,150 N, $\Delta R/R$ at the center was -1.62 % and at the perimeter 0.92 %. $\Delta R/R$ at the center was 80 % and at the perimeter 39 %, comparing with analytical values. As shown in Fig. 6, the difference between each pair of $\Delta R/R$ *is* thought to be due to alignment error of the rod and non-uniform stress distribution caused by surface roughness on the contact area (between rod bottom and sensor chip surface).

As shown in Fig. 7, the nonlinearity of the output characteristic was ±0.3 % F.S.. The experimental value of the output characteristic was 50 % of the analytical value. As shown in Fig. 8, the sensitivity temperature characteristic of the force sensor was within ±0.02 % F.S. / ℃ in the range from room temperature to 150 ℃.

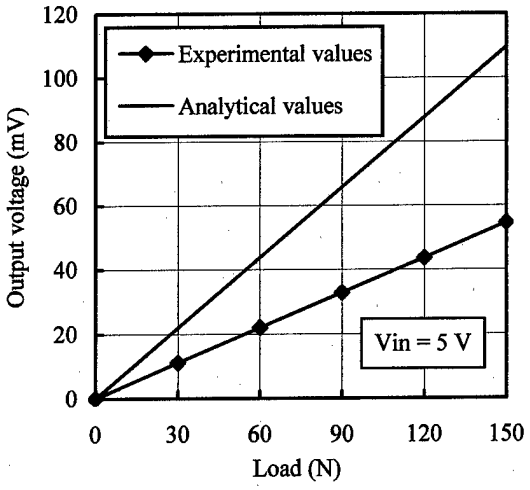


Fig. 7. Output characteristics of the force sensor under room temperature.

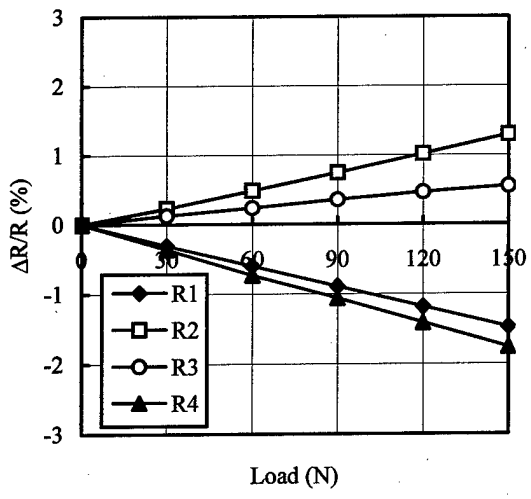


Fig. 6. Resistance changes in piezoresistors versus applied loads under room temperature.

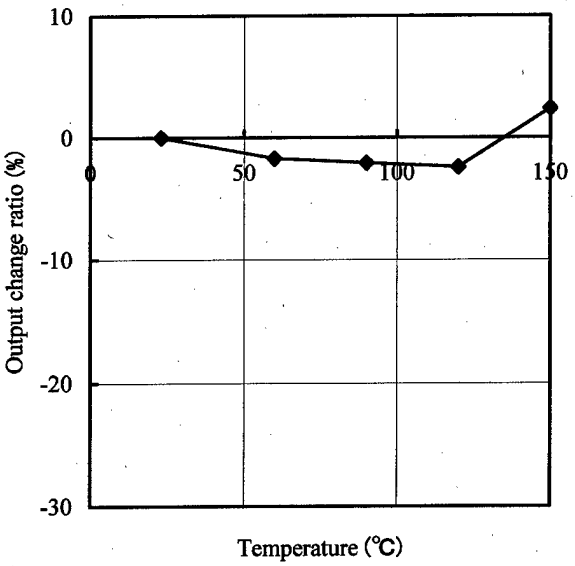


Fig. 8. Output change ratios of the force sensor under elevated temperature.

3. HIGH PRESSURE SENSOR

3.1 Principle

Figure 9 shows a schematic for the high pressure sensor structure. The high pressure sensor has an SUS630 diaphragm of 10mm-diameter and 1mm-thickness.

Pressure applied to the metal diaphragm is transmitted into the force sensor. When the high pressure sensor is fixed by a screw and sealed by a metal seal into a measuring instrument, the embedded force sensor unit can be prevented from being subjected to any stresses during sealing. As shown in Fig.9, the metal diaphragm component containing the force sensor unit is enclosed within the metal case just above the metal seal section. Therefore, the stress due to sealing is applied to just below the metal seal section and the embedded force sensor unit is stress free during sealing. The embedded force sensor unit can measure various ranges of pressure by changing the metal diaphragm thickness.

Figure 10 shows the components of the high pressure sensor. We recall that each part was bonded by an epoxy bonding agent.

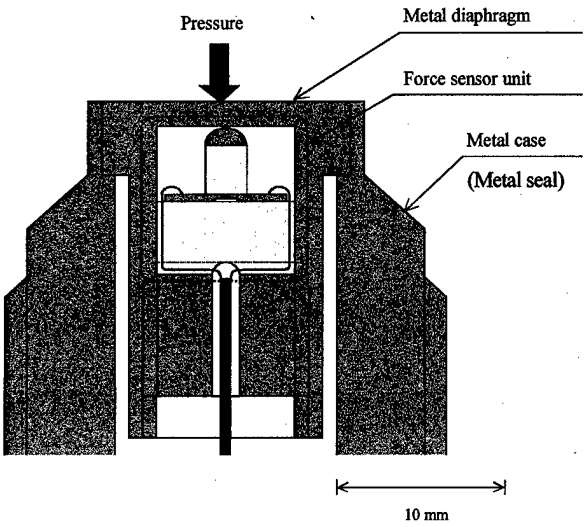


Fig. 9. Structure of the high pressure sensor.

3.2 Characteristics

High pressure up to 150 MPa per 30 MPa steps was applied to the pressure sensor, which is fixed into a temperature control furnace, by a manual cylindrical oil pressure pump under a temperature range from room temperature to 150 ℃.

In order to prevent causing a gap between the metal diaphragm and the force sensor under elevated temperature due to a difference in the thermal expansion of the component materials, a preload of 100N was applied to the embedded force sensor by the metal screw, prior to the experiment (see Fig.9).

Figure 11 shows the output voltage against applied pressure under a range from room temperature to 150 ℃. The nonlinearity of the output characteristic was 2.5 % F.S. at room temperature and 5.3 % F.S. at 150 ℃. The nonlinearity increased with temperature elevation. Figure 12 shows the sensitivity temperature characteristic. The sensitivity temperature characteristic was within 0.11 % F.S. / ℃ under a range from room temperature to 150 ℃.

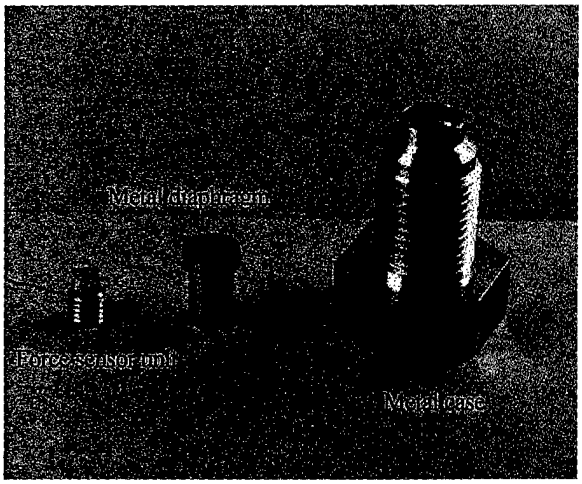


Fig. 10. Components of the high pressure sensor.

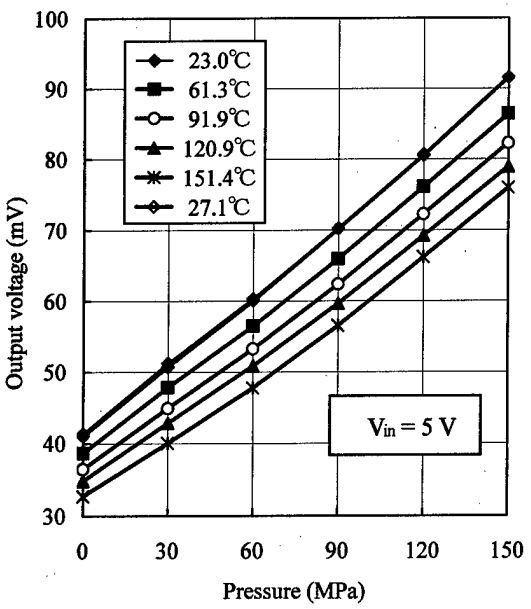


Fig. 11. Output characteristics of the high pressure sensor under elevated temperature.

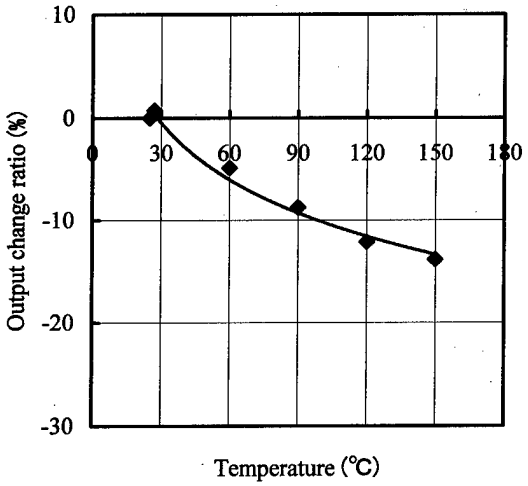


Fig.12. Output change ratios of the high pressure sensor under elevated temperature.

4. CONCLUSIONS

A piezoresistive high pressure sensor, having an SUS630 stainless steel diaphragm of 10 mm-diameter and 1 mm-thickness, was fabricated. An output voltage of more than 50 mV / 5 V at 150 MPa and a sensitivity temperature characteristic of 0.11 % F.S. / ℃ in the range from room temperature to 150 ℃ were realized.

ACKNOWLEDGEMENTS

The authors would like to thank Mr. K. Akagi, Mr. Y. Ota and Mr. T. Hatasaki at Riken Keiki Nara Mfg., Co., Ltd. for fabrication, measurement and discussion of the force sensor, Mr. H. Iwata and Mr. K. Itoigawa at Tokairika Co., Ltd. for supplying sensor chips, Mr. F. Akiyoshi at Asahi Techno Glass Co., Ltd. for supplying glass rods and glass base plates, and Mr. Y. Nasu and Dr. T. Imamichi at Industrial Research Center of Shiga Prefecture for helping with the measurement of the force sensor.

REFERENCES

[1] S.Otake, M.Onoda and K. Nagase, "Automotive High Pressure Sensor", SAE Paper, 980271, pp.61-68, 1998.

[2] Toyoda Machine Works, Ltd. "Semiconductor Transducers Catalog", no.EKA013-12JE, 1994.

[3] H. Nakamura and S. Sugiyama "Crystal Orientation Dependence of Piezoresistive Effect in Silicon", A Monthly Publication of The Japan Society of Applied Physics, vol.45 no.2, pp.179-182, 1976 (in Japanese).

[4] C. S. Smith, "Piezoresistance Effect in Germanium and Silicon", Physical Review, vol.94 no.1, pp.42-49, 1954.

[5] W.G.Pfann and R.N. Thuston, "Semiconducting Stress Transducers Utilizing the Transverse and Shear Piezoresistance Effects", Journal of Applied Physics, vol.32 no.10,pp.2008-2019, 1961.

[6] K. E. Petersen, "Silicon as a Mechanical Material", Proceedings of the IEEE, vol.70 no.5, pp.420-457, 1982.

Technical Session D-1

Microcomponents and Microdevices II

Fabrication of Micromotors Using LIGA Process

Shinsuke Takimoto, Ryoji Kondo, Kenichiro Suzuki and Susumu Sugiyama*
Faculty of Science and Engineering, Ritsumeikan University
1-1-1 Noji-Higashi, Kusatsu, Shiga 525-8577, Japan
phone: +81-77-561-2845, facsimile: +81-77-561-2845, e-mail: rm082955@se.ritsumei.ac.jp
*NEC Corporation, 34 Miyukigaoka, Tsukuba, Ibaraki 305-0841, Japan

Abstract:

An electrostatic wobble micromotor and a comb drive microactuator were fabricated by the LIGA process. The following design rules for the micromotors were decided: a height of 100 μm, a maximum width for movable parts of 10 μm, a minimum width for fixed parts of 40 μm, a driving voltage of about 100 V, and a minimum gap of 2 μm between movable parts and fixed parts. Calculated torque outputs for the wobble motor and the comb drive actuator were 3.19×10^{-8} Nm and 11.33×10^{-8} Nm respectively under a driving voltage of 100 V. The basic structure of the micromotors was composed of movable and fixed electrodes of Ni and a sacrificial layer of SiO_2 on a Si substrate. These micromotors were fabricated by a single mask process using LIGA. In this process, the difficult phase is removing the PMMA molds before the sacrificial layer etching of SiO_2. The residual PMMA was removed by the GG developer after a second X-ray exposure without a mask. When the residual PMMA was left between the micropatterns, it was removed completely by using an organic solvent and so on. Therefore, the sacrifice layer etching and drive of the micromotors were successful. Actuation of the micromotors was confirmed. The applied voltage to the wobble motor and the comb drive actuator were 125 V and 65 V respectively. The maximum oscillation of the comb drive actuator was 4.54 μm under a frequency of 2.0×10^3 Hz.

1. INTRODUCTION

Recently, there have been many examples of microstructures fabricated by the LIGA (German acronym for Lithographie, Galvanoformung, Abformung) process [1]. The LIGA process can make high aspect ratio (height /width) microstructures. As driving source for microactuators, electrostatic force is mostly adopted because there is an advantage in the view point of size effect against magnetic force, piezoelectric force, thermoelectric force and so on [2]. An another advantage of electrostatic force for micromotors is as follows.

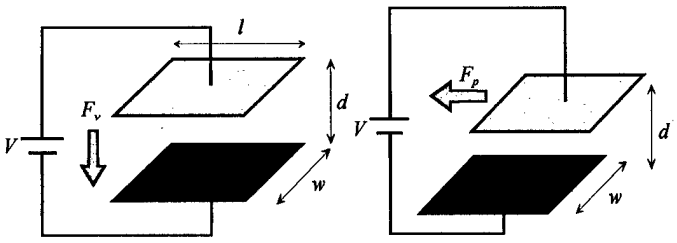
The electrostatic force is shown in Fig 1. There are two types of the electrostatic force, vertical force and parallel force, as the electrostatic force which acts between two electrodes [3]. A wobble motor is driven by the vertical force and a comb drive actuator is driven by the parallel force:

$$F_v = \frac{1}{2}\frac{\varepsilon w l}{d^2}V^2 \quad : \text{Vertical force}$$

$$F_p = \frac{1}{2}\frac{\varepsilon w}{d}V^2 \quad : \text{Parallel force}$$

where ε is the dielectric constant, w is the electrode width, d is the gap between the electrodes, l is the electrode length and V is the applied voltage. So, microstructures which have a small gap between the two electrodes and a high structure are expected to fabricate micromotors with high power. We have therefore adopted the electrostatic force as a driving source for micromotors.

In this paper, we will present a fabrication process for micromotors using the LIGA process and characteristics of the micromotors.



Vertical force Parallel force

Fig. 1. Electrostatic forces

1999 INTERNATIONAL SYMPOSIUM ON
MICROMECHATRONICS AND HUMAN SCIENCE
0-7803-5790-6/99/ $10.00 ©1999 IEEE.

2. DESIGN

The design rules were decided as follows: a resist minimum width of 2 μm, a resist height of 120 μm, consideration of the lateral etching length of SiO_2, a maximum width for movable parts of 10 μm, a minimum width of fixed parts of 40 μm, a minimum gap of 2 μm between movable parts and fixed parts and an applied voltage of 100 V.

Figure 2 shows the basic structure of the micromotors in this work. The structure is composed of 100 μm-high Ni microstructures, an isolation layer of 2 μm-thick SiO_2 and a Si substrate. The Ni microstructures are fabricated by a single mask process using LIGA. The Ni microstructures compose a movable electrode, a spring beam, an anchor portion and a fixed electrodes. The movable electrode is supported by the spring beam, the end of which is fixed to the anchor portion.

A wobble motor and a comb drive actuator as shown Fig. 3 and Fig. 4 were designed. The wobble motor is composed of a rotor, a rotor electrode and stators. The rotor contacts the rotor electrode, and receives electrical potential. The stators are arranged inside the contact points with the rotor and the rotor electrode. The rotor can be rotated by applying voltage to successive stators. The transmission of the torque is facilitated by the arrangement of the rotor outside the stator.

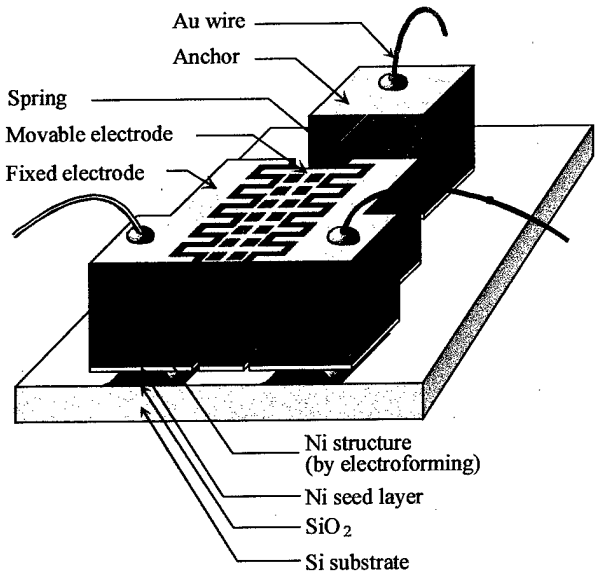


Fig. 2. A basic structure

The reduction ratio of the wobble motor is as follows: [1]

$$r = \frac{R_r - R_s}{R_r}.$$

Where, *Rr* is the radius of the rotor, *Rs* is the maximum radius

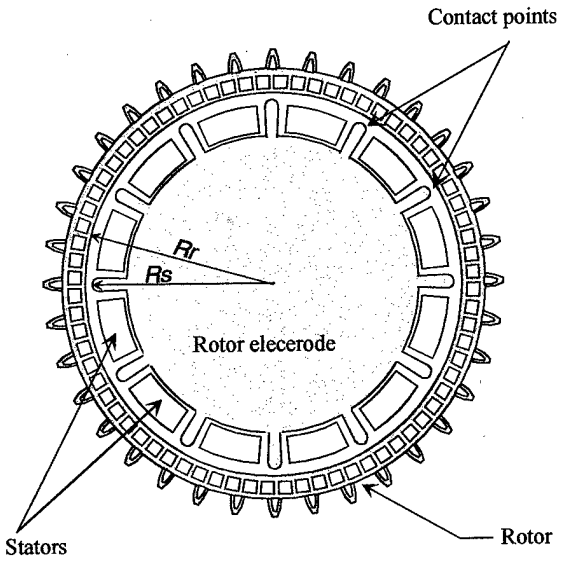


Fig. 3. A design of the wobble motor

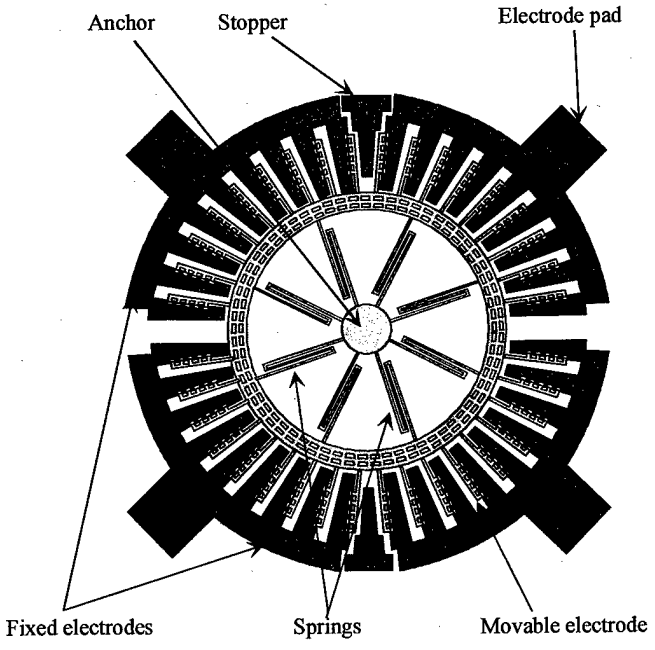


Fig. 4. A design of the comb drive actuator

of the rotor electrode. The wobble motor is a low speed and high torque type, with a large reduction ratio of 1:201. This decreases the shaft shake because the movement of the rotor is nearly a sheer circular orbit. Friction between the rotor of Ni and the Si substrate must be taken into consideration. Generally, a coefficient of friction between materials in micro scale is not constant because of differences in the surface condition during the fabrication process and so on. The calculated torque of the wobble motor is 3.19×10^{-8} Nm under an applied voltage of 100 V when coefficients of static friction and dynamic friction are 1 and 0.5 respectively.

The comb drive actuator is composed of a movable electrode, fixed electrodes, springs, an anchor, stoppers and electrode pads. The movable parts are supported by the springs. The comb drive actuator is a vibration type capable of minute displacement. The movable electrode receives electrical potential through the springs from the anchor, and the fixed electrodes receive potential from the electrode pads. The stoppers prevent the mutual electrodes from contacting.

3. FABRICATION PROCESS

Ni electrostatic microactuators were fabricated by the LIGA process, as shown in Fig. 5. The process flow is as follows.

①A 3 μm-thick isolation layer of SiO_2 and a 50 nm-thick seed layer of Ni were deposited on a Si wafer. A 120 μm-thick PMMA (polymethyl methacrylate) X-ray resist layer was formed on the substrate. PMMA is an excellent X-ray resist, because it has high resolution in spite of its low sensitivity. The PMMA layer was formed by polymerizing a base resin directly onto the substrate. The resin was composed of MMA (methyl methacrylate)-PMMA mixed resin, benzoyl peroxide as starter, N,N-dimethylaniline as hardener and triethylene glycol dimethacrylate as cross-linker.

②X-ray mask patterns were transferred to the PMMA resist by deep X-ray lithography. The X-ray mask was composed of a 7 μm-thick Au absorber and a 2 μm-thick poly-Si membrane [5]. Although the photon energy of the SR light source is relatively low, a high photon density is obtained at the resist

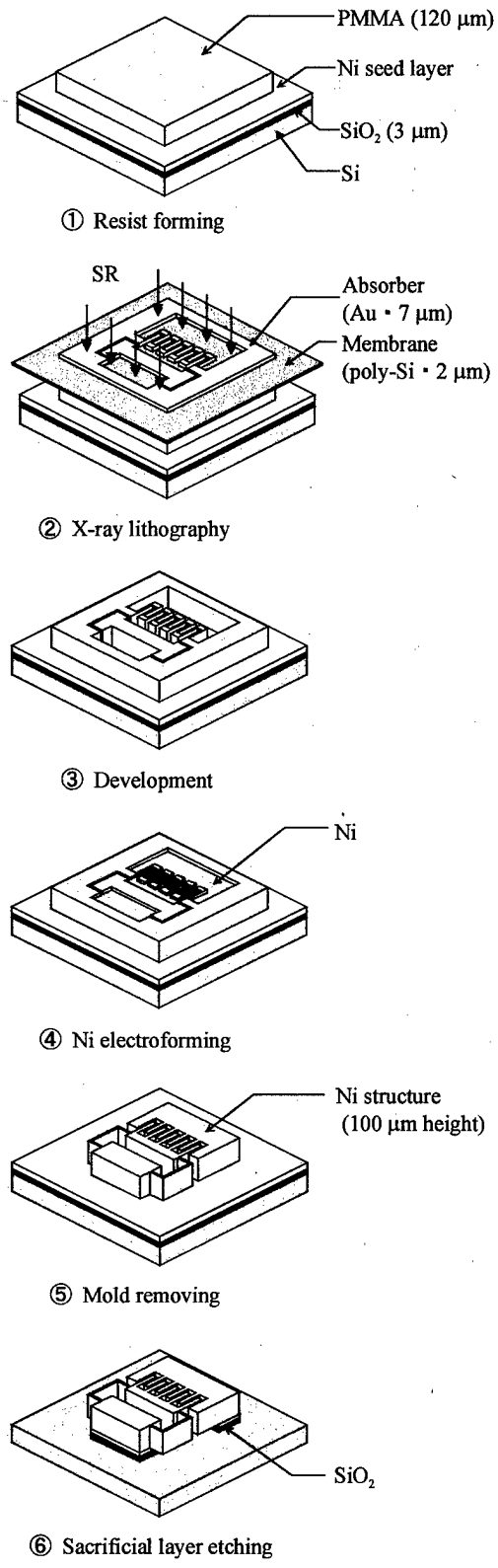


Fig. 5. Fabrication process for micromotors

surface, because it is possible to expose at a distance of only 3 m from the SR light source.

③The exposed PMMA was developed by using GG developer (a mixture of 2-2-butoxyethoxy ethanol, morpholine, 2-aminoethanol, and water) for 60 min at 37 ℃. PMMA structures 120 μm high and with a minimum width of 2 μm (aspect ratio of 60), were fabricated. These structures were used as molds for Ni electroforming. Examples of PMMA molds are shown in Fig. 6 and Fig. 7.

④Ni microstructures were formed by using a Ni sulfamate plating bath at 37 ℃ with a current density of 2.8 A/dm^2, giving a deposition rate of about 0.28 μm/min. The advantages of the plating bath are that the deposition rate is relatively high and the residual stress of deposited Ni is relatively low.

⑤Most of the PMMA molds on the substrate were removed by the GG developer after a second X-ray exposure without a mask. Residual PMMA was removed by an organic solvent, i.e. 2-Butanone. Finally the GG developer was reapplied after a further X-ray exposure without a mask. As a result, Ni microstructures with 100 μm-height, 2 μm-minimum width and with a maximum aspect ratio of 50 were fabricated. SEM images of the fabricated Ni microstructures are shown in Fig. 8 and Fig. 9.

⑥The Ni seed layer was removed by etching with diluted HNO_3. The movable parts of the Ni microstructures were separated from the substrate by lateral etching of the SiO_2 isolation layer using buffered HF. SiO_2 lateral etching was performed until the isolation layer was 8μm wide. There was the possibility that movable parts which were separated by etching would re-adhere due to the surface tension of rinse water during the drying step. Therefore a freeze drying method utilizing t-butyl alcohol was used [6]. In this way, the movable parts of Ni microstructures were able to be separated from the substrate.

4. MICROMOTOR CHARACTERISTICS

A wobble motor with 100 μm-height, 2 μm-minimum width and with a maximum aspect ratio of 50 was fabricated. Rotation of the wobble motor was confirmed when the applied voltage was 125 V and the excitation frequency was 8 kHz.

A comb drive actuator with 100 μm-height, 5 μm-minimum width and with a maximum aspect ratio of 20 was fabricated. Displacement lengths of the comb drive actuator were measured. The maximum oscillation of the comb drive actuator was 4.54 μm under a frequency of 2.0 kHz and an applied voltage of 100 V. The output torque was 111.7 nNm.

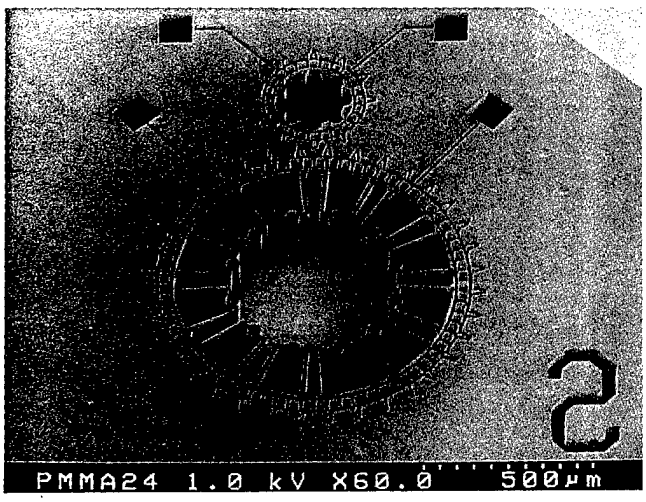


Fig. 6. SEM image of PMMA mold for the wobble motor

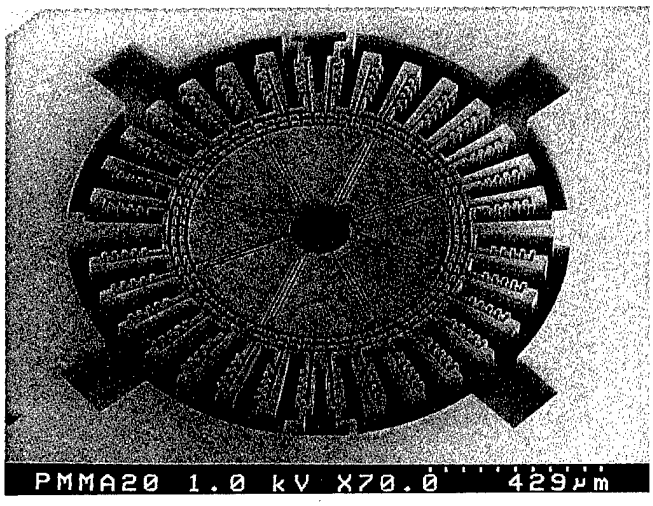
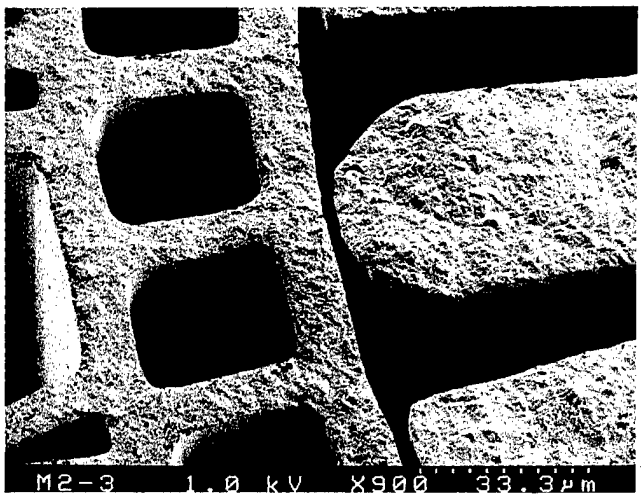


Fig. 7. SEM image of PMMA mold for the comb drive actuator



Close-up

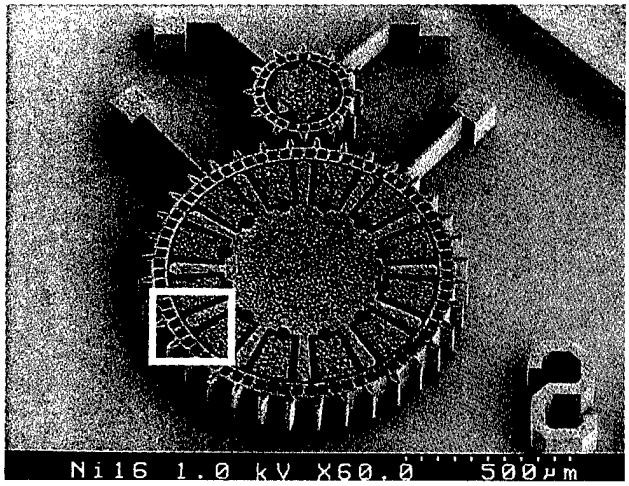
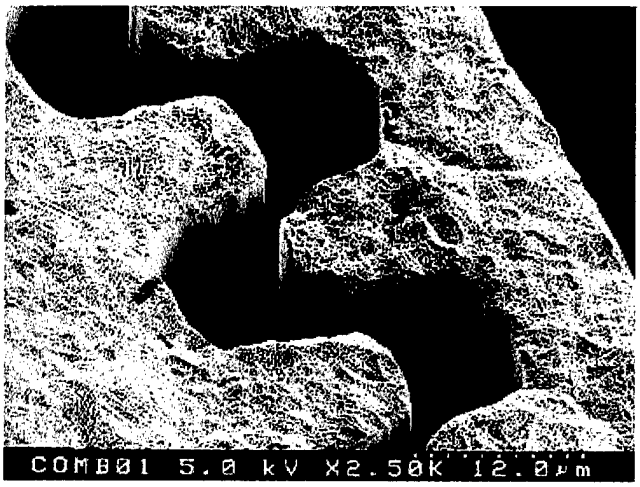


Fig. 8. SEM image of the wobble motor of Ni



Close-up

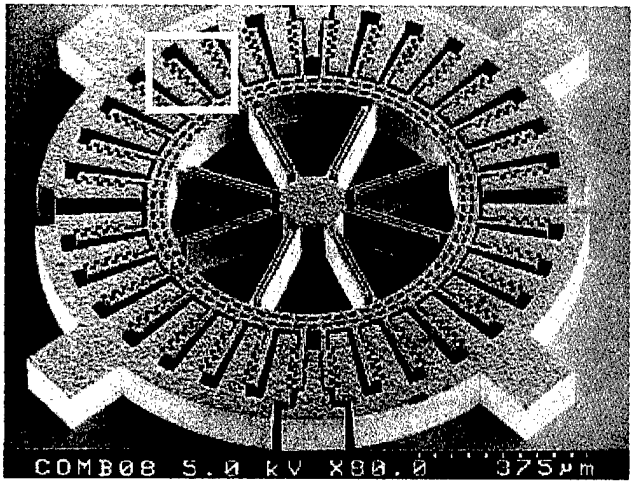


Fig. 9. SEM image of the comb drive actuator of Ni

Measured resonant frequency of the comb drive actuator was 2.0 kHz compared to 1.4 kHz in design. This difference is explained by the fact that there was no load applied during measurement compared to a load of 1 mg in design. Therefore the measured characteristics approximate closely the design.

5. CONCLUSIONS

A wobble motor and a comb drive actuator were designed. Calculated torque of the wobble motor and the comb drive actuator were 31.9 nNm and 113.3 nNm respectively under an applied voltage of 100 V. PMMA molds for the micromotor were fabricated by a single mask process using LIGA. Most of the PMMA molds on the substrate were removed by GG developer after a second X-ray exposure without a mask. Residual PMMA was removed by an organic solvent, i.e. 2-Butanone. Finally GG developer was reapplied after a further X-ray exposure without a mask. A wobble motor with 100 µm-height, a 2 µm-minimum width with a maximum aspect ratio of 50 and a comb drive actuator with 100 µm-height, 5 µm-minimum width and with a maximum aspect ratio of 20

were fabricated. Ni microstructures used for movable electrodes were separated from the substrate by lateral etching of SiO_2 layer. After wiring, actuation of a comb drive actuator and a wobble motor was confirmed. The applied voltage of the wobble motor was 125 V, the excitation frequency was 8 kHz and the motor speed was about 199 rpm. The maximum oscillation of the comb drive actuator was 4.54 μm under frequency of 2.0 kHz and applied voltage of 100 V.

It is concluded from these results that the LIGA process can be used to fabricate practical high power micromotors with a high aspect ratio. We are convinced that high performance micromotors can be fabricated, provided we investigate further the characteristics of micromotors.

6. ACKNOWLEDGMENTS

This work was partly supported by the Japanese Ministry of Education, Science, and Culture under a Grant-in-Aid for Developmental Scientific Research (No.08455046), and by the Micromachine Center for Micromachine Technology Research Grant.

REFERENCES

[1] V. D. Samper, A. J. Sangster, R. L. Reuben, and U. Wallrabe, "Multistator LIGA-Fabricated Electrostatic Wobble Motors with Integrated Synchronous Control", IEEE, Jounal of Micrielectromechanical Systems, Vol.7, No.2, 1998, pp214～223

[2] H. Nakazawa, The R&D trend of Micro-Actuator Technology, The Fourth International Micromachine Symposium, 1998, pp215-220

[3] e.g.:Digest of Technical Papers of TRANSDUCERS97, Chicago, 1997.

[4] S. Sugiyama, Y. Zhang, H. Ueno, M. Hosaka, T. Fujimoto, R. Maeda and T. Tanaka, "A compact SR beamline for Fabrication of High Aspect Ratio MEMS Microparts", Proceedings of MHS'96, 1996, pp.49-54

[5] K. Suzuki, H. Nakamura, H. Ueno, N. Nakamura and S. Sugiyama, "An X-ray Mask with a Low-Stress Controlled Polysilicon Membrane in Use for High Aspect Ratio Pattern Lithography", Technical Digest of the 15th Sensor Symposium, 1997, pp.197-200

[6] N.Takeshima et al, "A New Freeze Drying Method for Sacrificial Layer Etching", NATIONAL CONVENTION RECORD I.E.E. JAPAN,4-1,1991 (In Japanese).

[7] Koichi Suzumori, "Electrostatic Actuators", JRSJ, Vol.15, No.3, 1997, pp342～346

Development of a Planar Type Micro Electro Magnetic Distance Sensor using High Aspect Ratio Photoresist and Its Application

Xianhe DING, Katsutoshi KURIBAYASHI and Takao HASHIDA
Faculty of Engineering, Yamaguchi University
2-16-1 Tokiwadai UBE, 755-8611 JAPAN

ABSTRACT

In this paper, a planar type micro electro magnetic distance sensor has been developed for the distance sensor of micro mobile robot. So far, because of the use of common photoresist, the thickness of the sensors only get several μ m [1][2]. Therefore the sensors fabricated have low measuring accuracy. In order to obtain high sensivity, using ultrathick high aspect ratio photoresist SU-8, a 300- μ m-thick microcoil has been fabricated by micromaching technique based on sputtering and electroplating methods. The microcoil has a spiral planar ultrathick structrue. The static characteristics and frequency response of the microcoil have been measured, and sensitivity and position control of the microcoil were measured. The experimental results show that as electro megnetic distance sensor it has wide frequecy response and high measuring accuracy.

1 INTRODUCTION

Among the many different fabrication techniques of micro system technology, surface micromachining is most promising and fast developing. Many kinds of micro distance sensor have been fabricated [1]~[3], and untill now, many of their structures have relatively low aspect ratio characteristics. But high aspect ratio structures of the microsensor are offen required, because the high aspect ratio of the microsensor can lead to a low resistance, thereby reducing ohmic losses and increacing the S/N and sensitivity [4].

To get a high aspect-ratio structure, a new fabrication technique has been demonstrated [5]. This technique is based on the use of ultrathick photoresist SU-8, the photoresist has two important properties suited for ultrathick application, its low molecular weight dissolution and spectrum [6]. With SU-8 photoreist, 400- μ m-thick microcoil mold was fabricated.

By the ultrathick, high aspect ratio photoresist SU-8 combined with electroplating of nickel, a planar highly intergrated electromagnetic coil of thickness of Ni plate 300 μ m, and outer diameter 3000 μ m has been fabricated. With help of testing circuit, the static characteristics and frequency response of the microcoil were measured, and sensitivity and closed-loop position control respose using the microcoil distance sensor developed were measured.

2 PRINCIPLE OF THE SENSOR

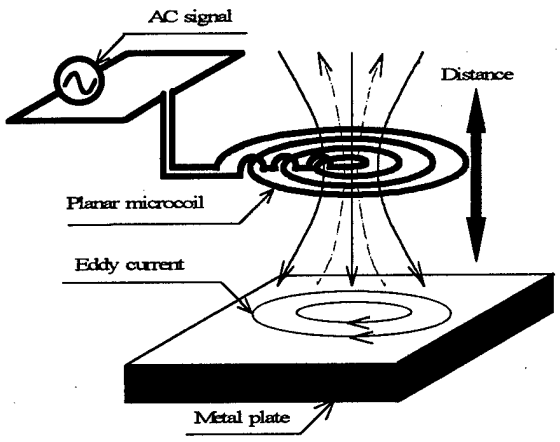


Fig1 Principle of the planar type micro electro magnetic distance sensor

The micro electro magnetic distance sensor is based on the measurment of the microcoil inductance variation. Fig 1 shows its principle diagram.

When the microcoil is supplied high frequency AC signal, it will generate electromagnetic field which induces an eddy

1999 INTERNATIONAL SYMPOSIUM ON
MICROMECHATRONICS AND HUMAN SCIENCE
0-7803-5790-6/99/ $10.00 ©1999 IEEE.

current on the metal plate, the eddy current will lead to a variation of microcoil inductance. Since a change of the distance (Z) between the sensor and the metal plate affect the eddy current value, its presence can be detected from the variation of the coil inductance.

If the metal plate is regarded as a short circuit coil, we can get its equivalent circuit in [Fig 2].

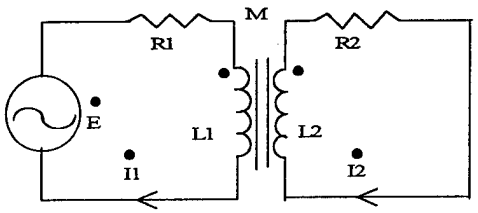


Fig2 Equivalent circuit of the Fig1

$R1*\dot{I}1+j\omega*L1*\dot{I}1-j\omega*M*\dot{I}2=\dot{E}$ (2.1)

$-j\omega*M*\dot{I}1+R2*\dot{I}2+j\omega*L2*\dot{I}2=0$ (2.2)

Thus equivalent impedance of the microcoil

$Z=\dot{E}/\dot{I}1=R1+R2*Y+j(\omega*L1-\omega*L2*Y)$ (2.3)

$\{Y=\omega*\omega*M*M/(R2*R2+\omega*\omega*L2*L2)\}$

Equivalent inductance of the mcrocoil

$L=L1-L2*Y$ (2.4)

R1-----Coil resistance

R2-----Metal resistance

E------AC signal

L1-----Coil inductance

L2-----Metal inductance

M------Mutual inductance

$\dot{I}1$-----Coil current

$\dot{I}2$-----Metal current

ω-----Frequency

3 FABRICATION PROCESS

3.1 Photomask design

Table 1 Microcoil size

a(Maximum diameter of a coil)	3000(μ m)
b(Center diameter of a coil)	300(μ m)
c(Width)	100(μ m)

In the fabrication process the photomask design is necessity, because the size and shape of the microsensor is decided by photomask.

Generally the microcoil is requested to have a high inductace and low resistance [7]. In comparison to different planar coil structures, the spiral coil can obtain the highest inductance [8], and high inductance also depends on increasing the total number of the microcoil turns. The low resistance can be obtained by increasing the width and thickness of the micocoil [9][10].

Considering high inductance, low resistance and small size, the final size and shape of microcoil is presented in Fig3 and Table1.

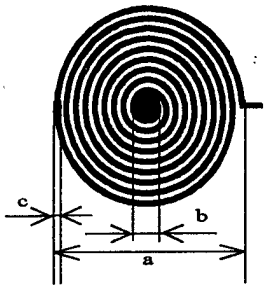


Fig3 Mask Sample

3.2 Fabrication process of the microcoil

A new fabrication process of the microcoil is schematically described in Fig4.

1) The seed layer (Cu/1 μ m) were sputtered on the glass plate. The sputtering condition is shown in Table2.

Table2 sputering condition

Method	Sputtering
Meterial	Glass
Target	Cu
Presputtering time	10 min
Sputtering time	12 min
Chamber presure	6.2*10-7 torr
Ar gas presure	1.4*10-3 torr
RF Power	300w

2) A resist is spin-coated

In the fabrication of the microcoil mold, the photoresist SU-8 is used. According the SU-8 properties, the spinning speed, the pre-bake time, the exposure dose and the development time of the microcoil mold are dependent on the photoresist thickness[11]. For a 400-μ m-thick photoresist, the spin is done in two steps which have a total duration of 40 s, The first step consists of a ramp from 200 rpm to the final speed 900 rpm with an acceleration of 100 rpm/s and the

second step is a sustained spin at the final speed, the wafer is pre-baked at 95℃ on a flat hot plate for 15 min. The exposure is performed on a UV light, a dose of 300-400 $mJcm^{-2}$ measured at 365nm is necessary for the complete cross-linking of the photoresist which is accelerated by a post-bake of 15 min on a hot plate.

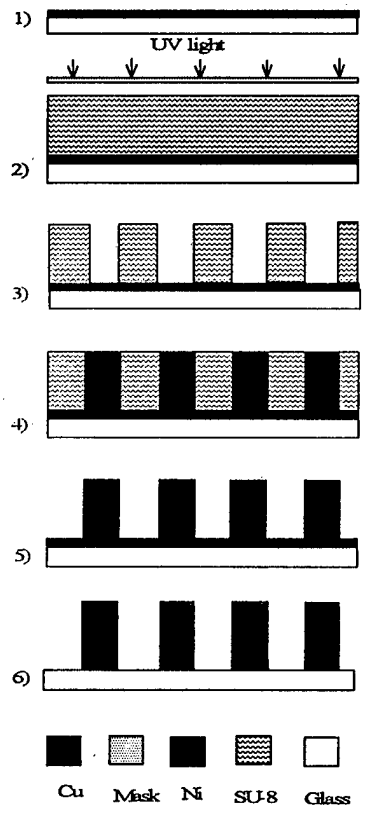


Fig4 Fabrication process of the sensor

3)Development is done in PGMEA (propyleneglycol monomethylether acetate) for 15 min and finally the wafer is rinsed with isopropanol.Stripping can be achieved with hot N-Methyl-pyrrolid-inone [12].

4)Electroplating

The high aspect ratio microstructure of microcoil is achieved by Ni electroplating using ultrathick photoresist SU-8 mold. The Table3 shows elecroplating condition. Ni thickness of up to 300 μ m has been obtained.

5)The photoresist SU-8 is removed.

6)Cu is etched. The microcoil sample fabricated is shown in Fig 5, it has high aspect ratio and ultrathick structure.

Table3 The electroplating condition

Plating thickness		300 μ m
Composition of the electroplating liquid	sulfinic acid nickel	450 g/l
	chlorinated nickel boric acid	30 g/l
Electrolytic current		50 mA
The liquid temperature		55 ℃

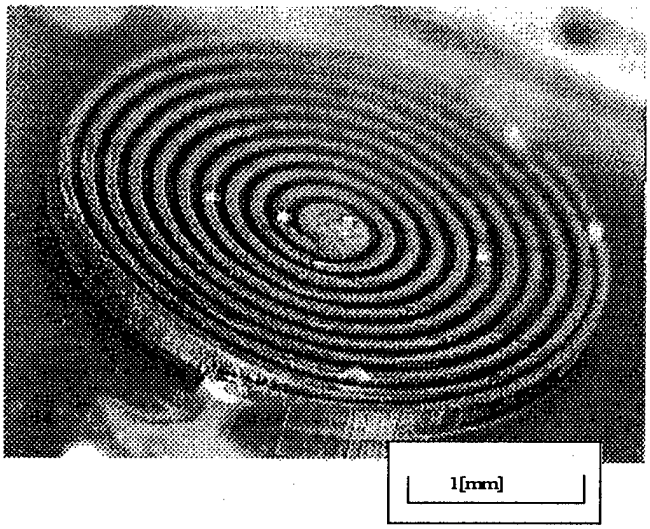


Fig5 Microcoil sample fabricated

4 THE STATIC CHRACTERISTCS

4.1 The measurement and the theory of the impedance characteristics of the sensor.

In the Fig6, by controlling the position of XYZ stage along Z directon, the variation of the microcoil inductance can be measured from the inpedance meter. Fig7 shows the microcoil inductance measured as a function of the distance between the microcoil and metal plate which is aluminium plate.

From the Fig2, $R2 = \rho * D/S$

But $Z \propto 1/S$, $Z \propto 1/M$ and $Z \propto L2$

According equation 2.4

$L = L1-L2*Y$

$\{Y= \omega * \omega *M*M/(R2*R2+ \omega * \omega *L2*L2)\}$

L1 is constant

Thus $L2*Y \propto 1/Z$,

$L \propto Z$

S------eddy current square on the metal plate

D----- eddy current deep

ρ -----resistance coefficient

Therefore the experimental result is corresponding with theory analysis.

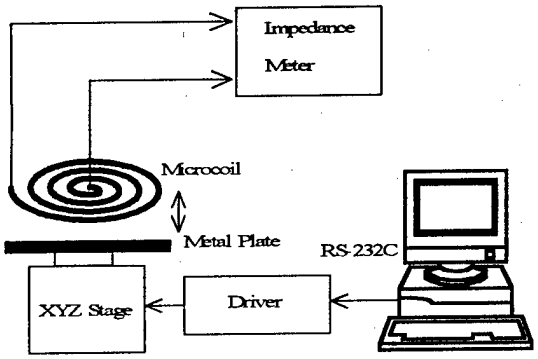


Fig6 Testing system frame of the impedance characteristics

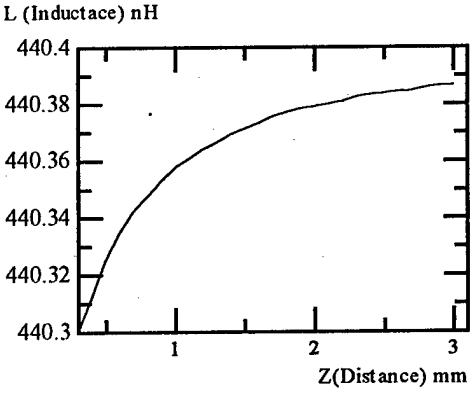


Fig7 L-Z Experimental result of the static characteristics of the sensor

4.2 The measurement of output characteristics of the sensor

The Fig8 shows the testing system of the output chatacteristics of the mirocoil. To achieve high sensitivity, the tranceformer T is used , n1/n2=80/1.

Firstly the computer controls the position of XYZ stage, at the same time, by F/V and A/D transformation, the microcoil output will be obtained. The curve of distance with the voltage of the microcoil and its approximate curve which was produced by minimizing e^2 is shown in Fig9. Fig9 shows that the microcoil has better outputer characteristcs at distance of 0 to 1mm.

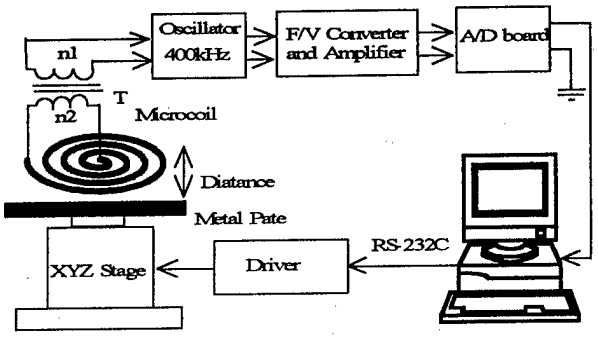


Fig8 Experimental system to measure output Voltage characteristics of the sensor

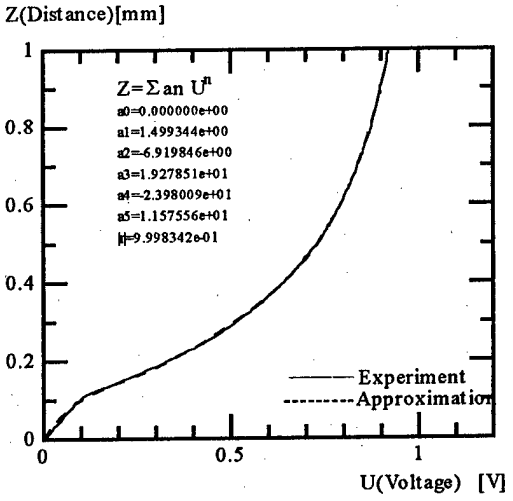


Fig9 Expermental static charactristic of the microcoil and its inverse function approximated by 5 th order polinomial

5 FREQUENCY RESPONSE of THE SENSOR

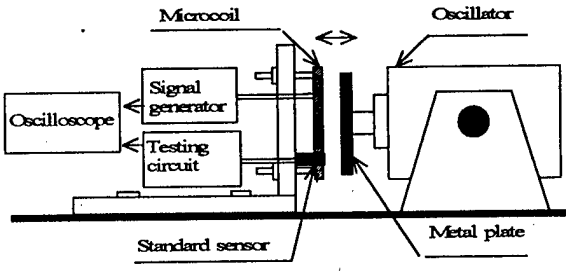


Fig10 Experimental system of frequency response] of the microcoil distance sensor

Table4 Specifications of the oscillator

Maximum oscillation torque	5Kgf±5%
Maximum acceleration	38G±5%
Range of the oscillation frequency	1Hz～10KHz
Maximum amplitude	7mm
Maximum speed	114cm/s

The frenquency response of the microcoil has been measured.The experimental system used is shown in Fig10. The specifications of the oscillator are shown in Table4. By controlling amplitude and frequency of the oscillator, the output of the microcoil can be gotten from the oscilloscope.

G(Gain)=20log V/V0

V ---- output of the standard sensor

V0 ---- output of the microcoil.

The experimental results are shown in the Fig 11 and shows that the frequency working range of the microcoil is from oHz to 1kHz. U shows the bias value of the sinusoidal wave for the frequency response.

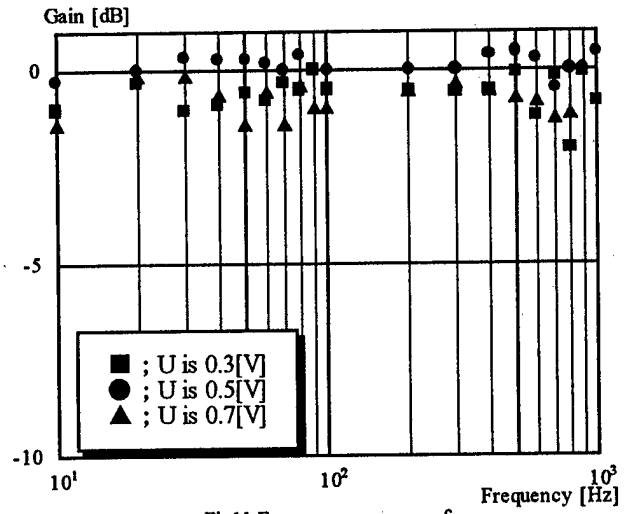


Fig11 Frequency response of the microcoil distance sensor

6 CONTROL EXPERIMENTS

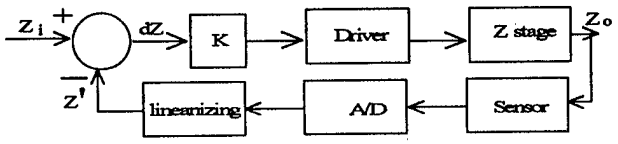


Fig12 Controlling System

In order to measure the output linearity and response speed of the sensor system, the following experiments were performed. Fig12 shows the closed-loop position control system based on the microsensor measurement.

Firstly, by controlling Z stage to move to some position Z_O, the sensor will output corresponding voltage, after A/D conversion and lineanizing which is realized by relation between the output voltage and distance in the Fig9, the distance Z' measured is obtained. The linearized distance characteristics of the sensor system is gotten in Fig13.The experimental result shows the microsensor has good linearity for the measured range of 0 to 1mm.

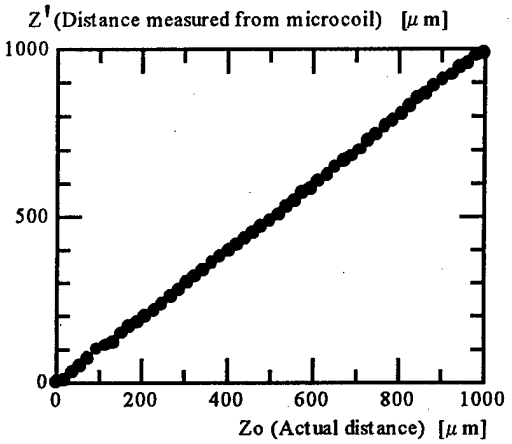


Fig13 Linearized distance characteristic

The experimental result of the closed-loop position feedback control of the microcoil is shown in the Fig14. In this control system, proportional control was used. In the position of 0.5mm, 3 position control curves are obtained at 3 different proportional refrences. The Fig14 shows that the microcoil has good tracking characteristics.

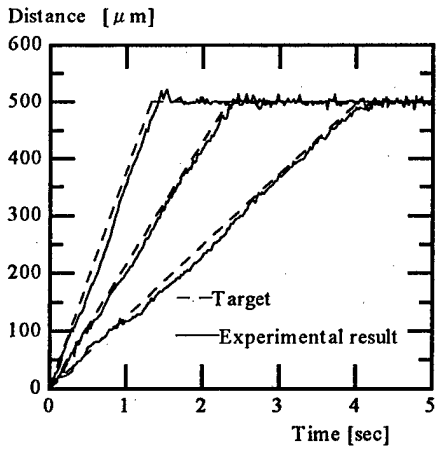


Fig14 Experimental response of the distance of the control system

7 CONCLUSIONS

1) Micro distance sensor using microcoil was developed .
2) A microcoil of thickness of Ni 300 μ m, and outer diameter 3000 μ m was fabricated successfully by using ultrathick high-aaspect-ratio photoresist SU-8 and Ni electroplating method.
3) The linearity and frequency response characteristics of microcoils have been measured by detecting circuit. Experimental results show the microcoil has good linearity at the range of 0 to 1mm,and its frequency response range is from 0Hz to 1000Hz.
4) Closed-loop position control characteristics of the microcoil has been measured. The microcoil as a micro distance sensor has good positional tracking function at 0 to 1mm.

REFENRENCE

[1]K.Murakami, K.Minami and M.Esashi "High Aspect Ratio Fabrication Method Using O2 RIE and Electroplating" Applied Surface Science 79/80(1994),143-152

[2]B.Lochel, A.Madciossel, M.Rothe and W.Windbracke "Microcoils Fabricated by UV Depth Lithography and Galvanoplating" Transducers'95, 264-267

[3]G.Engelmann, O.Ehrmann, J.Simon and H.Reichl "Fabrication of High Depth-to-Width Aspet Ratio Microstructures" MEMS' 92 93-98

[4]M.Despont, H.Lorenz,and P.Vettiger "High-Aspect-Ratio, Ultrathick, Negative-Tone Near-UV Photoresist for MEMS Applications" 1997IEEE 518-522

[5]H.Lorenz, M.Despont "High-aspect- ratio ultrathick, negative-tone near-UV photoresist and its applications for MEMS " Sensors and Actuators Mar,1998,33-39

[6]H.Lorenz, M.Despont, N.Fahrni, N.Labianca and P.Renaud "SU-8: a Low-cost Negative Resist for MEMS" j.Micromech.Microeng.7(1997), 121-124

[7]A.Meckes,J.Behrens and W.Benecke "Electromagnetically Driven Microvalve Fabricated in Silicon" Transducers '97, 821-824

[8]K.Muraki and K.Kuribayashi "New Fabrication Method of Multiple-Layer Microcoil Using Anodic Oxidized Aluminum" PROC. Advanced Mechatronics 1998, 484-488

[9]Y.Hamasaki and T.Ide "Fabrication of Multi-layeer Eddy Current Micro Sensors for Non-destructive Inspection of Small Diameter Pipes" 1995 IEEE 232-237

[10]Y.Hamasaki and T.Ide "a Multi-layer Eddy Current Micro Sensor for Non-destructive Inspection of Small Diameter Pipes" Trnsducers'95, 136-139

[11]M.B.Stern, S.C.Palmateer "Profile control in dry development of high-aspect-ratio resist structures" J.Vac.Sci.Technol. Nov, 1995, 3017-3021

[12]K.Y.Lee, N.Labianca "Mciromachinig application of a high resolution ultrathick photoresest" J.Vac.Sci.Technol. pp3012-3016 Nov, 1995, 3012-3016

Structure of Microrobots Using Electromagnetic Actuators

Akihiro TORII, Tomohiro KOYANAGI, Akiteru UEDA
Dept. of Electrical Eng., Aichi Institute of Technology
1247 Yachigusa, Yakusa, Toyota 470-0392, Japan
Tel: +81 565 48 8121 ext. 2012
Fax: +81 565 48 0010
Email: torii@ee.aitech.ac.jp

Abstract :

We have been developing microrobots which are driven by the clamping of electromagnetic actuators and by the thrusting of piezoelectric transducers. The principle of the microrobots is based on an inchworm motion. The microrobots have three degrees of freedom and realize the linear and the rotational displacements not only on a horizontal plane but also on a slope. Less than 1 μm resolution in the linear displacement and less than 1 μrad resolution in the rotational displacement were obtained on a flat surface. However our microrobot could not climb on a steep slope.

In this paper we discuss the structures of microrobots from the viewpoint of an electromagnetic force. We consider the electromagnetic forces of three microrobots theoretically and experimentally. The electromagnetic force is determined by a magnetic flux which is determined by an electromotive force and reluctance of a magnetic path. Since the microrobots differ in their electromagnetic paths, their reluctances and electromagnetic forces are different from each other. We also discuss the linear and rotational displacements of the microrobots theoretically and experimentally.

1 Introduction

Fast deformation of piezoelectric transducers (PZTs) are used for precision positioning [1, 2]. This microrobot consisting of an electromagnetic wobble motor was proposed[5].

We proposed the microrobots which consisted of electromagnets and stacked-type piezoelectric transducers (PZTs) [3, 4]. Three electromagnets and three PZTs were combined together to produce a Y-shaped and Δ-shape microrobot. The principle of the microrobots was based on an inchworm motion. The microrobots were driven by clamping of the electromagnets and by thrusting of the PZTs. These microrobots could move in X, Y and Θ directions not only on a horizontal plain but also on a slope. A 100 nm resolution of the linear displacement and a 500 nrad resolution of the rotational displacement were obtained. However, the displacement obtained on a wall was different from that on a flat plane.

We also developed the microrobot which had improved electromagnets. A Y-shaped steel frame was used as the core of an electromagnet, which adhered the microrobot to the magnetic floor. A closed-loop magnetic field is the merit of the microrobot. PZTs were used to thrust the Y-shaped steel frame. Though the electromagnetic force generated by the microrobot was improved, the microrobot was difficult to construct.

The novel structure of a microrobot is described in this paper. A steel plate, three electromagnets and three PZTs are used as components of the microrobots whose principle is the same as the previous microrobot. The simple structure is the merit of this microrobot.

In this paper, we describe these microrobots from the viewpoint of the electromagnetic force. First, the structures of the microrobots are described. The electromagnetic circuits are analyzed theoretically and the electromagnetic flux and electromagnetic force of the circuit are discussed. Then, the linear motion and rotational motion of the microrobots are described. Next, the electromagnetic force and the displacements are measured experimentally. Finally, we discuss the relation between the electromagnetic forces and the structure of the microrobots.

1999 INTERNATIONAL SYMPOSIUM ON
MICROMECHATRONICS AND HUMAN SCIENCE
0-7803-5790-6/99/ $10.00 ©1999 IEEE.

2 Microrobots

2.1 1st Microrobot

Figure 1 shows our first developed microrobots. Three

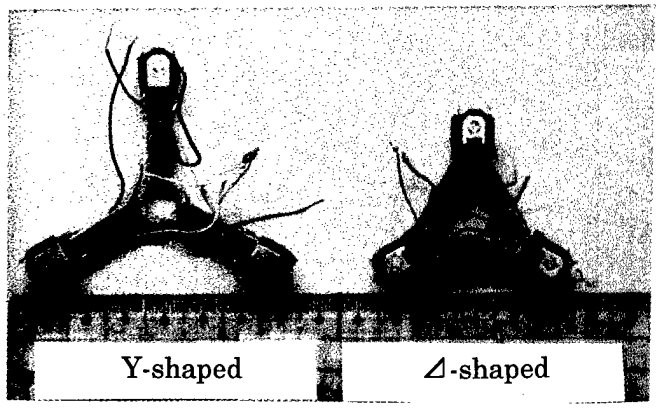


Figure 1: First developed microrobots.

electromagnets and three PZTs are used. The electromagnet, which consists of a magnetic core, a yoke and 3000-turn coil, is about 10 mm × 10 mm × 10 mm. The electromagnets are used to hold the microrobot on a magnetic surface. The stacked-type PZT is about 5 mm × 5 mm × 18 mm and its deformation is about 0.08 μm/V. The PZTs are used to push the electromagnets. We combined these components into the Y shape and Δ-shape as shown in Figure 1 Three PZTs are used as frames of the microrobot and three electromagnets are connected at every vertex. The microrobot can move precisely in X, Y and Θ directions by an inchworm motion. The principle of the displacement is described in the following chapter.

An equivalent electrical circuit of the electromagnet is shown in Figure 2. The Symbols Φ, NI, R, R_g

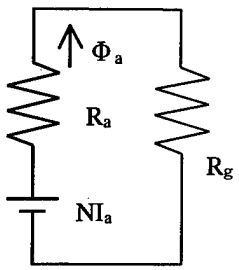


Figure 2: Equivalent circuit.

denote a magnetic flux, an electromotive force, a reluctance of the core and yoke, and a reluctance of an airgap between the yoke and substrate. We obtain the following equation.

$$NI = (R + R_g) \cdot \Phi \tag{1}$$

The magnetic flux Φ is expressed by

$$\Phi = \frac{NI}{R + R_g}. \tag{2}$$

Since the reluctance of air is much larger than that of the magnetic material, the magnetic flux Φ is largely influenced by the reluctance of air. The electromagnetic force F is given by

$$F = \frac{\Phi^2}{2\mu_0 S}, \tag{3}$$

where μ_0 is the permittivity of air and S is the cross section of the flux. Therefore, the small airgap decreases the magnetic flux and the electromagnetic force.

2.2 2nd Microrobot

Figure 3 shows the microrobot whose electromagnetic force is further developed. Magnetic material (steel)

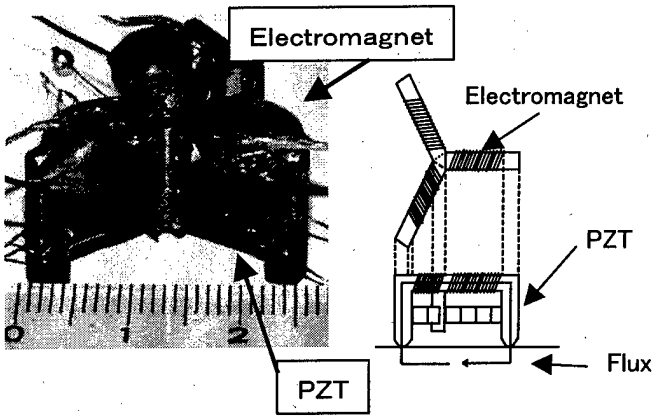


Figure 3: Microrobot with three legs.

is used as the Y-shaped frame of the microrobot. We wind enamel wire to the frame. Each coil is 1000 turns (84 Ω, 34 mH). Stacked-type PZTs are about 2 mm × 3 mm × 9 mm, and their deformation is about 0.08 μm/V. The total weight of the microrobot is about 10 g. Electromagnets are used to hold the microrobot on a magnetic surface. There is a pole at the center of the Y-shaped frame. The three ends of the frame bend in the same direction. The bent ends which contact the substrate are called "legs". The PZTs are placed between the legs and the center pole. The microrobot can

move precisely in X, Y and Θ directions by an inchworm motion. The details of its motion are described in the next chapter.

An equivalent electrical circuit is shown in Figure 4. The circuit shows that there is no airgap nor

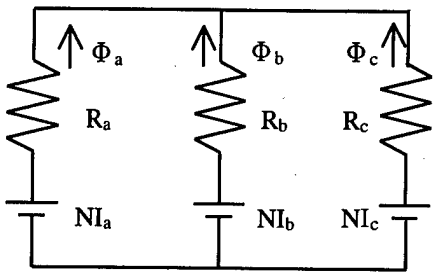


Figure 4: Equivalent circuit.

reluctance of air. The magnetic flux is expressed by

$$\begin{pmatrix} \Phi_a \\ \Phi_b \\ \Phi_c \end{pmatrix} = \frac{1}{R_aR_b + R_bR_c + R_cR_a} * \\ * \begin{pmatrix} R_b + R_c & -R_c & -R_b \\ -R_c & R_c + R_a & -R_a \\ -R_b & -R_a & R_a + R_b \end{pmatrix} \begin{pmatrix} NI_a \\ NI_b \\ NI_c \end{pmatrix} \quad (4)$$

The line of magnetic force passes through the frame and the magnetic floor. The direction of the line of magnetic force is decided by the wind of the coil.

2.3 3rd Microrobot

Figure 5 shows the microrobot we are developing now. The microrobot is the same size as the microrobot

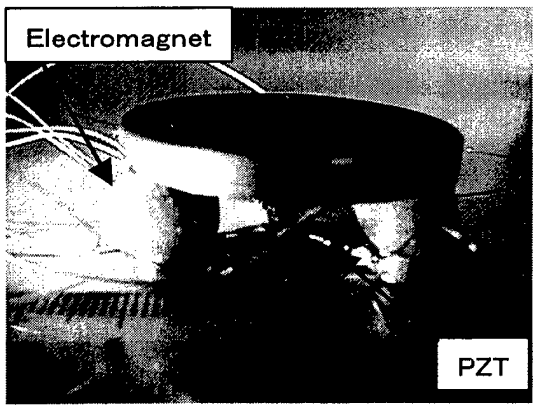


Figure 5: 3rd microrobot.

shown in Figure 3. We used three electromagnets as three "legs". The microrobot shown in Figure 5 and the microrobot shown in Figure 3 have similar electromagnetic circuits. However the fabrication process is different. The microrobot shown in Figure 3 is manufactured by winding a wire to a frame with a complex shape. The microrobot shown in Figure 5 is a combination of a circular plate and an electromagnet with a screw. Therefore, it is easy for us to fabricate the microrobot shown in Figure 5. The reluctance of the electromagnetic circuit without an airgap is so small that the generated electromagnetic force will increase. The circular plate is used to carry a small part on it.

3 Principle of Displacement

In this chapter, the principle of displacement is described. Since the Y-shaped microrobots that we developed are driven by the same principle, we explain the principle of the microrobots by using schematic diagrams of the Y-shaped microrobot as shown in Figure 1.

3.1 Linear Displacement

Figure 6 shows the principle of linear displacement and control waveforms. The black square denotes the elec-

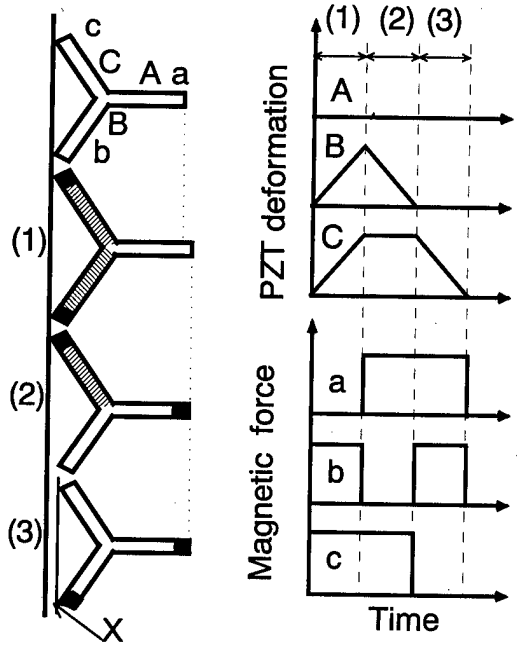


Figure 6: Principle of linear displacement and input waveforms.

tromagnet which adheres to the magnetic substrate, and the white square denotes the electromagnet which does not adhere to the magnetic substrate. The shaded rectangle denotes the PZT which is extended by the applied voltage, and the white rectangle denotes the PZT which is not extended. The principle of the forward motion is as follows: (1) The coils b and c make the electromagnetic legs adhere to the substrate by the applied voltage. The piezoelectric actuators B and C are extended by the applied voltage. At this time a closed-loop magnetic field passes through the coils b and c and the magnetic substrate. (2) The coil a and c make the electromagnetic legs adhere to the substrate by the applied voltage. The PZT B is contracted by stopping voltage. At this time a closed-loop magnetic field passes through the coils a and c and the magnetic substrate. (3) The coil a and b make the electromagnetic legs adhere to the substrate by the applied voltage. The PZT C is contracted by removing voltage. At this time a closed-loop magnetic field passes through the coils a and b and the magnetic substrate. The microrobots moves in the X direction by repeating the intervals (1), (2) and (3).

3.2 Rotational Displacement

Figure 7 shows the principle and the control waveforms of the rotational displacement. The principle of the rotational displacement is as follows: (1) The coils a and b make the electromagnets adhere to the substrate by the applied voltage. The PZT A is extended by the applied voltage. The PZT B is contracted by removing voltage. At this time a line of magnetic force passes through the coils a and b and the substrate. (2) The coils a and c make the electromagnets adhere to the substrate by the applied voltage. The PZT C is extended by the applied voltage. The PZT A is contracted by removing voltage. At this time a line of magnetic force passes through the coils a and c and the substrate. (3) The coils b and c make the electromagnets adhere to the substrate by the applied voltage. The PZT B is extended by the applied voltage. The PZT C is contracted by removing voltage. At this time a line of magnetic force passes through the coils b and c and the substrate. The microrobots rotate to the left by repeating the intervals (1), (2) and (3).

4 Experiments

The microrobot shown in Figure 3 is used in the experiments. Control waveforms are made by a computer and applied to the microrobot through a D/A

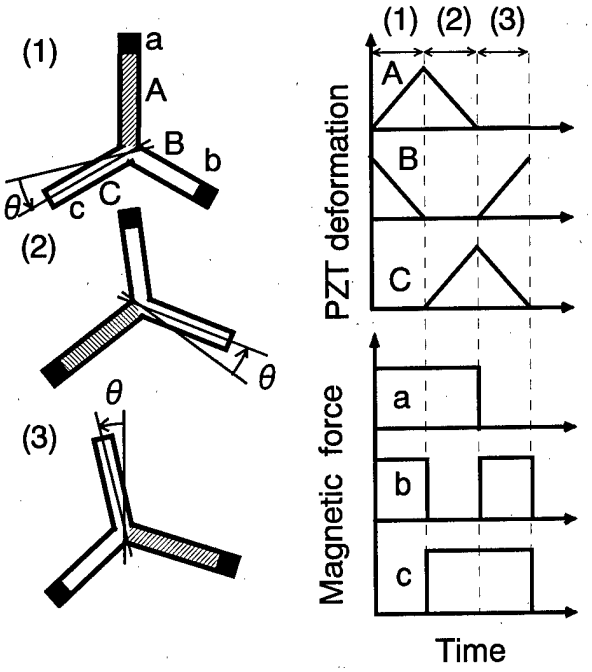


Figure 7: Principle of rotational displacement and input waveforms.

board. Electromagnetic force is measured with a commercially available force gauge. The linear and rotational displacements are measured with an optical displacement sensor (OPTOMETRIC; SUNTECHNO, OM-10, 0.012 μm/mV). The values measured with the OPTOMETRIC are drawn with an A/D board and processed to a computer. The resolution of the measuring instrument is about 30 nm. Experiments are carried out on a slope.

5 Results and Discussion

5.1 Electromagnetic Force

Electromagnetic force is measured by a force gauge. Two coils are excited by an applied voltage and electromagnetic flux passes through two legs and a magnetic substrate. Figure 8 shows the electromagnetic force as a function of the applied voltage to an electromagnet. The two coils of the three coils are excited and the electromagnetic forces of the legs are measured. The legs clamping to the substrate are indicated in the figure.

The electromagnetic force becomes larger as the applied voltage increases the electromotive force. Note that the electromagnetic force of a leg, which connects a non-excited coil, is not zero. The electromagnetic

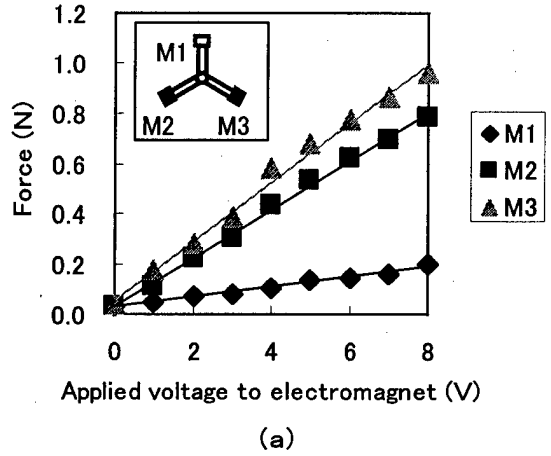


Figure 8: Electromagnetic force.

forces of two legs, which connect two excited coils, are not equal. This is caused by the fact that the reluctances of three legs differ from each other. The electromagnetic force is about 0.9 N when the applied voltage to the electromagnet is 8 V.

5.2 Linear Displacement

Figure 9 shows the relationship between the linear displacement and the slope angle. The microrobot is climbing on a slope. The applied voltage to the electromagnet is 8 V, which indicates the electromagnetic force of 0.9 N. Parameters are the applied voltage to the PZTs. The displacement becomes smaller as the slope becomes steep. This is why the microrobot slips a little on a slope. It is natural that the large applied voltage to the PZTs gives larger displacement.

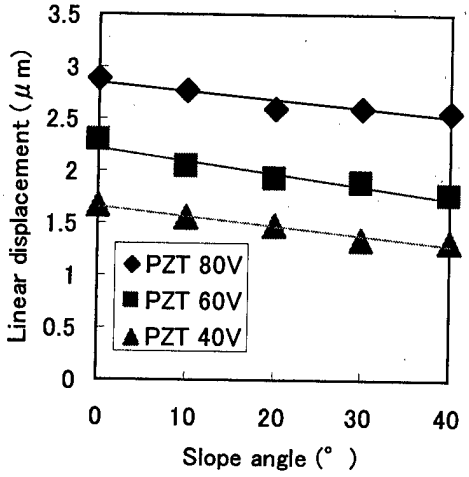


Figure 9: Displacement vs. slope angle.

Figure 10 shows the displacements of the microrobot. The parameters are the applied voltage to the electromagnet which holds the microrobot on a slope. The experiments are carried out on a slope of 30 degrees and the applied voltage to the PZT is 60 V. The horizontal axis denotes the time and the vertical axis denotes the linear displacement. The parameters are the applied voltage to the electromagnet, *i.e.* electromagnetic force. The displacement of the microrobot is an increasing function at 8 V (0.9 N). However, the displacements at 7 V (0.8 N) or 6 V (0.7 N) are not. The decreases are caused by a slip of the microrobot, so the small electromagnetic force makes a large drop. The smallest electromagnetic force which does not make the microrobot slip is about 0.9 N in our experimental conditions. The step displacement is about 1.8 μm when the electromagnetic force is 0.9 N.

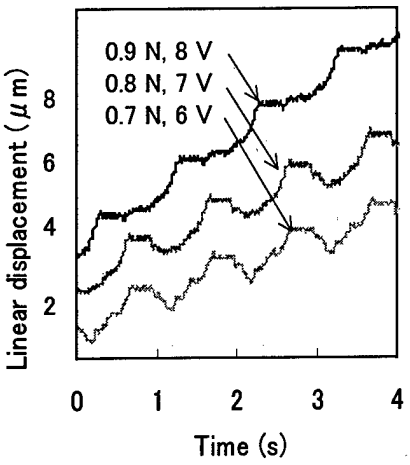


Figure 10: Linear displacement.

5.3 Rotational Displacement

Figure 11 shows the relationship between the rotational displacement and the angle of a slope. The

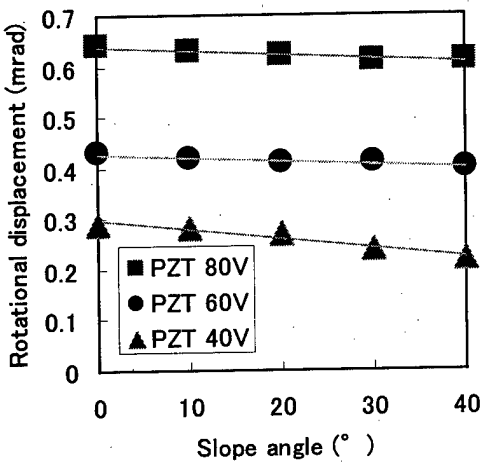


Figure 11: Rotational displacement vs. slope angle.

horizontal axis denotes the angle of a slope, and the vertical axis denotes the rotational displacement. The applied voltage to the electromagnet is 5 V, which indicates the electromagnetic force of 0.4 N. Parameters are the applied voltage to the PZTs. The displacement becomes smaller as the slope becomes steep. This is why the microrobot slips a little on a slope.

Figure 12 shows the results of real-time operation of the microrobot. The parameters are the applied voltage to the electromagnet which holds the microrobot on a slope. The experiments are carried out on the slope of 30 degrees and the applied voltage to the PZT is 60 V. The horizontal axis denotes the time and

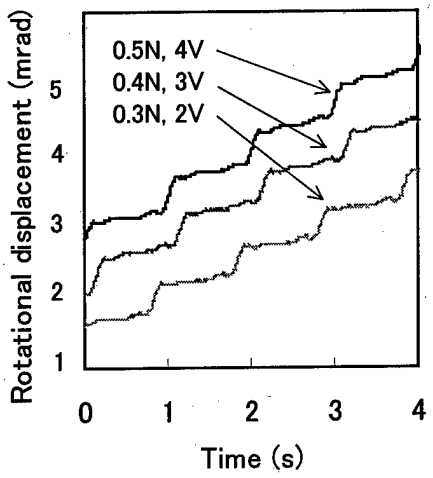


Figure 12: Rotational displacement.

the vertical axis denotes the linear displacement. The parameters are the applied voltage to the electromagnet, *i.e.* electromagnetic force. The results are increasing functions. Since the axial displacement is much larger than the radial displacement, the small drop appeared in the linear displacement measurement is now shown in the rotational displacement. The Y-shaped structure causes the result. The step rotational displacement is about 0.5 mrad in all cases.

6 Summary

In this paper, we described the structure of the microrobot from the viewpoints of the electromagnetic force. We examined the linear and rotational displacement as a function of the applied voltage to the electromagnets and the PZTs. The feasibility of the operation of the microrobot on a wall or a ceiling is indicated. We confirmed the operation of the developed microrobot on a slope from 0 degree to 40 degrees. In one experimental condition, the step linear displacement was 1.8 μm and the step rotational displacement was 0.5 mrad.

Since the electromagnetic field have a close relation to the operation of our developed microrobot, our next project is to design an optimal magnetic field by using a finite element method.

References

[1] T. Higuchi, et al., "Precise Positioner Utilizing Rapid Deformations of a Piezoelectric Element", Journal of the Japan Society for Precision Engineering, Vol.54, No.11, pp.75-80 (1988) (in Japanese)

[2] Yasuhiro Okamoto, et al., "Development of Linear Actuator Using Piezoelectric Element", Trans. of IEICE, Vol.j80-A, No.10, pp.1751-1756 (1997) (in Japanese)

[3] H. Kato, et al., "XYΘ Actuator Using Piezoelectric and Electromagnetic Actuators", Trans. IEE of Japan, Vol.119-C, No.1, pp. 57–62 (1999) (in Japanese)

[4] A. Torii, et al., "A Microrobot Actuated by Piezoelectric and Electromagnetic Actuators", Proc. of the 1st Euspen Conference, pp. 510–513, Bremen, Germany (1999)

[5] Paolo Dario, et al., "A Mobile Microrobot Actuated by a New Electromagnetic Wobble Micrometer", IEEE/ASME Transactions on Mechatronics, Vol.3, No.1, pp.9-16 (1998)

Optical Micro Energy and Information Transmission System

Hidenori ISHIHARA*1 and Toshio FUKUDA*2

*1: Dept. of Intelligent Mechanical Systems Eng., Kagawa University
E-mail: ishihara@eng.kagawa-u.ac.jp
*2: Center for Cooperative Research of Advanced Science and Technology, Nagoya University
E-mail: fukuda@mein.nagoya-u.ac.jp

Abstract: We propose the optical multi-transmission system using pyroelectric and optical piezoelectric element as the transmitter for the transmission system of micromachine system. We apply the PLZT element to the proposed system as a main component, transmitter. The PLZT element generates the electric charge according to the change of temperature and strength of the irradiation of ultraviolet ray. We aim at the energy supply system using the pyroelectric effect, and the information transmission system using the optical piezoelectric effect. We show the numerical model of the transmission system using the PLZT element and the simulation results of the transmitting the photo energy and information source to the electric information. Then, the experimental results explains the performance of the developed transmission system and the ability of proposed system.

1. Introduction

Recently, the various research on the MEMS (Micro Electro Mechanical Systems) and Micromechatronics have been investigated and reported from various fields. The previous studies have reported microactuators and microsensors made by semi conductive machining or precise machining. Some microsensors have been applied to some fields such as car electronics/\ and consumer products. The microactuator have also been developed, and utilized some mechanisms such as electrostatic actuator, electromagnetic actuator, piezoelectric actuator and shaped memory alloy actuator. Especially, the solid actuator using the functional element such as the piezoelectric actuator is expected as a new principle actuator. However, there are no integrated system with the microactuator produced by semi conductive micromachining. Various reasons are proposed in some research, and we have taken account into energy supply problems to micro system.

We have proposed the non contact optical energy supply system using the pyroelectric element and developed the micro mobile robotic system driven this energy supply system. The pyroelectric element generates the electric charge in proportion to the temperature of the element. On the other hand, we have investigated on the optical actuator driven directly by the light beam. When the light is utilized as the driving energy of actuators, the following advantages are considered:

1) the power of energy concentration is large, and its distribution is easy;
2) the efficiency in energy transformation is high;
3) the use of natural energy is easy;
4) no induced noise is generated;
5) electric insulation is unnecessary;
6) non-contact connections are between cable and radio transmissions. The optical actuator have been expected to the various fields such space and under water according to above properties.

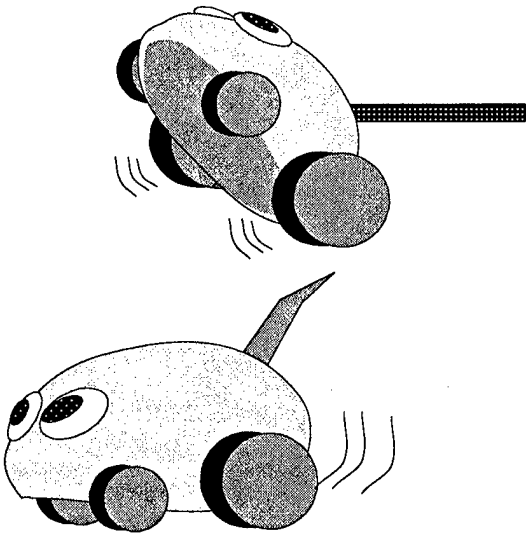


Fig. 1 Influence of Energy Cable on Micro Robot

Optical actuators using optical piezoelectric elements with a photostrictive effect are drawing particular attention, because they can transform light energy directly into mechanical motion called the generation of strain. The photostrictive phenomenon generated in these optical piezoelectric element is considered to be the phenomenon that the voltage generated by the load generated by the

1999 INTERNATIONAL SYMPOSIUM ON
MICROMECHATRONICS AND HUMAN SCIENCE
0-7803-5790-6/99/ $10.00 ©1999 IEEE.

activation of optical piezoelectric elements due to light radiation is transformed into a strain by the piezoelectric effect found in the optical piezoelectric element. However, the strain generated by the light irradiation is so slight and the response is so slow that it is difficult to apply into the integrated micro mechanical system. Therefore, we apply the optical piezoelectric element to the energy transmission system.

As the non-contact energy supply system except the optical supply system, microwave, electromagnetic wave and ultrasonic wave have been proposed as the medium of the supply system. Almost supply system supply only the energy, and controls the object by the switching of medium. However, a kind of system as computer and logic circuits needs continuous energy, and so conventional supply system is not suitable for these system. Therefore, the energy and control signal is supplied independently.

This paper deals with the optical multi-transmission system using the pyroelectric and optical piezoelectric element, PLZT element. We propose the numerically physical model of energy transmission system, and evaluate the model. By the experiment, we estimate the physical properties of the prototype of the transmission system.

2. Optical Energy-Information Transmission System

This paper proposes the Optical Energy-Information Transmission System (OPENITS). The OPENITS consists of only the functional elements with pyroelectric and optical piezoelectric effect, and utilizes the PLZT elements as such functional elements. The PLZT is well-known as the optical piezoelectric element, and is applied to the optical actuator. The PLZT element shows the specific properties that the displacement appears in proportion to the strength of the irradiation of UV ray, but the displacement is very slight and the time response is wrong. Therefore, we have applied the PLZT element into the energy transmission system to convert the optical energy to the electric energy, and developed the optical micro mobile robotic system. In previous studies, we have applied the pyroelectric effect of the PLZT element rather than the optical piezoelectric effect, since the pyroelectric effect generates the larger electric current than the optical piezoelectric effect. In the other studies, the independence between the pyroelectric effect and optical piezoelectric effect have been confirmed. The pyroelectric effect generates the electric charge in proportion to the differential of temperature, and the optical piezoelectric effects is depend on the UV irradiation.

The OPENITS utilizes the independence between such two effects. Figure 1 shows the concept and basic structure of the OPENITS. The main component of the OPENITS is only the PLZT element, and the PLZT element plays the role of extinction and transmission. The mediums to supply the energy and information are Infrared (IR) ray and ultraviolet (UV) ray, and especially for this simulation and experiment wave length of UV ray is 365 nm and IR ray is 950 nm.

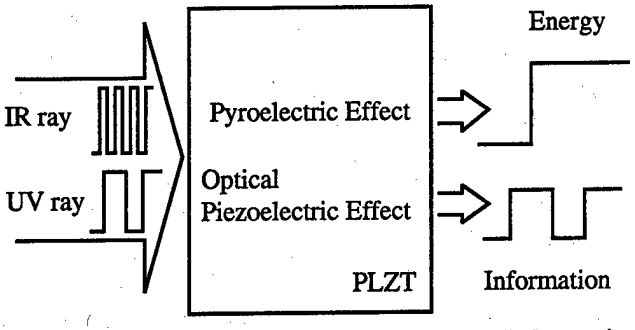


Fig. 2 Architecture of Optical Energy-Information Transmission System

The conventional non-contact energy supply system transmits only the energy, and the control the object by the shattering the medium of supplying the energy. However, to drive the electric circuits, it is need to supply the energy continuously. Therefore, it is required to supply the continuous energy and information independently as proposed method.

The Specifications of functional element, the pyroelectric and optical piezoelectric element, is the key of the properties of the transmission system, since proposed system consists of only the functional element. The OPENITS proposing in this paper utilizes the PLZT element as the key component. The PLZT element is a ceramic polycrystalline material formed by adding La2O2 to a solid solution Pb(Zr,Ti)O3 of PbTiO3 and PbZrO3. It is known that this material shows various crystalline structures and dielectric properties depending on its composition, and displays a variety due to compositional changes, which is peculiar to ceramic polycrystalline materials.

In this experimental systems, PLZT (3/52/48) with 3 weight % of La, is considered to have the highest photostrictive effect, and a mole ratio between PbZrO3 and PbTiO3 of 52/48. The PLZT thus composed is a ferroelectric with a tetragonal system and a structure, which causes residual polarization when polarization processing is carried out by an electric field and has spontaneous polarization.

3. Numerical Transmission Model

Figure 2 shows the numerical model of the OPENITS based on the Hattori's model. The parameters of the model is as follows:

[1] Physical Parameters of PLZT element

S: surface area of PLZT element

L: thickness of PLZT element

$\theta(x, t)$: temperature of PLZT element

k : thermal conductivity

c_p : thermal capacity at constant pressure

density of element

h_1 : heat emission coefficient to air obeying Newton's law of cooling

h_2 : heat emission coefficient to basis.

φ_{th}: coefficient of pyroelectric current conversion

φ_{op}: coefficient of optical piezoelectric current conversion

ξ_{th}: heat absorption coefficient

ξ_{op}: ultraviolet ray absorption coefficient

[2] Parameters of Input energy

$H(\lambda, t)$: thermal energy,

$U(\lambda, t)$: power of ultraviolet ray,

λ: wave length

[3] Electronics

I_{th}: electric current by pyroelectric effect

I_{op}: electric current by optical piezoelectric effect

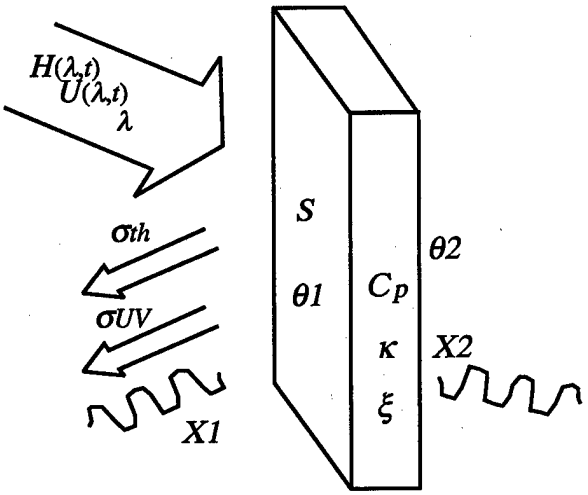


Fig. 3 Physical model of optical Model

The following equation is obtained on the basis of the one-dimensional heat conduction partial differential equation based on the physical model as shown in Fig. 3.

$$\frac{\partial \theta}{\partial t} = \alpha \frac{\partial^2 \theta}{\partial x^2} \qquad (1)$$

where the boundary conditions and initial conditions are as follows:

$$\frac{\partial \theta(0,t)}{\partial t} = \xi_{th} H(t) - \alpha\theta(0,t) - \beta_1 \theta(0,t) \qquad (2),$$

$$\frac{\partial \theta(L,t)}{\partial t} = \alpha\theta(0,t) - \beta_2 \theta(0,t) \qquad (3),$$

$$\theta(x, 0) = T_1 \qquad (4),$$

in Eqs. (1) to (4),. α, β_1 and β_2 is expressed as follows:

$$\alpha = kC_p^{-1}\rho^{-1} \qquad (5),$$

$$\beta_1 = h_1 k^{-1} \qquad (6),$$

$$\beta_2 = h_2 k^{-1} \qquad (7),$$

and α is the thermal diffusion. β_1 and β_2 are heat emission. In this situation, the pyroelectric current, Ith(t), is expressed by the following equation:

$$I_{th} = \frac{\varphi_{th}}{L} \int_0^L \theta(x,t)dx \qquad (8).$$

Then, the photo electromotive current, Iop(t), which is a factor in causing a photostrictive effect, is expressed by the following equation:

$$\frac{\partial I_{op}}{\partial t} = \varphi_{op}\xi_{op}U(\lambda, t) \qquad (9).$$

Based on the above equations, the total voltage generated by these effect is represented by the following equation:

$$V = R\left(I_{th} + I_{op}\right) \qquad (10),$$

where R is electric resistance of PLZT element

Above equations is solved by the following conditions:

(1) thickness of PLZT element is so thin that $\partial\theta / \partial t = a(t)$. (a(t) is constant at time t)

(2) Since on the both side of the PLZT element is air, $\beta_1 = \beta_2$.

4. Numerical Simulation

The numerical simulation uses the following parameters:

$a = 8\text{x}10\text{-}5\text{m}^2\text{s}^{-1}$, $k = 10\ \text{Wm}^{-1}\text{K}^{-1}$,
$h_1 = 15\ \text{Wm}^{-2}\text{K}^{-1}$, $h_2 = 30\ \text{Wm}^{-2}\text{K}^{-1}$,
$L = 0.002$ m, $\text{Ps} = 6\text{x}10^{-9}$

These parameters are selected according to the Hattori's model[9]. Input signal, H() and U(), areFig. 4 shows the simulation results when the infrared ray in 10 Hz and

ultraviolet ray in 2 Hz are supplied. At the results of simulation, the energy of 30 nA and the signal of about 3 nA are confirmed. We have expected to generate the constant value of the energy, but the energy become reducing. At the simulation results when the frequency of UV ray and IR ray is changed, the frequency area of performing as the transmission system is acquired as shown in Table 1, and the typical results is shown in Figs. 5 and 6.

From the simulation results, one of the problems is the dependence of electric current onto the frequency of the input signal. Especially, the effect of transmission of the energy is strongly dependent on the frequency. Therefore, it is need to adjust the parameter as frequency to the properties of PLZT element.

Table 1 Frequency Area of Performing as the Transmission System

	UV ray(100mW/cm2)	IR ray (50mW/cm2)
Upper Frequency	7 Hz 1.8 nA	12 Hz 89 nA
Lower Frequency	———	4 Hz 107 nA

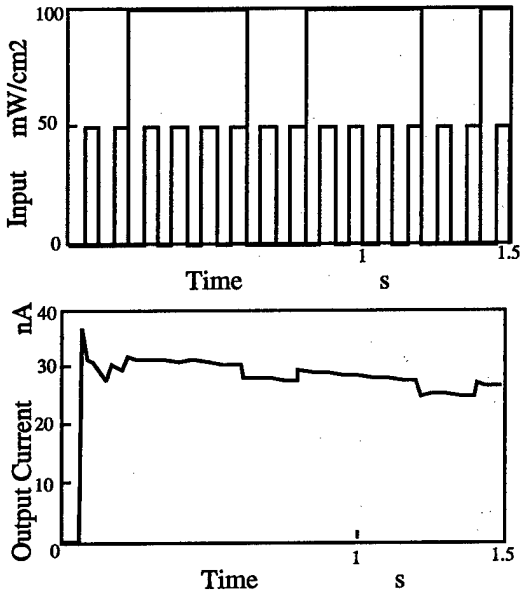


Fig. 4 Simulation Result: Input : Infrared Ray - 50mW/cm2 in peak, 10Hz, Ultraviolet Ray - 100mW/cm2 in peak, 2Hz

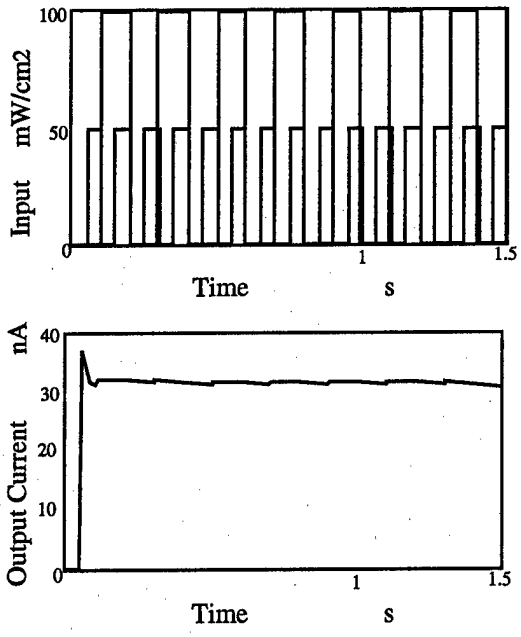


Fig. 5 Simulation Result: Input : Infrared Ray - 50mW/cm2 in peak, 10Hz, Ultraviolet Ray - 100mW/cm2 in peak, 5Hz

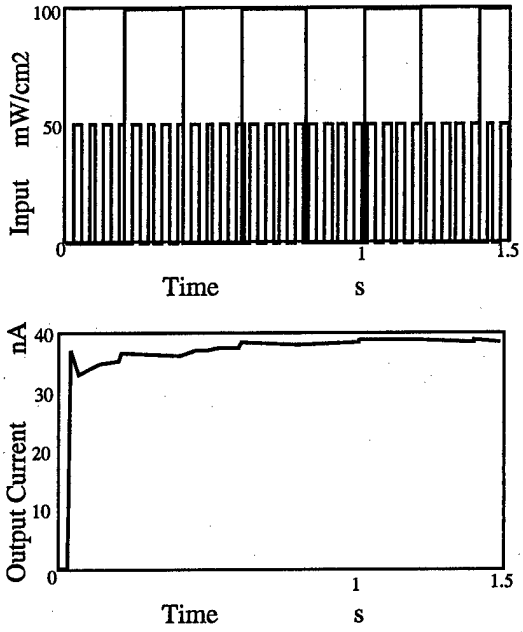


Fig. 6 Simulation Result: Input : Infrared Ray - 50mW/cm2 in peak, 20Hz, Ultraviolet Ray - 100mW/cm2 in peak, 2Hz

5. Experiments

The experiments aims at the realization of the OPENITS and the confirmation of the theoretical design of the OPENITS. The experimental system requires the two light source of IR and UV ray and the control system of the

optical lights. The experimental optical system consists of the UV and IR light sources and the filters and light guides with mirrors and prisms. Figure 7 shows the outline of experimental system. The source of UV ray irradiate the UV ray in 365 nm wave length in peak of 320 mW/cm2 in maximum, and after being narrow banded by a 320-420 nm band pass filter, the beam was radiated uniformly over the entire surface of the PLZT element. The intensity of the UV light beam is controlled to 135 mW/cm2 in maximum. Figures 8 and 9 show the experimental results. As the results shown in Figs. 8 and 9, the voltage of output is so unstable that it fell short to our expectation. Table 10 shows the experimental results of the properties of transmission through the PLZT on frequency. These resutls appears some problems of response to convert the energy.

The experimental system reconfigurates the signal from the voltage outputted through the PLZT element. Figure 10 shows one of the reconstructed signal in the case of experiment of Fig. 8. In this experiment, the signal processing is out of the realtime process. Unfortunately, it is difficult to distinguish the information signal from the output voltage since difference of the output voltage of information signal is little. Therefore, it is need to increase the output voltage of the information signal according to the optical piezoelectric effect.

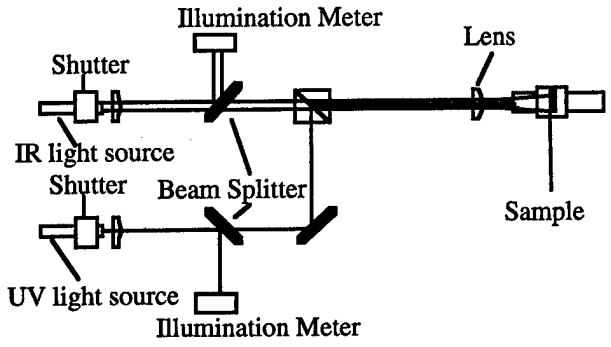


Fig. 7 Experimental Optical System

Table 2 Experimental Results of Frequency Response

	highest	lowest
IR ray	8.5 Hz in 124 mW/cm2	4.5 Hz in 124 mW/cm2
UV ray	1.8 Hz in 62 mW/cm2	-

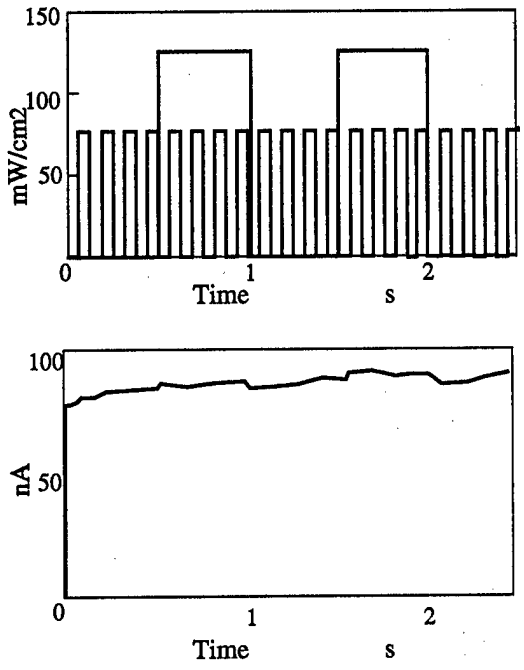


Fig. 8 Experimental Results: Input; Infrared ray - 62 mW/cm2 in peak, 8 Hz, Ultraviolet ray - 124 mW/cm2 in peak, 0.5 Hz

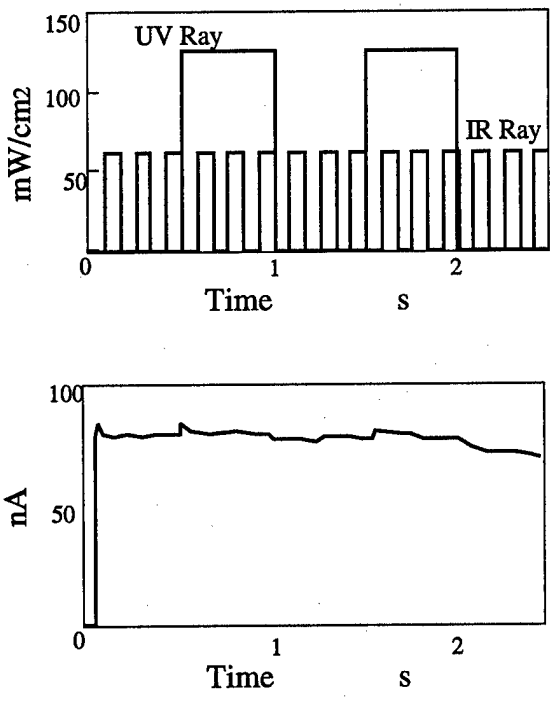


Fig. 9 Experimental Results: Input; Infrared ray - 62 mW/cm2 in peak, 6 Hz, Ultraviolet ray - 124 mW/cm2 in peak, 0.2 Hz

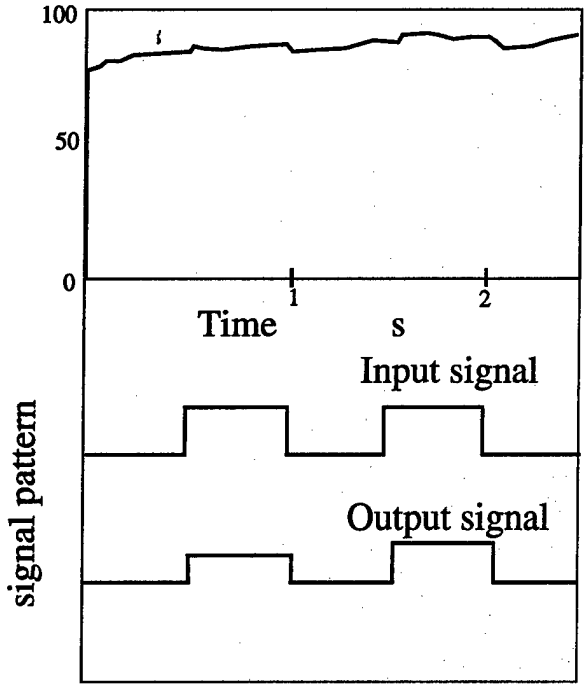


Fig. 10 Reconstructed signal from the output through the PLZT element of OPENITS

6. Discussions and Conclusions

This paper proposes the Optical Energy-Information Transmission System (OPENITS) using the Pyroelectric and optical -piezoelectric element as the transmitter. This system is constructed by so simple structure that it is possible to miniaturize it, since the OPENITS consists of only the PLZT element. Besides, this system has several problems to introduce to the micro robotic system as follows:

(1) constant supply of generating the electric voltage,
(2) response against illumination of UV and IR ray,
(3) thermal isolation,

These problems are depend on the properties of the element, and so it is required to improve its characteristics. However, it is difficult to arrange the properties of the element. Miniaturization is an usual method of improving the performance of the system. Reduction of volume of the PLZT element decrease the thermal capacity of the element, and uplift the response of the pyroelectric effect and photostrictive effect. Besides, the PLZT element, which volume is less than a threshold, declines its properties.

This experiment measures only the electric current, but we must design the electric circuits to apply the OPENITS into the robotic system. The electric current is too slight to be consumed in the circuits. To prevent the consumption of the electric current, monoblock machining is effective for the producing the electric circuits, and the semi conductive micromachining is important technology.

This paper shows the proposal of the optical energy-information transmission system using the functional element with pyroelectric and photostrictive effect. Through the numerical simulation and experiment, independent supply of energy and information is confirmed. However, electric current measured at the experiment is less than the results of simulation, and response is wrong. Next target of this project is the improvement of such properties and development of integrated micro robotic system using the OPENITS.

References

[1] S. Egawa and T. Higuchi: Multi-Layered Electrostatic Film Actuator, Proc. IEEE Micro Electro Mechanical Systems, pp.17-24, 1989

[2] H. Fujita et al.: An Integrated Micro Servo system, IEEE Int. Workshop on intelligent Robot and Systems pp.15-20, 1988

[3] T. Fukuda et al.: Design and Dexterous control of micro manipulator with 6 D.O.F., in Prof. IEEE Advanced Robotics, pp.343-348, 1991

[4] S. Konishi, et al.: System Design for Cooperative Control of Arrayed Microactuators, Proc. IEEE Workshop on Micro Electro Mechanical Systems (MEMS'95), pp. 322-327, 1995

[5] H. Ishihara, F. Arai and T. Fukuda: Micro Mechatronics and Micro Actuator, IEEE/ASME Transaction on Mechatronics, Vol.1, No.1, pp.69-79, 1996

[6] M. Irie: Photoresponsive Polymers. Reversible Bending of Rod-Shaped Acrylamid Gels in an Electric Field, Macromolecules, Vol. 19-11, pp. 2890-2892, 1986

[7] P.S. Brody: High Voltage Photovoltaid Effect in Barium Titanate and Lead Tinanate-Lead Zirconate Ceramics, J. of Solid State Chemistry-12, pp.193-200, 1975

[8] K. Uchino and M. Aizawa: Photostrictive actuator using PLZT ceramics, Jap. J. Apply. Phys. 24, suupl. 42-3, pp.139-142, 1985

[9] S. Hattori, T. Fukuda and S. Nagamori: A Study on Optical Piezo-Electric Actuator (Response Experiments by U.V. Beam and Photo Response Model), J. of Robotics and Mechatronics, Vol.4, No. 4, pp.321-329

[10] M. Inoue, T. Sada and K. Uchino: Photo driven relay using PLZT ceramics, ISAF'86 Proc. of the Sicth IEEE Internat. Symp. Appl. Ferroelectrics, pp.16-19, 1986

[11] H. Ishihara et al.: Micro Optical Robotic System (MORS), Proc. Fourth Int. Symp. Micro Machine and Human Science (MHS'93), pp.105-110, 1993

Improvement of Sensing and Actuating Property of Parallel Beam Gyroscope

Hiroshi SATO[*1], *Toshio FUKUDA*[*2], *Fumihito ARAI*[*1],
Kouichi ITOIGAWA[*3] *and Yasuhisa TSUKAHARA*[*3]
[*1] Department of Micro System Engineering, Nagoya University
[*2]Center for Cooperative Research in Advanced Science and Technology, Nagoya University
Furo-cho, Chikusa-ku, Nagoya 464-01, JAPAN
[*3]Tokai Rika Co.,LTD. Oguchi-cho, Niwa-gun, Aichi-Ken 480-01, JAPAN

Abstract

Parallel beam structure has many significant features as follows: (i)The tip moves in parallel at the end. (ii)This structure converts the small displacement into the large strain. (iii)Strain is concentrated on the boundary point between the parallel-beam part and the supporting part. (iv)Being Piled up this structures, each unit doesn't interfere to the other units. (v)The lateral rigidity is high. We propose this structure for piezoelectric vibrating gyroscope(angular rate sensor), and detected angular rate using this gyroscope.

In this paper, it is shown the method for super sensitizing by bringing two resonance frequencies(drive resonance frequency and sensing resonance frequency) close. Then we propose the suppression method of the mechanical coupling that arises by bringing two resonance frequencies close. From this result, this structure suits for the gyroscope.

1 Introduction

In recent years, it is expected to develop a small, highly accurate, and low cost gyroscope (angular rate sensor), which is used for industrial applications, such as the car attitude control and the portable VTR vibration control system. The piezoelectric vibrating gyroscope can be made in low cost.[1] [2] [3] This gyroscope detects a Coriolis force by direct piezoelectric effect based on the deformation of the sensing piezoelectric material. However Coriolis force is not so strong, it is difficult to make highly accurate gyroscope.

Our approach concentrates on the strain cause by the Coriolis force using the parallel beam structural features. This structure has many significant features as follows. The tip moves in parallel at the end. This structure converts the small displacement into the large strain. Strain is concentrated on the boundary point between the parallel-beam part and the supporting part. Being Piled up this structures, each unit doesn't interfere to the other units. The lateral rigidity is high. So, using this features, it is possible to make the highly accurate gyroscope. We have reported a new piezoelectric vibrating gyroscope using parallel beam structure, and detected a Coriolis force.[4] , [5]

And the vibrating gyroscope can be made supersensitized by bringing the resonance frequency of the drive unit and sensor unit close. [2] But if the resonance frequency of sensor unit and drive unit close, leakage vibration is occured by the mechanical coupling. The sensitivity of the gyroscope has deteriorated by this leakage vibration. Therefore, the sensitivity depends the trade-off of two parameters, resonance frequency and mechanical coupling.

In this paper, we solved those problem by new methods, control of resonance frequency by structural feature, and suppress mechanical coupling by piezoelectric effect. From this result, this structure suits for the gyroscope.

2 Parallel Beam Structure

Figure 1 shows the parallel beam structure. Square hole is made through the rectangular solid. Then the thin parallel beam structure is constructed. Section modulus of parallel beam is decreased by the square hole. Hatamura et al. analyzed this structure.[6] Until now, this structure has been used for pin-type load cell

1999 INTERNATIONAL SYMPOSIUM ON
MICROMECHATRONICS AND HUMAN SCIENCE
0-7803-5790-6/99/ $10.00 ©1999 IEEE.

and 6-axis force sensor.[7] [8]

The parallel beam structure is characterized by the peculiar deformation, when the force is applied at the free end of the structure from X-direction and Y-direction. When we applied a force at the free end in drive direction(X-direction), then the parallel beam structure deformed, as shown in Figure 2-(a). This figure shows FEM analysis by ANSYS software. The gray zone means small stress. And as it changes to white, tensile stress increases. As it changes to black, compressive stress increases. Strain of the parallel beam is concentrated on the boundary four point between parallel beam part and supporting part. Next, we applied a force at the free end in perpendicular direction (Y-direction), then the parallel beam structure deformed, as shown in Figure 2-(b). This structure deformed like the cantilever beam. In this case, strain does not concentrated in the parallel beam. This structure is difficult to be deformed to this direction.

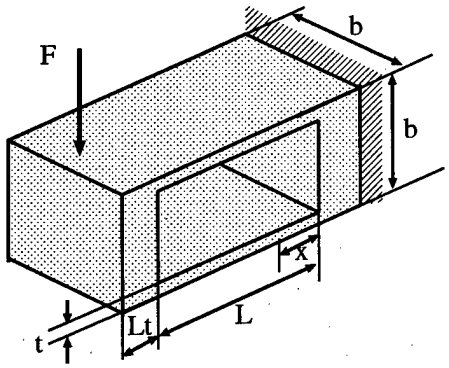


Figure 1: Parallel Beam Structure

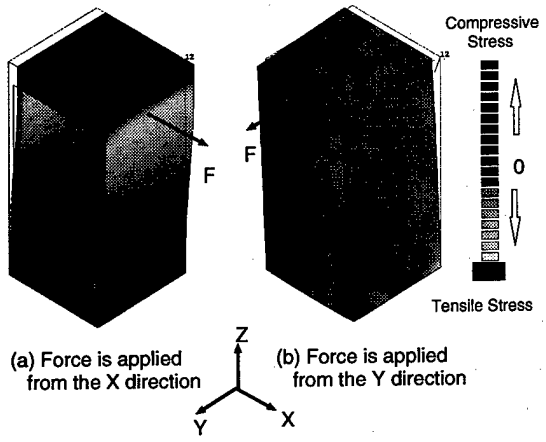


Figure 2: Deformation of Parallel Beam Structure

Parallel beam structure has those following advantage.

- The tip moves in parallel at the end.
- This structure converts the small displacement into the large strain.
- Strain is concentrated on the boundary point between the parallel-beam part and the supporting part.
- The lateral rigidity is high.

3 Parallel Beam Gyroscope

We made the vibration gyroscope that piled up two parallel beam structures as shown in Figure 3. We used the metal(SUS304) in this structure. The length of this structure is 5mm, width is 5mm, and height is 24mm. At first, we opened the hole(upper hole:width 4.5mm height 8mm, lower hole:width 4.5mm height 10mm) from X-direction and Y-direction by the cutting work. Thickness of the parallel beam part is 250μm.

pAfter, we put piezoelectric plate(PZT plate:width 5mm, height 12mm, thickness 150μm) on the both side. The lower unit works as an actuator(drive unit) to generate the reference vibration. And the upper unit works as a sensor(sensor unit) to detect a Coriolis Force.

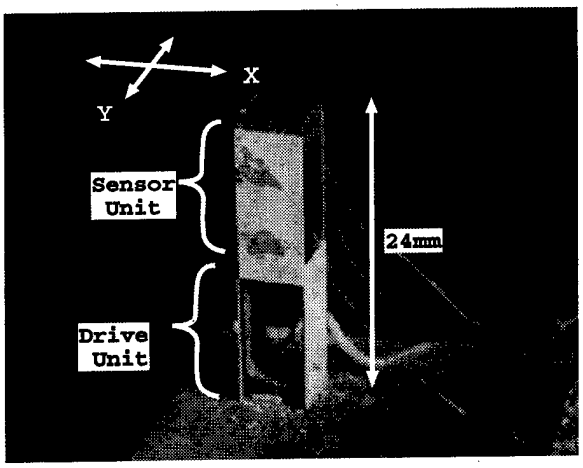


Figure 3: Parallel Beam Gyroscope

3.1 Principle of Parallel Beam Gyroscope

Figures 4 show principle of parallel beam gyroscope. Piezoelectric material can be used for the sensor and actuator by the direct piezoelectric effect and the converse piezoelectric effect. By the direct piezoelectric effect, electric polarization is produced by mechanical stress. Closely related to it is the converse piezoelectric effect, whereby a crystal becomes strained when an electric field is applied.[9] Using piezoelectric material, it is possible to converts mechanical energy and electrical energy.

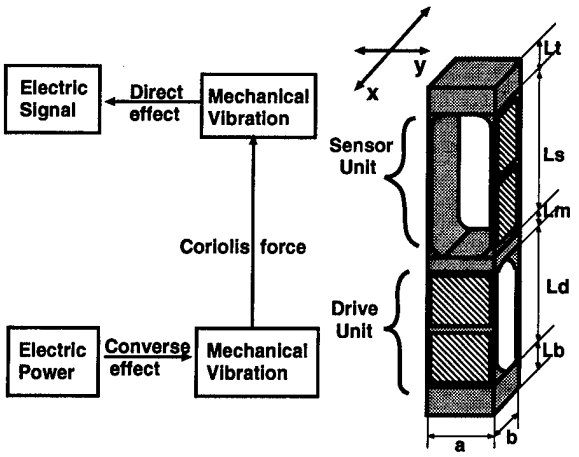


Figure 4: Principle of Parallel Beam Gyroscope

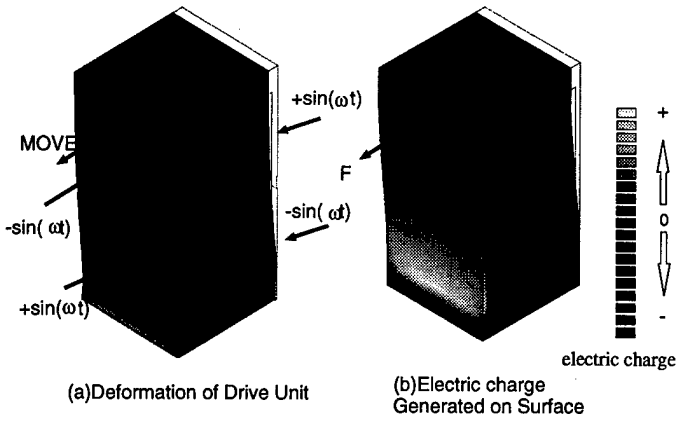


Figure 5: Deformation of Parallel Beam Gyroscope

At first, we applied AC voltage to drive unit. Then PZT plate are deformed by the converse piezoelectric effect, as shown in Figure 5-(a). Those figure show the deformation when we applied voltage to parallel beam structure with PZT plate by ANSYS software. And drive unit vibrate to X-direction. When this structure is rotated, Coriolis force occurs to perpendicular direction(Y-direction). Then PZT plate generate the electric charge by direct piezoelectric effect, as shown in Figure 5-(b) We detect angular velocity calculate electric charge.

3.2 Advantage of Parallel Beam Gyroscope

We proposed the new gyroscope which piled up two parallel beam structures. By using such structure, it is possible to make the vibration gyroscope advantage of the parallel beam structure. When a force applied to piled up structure, each unit deformed only drive direction as shown in Figure 6. This Figure shows deformation of piled up structure when the force applied X and Y direction.

Using this structure for gyroscope, lower unit(drive unit) generate the reference vibration only X direction, upper unit(sensor unit) deform only Coriolis force which perpendicularly arises with the reference direction. And this structure converts the force into the concentrated strain.

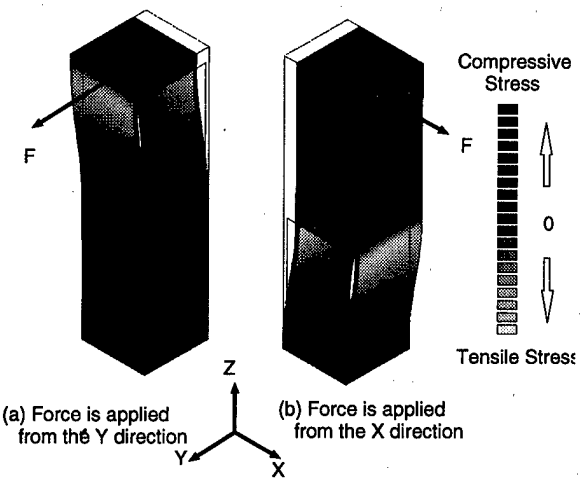


Figure 6: Deformation of Piled up Structure

So, it is possible to make vibration gyroscope with the advantage like the following.

- Sensor unit doesn't interfere to the drive unit's reference vibration.
- This structure converts the Coriolis force into the concentrated strain.

4 Improvement of the Sensitivity

The vibrating gyroscope can be made super-sensitized by bringing the resonance frequency of the drive unit and sensor unit close.[1] Therefore, it becomes important to simply bring the resonance frequency of drive unit and detecting unit close.

However, the phenomenon of the mechanical coupling (reference vibration leaks out in the sensing direction) occurs when the resonance frequency of sensor unit and drive unit close. This leakage vibration generate a offset output. The sensitivity of the gyroscope has deteriorated by this offset. Therefore, the sensitivity depends the trade-off of two parameters, resonance frequency and mechanical coupling.

In the parallel beam gyroscope, those problem has been solved by two way, control of resonance frequency and suppress mechanical coupling.

4.1 Control of Resonance Frequency

In the parallel beam gyroscope, it is easy to adjust the resonance frequency of each unit.

First, In the parallel beam structure, the resonance frequency(F_n) is given as follows, as shown in Fig.1 [6]

$$\mathrm{F_n} = \frac{1}{2\pi}\sqrt{\frac{\mathrm{K}}{\mathrm{m}}} = \frac{1}{2\pi}\sqrt{\frac{2\mathrm{Ebt^3}}{\mathrm{mL^3}}} \qquad (1)$$

Where m is the mass of the top. E is Young's modulus, L, t and b are the length, the thickness and the width of the parallel beam. Rigidity K of this structure is the ratio between load and maximum deflection.

It is possible to consider the parallel beam gyroscope similarly, as shown in Figure 4. The resonance frequency of the sensor unit and drive unit are shown as follows by equation (1).[10]

$$\mathrm{F_{sensor}} = \frac{1}{2\pi}\sqrt{\frac{2\mathrm{Ebt^3}}{\mathrm{m_t L_s^3}}} \qquad (2)$$

$$\mathrm{F_{drive}} = \frac{1}{2\pi}\sqrt{\frac{2\mathrm{Eat^3}}{\mathrm{m_d L_d^3}}} \qquad (3)$$

Where $\mathrm{L_s}$, t and b are the length, the thickness and the width of the parallel beam of the sensor unit. $\mathrm{L_d}$, t and a are the length, the thickness and the width of the parallel beam of the drive unit. $\mathrm{m_t}$ is the mass at the top. $\mathrm{m_d}$ is the mass of the sensor unit.

Table 1: Parameter value of Parallel Beam Gyroscope

Parameter		value
width	a,b	5.0 mm
length of the tip	L_t	1.0-3.0 mm
length of the parallel beam (sensor unit)	L_s	10 mm
length of the connection	L_m	1 mm
length of the parallel beam (drive unit)	L_d	8.0 mm
length of the base	L_b	1 mm
thickness of the parallel beam (drive unit and sensor unit)	t	250 μm
density	ρ	$4540 kg/m^3$
Young's modulus	E	$1157 \times 10^8 N/m^2$

Equations (2) and (3) may become equal in order to super-sensitive. Figure 7 shows relationship between resonance frequency of each units and the length of tip($\mathrm{L_t}$), using equation (2), (3), and modal analysis of FEM by ANSYS software. It is proven that the resonance frequency of sensor unit rises from resonance frequency of drive unit, when the length of tip($\mathrm{L_t}$) is lengthened. In two analysis, there is a difference for the value of the resonance frequency. This difference is due to be calculated without considering the mass in the parallel beam in the equation (2), (3).

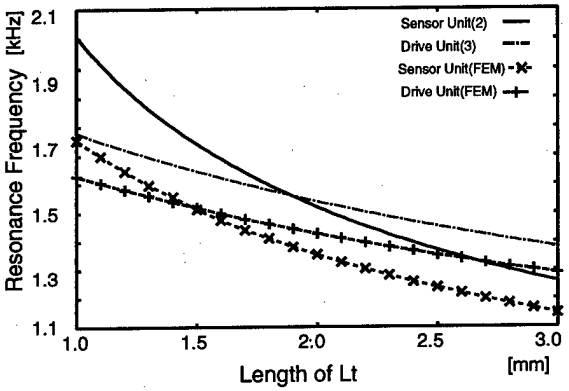


Figure 7: Fluctuation of Resonance Frequency

From the result, it is shown that the resonance frequency of drive unit and sensor unit can be adjusted

by changing the mass at the tip.

In this prototype, resonance frequency of drive unit and sensor unit were $2.18KHz$ and $2.28KHz$ each. After we put the mass at the tip. Both resonance frequency changed to $2.10KHz$ and $2.06KHz$ each.

4.2 Suppress of Mechanical Coupling

In the parallel beam gyroscope, sensor unit doesn't interfere to the drive unit's reference vibration. However, the phenomenon of the mechanical coupling occurs when the resonance frequency of the sensor unit and the drive unit close by the error of the symmetry of the structure.

Figure 8 show the locus of the tip when the prototype vibrate near the resonance frequency. We applied AC Voltage($7V_{pp}$ $2.08KHz$) to drive unit. And we detected X, Y directional vibration of the tip using the laser doppler vibration meter. Figure 8-(a) shows about $10\%(1.5\mu m_{pp})$ of drive vibration leaked out in the sensing direction by the mechanical coupling. And this leakage vibration generated offset voltage about $1.77V_{pp}$.

After, we suppressed the leakage vibration by the mechanical coupling using actuator for sensor unit. We applied $0.4V_{pp}$ voltage which is suppressed the leakage vibration to lower two electrode of sensor unit, as shown in Fig.9. By this suppression, drive vibration leakage decrease less than 5 % ($0.6\mu m_{pp}$), as shown in Figure 8-(b). And offset voltage also decrease about $0.56V_{pp}$.

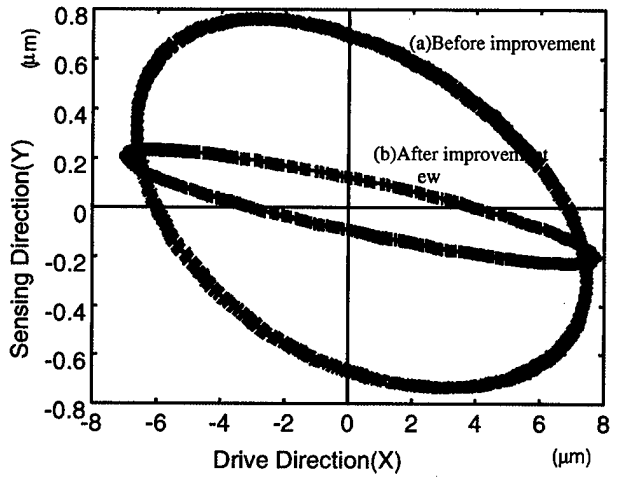


Figure 8: Trajectory of the Top

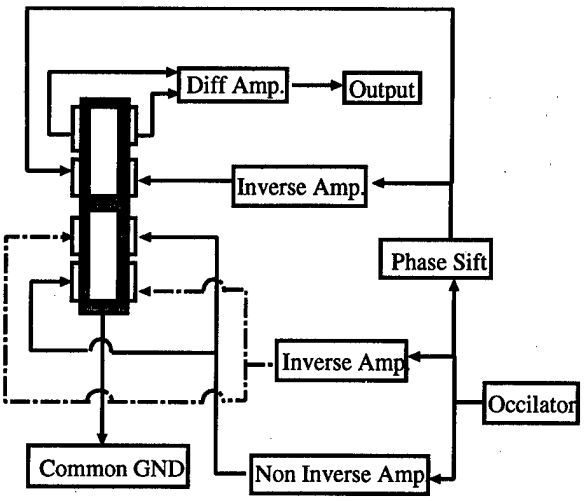


Figure 9: Control Circuit of Parallel Beam Gyroscope

4.3 Result

Figure 10 shows relationship between output voltage and rotation speed.

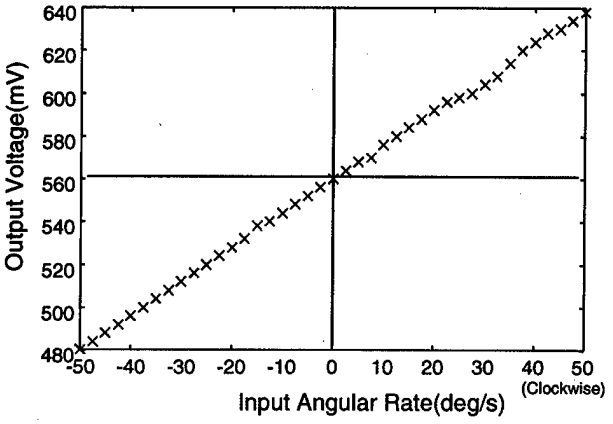


Figure 10: Relationship between Output and Rotation

We applied $7V_{pp}$ voltage for drive unit to generate reference vibration, and $0.4V_{pp}$ voltage for sensor unit to suppress leakage vibration. Frequency is about 2.08kHz. Angular velocity calculates form the difference of two upper electrodes.

This graph shows, $0.56V_{pp}$ offset voltage occurs by leakage vibration, and output voltage is proportional to rotation speed. The sensitivity of this sensor is $1.7mV/deg./sec.$

5 Summary

In this paper, we propose new vibration gyroscope using parallel beam structure. and shows two improve method, control resonance frequency and suppress the mechanical coupling. From this result, this structure suits for the gyroscope. And we made this gyroscope put a PZT plate on the side of the parallel beam structure. This gyroscope detected a angular rate, and proportional to the rotational speed.

The advantage of parallel beam gyroscope rather than other vibration gyroscope(Quadratic type, Tuning Fork type, Triangular type) are follows.

- The sensor unit does not interfere to the reference vibration of the drive unit.
- This structure can converts the small Coriolis force into large strain.
- Resonance frequency of the drive unit and sensor unit can be easily adjusted by changing the mass of the tip.
- Mechanical coupling can be suppessed by applied voltage to sensor unit.

Using the parallel beam structure, it is possible to make a highly accurate gyroscope.

References

[1] W.D.Gates, "Vibrating angular rate sensor may threaten the gyroscope" Electronics, 41 (10) (1968) 130-134

[2] Jan Söderkvist"Micromachind gyroscopes" Sensors and Actuators A,43(1994)65-71

[3] S. Fujishima, T. Nakamura and K. Fujimoto, "Piezoelectric vibratory gyroscope using flexural vibration of a triangular bar" Proc. 45th Symp. Frequency Control, Los Angeles, CA, USA, 1991,pp.261-264

[4] H. Sato, F. Arai,H. Ishihara, T. Fukuda, H. Iwata, K. Itoigawa "New PZT Actuator Using Piezoelectric Thin Film on Parallel Plate Structure" MHS'97 Proseedings. A2,79-84(1997)

[5] T. Fukuda, H. Sato, F. Arai, H. Iwata, K. Itoigawa "Parallel Beam Micro sensor/Actuator Unit Using PZT Thin Films and Its Application Example" Proc.of Int. Conf. Robotics and Automation,1498-1503(1998)

[6] Y. Tani,Y. Hatamura, T. Nagao and N.Takenaka "A Study on the Dynamometer Using the Structure of Parallel Beams for Grinding(1st Report)" Journal of the Japan Society of Precision Engineering、48,6(1982)、(in Japanese)

[7] Y Hatamura, K Iino, K Ono and R Takada "A Trial on a 6-axis Force Sensor for Robots" Transactions of the Japan Society of Mechanical Engineers. C54.497(1993)、(in Japanese)

[8] Yotaro Hatamura and Ryouji Takada "Development of a Pin-Type Loadcell" Transactions of the Japan Society of Mechanical Engineers. C54.497(1993)、(in Japanese)

[9] Kenji Uchino "Piezoelectric acutators and ultrasonic motors" Kluwer Academic Publishers(1997)

[10] T. Fukuda, H. Sato, F. Arai, H. Iwata, K. Itoigawa "Analysis of Parallel Beam Gyroscope"Proc.of Int. Conf. Robotics and Automation,1632-1637(1999)

Technical Session D-2

Mesurement and System Control

Fire Flame Detection Algorithm Using a Color Camera

Hideaki Yamagishi *Jun'ichi Yamaguchi*
Engineering Institute, Sogo Keibi Hosho Co., Ltd.
Koutou-ku, TOKYO 135-0014
JAPAN

Abstract:

In fire detection using image processing, it is required that a system has enough robustness and elimination of an influence of a disturbance. The authors have developed a method which fire flame can be detected by calculating a space-time fluctuation data on a contour of the flame area extracted by a color information. In this paper, the fire flame detection algorithm using a color CCD camera is explained and the results of the experiment, which is performed to verify the effectiveness of our method, are demonstrated.

1. INTRODUCTION

Recently, using image processing, a fire detection method for automatic extinguishing or automatic fire alarm is investigated [1], [2]. The proposed conventional ways are useful in case of a stabilizing background or a restricted condition. However, as affairs stand, it is difficult that these ways are used in an ordinary scene, because they don't have enough robustness and elimination of an influence of a disturbance. Especially, in outdoors, it is required that the system is not sensitive to an artificial light (flashlight, head light, rotating light, ...), the change of the sunlight and so on. On the other hand, there is a problem that a detecting accuracy is low in case of the flame change (size and shape) caused by the wind and the distance between the system and the fire. Thus, there are some problems for fire detection in the ordinary scene. Therefore, it is necessary to develop a fire detection method which can be widely used by solving these problems.

The authors have developed a fire flame detection method which eliminates the influence of the artificial light, the wind and the distance, by calculating a space-time fluctuation data on a contour of the flame area extracted by color information.

In our method, the contour of the flame area, which is normalized in size, is extracted. The extracted contour data is calculated by a polar coordinate transformation. The results of the polar coordinate transformation of every input image are placed in time series [3]. Then we get a fluctuation data, as a space-time data on the contour. Further, a pattern of the frequency component distribution is obtained by Fourier transform of the fluctuation data. Entering the pattern into a neural network, the fire flame is detected [4].

In this paper, the fire flame detection algorithm using a color CCD camera is explained and the experimental results are demonstrated.

2. FIRE FLAME DETECTION ALGORITHM

2.1 Extraction of the flame area

In our method, a RGB data obtained from a color camera is transformed into HSV color specification data. Then, if a pixel's color is transformed into the flame color region in the HSV space (Fig.1), the pixel is regarded as a flame color area in the input image. The color information is used for quick attention to the flame area. The values of H, S and V for the flame color region in the HSV space are decided by an experiment. Next, in the extracted flame color area, some groups are detected by segmentation and labeling. The group detection is needed to determine the processing order of priority in case of following scenes: both the fire flame and the

1999 INTERNATIONAL SYMPOSIUM ON
MICROMECHATRONICS AND HUMAN SCIENCE
0-7803-5790-6/99/ $10.00 ©1999 IEEE.

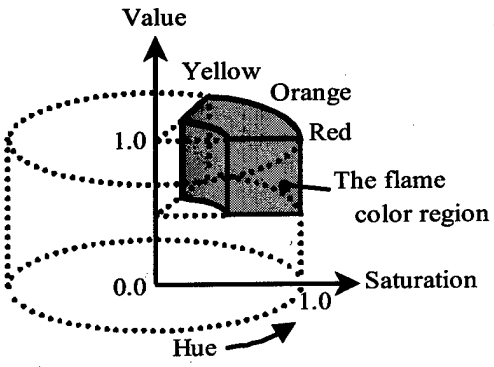
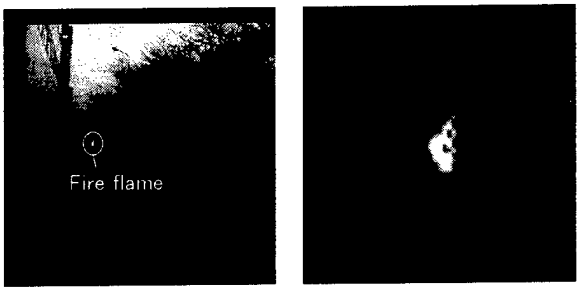


Fig.1 Fire flame color region in HSV space



(a) Input image (b) Extracted flame area

Fig.3 An example of the extracted fire flame area

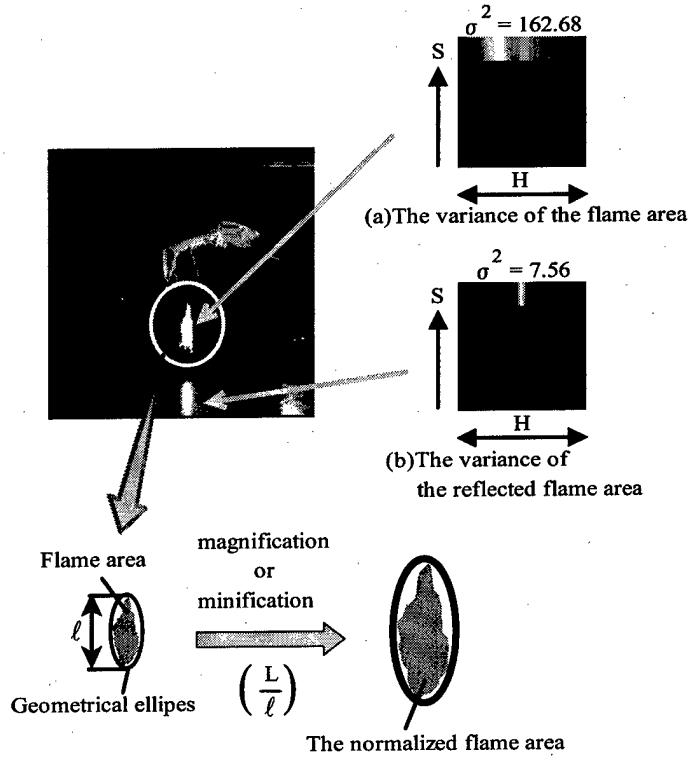


Fig.2 Variance of flame color area and the normalization on size

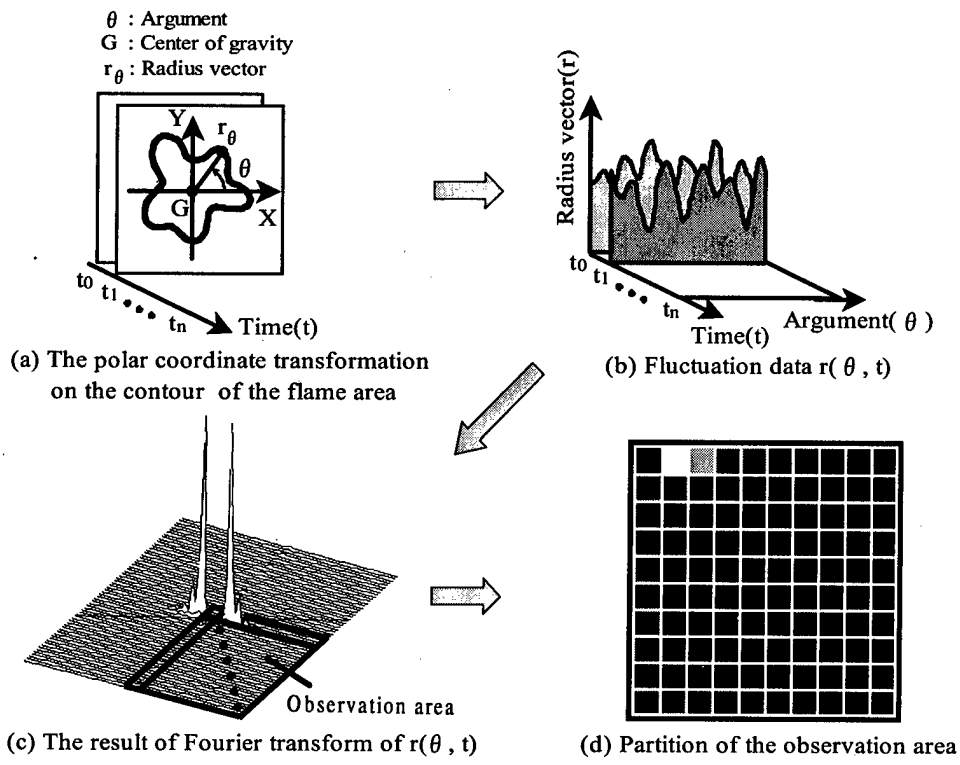
artificial light, fake fire flames caused by reflecting on the wall, the road and so on. It is also needed to detect the position of flame. In the method, the HSV transformed data is projected on the HS (Hue-Saturation) plane. Using the data of high level S region in the HS plane, the value of variance of H is calculated (Fig.2). Then the flame color area which the value of variance is the highest in all flame groups is selected. A geometrical ellipse fit the selected flame color area is calculated [5]. Comparing a length ℓ of a major axis of the ellipse with a referential length L prepared beforehand, a value L/ℓ is obtained. Using the value L/ℓ, the flame color area is normalized by the magnification or the minification (Fig.2). Consequently, the size of the extracted flame area is similar in case of any fire scene.

Fig.3 shows an example of the extracted fire flame color area in case of the flame 50 meters distance.

2.2 The space-time fluctuation on the contour

The contour of the flame area which is normalized in size is extracted by using an edge operator. The extracted contour data is calculated by the polar coordinate transformation, using an angle θ against the horizontal axis and a distance r between the contour and a position G of center of gravity (Fig.4 (a)). The results of the polar coordinate transformation of every input image are placed in time series. Then a fluctuation data $r(\theta, t)$, as a space-time data on the contour for a given period of time, is obtained (Fig.4(b)). Using two dimensional Fourier transform of $r(\theta, t)$ and the normalization on the power, a quantities on the space-time fluctuation is obtained (Fig. 4(c)).

We pay attention to a distribution of the frequency component in an observation area shown in Fig.4(c). The observation area is divided into $n \times n$ (Fig.4(d)). We determine the divided area which a peak of the distribution on fire flame and a peak of the distribution on artificial light should be distinguished: the



(a) The polar coordinate transformation on the contour of the flame area

(b) Fluctuation data r(θ , t)

(c) The result of Fourier transform of r(θ , t)

(d) Partition of the observation area

Fig.4 A space-time fluctuation data on a contour of the flame area

observation area is divided into 10 × 10 in the experiment. The value of one divided area is the sum of the frequency component in the area.

Fig.5 shows that the left column is the examples of fluctuation data r (θ , t) and the right column is the examples of the divided area. In case of fire, r (θ , t) shows a tendency that the components concentrate near the upper left corner of the observation area.

2.3 Detection of the fire flame

The frequency component distribution on the pattern of the observation area shows the space-time fluctuation on the contour. Using the distribution, it is possible to distinguish between the fire flame and the artificial light. However, the flame contour shape is changed by inflammable material, air supply flow rate, wind and so on. So the position of the concentration of the frequency component and the pattern of the component distribution are changed in the observation area. Likewise, in case of the artificial light, the position of the concentration of the frequency component and the pattern of the component distribution are changed by a radial pattern, partial appearance and disappearance and so on. Accordingly, it is difficult that the flame is detected determinately by the pattern of the component distribution. So a learning facility and a generalization facility of a neural network are used.

Fig.6 shows the neural network which is composed of three layers. The learning way is the back propagation algorithm. The input layer is composed of a matrix by n ×n input units. The number of the input units is same with the number of the divided area of the observation area. The value of the divided area is entered to the corresponding unit in the input layer. The output layer has two output units. The value from one output unit shows a recognition result on the fire flame and the value from another output unit shows a recognition result on non-fire.

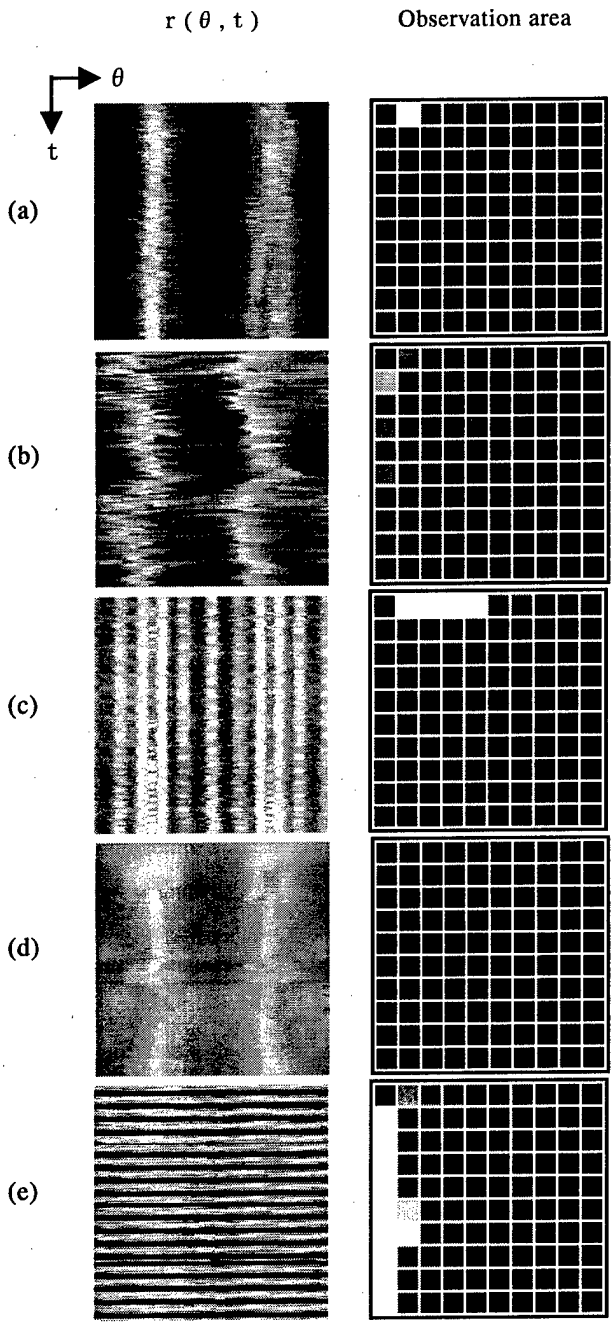


Fig.5 Example of r (θ , t) and the observation divided area. (a) the windless flame, (b) the flame blowing in the wind, (c) the flashlight with radiation, (d)the flashlight with no radiation, (e)the rotating light.

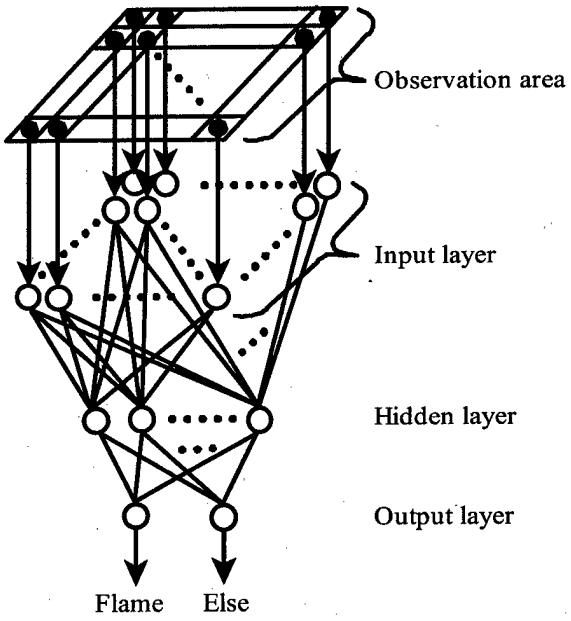


Fig.6 The neural network

3. RESULTS OF THE EXPERIMENT

In the experiment, the observation time is 8 seconds and the angular resolution of argument θ in the polar coordinate transformation is 360/256 degree. The input image is 512×512 on size and is 256 on gradation of R, G and B image. Both the number of the input unit and the number of the divided area of the observation area are 10×10. The number of the hidden unit is 50 and the number of the output unit is 2. Before the experiment, the neural network learned five scenes that were the windless flame, the flame blowing in the wind, the flashlight with radiation, the flashlight with no radiation and the rotating light in laboratory. In experiment, the unknown scenes including test scenes in outdoors were used.

Fig.7 shows the experimental results. (a) ～ (d) show the results of test on the artificial light and (e) ～ (h) show the results of test on the flame. If a faraway person has the flashlight and the flashlight is swinging, we may misjudge (Fig.7(d)). In this case, the contour shape and the pattern of the frequency component

distribution are similar to fire flame. In this way, there are some cases that the artificial light may be misjudged. But the experimental results are good enough. The scene of Fig.7(g) shows that the flame is faraway and blowing in the strong wind. The flame contour shape and size are changed violently. The experimental result is good and it is shown that our method is robust. The scene of Fig.7(h) shows that white smoke obtained by smoke machine is filling in the room and the flame is dim. It is shown that our method can't be influenced by white smoke.

In case of other scenes, the experimental results are good enough. Accordingly, it is considered that our method is useful for detection of the fire flame. As future work, we should add a processing for eliminating the influence of black smoke which causes flame splitting, flame appear and disappear.

4. CONCLUSION

In this paper, we described the fire flame detection method using a color CCD camera, and showed the result of experiment which is performed to verify the effectiveness of our method. In this method, the flame color area is extracted and the processing order of the extracted area is determined by the variance, using the color information. A space-time fluctuation data on the contour of the flame color area is produced by the polar coordinate transformation and the time series processing. Entering the distribution of frequency component on the space-time data into the neural network, the fire flame is detected. As a result of the experiment, it was shown that our method could not be influenced by the wind, the distance, the flame size changing, the flame shape changing, the white smoke and so on. Accordingly, it is considered that our method is useful for fire detection in the ordinary scene. We will investigate eliminating of the influence of the black smoke, detecting 3D position of flame and so on.

REFERENCES

[1] Tanaka, Tuchiya, Yamamoto, Tahara, Nishiyama and Suzuki, "Development of fire sensing system with CCD camera", Japan association for fire science and engineering, pp.8-9, 1996.

[2] Nemoto, Miyao and Yamauchi, "A real-time method of extracting flame fluctuation from CCTV pictures - An Application for fire protection", Japan association for fire science and engineering, pp.36-39, 1996.

[3] Yamagishi and Yamaguchi, "Fire Flame Detection Using Contour Fluctuation Information", Proceedings of the 1999 IEICE general conference, D-11-91, pp.91, 1999.

[4] Yamagishi and Yamaguchi, "Development of Fire Flame Detection Using Contour Fluctuation Information", The 5th Symposium on Sensing via Image Information, pp.7-12, 1999.

[5] Yamaguchi, Nakazawa and Nakajima, "A Real Time Intruder Finding System using Fiber Grating", T. IEE Japan, Vol. 110-D, No.7, pp.814-820, 1990.

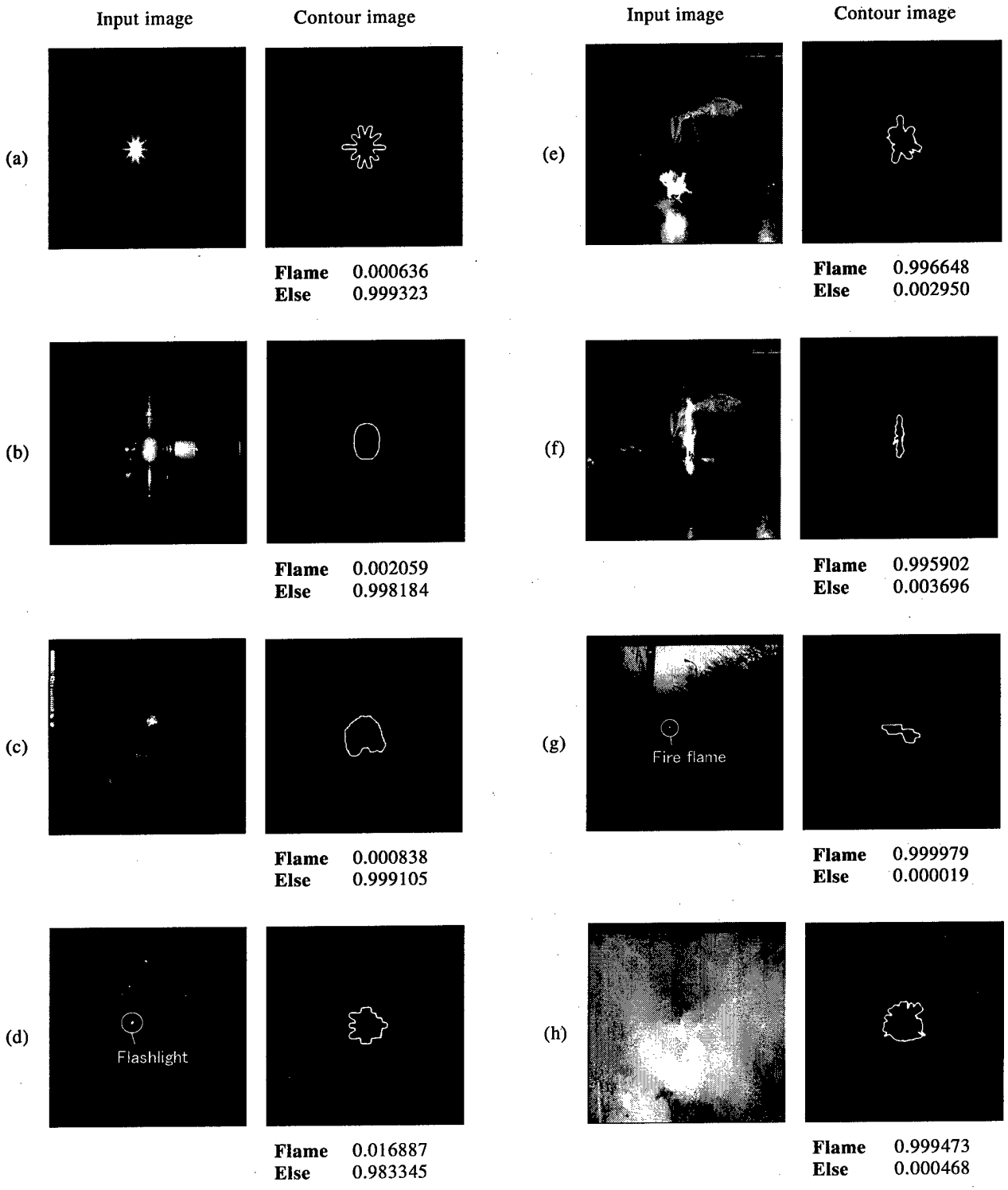


Fig.7 The experimental results. (a) Flashlight with radiation, (b) Flashlight with no radiation, (c) Rotating light, (d) Flashlight 50 meters distance (swinging), (e) Corrugated cardboard burning, (f) Dead branch burning, (g) Fire flame 50 meters distance (blowing in the strong wind), (h) Flame in the white smoke (dim flame). The value of Flame and Else are the output values of the neural network.

Analysis of Left Ventricular Wall Locus Tracing and Motion by Optical-Flow Using MRI

Kazuo YAGI, Masataka TOKUDA*,Yutaka SAWAKI*, Tadashi INABA*, Atushi YAMAMOTO*, Kiyotugu SEKIOKA*

Tokyo Metropolitan University of Health Science, 7-2-10,Higashi-ogu, Arakawa,116,Tokyo

*Mie university, 1515, Kamihama, Tsu,514, Mie

Abstract: The micro space transition, locus tracing and principal strain were calculated to be tried dynamics evaluation of the myocardial wall motion. This research was concentrated on the left ventricle in which during the one heart period was taken as the MR-images. And the change of pixel intensity between two continued images were visibility by the Optical Flow calculation. Optical Flow images could read deformation around the anti-watch more than the indication vector with the image of the ejection early phases, and anterior and septal were greatly indicated of movement. It were understood that phases were delicately different from each of base, middle, apex regions. It goes i center direction to inside of endomyocardial in lateral, posterior, and vector were indicated in equator pa (middle) and apex. It were understood it puts it on the apex from base, and about transition quantity the locus tracing increases from the viewpoint of grade and it were doing in the image of locus tracing calculation. It became the value that the means of strain of anterior which was the fatness part of the heart disease example when principle strain of normal volunteers were compared with the heart disease example decreased to about 70%.

1. Introduction

Recently, it is becomes popular research of the biomechanics which studies a like a bone of strong function and a character light and such as the muscle was smooth movement. Among them, the myocardium, which had such complicated movement as shrinking, expansion, rotation, twist, had very excellent durability as several decades.

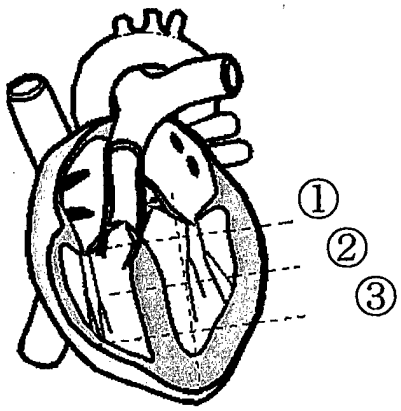


Fig.1 Schematic of ventricle region

In order to get the engineering application of such cardiac function, the quantitative analysis of the cardiac movement was necessary. Therefore this research was concentrated on the left ventricle, which lasts one cycle was taken as the imagines.

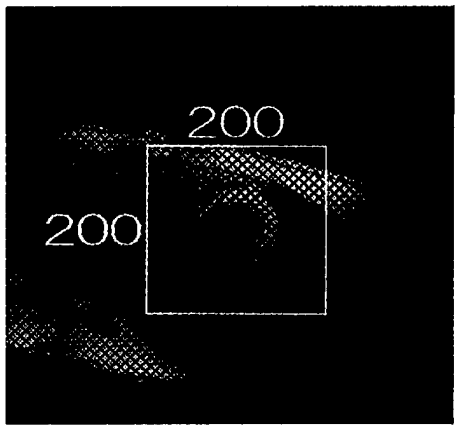


Fig.2 MR Tagg-image of ventricle region

And the movement of the pixel between two continued imagines is visibility by the

1999 INTERNATIONAL SYMPOSIUM ON MICROMECHATRONICS AND HUMAN SCIENCE
0-7803-5790-6/99/ $10.00 ©1999 IEEE.

Optical Flow calculation.The transition in the micro space, locus tracing and principal strain were calculated to be tried dynamics evaluation of the myocardial wall motion And, though Optical flow method was used as a means that a living body was analyzed, the precision evaluation was done by comparing a heart disease example with the normal example. And, it can be analyzed toward all image pixels contained in the image by to use Optical flow method law for the analysis, and local evaluation is possible.

2. Materials and Methods

2.1 Research of MR- I mage

As for the MRI image used for this research by using the electrocardiogram synchronous cine MR scan method、Targeting the left ventricle of heart of the normal volunteer 5 example were scanned in base, middle, apex and every department place in 3 section of short axisis, as for the number of sheets of 1 heart period (about 0.8 seconds caused by movement), got the image of the size of 512x512, 1 beat with 24 frame. As for this image, is done in (1 side 320mm) which pixel, slice width 7mm, a section interval 2cm. Shematical figure of the slice section in the left ventricle sagital side is shown in Fig.1. Volunteer A left ventricle territory in the image which could get it, it is cut off in the size of 200x200 pixel. An analysis was done after smooth process median filter treatment was done. A MRI image and the applicable department place was shown in Fig.2. And, as for the image used this time a lattice-shaped pattern (Tagg) was put artificially to make intensity of gradient for which to be in the image because an error is often brought about for the selection of a difference in concentration by the Optical Flow calculation as the concentration territory in the heart organization was narrow. Tagg-image was shown in Fig.3.

2.2 Calculation of Optical Flow

It was called the quantity that each image pixel in the process that it reaches the next frame from a certain frame into image was moved, and the distance of the movement were shown with the velocity vector place. This velocity vector place was called Optical Flow.

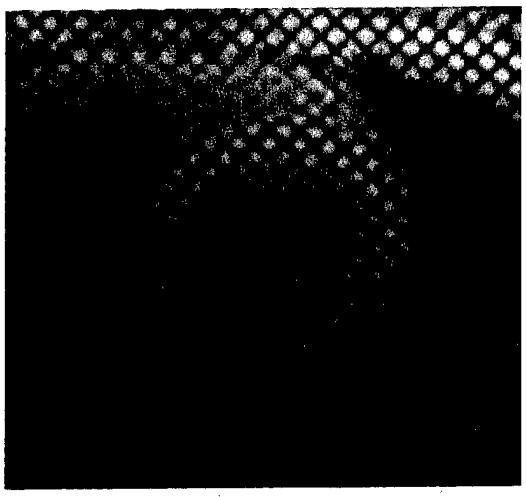


Fig.3 Analysis ventricle Tagg-image(200x200 pixel)

How to calculate Optical Flow used the technique of Tretiak (1) other, which was the algorithm of the typical slope law which the secondary partial derivative function of a degree of image intensity was used for by this research. The fundamental algorithm was shown in the following The next type could exist when it was moved to the coordinate (x+dx, y+dy) with a degree of image intensity of the point (x, y) in the t time being shown with G (x, y, z) and this point keeping a degree of image intensity in the constant after the dt time.

$$G(x, y, t) = G(x+dx, y+dy, t+dt) \quad (1)$$

Tayler polynominal function、

$$\frac{\partial G}{\partial x}\frac{dx}{dt} + \frac{\partial G}{\partial y}\frac{dy}{dt} + \frac{\partial G}{\partial t} = 0 \quad (2)$$

It gets (2) . Here.

$$\frac{\partial G}{\partial x} = Gx, \frac{\partial G}{\partial y} = Gy, \frac{\partial G}{\partial t} = Gt, \frac{dx}{dt} = U, \frac{dy}{dt} = V$$

When it is put, as for the ceremony (2)

$$Gx\,U+Gy\,V+Gt=0 \quad (3)$$

It becomes (3). Furthermore, this was computed about x and y with partial derivative.

$$GxxU+GxUx+GyxV+GyVx+Gtx=0 \quad (4)$$

$$GyyU+GyUy+GyyV+GyVy+Gty=0 \quad (5)$$

Two ceremonies are made, and U, V were

calculated to less than a decimal point six digits, and a speed vector place was computed.

Moreover, it could be chased automatically by using Optical Flow, and local evaluation was possible.

2.3 Strain Analysis

It was based on end-diastole period, and minimum principal strain until end-ejection period was calculated to evaluate the amount of contraction of the heart muscle. Three optional points were chosen on the heart muscle each department place, and the deformation of 3 corner shape to draw was applied to the following (4) (5) ceremony, and three points asked a strain calculation.

$$\left(ds_i^2 - dS_i^2\right)/2 = \varepsilon_{xx}dx_i^2 + 2\varepsilon_{xy}dx_i dy_i + \varepsilon_{yy}dy_i^2 \quad (6)$$

$$\varepsilon_2 = \frac{1}{2}\left(\varepsilon_{xx} + \varepsilon_{yy}\right) - \frac{1}{2}\sqrt{\left(\varepsilon_{xx} - \varepsilon_{yy}\right)^2 + 4\varepsilon_{xy}^2} \quad (7)$$

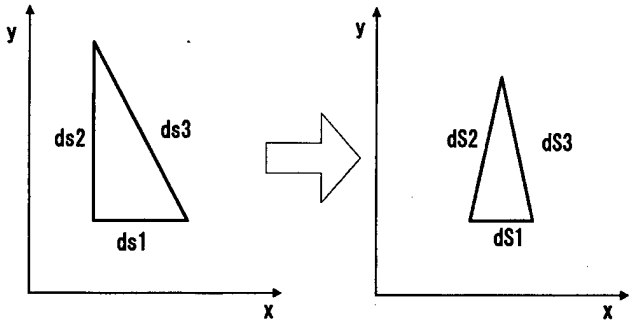


Fig.4 Schematically model of strain calculation

Before ds1, ds2, ds3 are transformed, it was the length of the side after dS1, dS2, dS3 were transformed in Fig.4. A heart short axisis 3 section was divided into a anterior, the lateral, a posterior, four department places of septal, was thought to be large intensity gradient was connected with triangle which the lattice point of tagg was computed by this research in the whole territory.

3. Result s and Discussion

Optical flow images in ejection period (frame2) of the large deformation in 1 heart period of normal volunteer A were shown in Fig.5~Fig.7.

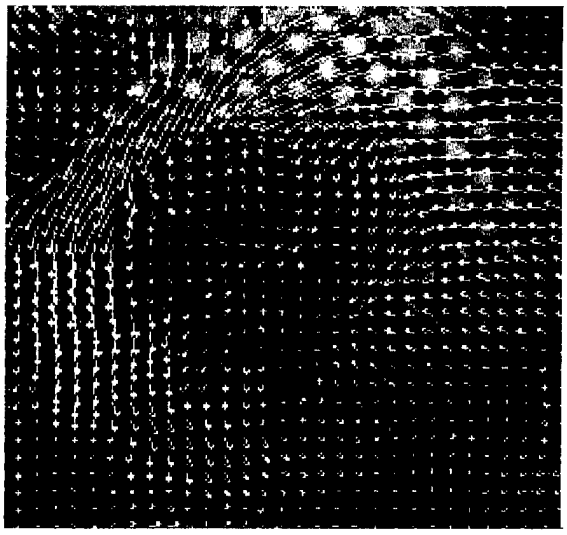


Fig.5 Axial slice image of base section ①, Calculated Optical flow image

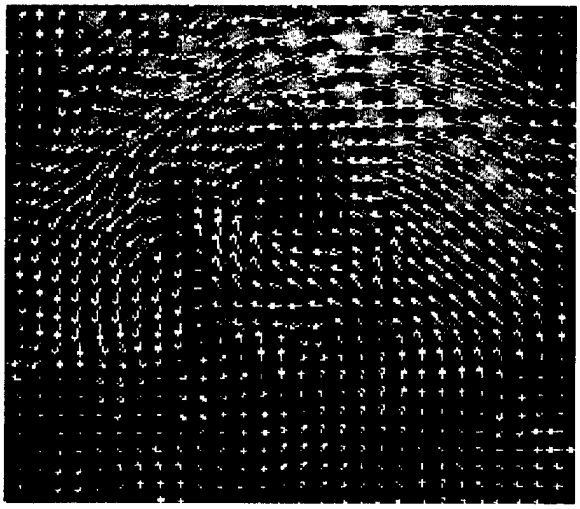


Fig.6 Axial slice image of middle section ②, Calculated Optical flow Image

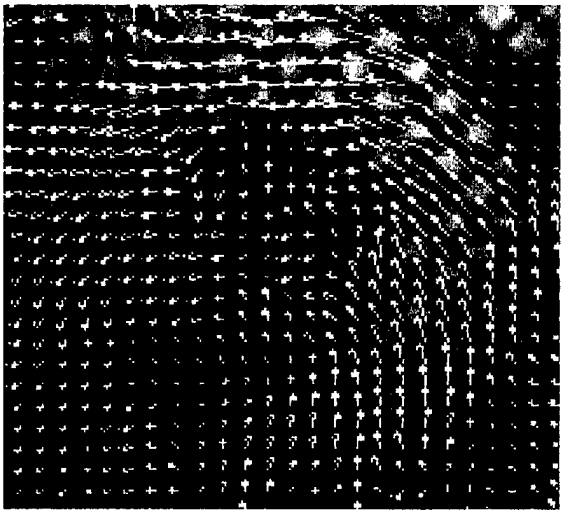


Fig.7 Axial slice image of Apex section ③, Calculated Optical flow Image

Vector images of Optical flow to frame13 of endejection period from frame1 of isometric

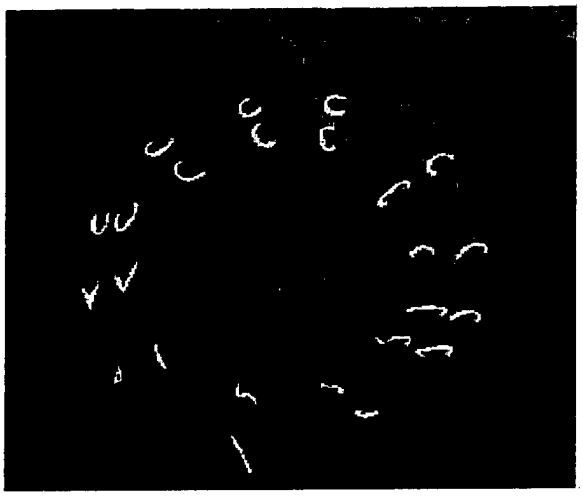


Fig.8 Axial slice image of base section ①, Locus image of left ventricle wall at ejection period

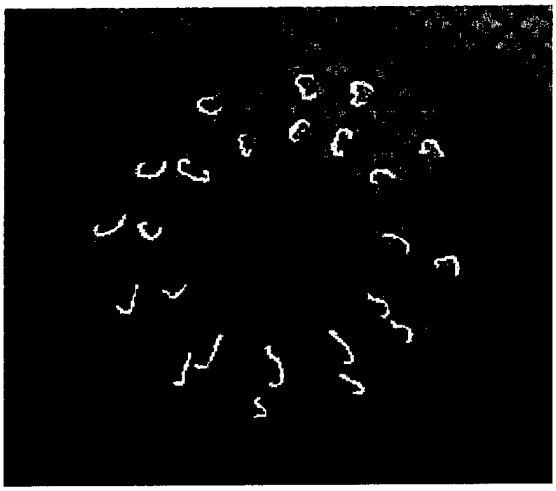


Fig.9 Axial slice image of middle section ②, Locus image of left ventricle wall

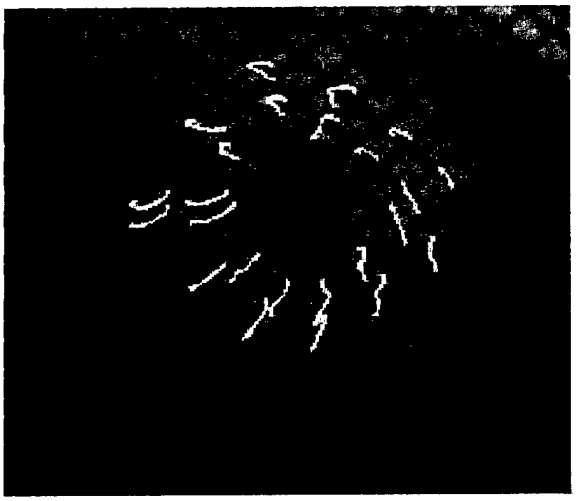


Fig.10 Axial slice image of Apex section ③, Locus image of left ventricle wall

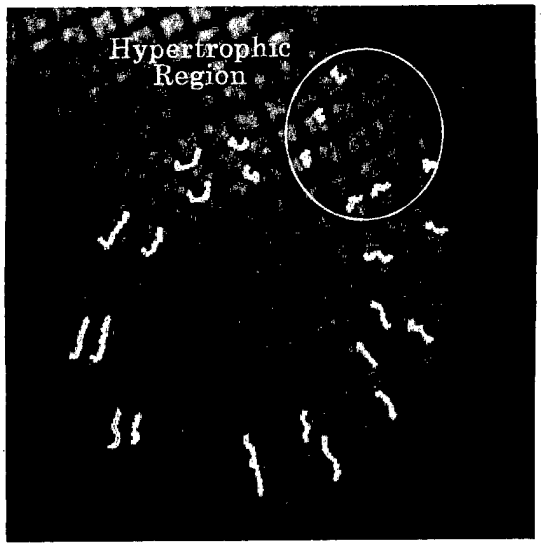


Fig.11 Axial slice image of Diseased Middle section② Locas image of left ventricle wall

endcontraction period such as normal volunteer A and heart disease patient F (HCM:Hyper trophic cardiomyopathy) were connected to make a path together for locus tracing were illustrated in Fig.8 - Fig.11.

Vectors indicated about deformation in the minute space with Optical flow images which visibility turned to by the intensity movement of image pixel by Optical flow calculation between two sheets of images which continued during the one heart period Moreover, deformation around the anti-watch could be read from Fig.5 - Fig.7 images of ejection early phase, and anterior and septal were greatly indicated. Furthermore, phase was delicately different from each of base, middle, apex.

It goes in the center direction to inside of endomyocardial in lateral, posterior, and vectors were indicated in middle and apex. It were understood it puts it on the apex more than Fig.8 ~ Fig.10 from base, and about transition quantity of the path increases from the viewpoint of grade and it were doing in the image of the path calculation.

It were understood that it goes through ejection with facing once in the perimeter direction inside the heart muscle walls in anterior and septal and turning in the anti-watch neighborhood direction and turning in the watch neighborhood direction after that when ejection were done again.

It was understood that Locus of Anterior which

disease region was very small in comparison with lateral, posterior and septal and it was hardly moving in locus calculation image of HCM case.

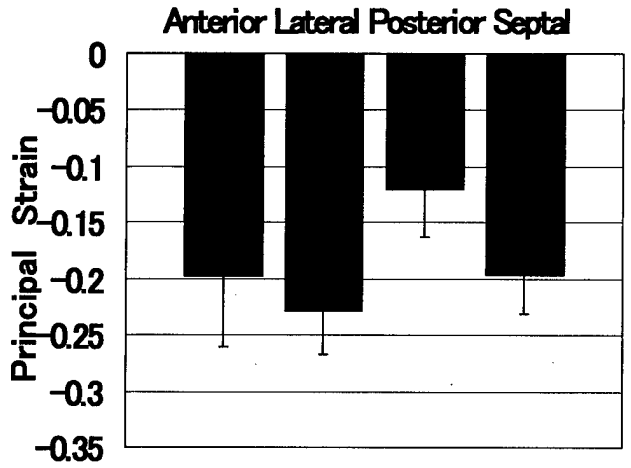


Fig.12 Principle Strain in Base Slice ①

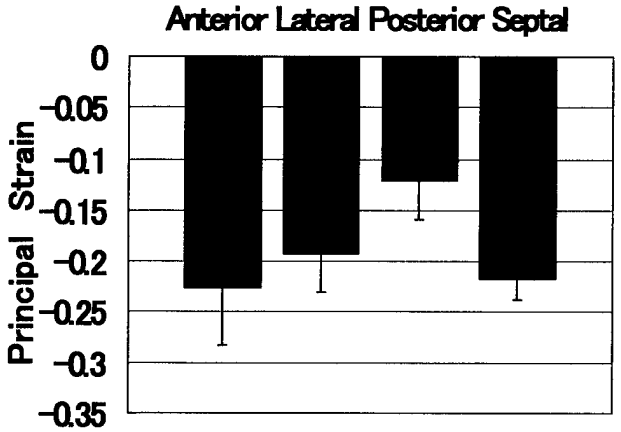


Fig.13 Principle Strain in Middle Slice ②

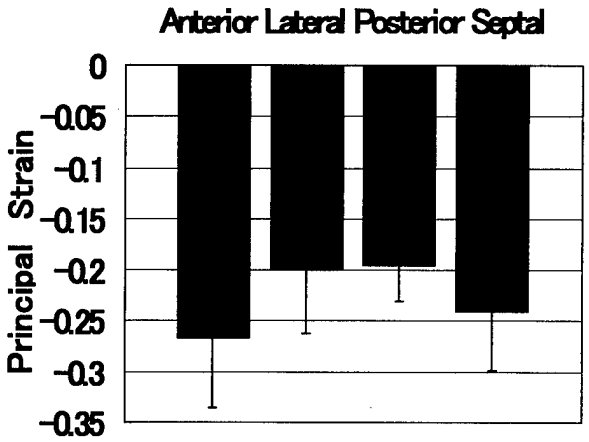


Fig.14 Principle Strain in Apex Slice ③

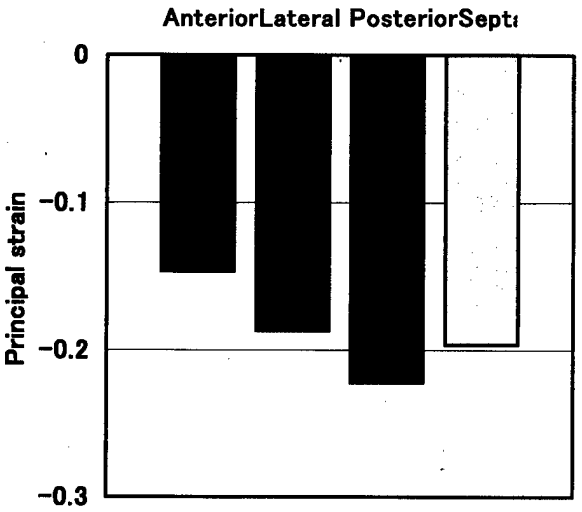


Fig.15-1 Principle Strain in Mid Slice ② with patient

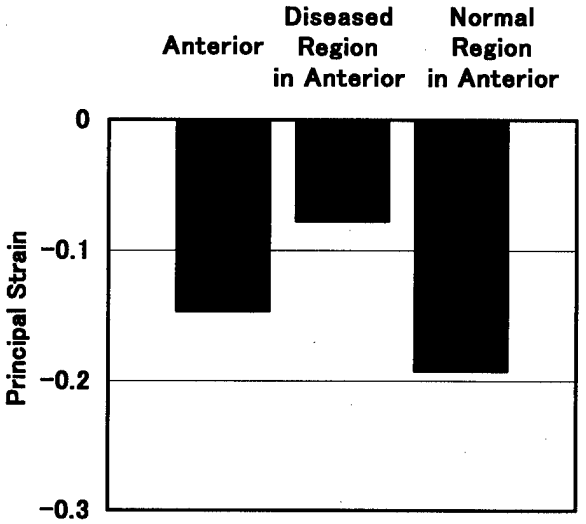


Fig.15-2 Principle Strain in Mid Slice ② with patient

Next, the calculation result of the minimum principal strain were shown in Fig.12 - Fig.15.

These graphs took average of normal volunteer 5 examples in anterior, lateral, posterior, septal by the thing of base, middle, apex in each of orders. And, an error shows standard deviation.

And, Fig15-2 was the graph which a reason compared Anterior which became the value that principal strain was smaller than Fig15-1 with in the HCM and Normal region.

It became -0.2 ～ -0.25 more than the calculation result in other department places though the minimum principle strain of posterior was small by about 30-40% in

comparison with other department places with -0.125 in base, middle. Moreover, it was put on apex from the base side, and the tendency that principle strain became big gradually was shown.

It became the value that the means of strain of anterior of HCM example when principle strain of normal volunteers are compared with the heart disease example decreased to about 70%. So, though it decreased to about 50% in the fatness part, the strain values which were about the same as normal volunteers were calculated in the normality parts as results that anterior of HCM was calculated with divide in the fatness part and the normality part.

4. Conclusions

This study, it learned to do used of optical-Flow techniques for dynamics deformation analysis with the locus images of left ventricle wall motion under the movement condition, Principle Strain, and so on.

It were proved that there were different characteristic movements in each department regions with perimeter direction and radius direction of straight lines or curve lines as analyze results of locus images with base, middle, apex.

It faces with apex though ejection movement has been done since ejection early times, and it goes in the anti-watch neighborhood direction with base, middle between freme1~fmare4s the rotation movement.

It guesses this movement the warm-up to do ejection, and it thinks about it with the reaction movement for a heart to produce bigger eject power with the smaller power. It is understood that locus images are very small and these are hardly moving in the heart disease region.

It was found out more than the result that it went through ejection with the biggest and -0.25 the smallest and the value of principle strain showing -0.12 and a heart entailing about 20% of the deformation.

Principle strain of the heart disease region became -0.08, and half of principle strain of apex which is a fatness part became the following value of the normality region. Therefore, it is effective to analyze it in the one by the territory, the one by the region to examine the motion of the heart muscle.

The heart of normal volunteer 5 example and heart disease patient were analyzed and judged with the thing which could do the analysis whose reliability were very high from standard deviation's being less than 0.07 as for the department place as well whose error were the biggest.

5. Reference

(1) Tretiak. O, other, Velocity estimation from image sequence with second order differential operatios: Proc. Int. conf. Pattern Recognition, Montreal, Que. pp16-19, 1984

(2) K. Yagi, other, Analysis of left ventricular deformation and local strain using optical-Flow: Proc.of IMMM'97,pp.673-682

Distributed Behavior Arbitration Network: An Autonomous Control Architecture for Humanoid Robots

Masaharu Shimizu, Takayuki Furuta and Ken Tomiyama
Department of Mechanical Engineering, Aoyama Gakuin University,
6-16-1 Chitosedai Setagaya-ku, Tokyo 157-0071, JAPAN

Abstract

This paper proposs an autonomous control architecture for humanoid robots that is called Distributed Behavior Arbitration Network. In the proposed architecture, robot's competence is differentiated based on the concept of behavior-based AI and these differentiated competencies are realized in individual agents. Here, 'fall avoidance' and 'goal search' behaviors are implemented on humanoid robots using proposed architecture to demonstrate its validity.

1. Introduction

This paper proposes an autonomous control architecture for humanoid robots that is called Distributed Behavior Arbitration Network (DBANet). In the proposed architecture, total capability of the robot is differentiated based on the concept of behavior-based AI and the differentiated individual capabilities are represented by separate agents.

In the field of autonomous mobile robots, shapes of robots have evolved from a wheel type to a polypod type and to a humanoid type. This evolution occurred because these robots are required to have multi-faceted competence[1] and to adapt to dynamic environments of every-day life. Especially, humanoid type robots have many actuators within their bodies. They can execute composite tasks that satisfy multiple purposes using them. For instance, they can hold an object with their arms while walking towards a goal with their legs. Another example would be fall avoidance where coordinated motions of whole body are needed.

There are however a few difficulties in pursuing multiple aims or in realizing cooperative behavior using a single algorithm[2]. For example, it is very difficult to develop an algorithm that is applicable to every conceivable situations. It is also true that a robot with single algorithm can be susceptible to even a small disturbance because it may cause a total system failure. Various multi-agent systems are proposed to alleviate these difficulties[2][3]. Most of them apply multi-agent system to a group of robots where each robot is an agent and an objective is achieved by a group of robots. Here, the multi-agent idea is applied to a behavior controller of a single robot to develop DBANet. This makes DBANet a multi-agent robot control architecture. It has a distinctive advantage that abilities of a humanoid robot are increased by simply adding new agents.

To realize this feature in the proposed architecture, distinct behavior patterns of the robot are implemented by individual agents and executed in parallel. Each agent is composed of NetIBSI[4] and Conflict Resolution Strategy (CRS) to be able to arbitrate among agents autonomously and distributedly. It is emphasized that the ability of each agent is determined by the behavior that is realized by the agent. This makes the proposed architecture behavior-based as well as multi-agent one.

In the next section, the concept of DBANet is explained in detail. Two humanoid robots used for experiments are introduced in **Section 3**. Then, implementation of the proposed architecture onto the robots is described in **Section 4** and a set of evaluation experiments is discussed in **Section 5**. **Section 6** concludes this study.

2. Distributed Behavior Arbitration Network

Distributed Behavior Arbitration Network for behavior management of humanoid robots is discussed here in detail (See **Fig.1**). First, a set of basic policies in developing DBANet architecture is described. Second, the whole structure of DBANet is outlined and then its components, NetIBSI and CRS, are explained.

2.1. A Set of Basic Policies

The first policy is to adopt the concept of behavior-based multi-agent system to construct a behavior managing architecture for humanoid robots. Thus, the total capability of the robot is differentiated based on the concept of behavior-based AI and these differentiated capabilities are represented by distinct agents. Each agent therefore has competence of executing well-defined identifiable behavior pattern by itself.

Second, an internal state of each agent is positively modeled within that agent and is made available to other agents. This makes it possible for multiple agents to arbitrate among themselves. This even opens up a possibil-

1999 INTERNATIONAL SYMPOSIUM ON
MICROMECHATRONICS AND HUMAN SCIENCE
0-7803-5790-6/99/ $10.00 ©1999 IEEE.

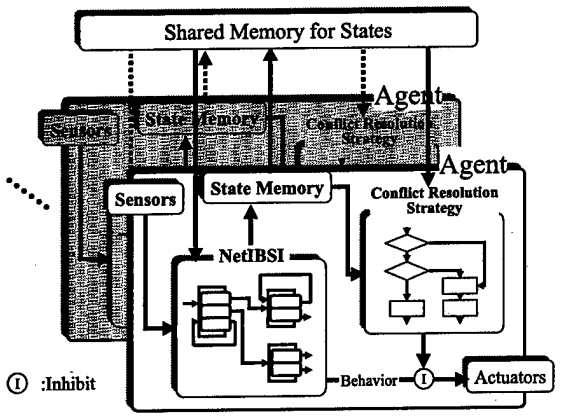


Figure 1: Distributed Behavior Arbitration Network

ity of composite behavior due to cooperation of multiple agents. Subsumption Architecture (SA) is known as the first behavior-based scheme[5] with real-time arbitration capability. SA can quickly control robot behavior in dynamic environment because it does not use any model. This, however, makes arbitration of behavior patterns be necessarily simple and rigid. On the other hand, the models in agents in the proposed architecture can make significant contribution in realizing efficient distributed autonomous arbitration among agents.

Third, the proposing architecture must be able to handle a large number of actuators. This is because the architecture is for behavior control of a humanoid robot with many joints on its body including two arms and two legs.

Forth, the controller must be able to realize both quick responsive behavior and a well-planned series of behavior patterns that achieves a given purpose. It is noted that these two behavior patterns, although needed for realistic humanoid robots, have fundamentally different characteristics and are not easily build into a single controller.

A successful controller must therefore be designed taking these basic policies into consideration. We follow these policies and propose DBANet as a new concept of an autonomous control architecture for humanoid robots.

2.2. Whole Structure of DBANet

Following the above policies, DBANet is composed of many agents that are individually assigned for a single capability of a humanoid robot (See **Fig.1**). That is to say, distinct behavior patterns of the robot are implemented by individual agents and executed in parallel. As stated in **Section 1**, each agent consists of NetIBSI and CRS. NetIBSI is an architecture that integrates behavior and sensation using state transition network and a behavior-based scheme. Here, a state in the state transition network represents an internal state of an agent. CRS clears situations where multiple agents simultaneously demand use of the same bodily resources. DBANet also includes shared memory for states. The information modeled by the agents is preserved in the shared memory. Thus, all agents are able to refer the information through the shared memory. DBANet does not have a supervisor or an observer that manages the total behavior in top level. Thus, the proposed architecture is a completely autonomous distributed multi-agent system.

2.2.1 NetIBSI: NetIBSI is an architecture that decides behavior of the agent in the proposed architecture. According to the set of basic policies, a robot acting in real environment must be able to respond quickly and to execute a desired goal systematically. NetIBSI therefore needs to represent both behavior patterns and uses states and transitions of states for this purpose. A single behavior pattern is defined by a state termed as Behavior State. A series of behavior patterns for a given intention can therefore be represented by a transition network of those Behavior States. Each Behavior State consists of several Sensor State-Behavior modules (SS-B modules)(See **Fig.2**). An SS-B module includes sensor infor-

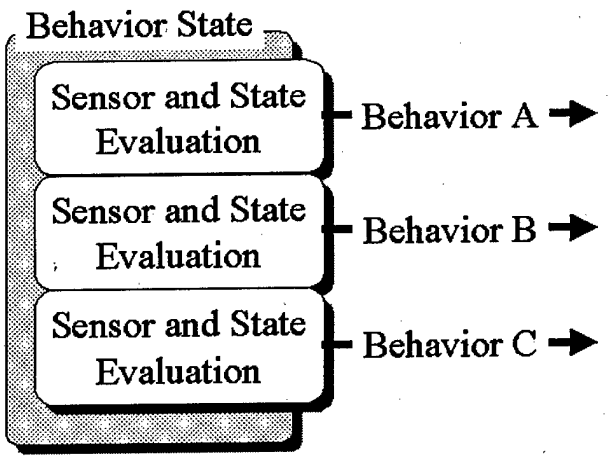


Figure 2: SS-B modules in Behavior State

mation and/or other agent states as inputs and a behavior pattern corresponding to the input information as an output. An SS-B module becomes active when the input information coincides with the input specification that is described in that module. They are layered from top to bottom according to their priorities in the Behavior State. The behavior pattern of an SS-B module that is active and has the highest priority is chosen by the Behavior State. The agent's state is then transformed from the current Behavior State to a next Behavior State that is specified by the chosen SS-B module.

A sample schematic diagram of NetIBSI is shown in **Fig.3**. It is assumed that this NetIBSI is a part of Agent I. State transition under NetIBSI is illustrated in detail using this figure. First, it is assumed that Agent I is in Behavior State A. There are three SS-B modules in this Behavor State. SS-B modules are placed from top to bot-

tom in the descending order according to their priorities. Suppose that Sensor 2 has activated and the current state of another Agent II is State α. Then Agent I executes Behavior Pattern C and the Behavior State of Agent I is transformed to Behavior State C. State of the robot and/or the environment are observed by new SS-B modules in Behavior State C.

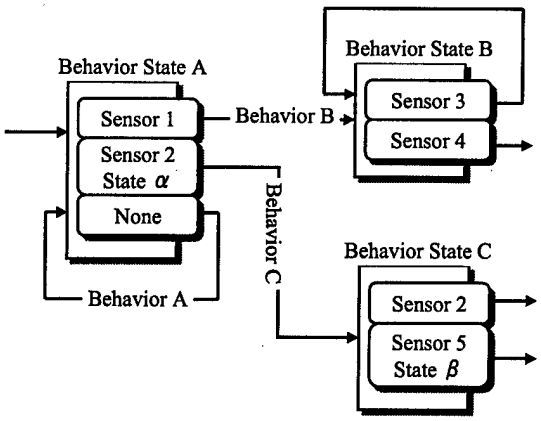


Figure 3: A Sample of NetIBSI

2.2.2 Conflict Resolution Strategy: Conflict Resolution Strategy (CRS) clears a conflict among the agents using priorities. A way of deciding the priority is explained first. Then, a flow of the strategy is discussed.

The priority is determined based on the following rules.

1. Behavior that is unsuccessful takes precedence. In other words, the agent whose behavior is prevented takes precedence.
2. It is checked that an agent is able or unable to execute behavior. This decision condition is given in advance.
3. The agent that uses smaller number of body parts is given precedence when the conflict is not cleared by the above two rules.

The priority is represented by a set of binary digits that is composed of **Fail Flag** bits as higher bits and **Body Flag** bits as lower bits (See **Fig.4**). The number represented by the whole bits is the numerical value of the priority. Here, it is considered that the larger the number is the higher the priority. **Fail Flag** bits are set (=1)



Figure 4: Format of a Priority Described Binary Digits

when the intended behavior is not executed and is cleared (=0) when it is executed. The position of a bit for an individual agent is determined based on the design criteria, namely, bits for more important agents are placed higher. An example of bit assignment is further discussed in **Section 4. Body Flag** bits are set at 0 if the agent uses the body part represented by that digit, otherwise are set at 1. Higher digits are allocated for the use of more significant body parts, for instance, the most significant digit of **Body Flag** represents the use of the right leg. It can easily be seen that the priority of an agent using less body parts becomes larger. It is noted that there is the shared memory to which all agents report their current priority. This makes it possible for all agents to refer to priorities of other agents.

Under the CRS, all agents individually execute this strategy and resolve conflicts by themselves. Here a conflict is defined by the following: multiple agents demand the use of the same body part(s) at the same time. The conflict occurs because the robot competence is not divided to agents according to the parts of the robot body. Each agent must decide between activating its behavior and stopping behavior when a conflict occurs. Agents use the logic in **Fig.5** for this purpose. First, the agent checks

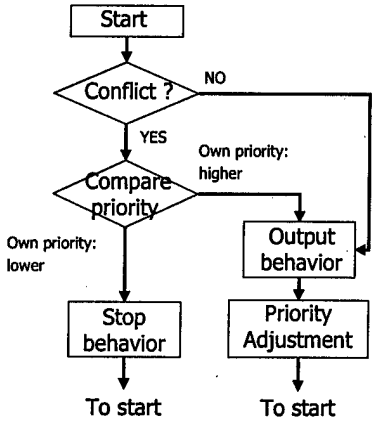


Figure 5: Conflict Resolution Strategy

existence of a conflict with other agents. It does this by referring priorities of other agents from the shared memory because the priorities represent states and the usage of body parts of all the agents. If conflicts are detected, own priority is compared with priorities of all conflicting agents. The agent with the highest priority activates own behavior and all other agents become dormant. Then, the priorities of all the agents that able to execute their behavior are adjusted as explained in above.

3. Experimental Platform

In this section, we introduce the experimental platform that is used for evaluating the proposed architecture. The experimental platform consists of a real-time controller and two humanoid robots. First the system configuration of the experimental platform is discussed and then two robots are explained.

3.1. System Configuration

The schematic diagram of our experimental system is drawn in **Fig.6**. This system consists of a humanoid robot, a VME-bus based controller and a UNIX workstation. The controller consists of a CPU board with VxWorks real-time operating system. The controller is connected to a network with multiple UNIX workstations, one of them is used as a host for data processing. This controller sends the motor control data to the robot through a pair of wireless transmitter and receiver. Sensor signals captured by a CPU board with one-chip CPU PIC16C73A(10MHz) implemented on the robot is send back to the controller through a pair of wireless modems. This signal is used to detect behavior states of the robot.

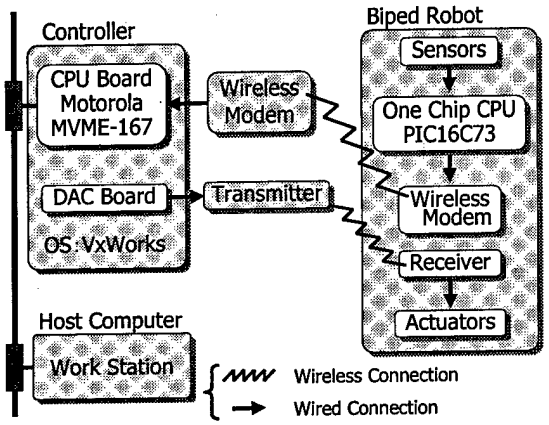


Figure 6: Schematic Diagram of the Robot System

3.2. Mk. 2 Robot

A back view of a robot called Mk. 2 is shown in **Fig.7**. Mk. 2 robot has two arms and two legs and is 0.40 [m] in length and 3.0[kgf] in weight. The robot is constructed for evaluating performances of an agent that has the task of keeping robot standing. Therefore, the task specifications are set as follow: to avoid falling down if possible. For realizing this specification, the robot must be equipped with sensors that can detect states of falling down. The following sensors are implemented for this purpose: i) two infrared proximity sensors, ii) a clinometer and iii) four touch sensors. The proximity sensors are located at the upper portion of the front and the back of the robot. The clinometer is installed approximately at the center of the body. The touch sensors are fixed on the back of both feet, two per foot at the front and the back of their outer sides.

3.3. Mk. 3 Robot

A view of a biped robot called Mk. 3 is shown in **Fig.8**. Mk. 3 robot is 0.30[m] in length and 1.6[kgf] in weight and is able to perform a dynamic biped walking. The robot is built for the task of reaching a goal while avoiding obstacles. Thus the specifications of Mk. 3 are set as the

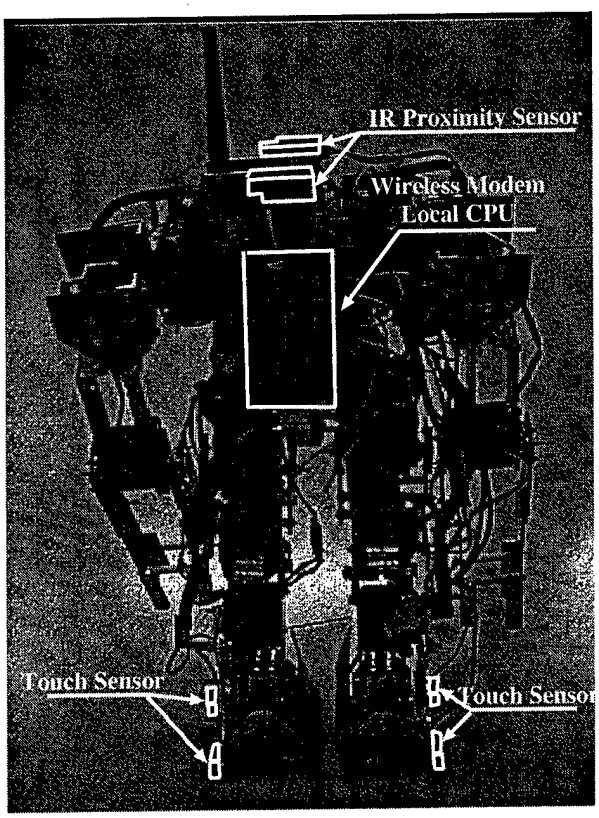


Figure 7: Mk. 2 Humanoid Robot

following: i) able to stop dynamic biped walking within 2 steps to avoid obstacles, ii) able to turn around and iii) be equipped with sensors that sense obstacles and a goal. To realize i) and ii), the algorithm of dynamic biped walking proposed by Furuta and Yamato [6] is used. Following sensors are installed to detect obstacles and a goal: i) one infrared detector and ii) one infrared proximity sensor. The proximity sensor is installed at the top portion of the body and can detect obstacles in front of the robot. The infrared detector is located on the head of the robot and is capable to sense a goal that emits infrared signals.

4. Two Behavior Types Needed by The Robots

Robots acting in real environment need two behavior types according to the basic policies as stated in **Section 3**. One is a reaction type that includes simple action but requires fast response. Another one is a mission type that requires non-trivial planning and often results in a complicated behavior. The mission type behavior can be represented by a composition of simple behavior patterns. The proposed architecture is capable of generating both types of behavior. Two sample cases, one from each behavior type, are considered to demonstrate this. The first one is an action of fall avoidance. The second behavior is the

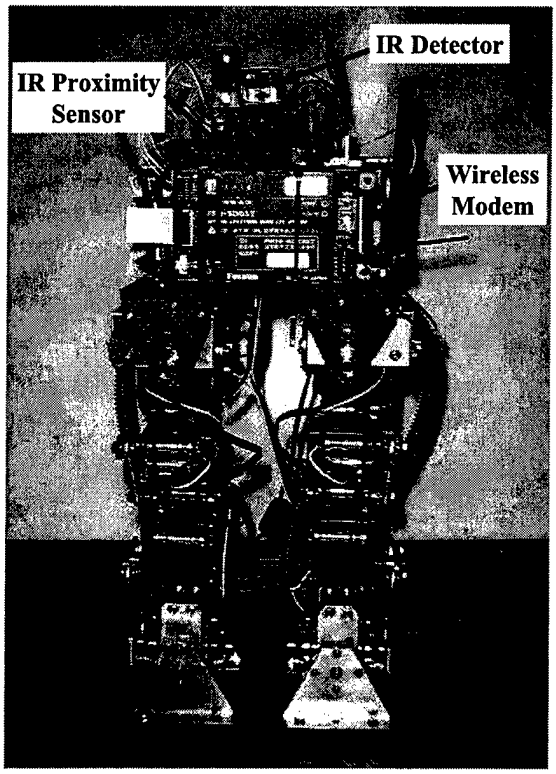


Figure 8: Mk. 3 Biped Robot

goal search and approach where the robot searches a goal and approaches it. Software configurations constructed for the two sample cases are explained here.

4.1. Fall Avoidance

The NetIBSI representation of fall avoidance and recovering of standing position is discussed here. It is noted that this capability is realized by a single agent called the Fall Avoidance agent. A network of Behavior States that constitutes NetIBSI is shown in **Fig.9**. Behavior States in **Fig.9** are listed and explained below:

STANDING: The robot is standing. SS-B modules to detect falling down are active prepared in this state.

HOLDING_OUT_F: The robot holds out front when a falling forward is sensed.

HOLDING_OUT_B: The robot holds out back when falling backward is sensed.

STRAIGHTENING_UP1: The robot straightens up from the crouching position. The arms are retracted to the standard position from forward position.

STRAIGHTENING_UP2: The robot straightens up from the crouching position. The arms are retracted to the standard position from backward position.

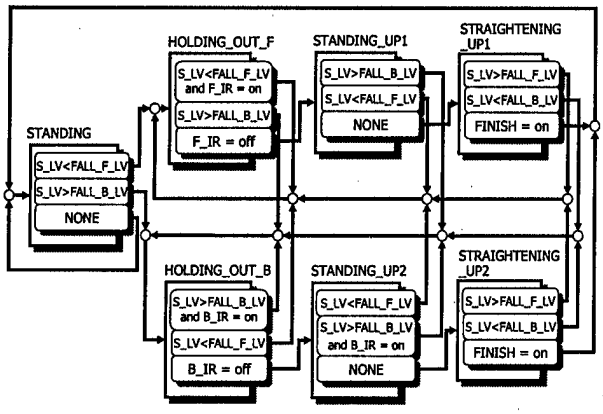


Figure 9: 'Fall Avoidance' Motion Described by NetIBSI

STANDING_UP1: The robot changes its position from holding out front to crouching position. This moves the projection of the center of gravity within the robot foot and makes it possible to lift arms.

STANDING_UP2: The robot changes its position from holding out back to crouching position. This moves the projection of the center of gravity within the robot foot and makes it possible to lift arms.

4.2. Goal Search and Approach

Two agents are constructed to realize the composite behavior that consists of searching and approaching a goal while avoiding obstacles. The first one is the Search agent that is capable to search a goal and to approach it. Another one is the Avoid agent whose competence is to avoid obstacles. It is expected that if these two agents work as planned, the robot controlled by them would achieve a composite behavior of finding a goal and approaching it while avoiding obstacles. The two agents are constructed and are implemented onto Mk. 3 robot. Configurations of them are explained in the next.

4.2.1 Search Agent: Behavior patterns of the Search agent, represented by NetIBSI, are shown in **Fig.10**. Behavior states symbolized in this figure are explained below.

FORWARD: The robot moves towards the detected goal in this Behavior State. This Behavior State is a successful state because the robot is approaching the goal when it is active. All other Behavior States in this agent are unsuccessful states.

NECK_RIGHT: The neck turns right to seek the goal.

RIGHT_TURN: The robot turns right because of detecting the goal while rotating the neck. The turn angle is the same as the rotate angle of neck in

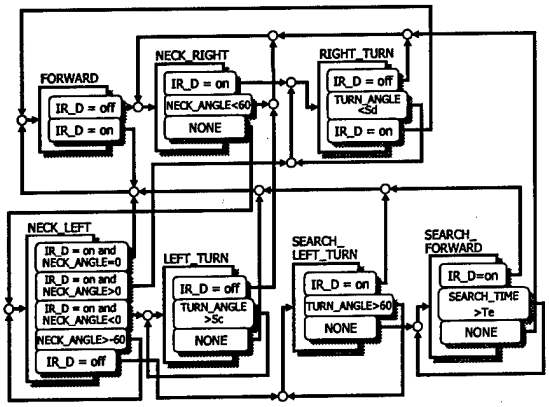


Figure 10: Behavior Part of the Search Agent Described by NetIBSI

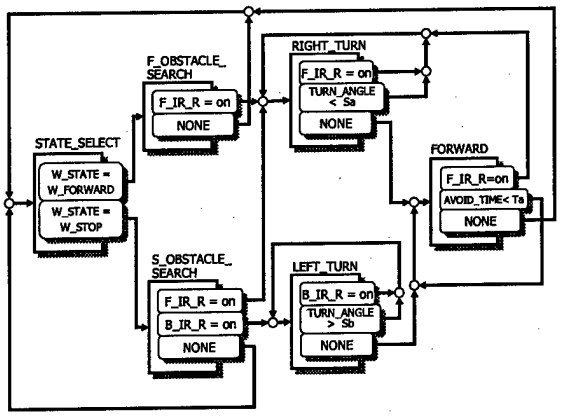


Figure 11: Behavior Part of the Avoid Agent Described by NetIBSI

rotates counterclockwise while the robot turns in order to keep the goal in sight. A direction of the robot body faces the goal after completing this Behavior State.

NECK_LEFT: The neck turns left in this Behavior State.

LEFT_TURN: The robot turns left to face the goal. The neck rotates roight not to miss the goal.

SEARCH_LEFT_TURN: The robot turns left to seek a goal. This is activated when a neck turn is not successful in finding the goal.

SEARCH_FORWARD: The robot walks forward to change a place.

As mentioned above, **FORWARD** is the only successful state and all other states are unsuccessful ones for the Search agent. This distinction is important in deciding the priority of this agent using CRS.

4.2.2 Avoid Agent: Behavior patterns of the Avoid agent are shown in **Fig.11**. Behavior States symbolized in this figure mean as follows.

STATE_SELECT: A state where the walking condition of the robot is observed through the states of other agents. A state that is appropriate for the current walking condition is selected and a state transition to that state occurs. Next Behavior State is selected based on this state.

F_OBSTACLE_SEARCH: The robot watches obstacles in front while walking forward.

S_OBSTACLE_SEARCH: Obstacles in front and rear are monitored while the robot is standing.

RIGHT_TURN: The robot turns right to avoid obstacles that are detected in front.

LEFT_TURN: The robot turns left to avoid obstacles that are detected behind.

FORWARD: The robot walks forward for a fixed time duration after avoiding obstacles.

Here, **STATE_SELECT**, **F_OBSTACLE_SEARCH** and **S_OBSTACLE_SEARCH** are defined to be successful states and the rests are unsuccessful states. This is based on the claim that the robot can perform its intended task of approaching the goal when no obstacles are detected.

4.2.3 Priority of CRS: The priorities, that are represented by binary digits, of the Avoid and the Search agents are established based on the rules of **Section 3.** These are shown in **Table 1. Success** denotes that the agent is in one of the successful states and **Failure** denotes otherwise. The placement of **Fail Flag** bits for various agents depends on criticality of the behavior patterns of agents. For example, the Search agent can make the robot approach a goal provided that obstacles are avoided. It therefore cannot execute its behavior while the Avoid agent is failing. Then, **Fail Flag** of the Avoid agent is necessarily placed in a higher position than that of the Search agent. This makes the priority of the Avoid agent become higher than one of the Search agent. The bits in **Body Flag** digits signify the right leg, the left leg, the right arm, the left arm and the neck in this order from higher bits.

Table 1: Assignment of Binary Digits to Behavior and State

Behavior	State	Fail Flag	Body Flag
Search	Success	0 0	0 0 1 1 0
	Failure	0 1	0 0 1 1 0
Avoid	Success	0 0	1 1 1 1 1
	Failure	1 0	0 0 1 1 0

5. Experimental Evaluation

To evaluate capabilities of the proposed architecture, NetIBSI and DBANet explained in the last section are implemented onto the robots. Here, we discuss two evaluation experiments and report the results of them.

5.1. Experiment of Fall Avoidance

Fall avoidance of humanoid robots requires fast response and is used to evaluate real-time capability of the controller. It therefore can be confirmed if the controller, that is a single NetIBSI here, satisfies the basic policies in **Section 2**. It is natural that a fall of a robot can be initiated suddenly and the state of the robot can start changing rapidly. Moreover, the robot needs to recover standing straight status via a series of planned motions after a fall is avoided by holding out. Therefore, fall avoidance is a good function to evaluate capability of a behavior controller in dealing with rapid phenomena and recovering from them according to planned strategies.

The method of this experiment is simple. The NetIBSI representing behavior patterns that realize fall avoidance and recovering its posture is implemented onto the Mk. 2 robot. Then, a fall is forcibly initiated by adding force to the upper body of a standing Mk. 2 robot and the reaction of the robot is recorded.

5.1.1 Result and Consideration: Actual standing up motion sequence from leaning forward is shown in **Fig.12**. The robot executes these motions in the order of

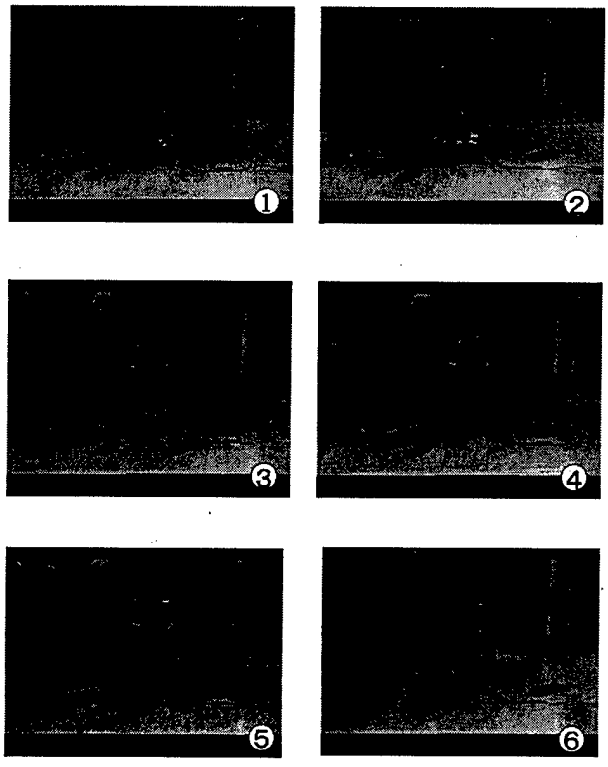


Figure 12: Actual 'Standing Up' Motion from Leaning Forward

the numbers in this figure. The robot can avoid falls most of the time and can recover a posture as shown in **Fig.12**. We can confirm the following facts from the results of experiments.

- The robot controlled by NetIBSI can rapidly move to avoid falls.
- Appropriate motions to recover the standing position are initiated by checking the own state after avoiding a fall. The robot is able to recover the standing position most of the time.
- When the falling speed is too large, there are cases where the robot falls due to a hardware limitation. The sampling period of the colinometer is 0.3[s] and is not short enough to detect a fall in time.
- The behavior of fall avoidance using the whole body of the humanoid robot can be represented by NetIBSI. The real robot functions according to the representation.

As stated above, it is shown that NetIBSI can realize both real-time capability and planned sequence of behaviors.

5.2. Experiment of Approaching a Goal

Conflict resolution capability of DBANet is evaluated in this experiment. The situation is that a robot approaches a prescribed goal while avoiding obstacles is selected for this purpose. The robot needs two agents to deal with this situation. One has the ability to approach a goal and another one is capable to avoid obstacles as stated in **Section 4**. We can check the conflict resolution capabilities between two agents in this situation.

Mk. 3 robot, a single obstacle and a goal are placed as shown in **Fig.13**. Because of this arrangement, both behavior patterns of avoiding the obstacle and approaching the goal need to be executed by the robot in order to accomplish its mission. That is to say, the robot must avoid the obstacle to approach the goal in this situation.

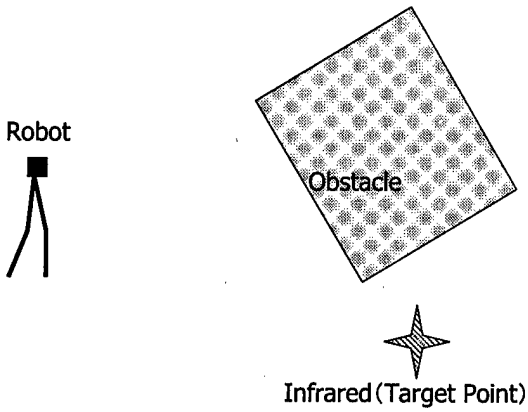


Figure 13: Experimental Environment

5.2.1 Result and Consideration: The robot is able to achieve its objective of approaching the goal while avoiding the obstacle as shown in **Fig.14**. In this figure, numbers denote the order of executing behavior and circles represent the goal point (a source of infrared light). A typical history of transitions of the priorities of two agents is shown in **Fig.15**.

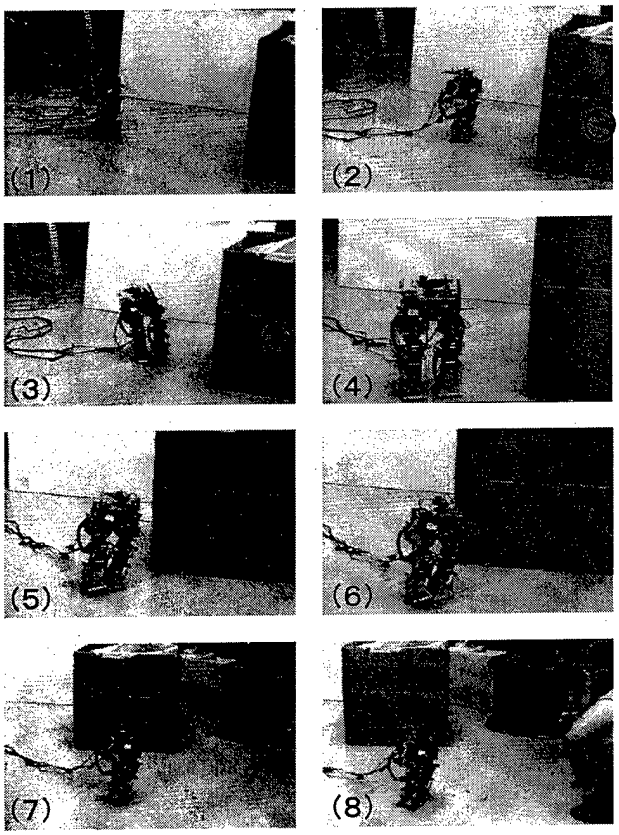


Figure 14: The robot approaches the goal while avoiding the obstacle.

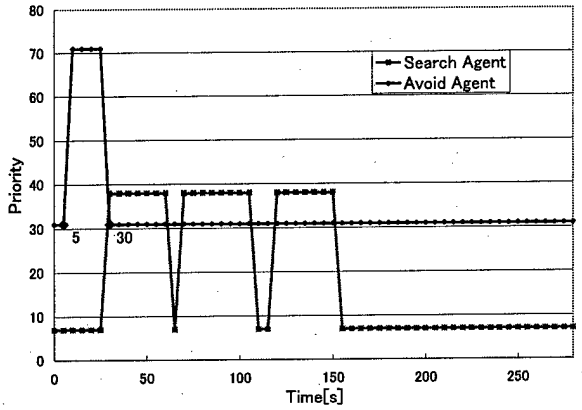


Figure 15: Priority History

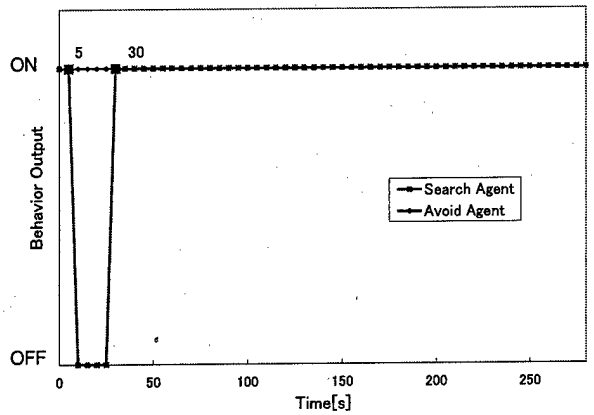


Figure 16: Behavior Activation History

The priority of the Avoid agent becomes high at five seconds mark in **Fig.15** while the robot is moving forward because the robot has sensed the obstacle (See **Fig.14** (2)). Since the obstacle is found but not avoided yet, the priority of the Avoid agent is high and the obstacle avoidance behavior is initiated by this agent. The priority of the Avoid agent is high until the robot has avoided the obstacle (See **Fig.14** (4)). The Search agent conflicts with the Avoid agent because both agents demand the legs simultaneously while the robot detects the obstacle (from five seconds to thirty seconds). The Search agent stops executing its own behavior in this period by itself (See **Fig.16**) because the own priority is lower than that of the Avoid agent (See **Fig.15**). Thus, the arbitration between the agents succeeds and composite behavior is realized by the proposed achitecture.

6. Concluding Remarks

In this study, the DBANet is proposed as a new concept for generating composite behavior of humanoid robots. It is based on the concept of multi-agent behavior-based scheme. The proposed architecture is implemented onto two humanoid robots to perform fall avoidance and goal search and approach behaviors. Experiments are successfully accomplished. This proves that the intended capability of the proposed control architecture is practically realizable.

References

[1] Toshihiro Matsui. How humanoid robots come closer to humans. *Journal of the Robotics Society of Japan*, 15(7):961–963, 1997.

[2] Shin Kato and Jun'ichi Takeno. Cooperation of multiple mobile robots. *Journal of the Robotics Society of Japan*, 12(6):785–790, 1994.

[3] Toru Ishida. Communication among autonomous agents. *Journal of the Robotics Society of Japan*, 12(6):802–807, 1994.

[4] Takayuki Furuta, Masaharu Shimizu, and Ken Tomiyama. Interactive behavior-sensing interface for mobile robot. *Intelligent Autonomous System IAS-5*, pages 407–414, 1998.

[5] Rodney A. Brooks. A robust layered control system for a mobile robot. *IEEE Journal of Robotics and Automation*, RA-2(1):14–23, 1986.

[6] Takayuki Furuta, Hideaki Yamato, and Ken Tomiyama. Biped walking using five-link virtual inverted pendulum model. In *Proc. of 3rd Int. Conf. on Advanced Mechatronics*, pages 614–619, 1998.

FUZZY-NEURAL BASED MULTI-AGENT STRATEGY FOR BIPED MOTION CONTROL

Amar Khoukhi[1,2], Lyes Khoukhi[1]

[1]Institut d'Informatique USTHB BP32 El-alia Bab-Ezzouar Alger Algérie
[2]Groupe ESIEE Dépt Automatique 2 Bd Blaise Pascal Noisy le Grand 93400 France

Abstract:

In this paper the problem of motion control of biped is considered. We develop a new method based on multi-agent associated Fuzzy-Neural and Adaptive Stochastic Petri Nets strategy. This method deals with organization and coordination aspects in an intelligent modeling of human motion. We propose a cooperative multi-agent model. Based on this model, we develop a control kernel named IMCOK (Intelligent Motion COntrol Kernel), which consists of a controllor, coordinator and executor of different cycles of motion of biped. When walking, IMCOK receives messages and sends offers. A decision making of actions (DMA) is developed at the supervisor level. The articulator agents partially planify the motion of non-articulator agent associated. The system is hybrid and distributed functionally. In the conflictual situations of sending or receiving messages we apply a new strategy: The Adaptive Stochastic Petri Nets (ASPN) which deals with all these situations. Cognitive agents communicate with reactive agents (non-articulator) in order to generate the motion.

Key Words : ***Biped, Multi-Agent, Articulator and non-Articulator Agent, IMCOK, ASPN, Fuzzy-Neural.***

1. Introduction

Multi-agent systems (MAS) have an explicit representation of their environment on which they can reason and from which they can predict future events[1]. Many architecture or theories about cognitive and reactive agents have been proposed[6,8,19]. It concerned with the behavior of a collection of autonomous agents aiming at solving a given problem.[7] .

However, for the past several years, the neural computation approach has emerged[20] to take problems for which several conventional computational approaches have been proven ineffective. Hence, there have been a lot of interests in applying new methods to solve the problems of motion control of walkers robots. For instance Beer(1990) showed how to build a vivant like agent made of ''neurons'' to perform various tasks and survived in a simulated environment. Usually a simple network cannot accommodate complex task performances[1]

The researches have studied the problem of motion of biped from several sides such as autonomy and locomotion [1], methods based phase movement [7]. Recently, many researches investigated biped robots and walkers on surface, like that can climb a sloping surface [17]. Presented hereafter is using the multi-agents systems associated with neural approach , in order to learn our biped. To solve conflictual messages, we use stochastic Petri nets approach. Hence, we consider principles and fundaments of Distributed Artificial Intelligence (D.A.I) in order to build cooperation and communication system between agents.

The model is called Multi-agent Biped System (MABS) and the control kernel is called Intelligent Motion COntrol Kernel (IMCOK). The biped learns and recognizes different forms of movement. Actually, the coordination between the biped members makes its movement. The present scheme is a representation of a biped.

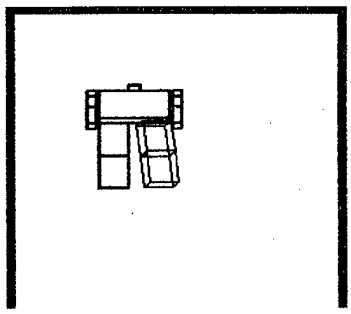


Figure1: Schematic representation of biped

1999 INTERNATIONAL SYMPOSIUM ON
MICROMECHATRONICS AND HUMAN SCIENCE
0-7803-5790-6/99/ $10.00 ©1999 IEEE.

2. System description

2.1 Definition

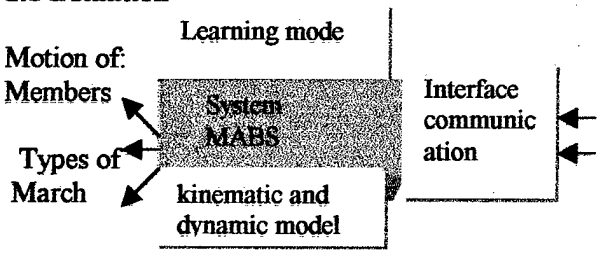


Figure 2: knowledge of MABS

The system is hybrid and distributed in terms of function and scheduling, i.e. it constitutes of a set of hybrid agents (cognitive and reactive) that cooperates to accomplish functions of control of biped. Agents use a dynamic organization strategy based on the use of the negotiation technique based on communication protocol DDE_ inter-agent. This technique allows messages exchanging between agents.

2.2. Actions of MABS

The main features of this model is to permit a scheduling distributed of several agents, and facilitates the communication with the user via the interface of communication. It gives a new strategy of organization: The parallel communication between agents, the execution of several operations (intra-agents or inter-agents) and the flexibility and extensibility. It allows a distributed scheduling too. It also admits new articulator agents.

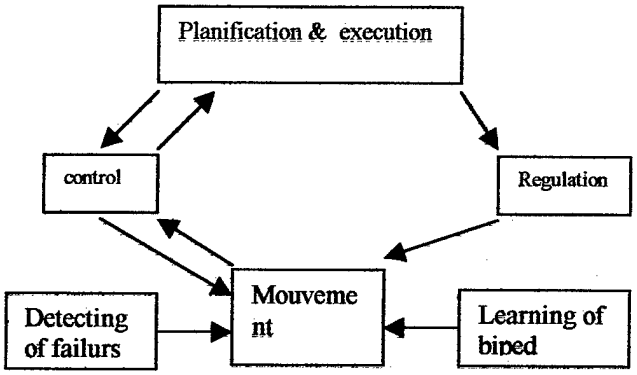


Figure 3: the scheme of a general action

The scheme below shows the different levels of our architecture, the user can communicate with MABS via interface of communication

The operation :

It is based on the following algorithm, followed by every agent:

- Message receiving.
- Scheduling.
- Sending results.

2 Architecture of MABS system

MABS is constituted of (figure 3):

-Kernel (IMCOK) Intelligent Multi-agent COntrol Kernel that is composed of supervisor agent, PERCR agent, equilibrator agent and regulator agent.

- The mode of learning
- Tools for detection of failures
- Interface of communication
- Articulator agents
- Non-articulator agents

3.1 Articulator agents

These agents are homogeneous in their structures, but differentiate by their associated functions

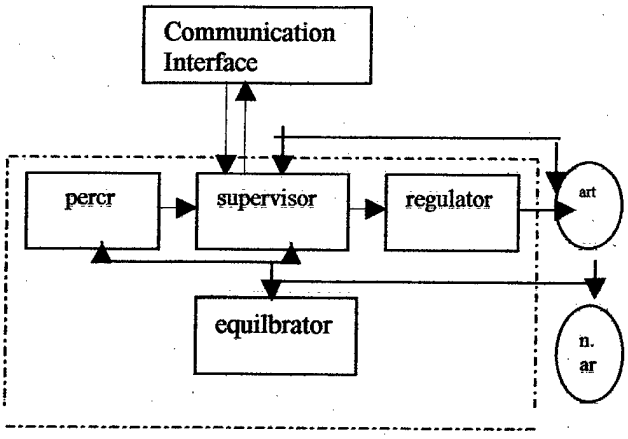


Figure 3: MABS and IMKOC
Architectures of movement.

Our articulator agent has three processes: Process of communication, process of decision and Process of scheduling.

- Process of communication: It receives the message coming from the supervisor or other

components by the Process of Input Communication (PIC), it shapes it the Internal Message File (IMF), and transmits the results of scheduling by Process of Output Communication (POC).

- Process of decision: at the receipt of a message from the regulator agent, the articulator agent decides after consulting the scheduling process, whether it sends a control to the non-articulator agent or no.

¨ Process of scheduling: this process is constituted of library of plans: the necessary data allowing the process of decision either to send a signal of activation or not to the non-articulator agent, are contained in the library of plans (like max and min limit for rotation of the non-articulator agent partner). The ability of articulator agents resides in their plans.

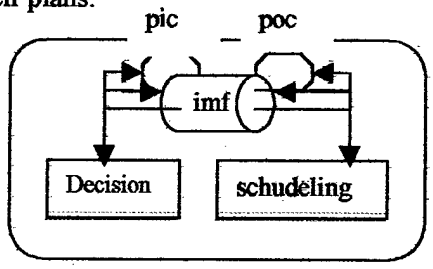


Figure 3 :articulator agent architecture

3.Non Articulator agents

It doesn't arrange a process of decision. Its primary function is clearly the execution of the movement. So, it represents a reactive agent. It constitutes of

-Process of communication:

-Process of scheduling: The necessary data allowing the non-articulator agent to plan its trajectory of reference and then to follows it, are contained in the library of plans.

3.3 Regulator agent

It is constituted of process of communication, process of regulation, motor process, process of scheduling.

· *Process of Regulation*: its function is the regulation of the speed of members given by the supervisor.

· *Motor process:* its unique function is the generation of a signal (message) called message motor.

· *Process scheduling:* this process contains the necessary information to the treatment.

3.4 PERCR

. After having received signals of the environment (reversed picture), the cerebellum of our system is going to construct the real picture of the environment, it is the perception of the environment. Then the resulting signal is going to be transmitted to the supervisor.

Pecr receives two types of signals, one from sensors, the other from the agents.

· Process of perception: this process ensures the perception of the environment signals.

· Process of scheduling: it contains a library of plans: One distinguishes two essential data parts: data specified for the perception that ensures the management of the system of picture treatment (SYPT). And data specified for the control, which ensures the management of the control system by sending data concerning states of the different members in progress with each cycle of movement.

· Process of control (SYMOC): SYstem of Movement Control : an agent that transmit his information on the states of agents to control system

3.5 Supervisor

The supervisor receives the already quoted signals from agents, treat them and generate new signals of command or answer (structures of solution to problems met by the other agents of MABS). One distinguishes two types of communications, at the level of the supervisor:

-Intra-supervisor Communication (between its different constituents) performed via the Internal Messages File (IMF), and

-Inter-supervisor Communication performed via DISI DIspatcher of SIgnals, and PIC process of exit communication. Signals coming from the different components are identified and recognized by RISI. All the components of MABS system are managed by their respective managers.

MC: manager of communication
ME: manager of equilibrator
MR: regulating manager
MO: manager of control
MA: manager of articulator agent
MN: manager of non-articulator agent

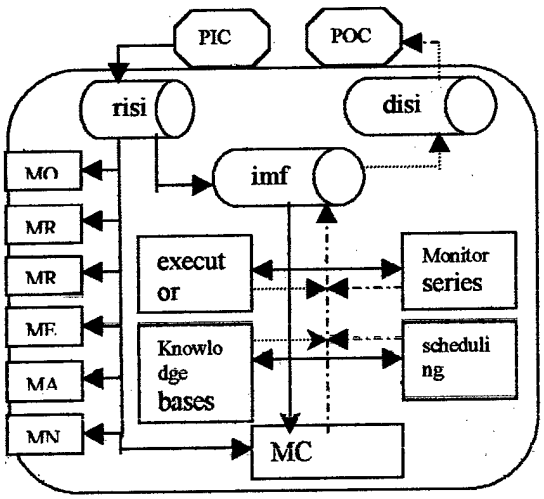


Figure 5: Supervisor agent

We explain few processes: The library of plans contains the command or the necessary tools for the management of the components of MABS system.

3.5.1 Basis of knowledge: It is the data basis of MABS. Containing all information on the different components of the system, and of each cycle of movement (4 cycles, two for double and two for single support).

3.5.2 Monitor of Series (MS)
Its main role is the coordination between the intra-supervisor actions. One can associate different strategies to plan activities of this monitor:

-- With static priority: once a priority is affected into a program, this one won't change until the end of execution of this program.

-- With dynamic priority: the priority affected into program changes according to the environment of execution of this one (load of system, types of actions to be executed...).

3.5.3 Executor: The allowance of executor to the program can make it according to the affected priorities to program them automatically (for example one is going to give to every signal coming from an organ a priority, with of course their organization), or by an external manner by the person responsible of exploitation, the priority can be allocated statically or dynamically.
After execution, the result will be transmitted to the DIspatcher of SIgnals in order to transmit it to the concerned agent.

3.5.4 Receiver and Identifier of the SIgnals (RISI): Contrarily to other agents of MABS, the supervisor has a superior work load, that requires a loaded element of identification and to send received messages from the outside into processes or the corresponding manager in the supervisor.

3.5.5 DIspatcher of SIgnals (DISI)
Play an important role in the diffusion of signals (either signals that have just been executed, or those that has just been managed without being executed).

3.5.6 Managers: ensure the management of agents of MABS system. The manager sends a message of working to the agent managing.

3.6 Equilibrator

This process ensures the balance of the biped during the march or during the station. The physical conditions, such that the robot is in state of balance, are the center of gravity of the body on the surface of lift (surface taken between elements in contact with the soil). It is constituted of a process of communication, process of scheduling and process of equilibration.

The equilibrator receives the answer from articulator agents via the process of communication, after a treatment, the process of equilibration gives the state of balance of the biped, and transmits them to the supervisor.

The supervisor contains the necessary plans of motion forms, the neuron of degrees (for example) is in relation with supervisor because it contains the degrees of each member.

4. The communication:

MABS agents communicate between them by sending messages.
Every signal (message) represents the information needed by the agent (a control to be achieved) and as the result of treatment of the previous agent.

5. Neural approach

The Neural method for learning the biped for several cases of motion is applied in our system. So The Decision Making is affected on the level of Supervisor , MABS can be looked at this form :

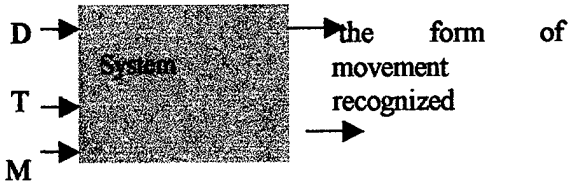
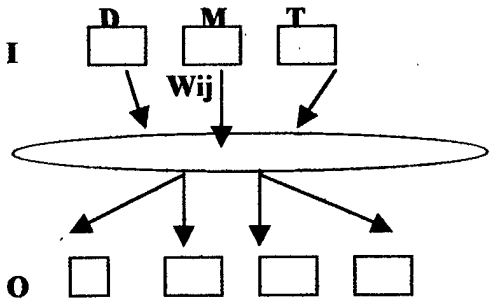


Figure6 : the representation of neural system

The degrees, type and member data (the entrances of our neural system) are taken from outside of the supervisor, are treated and used to learn biped and which how form of movement learned by biped and then are arranged in supervisor agent.

The different levels of the this neural scheme are presented as follow :



And in order the biped learns the form of movement we use the retro-propagation algorithm,

we apply some equation :
Oj = 1/1+exp(-netj) ;

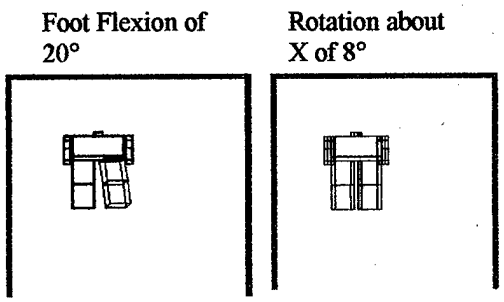
$$netj = \sum WijOi;$$

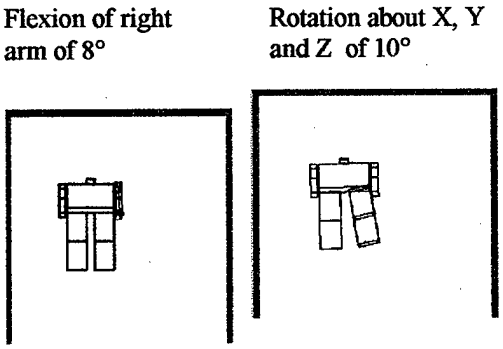
$$\delta j = Sj(1-Sj)\sum_K \delta_K wjk$$

The new wij will be calculating by

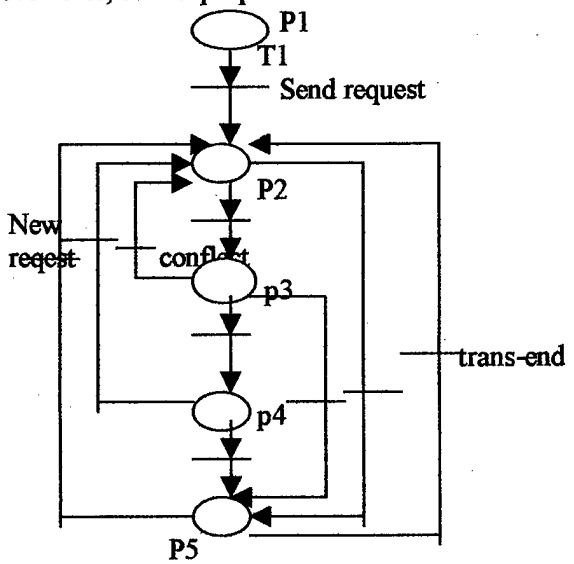
$$Wij(n+1)=wij(n)+\alpha\delta jSi + B[(wij(n)-wij(n-1)]$$

The outputs shows this files **(Simulations1)** :





We have associated the Stochastic Petri Nets for studying different conflictual situations of movements, so we propose this scheme:



After we have determined the graph associated, we determine all situations generating a conflict. So, we notice :

P(Si+1/Si) to represent the probabilty of transition from the state Si to the state Si+1.
P(Si) represents the probability that request is in state Si

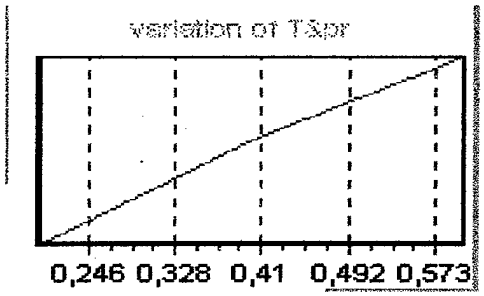
We have :

$$\begin{cases} P.Q=0; \\ \sum_{1}^{n+2} pi=1 \end{cases}$$

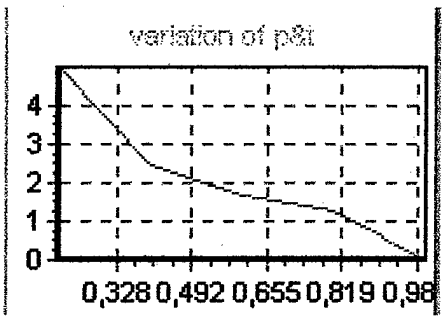
than we can calculate the average time in each place with :
T*(Pi)=M*(Pi) / Post(Pi, .) . F*
And the average transition of each transformation with :

$$F^*(ti)=\sum \lambda i(Mi)\pi i \quad j \in SMj$$

Simulation :
In order to show efficiency of our methodology, some simulations were performed:
Variation of generation rate (T, axis Y) in function of average time (Pr, axis X)



Variation of function of time de séjour in place (P, axe of Y) on function of probabilties de franchissement (t, axe of X).



References

[1] J.Ferber "Reactive Distributed Artificial Intelligence: Principe and Application, In Foundations of Distributed Artificial Intelligence, 1996.

[1] M.Nilsson "Snake robot" IEEE conf control systems. Apr 1997, pp. 21-26.

[2] S.kajita and al. "dynamic walking control of a biped robot along a potential energy conserving orbit" IEEE trans. robotics Automat., vol 8, no. 4, pp. 431-437, aug 1992.

[3] C.Chevallereau, A. Formal'sky, B. Perrin, "low energy cost reference trajectories for a biped robot" IEEE conf., Robotics Automat. May 1998, pp. 1398-1404.

[7] M. Rostami and Guy Bessonet"Impactless sagittal gait of a biped robot during the single support phase" IEEE conf. Robotics Automat. , May 1998, pp.1385-1391.

[1] M.Nilsson "Snake robot" IEEE Conf. control systems. Apr 1997, pp. 21-26.

[6] B. Moulin and B.Caib-draa"An Overview of Distributed Artificial Intelligence", in Foundation of distributed Artificial Intelligence, 1996.

[7] L.Khoukhi "general view and analysis of multi-agent systems" internal report, USTHB.jan- 1999.

[8] H. Van Dyke Parunak "Applications of Distributed Artificial Intelligence in Industry" in Foundation of distributed Artificial Intelligence, 1996.

[9] S. Kagami, and al. "Design and Developement of a Legged Robot Research Platform JROB-1" conf of IEEE robotics Automat., May 1998, pp.146-151.

[10]A.Khoukhi,L.Khoukhi,R.Ouguini,and N.Ababou "Multi-Agent Based Strategy for Biped Motion control" ICRAM'99 Istanbul May 24-26.

[10] C. Yu-Yung, L.Fu and C. Yu-Chien "Multi-agent Based Dynamic Scheduling for a Flexible Assembly System" IEEE Conf. Robotics Automat., May 1998, pp.2122-2128.

[11] S. Liu, L. Fu and J.Yang "Multi-Agent Based Control Kernel for Flexible Automated Production System" IEEE Conf. Robotics Automa., 1998, pp-2134-2139.

[12] D. Steiner "An Integrated Environment for Constructing Distributed Artificial Intelligence Systems" Foundation of distributed artificial Intelligence, 1996.

[13] K.Fischer, J.Muller and M.pischel"A. Geral Testbed Artificial Intelligence Applicat-

ions''. Foundation of distributed Artificial Intelligence, 1996.
[14] J. Ferber ''Reactive Distributed Artificial Intelligence : Principles and Application ''96.
[17] Y.F.Zheng and J.Shen,''Gait synthesis for the SD-2 biped robot to climb sloping surface,'' IEEE Tran. Robotics Automat., vol. 6, no .1, pp.86-96, feb 1990.
[18] Bernard moulin and Brahim Chaib-Draa'' An Overview of Distributed Artificial Intelligence '' Foundations of Distributed Artificial Intelligence, 1996.
[19] H. Van Dyke Parunak ''Applications of Distributed Artificial Intelligence in Industry'', Foundations of Distributed Artificial Intelligence, 1996.
[20]R,P Lippmann, ''An introduction to computing with neural nets'' ASSP.Mag., Vol 4, pp 4-22, Apr 1987.

International Micro Robot Maze Contest
November 23, 1999
Nagoya Congress Center
- Authorized by RoboFesta 2001 -

Cosponsored by :
City of Nagoya
The Chubu Industrial Advancement Center
Nagoya University
Chubu Science & Technology Center
Japan Society of Mechanical Engineers
Robotics Society of Japan
Society of Instrument and Control Engineers
IEEE Industrial Electronics Society
IEEE Robotics and Automation Society
Research Committee on Micromechatronics
Technical Committee on Micro-mechanisms
of Japan Society of Precision Engineering

In Cooperation with :
Chubu Bureau of International Trade & Industry of MITI
Micromachine Center
Federation of Micromachine Technologies
Aichi Prefecture
Gifu Prefecture
Mie Prefecture
Shizuoka Prefecture
Nagano Prefecture
Nagoya Chamber of Commerce & Industry
Chubu Economic Federation
Nagoya Junior Chamber

The International Micro Robot Maze Contest are held on November 23, 1999 in parallel with the 1999 International Symposium on Micromechatronics and Human Science (November 23-26, 1999). The Goal of the contest is to promote the development of autonomous micro robots. In the contest, two categories are opened for, 1) micro mobile robots, 2) teleoperated mountain climbing micro robots and 3) autonomous mobile robots. The micro mobile robots, whose dimensions are less than 1.0 cm x 1.0 cm x 1.0 cm, teleoperated micro robots, whose dimensions are less than]1.0 cm x 1.0 cm x 1.0 cm, and autonomous micro robots, whose dimensions are less than 2.54 cm x 2.54 cm x 2.54 cm, will compete in time trial contest. Robots are required to pass through several selected points in a maze in going from start to finish. Many teams from academia, companies, private teams, individuals, etc. are participated.

Contest Rules:
Category 0 : Teleoperated Micro Racer

0-1) The maximum demensions of the body are 1.0 cm x 1.0 cm x 1.0 cm. The robot must have the basic ability of moving on the flat surface: going a straight line, and turning left and right.

0-2) Energy or control signal can be provided from cables or flexible tubes outside. However, the robot should not be pushed directly by air or tube.

0-3) The robot must clear two kinds of events: a) time trial on the straight line (Fig.1) and b) slalom (Fig.2). The contest ground will be unveiled at the contest site. The amaterial of this ground is a glass and its surface is finished flat and smooth.

Contest Rules:

Category 1 : Teleoperated Mountain Climbing Micro Robots

1-1) A robot must climb up a mountain after leaving the Start Point, and then pass through whole Control Points in the maze. At last, the robot must reach the Goal Point. The location of the Control Points for the contest will be unveiled at the contest site.

1-2) The layout of contest ground is shown in Figs. 1 and 2. The material of ground is an aluminum alloy to avoid electrostatic charge and its surface is finished with fine aventurine so that robot should not slip.

1-3) The maximum dimensions of the body are 1.0 cm x 1.0 cm x 1.0 cm.

1-4) Energy or control signal can be provided from cables or flexible tubes outside. However, the robot should not be pushed directly by air pressure, a stick, and so on. These cables or tubes will not be counted as part of the robot.

Category 2 : Wireless Autonomous Mobile Micro Robots

2-1) The robot must pass through several control points in the maze and then reach the Goal Point.

2-2) The layout ; of contest ground is shown in Figs. 3 and 4. The material of this ground is an aluminum alloy to avoid electrostatic charge. The surface of ground is finished with fine aventurine so that robots should not slip, and the surface of side wall is polished so that the light should reflect.

2-3) The maximum dimensions of the body are 2.54 cm x 2.54 cm x 2.54 cm (1 inch cube)

2-4) Only control signal may be provided using wireless communication system from outside. However, the robot should not be controlled by cables or flexible tubes, a stick and so on. The antenna system will not be counted as part of the robot. Autonomous robots with CPU and sensors are welcome.

Judgment:

In all categories, the preliminary heats will be held and the entries for the final will be selected by the results of the preliminary heats. The judgment will mainly be depend on time to reach Goal in final. The judgment will be also considered by the following view points:

a) idea, b) possibility of miniaturization, c) running performance, d) humor, e) autonomy, and so on.

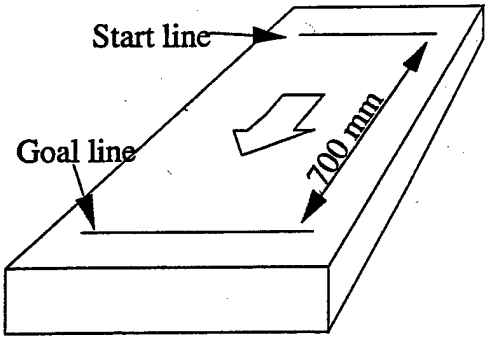


Fig. 1 Layout of Category 0 : Straight line

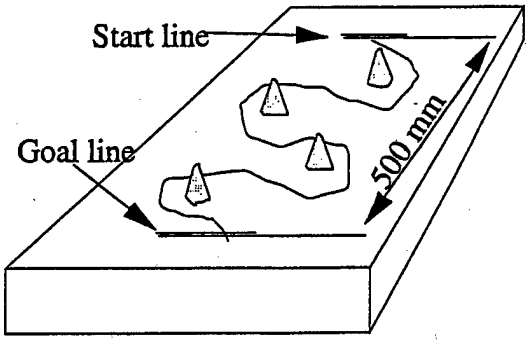


Fig. 2 Layout of Category 0: Slalom

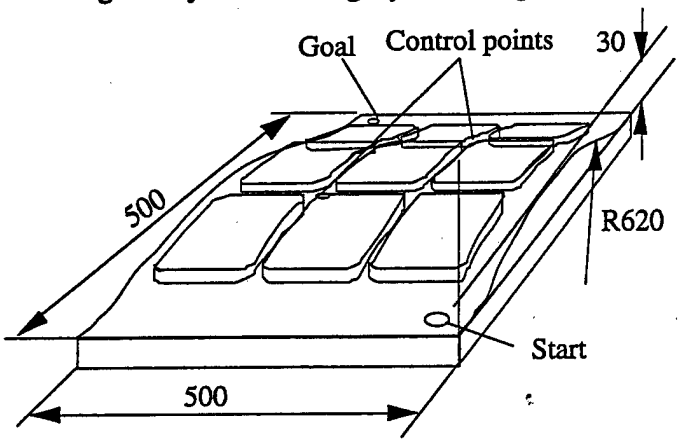


Fig. 3 Layout of Contest Ground for Category 1

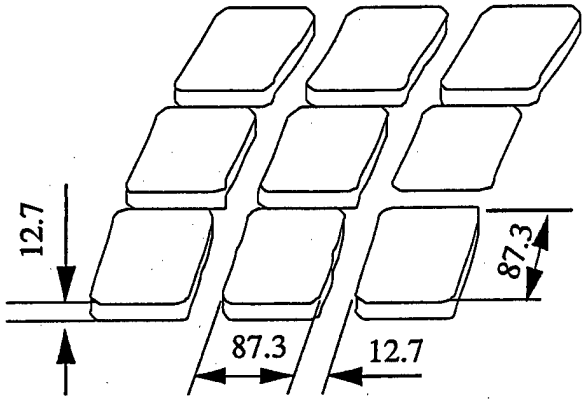


Fig. 4 Details of Maze for Category 1

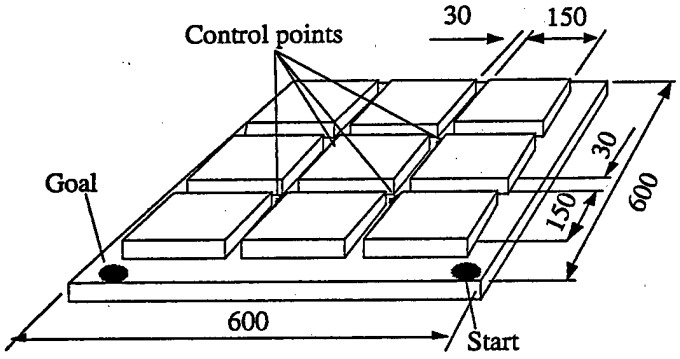


Fig. 5 Layout of Contest Ground for Category 2

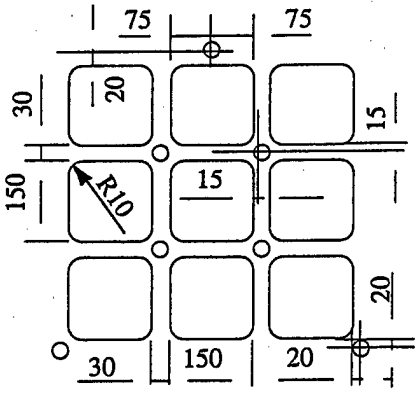


Fig. 6 Details of Maze for Category 2

We wish to thank the following for their contribution
to the success of this conference:

United States Air Force Asian Office of Aerospace Research and Development,
United States Army Research Office Far East,
United States Office on Naval Research International Field Office Asia.

Authors Index

F. Arai 71, 79, 207, 249
Y. Araki.....11
G. Caprari.....129
X. Ding.....227
T. L. Edwards.....19
W. Ehrfeld.....27
T. Estier.....129
V. Fascio.....179, 185
A. B. Frazier.....19
M. Freese 129
T. Fukuda.....71, 79, 135, 207, 243, 249
T. Furuta 267
B. K. Gale 19
Z. Gong.....153
V. Grosser.....193
S. Guo 135
J. Han 199
S. Hasegawa 99
T. Hashida.....227
H. Hashimoto.....35
I. Hayashi.....149
S. Hirano.....11
Y. Ichiminami.....113
T. Ikoma.....1
K. Ikuta 123, 173
T. Inaba.....261
H. Ishihara 243
Y. Ito.....11
K. Itoigawa.....71, 207, 249
N. Iwatsuki 149
T. Kadowaki 199
M. Kaelin.....129
Y. Kagawa.....149
P. Kallio.....79
T. Kaneko.....141
Y P Kathuria 169
K. Kato 11
T. Katoh 93
N. Kawahara.....141
A. Kawaji.....71
S. Kawakita.....141
A. Khoukhi 275
L. Khoukhi.....275
K. Kikuta 11
T. Kishita.....157
T. Kobayashi 157
Y. Kogure 65
T. Kohigashi 11
H. N. Koivo 79
R. Kondo.....221
S. Konishi 93
T. Koyanagi.....235
K. Kuribayashi 99, 227
H. Langen.....179, 185
J-M. Lehky.....129
L. Lian.....153
A. Maeda 71
S. Maruo.....173
H. Matsuura.....51
F. Michel 27
B. Michel.....193
N. Mitumoto 141
K. Morikawa.....149
T. Nakamura 65
K. Nakamura.....149
M. Nakano 51
N. Nishi 87, 93
H. Nishikawa.....141
M. Nokata 123
S. Ogasahara.....11

K. Oguro 135
I. Papautsky 19
L. Poom 71
X. Qin 153
H. Reichl 193
Y. Saito 43
M. Saitoh 11
W. Sakamoto 11
T. Sasaya 141
H. Sato 249
K. Sato 199
K. Sawa 215
Y. Sawaki 261
M. Schuenemann 193
K. Sekioka 261
T. Shibata 141
M. Shikida 199
K. Shimamura 65
M. Shimizu 267
M. Shimodaira 59
R. Siegwart 129
M. Sitti 35
K. Sugano 163
T. Sugiyama 71
S. Sugiyama 87, 93, 215, 221
L. Sun 153
P. Sun 153
K. Suzuki 11
K. Suzuki 107
K. Suzuki 221
O. Tabata 163
Y. Takeichi 11
S. Takimoto 221
Y. Tanimoto 215
M. Tokuda 107, 113, 157, 261
K. Tomiyama 267
A. Torii 59, 235
T. Toriyama 215
Y. Tsukahara 249
J. Tsuruno 207
K. Uchino 3
T. Ueda 99
A. Ueda 59, 235
H. Ueno 87, 93
H. Ukai 11
D. Viquerat 179, 185
R. Wüthrich 179, 185
K. Yagi 107, 113, 157, 261
H. Yamagishi 255
T. Yamaguchi 149
J. Yamaguchi 255
A. Yamamoto 261
T. Yogo 11
H. Yoshidome 107
T. Yoshikawa 113
Q. Zhou 79